

Lecture Notes in Mechanical Engineering

P. Pradeep Pratapa
G. Saravana Kumar
Palaniappan Ramu
R. K. Amit *Editors*


Advances in Multidisciplinary Analysis and Optimization

Proceedings of the 4th National
Conference on Multidisciplinary Analysis
and Optimization

 Springer

Lecture Notes in Mechanical Engineering

Editorial Board

Francisco Cavas-Martínez , Departamento de Estructuras, Construcción y Expresión Gráfica Universidad Politécnica de Cartagena, Cartagena, Murcia, Spain

Francesca di Mare, Institute of Energy Technology, Ruhr-Universität Bochum, Bochum, Nordrhein-Westfalen, Germany


Mohamed Haddar, National School of Engineers of Sfax (ENIS), Sfax, Tunisia

Young W. Kwon, Department of Manufacturing Engineering and Aerospace Engineering, Graduate School of Engineering and Applied Science, Monterey, CA, USA

Justyna Trojanowska, Poznan University of Technology, Poznan, Poland

Series Editors

Fakher Chaari, National School of Engineers, University of Sfax, Sfax, Tunisia

Francesco Gherardini , Dipartimento di Ingegneria “Enzo Ferrari”, Università di Modena e Reggio Emilia, Modena, Italy

Vitalii Ivanov, Department of Manufacturing Engineering, Machines and Tools, Sumy State University, Sumy, Ukraine

Lecture Notes in Mechanical Engineering (LNME) publishes the latest developments in Mechanical Engineering—quickly, informally and with high quality. Original research reported in proceedings and post-proceedings represents the core of LNME. Volumes published in LNME embrace all aspects, subfields and new challenges of mechanical engineering. Topics in the series include:

- Engineering Design
- Machinery and Machine Elements
- Mechanical Structures and Stress Analysis
- Automotive Engineering
- Engine Technology
- Aerospace Technology and Astronautics
- Nanotechnology and Microengineering
- Control, Robotics, Mechatronics
- MEMS
- Theoretical and Applied Mechanics
- Dynamical Systems, Control
- Fluid Mechanics
- Engineering Thermodynamics, Heat and Mass Transfer
- Manufacturing
- Precision Engineering, Instrumentation, Measurement
- Materials Engineering
- Tribology and Surface Technology

To submit a proposal or request further information, please contact the Springer Editor of your location:

China: Ms. Ella Zhang at ella.zhang@springer.com

India: Priya Vyas at priya.vyas@springer.com

Rest of Asia, Australia, New Zealand: Swati Meherishi at swati.meherishi@springer.com

All other countries: Dr. Leontina Di Cecco at Leontina.dicecco@springer.com

To submit a proposal for a monograph, please check our Springer Tracts in Mechanical Engineering at <https://link.springer.com/bookseries/11693> or contact Leontina.dicecco@springer.com

Indexed by SCOPUS. All books published in the series are submitted for consideration in Web of Science.

P. Pradeep Pratapa · G. Saravana Kumar ·
Palaniappan Ramu · R. K. Amit
Editors

Advances in Multidisciplinary Analysis and Optimization

Proceedings of the 4th National Conference
on Multidisciplinary Analysis
and Optimization

 Springer

Editors

P. Pradeep Pratapa
Department of Civil Engineering
Indian Institute of Technology Madras
Chennai, India

G. Saravana Kumar
Department of Engineering Design
Indian Institute of Technology Madras
Chennai, India

Palaniappan Ramu
Department of Engineering Design
Indian Institute of Technology Madras
Chennai, India

R. K. Amit
Department of Management Studies
Indian Institute of Technology Madras
Chennai, India

ISSN 2195-4356

ISSN 2195-4364 (electronic)

Lecture Notes in Mechanical Engineering

ISBN 978-981-19-3937-2

ISBN 978-981-19-3938-9 (eBook)

<https://doi.org/10.1007/978-981-19-3938-9>

© The Editor(s) (if applicable) and The Author(s), under exclusive license to Springer Nature Singapore Pte Ltd. 2023

This work is subject to copyright. All rights are solely and exclusively licensed by the Publisher, whether the whole or part of the material is concerned, specifically the rights of translation, reprinting, reuse of illustrations, recitation, broadcasting, reproduction on microfilms or in any other physical way, and transmission or information storage and retrieval, electronic adaptation, computer software, or by similar or dissimilar methodology now known or hereafter developed.

The use of general descriptive names, registered names, trademarks, service marks, etc. in this publication does not imply, even in the absence of a specific statement, that such names are exempt from the relevant protective laws and regulations and therefore free for general use.

The publisher, the authors, and the editors are safe to assume that the advice and information in this book are believed to be true and accurate at the date of publication. Neither the publisher nor the authors or the editors give a warranty, expressed or implied, with respect to the material contained herein or for any errors or omissions that may have been made. The publisher remains neutral with regard to jurisdictional claims in published maps and institutional affiliations.

This Springer imprint is published by the registered company Springer Nature Singapore Pte Ltd. The registered company address is: 152 Beach Road, #21-01/04 Gateway East, Singapore 189721, Singapore

Conference Committee

Patrons

Prof. Bhaskar Ramamurthi, Director, IIT Madras
Dr. Kota Harinarayana, Chairman, Design Division, AeSI

Advisory Committee

Prof. G. K. Ananthasuresh, IISc Bangalore
Prof. Chakravarthi Balaji, IIT Madras
Prof. Gengdong Cheng, Dalian University of Technology, China
Prof. Kalyanmoy Deb, Michigan State University, USA
Dr. Pankaj Priyadarshi, VSSC, ISRO
Prof. Raghunathan Rengaswamy, IIT Madras
Dr. Ravi Salagame, APTIV, India
Prof. Shankar Krishnapillai, IIT Madras
Prof. Sudhakar (Retd.), IIT Bombay
Mr. Vinay Ramanath, Siemens, India

Core Committee

Prof. Abdus Samad, IIT Madras (Sponsors)
Prof. R. K. Amit, IIT Madras (Papers)
Prof. Palaniappan Ramu, IIT Madras (General)
Prof. P. Pradeep Pratapa, IIT Madras (Papers)

Prof. Ramanathan, IIT Madras (Website)
Prof. Ratnakumar A, IIT Madras (Sponsors)
Prof. Saravana Kumar G, IIT Madras (General)
Prof. Sayan Gupta, IIT Madras (Speakers)
Prof. Sourav Rakshit, IIT Madras (Finance)

Preface

This book contains selected papers from the 4th National Conference on Multidisciplinary Design, Analysis and Optimization (NCMDAO-4) which was held at Chennai between October 7 and 9, 2021. The virtual conference was organized by the Department of Engineering Design, the Indian Institute of Technology Madras (IITM), in collaboration with the mechanical engineering department at the Indian Institute of Science, Bengaluru (IISc), and the Design Division of the Aeronautical Society of India (AeSI). This conference was the fourth in an annually planned event to create a platform for researchers in academia, government labs and industry professionals working in the areas of multidisciplinary design, analysis and optimization to share their current work.

Optimization is imperative in today's multidisciplinary R&D environment to push the envelope in design. Several domains such as aerospace, automotive, manufacturing and biomedical among others significantly benefit from optimization and gain a competitive edge. Advances in optimization theory, algorithms and the ecosystem for large computations have made it possible to improve the performance and economy of components, devices, processes and entire systems. Efficient analysis and design are possible even for those complex problems where analytical and computational models are not typically available. Design under uncertainty, emerging techniques that use machine learning and quantum computing to accelerate optimization are also pursued vigorously. The conference was organized with these goals in mind.

The response from various government laboratories, academic institutions and private companies was overwhelming with roughly 145 registered participants attending the two-day conference. Over 25% of the contributed papers were from the manufacturing and consulting industries, while the rest of them were from academic institutions and government research laboratories such as ISRO, ADA and NAL. Over the two days of the conference, about 79 papers were presented out of which over 71 full papers were contributed. These papers were peer-reviewed by the papers committee, and a total of 48 high-quality papers are included in this proceedings.

The conference was held over two days with a pre-conference masterclass. Masterclass included a talk and hand-on session on polynomial chaos expansions (PCE) and UQLab by Prof. Bruno Sudret and Ms. Nora Luthen, ETH Zürich. The second

masterclass was on graphs and physics-informed neural networks (PINN) for hybrid modeling and uncertainty quantification by Prof. Felipe A. C. Viana, University of Central Florida.

A student design competition on the optimal design of heat exchangers for solar still application was also conducted. The main conference included two keynotes, three invited talks, two impact talks and three sponsor presentations. The keynotes were delivered by Dr. William Baker of Skidmore, Owings and Merrill on Maxwell, Rankine, Airy and Modern Structural Engineering Design, and by Prof. Wei Chen of Northwestern University on Interdisciplinary Data-driven Design of Engineered Materials Systems. Invited talks were delivered by Dr. Arvind Kumar of Optym on using Optimization for Managing Electric Vehicle (EV) Loads on Power Grid, by Dr. S. A. Ilangoan from ISRO on Batteries for Space: Design and Challenges, and by Dr. N. R. Srinivasa Raghavan of Tarxya Limited on Industrial Applications of AI/ML/Optimization. Impact talks were delivered by Mr. Suresh Kumar of Pepul on Process Innovation in HR Policies—a Systems Perspective in Building a Million-dollar Company and by Mr. Ramasubramanian of VillageRES on Decentralising and Demystifying Renewable Energy Technologies for the Remote Rural Population.

The conference agenda was divided into six parallel sessions. Each session had roughly five papers. Each paper was scheduled based on a session theme. The following were the themes of the conference:

- S1T1 Data-Driven Decision/AI/ML
- S1T2 Aerodynamics/CFD
- S1T3 Aircraft Design 1
- S1T4 Space
- S2T1 Structures 1 and Space
- S2T2 3DP
- S2T3 Fluids 1
- S2T4 TO 1
- S3T1 Structures 2
- S3T2 UQ/Statistics 1
- S3T3 TO 2
- S3T4 Manufacturing 1
- S4T1 UQ/Statistics 2
- S4T2 Surrogates
- S4T3 Structures 3
- S4T4 MDO 1
- S5T1 Materials
- S5T2 TO 3
- S5T3 SC
- S5T4 MDO 2
- S6T1 Aircraft Design 2
- S6T2 Fluids 2
- S6T3 Structures 4
- S6T4 Manufacturing 2

The conference was sponsored by leading industries in the field of optimization such as AUTODESK, ANSYS and BETA simulation solutions besides strong support from SAEINDIA and Springer.

The papers included in this proceedings were selected based on a rigorous review considering the theme of the conference in mind. We hope that this collection of work would ignite further interest in this field in the country and elsewhere and will continue to be active for years to come with an increased contribution.

Chennai, India

Prof. P. Pradeep Pratapa
Prof. G. Saravana Kumar
Prof. Palaniappan Ramu
Prof. R. K. Amit

Acknowledgements

We thank Dr. Kota Harinarayana and Prof. K. Sudhakar for continued advice on MDAO-related activities in the country. We thank Prof. Bhaskar Ramamurthi, Director, IITM, for wholeheartedly supporting the event. We are grateful to our sponsors Ansys, Autodesk and Beta. We thank SAEINDIA for their partnership with us. On the logistics side, we thank the faculty members from across different departments at IITM who headed different verticals at the conference. We thank the several student volunteers for their commitment and dedication. In addition, we also thank the Center for Continuing Education, IIT Madras, for managing the funds. We thank the Department of Mechanical Engineering at the Indian Institute of Science, Bengaluru, and the Design Division of the Aeronautical Society of India for their support.

Contents

Optimization Applications: Aerospace

Optimization of Blunt Nose Semi-spherical Heat-Shield in Hypersonic Flow at Mach 7.99	3
Chandan Kumar and Akshay Prakash	
Automation of Launch Vehicle Telemetry—Requirement Capture to Analysis of Data	21
S. J. Anjana, P. Renjith, Kuntamukkala S. Manyam, J. Abey Rose, L. S. Syamlal, S. Praseetha, L. Jayalekshmi, C. Chandrasekharan, and Anna Priya Koshy	
Design Exploration of a Scramjet Inlet upto Three External Ramp	29
Kunal Garg, G. Vidya, M. M. Patil, and V. Ashok	
Supply Chain Optimization for Mainstreaming SAF in the Indian Aviation Sector	35
Arvind Ravi, Shirish Nanda Potu, Stephen Varghese, Valliappan Valliappan, and Vishwanath Doddamani	
Analysis of Direct Interplanetary Transfers Using Solar-Electric Propulsion	45
Suchismita Choudhury, Pooja Dutt, Deepak Negi, Abhay Kumar, and V. Ashok	
A Multi-fidelity Aeroelastic Optimization of an Aircraft Wing Using Co-Kriging	57
Partha Ajit Surve, Palaniappan Ramu, and Devendra Ghate	
Effect of Pulsed Fuel Injection on Scramjet Combustion Efficiency Using OpenFOAM	65
Singeetham Pranaykumar and Akshay Prakash	

Optimal Impulsive Maneuver Planning for Station Acquisition of Geosynchronous Satellites	73
M. R. Srivatsa and Gurpreet Singh	
Assessment of Nonlinear Optimization Algorithms on Weighted Least-Square-Based Method for Re-Entry Prediction	89
Pooja Dutt, Deepak Negi, Abhay Kumar, and V. Ashok	
Multidisciplinary Design Optimization (MDO) of a Typical Civil Aircraft Wing Using 3DEXPERIENCE Platform from Dassault Systemés	97
Bharath Kanaparthi, Emlin Vathsalan, Dayanidhi Panda, Ganesh Prasad, G. Umashankar, Srikrishna Srinivasa Chittur, Geetha Avula, Abhay Pashilkar, A. C. Pankaj, Devendra Singh, and Vijayakrishnan	
On-Off Control Scheme Using Reaction Control Thrusters for Pitch Stability During Atmospheric Abort of Crew Module	113
Swetha Sakunthala, Nikunj Gupta, Aprameyo Roy, and Kapil Kumar Sharma	
Sensitivity Analysis and Optimization for a Trainer Aircraft Configuration	123
M. B. Subrahmanya, V. K. Suman, K. N. Kaushik, S. Raghavendra Rao, and Gopinath L.	
Mathematical Modelling and Numerical Simulations of Underslung Dynamics	129
K. L. N. Sai Nitish, S. Kumanan, N. Remesh, and B. Karthik	
A Genetic Algorithm-Based Optimization of a Generic Winglet	139
V. K. Suman, Abhijith J. Patil, M. B. Subrahmanya, K. N. Kaushik, Sintu Singha, Raghavendra, Abhay Pashilkar, and V. R. Ramesh	
Optimization of Oil Cooler Duct Shape of a Generic Transport Aircraft Using Numeca	145
A. Shikhar Jaiswal, C. K. Niranjana, and T. N. Venkatesh	
External Aerodynamic Optimization of a 19-Seater Turboprop Aircraft During Preliminary Design Stage	151
C. K. Niranjana, A. Shikhar Jaiswal, Raghavendra, and T. N. Venkatesh	
Winglet Aerodynamic Optimization of a 19-Seater Turboprop Aircraft	157
C. K. Niranjana, C. Arshad Shameem, A. Shikhar Jaiswal, and T. N. Venkatesh	
Design and Position Sensitivity Analysis of Close-Coupled Canard for Naval Fighter Aircraft	165
Sathish Sunnam, C. Muthuraj, and S. Ragul	

Optimization Applications: Automobile

Seating System in Indian Public Transport 187
 Surya Chaurasiya and Tripti Singh

Strategic Optimization of Lubricant Base Oil Formulations and Supply Portfolio 199
 Senthil K. Vadivelu, G. R. Gauri Shanker, Sudarshan Kasthurirangan, and Ben Bosmans

Optimization of Lot Size in Lubricant Blending Plants 203
 G. R. Gauri Shanker, Ramya C. Sreeram, Michael Mortlock, and Danielle Zennemers

Optimization of Aluminum Extrusion Battery Side Rail for Crashworthiness 211
 Rajapandian Ramamoorthy, Sriram Seshadri, Gaurav R. Kanvinde, and Tejas Bhavsar

A Methodology for Multi-objective Design Optimization (MDO) of Automotive Transmission Systems 217
 Saurabh Sameer Kamat, Srinivas Gunti, Bonda Veerababu, and Shankar Venugopal

Numerical Investigation and Multi-objective Optimization of the Aerodynamics of a Hyperloop Pod 229
 Nivedan Vishwanath, Tushar Maloo, Prithvi Ramesh, and Dheeraj Agarwal

Molecular Dynamics of Carbon Capture from the Emissions of an IC Engine Using ZSM-5 237
 L. Deepak, A. Ganesh, R. S. Dit, S. H. Sreehari, V. Vinod, and G. P. Krishnamohan

Surrogate Modelling of the Retaining Ring Shrink Fit in a Turbogenerator 241
 Abhishek Sharma, Aditi Khandelwal, and Rishi Relan

A Methodology for Multi-objective Design Optimization (MDO) of Automotive Suspension System 253
 Lingadalu Ganesh, Srinivas Gunti, N. Balaramakrishna, and Shankar Venugopal

Optimization Applications: Materials and Structures

Optimization and Prediction of Transverse Shear Property of the Bioinspired Cell Core Using PSO and ANN 269
 Muthukumaran Gunasegeran and P. Edwin Sudhagar

Adaptable and Robust Origami Metamaterials with Controllable Poisson’s Ratio Over Large Deformations 285
Siva P. Vasudevan and P. Pradeep Pratapa

Design and Optimization of Bio-inspired Fluidic Diode for Wave Energy Harvesting System 293
Doddamani Hithaish and Abdus Samad

Prediction of the Propagation of Fatigue Cracks for a Beam Specimen in Four-Point Bending Using CASCA and FRANC2D 301
H. M. Vishwanatha, Pawan Kumar, Anshuman Das, Ashish Agrawal, Ch. Satheesh Kumar, and B. B. Verma

Topology Optimization

Topology Optimization of Vehicle Components for Nonlinear Load Cases 309
Rajapandian Ramamoorthy

Topology Optimization of a Coupled Aerothermoelastic System 319
Pankil N. Mishra and Abhijit Gogulapati

Topology Optimization for Designing a Wheel Rim 331
Pilla Sai Priyatham, Dheeraj Agarwal, and Amit Kumar Gupta

Topology Optimization with Orthotropic Material Model for Design-Dependent Loads 339
Rahul Ramachandran, Sourav Rakshit, and G. Saravana Kumar

Lattice Topology Optimization of Hip Bone Microstructure 353
S. Rajaraman and Sourav Rakshit

Optimization Applications: Manufacturing

Optimization of Fused Filament Fabrication for Maximum Stiffness Considering Anisotropy 367
Rahul Ramachandran and G. Saravana Kumar

Investigations on the Machining of Inconel X-750: Effect of Cutting Speed, Feed, Forces, Energy Consumption and MRR 377
Vishal Yashwant Bhise and Bhagwan F. Jogi

DMLS Support Structure Optimization Using Homogenized Model Distortion Prediction 391
A. Varun and G. Saravana Kumar

Design Optimization of Nd:YAG Laser Welded Inconel 718 Alloy Joints by Taguchi Method 399
P. Thejasree and P. C. Krishnamachary

General Applications of Optimization

A State Estimation, Kalman Filter Auto-tuning and Uncertainty Quantification Framework with Application to Industrial Storage Tank-farms 407
 Shirish Nanda Potu, Rihab Abdul Razak, and Senthil K. Vadivelu

3-D Spatio-Temporal Prediction of Atmospheric Quantities for Cn2 Modelling Using Machine Learning 415
 Suraj Subramanian and Rishav Kanth

To Evaluate the Performance of Cooling Tower Using Different Filters 421
 Rutuja Kapote, Kumar Vivek, and Ajit Dorwat

Extension of Particle Swarm Optimization Algorithm for Solving Priority-Based Time Minimization Transportation Problem 429
 Gurwinder Singh, Amarinder Singh, and Prabhjot Kaur

Parametric Modelling, Analysis and Design of Compact Diffuser for Heat Exchanger 437
 Kumud Mittal, G. Saravana Kumar, K. Arul Prakash, Sreenivas Jayanti, and S. Vengadesan

Thermal Frequency Stability Test for Multiple ICs 447
 Merlyn Kuriakose and A. N. Aryadevi

Synthesis and Fatigue Life Optimization of a Spring-Less Compliant Robot Leg Design 451
 Rohan Vijay Khatavkar and Ajay Pandit Bhattu

Differential Evolutionary (DE) Method for Strut Performance Design and Optimization Using Machine Learning-Based Meta-Models Prediction 461
 Balasubramanian Shanmugam, Arun Shanthkumar Bhaire, Sritharan Gopal, and Fan Li

Editors and Contributors

About the Editors



P. Pradeep Pratapa is an Assistant Professor in the Department of Civil Engineering at the Indian Institute of Technology (IIT) Madras. He obtained his Ph.D. from Georgia Tech, Atlanta, USA, and later worked with Prof. Glaucio H. Paulino as a postdoc where he was inspired by the ideas of origami engineering, metamaterials, and topology optimization. His current research focuses on exploring the use of optimization and origami principles in structural mechanics and engineering. His research interests also include the topics of lattice structures and 3D printing. His work has been published in highly reputed journals like *Physical Review Letters* and *Journal of the Mechanics and Physics of Solids*. Dr. Pratapa has a Bachelor's degree from IIT Madras and a Master's degree from The University of Texas at Austin, both in Civil Engineering.



G. Saravana Kumar is a Professor in the Department of Engineering Design at the Indian Institute of Technology (IIT) Madras. His research aims at development of representational and computational tools for virtual and physical prototyping applied to arrive at solutions to design problems. Some of the specific research areas include CAD, design optimization, and design for additive manufacturing. His current research focuses on exploring the capabilities of additive manufacturing to design novel structures for various applications including light weighting, compact heat exchangers, and orthopaedic implants. He has more than 100 publications in international journals and conferences. Dr. Saravana Kumar has a Bachelor's degree from the University of Madras and a Ph.D. from IIT Kanpur, both in Mechanical Engineering.



Palaniappan Ramu is an Associate Professor in the Department of Engineering Design at the Indian Institute of Technology (IIT) Madras. His research interests revolve around the treatment of uncertainties in design. His philosophy on the treatment of uncertainties is 'More out of less' - to obtain more information with limited experiments or computer simulations and how not to be fooled by randomness. With this focus, he works on diverse problems which are predominantly data driven. Application areas include automotive/space structures, wind turbines, and internet marketing.



R. K. Amit is currently a Professor in the Department of Management Studies, Indian Institute of Technology (IIT) Madras, Chennai, India. He completed his undergraduate studies at IIT Kanpur, and his doctoral studies at the Indian Institute of Science (IISc), Bangalore. His research and teaching interests are game theory and decision theory, and their applications in operations management. His research has been published in journals of national and international repute. He is currently working on numerous industry-sponsored research projects in the areas of electric mobility, emergency medical services, and airlines revenue management.

Contributors

Agarwal Dheeraj School of Engineering, University of Liverpool, Liverpool, England

Agrawal Ashish Department of Mechanical Engineering, Madhav Institute of Technology and Science, Gwalior, Madhya Pradesh, India

Anjana S. J. Vikram Sarabhai Space Centre (VSSC), Thiruvananthapuram, India

Arshad Shameem C. CSIR-National Aerospace Laboratories, Bangalore, India

Arul Prakash K. Department of Applied Mechanics, IIT Madras, Chennai, India

Aryadevi A. N. VSSC, Thiruvananthapuram, India

Ashok V. ADSG/AERO, Vikram Sarabhai Space Centre, ISRO, Thiruvananthapuram, India

Avula Geetha Dassault Systemés, Bengaluru, India

Balaramakrishna N. Mahindra & Mahindra Ltd., Chengalpattu, Tamil Nadu, India

Bhaire Arun Shanthkumar Tata Consultancy Services, Bangalore, India

Bhattu Ajay Pandit College of Engineering Pune, Pune, India

Bhavsar Tejas General Motors LLC, Detroit, USA

Bhise Vishal Yashwant Dr. Babasaheb Ambedkar Technological University, Lonere, India

Bosmans Ben Shell Lubricants Supply Company BV, Hague, The Netherlands

Chandrasekharan C. Vikram Sarabhai Space Centre (VSSC), Thiruvananthapuram, India

Chaurasiya Surya Design Discipline, Indian Institute of Information Technology Design and Manufacturing, Jabalpur, India

Chittur Srikrishna Srinivasa Dassault Systemés, Bengaluru, India

Choudhury Suchismita Vikram Sarabhai Space Centre, ISRO, Thiruvananthapuram, India

Das Anshuman Department of Mechanical Engineering, DIT University, Dehradun, India

Deepak L. Department of Mechanical Engineering, MBCET, Thiruvananthapuram, Kerala, India

Dit R. S. Department of Mechanical Engineering, MBCET, Thiruvananthapuram, Kerala, India

Doddamani Vishwanath Shell India Markets Pvt. Ltd., Bengaluru, India

- Dorwat Ajjit** Sinhgad College of Engineering, Pune, Maharashtra, India
- Dutt Pooja** Vikram Sarabhai Space Centre, ISRO, Thiruvananthapuram, India
- Edwin Sudhagar P.** School of Mechanical Engineering, Vellore Institute of Technology (VIT), Vellore, Tamil Nadu, India
- Ganesh A.** Department of Mechanical Engineering, MBCET, Thiruvananthapuram, Kerala, India
- Ganesh Lingadalu** Mahindra & Mahindra Ltd., Chengalpattu, Tamil Nadu, India
- Garg Kunal** ACMD/ADSG/AERO, VSSC, ISRO, Trivandrum, India
- Gauri Shanker G. R.** Shell India Markets Pvt. Ltd, Bangalore, India
- Ghate Devendra** Indian Institute of Space Science and Technology, Thiruvananthapuram, Kerala, India
- Gogulapati Abhijit** Department of Aerospace Engineering, Indian Institute of Technology Bombay, Mumbai, Maharashtra, India
- Gopal Sritharan** Tata Consultancy Services, Bangalore, India
- Gunasegeran Muthukumaran** School of Mechanical Engineering, Vellore Institute of Technology (VIT), Vellore, Tamil Nadu, India
- Gunti Srinivas** Mahindra & Mahindra Ltd., Chengalpattu, Tamil Nadu, India
- Gupta Amit Kumar** Department of Mechanical Engineering, BITS Pilani Hyderabad Campus, Secunderabad, Telangana, India
- Gupta Nikunj** Vikram Sarabhai Space Centre, Trivandrum, India
- Hithaish Doddamani** Department of Ocean Engineering, IIT Madras, Chennai, India
- Jayalekshmi L.** Vikram Sarabhai Space Centre (VSSC), Thiruvananthapuram, India
- Jayanti Sreenivas** Department of Chemical Engineering, IIT Madras, Chennai, India
- Jogi Bhagwan F.** Dr. Babasaheb Ambedkar Technological University, Lonere, India
- Kamat Saurabh Sameer** Vellore Institute of Technology, Vellore, Tamil Nadu, India
- Kanaparthi Bharath** Dassault Systemés, Bengaluru, India
- Kanth Rishav** Zeus Numerix Pvt. Ltd., Pune, India
- Kanvinde Gaurav R.** Tata Consultancy Services, Bangalore, India
- Kapote Rutuja** Sinhgad College of Engineering, Pune, Maharashtra, India

- Karthik B.** Vikram Sarabhai Space Centre, I.S.R.O, Trivandrum, India
- Kasthurirangan Sudarshan** Shell India Markets Pvt. Ltd., Bengaluru, India
- Kaur Prabhjot** University Institute of Engineering and Technology, Panjab University, Chandigarh, India
- Kaushik K. N.** CSIR -NAL, Bangalore, India
- Khandelwal Aditi** Department of Electrical Engineering, IIT Delhi, New Delhi, India
- Khatavkar Rohan Vijay** College of Engineering Pune, Pune, India
- Koshy Anna Priya** Vikram Sarabhai Space Centre (VSSC), Thiruvananthapuram, India
- Krishnamachary P. C.** JB Institute of Engineering and Technology, Hyderabad, India
- Krishnamohan G. P.** Department of Science and Humanities, MBCET, Thiruvananthapuram, Kerala, India
- Kumanan S.** Vikram Sarabhai Space Centre, I.S.R.O, Trivandrum, India
- Kumar Abhay** Vikram Sarabhai Space Centre, ISRO, Thiruvananthapuram, India
- Kumar Chandan** Indian Institute of Technology, Kharagpur, India
- Kumar Pawan** Department of Engineering Metallurgy, Faculty of Engineering and the Built Environment, University of Johannesburg, Johannesburg, South Africa
- Kuriakose Merlyn** VSSC, Thiruvananthapuram, India
- L. Gopinath** CSIR -NAL, Bangalore, India
- Li Fan** General Motors LLC, Detroit, USA
- Maloo Tushar** Department of Mechanical Engineering, BITS Pilani, K K Birla Goa Campus, Goa, India
- Manyam Kuntamukkala S.** Vikram Sarabhai Space Centre (VSSC), Thiruvananthapuram, India
- Mishra Pankil N.** Department of Aerospace Engineering, Indian Institute of Technology Bombay, Mumbai, Maharashtra, India
- Mittal Kumud** Department of Engineering Design, IIT Madras, Chennai, India
- Mortlock Michael** Shell Eastern Trading Pvt. Ltd., Singapore, Singapore
- Muthuraj C.** Aeronautical Development Agency, Bangalore, India
- Negi Deepak** Vikram Sarabhai Space Centre, ISRO, Thiruvananthapuram, India
- Niranjanan C. K.** CSIR-National Aerospace Laboratories, Bangalore, India

- Panda Dayanidhi** Dassault Systemés, Bengaluru, India
- Pankaj A. C.** CSIR-NAL, Bengaluru, India
- Pashilkar Abhay** CSIR-NAL, Bengaluru, India
- Patil Abhijith J.** CSIR-NAL, Bangalore, India
- Patil M. M.** AD SG/AERO, VSSC, ISRO, Trivandrum, India
- Potu Shirish Nanda** Shell India Markets Pvt. Ltd., Bengaluru, India
- Prakash Akshay** Indian Institute of Technology, Kharagpur, India
- Pranaykumar Singeetham** Indian Institute of Technology, Kharagpur, India
- Prasad Ganesh** Dassault Systemés, Bengaluru, India
- Praseetha S.** Vikram Sarabhai Space Centre (VSSC), Thiruvananthapuram, India
- Pradeep Pratapa P.** Indian Institute of Technology Madras, Chennai, India
- Priyatham Pilla Sai** Department of Mechanical Engineering, BITS Pilani Hyderabad Campus, Secunderabad, Telangana, India
- Raghavendra Rao S.** CSIR -NAL, Bangalore, India
- Raghavendra** CSIR-National Aerospace Laboratories, Bangalore, India
- Ragul S.** Aeronautical Development Agency, Bangalore, India
- Rajaraman S.** Department of Mechanical Engineering, Machine Design Section, Indian Institute of Technology Madras, Chennai, Tamil Nadu, India
- Rakshit Sourav** Department of Mechanical Engineering, Machine Design Section, Indian Institute of Technology Madras, Chennai, Tamil Nadu, India
- Ramachandran Rahul** Department of Engineering Design, Indian Institute of Technology Madras, Chennai, India
- Ramamoorthy Rajapandian** Tata Consultancy Services, Bangalore, India
- Ramesh Prithvi** Department of Mechanical Engineering, BITS Pilani, K K Birla Goa Campus, Goa, India
- Ramesh V. R.** CSIR-NAL, Bangalore, India
- Ramu Palaniappan** Indian Institute of Technology Madras, Chennai, Tamil Nadu, India
- Ravi Arvind** Shell India Markets Pvt. Ltd., Bengaluru, India
- Razak Rihab Abdul** Shell India Markets Pvt. Ltd., Bengaluru, India
- Relan Rishi** Generator R&D, Siemens Limited, Gurgaon, India
- Remesh N.** Vikram Sarabhai Space Centre, I.S.R.O, Trivandrum, India

- Renjith P.** Vikram Sarabhai Space Centre (VSSC), Thiruvananthapuram, India
- Rose J. Abey** Vikram Sarabhai Space Centre (VSSC), Thiruvananthapuram, India
- Roy Aprameyo** Vikram Sarabhai Space Centre, Trivandrum, India
- Sai Nitish K. L. N.** Vikram Sarabhai Space Centre, I.S.R.O, Trivandrum, India
- Sakunthala Swetha** Vikram Sarabhai Space Centre, Trivandrum, India
- Samad Abdus** Department of Ocean Engineering, IIT Madras, Chennai, India
- Saravana Kumar G.** Department of Engineering Design, IIT Madras, Chennai, India
- Satheesh Kumar Ch.** Department of Mechanical Engineering, Madanapalle Institute of Technology & Science, Madanapalle, Andhra Pradesh, India
- Seshadri Sriram** Tata Consultancy Services, Bangalore, India
- Shanmugam Balasubramanian** Tata Consultancy Services, Bangalore, India
- Sharma Abhishek** Generator R&D, Siemens Limited, Gurgaon, India
- Sharma Kapil Kumar** Vikram Sarabhai Space Centre, Trivandrum, India
- Shikhar Jaiswal A.** CSIR-National Aerospace Laboratories, Bangalore, India
- Singha Sintu** CSIR-NAL, Bangalore, India
- Singh Devendra** CSIR-NAL, Bengaluru, India
- Singh Gurpreet** Flight Dynamics Group, UR Rao Satellite Center, Bengaluru, India
- Singh Gurwinder** Chandigarh University, Gharuan, Mohali, Punjab, India
- Singh Tripti** Design Discipline, Indian Institute of Information Technology Design and Manufacturing, Jabalpur, India
- Singh Amarinder** Chitkara University Institute of Engineering and Technology, Chitkara University, Rajpura, Punjab, India
- Sreehari S. H.** Department of Mechanical Engineering, MBCET, Thiruvananthapuram, Kerala, India
- Sreeram Ramya C.** Shell India Markets Pvt. Ltd, Bangalore, India
- Srivatsa M. R.** Flight Dynamics Group, UR Rao Satellite Center, Bengaluru, India
- Subrahmanya M. B.** CSIR-NAL, Bangalore, India
- Subramanian Suraj** Zeus Numerix Pvt. Ltd., Pune, India
- Suman V. K.** CSIR-NAL, Bangalore, India
- Sunnam Sathish** Aeronautical Development Agency, Bangalore, India

- Surve Partha Ajit** Vikram Sarabhai Space Centre, Thiruvananthapuram, Kerala, India
- Syاملal L. S.** Vikram Sarabhai Space Centre (VSSC), Thiruvananthapuram, India
- Thejasree P.** Sree Vidyanikethan Engineering College, Tirupati, India
- Umashankar G.** Dassault Systemés, Bengaluru, India
- Vadivelu Senthil K.** Shell India Markets Pvt. Ltd., Bengaluru, India
- Valliappan Valliappan** Shell India Markets Pvt. Ltd., Bengaluru, India
- Varghese Stephen** Shell India Markets Pvt. Ltd., Bengaluru, India
- Varun A.** Department of Aerospace Design, Honeywell, Bangalore, India
- Vasudevan Siva P.** Indian Institute of Technology Madras, Chennai, India
- Vathsalan Emlin** Dassault Systemés, Bengaluru, India
- Veerababu Bonda** Mahindra & Mahindra Ltd., Chengalpattu, Tamil Nadu, India
- Vengadesan S.** Department of Applied Mechanics, IIT Madras, Chennai, India
- Venkatesh T. N.** CSIR-National Aerospace Laboratories, Bangalore, India
- Venugopal Shankar** Mahindra & Mahindra Ltd., Chengalpattu, Tamil Nadu, India
- Verma B. B.** Department of Metallurgical and Materials Engineering, National Institute of Technology Rourkela, Rourkela, India
- Vidya G.** ACMD/ADSG/AERO, VSSC, ISRO, Trivandrum, India
- Vijaykrishnan** CSIR-NAL, Bengaluru, India
- Vinod V.** Department of Mechanical Engineering, MBCET, Thiruvananthapuram, Kerala, India
- Vishwanatha H. M.** Department of Mechanical and Manufacturing Engineering, Manipal Institute of Technology Manipal, Manipal Academy of Higher Education, Manipal, Karnataka, India
- Vishwanath Nivedan** Department of Mechanical Engineering, BITS Pilani, Hyderabad Campus, Hyderabad, India
- Vivek Kumar** Sinhgad College of Engineering, Pune, Maharashtra, India
- Zennemers Danielle** Société des Pétroles Shell, Paris, France

Optimization Applications: Aerospace

Optimization of Blunt Nose Semi-spherical Heat-Shield in Hypersonic Flow at Mach 7.99



Chandan Kumar and Akshay Prakash

1 Introduction

A flow is stated as hypersonic flow if its Mach number is five or above. Such flows are generally encountered during atmospheric entry or in the case of hypersonic missiles. There is intense shear and thermal loads to the surface at such a high speed. In order to protect the vehicle from this extreme heat, Thermal Protection System (TPS) is used. There are different ways to protect the vehicle thermally, commonly using a heat-shield or active and passive cooling. It is not possible to employ the active and passive cooling system due to limited energy resources and geometrical constraints at hypersonic speed [1]. Hence, the only way left to dissipate the extreme thermal energy on the surface of the vehicles is to use a heat-shield. In general, heat-shields are made up of ablative or non-ablative materials [2]. Ablative materials work by ablation; that is, part of it melts, vaporizes, and breaks off to carry away heat harmlessly, as illustrated by Niehaus [2]. In contrast, non-ablative materials undergo pure conduction till failure or deformation in some cases prior to failure depending on the materials' properties. Curry [3] performed the thermal analysis of a one-dimensional ablative heat-shield with the backup structures at the inner cabin. The backup structures were considered to be made up of non-ablative materials. The time-dependent heat flux was applied as a boundary condition at the outer surface of the heat-shield rather than using any fluid solver to compute the heat flux. Balakrishnan et al. [4] presented a detailed analysis of the heat-shield of Galileo probe, which was designed to study the Jovian atmosphere. The heat-shield was made up of carbon-phenolic. The forebody, except the nose, was divided into frustums. At an off-stagnation location, peak heating was observed near a reattachment point. The final mass of the heat-shield was reduced by 89 kg. The forebody contributed 90% to the reduction in the final mass, while the aft section of the heat-shield con-

C. Kumar (✉) · A. Prakash
Indian Institute of Technology, Kharagpur, India
e-mail: chandankr@iitkgp.ac.in

© The Author(s), under exclusive license to Springer Nature Singapore Pte Ltd. 2023
P. Pradeep Pratapa et al. (eds.), *Advances in Multidisciplinary Analysis and Optimization*,
Lecture Notes in Mechanical Engineering,
https://doi.org/10.1007/978-981-19-3938-9_1

tributed 10%. Mazzaracchio and Marchetti [5] performed the thermal analysis of a one-dimensional ablative heat-shield. The uncertainty and sensitivity analysis was performed to estimate the probability of maintaining the specified temperature of the underlying material. Three different cases with different materials and missions were considered: Stardust return capsule, Mars rover capsule, and aerocapture mission for Neptune. Their study showed 17% reduction in the overall weight of the TPS when the input uncertainty values were halved. In 2013, Ewing et al. [6] developed a numerical tool for 1D ablation problem based on a control volume approach with the variable grid to include the effect of surface movement. Other non-traditional complexities were considered, such as material swelling and mechanical erosion (spallation). It was claimed that their approach provides stable results even in case of extreme heat flux and ablation conditions, unlike the CMA (Charring Material Ablation) program [7] which suffers solution instabilities and fails to converge due to grid refinement issues. A combined computational and experimental study of an ablative heat-shield was conducted on a scaled model of NASA's Orion Multi-Purpose Crew Vehicle by Combs et al. [8] in 2017. The ablative heat-shield was made up of naphthalene, and the study was mainly focused on the visualization of ablation products using laser-induced fluorescence technique. The visualization process showed that the boundary layer carried the ablating naphthalene product into the different regions: over the capsule shoulder, separated shear layer, and back-shell re-circulation zone. It was found that the separated flow region has a higher naphthalene concentration than any other location.

The ablative heat-shield undergoes pyrolysis when subjected to the thermal loads, and as a result, gaseous products release through its surface into the boundary layer. The outgoing gaseous products affect the boundary-layer profile and incoming heat fluxes through the surface. The properties of the ablative materials are largely experiment-dependent. Due to lack of access to such experimental facilities and experimental data, which generally falls under classified research, a non-ablative heat-shield is considered, which works by pure conduction. The objective of the present work is to perform a thermal analysis of a blunt nose semi-spherical non-ablative heat-shield coupled with a hypersonic fluid flow solver. The thermal load at the surface is computed using the fluid solver, which uses a shock-fitting technique to solve the hypersonic flow-field. Based on the inner cabin temperature predicted within the specified limit by the solid solver, the thickness of the heat-shield is optimized using the Newton-Raphson method at different locations in the body curvature direction and hence reduces its overall weight.

2 Mathematical Formulation

The governing equation for a perfect gas, laminar flow, is given by the Navier-Stokes equation in vector form as

$$\frac{\partial U}{\partial t} + \frac{\partial F_j}{\partial x_j} + \frac{\partial G_j}{\partial x_j} = 0 \quad (1)$$

$$U = \begin{bmatrix} \rho \\ \rho u_1 \\ \rho u_2 \\ \rho u_3 \\ E \end{bmatrix} \quad F_j = \begin{bmatrix} \rho u_j \\ \rho u_1 u_j + p \delta_{1j} \\ \rho u_2 u_j + p \delta_{2j} \\ \rho u_3 u_j + p \delta_{3j} \\ (E + p)u_j \end{bmatrix} \quad G_j = \begin{bmatrix} 0 \\ \tau_{j1} \\ \tau_{j2} \\ \tau_{j3} \\ \tau_{ji}u_j + k \frac{\partial T}{\partial x_j} \end{bmatrix} \quad (2)$$

$$\tau_{ij} = \mu \left(\frac{\partial u_i}{\partial x_j} + \frac{\partial u_j}{\partial x_i} \right) - \frac{2}{3} \mu \frac{\partial u_k}{\partial x_k} \delta_{ij} \quad (3)$$

where U is a conservative variable vector. The flux vector is symbolically broken into inviscid and viscous flux denoted by F_j and G_j , respectively. The subscript j represents a direction and has the value $j = 1, 2, 3$ which corresponds to the x , y , and z directions, respectively. The equation of state for a perfect gas is used to relate the pressure and temperature. In U , F , and G vectors, the first row represents continuity equation, the next three rows represent momentum equation, and the last row represents energy equation. The total energy E in the last row is given by

$$E = \rho \left(C_v T + \frac{1}{2} \sum_i u_i u_i \right) \quad (4)$$

The unsteady Navier-Stokes equations are solved in the region between shock and the semi-spherical blunt body (shock-fitting technique) and solved numerically. The convective terms are collected as inviscid terms and solved using the flux-splitting method [9], while the diffusion terms are collected as viscous terms and solved using a high-order central difference scheme [9]. The governing equations are transformed into the body-fitted curvilinear coordinates (ξ, η, ζ) as

$$\begin{cases} \xi = \xi(x, y, z) \\ \eta = \eta(x, y, z, t) \\ \zeta = \zeta(x, y, z) \\ \tau = t \end{cases} \iff \begin{cases} x = x(\xi, \eta, \zeta, \tau) \\ y = y(\xi, \eta, \zeta, \tau) \\ z = z(\xi, \eta, \zeta, \tau) \\ t = \tau \end{cases} \quad (5)$$

$$\frac{1}{J} \frac{\partial U}{\partial \tau} + \left(\frac{\partial E'}{\partial \xi} + \frac{\partial F'}{\partial \eta} + \frac{\partial G'}{\partial \zeta} \right) + \left(\frac{\partial E'_v}{\partial \xi} + \frac{\partial F'_v}{\partial \eta} + \frac{\partial G'_v}{\partial \zeta} \right) + U \frac{\partial \frac{1}{J}}{\partial \tau} = 0 \quad (6)$$

where

$$E' = \frac{F_1 \xi_x + F_2 \xi_y + F_3 \xi_z}{J} \quad (7)$$

$$F' = \frac{F_1 \eta_x + F_2 \eta_y + F_3 \eta_z}{J} \quad (8)$$

$$G' = \frac{F_1 \zeta_x + F_2 \zeta_y + F_3 \zeta_z}{J} \quad (9)$$

$$E'_v = \frac{G_1 \xi_x + G_2 \xi_y + G_3 \xi_z}{J} \quad (10)$$

$$F'_v = \frac{G_1 \eta_x + G_2 \eta_y + G_3 \eta_z}{J} \quad (11)$$

$$G'_v = \frac{G_1 \zeta_x + G_2 \zeta_y + G_3 \zeta_z}{J} \quad (12)$$

The superscript $'$ represents the transformed fluxes. J is a Jacobian of the transformation. F and G with subscript 1, 2, and 3 are inviscid and viscous fluxes in x , y , and z direction, respectively. E' , F' , and G' are the transformed fluxes in ξ , η , and ζ direction, respectively, and their corresponding viscous part is represented by subscript v . τ is the transformed time and should not be confused with viscous dissipation τ_{ij} in Eq. (2). The inviscid fluxes are split into two terms based on positive and negative eigenvalue as follow

$$\begin{aligned} F' &= F'_+ + F'_- \\ F'_\pm &= \frac{1}{2} (F' \pm \Lambda U) \\ A &= R \Lambda L \end{aligned} \quad (13)$$

R and L consist of right and left eigenvector arranged column-wise, respectively. Λ is a diagonal matrix holding eigenvalues as its diagonal. The spatial discretization of the flux derivative is given as

$$\frac{\partial F'}{\partial \eta} = \frac{\partial F'_+}{\partial \eta} + \frac{\partial F'_-}{\partial \eta} \quad (14)$$

The flux corresponding to positive eigenvalue is discretized using an upwind scheme, whereas the flux corresponding to negative eigenvalue is discretized using a downwind scheme. A fifth-order explicit scheme [9] is used for the discretization given as

$$u'_i = \sum_{k=-3}^3 \tilde{\alpha}_{i+k} u_{i+k} - \frac{\tilde{\alpha}}{6! b_i} \left(\frac{\partial u^6}{\partial \eta^6} \right)_i + \dots \quad (15)$$

This scheme has an adjustable parameter $\tilde{\alpha}$ which makes it upwind, downwind, or central. The scheme is upwind when $\tilde{\alpha} < 0$ and downwind when $\tilde{\alpha} > 0$. When $\tilde{\alpha}$ is zero, it becomes sixth-order central difference scheme. The dissipative nature of scheme is controlled by $\tilde{\alpha}$, and it is less dissipative when $\tilde{\alpha}$ closer to zero. In the present shock-fitting formulation, shock is located at

$$\eta(x, y, z, t) = \eta_{\max} = \text{constant}$$

and treated as a computational boundary. The grid points at η_{\max} are assumed to be immediately downstream of the shock. The condition behind the shock is calculated using Rankine-Hugoniot equation [9] given as

$$(\mathbf{F}_s - \mathbf{F}_\infty) \cdot l_s + (U_s - U_\infty) l_t = 0 \quad (16)$$

where,

$$\begin{aligned} \mathbf{F} &= F_1 \hat{i} + F_2 \hat{j} + F_3 \hat{k} \\ l_s &= \frac{\eta_x}{J} \hat{i} + \frac{\eta_y}{J} \hat{j} + \frac{\eta_z}{J} \hat{k} \\ l_t &= \frac{\eta_t}{J} \end{aligned}$$

The subscripts ∞ and s represent the variables ahead and behind of the shock, respectively. \mathbf{F} and U are flux and conservative variables vectors. l_s and l_t are the unit normal vectors to the shock for space and time, respectively. The above equation requires shock velocity which is computed using compatibility relation immediately behind the shock. The compatibility relation [9] is obtained by taking a derivative of Rankine-Hugoniot equation with respect to the computational time given as

$$\begin{aligned} (\mathbf{A}_s \cdot l_s) \frac{\partial U_s}{\partial \tau} - (\mathbf{A}_\infty \cdot l_s) \frac{\partial U_\infty}{\partial \tau} + (\mathbf{F}_s - \mathbf{F}_\infty) \cdot \frac{\partial l_s}{\partial \tau} \\ + \left(\frac{\partial U_s}{\partial \tau} - \frac{\partial U_\infty}{\partial \tau} \right) \cdot \frac{\partial l_t}{\partial \tau} \\ + (U_s - U_\infty) \cdot \frac{\partial l_t}{\partial \tau} = 0 \end{aligned} \quad (17)$$

where A is the flux Jacobean. Readers are advised to go through Zhong's work [9] for further details on shock-fitting formulation. The convective heat flux at the surface is computed using the temperature difference between solid and adjacent fluid as

$$q = h(T_f - T_s) \quad (18)$$

h is the convective heat transfer coefficient which is computed using a relation for Nusselt number as

$$Nu = \frac{hL}{K} = 0.332 \text{Pr}^{0.5} \text{Re}_x^{0.5} \quad (19)$$

$$\text{Pr} = \frac{\mu C_p}{K} \quad (20)$$

The distance between solid and adjacent fluid node is considered as the representative length L . The fluid viscosity (μ) is computed using Sutherland's law given by

$$\mu = \begin{cases} (1.458 \times T^{1.5}) / (T + 110.4) \times 10^{-5} & T > 110.4 \text{ K} \\ (0.693873 \times 10^{-6}) \times T & T < 110.4 \text{ K} \end{cases} \quad (21)$$

K is the thermal conductivity of the fluid and related to the viscosity via Prandtl number. The non-ablative heat-shield undergoes pure conduction. Hence, the thermal analysis is done using transient heat equation given as

$$\frac{\partial U}{\partial t} + \alpha \frac{\partial F_j}{\partial X_j} = 0 \quad (22)$$

$$U = [T] \quad F_j = \left[\frac{\partial T}{\partial X_j} \right] \quad (23)$$

where α is thermal diffusivity of the material under consideration. A transformation similar to the fluid solver is applied to the above unsteady heat equation to solve it on the curvilinear grid. A second-order central difference scheme is used to compute the derivative at the grid points next to the boundaries and a fourth-order central difference schemes [10] at the inner grid points.

3 Problem Description

3.1 Flow Conditions

The present numerical study is performed on a blunt nose semi-spherical heat-shield. The flow conditions for the test case [11] are as follows:

$$M_\infty = 7.99, \quad Re = \rho_\infty U_\infty r_n / \mu_\infty = 33449$$

$$\text{Freestream total pressure : } P_o = 4 \times 10^6 \text{ N/m}^2$$

$$\text{Freestream total temperature : } T_o = 750 \text{ K}$$

$$\text{Gas properties : } R = 287 \text{ J/kg.K, } \gamma = 1.4, \quad Pr = 0.72$$

$$\text{Freestream unit Reynolds number : } Re_u = 8.78 \times 10^{-6} \text{ m}^{-1}$$

$$\text{Material thermal diffusivity : } \alpha = 10^{-7} \text{ m}^2/\text{s}$$

$$\text{Heat-shield initial temperature : } T_{i=0} = 288 \text{ K}$$

$$\text{Spherical nose radius : Outer wall radius, } r_o = 3.81 \times 10^{-3} \text{ m}$$

$$\text{Inner wall radius, } r_i = 3.06 \times 10^{-3} \text{ m}$$

3.2 Computational Domain and Boundary Conditions

The computational domain is shown in Fig. 1a. The mesh specifications are as follows:

Mesh specifications:

$$\text{Fluid domain: } \xi \times \eta \times \zeta - 102 \times 120 \times 2$$

$$\text{Solid domain: } \xi \times \eta \times \zeta - 102 \times 50 \times 2$$

Figure 1a shows the computational domain for both the fluid and solid. The major part of the fluid domain is surrounded by the shock and the solid surface. The boundary conditions behind the shock are computed using the Rankine-Hugoniot equation. The symmetry boundary condition is applied along the stagnation line, whereas the variables are extrapolated from the inner grid point at the exit of the flow domain. The heat flux is computed at the solid-fluid interface for each node in the streamwise direction using the temperature difference. This computed heat flux is used as a boundary condition for thermal analysis in the solid. The inner wall boundary condition is set to adiabatic rather than a fixed temperature to monitor the temperature rise in the inner cabin. A fixed temperature boundary condition at the inner wall will work as a heat sink. Along the stagnation line in the solid domain, a symmetry boundary condition is used. The grid stretching is applied along streamwise (ξ) and wall-normal (η) direction in order to solve the flow-field effectively near the boundary and the front portion of the nose where the shock is almost normal. The flow is assumed to be axis-symmetry in the third direction (ζ). The grid stretching similar to the fluid domain is applied to the solid domain in the streamwise direction (ξ) to ensure that the grid points match at the solid-fluid interface. Figure 1b shows a zoomed view of the interface. The solid domain has uniform grid distribution in the

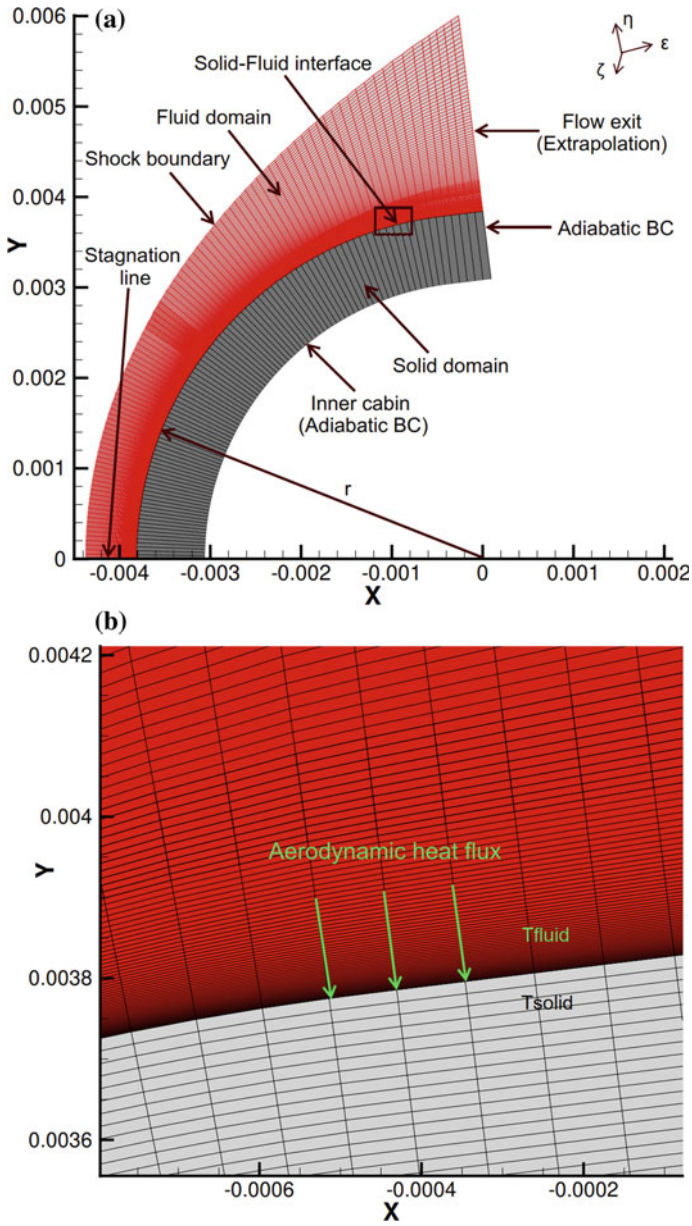


Fig. 1 a Computational domain and b solid-fluid interface

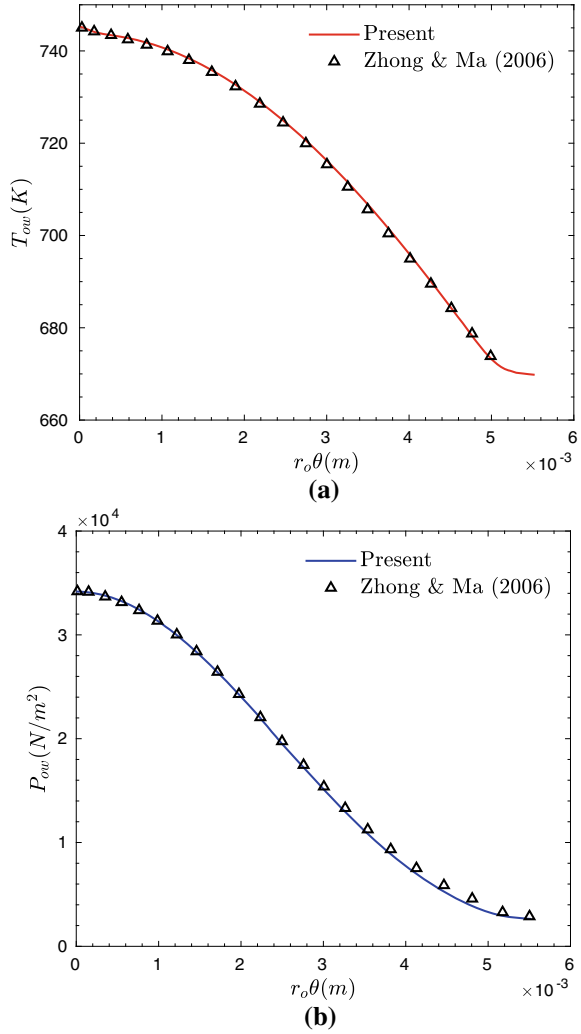
wall-normal direction (η), whereas the fluid domain has grid stretching with more grid points lying toward the solid-fluid interface. The grid points for solid and fluid match at the interface in the streamwise direction (ξ). The heat flux at the interface is computed using a temperature difference between two adjacent nodes to the interface.

4 Result and Discussion

Hypersonic fluid flow over blunt cone is solved using a high-order shock-fitting in-house fluid solver. Figure 2a, b shows temperature (T_{ow}) and pressure (P_{ow}) distribution on the outer wall predicted using fluid solver when solution has reached steady state. The present study is in good agreement with the published data in the literature [11]. The x-axis shows the distance along the curvature of the outer wall in ξ -direction. θ is an angle made by the radial vector with the negative x-axis (see Fig. 1a) and extends from 0° to 83° . The result is quite obvious and as expected. The shock is almost normal near the nose, and the shock angle decreases as we move downstream in ξ -direction. Hence, the higher temperature and pressure are observed at the nose and reduce downstream. Figure 3 shows the variation of streamwise velocity, temperature, and density along the stagnation line which extends from the surface to shock. $\eta = 0$ represents the surface. The streamwise velocity is zero, whereas temperature and density become maximum at the surface. Figure 4 shows the boundary-layer profile for streamwise velocity, temperature, and density at flow exit. Two planes are considered to visualize the flow-field in $\eta - \zeta$ space. The orientation of planes is shown in Fig. 5. Height (η) of the planes is normalized with their respective η_{max} , whereas width (ζ) is normalized with the twice of ζ_{max} . Plane 1 is located at a radial angle of $\theta = 27.6^\circ$ which is at around one-third of the total distance in ξ -direction from the nose, whereas plane 2 is at flow exit. Figure 6 shows the flow-field at both the planes. The shock angle is higher at plane 1 than plane 2. This creates lower streamwise velocity, higher temperature, higher pressure, and higher density behind the shock ($\eta/\eta_{max} = 1$) at plane 1 than plane 2.

Initially, heat flux at the surface (outer wall) is computed using the temperature difference between fluid and solid node adjacent to the interface with Eq. (18). This computed heat flux works as a boundary condition to the outer wall. As the heat propagates in the solid, the temperature at the solid node adjacent to the interface changes. Hence, the incoming heat flux at the outer wall changes with time. Figure 7 depicts the temperature contour at different time instants. The boundary edge of the solid domain is shown (black line) to identify the solid-fluid interface. The initial temperature for the heat-shield is set uniform at 288 K. The fluid solver generates higher temperature at the nose. Hence, there is higher heat flux at the nose than compared to any other location downstream. As time increases, the heat from the

Fig. 2 Flow-field at the outer wall in the streamwise direction ξ : **a** temperature and **b** pressure



outer wall propagates toward the inner wall and raises the inner wall temperature. It is observed that the temperature rise on the inner wall at the nose is higher than any other location downstream. This is due to higher heat flux at the nose. Figure 8 shows the inner wall temperature distribution at different time intervals. The temperature on the inner wall starts rising from the nose.

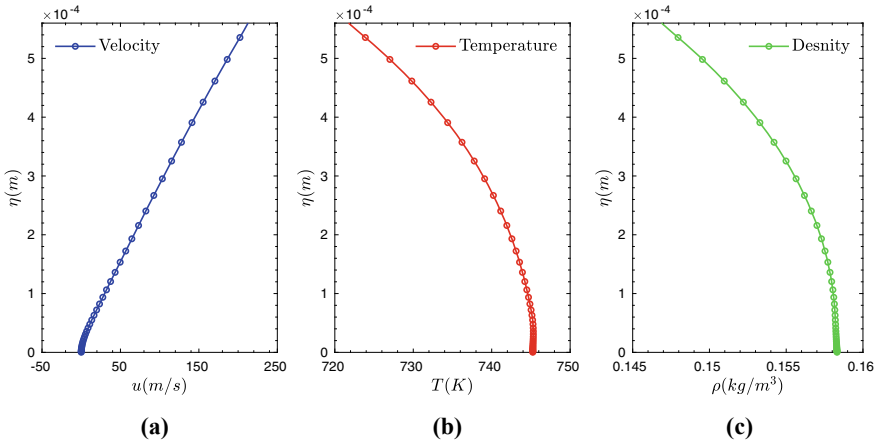


Fig. 3 Flow-field along the stagnation line: **a** streamwise velocity, **b** temperature, and **c** density. Note $\eta = 0$ represents the cone surface

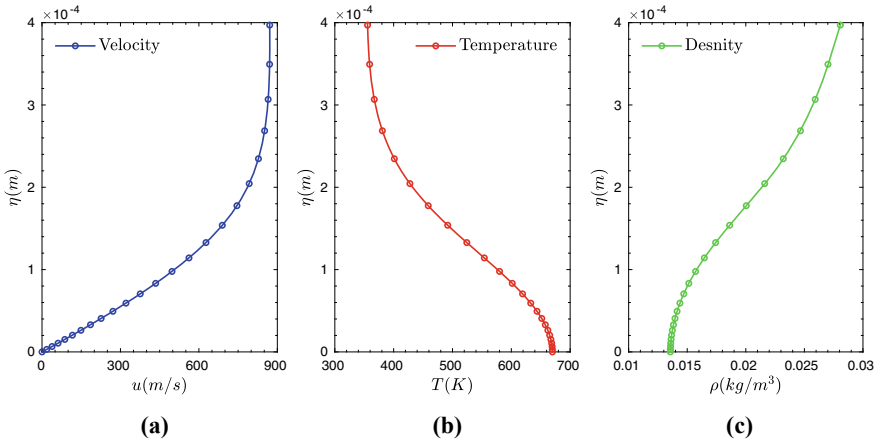


Fig. 4 Boundary-layer profile at flow exit: **a** streamwise velocity, **b** temperature, and **c** density

For an early time, it is observed that the temperature rises at the nose first, while the temperature at other downstream locations remains constant. But as the time increases, the temperature rises at all the downstream locations. The optimization of the heat-shield thickness is done based on the inner wall temperature prediction under the bearable limit. The bearable temperature limit is set at 318 K (45 °C). The temperature is measured at each and every node of the inner wall at every time step. If the temperature is less than 318 K, we keep marching forward in time. Once the temperature at any node of the inner wall achieves 318 K, the thickness optimization process starts. The flowchart for the process is shown in Fig. 11.

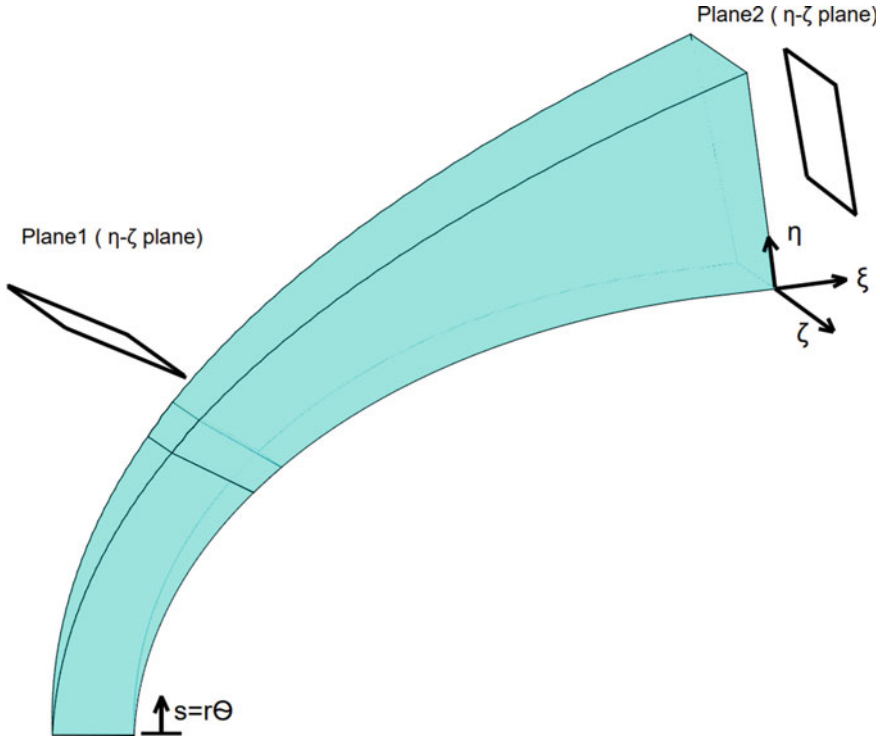


Fig. 5 Schematic of fluid domain with planes

In order to apply the optimization technique, the temperature of the heat-shield along j (wall-normal direction) at any location i (streamwise direction) is given as a function of heat-shield thickness along j . A desired thickness of the heat-shield is obtained when the function reaches a value of 318 K (bearable temperature), i.e.,

$$f(t) = T \quad (24)$$

$$\text{at desired thickness } t: f(t) = T_{\text{bearable temp.}} = 318 \quad (25)$$

$$g(t) = f(t) - 318 = 0$$

The Newton-Raphson iteration is used for the optimization

$$t^{n+1} = t^n - \frac{g(t^n)}{g'(t^n)} \quad (26)$$

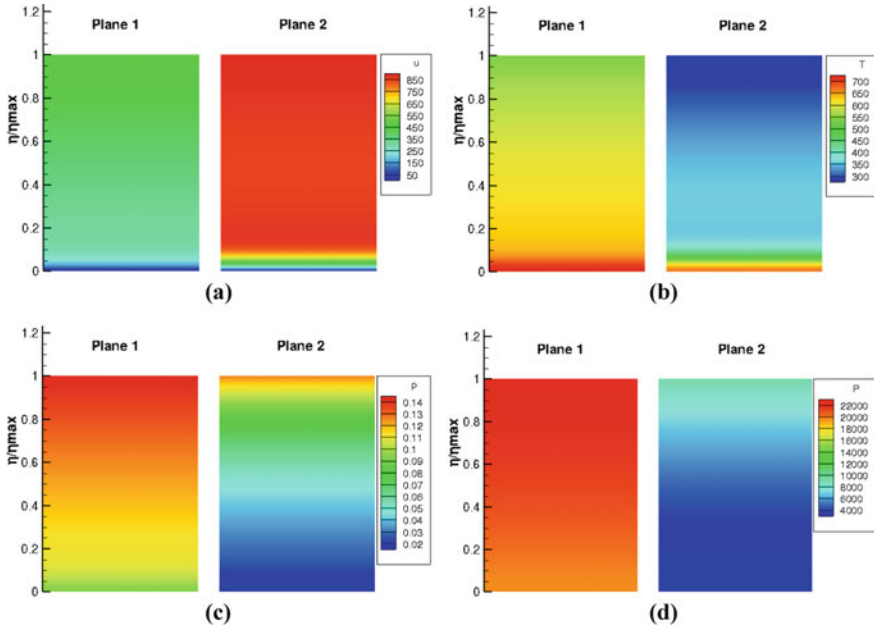


Fig. 6 Flow-field at plane 1 and plane 2: **a** streamwise velocity, **b** temperature, **c** density, and **c** pressure

t^n is the guessed thickness value to start the iteration which has been considered here as the initial heat-shield thickness. g' is the first-order derivative of g with respect to t . The convergence tolerance level is set 10^{-8} . As the tolerance level reaches its value, a optimized thickness is determined and grid points are redistributed. The same procedure is repeated for each streamwise location. Figure 9a shows the temperature contour for the case when temperature first reached 318 K at any node of the inner wall. Figure 9b shows the thickness optimized version of Fig. 9a. Figure 10 shows the variation of heat-shield thickness in the streamwise direction. Initially, thickness was uniform and reduced gradually toward the exit after the optimization process. The heat-shield thickness at the exit has been reduced by approximately half.

The percentage weight reduction is given by

$$\% \text{Weight reduction} = \frac{|W_i - W_f|}{W_i} \times 100 \quad (27)$$

where W_i and W_f are the initial and final weight of the heat-shield computed based on initial (V_i) and final (V_f) volume of the heat-shield. The V_i and V_f are given by

$$V_i = \frac{2}{3} \pi (r_{\text{outer}}^3 - r_{\text{inner}}^3) \quad (28)$$

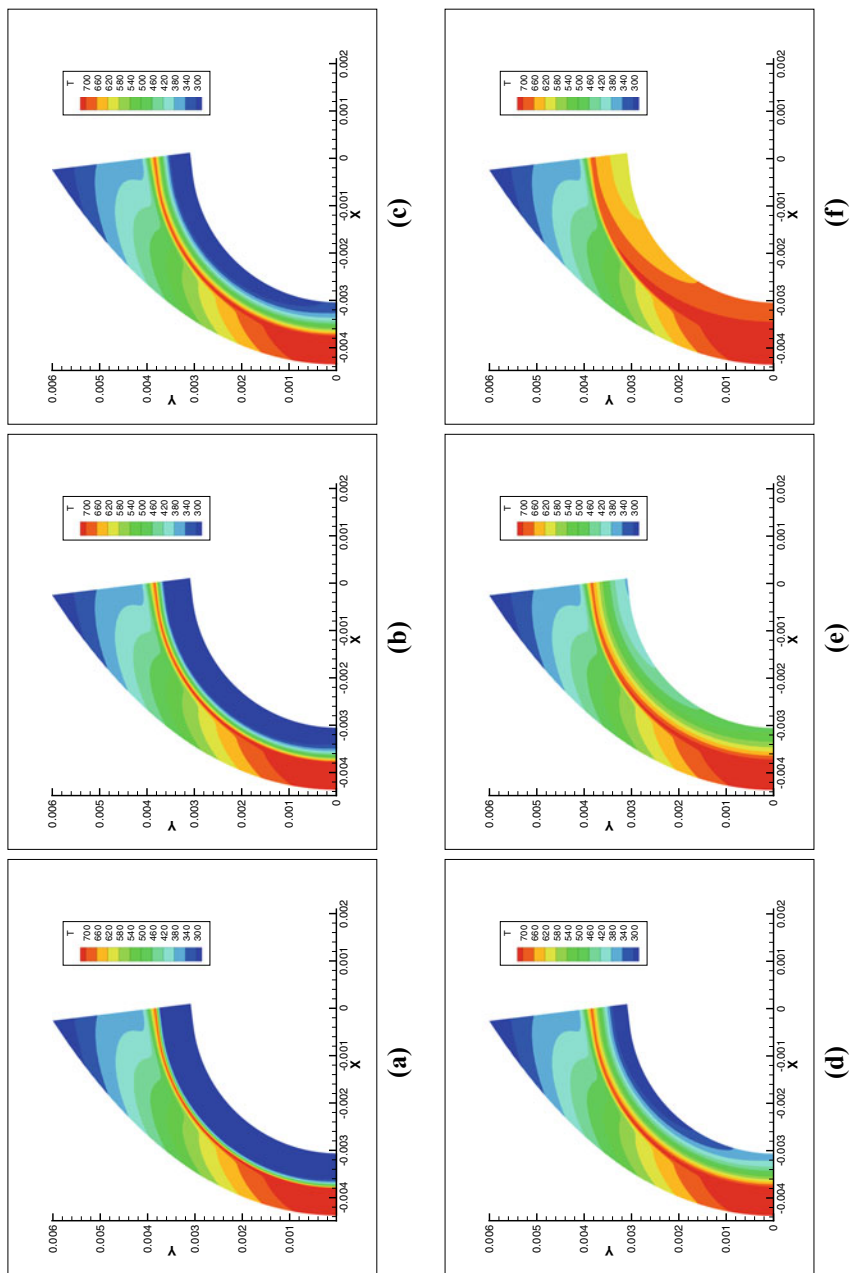


Fig. 7 Temperature contour at different time instants: **a** 2 s, **b** 5 s, **c** 10 s, **d** 15 s, **e** 25 s, and **f** 40 s. *Note* Edge of the solid domain is shown as black line

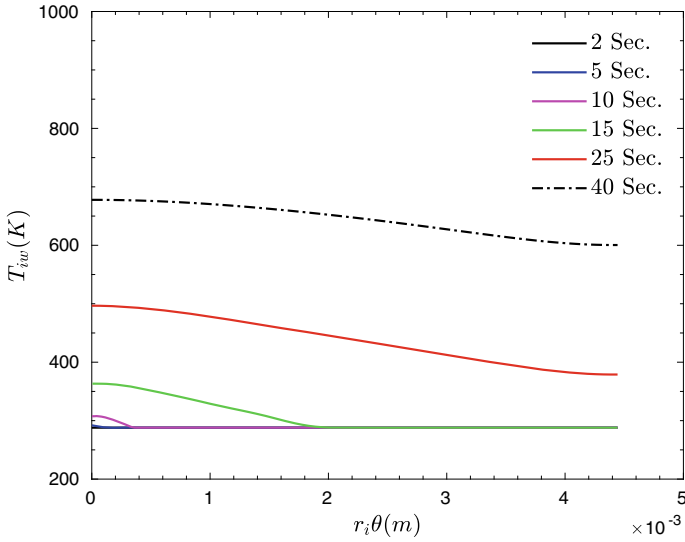


Fig. 8 Inner wall temperature distribution at different time instants

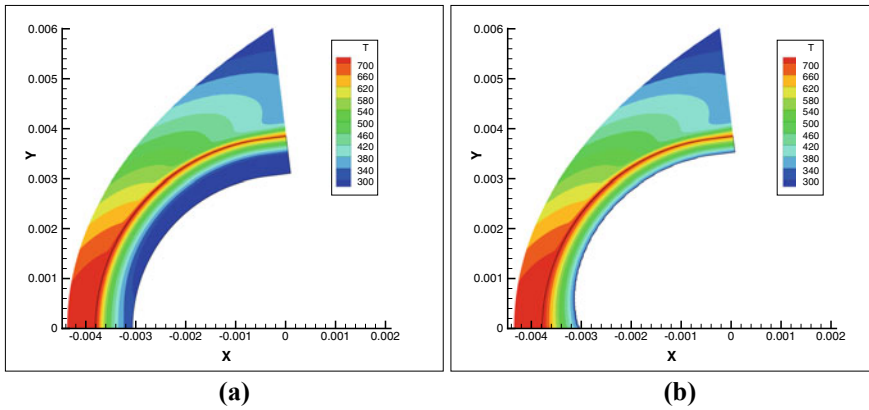


Fig. 9 Temperature contour as temperature reaches 318 K at any point in the inner cabin. **a** Initial heat-shield and **b** thickness optimized heat-shield

$$V_f = \frac{2}{3}\pi \left[r_{outer}^3 - \left(\frac{r_{inner_1} + r_{inner_2}}{2} \right)^3 \right] \tag{29}$$

Initially, the inner radius (r_{inner}) of the heat-shield was constant but after optimization, it gradually decreased from the nose to exit. For the latter case, r_{inner_1} and r_{inner_2} are the inner radius at nose and exit, respectively, and the overall inner radius is taken

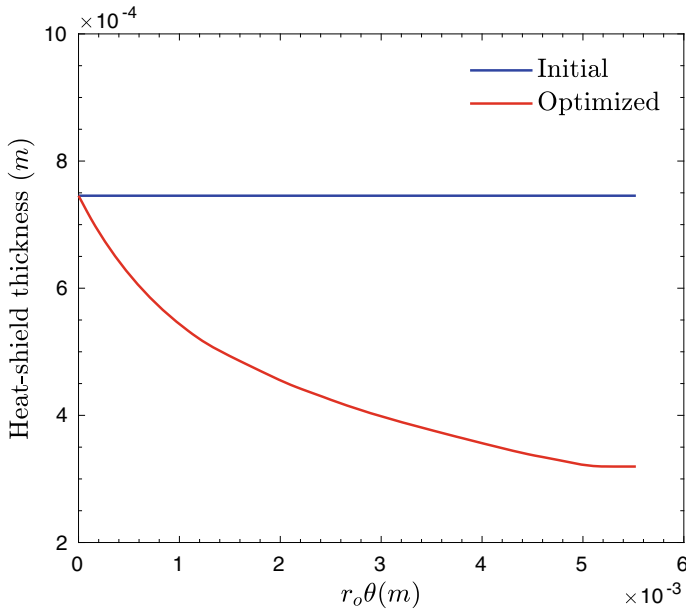


Fig. 10 Thickness distribution

as the average of these two. The above Eq. (27) is used to compute the percentage weight reduction, and a 24.23% weight reduction is observed for our present study.

5 Conclusion

The thermal analysis of a blunt nose semi-spherical non-ablative heat-shield coupled with the hypersonic fluid flow has been performed. The thermal load at the surface has been computed using the fluid solver, which uses a shock-fitting technique to solve the hypersonic flow-field. The computed heat flux at the surface is used for transient thermal analysis of the heat-shield. Based on the inner cabin temperature predicted using thermal analysis, the thickness of the heat-shield has been optimized with the help of the Newton-Raphson method. The reduction in heat-shield thickness reduces its volume and weight. By computing the initial and the final weight, a 24.23% reduction in the weight of the heat-shield has been observed.

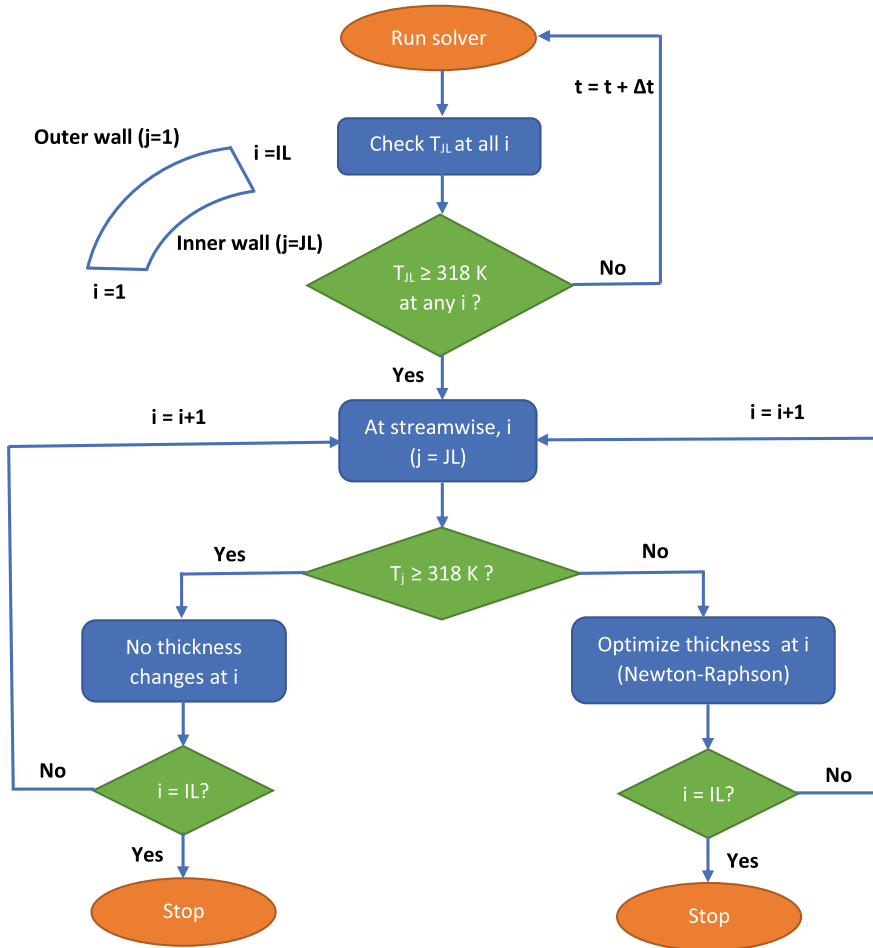


Fig. 11 Computational steps

References

1. Johnson Joshua E, Starkey Ryan P, Lewis Mark J (2007) Aerothermodynamic optimization of reentry heat shield shapes for a crew exploration vehicle. *J Spacecr Rockets* 44(4):849–859. <https://doi.org/10.2514/1.27219>
2. Niehaus W (1963) Heat shield concept and material for reentry vehicles. In: Defence Documentation Centre, Cameron Station, Alexandria, Virginia. <http://apps.dtic.mil/sti/citations/AD0439449>
3. Curry DM (1965) An analysis of a charring ablation thermal protection system. In: NASA technical note NASA TN D-3150. <http://ntrs.nasa.gov/citations/19660003941>
4. Balakrishnan A, Nicolet W, Sandhu S (1979) Galileo probe thermal protection: entry heating environments and spallation experiment design. In: NASA contractor report-152334. <http://ntrs.nasa.gov/citations/19800005927>

5. Mazzaracchio A, Marchetti M (2010) A probabilistic sizing tool and Monte Carlo analysis for entry vehicle ablative thermal protection systems. *Acta Astronautica* 66(5):821–835. <https://doi.org/10.1016/j.actaastro.2009.08.033>
6. Ewing ME, Laker TS, Walker DT (2013) Numerical modeling of ablation heat transfer. In: *J Thermophys Heat Transfer* 27(4):615–632. <https://doi.org/10.2514/1.T4164>
7. Kendall RM, Bartlett EP, Rindal RA, Moyer CB (1967) An analysis of the coupled chemically reacting boundary layer and charring ablator. In: NASA contractor report No. 66-7. Aerotherm Corporation, Mountain View, CA. <http://ntrs.nasa.gov/citations/19690008458>
8. Combs CS, Clemens NT, Danehy PM, Murman SM (2017) Heat-shield ablation visualized using naphthalene planar laser-induced fluorescence. *J Spacecr Rockets* 54(2):476–494. <https://doi.org/10.2514/1.A33669>
9. Zhong X (1998) High-order finite-difference schemes for numerical simulation of hypersonic boundary-layer transition. *J Computat Phys* 144(2):662–709. <https://doi.org/10.1006/jcph.1998.6010>
10. Chang C-L, Malik MR, Erlebacher G, Hussaini M (1991) Compressible stability of growing boundary layers using parabolized stability equations. In: 22nd Fluid dynamics, plasma dynamics and lasers conference. <https://doi.org/10.2514/6.1991-1636>
11. Zhong X, Ma Y (2006) Boundary-layer receptivity of Mach 7.99 flow over a blunt cone to freestream acoustic waves. *J Comput Phys* 556:55–103. <https://doi.org/10.1017/S0022112006009293>

Automation of Launch Vehicle Telemetry—Requirement Capture to Analysis of Data



S. J. Anjana, P. Renjith, Kuntamukkala S. Manyam, J. Abey Rose, L. S. Syamlal, S. Praseetha, L. Jayalekshmi, C. Chandrasekharan, and Anna Priya Koshy

1 Introduction

The processor onboard launch vehicle, termed onboard computer (OBC), performs navigation, guidance, control (NGC) and stage sequencing functions. It is bus controller (BC) in MIL-STD 1553 Avionics data bus of distributed NGC system, interfacing with other subsystems configured as Remote Terminals (RT). Redundant NGC chains meet the reliability requirements of missions. Telemetry Control Unit (TCU) provides the interface to ground telemetry through Radio Frequency (RF) link, by functioning as a Monitor Terminal (MT) monitoring all messages transacted over the bus. In dual-redundant NGC chain, two TCUs are present, each one monitoring both buses. Prime OBC is BC in prime bus, and redundant OBC is BC in redundant bus. Prime and redundant RTs are connected to both buses in fully cross-strapped configuration. Each TCU is programmed to send data words selected from 1553 messages, through telemetry, along with the health status of all messages. Telemetry frames are designed to include critical parameters from both prime and redundant subsystems to ensure availability of data for non-identical failures, say BC/RT failure in one bus and a TCU failure in the other.

Messages over 1553 bus are designed for transaction of data between BC and RTs to achieve NGC system functionality, consolidating the requirements of hardware and software subsystems. A subset of data words from each RT is selected from RT-BC messages for telemetry. A few software parameters from NGC algorithms executed in OBC are also monitored through telemetry. Telemetry frame format requirements are currently generated in document form for use by TCU designers. The document also includes details like bit composition of software flags as reference for analysis

S. J. Anjana (✉) · P. Renjith · K. S. Manyam · J. A. Rose · L. S. Syamlal · S. Praseetha · L. Jayalekshmi · C. Chandrasekharan · A. P. Koshy
Vikram Sarabhai Space Centre (VSSC), Thiruvananthapuram 695022, India
e-mail: sj_anjana@vssc.gov.in

of pre-flight and post-flight data. Capturing and presenting data in software readable form, for ready use by downstream agencies, have been the motivation for this work.

Process engineering and workflows control and coordinate the complex activities and interactions among individuals and software components, thereby achieving the objective of improved quality and efficiency of computerized work [1]. The automation software discussed in this paper is a process improvement to minimize human interventions and scope of errors in NGC telemetry, saving time and effort. It embeds the workflow right from requirement capture till delivery of telemetry data in the required formats for various end users.

2 Problem Definition and Formulation

Telemetry requirements are currently received from multiple subsystem designers in document form. Details of interfaces among hardware packages and among the software elements residing in OBC are worked out in parallel. Design of messages for communication between BCs and RTs, adhering to 1553 protocol, is then carried out by system software designer of OBC, the BC in NGC system. Software parameters for telemetry are selected by the telemetry packing module in OBC and included in the broadcast message from BC to TCU. Data words corresponding to RTs are selected for telemetry from the corresponding RT-BC messages. Telemetry parameters are judiciously identified, after trade-off studies between the criticality of data and the available bandwidth for communication to ground. The specifications of telemetry frame formats are communicated thereafter to TCU designers in document form. The manual steps involved in mapping the parameters from 1553 message table and documenting words for TCU in the form $Mm, DW_{n1} - DW_{n2}$, where m is the message number and $n1-n2$ are data words for telemetry from message m , may lead to errors. Oversight in the depiction of bus, in various TCU frame formats, might surface as surprises during analysis of telemetry data from pre-flight tests.

Our aim is to optimize the existing practices and streamline the process of generating NGC telemetry requirements and formats for all missions. The scope of our work entails elicitation of telemetry requirements of NGC system designers, analysis and selection of essential parameters compliant to telemetry bit-rate constraints, finalization of file formats required by various stakeholders, and implementation of the automation software for online upload and retrieval of telemetry data frame formats and making it operational after thorough validations.

3 Methodology

The GUI-based software consolidates the telemetry requirements and generates relevant data as software readable files in the required formats for TCU programming, flight measurement plan generation, checkout stations, and simulation test beds. The

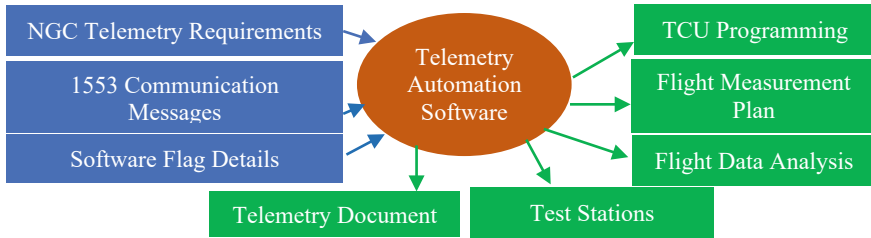


Fig. 1 Software system interfaces

details of parameters including unit and scale factor and bit definitions of software flags are captured. The associated documents, with 1553 message details of NGC system, TCU telemetry frame composition, details of each telemetry parameter, and the information on message errors reported by TCU are automatically generated for the various testing and data analysis teams, as depicted in Fig. 1.

3.1 NGC Serial Telemetry Configuration

In the dual-redundant NGC chain in Fig. 2, BUS1 is the 1553 bus with OBC—prime as BC and BUS2 is the bus with OBC—redundant as BC. TCU operating in monitor mode collects all messages from both buses in the system. It selects required data words from the identified messages, as programmed, and packs them in the telemetry data frames corresponding to one of the four NGC-TCU communication interfaces.

OBC(P) sends BC-RT message db1 to a paired (Pd) RT and message db2 to its cross-strapped (Xd) RT. Similarly, OBC(R) sends db3 and db4 messages to its Pd and Xd RTs. For RT-BC messages, duplicate messages are sent from an RT, one to its Pd BC and another to its Xd BC, i.e., dr1, dr2 from RT(P) and dr3, dr4 from RT(R). OBC

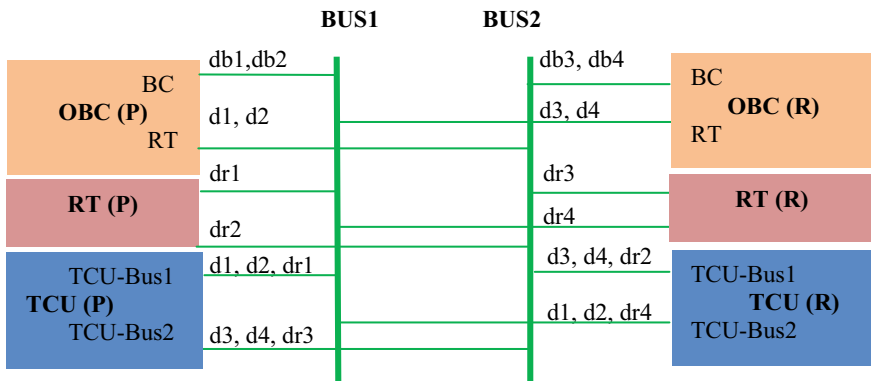


Fig. 2 Data flow: BC-to-RT, RT-to-BC, and broadcast messages

telemetry broadcast messages in BUS1 are denoted by d1, d2 and d3, d4 in BUS2. TCU(P) selects d1, d2, dr1 through TCU-Bus1 link and d3, d4, dr3 through TCU-Bus2 link for telemetry. Similarly, TCU(R) selects d3, d4, dr2 through TCU-Bus1 link and d1, d2, dr4 through TCU-Bus2 link. Thus, telemetry data is available in case of non-identical failures. All messages are analyzed for 1553 protocol adherence, and a composite indication is sent to telemetry. Four error bits for a message indicate format error, no response error, message error bit (MEB) setting, and wrong RT response. Different telemetry frame formats are generated in multiple phases of a mission, by eliminating parameters related to NGC systems getting separated from launch vehicle in each stage.

3.2 Features of Automation Software

The web-based tool features a GUI to accept inputs from the users and generates output files in software readable or document forms. NGC telemetry requirements and format can be generated from scratch for a new mission or evolved from existing mission data. User can create new missions and assign hardware packages. The tool accepts NGC system 1553 communication protocol and uses the information on data words of messages to identify the message source for telemetry format generation by TCU. Telemetry requirements are elicited from NGC system designers, including the parameters, legends, data types, scale factor, units, and periodicity of transmissions. Provisions are enabled for multiplexing parameters in telemetry slots for different phases of multi-staged launch vehicles. Interface is provided for entering the individual bit definitions of software flags.

The tool generates NGC serial telemetry requirements for TCU format as software readable text file with 1553 command words in BUS1 and BUS2, followed by telemetry words in BUS1-TCU(P)Bus1, BUS2-TCU(P)Bus2, BUS1-TCU(R)Bus2, and BUS2-TCU(R)Bus1 frames, in sequence. The telemetry words are represented as Mm , DW_{n1} - DW_{n2} , for data words DW_{n1} - DW_{n2} from message Mm . The tool also generates data files required by other user agencies by retrieving the required fields of telemetry database. Simulation and data analysis teams use these for pre-flight validations and post-flight data analysis. Files are provided in software readable form for test stations, where actual telemetry data from TCU is verified against TCU format using 1553 bus emulator.

With the entire telemetry space mapped to the database, the system generates NGC serial telemetry document. The telemetry format specifies the byte position of each parameter (position in TCU frame and within a package), legend, data type, and data word source in 1553 message. Scale factor and unit of relevant parameters are included as shown in Table 1. 1553 message table and software flag details in tabular form are also provided in the document. TCU message error status, where each byte contains the error status of two 1553 messages, and the summary table capturing the total number of words in each bus of both TCU are also generated by the tool.

Table 1 Telemetry frame template

Byte pos	Description	Legend	Data type	BUS1-TCU(P) Bus1	Scale factor	Unit	
1	1	Start of frame for BUS1 data (F0)	Start_id	Byte	START	–	–
<i>RT1—PRIME PAIRED LINK</i>							
3	1	Compensated body rate yaw	Body rate yaw	Short_integer	M4,DW1	16	rad/s
–	–	–	–	–	–	–	–
495	15	End of frame (CC)	End_id	Byte	STOP	–	–

3.3 Overview of Implementation

Workflows increase efficiency by separating the repetitive aspects of work into well-defined tasks, roles, rules, and procedures using Information Technology [2]. Workflow implemented for our automation software is depicted in Fig. 3, where owner represents the engineer responsible for NGC telemetry. Certain tasks in this workflow are executed by humans, and certain others are computer tasks like database management system.

The system implements password-based authentication and role-based authorization for performing various actions. Emails are sent to the users to alert on

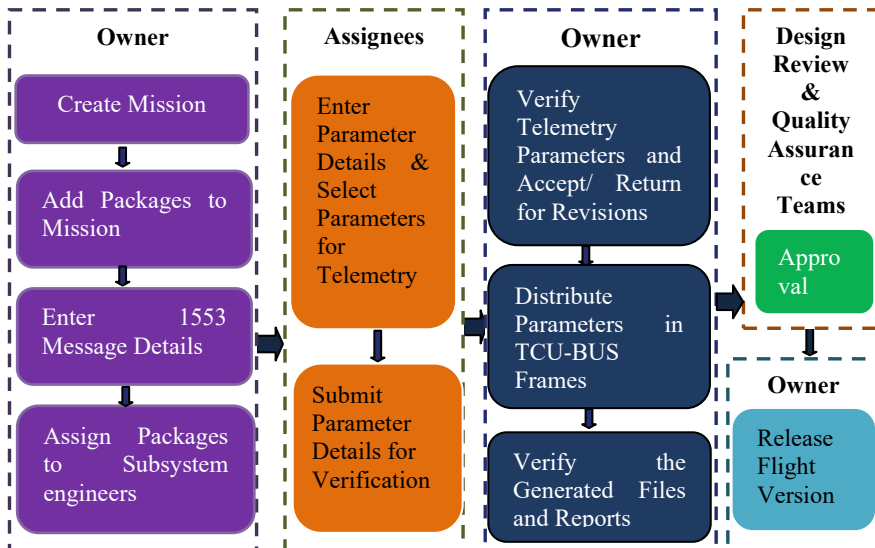


Fig. 3 Automation software workflow

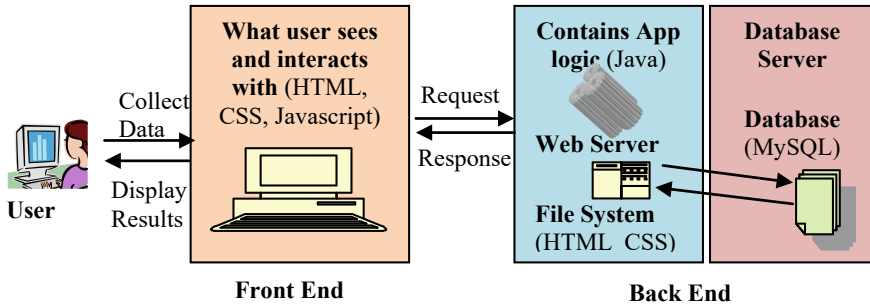


Fig. 4 Architecture of telemetry automation software

pending actions or specific milestones, in addition to notifications received upon logging to the system. System grants necessary privileges to enter/edit/delete data and approve the format for releasing a version. Change record from baseline is generated automatically for every new version.

The software is developed using three-tier architecture as shown in Fig. 4. The design of GUI is simple, with the interfaces following a standard approach for the look and feel. Front end is designed using Hypertext Markup Language (HTML) to create web pages, Cascading Style Sheets (CSS) to specify the presentation layout, colors, and fonts, and Bootstrap front-end library for the design templates. Client-side validation of user inputs is done using JavaScript and jQuery, a cross-platform library for HTML scripting. Server-side validations and business logic are implemented using Java, Java Server Pages (JSP), Servlets, and Asynchronous JavaScript and XML (AJAX). Application business logic is written in Java, with server-side validations for all user actions. JSP enables writing of dynamic, data-driven pages for java-based web applications. Servlets are used to access the data from HTML and interface with the database to provide dynamic content. Ajax allows web pages and applications to change content dynamically without the need to reload the entire page. The application is hosted in a tomcat server. User operations are implemented as transactions at the application level using Java Database Connectivity (JDBC) transaction management Application Programming Interface (API). MySQL, an open-source relational database management system, is used to store, update, retrieve, and delete user data and data on missions. Transactions at application and database levels can handle asynchronous and concurrent activities.

4 Results

Web-based automation software is designed and developed embedding the workflow to capture telemetry requirements from NGC designers and generate the inputs for programming TCU. It facilitates re-use of telemetry configurations generated for previous missions. Input telemetry data fed by the user is verified automatically with

Step No	Process Name	Remarks/Action	Status	Message No	Is Multiplexed	Legend	Parameter Description	Parameter Type	Data Type	Message Source from Word
1	Mission Creation	Created	✔	4	No	BodyRateYaw	Compensated Body Rate Yaw	NORMAL ✔	INT16	DW1
1	Bus Information	Added	✔	4	No	BodyRatePitch	Compensated Body Rate Pitch	NORMAL ✔	INT16	DW2
2	Package Adding	4 Packages Added	✔	4	No	BodyRateRoll	Compensated Body Rate Roll	NORMAL ✔	INT16	DW3
3	1553Comm Messages Entry	23 Messages Added	⚠	4	No	Aid_Q0	ECI to body Quaternion aided with NavIC-Q0	NORMAL ✔	Float32	DW8
4	Package Assignment	4 Packages Assigned	✔	4	No	Aid_Q1	ECI to body Quaternion aided with NavIC-Q1	NORMAL ✔	Float32	DW10

Fig. 5 Front end of web-based telemetry automation system

respect to total telemetry frame size and data types of all parameters. Testing of the utility is carried out, and pilot project is in progress. Sample screen of automation software is included in Fig. 5.

5 Discussion and Conclusions

Automation of NGC telemetry has been the need of the hour, considering the increasing frequency of space missions and the multi-disciplinary nature of launch vehicles. The software has been evolved after an in-depth study of the existing scheme and incorporating the industry-standard best practices for process automation. Its capability to generate the NGC telemetry requirements and format from scratch for a new mission as well as to evolve telemetry configuration from existing data will immensely benefit the authorized users of launch vehicle community. Equally significant is the details generated by the tool for test stations and data analysis agencies.

References

1. Cichocki A, Ansari HA, Rusinkiewicz M, Woelk D (2012) Workflow and process automation: concepts and technology
2. Georgakopoulos D, Hornick M, Sheth A (1995) An overview of workflow management: from process modeling to workflow automation infrastructure

Design Exploration of a Scramjet Inlet upto Three External Ramp



Kunal Garg, G. Vidya, M. M. Patil, and V. Ashok

1 Introduction

Scramjet vehicles are a special class of vehicles where aerodynamics and propulsion are highly intertwined leading to stringent design requirements. Thrust is generated by its integral propulsive elements comprising shock compression by ramps/corner/cowl which constitutes the inlet followed by heat addition at the supersonic speed which gets expanded through elongated divergent and further by nozzle [1]. In the hypersonic regime, flow at each station is governed by the flow at the preceding station enforcing severe design requirements on the inlet. Also, the hypersonic flow regime involves high-speed motion which reduces available reaction time for control forces to counteract disturbances hence requires inherent stability.

The high compression by inlet specifically ramps leads to high static pressure build-up which aerodynamically increases lift but also increases nose up pitching moment depreciating stability characteristics. Lowering compression will lead to poor combustion characteristics hence reduces thrust. The non-isentropic compression by ramps reduces the total pressure recovery (TPR) resulting in nozzle under-performance. Therefore optimum compression should be achieved through minimum entropy generation catering to both performance and stability. Vehicle mass

K. Garg (✉) · G. Vidya
ACMD/ADSG/AERO, VSSC, ISRO, Trivandrum, India
e-mail: kunal@vssc.gov.in

G. Vidya
e-mail: g_vidya@vssc.gov.in

M. M. Patil · V. Ashok
ADSG/AERO, VSSC, ISRO, Trivandrum, India
e-mail: mm_patil@vssc.gov.in

V. Ashok
e-mail: v_ashok@vssc.gov.in

is directly correlated to the length of the ramps which creates a flywheel effect on the design requirement and also need to be addressed. Therefore there exist many trade-off parameters but for the current study TPR and pitching moment coefficient has been used for carrying out optimization studies.

2 Methodology

Current studies focus on multi-objective optimization of Scramjet inlet employing the weighted sum technique using MATLAB. Oblique shock relations with a perfect gas assumption ($\gamma = 1.4$), the inviscid flow has been used to derive the 2-D flow field. Total pressure recovery across intake and pitching moment coefficient due to ramps are two objective functions that are used for current design exploration. The design variables are the pressure ratio (compression ratio) across each oblique shock. The problem is formulated as

$$\begin{aligned} \text{Minimize} & : w_1 \times C_m - w_2 \times \text{TPR} \\ \text{Subject to} & : M_4 = M_e, \quad \theta_i \geq 0 \\ \mathbf{X}: \{CR_i\}, & \quad 1.01 \leq CR_i \leq 7.0 \end{aligned}$$

where **CR**: Compression ratio, **TPR**: Total pressure recovery across intake, **M_e** isolator inlet Mach number.

This approach allows to convert multi-objective problems to a single objective problem which can be tackled with a wide variety of solvers, this study employs MATLAB “*fmincon*” for the same. The solver is based on SQP algorithm for faster convergence. To enhance the fidelity of the analysis the weights are varied over complete Cartesian space which results in Pareto front preserving the multi-objective nature of the problem.

The oblique shock solution starts with guessing the compression pressure ratios across individual oblique shock [2]. Based on pressure ratio across *i*th shock on the *i*th ramp, the *i*th shock angle is computed by Eq. 1 followed by the computation of *i*th ramp angle w.r.t to (*i* - 1)th ramp given by Eq. 2 and finally, the Mach after *i*th shock given by 3 is computed. After performing the computation for each ramp, finally, the reflected shock solution is computed and the flow conditions designated by subscript 4 and then compared to the constraints. The computation is transversed till convergence of 10^{-6} .

$$\beta_i = \sin^{-1} \left[\sqrt{\frac{\left((CR_i - 1) \left(\frac{\gamma+1}{2\gamma} \right) \right) + 1}{M_{i-1}^2}} \right], \quad CR_i = \frac{P_i}{P_{i-1}} \quad (1)$$

$$\theta_i = \tan^{-1} \left[2 \cot \beta_i \left(\frac{M_{i-1}^2 \sin^2(\beta_i) - 1}{M_{i-1}^2 (\gamma + \cos 2\beta_{i-1}) + 2} \right) \right] \quad (2)$$

$$M_i = \sqrt{\frac{\left(M_{i-1}^2 \sin^2(\beta_i) + \frac{2}{\gamma-1} \right)}{\left(\frac{2\gamma}{\gamma-1} M_{i-1}^2 \sin^2(\beta_i) - 1 \right)}} (\sin(\beta_i - \theta_i))^{-1} \quad (3)$$

The total pressure recovery across intake is cumulative multiplication of individual total pressure recovery across oblique shock which is given by Eq. 4. The pitching moment coefficient defined w.r.t cowl lip given by Eq. 5. The nomenclature, sign conventions are depicted are Fig. 1.

$$\text{TPR}_i = \left[\left(1 + \frac{\gamma-1}{2} M_i^2 \right)^{\frac{\gamma}{\gamma-1}} \text{CR}_i \left(1 + \frac{\gamma-1}{2} M_{i-1}^2 \right)^{\frac{-\gamma}{\gamma+1}} \right] \quad (4)$$

$$C_M = \frac{1}{0.5\gamma M_o^2 y_L(1)(1)} \sum \frac{P_i}{P_o} \times (x_i - x_{i-1}) \times (x_L - \frac{1}{2}(x_i + x_{i-1})) \quad (5)$$

A mixed compression inlet based on three external ramps and one internal reflected shock is considered for analysis. Though the algorithm is developed for analyzing three ramp systems it also considers one and two ramp systems as they are a subset of three ramp systems and hence the number of ramps up to three is a part of the optimization solution. The ramps provide pitch up moment which must be minimized for stability and total pressure recovery must be maximized for maximum thrust honoring the constraint of desired Mach number at isolator beginning. Wing and control surfaces counteract the pitch up moment so lowering the pitching moment

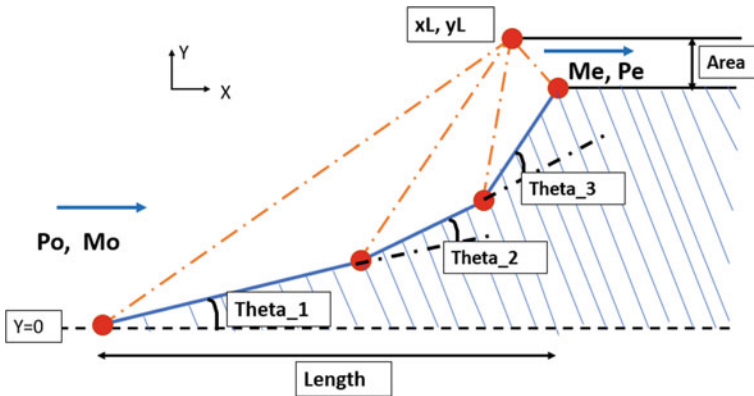


Fig. 1 Schematic of typical inlet with three ramps. Nomenclature and sign convention

also indirectly reduces drag offered by the wing and control surfaces as these can be smaller also the ramps beside the pitch up moment offer significant lift and drag. Higher lift and lower drag not only improves performance but also reduces wing requirement and thrust requirement, respectively. Although TPR and moment are optimized the lift and drag are also monitored. The ramp length, isolator area, ramp angles, total flow turning angle are also computed and their correlation with total pressure recovery is studied. The total temperature being constant across the shock, the temperature ratio across intake reduces to function of freestream Mach number and M_e (isolator beginning Mach) [3]. So the effect of M_e has also been studied on-ramp angles. Subsequently, variation of freestream Mach number on the ramp angles and pitching moment is discussed.

3 Results and Discussion

The ramp angles are optimized against objective function comprising TPR and pitching moment. The freestream Mach number is varied from 5.5 to 7.0. The isolator beginning Mach number is varied from 50 to 75% of the freestream Mach number. Pitching moment, lift, drag, ramp length, isolator area, ramp angles, total flow turning angle variation with TPR is studied and discussed.

3.1 Freestream Mach (M_o) 6.0, M_e 55 % M_o

The C_M -TPR Pareto is reported in Fig. 2a and correspondingly the lift and pressure ratio across ramps variation with TPR is reported in Fig. 2b, c. The Pareto suggests that pitching moment (nose up) increases as TPR increases, clearly stability is compromised on the cost of performance. The weight functions are complimentary so sum is always one; Therefore the extreme design points corresponds to minimum moment design and maximum pressure recovery design for a given M_e (isolator Mach number). Similar to C_M , C_L increases with TPR but drag is marginally affected and assumes values of approximately 0.16. On an average C_L increases by 13%, C_M by 58% with TPR increase of 31%. The moment and lift marginal increase is higher per unit TPR for higher TPR. Correspondingly linear variation with about 31% increase in pressure ratio is observed and interestingly higher the total pressure recovery higher is the pressure ratio for optimized designs.

Correspondingly length of the intake with higher pressure recovery is higher which is shown in Fig. 3a. On an average the length increases by 44%. Similar to moment, the marginal change of length per unit of TPR is higher for higher pressure recovery. The ramp angle variation with TPR and design points are plotted in Fig. 3b, c.

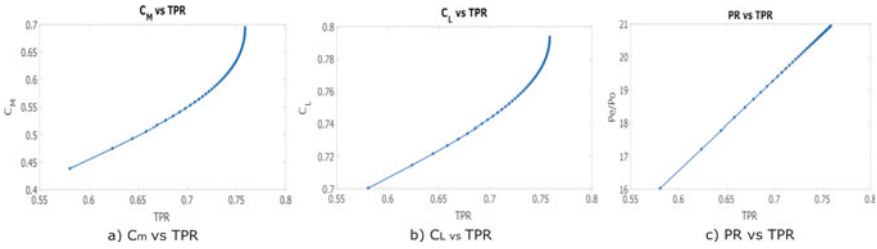


Fig. 2 Aerodynamic forces and pressure ratio variation with TPR

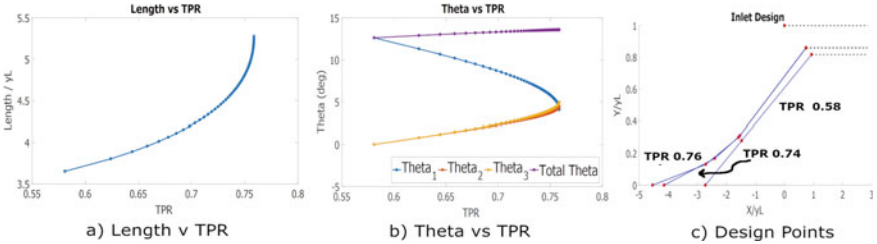


Fig. 3 Length variation and ramp angle variation with TPR and design points

Interestingly, the minimum moment design is nothing but single ramp system and maximum pressure recovery solution as expected is a three ramp system. The total flow turning only changes from 12.6° to 13.6° whereas large change is observed in first ramp angle which changes from 12.6° to 4° . Second ramp and third ramp increases from 0° to $4-5^\circ$.

3.2 Effect of M_e on the Design

The M_e is varied from 50 to 75% of the freestream Mach number. The aerodynamic moment and total turning angle is reported in Fig. 4a, b, respectively. Irrespective of the M_e (Mach at isolator beginning) the pitching moment increases with TPR and same holds true for lift also as depicted earlier. In general as the M_e decreases from 75 to 50%, the pitching moment is increased for a given TPR. Also with decrease in M_e , the total pressure recovery also decreases because higher shock strength is required. From Fig. 4a, it can be concluded that the pitching moment is more sensitive to TPR for higher M_e . Since drag is observed to approximately constant with TPR in Fig. 2c, the decreasing M_e merely increases the magnitude. The total turning angle as shown earlier increase with TPR but the magnitude increases with reduction in M_e .

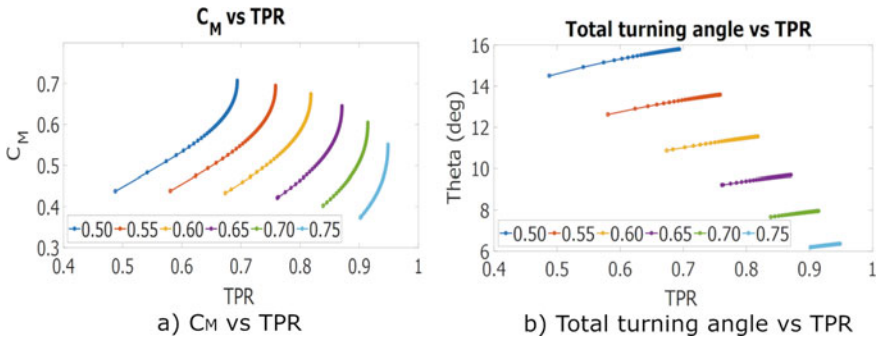


Fig. 4 Pitching moment and total turning angle variation with TPR for different M_e

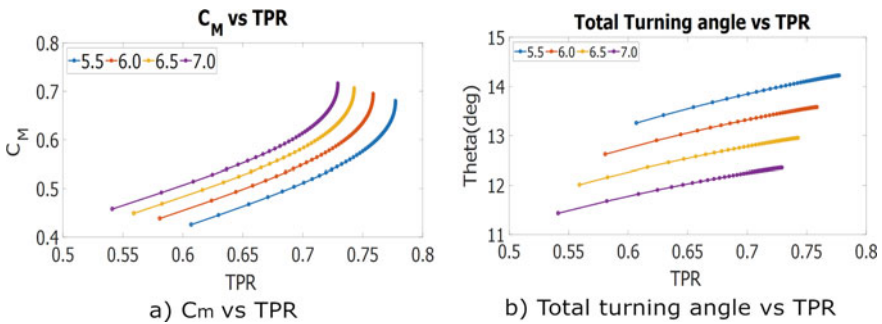


Fig. 5 Pitching moment and total turning angle variation with TPR for different M_o

3.3 Effect of M_e on the Design

The M_o is varied from 5.5 to 7.0 and the M_e is kept 55% of the freestream mach number (M_o). The aerodynamic moment and total turning angle is described in Fig. 5a, b, respectively. With increase in freestream Mach number, the pitching moment magnitude increases whereas similar trend is observed irrespective of M_o . Likewise, total turning angle linearly increases with TPR whereas the magnitude decreases with increasing Mach number.

References

1. Segal C (2009) The Scramjet engine, processes and characteristics. Cambridge University Press
2. Raj NOP, Venkatasubbaiah K (2012) A new approach for the design of hypersonic scramjet inlets. Phys Fluids 24:086103
3. Araújo PP, Pereira MV, Marinho GS, Martos JF, Toro PG (2021) Optimization of scramjet inlet based on temperature and Mach number of supersonic combustion. In: Aerospace science and technology, vol 116, p 106864

Supply Chain Optimization for Mainstreaming SAF in the Indian Aviation Sector



Arvind Ravi, Shirish Nanda Potu, Stephen Varghese, Valliappan Valliappan,
and Vishwanath Doddamani

1 Introduction

The UNFCCC Paris agreement calls for limiting global warming to below 2 °C relative to pre-industrial levels by 2100, while striving to be within 1.5 °C. Aviation accounts for 3% of global annual CO₂ emissions with a projected increase of 300% over 2005 levels by 2050. Due to the nascent stage of alternative propulsion and long operating life of new Aviation Turbine Fuel (ATF) powered aircrafts, there is an immediate need for a low emission drop-in fuel. With minimal changes to transport, storage, fueling and usage, Sustainable Aviation Fuel (SAF) offers the most achievable pathway to reduce life cycle emissions in the aviation industry [1].

The need to adapt and scale up SAF implementation is also reflected in the government policies. Norway now requires 0.5% of SAF usage in its aviation sector, growing to 30% by 2030 [1] with other countries instituting a carbon tax or cap-and-trade system. As a result, there have been cross-industry collaborations between companies like Shell, BP, SkyNRG, Rolls Royce, etc., paving the way for SAF commercialization in Europe and in the USA. In India, three SAF-powered demonstration flights have been conducted so far. The Indian government has acknowledged the strategic importance of biofuels due to their benefit to initiatives, like ‘Make in

A. Ravi (✉) · S. N. Potu · S. Varghese · V. Valliappan · V. Doddamani
Shell India Markets Pvt. Ltd., Bengaluru, India
e-mail: Arvind.R@shell.com

S. N. Potu
e-mail: Shirish.Nanda@shell.com

S. Varghese
e-mail: Stephen.Varghese@shell.com

V. Valliappan
e-mail: V.Valliappan@shell.com

V. Doddamani
e-mail: Vishwanath.Doddamani@shell.com

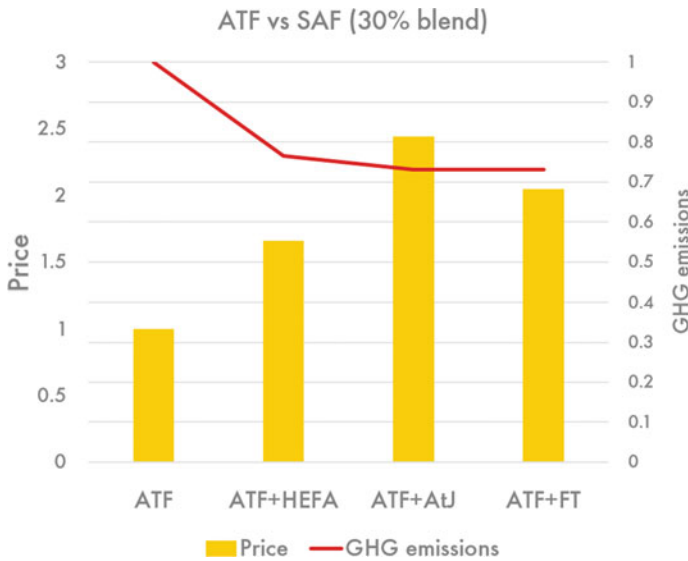


Fig. 1 ATF versus SAF (cost, GHG emissions)

India' and Swachh Bharat Abhiyan, and their natural integration with targets such as increasing farmer's income, import reduction, employment generation and waste to wealth creation. With the nation's feedstock-induced potential to produce 11 million tons of SAF per year [1] and encouragement from the 2018 national policy on biofuels for setting up of refineries and supply chain mechanisms for biofuel production in the country, a rapidly developing India shows good potential as an emerging SAF market. There are three potential SAF production pathways for India—hydro-processed esters and fatty acids (HEFA), Alcohol-to-Jet (AtJ) and Fischer–Tropsch (FT). Each of these technologies has different feedstock conversion rates, production costs and GHG emissions as shown in Fig. 1. For any pathway, the market cost for SAF is expected to be higher than ATF [1]. This is attributed to the establishment of a feedstock supply chain network, installation of new manufacturing facilities and R&D. This paper addresses the need for establishing an optimal feedstock-to-airport supply chain network to minimize the cost of transporting SAF to five airports in south India. The problem formulation and supply chain optimization framework are discussed in Sects. 2 and 3. The results are presented in Sect. 4, and with scope for future extensions and additional case studies discussed in Sect. 5.

2 Problem Definition and Formulation

The focus of the proposed case study is to optimize the supply chain network for delivering SAF blended ATF to five airports, viz. Chennai (MAA), Bengaluru (BLR), Cochin (COK), Thiruvananthapuram (TRV) and Madurai (IXM). Figure 2 highlights

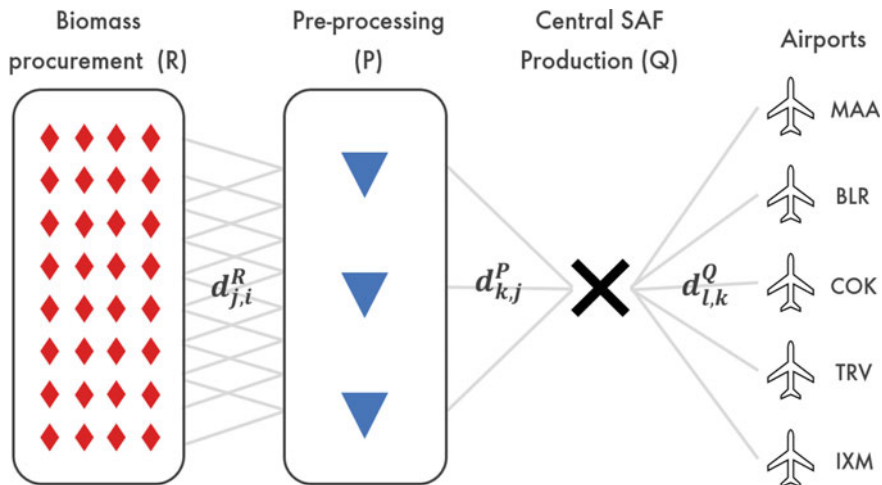


Fig. 2 Schematic of biomass to airports—SAF supply chain

the proposed supply chain network. The raw feedstock is procured from the biomass procurement points R , whose distribution across south India is mapped using Indian Space Research Organization's Visualization of Earth Observation Data and Archival System (VEDAS) [2]. This mapping has been shown in Fig. 3 while the VEDAS data for India has been shown in Fig. 8.

The procured biomass from R is distributed to the pretreatment facilities or pre-processing units P . The intermediate feedstock (biochar, pellets and bio-oil) produced at P is then transported to the central SAF production unit Q which supplies blended SAF to the above airports. At each stage, i.e. from R to P and from P to Q , there is a feedstock-to-product conversion factor which has been borrowed from literature [1]. The optimization cost function (Φ) is formulated using transportation cost parameters $\tau_{(j,i)}^P$, $\tau_{(k,j)}^Q$, $\tau_{(l,k)}^A$ ($\text{km}^{-1}\text{ton}^{-1}$) sourced from [3]. The terms m (ton) and d (km) represent mass and distance, respectively, with superscripts denoting the node connected upstream. The term α denotes the conversion factor at the intermediate nodes P and Q . The usage of α , therefore, results in the optimizer implicitly placing a higher weightage on the first term in the cost function. The impact of this parameter is discussed in Sect. 4.

$$\Phi = \sum_{i=1}^{ni} \sum_{j=1}^{nj} m_{j,i}^R d_{j,i}^R \tau_{j,i}^P + \sum_{j=1}^{nj} \sum_{k=1}^{nk} \alpha_j^P m_{k,j}^P d_{k,j}^P \tau_{k,j}^Q + \sum_{k=1}^{nk} \sum_{l=1}^{nl} \alpha_k^Q m_{l,k}^Q d_{l,k}^Q \tau_{l,k}^A \quad (1)$$

To mitigate the cost involved in the operation and maintenance of the facility, the case study explores the option of retrofitting the central facility (Q) inside one of three refinery complexes available in southern India. The study is constrained to

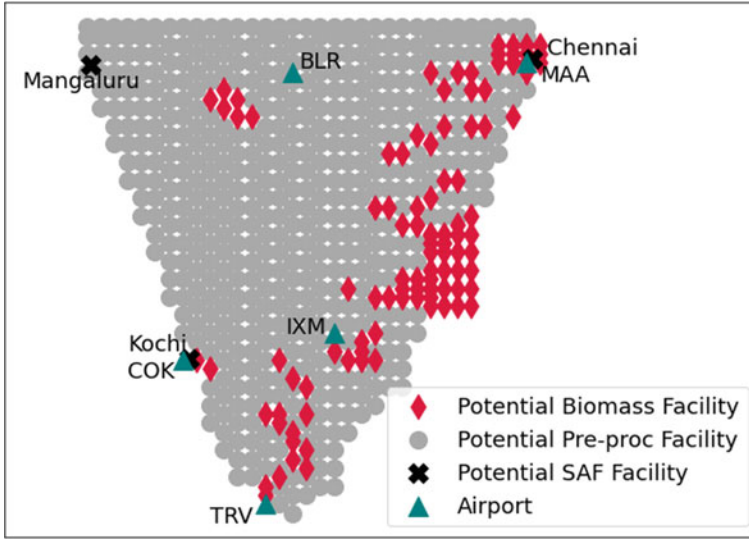


Fig. 3 Distribution of potential biomass procurement points, pre-processing units and central SAF production facilities in Southern India

utilizing this single SAF production unit in a centralized supply chain configuration and assumes fixed number of pre-processing units (three) with the flexibility to scale up based on requirement. Furthermore, static demand is assumed for the airports. Other assumptions include constant inventory per node and geographic limitations with regards to biomass distribution.

3 Methodology

The distribution of biomass reserves [2] is replicated in Fig. 3 along with the three potential locations for the central facility Q and the five airports. The central unit (Q) and the pre-processing units (P) are operated to cater to the downstream demand. The absolute distance between the various facilities and the initial biomass locations are mapped to compute the route-specific cost of transportation. The objective of the optimization is to compute the optimal locations of the facilities Q , P and R such that the cost of transportation is minimum for a constant supply of SAF to the airports. Here, the static end customer demand from the airports is used as an input to the framework. The optimal locations are then chosen from the potential biomass reserves (shown in red diamond) the pre-processing units (P) (grey) and the central facility (Q) (three refinery locations and black cross). The optimization framework incorporates integer binary decision variables for the choice of each facility. The other decision variables optimize the mass transported across R , P and Q , with constraints

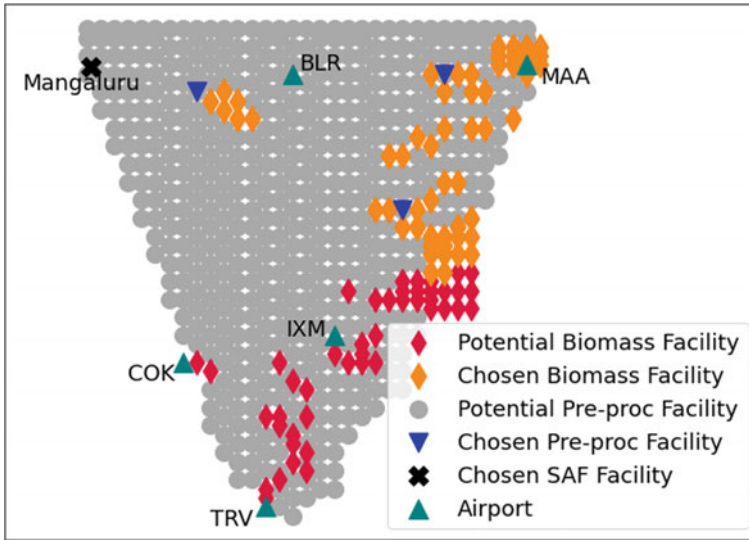


Fig. 4 Optimal supply chain network for a central SAF facility located at Mangaluru

to satisfy mass balance across the network. With the binary (location) and continuous (mass) variables and their associated constraints, the facility optimization is posed as a Mixed Integer Linear Programming (MILP) optimization problem which is setup in an open-source optimization framework Pyomo [4] and solved using the coin-or branch and cut (cbc) solver [5].

4 Results and Discussion

The supply chain optimization framework discussed in Sects. 2 and 3 ensures that the transportation cost of SAF is minimized across three levels: the biomass procurement points (R) to the pre-processing units (P), pre-processing units to the central SAF production unit (Q) and from the central SAF production unit to the five airports under consideration. Given the airport demand and feedstock availability in south India, the methodology yields the optimum

- Location of, and raw feedstock supply requirement from, each selected biomass procurement point.
- Location of, and raw feedstock demand and processed feedstock supply requirement from, each selected pre-processing unit.
- Location of, and processed feedstock demand requirement from, the central SAF production unit.

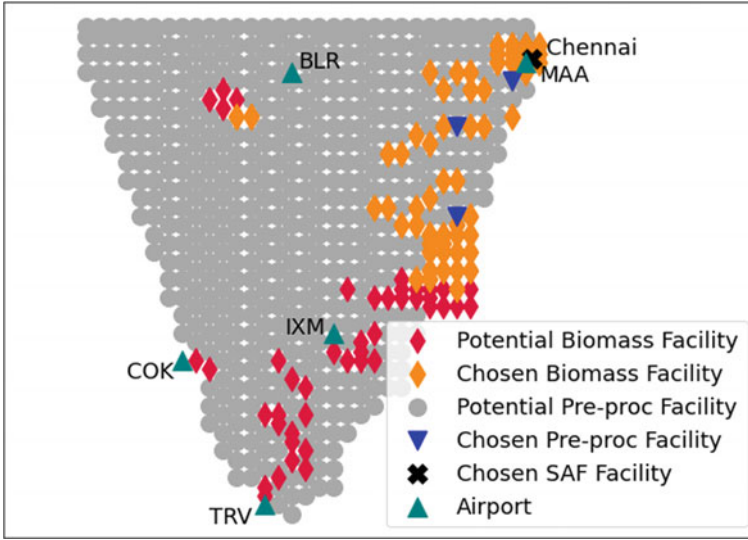


Fig. 5 Optimal supply chain network for a central SAF facility located at Chennai

As mentioned in Sect. 2, we consider the central SAF production facility being retrofit to existing refineries in south India as the most feasible option for pilot implementation. This assumption leads to three possible locations for Q - Mangaluru, Chennai and Kochi. The framework has been implemented for each of these locations, providing a scenario-wise optimal supply chain network as shown in Figs. 4, 5 and 6. For each of these networks, the distribution of the transportation costs has been shown as a bar chart in Fig. 7. It can be noticed in the figure that the cost of transporting biomass from its procurement point to the pre-processing unit (yellow) as well as that of transporting SAF from Q to the five airports (blue) is comparable across the three options. The cost that decides the optimal location of Q in this study is that of transporting processed feedstock from the pre-processing unit to central SAF facility at Q , i.e. the red portion of the bar charts in Fig. 7.

Considering feedstock-to-product conversion rate defined in Sect. 2, we estimated the largest share of transportation cost to be between biomass procurement points and the pre-processing units [1]. To minimize the same, the framework placed the pre-processing units closer to the procurement points and farther away from the central SAF facility. That in turn resulted in higher transportation cost between the pre-processing units and the central SAF facility, thus favouring that SAF facility which is closest to the pre-processing units. This is evident in the bar chart in Fig. 7.

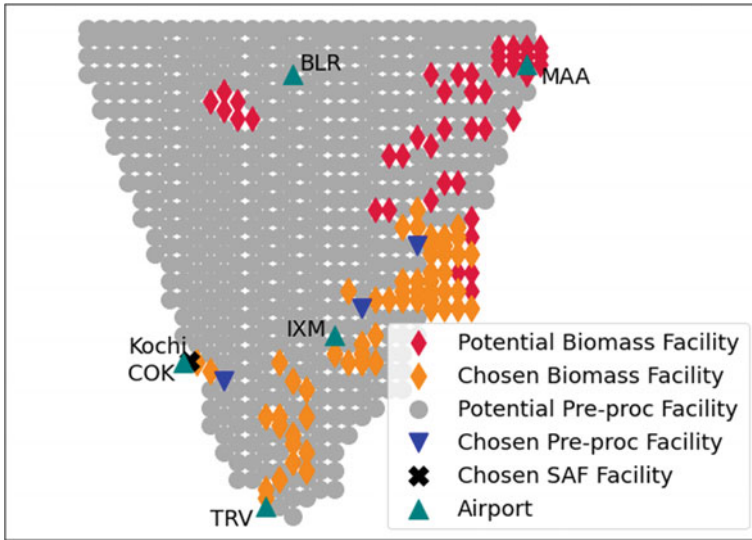


Fig. 6 Optimal supply chain network for a central SAF facility located at Kochi

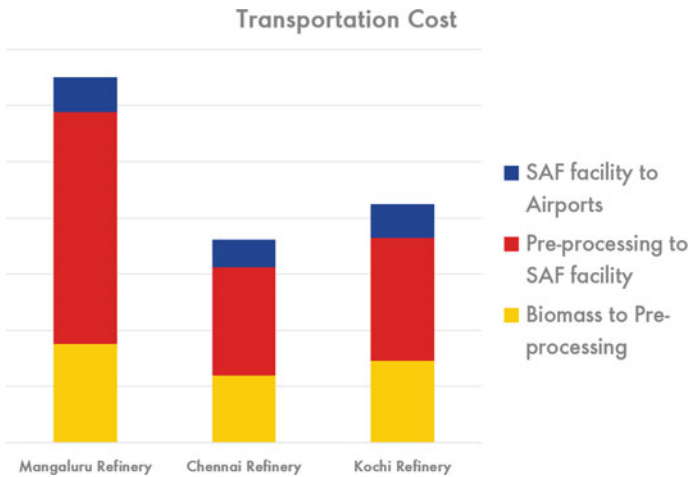


Fig. 7 Breakdown of supply chain transportation costs for each of the three SAF facilities

5 Conclusions and Future work

For this study, FT-based technology is chosen to estimate feedstock requirement based on airport SAF demand. The proposed framework can be extended to alternative technology pathways such as HEFA and ATJ. Furthermore, the results obtained from this study only consider biomass distribution across southern India as shown

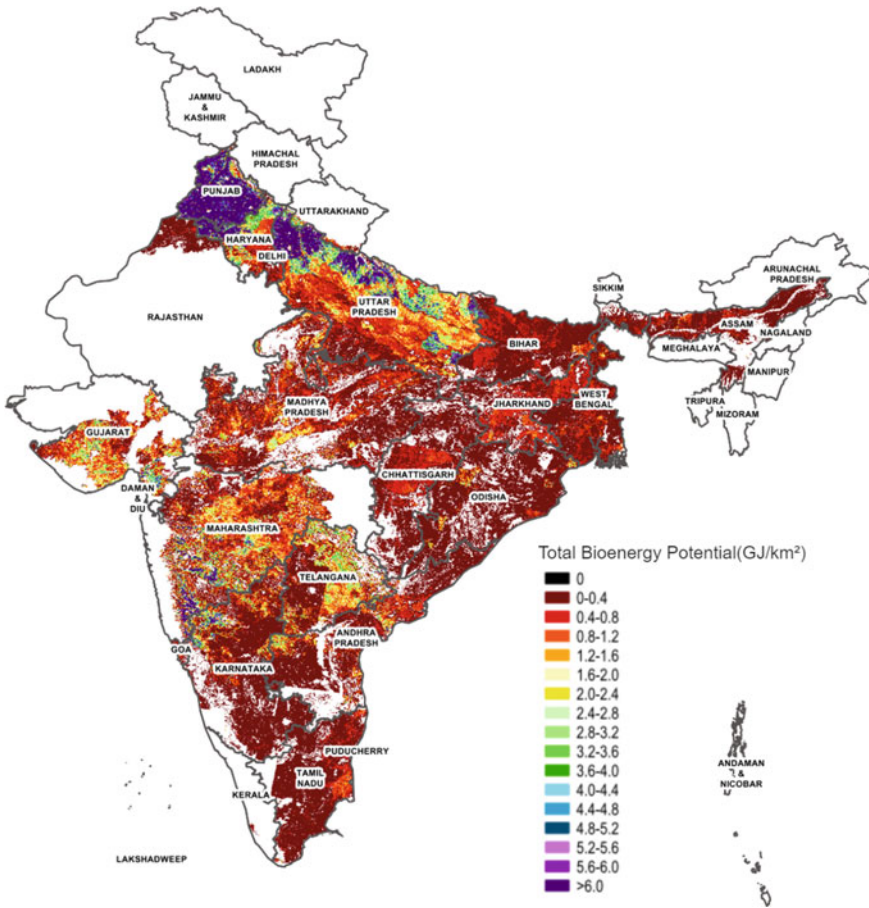


Fig. 8 Bioenergy potential of India [2]

in Fig. 3. However, Fig. 8 clearly highlights biomass availability in higher concentrations in the south-central, western and northern parts of the country. Using the framework described in this paper, further studies can be undertaken considering the effect of these different regions. This paper also assumes uniform cost of procurement of feedstock, transportation, taxation, land cost/availability, etc. The framework can be used to incorporate additional or more accurate input data which will affect the optimum location and capacity of the central facility, pre-processing units and procurement points. Extensions to the current framework in terms of transient supply and demand and multi-objective formulation [6] will aid future case studies on phased implementation of SAF production and supply in India.

On a concluding note, the authors would like to state that a spatial optimization of the supply chain network yields SAF which would still need to be priced significantly higher than the current ATF cost as shown in Fig. 1. The green premium associated

with the price difference must be borne either by the customers or subsidized by the government. To further drive down the premium, a spatio-temporal optimization problem may be formulated, to facilitate a phased role out. Phase-wise expansion of SAF production capacity and commissioning of new central SAF and pre-processing facilities will enable a reduction in the green premium in the initial years particularly in the absence of any government subsidies or incentives.

! Disclaimer

This paper is an independent contribution from the authors and does not represent *Shell* interests in any entities specified in the work and is therefore not to be interpreted as current or future investment proposition from *Shell*.

References

1. Clean skies for tomorrow: sustainable aviation fuels as a pathway to net zero aviation—2020 report. http://www3.weforum.org/docs/WEF_Clean_Skies_Tomorrow_SAF_Analytics_2020.pdf
2. Energy map of India. <https://vedas.sac.gov.in/energymap/view/powergis.jsp>
3. <https://nationalfreightindex.co.in/>
4. Hart WE, Laird CD, Watson J-P, Woodruff DL, Hackebeil GA, Nicholson BL, Siirola JD (2017) *Pyomo—Optimization modeling in Python*, vol 67, 2nd edn. Springer
5. CBC solver. <https://projects.coin-or.org/Cbc>
6. Huang E, Zhang X, Rodriguez L, Khanna M, De Jong S, Ting KC, Ying Y, Lin T (2019) Multi-objective optimization for sustainable renewable jet fuel production: a case study of Corn stover based supply chain system in Midwestern U.S. *Renew Sustain Energy Rev* 115:109403

Analysis of Direct Interplanetary Transfers Using Solar-Electric Propulsion



Suchismita Choudhury, Pooja Dutt, Deepak Negi, Abhay Kumar, and V. Ashok

Nomenclature

A_i, B_i	Coefficients of the parameterizing equations
a_T	Thrust acceleration, m/s ²
\bar{a}_T	Average thrust acceleration, mm/s ²
g	Acceleration due to Earth's gravitation, m/s ²
I_{sp}	Specific impulse, s
m	Spacecraft mass, kg
P	Input power, kW
P_0	Initial power at 1AU
r	Heliocentric radius of the orbit, km
t	Time, s
u	Control variable
v_r	Radial velocity, km/s
v_θ	Transverse velocity, km/s
x	State vector
α	Thrust-steering angle, rad

S. Choudhury (✉) · P. Dutt · D. Negi · A. Kumar · V. Ashok
Vikram Sarabhai Space Centre, ISRO, Thiruvananthapuram, India
e-mail: suchismita_choudhury@vssc.gov.in; smsmita121212@gmail.com

P. Dutt
e-mail: pooja_dutt@vssc.gov.in

D. Negi
e-mail: deepak_negi@vssc.gov.in

A. Kumar
e-mail: abhay@vssc.gov.in

V. Ashok
e-mail: v_ashok@vssc.gov.in

ΔV	Velocity change, m/s
η	Efficiency of the thruster (SEP in this case)
θ	Polar angle, rad
μ	Sun's gravitational parameter, km^3/s^2
θ_f	Total transfer angle, deg
θ_c	Coast arc angle, deg
ψ	Terminal state constraints

Subscripts

f	Final condition
T	Target orbit conditions
0	Initial orbit condition
H	Hohmann transfer (high thrust)

1 Introduction

Low-thrust transfer has been an area of interest for researchers for the past few decades since low-thrust spacecraft can deliver a greater payload fraction for a given space mission compared to chemical-propulsion spacecraft. The trade-off is higher flight duration. Low-thrust trajectory design is an optimization problem to determine a minimum-propellant or maximum-payload trajectory from starting orbit to a destination orbit. Such optimization problems are computationally intensive since there are large number of design variables. Initial trajectory is determined using a low-fidelity model and refined further using medium- and high-fidelity models. The “low-fidelity” models generally consist of analytical expressions so that the trajectory can be obtained quickly and are very useful for preliminary mission analysis and trade-off studies. The low-thrust trajectories are optimized by various indirect or direct method. Indirect methods based on calculus of variations, resulting in a two-point boundary value problem solved by the initial and final conditions is subject to extreme sensitivity to the initial guess of the variables—some of which are not physically intuitive. In direct methods however, the problem is parameterized and nonlinear programming techniques are used to optimize an objective function by adjusting a set of variables. A variety of methods of this type have been examined, and these are subject to the limitations of the nonlinear programming techniques [1, 2, 3, 4, 5].

The present work uses Kluever's analytical method [6] to study the optimal low-thrust trajectories for interplanetary transfers to various asteroids and inner planets. Section 2 gives the methodology, and Sect. 3 lists results and case studies. Section 4 concludes the study.

2 Methodology

The low-thrust trajectory optimisation problem between two coplanar circular orbits is given by [6]:

$$F(X) = -m(t_f) \quad (1)$$

subject to:

$$\dot{x} = f(x, u) \quad (2)$$

with an initial state:

$$x(0) = x_0 \quad (3)$$

and terminal state constraint:

$$\psi[x(t_f)] = 0 \quad (4)$$

So from Eq. (1), it is understood that the main goal of the problem is to obtain an orbit transfer that gives maximum final spacecraft mass or minimum propellant mass consumption.

Equation (2) can be represented by following system dynamics for the planar low-thrust transfer [6]:

$$\dot{r} = v_r \quad (5)$$

$$\dot{\theta} = v_\theta / r \quad (6)$$

$$\dot{v}_r = \frac{-\mu}{r^2} + \frac{v_\theta^2}{r} + a_T \sin \alpha \quad (7)$$

$$\dot{v}_\theta = \frac{-v_r v_\theta}{r} + a_T \cos \alpha \quad (8)$$

$$\dot{m} = \frac{-2\eta P}{(gI_{sp})^2} \quad (9)$$

So the state vector is $= [r\theta v_r v_\theta m]^T$, with $x_0 = [r_0\theta_0 0 \sqrt{\frac{\mu}{r_0}} m_0]^T$ as the initial state vector (where $r_0 = 1$ and initial polar angle $\theta_0 = 0$). The single control is the in-plane thrust-steering angle $u = \alpha$. The thrust-steering angle is measured positive

from the local horizon in the direction of motion. Input power of the system is inversely proportional to the square of the radial distance to the sun, i.e. $P = \frac{P_0}{r^2}$. Thrust acceleration is $a_T = \frac{2\eta P}{(mgI_{sp})}$, changes with mass m and power P [6].

It is assumed that the orbits are circular; for this, three final state constraints are imposed:

$$\psi_1[x(t_f)] = r(t_f) - r_T = 0 \quad (11)$$

$$\psi_2[x(t_f)] = v_r(t_f) = 0 \quad (12)$$

$$\psi_3[x(t_f)] = v_\theta(t_f) - \sqrt{\frac{\mu}{r_T}} = 0 \quad (13)$$

where r_T is the radius of the final orbit. There is no constraint imposed on the final polar angle.

The average thrust acceleration is given by [6]:

$$\bar{a}_T = \frac{1}{2}(a_T(0) + \hat{a}_T(t_f)) \quad (14)$$

where $a_T(0)$ is the initial thrust acceleration at 1AU and $\hat{a}_T(t_f)$ is the final thrust acceleration, i.e. at the target orbit, computed by:

$$\hat{a}_T(t_f) = \frac{2\eta P_0}{r_T^2 \hat{m}_f g I_{sp}} \quad (15)$$

\hat{m}_f is the approximate final spacecraft mass and can be computed using the Hohmann transfer velocity change ΔV_H :

$$\hat{m}_f = m_0 \exp[-\Delta V_H / (gI_{sp})] \quad (16)$$

The optimal trip time (t_f), total transfer angle (θ_f), the coast arc angle (θ_c) and the ΔV can be parameterized using the following function fits [6]:

$$t_f = A_{TOF} + \frac{B_{TOF}}{\bar{a}_T} \text{ days} \quad (17)$$

$$\theta_f = A_\theta + \frac{B_\theta}{\bar{a}_T} \text{ deg} \quad (18)$$

$$\theta_c = A_c + \frac{B_c}{\bar{a}_T} \text{ deg} \quad (19)$$

$$\Delta V = A_{\Delta V} a_T^{-B_{\Delta V}/\bar{a}_T} \quad \text{km/s} \quad (20)$$

where A_i and B_i are the hyperbolic (17–19) and geometric (20) fit coefficients and \bar{a}_T is the average thrust acceleration.

This is Kluever's analytical method [6] to obtain the optimal values of trajectory metrics for both inner and outer interplanetary transfers.

3 Results

Kluever's analytical method is used here to compute the total ΔV and flight duration for low-thrust transfers from Earth to Mars, Venus and various asteroids and is compared with Hohmann transfers (HT). The trajectory metrics have been calculated using Eqs. (17–20). This algorithm takes the initial radii, the target radii, the input power (P_0), the specific impulse (I_{sp}), the efficiency (η) and the initial mass of the spacecraft (m_0) as the input. Further, it computes the Earth Orbit Equivalent (EOE) radii for the inner or outer transfer, and the average thrust acceleration is calculated. The HT solution can also be calculated for this EOE radii. The EOE radii and the curve-fit coefficients are used for computation of curve-fit equations EOE trajectory parameters, and finally by scaling technique, we get the desired trajectory parameters [6].

For computation of ΔV , transfer time and mass of propellant consumed, using Kluever's analytical algorithm, the example of an SEP ion propelled system that has an initial mass $m_0 = 1300$ kg, initial power $P_0 = 12$ kW, specific impulse $I_{sp} = 3100$ s and efficiency $\eta = 0.65$ is considered [6]. Using these inputs, the ΔV , transfer time and mass of propellant consumed are calculated. For the Hohmann transfers, the specific impulse is taken to be $I_{sp_h} = 310$ s. Figure 1 compares the low-thrust and Hohmann transfers ΔV , time of transfer and mass of propellant consumed for various asteroids. It can be observed that though ΔV and time of transfer are more for the low-thrust transfer as compared to that of Hohmann transfer, there is a significant reduction in propellant mass consumption in case of low-thrust transfers over Hohmann transfer.

Further analysis was carried on to check the trend of trajectory parameters by varying the average thrust acceleration. It was expected that with increase in the average thrust acceleration the trajectory parameter will approach the Hohmann transfer (or high thrust) solution. Cases for various asteroids, Mars and Venus were studied.

In Figs. 2 and 3, with increase in the average thrust acceleration the transfer angle θ_f decreases and approaches the Hohmann transfer value of 180° . For transfer to a fixed target circle (1.523 AU and 2.360 AU, respectively), the coast arc increases and approaches the Hohmann transfer value of 180° . The coast arc becomes zero for very low-thrust acceleration, where the optimal orbit transfer consists of a single powered arc without coasting. As the average thrust acceleration becomes large, the

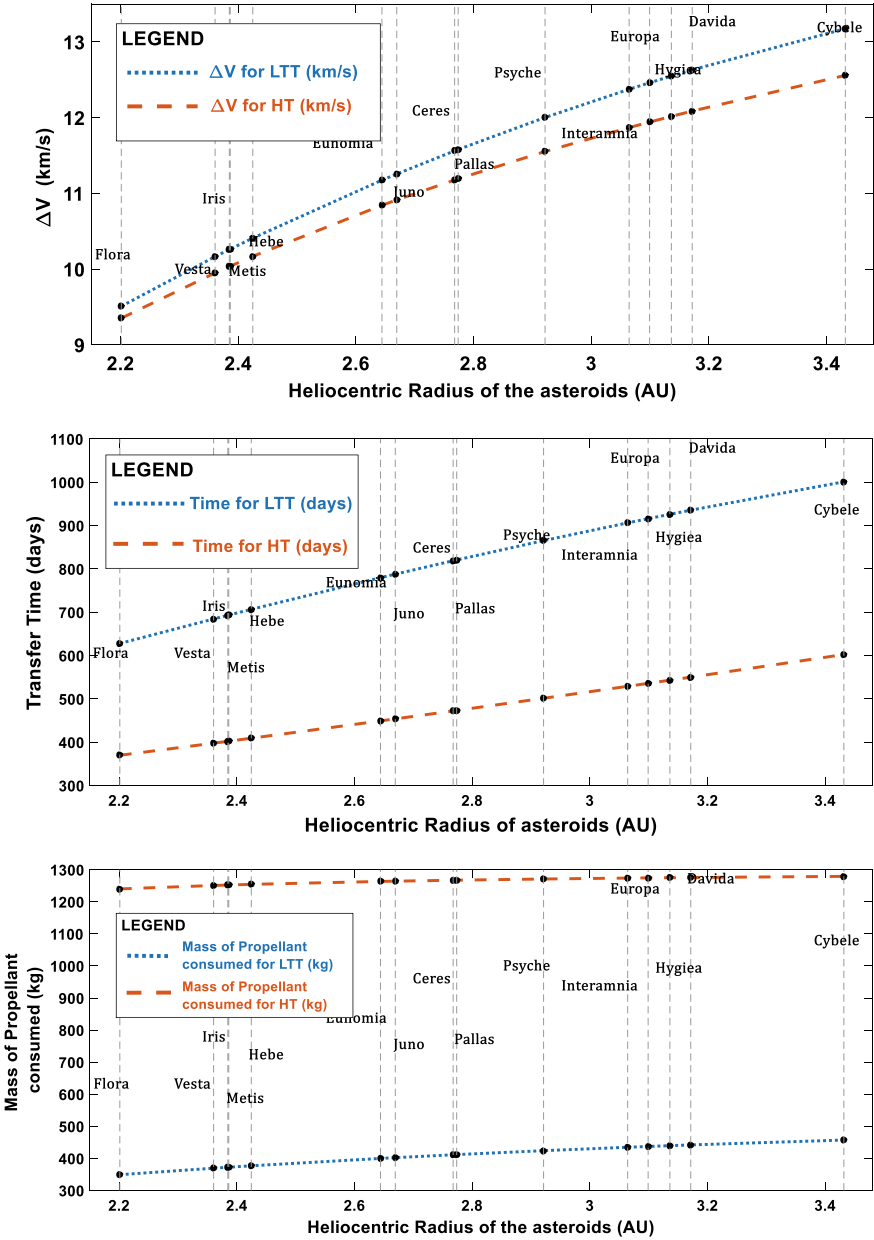


Fig. 1 Comparison of low-thrust and Hohmann transfer **a** ΔV , **b** time of transfer and **c** mass of propellant consumed for transfer from Earth to various asteroids

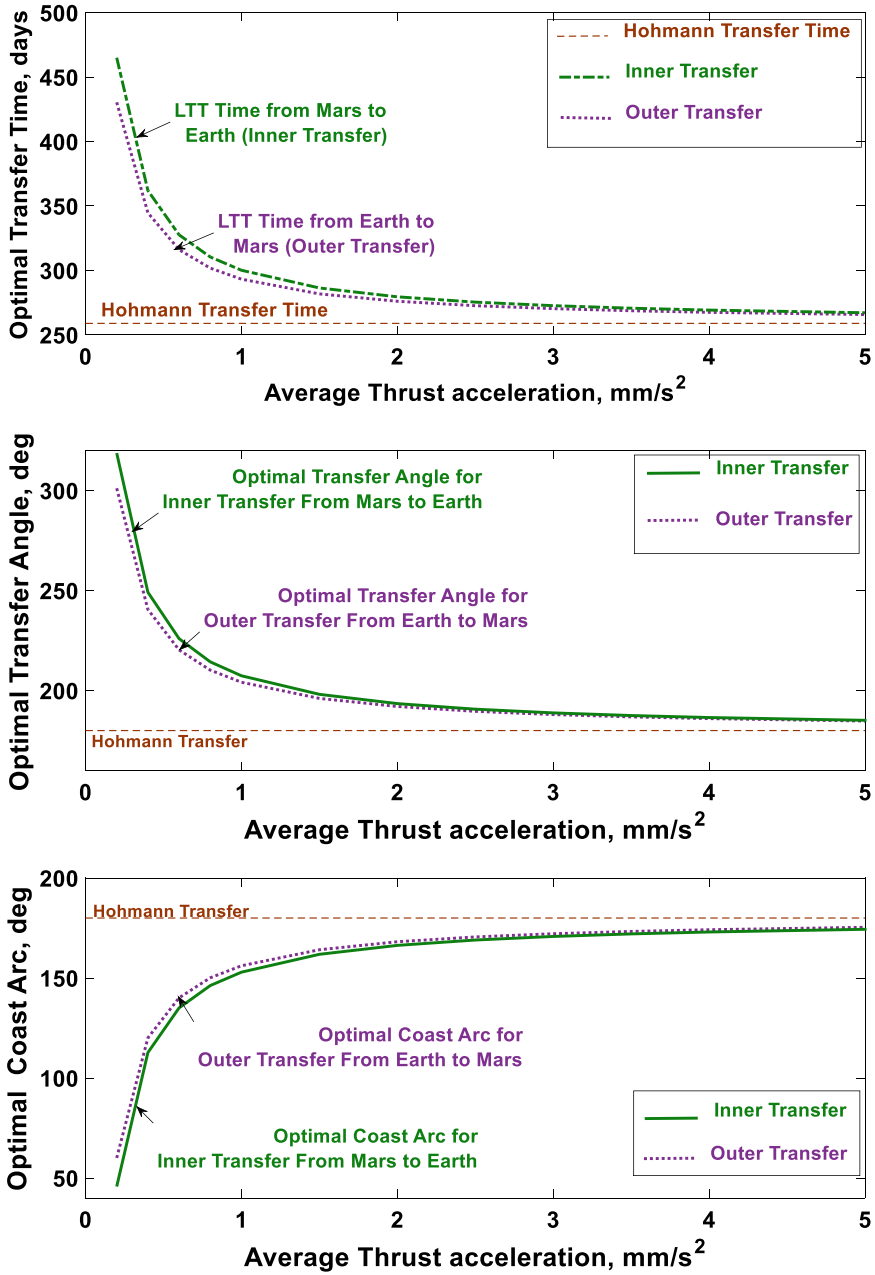


Fig. 2 Optimal a transfer time, b transfer angle, c coast arc and d LTT ΔV as a function of avg. Thrust acceleration for inner and outer transfer of Mars (1.523AU)

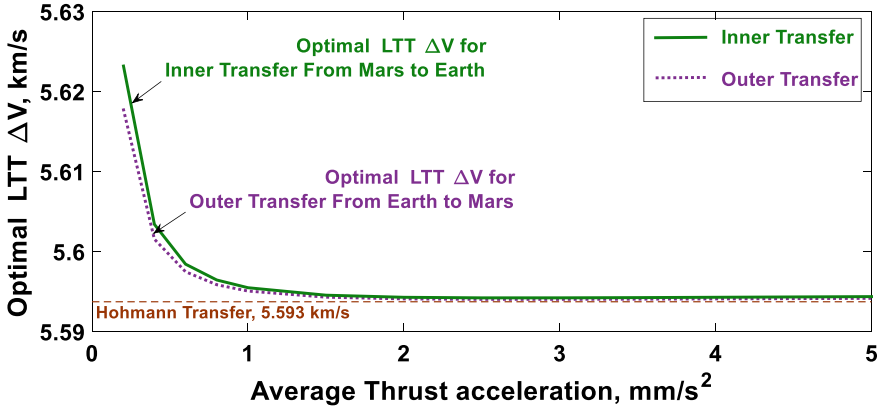


Fig. 2 (continued)

powered arcs become shorter, the coast arc increases, and the transfer time approaches the Hohmann solution. As the average thrust acceleration increases, the coast arc approaches its optimal solution (180° as in Hohmann transfer) and low-thrust ΔV approaches ΔV_H . However, in case of inner planet Venus, the results obtained from the analytical method deviate from the expected trend.

From Fig. 4, it can be observed that for the Venus, the variation in transfer time and ΔV deviates from the expected trend. For the transfer time, the optimal transfer time crosses the Hohmann transfer time in $0.4\text{--}0.6\text{ mm/s}^2$ and does not asymptotically approach the expected optimal solution. For Δv , it does not even approach the Hohmann solution rather the graph becomes parallel to the Hohmann solution line.

Also for outer asteroids like Hygiea (Radii 3.136 AU) as shown in Fig. 5, the analytical solution fails to give the expected trend. In this case, the transfer angle and coast arc first decrease and then increase with increase in average thrust acceleration, violating the regular trend.

4 Conclusion

Cluever’s analytical algorithm to obtain an optimal low-thrust direct interplanetary transfers using SEP [6] is studied and presented here. The advantage of this analytical method is that we can get quick estimate for trajectory metrics (namely ΔV , transfer time, transfer angle, coast arc and propellant mass) for a given average thrust acceleration value. This “low-fidelity” trajectory design tool is very helpful for preliminary mission design and analysis purposes. Both inner (transfer from outer radius to inner radius) and outer transfers can be computed using this method.

This algorithm has been used to obtain ΔV and transfer time for transfer from Earth to Mars and various asteroids. Also, detailed analysis is carried out for inner

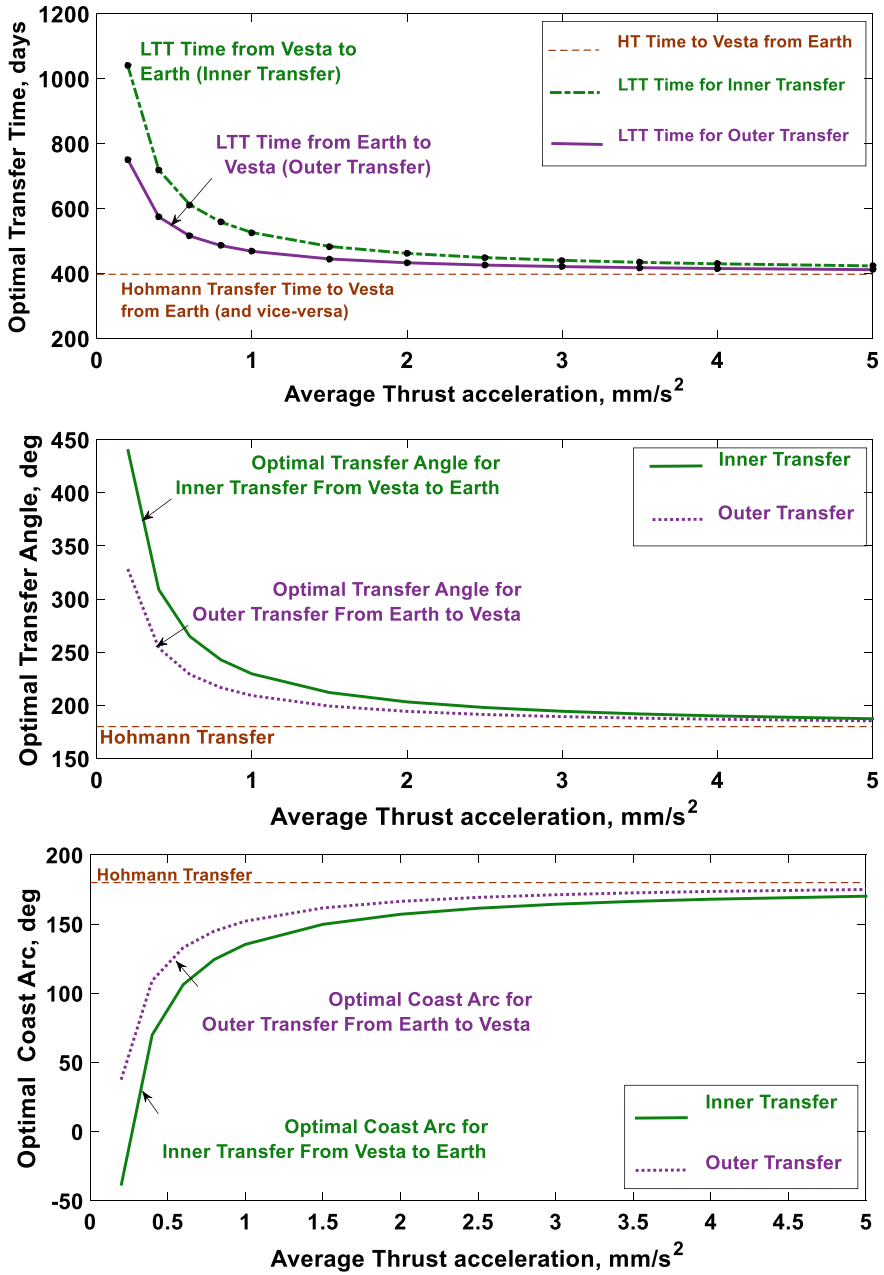


Fig. 3 Optimal a transfer time, b transfer angle, c coast arc and d LTT ΔV as a function of Avg. Thrust acceleration for inner and outer transfer for Vesta (Radii 2.360 AU)

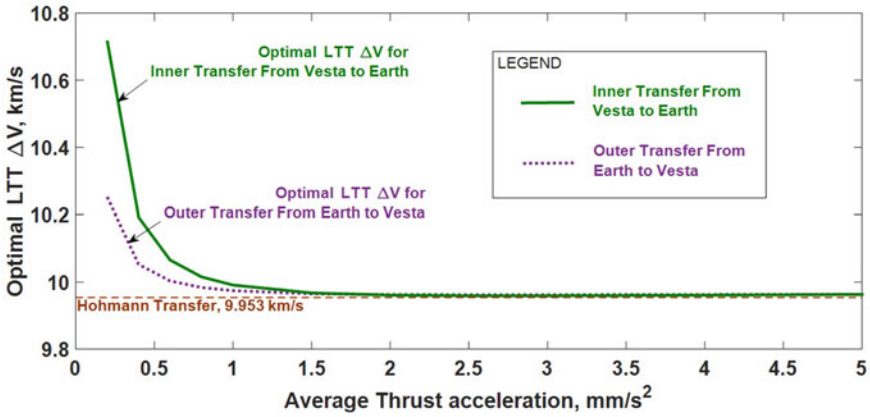


Fig. 3 (continued)

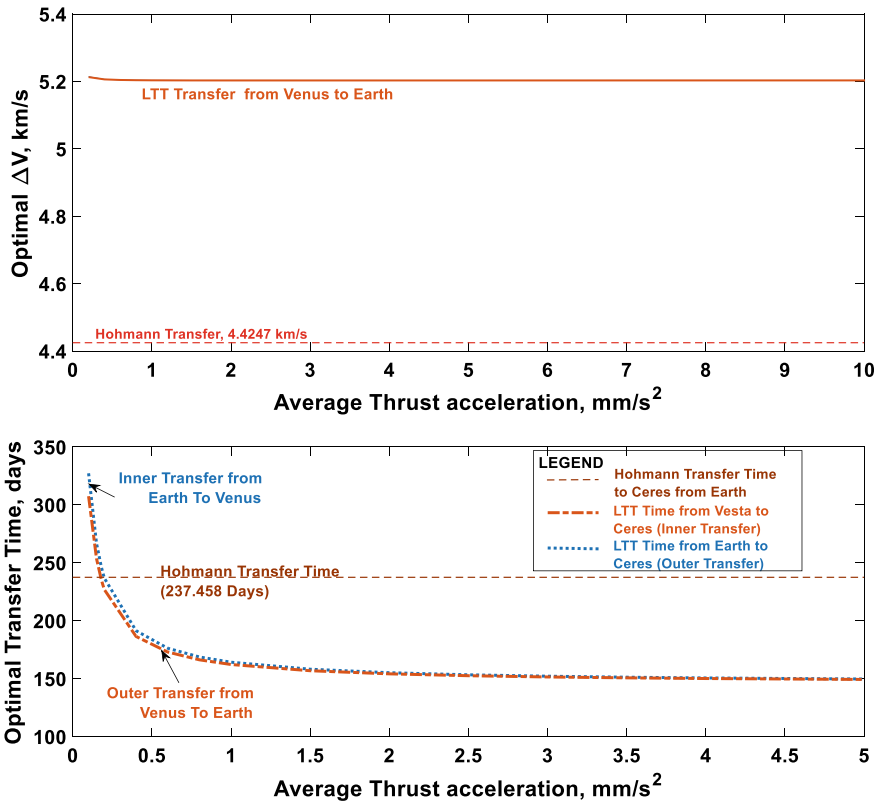


Fig. 4 Optimal a transfer time and b LTT ΔV versus average thrust acceleration for inner and outer transfer of Venus (Radii 0.723 AU)

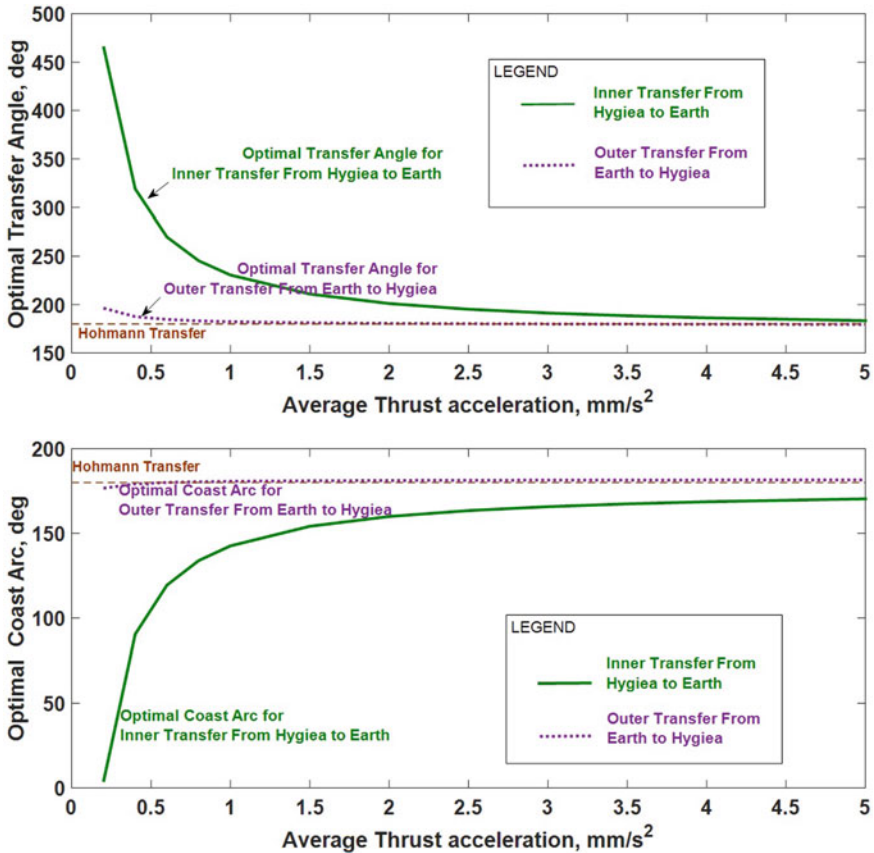


Fig. 5 Optimal **a** transfer angle and **b** coast arc as a function of Avg. Thrust acceleration for inner and outer transfer for Hygiea (Radii 3.136AU)

and outer transfers to/from Vesta, Mars, Hygiea and Venus. This paper also brings out the grey areas where this algorithm fails to give optimal estimates.

Acknowledgements The authors are grateful to Shri Jaison Joseph and Shri C. Ravikumar for their guidance, encouragement and suggestions throughout the work.

References

1. Bate RR, Mueller DD, White JE (1971) Fundamentals of astrodynamics. New York, Dover
2. Flanagan SN, Sims JA Preliminary design of low-thrust interplanetary missions
3. Flandro G (1966) Fast reconnaissance missions to the outer solar system utilizing energy derived from the gravitational field of Jupiter. Astronautica Acta 12(4)

4. Williams SN, Coverstone-Carroll V (1997) Benefits of solar electric propulsion for the next generation of planetary exploration missions. *J Astronaut Sci* 45(2):143–159
5. Wilson A (1990) *Space directory*. Jane's Information Group Inc., Alexandria, VA
6. Kluever CA (2015) Efficient computation of optimal interplanetary trajectories using solar electric propulsion. *J Guidance Control Dyn* 38(5)

A Multi-fidelity Aeroelastic Optimization of an Aircraft Wing Using Co-Kriging



Partha Ajit Surve, Palaniappan Ramu, and Devendra Ghate

1 Introduction

The twenty-first century has witnessed increasing sophistication in production for better performance. This has led to increasingly complex designs and algorithms. Even a minor increase in efficiency or energy saving can lead to reduced wastage and increased profit margins. In order to achieve this goal, various design optimization strategies are employed, which can be multi-disciplinary as well as multi-objective in nature. Especially, in aerospace and aircraft industry which involve numerous disciplines, Multi-disciplinary Optimization (MDO) can aid in exploring the design space and the interactions between the disciplines while providing a synergetic optimum solution.

The aircraft wing design, which has been a focus of numerous such studies in the past, is a good example of a multi-disciplinary design problem. A study by Breittkopf and Coelho [1] discusses the aeroelastic optimization problem of a supersonic business plane wing. The objective of their study was to determine the optimal wing thickness so as to minimize the supersonic drag and at the same time satisfying the aeroelasticity constraints. A sole aerodynamic optimization would lead to reduced wing thickness in order to reduce the wave-drag while the structural optimization would avoid very thin wings to prevent aeroelastic flutter problems. Paiva [2] have developed an MDO tool to carry out a preliminary design of wing. The aerodynamic

P. A. Surve (✉)

Vikram Sarabhai Space Centre, Thiruvananthapuram, Kerala 695022, India
e-mail: partha_surve@vssc.gov.in

P. Ramu

Indian Institute of Technology Madras, Chennai, Tamil Nadu 600036, India
e-mail: palramu@iitm.ac.in

D. Ghate

Indian Institute of Space Science and Technology, Thiruvananthapuram, Kerala 695547, India
e-mail: devendra.ghate@iist.ac.in

module uses vortex lattice code while the structural module employs equivalent plate model theory. Though such studies are prevalent in both academia as well as industry, they face a common bottleneck with respect to the high computational cost of implementing MDO with high fidelity disciplinary codes. The motivation behind this study was to develop an optimization process that explores the design space for any given multi-disciplinary problem effectively and at a lower computational cost without compromising on the accuracy of the solution. Thus, to circumvent this bottleneck, the Multi-disciplinary Analysis (MDA) [3] component of the optimization process was replaced with a multi-fidelity surrogate model. In recent years, numerous studies have been conducted on incorporating multi-fidelity strategies into MDO framework. Toal [4] discusses the factors that need to be taken into account while using multi-fidelity data to generate surrogate models.

Thus, in the present study, aircraft wing optimization problem has been used as a prototype to validate the MDO algorithm since it incorporates two of the most important disciplines, namely aerodynamics and structures. It can also be posed with multiple objectives. To relieve the computational cost of high fidelity solvers, the use of Co-kriging [5]—a multi-fidelity surrogate model is proposed. The resulting optimum wing configuration showed considerable improvement in performance compared to the baseline. A sensitivity analysis was also carried out to capture the correlation between the various design variables. The subsequent sections outline the optimization problem definition, methodology along with the relevant results and conclusions. All the flight mechanics symbols have their usual meaning.

2 Problem Definition

Wing design is very important in aircraft development. The aircraft performance and flight quality are heavily dependent on it. It is also a crucial component since it bears the varying loads during the entire flight regime. The current section provides details on the objective function, design variable and constraints employed in the current study.

2.1 Objective

Aircraft spend nearly 57% of their flight time in cruise condition at Mach 0.8 in the transonic regime as seen in Fig. 1a. In order to ensure better fuel efficiency, transonic drag (C_d) at cruise condition has to be minimized. Similarly, the weight (W) of the wing also plays a crucial role in aircraft performance. Thus the overall weight of the wing also needs to be minimized to ensure efficiency and profitability. Appropriate weights are provided to each of the objectives in the form of α and β in the final cost

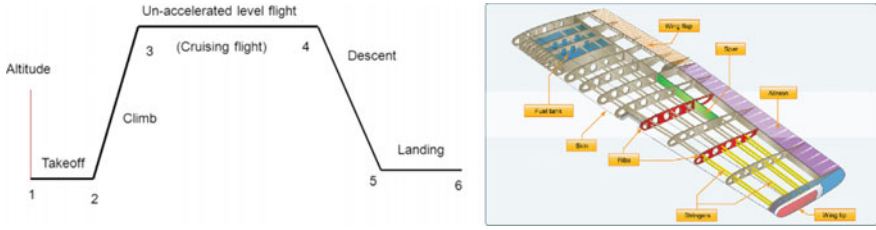


Fig. 1 a Mission profile of a civilian aircraft and b Internal structure of a typical aircraft wing [www.nomenclatur.com]

function ($\alpha = \beta = 0.5$). Thus, the twin objectives during cruise flight at Mach 0.8 at 10 km altitude can be posed as follows,

$$\text{Min}\{ \alpha C_d|_{M=0.8} + \beta W \} \tag{1}$$

2.2 Design Variables

The wing geometry was parametrized using a total of 11 design variables (10 continuous, 1 discrete). The airfoil cross-section is maintained constant throughout the wing, and the twist angle, leading edge and trailing edge sweep angles and dihedral angle are considered to be zero for simplification purpose. The airfoil shape was generated using a second-order Class Shape Transformation (CST) [6] with a total of six weight coefficients ($C1$ to $C6$).

A typical internal wing geometry is shown in Fig. 1b, which consists of various components such as ribs, stringer, skin and spars to provide structural rigidity. A compromise needs to be made on the weight contribution of each of these components and their contribution to the structural rigidity. The structural geometry of the wing was explored using five design variables, namely skin thickness, number of ribs, thickness of ribs, diameter of stringers and half span of the wing. The wing consist of four stringers and has a root chord of 3m. For simplification purpose, spars are not modelled.

2.3 Constraints

Aerodynamic as well as structural constraints were implemented in order to ensure the practicality of the final solution. Material properties of Aluminium alloy were utilized since it is one of the most widely used material in aircraft industry due to its light-weight and high strength. Constraints were placed on the maximum von-Mises

stress experienced by the structure ($\sigma_{\text{von-mises}} < 180 \text{ Mpa}$) with a factor of safety of 1.55. As the wing deflects, it leads to a lesser component of upward lift force, thus a constraint was implemented on the maximum allowable tip deflection of the wing.

Since one of the objectives is to minimize C_d , it may also leads to reduction in lift. For the wing to produce sufficient lift to maintain level flight during the cruise condition, a constraint needs to be placed on the aerodynamic efficiency ($E = C_l/C_d \geq 5$). It's possible that during optimization a thin airfoil is generated which in real life is not manufacturable. Thus a constraint needs to be placed on the minimum allowed thickness of the airfoil. Appropriate box constraints were imposed on all the 11 design variables. The subsequent section highlights the optimization methodology used to explore the defined design space.

3 Methodology

Exploring the design space with the 11 design variables discussed in the previous section with a conventional MDO algorithm and high fidelity disciplinary codes can be extremely challenging. The current study utilizes a multi-disciplinary feasible architecture (MDF) [3]. In an MDF architecture, the most computationally expensive part is the MDA loop. For a fluid-structure interaction (FSI) problem like the one at hand, at every design iteration, initially, the geometry is created using the design variables, then the flow solver is called upon and the displacement field of the structure is initialized to zero. After the flow solver has converged, the surface pressures are translated into nodal forces, and the structures solver is called upon. The new displacement field is then used to deform the CFD mesh and the flow solver is initiated again. This process continues until the norm of the flow solver and structural solver residuals has converged or the max number of iterations have been reached.

In the current study, the MDA loop is replaced with a multi-fidelity surrogate model using Co-kriging. The overall flow chart of the MDO methodology is outlined in Fig. 2a. Firstly, based on the 11 design variables initialized, a total of 100 design points were generated using Latin Hypercube Sampling. Out of which, 30 were used to perform high fidelity MDA simulations and the rest were used for low fidelity MDA simulations. The high fidelity MDA utilized unstructured Reynolds Averaged Navier-Stokes solver in FLUENT for aerodynamics and ANSYS® structural solver. For low fidelity MDA, Euler solver was used with the same structural solver. In this particular study, ANSYS® workbench is used to setup the FSI coupling, FLUENT is used for solving the flow physics around the wing and transient structural module is used for the structural domain. The analysis was carried out with unstructured mesh, and grid convergence studies were carried out for both the meshes. Figure 2b shows the wing geometry while Fig. 2c shows the CFD mesh. Appropriate environmental boundary conditions were implemented corresponding to the wing being at cruise condition at 10 km altitude with an Angle of Attack of 8° and the free stream velocity of Mach 0.8. A high fidelity MDA routine run had a computational time of 4 h while the low fidelity runs were of 30 min.

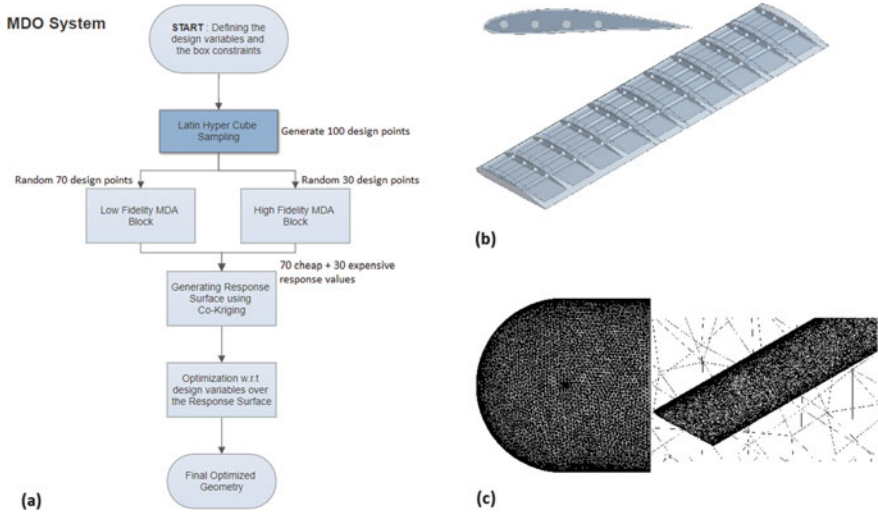


Fig. 2 a Flow chart of the optimization process, b Baseline Wing planform geometry and c CFD mesh of the domain and the refined mesh near the wing surface

The evaluated C_1 , C_d , $\sigma_{\text{von-mises}}$, δ and weight were stored and used to construct the Co-Kriging surrogate model. Genetic Algorithm was used as the optimizer at the top of the architecture in order to evaluate the optimal design with respect to design variables which minimizes the objective while satisfying the constraints. The optimization and the sensitivity analysis results are outlined in the subsequent section.

4 Results and Discussion

The comparison of outputs from the baseline and optimized geometry is provided in Table 1. The aerodynamic coefficients C_1 and C_d showed improvement of 4.69% and 17.9%, respectively, compared to the baseline values. The structural weight of the optimized geometry was reduced by 355.7 Kg, and there was 14.54% reduction in the max von-Mises stress in the optimized structure. The tip displacement has increased by 17.85 cm but it's still within the allowable displacement values. This is the result of the trade-off between weight and max stress. The deflected geometry of the wing is compared with the original geometry in Fig. 3a, this deflection is caused due to the action of aerodynamic forces on the wing surface.

A sensitivity analysis was carried out for the response values (C_1 , C_d , $\sigma_{\text{von-mises}}$, δ and W) with respect to the 11 design variables. Figure 3b shows one such contour plot highlighting the nonlinear correlation between skin thickness (t_{skin}) and number of ribs (N_{rib}) in the wing. It can be seen that as both t_{skin} and N_{rib} increase the C_1 also increases. This is because C_1 reduces for a wing with more deflection while both

Table 1 Comparison of response values between baseline and optimized geometries

	C_l	C_d	Weight (kg)	$\sigma_{\text{von-mises}}$ (Pa)	Displacement (m)
Baseline geometry	0.949	0.246	9270.6	1.65E+08	0.289
Optimized geometry	0.994	0.202	8914.9	1.41E+08	0.468



Fig. 3 a Comparison between original and displaced geometry for the optimized design point and b Variation of coefficient of lift with No. of ribs and skin thickness

t_{skin} and N_{rib} aid in stiffening the wing. Thus even structural parameters affect the aerodynamic coefficient of the wing which couldn't be captured in the case of a rigid wing with weak coupling.

5 Conclusion

A successful and computationally inexpensive coupled aeroelastic wing optimization methodology has been demonstrated using MDF architecture. Co-kriging-based surrogate model was shown to capture the design trends with a reduced number of high fidelity simulations. The optimum configuration showed improved performance compared to the baseline. This methodology can be seamlessly extended to other problems in aerospace industry.

Acknowledgements We are grateful to the Engineering Design department and CSG group of IIT-M for providing the necessary technical insight, software and computational power.

References

1. Breitkopf P, Coelho RF (eds) (2013) Multidisciplinary design optimization in computational mechanics, Chapter 1. Wiley
2. Paiva RM (2007) Development of a modular MDO framework for preliminary wing design. Ph.D. dissertation
3. Martins JRR, Andrew N (2021) Engineering design optimization, pp 471–534

4. Toal DJ (2015) Some considerations regarding the use of multi-fidelity Kriging in the construction of surrogate models. *Struct Multidisc Optim*, 1223–1245
5. David M (1977) *Geostatistical ore reserve estimation*. Elsevier, Amsterdam
6. Kulfan BM, Bussioletti JE (2006) ‘Fundamental’ parametric geometry representations for aircraft component shapes. In: 11th AIAA/ISSMO multidisciplinary analysis and optimization conference. AIAA, Portsmouth

Effect of Pulsed Fuel Injection on Scramjet Combustion Efficiency Using OpenFOAM



Singeetham Pranaykumar and Akshay Prakash

1 Introduction

Supersonic combustion ramjet happens to be most viable choice in powering the vehicles to hypersonic speeds. Successful scramjet design can decrease the launch vehicle cost significantly by utilizing the atmospheric oxygen during its flight and to reduce the total propellant required placing a payload into orbit. Despite having many advantages, this technology advancement has potential challenges. One of such challenges is achieving sustained and efficient combustion to produce useful thrust. The short residence time of the flow becomes an issue to attain efficient fuel–air mixing.

In order to overcome the issue of mixing and combustion, cavity configuration attachment to the combustor wall has been proposed. It can promote and stabilize the ignition and also improves the mixing. Gruber et al. [1] investigated the effect of offset ratio and ramp angles of the cavity for improving the fundamental understanding of flame holding mechanism in the presence of supersonic flow field. Independent to that of the cavity geometry, a commonly used fuel injection scheme for the scramjet combustor is transverse or wall normal fuel injection scheme. The flow structure associated with the wall normal injection has been studied in detail by various authors in the past. Kouchi et al. [2] found that the penetration height of the pulsed jet is higher than the steady injection in the case of wall normal fuel injection scheme.

Most of the research on cavity configuration is based upon the fuel injectors located inside or in front of the cavity. Although cavity possesses better flame holding characteristics, the interaction of the cavity flowfield and shock structure of the fuel injection slot is limited in the conventional cavity based scramjet combustor.

S. Pranaykumar (✉) · A. Prakash
Indian Institute of Technology, Kharagpur, India
e-mail: pranaysingeetham94@iitkgp.ac.in

A. Prakash
e-mail: ap@aero.iitkgp.ac.in

The objectives of the present study are to examine the effect of pulsed fuel injection frequency on the combustion efficiency, and simulations have been carried out with a cavity mounted upstream of the injection for two L/D ratios to understand the flow features. Dakota software [3] is used to solve an unconstrained optimization problem.

2 Numerical Approach

2.1 Flow Solver

OpenFOAM [4] has become a widely used C++ toolbox for solving variety of computational fluid dynamics problems based on finite volume framework. The solvers and various functionalities that are present in OpenFOAM has been tested and validated in many research fields. The flow governing equations of mass, momentum, energy and species equations are solved using URANS framework. In the present work, rhoCentralFoam [5] and reactingFoam solvers were chosen to build a new solver to simulate high-speed reacting flows. The convective terms are discretized using a second-order central upwind schemes of Kurgnaov, Noelle and Petrova (KNP) [5, 6], and diffusion fluxes are evaluated through the central differences. Temporal derivative is calculated with the Euler discretization of first-order accurate scheme. K-Omega-SST model is used to model the turbulence and the chemistry is modeled using 9 species 27 reactions steps of H₂-O₂ mechanism [7].

2.2 Validation

It is observed that the use of cavity configuration upstream to the fuel injection has not been studied before, and there is no experimental details available for this particular configuration [8]. Two independent test cases have been considered to validate the present solver which captures the fundamental flow structures such as jet-freestream interaction and cavity flows. It is reasonable to assume that the validation of the above cases can also model the combined flow field. Experimental and computed stream trace data of Gruber et al. [1] are used to compare the current simulation results. Figures 1 and 2 show the normalized pressure profiles along the cavity wall and streamline pattern for L/D ratios of 3 and 5, respectively.

The experiment conducted by Aso et al. [9] is used to validate the present numerical model for simulating the transverse fuel injection into main freestream flow. The computational domain has a fuel injection slot width of 1 mm which is located 330.5 mm from the leading edge of the plate, and the exit plane of the domain is located 221.5 mm from the centerline of the injection port. The details of the flow condition are available from the literature [9]. In the present case, jet-to-freestream

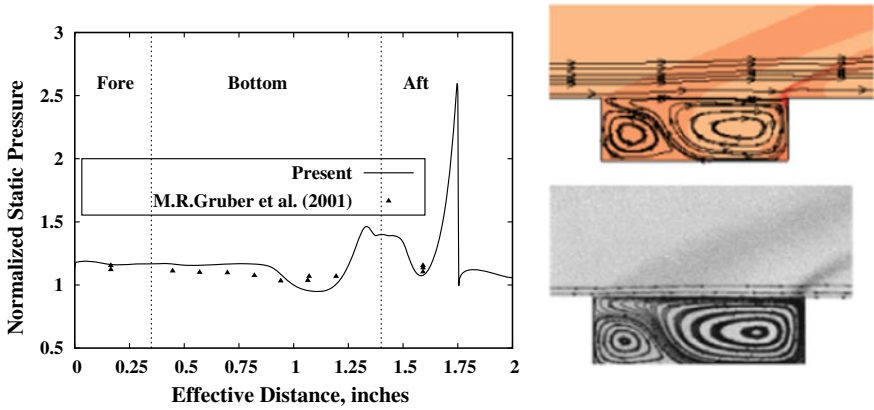


Fig. 1 Normalized static pressure variation along the cavity wall at $L/D = 3$ and comparison of computed stream traces

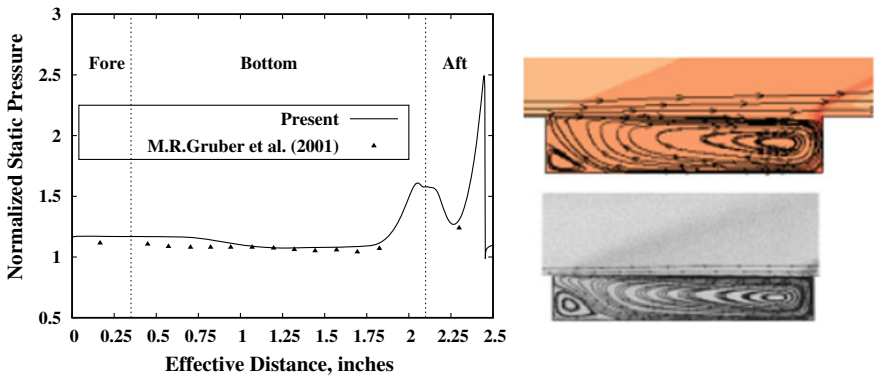


Fig. 2 Normalized static pressure variation along the cavity wall at $L/D = 5$ and comparison of computed stream traces

pressure ratio of 10.29 is selected. Normalized wall static pressure profile and flow structure around transverse jet are shown in Fig. 3. It is observed that the computational results are in reasonable agreement with experimental data.

2.3 Geometry, Boundary Conditions and Performance Parameters

The computational domain used in the present study is shown in Fig. 4. The leading edge of the cavity is located 29.5 mm from the inlet. The length of the cavity is 24 mm and depth is 1.2 and 4.8 mm for L/D ratio of 20 and 5, respectively. The inflow

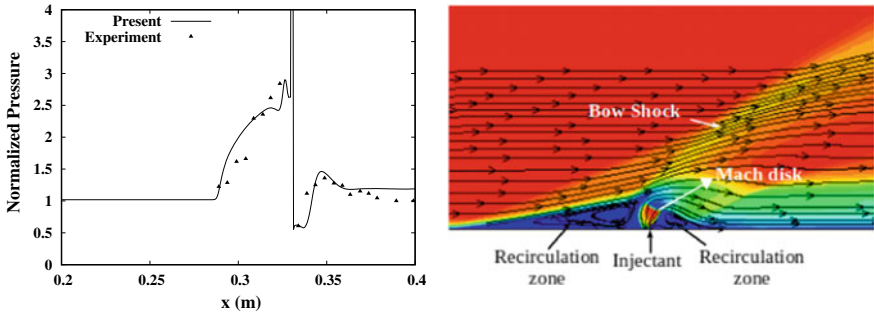


Fig. 3 Normalized static pressure variation with transverse injection and representation of the flow field

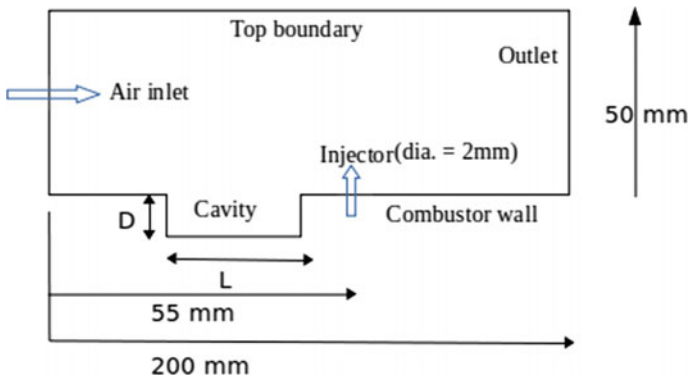


Fig. 4 Computational domain of an upstream cavity configuration

conditions are representation of an experiment with a static pressure of 0.341 atm, a static temperature of 1172 K and a Mach number of 2.05. Fuel is injected normal to the combustor wall at a total pressure of 189,292 Pa and total temperature of 360 K. Combustor walls are defined as adiabatic, and no slip condition is applied. For supersonic freestream and fuel inlet, fixed values of pressure, temperature and velocity are specified. Outflow boundary has been specified with Neumann conditions in which all variables are extrapolated from the inner domain.

Pulsed injection is defined as the pressure of the fuel jet inlet which is varying with time and variation follows sinusoidal with an amplitude (a) of 10^5 Pa, a steady injection pressure of 10^5 Pa and frequency of f , kHz is chosen. In order to study the effect of pulsed fuel injection on combustion efficiency, 6, 8, 10, 16, 20, 26, 30, 40 and 50 kHz frequencies are considered. Combustion efficiency is evaluated from the mass fraction of H_2O [10].

3 Results and Discussion

Cavity configuration modifies the flowfield around the wall normal injection jet. Location of the cavity placed upstream to the fuel injection could reduce the effect of bow shock due to the formation vortex structure inside the cavity and it further reduces the total pressure losses. Figure 5 shows contours of Mach number along with the streamline pattern and contours of pressure for two L/D cavity geometries. In the case of L/D ratio of 5, cavity vortex structure extends more into the core flow as compared to L/D ratio of 20. Due to this reason, shock structure in the vicinity of cavity and fuel jet shifts slightly upstream and fuel jet is exposed to different pressure levels in the case of L/D ratio 5. It is also observed that the penetration height is increased slightly than that of L/D ratio 20. This effect can be understood from the location of shock interactions which is above the large vortex structure behind the fuel injection. Location of the shock interaction is 74 mm from the inlet for L/D ratio 5 and it is 80 mm for the case of L/D ratio 20. Here, the bow shock places an important role in changing the shock interactions and penetration height. The near field mixing and combustion can have a great influence on the flame stabilization and length required for complete combustion would be smaller which can lower the weight of the engine.

Combustion efficiency is calculated at $x = 75, 125, 165, 195$ mm from the center-line of the injection port. Figure 6 shows the effect of pulsed excitation frequency on combustion efficiency at the specified x locations. Efficiency increases as the fuel jet frequency increases due to enhancement of fuel–air mixing. At a particular x location, frequency increases, reaches a maximum value and slightly decreases or reaches near plateau variation. The efficiencies corresponding to this variation are still above the steady injection efficiency. Steady fuel jet combustion efficiency corresponds to zero frequency value as shown from the Fig. 6. It was pointed out that there is an optimum frequency range for which performance can be enhanced. Too high or too

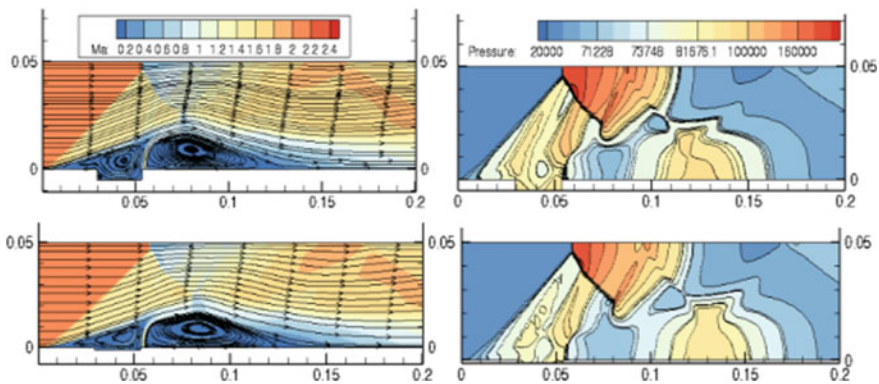


Fig. 5 Contours of Mach number for $L/D = 5$ (top left) and $L/D = 20$ (bottom left) and contours of pressure for both cases (right)

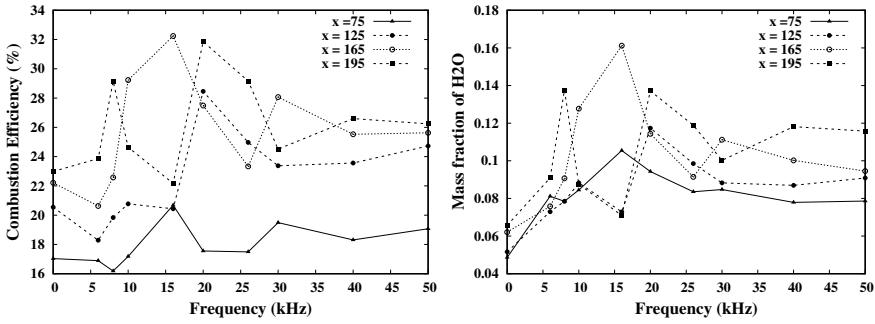


Fig. 6 Effect of pulse jet frequency on combustion efficiency and mass fraction of H₂O

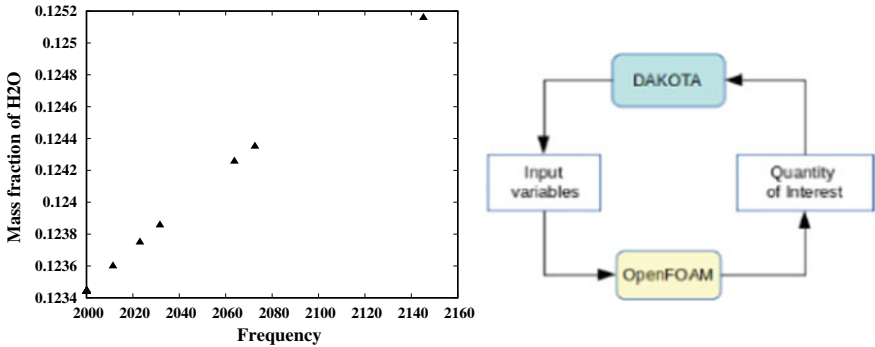


Fig. 7 Effect of frequency on mass fraction of H₂O and OpenFOAM-Dakota workflow

low frequency of the jet approach to the steady jet mode [11]. The area weighted average mass fraction of H₂O also shows the similar trend of combustion efficiency.

Fletcher-Reeves conjugate gradient is used to solve the unconstrained optimization problem. In this work, objective function is selected as the production of water vapor. The principal goal of optimization is to maximize the combustion by burning most of the fuel that is injected. The OpenFOAM-Dakota interface has been setup to maximize the mass fraction of H₂O at a specified location ($x = 90$ mm) by selecting the frequency of injection as a design variable space. From the Fig. 7, it has been observed that there is no significant improvement in the variation of the mass fraction of H₂O and this behavior of response function also changes the frequency input to very minimal. The range of design input parameter is 2–5 kHz. One of the ways to improve this method of optimization is to provide more constraints and increase number of design variable to meet the specific objective function requirement. The refinement in the design variables could predict better solution. This basic study has demonstrated the feasibility of coupling computational fluid dynamic solver with an open source toolbox of various optimization utilities. This is motivating in the further enhancement of the study and this approach could lead to achieve good inputs to develop an efficient scramjet engine.

Acknowledgements Most of the simulations were carried out on the Param Shakti supercomputer. We acknowledge Param Shakti National Supercomputing Mission, Government of India, for providing the computational resources.

References

1. Gruber MR, Baurle RA, Mathur T, Hsu K-Y (2001) Fundamental studies of cavity-based flameholder concepts for supersonic combustors. *J Propul Power* 17:146–153
2. Kouchi T, Sasaya K, Watanabe J, Sibayama H, Masuya G (2010) Penetration characteristics of pulsed injection into supersonic crossflow. In: 46th AIAA/ASME/SAE/ASEE joint propulsion conference exhibit. Nashville, TN
3. Dalbey K, Eldred MS, Geraci G, Jakeman JD, Maupin KA, Monschke JA, Seidl DT, Swiler LP, Tran A, Menhorn F, Zeng X (2020) Dakota a multilevel parallel object-oriented framework for design optimization parameter estimation uncertainty quantification and sensitivity analysis: version 6.12 theory manual, 5
4. OpenFOAM and Foundation, OpenFOAM v7 user guide
5. Greenshields CJ, Weller HG, Gasparini L, Reese JM (2010) Implementation of semi-discrete, non-staggered central schemes in a collocated, polyhedral, finite volume framework, for high-speed viscous flows. *Int J Numer Meth Fluids* 63(1):1–21
6. Kurganov A, Noelle S, Petrova G (2006) Semidiscrete central-upwind schemes for hyperbolic conservation laws and Hamilton–Jacobi equations read more. *SIAM J Sci Comput* 23(3):707–740. <https://epubs.siam.org/doi/abs/10.1137/s1064827500373413>
7. Marinov NM, Westbrook CK, Pitz WJ (1995) Detailed and global chemical kinetics model for hydrogen. In: 8th international symposium on transport properties. San Francisco, USA
8. Roos T, Pudsey A, Bricalli M, Ogawa H (2019) Cavity enhanced jet interactions in a scramjet combustor. *Acta Astronaut* 157:162–179
9. Aso S, Kawai M, Ando Y (1991) Experimental study on mixing phenomena in supersonic flows with slot injection. In: 29th aerospace sciences meeting. Reno, Nevada January
10. Bricalli MG, Brown L, Russell RG, Boyce R, Vanyai T, Pudsey AS (2018) Scramjet performance with nonuniform flow and swept nozzles. *AIAA J* 56
11. Cutler A, Harding G, Diskin G (2001) High frequency supersonic pulsed injection. In: 39th AIAA aerospace sciences meeting and exhibit. Reno, NV

Optimal Impulsive Maneuver Planning for Station Acquisition of Geosynchronous Satellites



M. R. Srivatsa and Gurpreet Singh

1 Introduction

Geosynchronous satellites are a major class of satellites serving various purposes like communication, scientific missions and earth observation used for both civilian and military activities. While most of the satellites in this class have an orbital inclination within 0.1° (geostationary), satellites like those belonging to a navigation system have higher inclinations. After being launched into a Geostationary Transfer Orbit (GTO), a series of Liquid Engine Burns (LEB) are carried out putting the satellite into a drift orbit with the desired inclination and right ascension of ascending node but requires finer in-plane corrections to achieve the final orbit that satisfies various mission requirements. These include the target longitude, longitudinal drift rate, and a specific eccentricity vector to adhere to station keeping and co-location requirements.

These fine in-plane corrections have to be performed satisfying mission constraints pertaining to the maximum velocity that can be imparted in a single operation (thruster hardware constraints, plume impingement, etc.) and minimum duration between consecutive maneuvers (for orbit determination). In order to satisfy these constraints while achieving the target orbit, multiple maneuvers are usually planned. Identifying the time of maneuvers and corresponding velocity impulses required for this phase is an optimization problem in which the total fuel consumed is minimized. Multiple maneuvers strategy allows to identify various possible solutions

M. R. Srivatsa (✉) · G. Singh
Flight Dynamics Group, UR Rao Satellite Center, Bengaluru, India
e-mail: svivatsa@ursc.gov.in

G. Singh
e-mail: gurpreet@ursc.gov.in

© The Author(s), under exclusive license to Springer Nature Singapore Pte Ltd. 2023
P. Pradeep Pratapa et al. (eds.), *Advances in Multidisciplinary Analysis and Optimization*,
Lecture Notes in Mechanical Engineering,
https://doi.org/10.1007/978-981-19-3938-9_8

with same(similar) cost function value and thus provides flexibility in planning. The present work addresses this optimization problem by splitting it into two phases, and the paper is organized accordingly.

2 Literature Review

Station acquisition and station keeping, both of which require simultaneous control of eccentricity vector and longitudinal drift rate (the difference being in the magnitude of maneuvers and thus orbital parameter changes), have been studied widely in literature. From systematically examining all the possible combinations of maneuvers and selecting those that satisfy mission constraints, early literature provides a few analytical methods for designing station acquisition maneuvers [5]. These methods were most often concerned with the longitudinal control and used analytical models of longitude evolution dynamics with the effect of maneuvers to come up with the impulses that satisfy the mission requirements. Over the time, simultaneous control of both longitude and eccentricity [12] became increasingly important due to the increase in number of satellites that are placed in close or same orbital slots demanding stricter control of the orbital parameters. As the magnitude of eccentricity influences the magnitude of longitudinal libration [10], simultaneous control of eccentricity vector is needed and has been studied extensively in literature from the station keeping perspective. Early works dealt with this using small number of maneuvers (one, two, or at-most three [1]) which was later extended to multiple maneuvers [7]. While multiple maneuvers add considerable operational flexibility, the algorithm in [7] assumes constant time intervals between these maneuvers. Although this is not a problem for station keeping which is performed in on-orbit mode, the same is not true for station acquisition phase which involves satellite drifting across a wide band of longitudes before being arrested at the target station. The presence of other satellites in these longitudes leads to operational constraints with respect to orbit determination and commanding requiring the maneuvers to be placed accordingly (not planning them close to the orbital slots of other satellites and adjusting drift to spend as less time as possible in those slots). Algorithms have been proposed for autonomous longitude and eccentricity control of geostationary satellites. In [2], an initial strategy for autonomous control is developed using simplified models and then is improved with differential corrections using high fidelity models. The focus of the work in [2] being autonomous control, the author acknowledges that the optimality of the velocity impulse imparted was not of primary concern.

The current work aims at addressing the points mentioned above. A methodology has been developed to provide enough flexibility in the maneuver planning and robust search of the decision space to find optimal maneuver sequences adhering to mission constraints. For this, the algorithm works in two phases. The first phase poses the station acquisition problem as an orbital reconfiguration problem using relative orbit elements with respect to a virtual satellite in the target orbit. Linearized relative orbit dynamics incorporating low fidelity force models (only central body/central body and

J2 perturbation) is used with maneuver locations and velocity impulse magnitudes as decision variables with box constraints. In order to search the decision space for global optima, Differential Evolution (DE) is used. In the second phase, the resulting decision vector from DE is used as an initial guess for a constrained numerical optimizer (Sequential Least Square Quadratic Programming) which seeks convergence to the corresponding minimum within specified tolerances. High fidelity force models significant for geosynchronous satellites—Gravity harmonics to a higher order and degree, Solar Radiation Pressure, and Third body perturbations from sun and moon—are incorporated while using numerical optimizer to ensure practical solutions. Using Differential Evolution as precursor removes the need to resort to trial and error for giving appropriate initial guess for the numerical optimizer.

3 Relative Orbit Dynamics

Following the conventions of previous works in literature [3, 4], six Relative Orbit Elements (ROEs) are defined as follows:

$$\delta\alpha = \begin{bmatrix} \delta a \\ \delta\lambda \\ \delta e_x \\ \delta e_y \\ \delta i_x \\ \delta i_y \end{bmatrix} = \begin{bmatrix} (a - a_t)/a_t \\ u - u_t + (\Omega - \Omega_t) \cos(i_t) \\ e \cos(\omega) - e_t \cos(\omega_t) \\ e \sin(\omega) - e_t \sin(\omega_t) \\ i - i_t \\ (\Omega - \Omega_t) \sin(i_t) \end{bmatrix} \quad (1)$$

where a, e, i, ω, Ω , and M denote the classical Keplerian elements with $u = M + \omega$. The subscript t denotes the elements of virtual target satellite. The ROEs at initial time t_0 and final time t_F are related as:

$$\delta\alpha_F = \Phi_{F,0} \alpha_0 \quad (2)$$

t_0 and t_F can be replaced with u_0 and u_F and the state transition matrix $\Phi_{F,0}$ is given by:

$$\Phi_{F,0} = \begin{bmatrix} 1 & 0 & 0 & 0 & 0 & 0 \\ -(3/2)(u_F - u_0) & 1 & 0 & 0 & \mu(u_F - u_0) & 0 \\ 0 & 1 & 0 & -\dot{\phi}(u_F - u_0) & 0 & 0 \\ 0 & 0 & \dot{\phi}(u_F - u_0) & 1 & 0 & 0 \\ 0 & 0 & 0 & 0 & 1 & 0 \\ 0 & 0 & 0 & 0 & \lambda(u_F - u_0) & 1 \end{bmatrix} \quad (3)$$

where:

$$\eta = \sqrt{1 - e^2}$$

$$\gamma = \frac{J_2}{2} \frac{R_\oplus^2}{a^2 \eta^4}$$

$$\mu = -\frac{21}{2} \gamma \sin(2i)$$

$$\dot{\phi} = \frac{3}{2} \gamma (5 \cos^2(i) - 1)$$

with Earth's radius R_\oplus and J_2 coefficient of the gravity harmonics. Let velocity impulse vector be:

$$\Delta \mathbf{V} = [v_t \ v_r \ v_n]^T \quad (4)$$

with components in T (tangential), R (radial), and N (Normal) frame centered at the spacecraft with respect to the orbital plane. Application of this impulse causes a jump in ROEs given by:

$$\Delta \delta \alpha_m = \mathbf{B}(u_m) \Delta \mathbf{V}_m \quad (5)$$

when impulse is applied at u_m with:

$$\mathbf{B}(u_m) = \begin{bmatrix} 2 & 0 & 0 \\ 0 & -2 & 0 \\ 2 \cos(u_m) & \sin(u_m) & 0 \\ 2 \sin(u_m) & -\cos(u_m) & 0 \\ 0 & 0 & \cos(u_m) \\ 0 & 0 & \sin(u_m) \end{bmatrix} \quad (6)$$

If acquisition is planned using N impulsive maneuvers, the final ROEs can be obtained using

$$\begin{aligned} \delta \alpha_1 &= \Phi_{1,0} \delta \alpha_0 + \mathbf{B}(u_1) \Delta \mathbf{V}_1 \\ \delta \alpha_2 &= \Phi_{2,1} \delta \alpha_1 + \mathbf{B}(u_2) \Delta \mathbf{V}_2 \\ &\vdots \\ &\vdots \\ &\vdots \\ \delta \alpha_N &= \Phi_{N,N-1} \delta \alpha_{N-1} + \mathbf{B}(u_N) \Delta \mathbf{V}_N \\ \delta \alpha_F &= \Phi_{F,N} \delta \alpha_N \end{aligned} \quad (7)$$

For station acquisition, ROEs are defined between the spacecraft in drift orbit and a virtual spacecraft in target orbit and $\delta \alpha$ must be driven to origin by choosing appropriate u_i , $\Delta \mathbf{V}_i$; $i = \{1, 2, 3, \dots, N\}$ while minimizing $\sum_{i=1}^N |\Delta \mathbf{V}_i|$. Differential Evolution is used to tackle this optimization problem and identify optimal maneuver sequence. This solution will then be used as an initial guess for a numerical optimizer to guarantee convergence. Formulation of same is presented in the following section.

4 Station Acquisition Formulation

Initial ROE ($\delta\alpha_0$) is defined using the classical orbital elements of the spacecraft in drift orbit and virtual spacecraft in target orbit at current epoch. Epoch and orbital elements of the drift orbit are taken as input from the mission planner. The orbital elements of target orbit are deduced from the station acquisition inputs which are: target longitude (equatorial crossing longitude in case of high inclination geosynchronous satellites) λ'_t , target longitudinal drift rate, D'_t , target eccentricity vector magnitude, e'_t and target eccentricity vector direction, β'_t . Let a, e, i, ω, Ω , and M be the drift orbit elements and $a_t, e_t, i_t, \omega_t, \Omega_t$, and M_t be the target orbit elements **at current epoch** (t_0). Let $a'_t, e'_t, i'_t, \omega'_t, \Omega'_t$ and M'_t be the target orbit elements at **acquisition epoch** (t_f) which is obtained by adding the maximum time allowed for station acquisition (dt_{acq}) to the t_0 . The parameters that need to be achieved after acquisition are longitudinal drift rate D'_t , longitude λ'_t , and eccentricity vector (ex'_t, ey'_t). It is assumed that the perturbations don't cause any significant change in orbital elements for the duration of station acquisition. Hence only M_t and M'_t differ, while other elements of the target virtual spacecraft remain unchanged.

4.1 Geostationary ($i \leq 0.1^\circ$)

- $a'_t = a_t = a_{geo}(1 - \frac{2}{3}D_t)$, where a_{geo} is the semi-major axis of an ideal geosynchronous orbit
- $e'_t = e_t$ is given as input
- As the corrections are aimed to be purely in-plane, we have: $i'_t = i_t = i$ and $\Omega'_t = \Omega_t = \Omega$
- $\omega'_t = \omega_t = \beta'_t - \Omega'_t$ (from the definition of eccentricity vector [10])
- Let v'_t be the true anomaly of the target orbit at acquisition epoch. We have:
 $v'_t = (\Theta' + \lambda'_t - \omega'_t - \Omega'_t) \bmod 2\pi$
 where Θ' is the Sidereal angle at acquisition epoch. Using relation between true anomaly and mean anomaly, M'_t can be obtained. Also we have: $M'_t - M_t = n(t_f - t_0)$ where n is the mean motion corresponding to the drift orbit obtained from the relation $n = \sqrt{\frac{GM}{a_t^3}}$ (GM - Gravitational constant of central body, Earth). u_t is then determined using (Fig. 1):

$$\begin{aligned} M_t &= (M'_t - n(t_f - t_0)) \bmod 2\pi \\ u_t &= M_t + \omega_t \end{aligned} \quad (8)$$

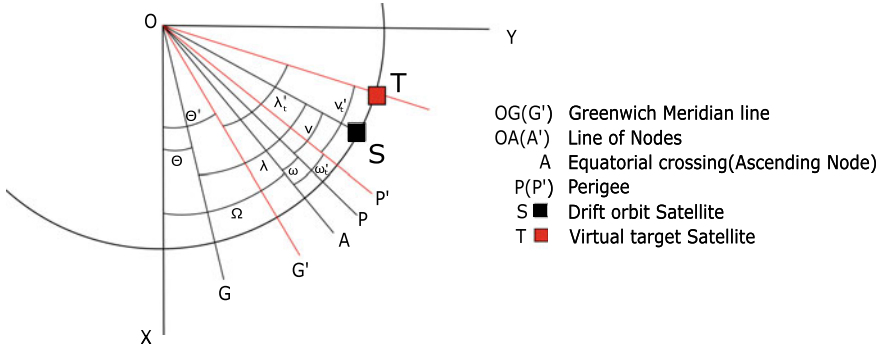


Fig. 1 Geostationary

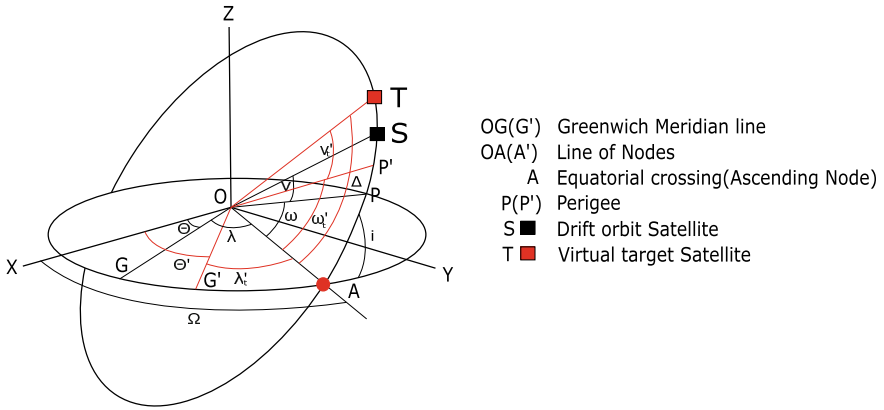


Fig. 2 Geosynchronous

4.2 Geosynchronous ($i > 0.1^\circ$)

- $a_t, e_t, i_t, \Omega_t,$ and ω_t are obtained as described above
- Target longitude λ'_t here corresponds to the equatorial crossing longitude. When the spacecraft is at equatorial crossing, we have the relations:

$$\Omega'_t = \Omega_t = \Theta' + \lambda_t$$

$$v'_t = 2\pi - \omega'_t(or)\omega_t \text{ from which } M'_t \text{ is obtained}$$

Depending on number of days since current epoch for planned acquisition at equatorial crossing, we have the relation:

$$dt_{acq} = (t_F - t_0) = (\text{int}(\text{no. of days for acquisition}) * 2\pi + \Theta' - \Theta) / \phi$$

where ϕ is the angular velocity of rotation of the Earth. Using above relations and Eq. 8, M_t and u_t are determined (Fig. 2).

5 Generation of Initial Guess Using Differential Evolution

For the purpose of optimization, angular separation between consecutive maneuvers are chosen instead of absolute angles to simplify specification of box constraints. Also, all the impulses are tangential as is the case in practical missions. Thus, the decision vector is defined as:

$$\mathbf{x} = [\Delta u_1 \ \Delta u_2 \ \dots \ \Delta u_N \ v_{t1} \ v_{t2} \ \dots \ v_{tN}]^T \quad (9)$$

where $\Delta u_i = u_i - u_{i-1}$ and v_{ti} are the tangential component of i th maneuver (other components are zero for in-plane maneuvers). The search space is defined using box constraints on the individual components of \mathbf{x} . The lower and upper limits are chosen based on mission constraints, i.e.:

$$\begin{aligned} du_i^l &< \Delta u_i < du_i^u \\ dv_i^l &< v_{ti} < dv_i^u \end{aligned} \quad (10)$$

which arise out of constraints pertaining to minimum time between consecutive maneuvers for orbit determination and limits on magnitude of velocity impulses realizable in each firing.

Differential Evolution (DE) is an evolutionary optimization algorithm [11]. It uses selection, mutation, and crossover operators similar to those used in genetic algorithms. DE works well for search spaces of real valued decision vectors due to the usage of real coding. It is a population-based method which improves the best individual over generations by using the above mentioned operators. Usage of DE is detailed in this section.

1. **Initialization of population:** Each individual in a population is initialized randomly using uniform distribution using:

$$\begin{aligned} x_{k,j,0} &= x_k^l + \text{Random}(0, 1)(x_k^u - x_k^l) \\ k &\in [1, 2 \dots 2N] \\ j &\in [1, 2 \dots \text{pop}] \end{aligned} \quad (11)$$

where pop is the population size of the generation.

2. **Mutation:** The success of DE is attributed to the effective generation of a donor vector $\mathbf{x}_{j,G}^d$ corresponding to every parent vector $\mathbf{x}_{j,G}$ in G th generation ($j \in [1, 2, 3, \dots, \text{pop}]$). Several mutation strategies are proposed in literature the simplest being of the form [13]:

$$\begin{aligned} \mathbf{x}_{j,G}^d &= \mathbf{x}_{r1,G} + F(\mathbf{x}_{r2,G} - \mathbf{x}_{r3,G}) \\ j, r1, r2, r3 &\in [1, 2, 3, \dots, \text{pop}] \text{ and } r1 \neq r2 \neq r3 \neq j \\ F &\in [0, 1] \end{aligned} \quad (12)$$

Larger value of F promotes the exploratory capability of DE. A donor vector is generated for every parent vector in the population and is passed on to the crossover operator.

3. **Crossover:** After generating a donor vector for each parent vector in population of a given generation, a new individual $\mathbf{x}_{j,G}^c$ is generated as follows:

$$\mathbf{x}_{k,j,G}^c = \begin{cases} x_{k,j,G}^d & \text{if } \text{random}(0, 1) \leq C \\ x_{k,j,G} & \text{if } \text{random}(0, 1) > C \end{cases} \quad (13)$$

$$k \in [1, 2, 3, \dots, 2N]$$

$$j \in [1, 2 \dots \text{pop}]$$

It is possible for the components of $\mathbf{x}_{j,G}^c$ to violate the box constraints imposed. Hence, various box constraint handling techniques are used. The method used here is as follows:

$$\text{if } x_{k,j,G}^c < x_k^l \text{ or } x_{k,j,G}^c > x_k^u :$$

$$x_{k,j,G}^c = x_k^l + \text{Random}(0, 1)(x_k^u - x_k^l) \quad (14)$$

$$k \in [1, 2, 3, \dots, 2N]$$

$$j \in [1, 2 \dots \text{pop}]$$

This ensures that the trial vector thus generated satisfies box constraints imposed. $\mathbf{x}_{j,G}^c$ thus produced is called trial vector.

4. **Selection:** For every parent vector in a generation, the selection operator compares the cost function of parent and corresponding trial vector and replaces parent if trial vector is a better performer. That is:

$$\mathbf{x}_{j,G+1} = \begin{cases} \mathbf{x}_{j,G} & \text{if } f(\mathbf{x}_{j,G}) < f(\mathbf{x}_{j,G}^c) \\ \mathbf{x}_{j,G}^c & \text{if } f(\mathbf{x}_{j,G}^c) < f(\mathbf{x}_{j,G}) \end{cases} \quad (15)$$

where f is the cost function to be minimized.

5. **Termination Criteria:** DE is terminated if the cost function value of the best individual in the population and worst individual in population differs by less than a specified threshold (ϵ) indicating convergence or if number of generations exceed a set limit.

With the objective to minimize total magnitude of $\Delta \mathbf{V}$ used for station acquisition, the following cost function was defined:

$$f(\mathbf{x}) = w_1 \sum_{i=1}^n |\Delta \mathbf{V}_i| + w_2 |\delta \alpha_F| \quad (16)$$

where $|\Delta \mathbf{V}_i| = |x_{N+i}|$ and $\delta \alpha_F$ are determined using Eq. 7. w_1 and w_2 were tuned considering the scale and after testing convergence for various values. The population size in this implementation is set to 100, the maximum number of generation is set to 5000, ϵ to $1e-5$, F was set to 0.9 and C to 0.8. The weights w_1 and w_2 were set to 10 and 1000, respectively.

6 Checking the Quality of Initial Guess Resulting from DE

In theory, an optimal maneuver sequence depends on if major correction is required in the drift (δa) or eccentricity ($\Delta \mathbf{e}$). The following inequalities are valid for multiple tangential maneuver sequence at arbitrary times obtained from linearized models [10]:

$$\begin{aligned} \sum_{i=1}^N |\Delta \mathbf{V}_i| &\geq (V/3) |\Delta D| \quad (\text{or } \Delta V_{\text{drift}}) \\ \sum_{i=1}^N |\Delta \mathbf{V}_i| &\geq 0.5V |\Delta \mathbf{e}| \quad (\text{or } \Delta V_{\text{ecc}}) \end{aligned} \quad (17)$$

where V is the geosynchronous velocity, ΔD is the magnitude of change in longitudinal drift rate required, and $|\Delta \mathbf{e}|$ is the magnitude of change in eccentricity vector required from drift orbit to target orbit. Optimal maneuver sequence is obtained if at least one of the two inequalities becomes an equality. For an optimal sequence:

- If $\Delta V_{\text{drift}} > \Delta V_{\text{ecc}}$, all impulses are expected to be in same direction with little significance to maneuver locations.
- If $\Delta V_{\text{ecc}} > \Delta V_{\text{drift}}$, maneuvers are expected to occur separated by multiples of half a sidereal day with alternating east and west thrusts.

The appropriateness of the initial guess resulted from DE can be checked using the above criteria. For scenarios with major drift correction, initial guess resulting in total ΔV close to ΔV_{drift} can be readily used. For scenarios with major eccentricity vector correction, Δu_i is expected to be close to integral multiples of π and ΔV close to ΔV_{ecc} in which case a good initial guess is generated. This fact can also be used to tune the parameters of DE to arrive at a good enough initial guess and reduce the number of generations.

7 Final Solution Using Constrained Nonlinear Programming

Using DE and low fidelity dynamics, we have generated a candidate solution. The final solution is expected to incorporate all significant force models for geostationary spacecraft dynamics as well as guarantee convergence to a minima which is not ensured from DE. Hence, the candidate solution thus obtained is used as an initial guess for station acquisition maneuver plan which will be posed as a constrained nonlinear programming (NLP) problem using appropriate force models. Sequential Quadratic Programming (SQP) is chosen as the optimizer for this purpose.

SQP is widely used as a robust and efficient algorithm for solving NLPs subject to equality, inequality, and box constraints. An iterative approach is used to arrive at solution using an appropriate search direction and step length in each iteration. The search direction is determined by formulating a quadratic approximation of the Lagrange function of NLP and a linear approximation of the constraints imposed. The step length is adjusted depending on the relative location of decision vector from optimum in each iteration. The Hessian of Lagrange function is estimated using the first-order information. In the present work, SQP as implemented by Dieter Kraft [8] and available in Python's Scipy library has been used. The formulation of constrained NLP problem is described below.

- **Decision vector**

For the purpose of having direct access to time for calculating various components of force model and constraints, the decision vector was chosen to be:

$$\mathbf{x} = [t_1, t_2, \dots, t_N, v_1, v_2, \dots, v_N]^T \quad (18)$$

where t_i corresponds to the time of flight between i th and $i + 1$ th maneuver (t_0 being the time of flight from reference epoch to first maneuver).

- **Objective Function**

With the aim of having a well behaved objective function, the L2 norm of the velocity components of the decision vector was chosen as the function to be minimized:

$$f(\mathbf{x}) = \sum_{i=1}^N x_{N+i}^2 \quad (19)$$

where $x_{N+i} = v_i$, the tangential velocity impulse of the maneuver thus minimizing the total fuel consumed.

- **Box Constraints**

The box constraints used for DE in terms of angles are directly transformed to box constraints in time of flight between maneuvers. Constraints used in DE for velocity impulses are used for SQP as well.

- **Terminal Constraints**

Tolerance bands are prescribed for the deviation in attained parameters from target parameters of spacecraft by the user. These tolerance bands are used to define inequality constraints for the NLP. The constraint vector function is structured as follows:

Let \mathbf{SV} be the state vector of spacecraft at time T :

$\mathbf{g}(\mathbf{x})$:

\mathbf{SV}_0 and T_0 specified as inputs

for in $[1, 2, \dots, N]$:

propagate state \mathbf{SV}_{i-1} of spacecraft from T_{i-1} to $T_i + x_i$ using full force model

Add tangential impulse of x_{N+i} to resulting state to get \mathbf{SV}_i

$T_i = T_{i-1} + x_i$

Use T_N and \mathbf{SV}_N to calculate the attained parameters D_{att} , λ_{att} , ex_{att} and ey_{att}

calculate the deviation from targetted parameters

$\Delta D_{\text{att}} = D_{\text{att}} - D_t^l$

$\Delta \lambda_{\text{att}} = \lambda_{\text{att}} - \lambda_t^l$

$\Delta ex_{\text{att}} = ex_{\text{att}} - ex_t^l$

$\Delta ey_{\text{att}} = ey_{\text{att}} - ey_t^l$

return

$$\begin{bmatrix} w_{\text{drift}}(\Delta D_{\text{att}} - D_{\text{tol}}^l) \\ w_{\text{drift}}(D_{\text{tol}}^u - \Delta D_{\text{att}}) \\ w_{\text{long}}(\Delta \lambda_{\text{att}} - \lambda_{\text{tol}}^l) \\ w_{\text{long}}(\lambda_{\text{tol}}^u - \Delta \lambda_{\text{att}}) \\ w_{\text{ex}}(\Delta ex_{\text{att}} - ex_{\text{tol}}^l) \\ w_{\text{ex}}(ex_{\text{tol}}^u - \Delta ex_{\text{att}}) \\ w_{\text{ey}}(\Delta ey_{\text{att}} - ey_{\text{tol}}^l) \\ w_{\text{ey}}(ey_{\text{tol}}^u - \Delta ey_{\text{att}}) \end{bmatrix}$$

(20)

where w_{drift} , w_{long} , w_{ex} , and w_{ey} are weights used to scale each component appropriately and $(D_{\text{tol}}^l, D_{\text{tol}}^u)$, $(\lambda_{\text{tol}}^l, \lambda_{\text{tol}}^u)$, $(ex_{\text{tol}}^l, ex_{\text{tol}}^u)$, $(ey_{\text{tol}}^l, andey_{\text{tol}}^u)$ are the tolerance ranges for deviations. Constraints are of the form $g_i \geq 0$. A successful termination ensures this inequality with an accuracy specified by the user. The values $w_{\text{drift}} = 100$, $w_{\text{long}} = 10$, $w_{\text{ex}} = 10$, and $w_{\text{ey}} = 10$ were set after studying the behavior of convergence to the accuracy expected in each parameter. The algorithm is developed in Python, and OREKIT [9] was used to formulate the force models required.

8 Results

Two mission scenarios and resulting maneuver plan from the developed algorithm are presented below.

8.1 Geostationary ($i \leq 0.1^\circ$)

A mission constraint on maximum velocity impulse magnitude of 1 m/s has been imposed. This requires splitting the acquisition into multiple maneuvers to achieve the net required velocity impulse and is separated adequately for orbit determination process. To test the flexibility of planning large number of maneuvers, a 11 maneuver plan was worked out. The following table summarizes the plan generated using the proposed algorithm (Table 1).

Table 1 Maneuver plan for geostationary case

Maneuver plan				
Maneuver plan				
Man No.	Epoch (UTC)	ΔV (m/s)	Long (Deg)	Drift (Deg/Day)
1	2018-12-11T03:13:51	0.5063	67.13	1.275
2	2018-12-13T02:55:42	0.5325	69.68	1.082
3	2018-12-13T14:50:55	-0.5563	70.10	1.276
4	2018-12-14T02:45:54	0.5455	70.87	1.084
5	2018-12-15T02:36:58	0.5587	71.97	0.885
6	2018-12-16T02:29:15	0.5719	72.87	0.682
7	2018-12-17T02:22:16	0.5852	73.57	0.476
8	2018-12-18T02:16:43	0.5987	74.06	0.266
9	2018-12-19T02:12:25	0.6122	74.34	0.053
10	2018-12-21T02:04:39	0.6394	74.49	-0.162
11	2018-12-23T13:56:53	-0.4251	74.0	0.0
Total $ \Delta V $		6.132 m/s		

This particular case is an example where the major correction corresponds to eccentricity correction and thus it is seen that the maneuvers are scheduled almost half a sidereal day apart (eccentricity vector evolution approximately along a straight line). From Eq. 17 which gives the lower bounds for total velocity impulse derived from linearised motion, the approximate value of the optimal total impulse is the maximum of $(V/3)|\Delta D| \approx 4.05$ m/s and $0.5V|\Delta e| \approx 6.06$ m/s. The optimal value achieved using high fidelity dynamics (6.132 m/s) closely agrees with this value (Fig. 3, and Tables 2, 3 and 1).

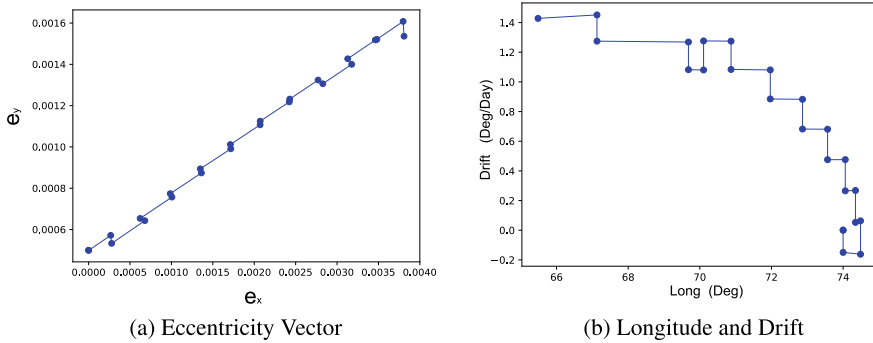


Fig. 3 Target parameters evolution for geostationary STAQ plan with developed algorithm

Table 2 Drift orbit parameters

Epoch (UTC)	Keplerian					
	a (km)	e	i (deg)	Ω (deg)	ω (deg)	v (deg)
2018-12-10T08:30:00.000	42,053.29,173	0.004107	0.095632	286.975	94.982	250.050
	Equinoctial					
	a (km)	e_x	e_y	i_x	i_y	TrueLong (deg)
	42,053.291733	0.003809	0.001536	0.000244	-0.000798	272.008

Table 3 Target parameters

Drift (deg/day)	e-Magnitude	e-Direction (deg)	Long (deg)
0.0	0.0005	90.0	74.0

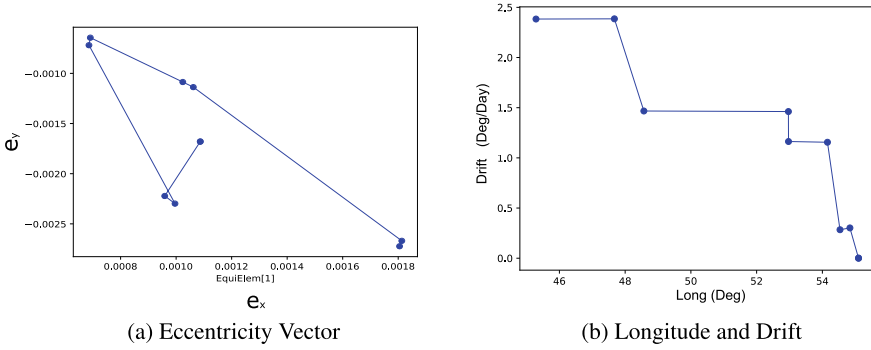


Fig. 4 Target parameters evolution for geosynchronous STAQ plan with developed algorithm

Table 4 Drift orbit parameters

Epoch (UTC)	Keplerian					
	a (km)	e	i (deg)	Ω (deg)	ω (deg)	v (deg)
2018-04-15T15:38:02.144	41978.91308	0.003267	28.502	123.072	180.466	180.01
Equinoctial						
	a (km)	e_x	e_y	i_x	i_y	TrueLong(deg)
	41978.91308	0.001805	-0.002723	-0.138602	0.21284	123.548

Table 5 Target parameters

drift (deg/day)	e-Magnitude	e-Direction (deg)	Long (deg)
0.0	0.002	302.92	55.08

8.2 Geosynchronous ($i > 0.1^\circ$)

In this particular scenario, the velocity impulse needed for drift correction is more than that required for eccentricity correction. This in theory allows us to execute maneuvers which are not necessarily separated by multiples of half a sidereal day intervals. Again from Eq. 17, the lower bounds for total velocity impulse derived from linearized motion, the approximate value of the optimal total impulse is the maximum of $(V/3)|\Delta D| \approx 6.77$ m/s and $0.5V|\Delta e| \approx 1.95$ m/s. The optimal value achieved using high fidelity dynamics (6.811 m/s) closely agrees with this value (Fig. 4 and Tables 4, 5 and 6).

Table 6 Maneuver plan for geosynchronous case

Man No.	Maneuver plan			
	Epoch (UTC)	ΔV (m/s)	Long (Deg)	Drift (Deg/Day)
1	2018-04-17T14:41:38	2.6276	48.57	1.467
2	2018-04-19T15:05:08	0.8519	52.97	1.163
3	2018-04-21T01:09:38	2.4755	54.54	0.284
4	2018-04-22T11:24:04	0.8563	55.1	0.0
Total $ \Delta V $	6.811 m/s			

9 Conclusion

A new algorithm was developed to generate optimal multiple impulse station acquisition maneuvers for geosynchronous spacecrafts. The developed novel methodology allows for specifying the mission constraints in terms of time intervals between successive maneuvers and limits on magnitude of velocity impulses allowed by thrusters and generates a corresponding maneuver sequence targeting the station acquisition parameters and alleviates the need to find a suitable initial guess by trial and error. Differential Evolution proves to be a robust algorithm for searching a feasible near optimal solution which is further refined using SQP. The results obtained using the final optimization incorporating high fidelity dynamics show close match with theoretical minimum derived using linearized models. Future work is aimed at incorporating multi-objective optimization to obtain Pareto optimal solution set that minimize station acquisition duration as well.

Acknowledgements The first author acknowledges the guidance and support provided by Dr. MP Ramachandran, Ex-GD, FDG, URSC for carrying out this work. We would also like to thank Shri. Kiran BS, DD, MDA, URSC and Shri. Kannan S, GD, FDG, URSC for their support.

References

1. Eckstein MC (1986) Station keeping strategy test, design and optimization by computer simulation. Space dynamics and celestial mechanics. Springer, Dordrecht, pp 411–412
2. Emma Brian P, Pernicka Henry J (2003) Algorithm for autonomous longitude and eccentricity control for geostationary spacecraft. J Guid Control Dyn 26(3):483–490
3. Gaias Gabriella, D’Amico Simone (2015) Impulsive maneuvers for formation reconfiguration using relative orbital elements. J Guid Control Dyn 38(6):1036–1049

4. Gaias Gabriella, D'Amico Simone, Ardaens Jean-Sébastien (2015) Generalised multi-impulsive manoeuvres for optimum spacecraft rendezvous in near-circular orbit. *Int J Space Sci Eng* 3(1):68–88
5. Gartrell CF (1985) An analytical approach to geosynchronous station acquisition. *J Guidance Control Dyn* 8(4): 535–537
6. Gazzino C (2017) Dynamics of a geostationary satellite. Diss, LAAS-CNRS
7. Kelly TJ, White LK, Gamble DW (1994) Stationkeeping of geostationary satellites with simultaneous eccentricity and longitude control. *J Guid Control Dyn* 17(4):769–777
8. Kraft D (1985) On converting optimal control problems into nonlinear programming problems. *Computational mathematical programming*. Springer, Berlin, pp 261–280
9. Maisonobe L, Pommier V, Parraud P (2010) Orekit: an open source library for operational flight dynamics applications. In: 4th international conference on astrodynamics tools and techniques
10. Soop EM (1994) Handbook of geostationary orbits, vol 3. Springer Science & Business Media
11. Storn R, Price K (1997) Differential evolution—a simple and efficient heuristic for global optimization over continuous spaces. *J Global Optim* 11(4):341–359
12. Sweetser T (2010) How to maneuver around in eccentricity vector space. In: AIAA/AAS astrodynamics specialist conference
13. Zhu Y, Wang H, Zhang J (2015) Spacecraft multiple-impulse trajectory optimization using differential evolution algorithm with combined mutation strategies and boundary-handling schemes. *Mathem Probl Eng*

Assessment of Nonlinear Optimization Algorithms on Weighted Least-Square-Based Method for Re-Entry Prediction



Pooja Dutt, Deepak Negi, Abhay Kumar, and V. Ashok

1 Introduction

Since the launch of Sputnik 1 in 1967, there has been continuous increase in space object population which include fragments and intact rocket bodies ranging from 1 mm to more than 25 m in size. Some of these space object re-enter Earth's atmosphere. There have been cases when intact upper stage along with satellite failed to reach orbit and then subsequently re-entered Earth's atmosphere, for example Phobos-Grunt. Occasionally, re-entering space objects consist of components which survive re-entry or contain toxic materials onboard and hence cause risk to life and property. Hence, an accurate prediction of re-entry time of these space objects along with impact location is very important.

Re-entry prediction of uncontrolled space objects close to re-entry still remains a challenging problem. There are several factors which cause uncertainty in re-entry prediction, namely its initial state, complicated shape and unknown attitude evolution, propagation model, conversion between mean and osculating elements and prediction of atmospheric drag as a function of solar and geomagnetic activity.

Gupta and Anilkumar [1] developed an integrated model with multi-objective error function minimization to estimate an essential ballistic parameter (EBP) which is used for re-entry prediction. The estimated EBP absorbs the uncertainties in measurements, models and other input parameters. The above methodology is named

P. Dutt (✉) · D. Negi · A. Kumar · V. Ashok
Vikram Sarabhai Space Centre, ISRO, Thiruvananthapuram, India
e-mail: pooja_dutt@vssc.gov.in

D. Negi
e-mail: deepak_negi@vssc.gov.in

V. Ashok
e-mail: v_ashok@vssc.gov.in

STKOptim (Optimization using System Tool Kit), and it has been used for re-entry predictions of decaying space objects. The procedure to estimate EBP and then predict re-entry time consisted of manual intervention. This paper presents the implementation of optimization logic for STKOptim methodology to reduce user-interference and automatize the complete re-entry prediction procedure. This is based on assessment of optimization algorithms for different space objects based on their sensitivity to initial guess, convergence and number of function evaluations.

2 Problem Definition and Formulation

STKOptim methodology requires a set of two-line element (TLE) data of the decaying space object (obtained from public domain) as input. Mean orbital parameters are extracted from this TLE data set. These parameters are plotted for outlier detection/trend analysis. A pivot TLE is selected by the user from the set of TLE data. The pivot TLE is propagated for various ballistic coefficients. The propagated profiles of orbital parameters are compared with the observed TLE data to obtain weighted least-square error (WLSE).

Assume that the observations are available at ' N ' TLE epochs t_i , $i = 1, 2, \dots, N$ and $sma_{i(\text{obs})}$, $a_{i(\text{obs})}$, $p_{i(\text{obs})}$, $pa_{i(\text{obs})}$ are semi-major axis, apogee altitudes, perigee altitudes and parameter at the respective TLE epochs. For a given ballistic parameter β , the osculating states obtained from the pivot TLE is propagated using numerical orbit propagator to obtain trajectory profiles for semi-major axis, apogee, perigee and parameter. Assume that, for the ballistic parameter β , the predicted semi-major axis, apogee, perigee altitudes and parameter at the i th TLE epoch, by propagating the pivot TLE, are $sma_{i(\text{pred})}$, $a_{i(\text{pred})}$, $p_{i(\text{pred})}$, $pa_{i(\text{pred})}$, respectively.

The error functions Φ_{sma} , Φ_a , Φ_p and Φ_{pa} are defined as:

$$\Phi_{sma} = \frac{1}{N} \sqrt{\sum_{i=1}^N [sma_{i(\text{obs})} - sma_{i(\text{pred})}]^2} \quad (1)$$

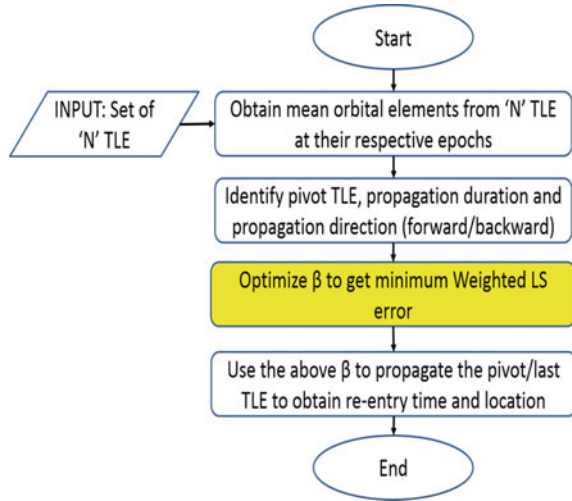
$$\Phi_a = \frac{1}{N} \sqrt{\sum_{i=1}^N [a_{i(\text{obs})} - a_{i(\text{pred})}]^2} \quad (2)$$

$$\Phi_p = \frac{1}{N} \sqrt{\sum_{i=1}^N [p_{i(\text{obs})} - p_{i(\text{pred})}]^2} \quad (3)$$

$$\Phi_{pa} = \frac{1}{N} \sqrt{\sum_{i=1}^N [pa_{i(\text{obs})} - pa_{i(\text{pred})}]^2} \quad (4)$$

$$f = w_1 \times \Phi_{sma} + w_2 \times \Phi_a + w_3 \times \Phi_p + w_4 \times \Phi_{pa} \quad (5)$$

Fig. 1 Algorithm to estimate EBP and re-entry time using STKOptim methodology



where w_1, w_2, w_3 and w_4 are normalized weights ($\sum_{i=1}^4 w_i = 1$) assigned to the WLSE function.

The above procedure is presented here in the form of a flowchart in Fig. 1. In order to automatize the STKOptim methodology, the crux of the problem lies in finding a suitable optimization logic to estimate the ballistic coefficient which minimizes the WLSE. This optimized ballistic coefficient is called essential ballistic parameter (EBP) and is used to propagate the pivot/latest TLE to obtain re-entry epoch.

3 Methodology and Results

Minimization of WLSE to find EBP using the STKOptim methodology requires manual intervention due to the following reasons:

- (i) Identification and removal of TLE outliers,
- (ii) the search range is wide as different space objects have different ballistic coefficients,
- (iii) lack of good initial guess, especially in the beginning of re-entry exercise,
- (iv) during re-entry prediction, certain ballistic coefficient values lead to re-entry even before the propagation duration, especially near re-entry time and
- (v) variation in EBP during the re-entry exercise, especially near re-entry time.

Conventional (derivative-based) optimization algorithms namely sequential quadratic programming (SQP, implemented in MATLAB’s `fmincon()`) and Quasi-Newton BFGS (MATLAB’s `fminunc()`) [2] were compared with non-conventional methods, namely Nelder–Mead simplex algorithm (MATLAB’s `fminsearch()`) and genetic algorithm (GA, MATLAB’s `ga()`) [3] for various re-entry predictions using

different TLE sets at various time intervals during the entire re-entry exercise (10–15 days prior to re-entry epoch till the re-entry epoch). These predictions were carried out for decayed space objects, namely Starlink-26 (44,240), CZ-5B Rocket Body (48,275) and Electron Rocket Body (43,166), and the re-entry time predictions were compared with their actual re-entry epochs. All the case studies were executed in the same computer. The comparison of the above-mentioned optimization algorithms is presented in Table 1, in terms of their success rate (convergence), average number of function evaluations and average execution time.

It was found that Nelder–Mead simplex algorithm and GA could give satisfactory results for all space objects considered here. Figures 2 and 3 show the sensitivity of initial condition to converged EBP for SQP and BFGS for test object Starlink-26 (pivot TLE Epoch: April-09-2021 14:56:08 UTC). The evolutionary algorithms take unacceptably long time for convergence for the present problem. Even Nelder–Mead simplex algorithm requires 40–75 function evaluations. The number of function evaluations matters because farther we are from re-entry, longer is the propagation duration and hence more execution time. Hence, to explore any possibility to reduce the number of function evaluations, and in turn execution time, the following study was carried out.

Given an interval of ballistic parameter (β -interval), there are two possibilities (i) minima lies within the interval (Fig. 4), or (ii) minima lies either on the left or on the right side of the interval (Fig. 5). First, the function is evaluated at grid points within

Table 1 Comparison of optimization methods for EBP estimation using STKOptim methodology

Optimisation algorithm	Success rate (%)	Average no. of function evaluations	Average execution time (min)
SQP	22	60	1.6–2.3
Nelder–Mead simplex algorithm	100	64	1.7–2.1
BFGS	72	40	1.1–2.0
GA	100	3268	80–130
Proposed scheme	100	30	1.0–2.0

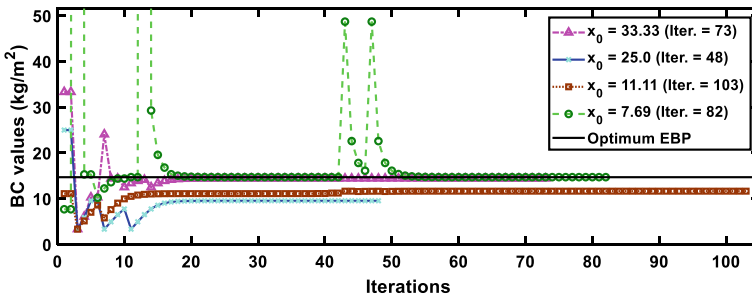


Fig. 2 Sensitivity to initial conditions using SQP

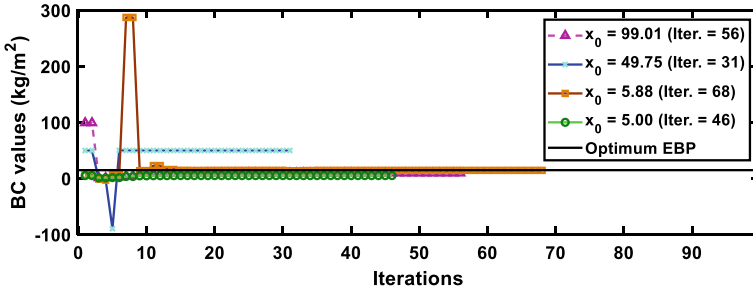


Fig. 3 Sensitivity to initial conditions using BFGS

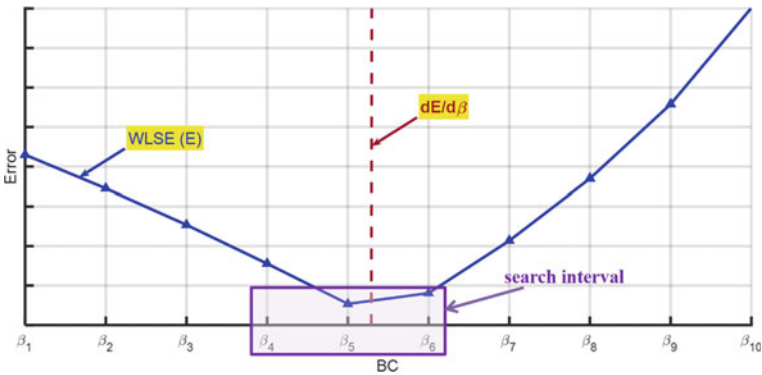


Fig. 4 Search interval when derivative test is successful

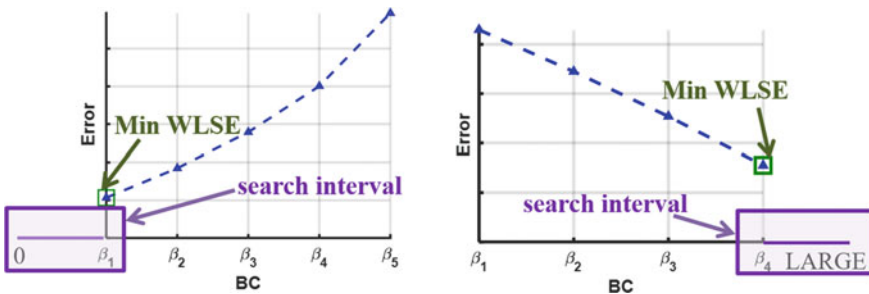


Fig. 5 Extended search interval when derivative test fails

the given β -interval and derivative test is performed to find the possible minima.

Derivative Test: Given, a set of ballistic parameters ($\beta = 1/BC = C_D \cdot A/m$, BC is ballistic coefficient, m is mass, A is the area, and C_D is drag coefficient of space object) is evaluated. The derivative of error function ($dE/d\beta$) is computed using the formula (6) for a set of dependents or error values $\{E_1, E_2, \dots, E_n\}$ and independent

values $\{\beta_1, \beta_2, \dots, \beta_{cn}\}$, where n is number of ballistic coefficients considered.

$$\frac{dE_i}{d\beta_i} = \frac{E_{i+1} - E_i}{\beta_{i+1} - \beta_i}, i = 1 \text{ to } n - 1 \quad (6)$$

Case (i): If derivative test is successful, then the sub-interval containing the minima is identified and Fibonacci search is called for a reduced search interval as shown in Fig. 4. Fibonacci search usually converges within 20 iterations for tolerance of 10^{-4} (sufficient for the re-entry prediction of space object considered in this study using STKOptim methodology).

Case (ii): If the minima lies outside the given β -interval, nonlinear optimization method is called for an extended search interval as shown in Fig. 5. If the minima lies on the left-hand side of the given β -interval, then the extended search interval will be $[0, \beta_1)$. If the minima lies on the right-hand side of the β -interval, then the extended search interval will be $(\beta_n, \text{LARGE}]$. The upper bound for this search interval is named as ‘LARGE,’ and its value is fixed based on study of re-entry of various space objects. This way, reducing the search interval for nonlinear optimizer will improve its performance compared to the cases discussed above. The flowchart for STKOptim with the derivative test is shown in Fig. 6.

Another problem faced during re-entry prediction near to re-entry time is that while scanning through the β -interval, some of the β values might lead to early re-entry, even before the latest TLE epoch. Such β s are identified and tagged as ‘invalid’ so that they are not used for further scanning by the optimizer.

On an average, Fibonacci search requires 15 iterations to converge to minima, while derivative test requires 10 function evaluations. Thus on an average total 25 function evaluations for the proposed scheme. In the beginning of re-entry campaign, a wide range of BC values can be scanned, and once EBP is estimated, BC range can be reduced for the later re-entry predictions. This logic has significantly reduced the execution time without loss in accuracy. The proposed STKOptim methodology is implemented in MATLAB and System Tool Kit (STK).

For a typical re-entry prediction, carried out 20 days prior to re-entry time, required 5 function evaluations for the derivative test while 18 function evaluations by `fminbnd()`. The execution time was 2.3 min which includes setting up an STK scenario, finding interval containing EBP, finding EBP, then propagation of pivot TLE to the re-entry epoch and determination of upper and lower bounds.

4 Conclusion

The STKOptim methodology is used for re-entry prediction of uncontrolled space objects. It is based on the method of minimizing weighted least-square error to estimate an essential ballistic parameter (EBP). The inaccuracies in TLEs, uncertainties in parameters like solar flux (F10.7) and geomagnetic indices (A_p) values, the inaccuracies in the atmospheric model and the propagation model are all absorbed in the

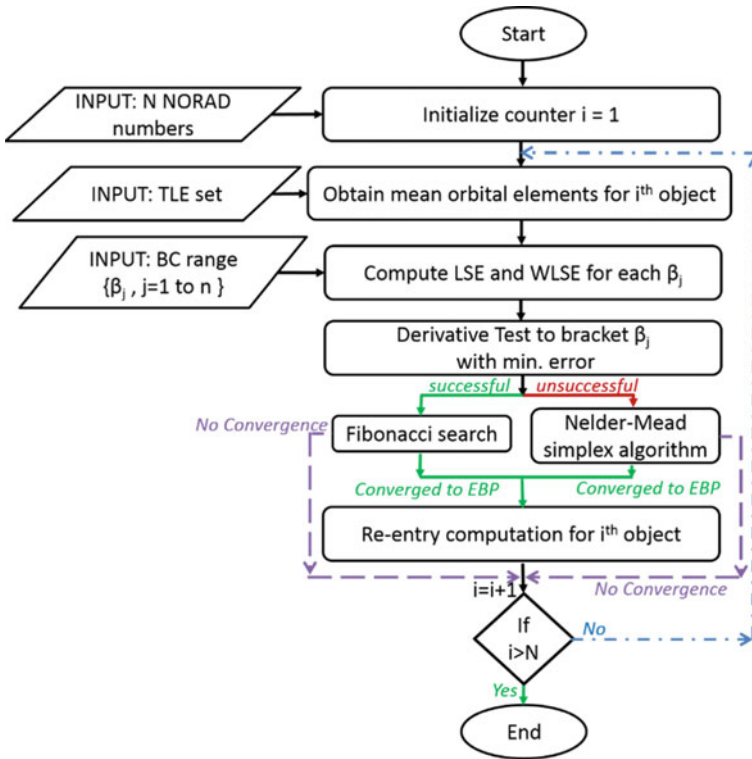


Fig. 6 Algorithm for STKOptim (in batch processing mode) with derivative test

estimated EBP. This estimated EBP is used to predict the re-entry time of the object from the pivot/latest TLE. The implementation of optimization logic for STKOptim methodology based on assessment of optimization algorithms is discussed. The assessment of optimization algorithms is carried out for different space objects on the basis of initial guess sensitivity analysis, convergence and number of function evaluations. Some failure cases and optimization logic to overcome them are presented.

Acknowledgements The authors would like to thank Shri. Jaison Joseph, GH, FMG, and Shri. C. Ravikumar, GD, AFDG, for their support and encouragement.

References

1. Gupta S, Anilkumar AK (2015) Integrated model for prediction of reentry time of risk objects. *J Spacecraft Rockets* 52(1)
2. Chong EKP, Zak SH (2001) *An introduction to optimization*, 2nd edn, Wiley-Interscience Series in Discrete Mathematics and Optimization, Wiley
3. Deb K (2001) *Multi-objective optimization using evolutionary algorithms*. 1st edn, Wiley

Multidisciplinary Design Optimization (MDO) of a Typical Civil Aircraft Wing Using 3DEXPERIENCE Platform from Dassault Systemés



Bharath Kanaparathi, Emlin Vathsalan, Dayanidhi Panda, Ganesh Prasad, G. Umashankar, Srikrishna Srinivasa Chittur, Geetha Avula, Abhay Pashilkar, A. C. Pankaj, Devendra Singh, and Vijayakrishnan

1 Introduction

Multidisciplinary optimization (MDO) of an aircraft wing is critical in the design stage of a civil aircraft to obtain enhanced performance with minimum possible structural weight. The approach of using the 3DEXPERIENCE platform as a collaborative environment is a game changer to accelerate the product development cycle by increasing virtual collaboration, improving execution, and accelerating innovation. The parametrized design variables considered in this study for the aerodynamic optimization of the wing planform are wing area, aspect ratio, and taper ratio. The design variables for the structures are the thickness of spar, rib, stringers and skin. The specified constraints are the fuel volume dominated by the space between front and rear spar of the wing, the permissible stress, and buckling factor. The location of the ribs and spars has also been parametrized during the optimization process. The aerodynamic loads for the cruise angle of attack are computed using CFD on the CAD models generated in the design space using CATIA apps and transferred to the structural mesh model for further stress and buckling analyses on using SIMULIA apps on the 3DEXPERIENCE platform. The analyses have been carried out for the extreme load factors at the designed dive speed. The optimization by design of experiments is carried out in the form of a nested approach, i.e., the structural optimization within an aerodynamic optimization loop. The set objective has been to obtain optimal performance of a wing with a maximum lift- to-drag ratio with minimum structural weight subjected to fuel volume, stress, and buckling constraints. The industry best practice

B. Kanaparathi (✉) · E. Vathsalan · D. Panda · G. Prasad · G. Umashankar · S. S. Chittur · G. Avula
Dassault Systemés, Bengaluru, India
e-mail: bharath.kanaparathi@3ds.com

A. Pashilkar · A. C. Pankaj · D. Singh · Vijayakrishnan
CSIR-NAL, Bengaluru, India

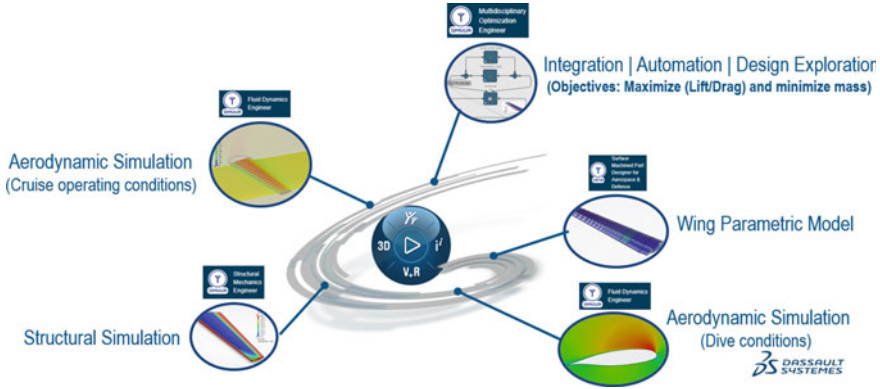


Fig. 1 Fully automated and integrated model-based platform approach

methodology shown in Fig. 1, proposed by Dassault Systemés, is fully integrated and automated ensuring digital continuity employing a unified environment for multidisciplinary optimization. The individual simulation solver technologies available on the 3DEXPERIENCE platform are validated for real-world performance assessment. The proposed workflow is re-usable and replicable for similar problem statements. Thus, the target process enables simulation-driven design decisions through a model-based data-driven approach on the 3DEXPERIENCE platform with the automation of simulation processes. The key value of the platform approach is to provide an end-to-end solution leveraging digital continuity, thereby accelerating the overall design and development cycle.

2 Description of Modeling and Approach

2.1 CAD Model

The significant aspect of an automated design iteration process is to have a robust and completely parametrized CAD. Semi-span of wing CAD is built using CATIA based on the case data provided by NAL.

According to the CAD modeling workflow presented in Fig. 2, airfoil smoothing is performed as a first step. The planform parametrization is done in terms of wing surface area, taper ratio, aspect ratio, root incidence, dihedral angle, and geometry twist on the semi-span wing model. Once the robustness of planform parameters are validated, the wing structure is parametrized in terms of rib thickness, number of ribs and their location, front and rear spars location. Through the parametrization of wing planform, the fuel volume is computed and exposed as an output variable to be monitored during the optimization study. The whole process of parametrization is based on general rules presented in Fig. 3. The complete wing parametric model

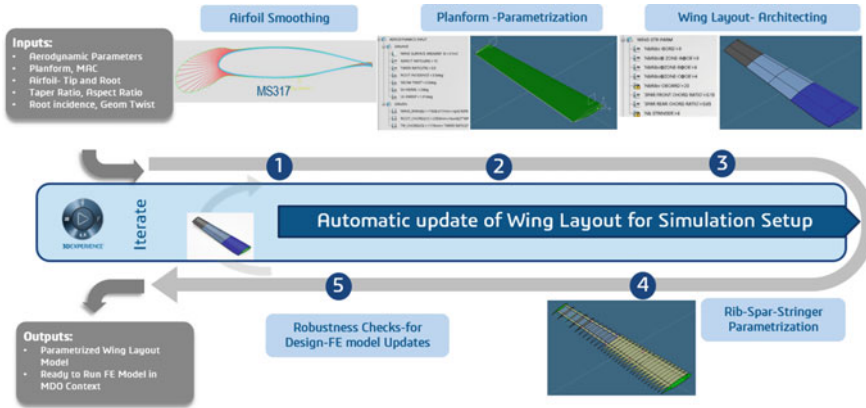
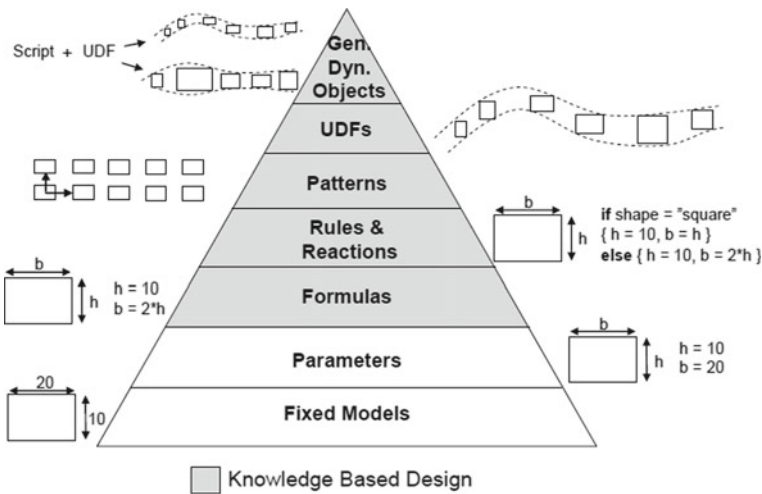


Fig. 2 CAD modeling workflow



Different levels of parametrization (adapted from Ledermann et al. [24])

Fig. 3 Parametrization rules

to be used in the simulation processes is shown in Fig. 4.

2.2 CFD Model

The Fluid Dynamics Engineer role on the 3DEXPERIENCE platform leverages 3DSFlow, a RANS-based finite volume solver to perform steady-state external flow

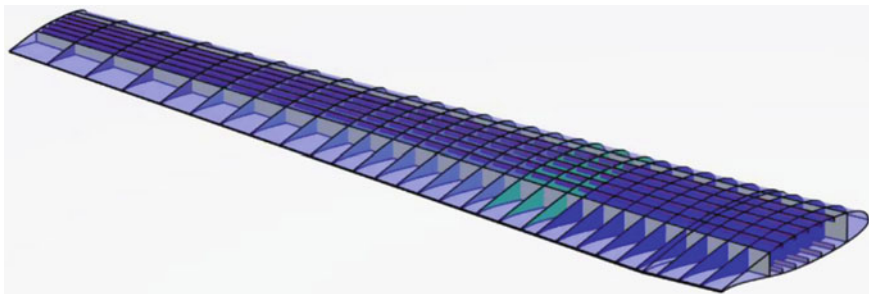


Fig. 4 Fully parametrized CAD of wing semi-span

simulations for assessing aerodynamic performance of the wing during dive and cruise conditions. Dassault Systemés SIMULIA’s body-fitted meshing technology called Hex-Dominant Mesher (HDM) not only reduces model build efforts with automatic fluid domain extraction but also generates finite volume mesh with prism boundary layers directly on native CAD geometry. This CAD-embedded CFD solution automatically updates the simulation model (mesh and scenario) when design changes occur during optimization loop. Aerodynamic simulation on parametrized wing semi-span is performed using Fluid Dynamics Engineer (FMK) role for 3 load cases, viz., upbending dive condition, downbending dive condition and cruise operating conditions as shown in Table 1.

The required angles of attack are estimated by the angle of attack (AoA) estimator, a 0D calculator, and given as input to Fluid Dynamics Engineer role. The fluid domain is tilted based on the AoA estimator output. Airflow simulation is performed assuming that the wing is static, and the incoming airflow is inclined with respect to the estimated AoA. The geometry is kept static in order to eliminate remeshing for every optimization loop, hence to save time for each CFD iteration. The planform parameters that are considered for aerodynamic DOE as design variables are listed in Table 2.

Table 1 Operating conditions

Operating conditions	Dive	Cruise
Pressure	101,320 Pa	52,423.8 Pa
Temperature	288.15 K	258.435 K
Velocity	139.5 m/s	111.11 m/s

Table 2 Aerodynamic design variables

Planform parameters	Baseline value	Lower bound	Upper bound	Intervals
Wing area (S)	31 m ²	28 m ²	32 m ²	0.5 m ²
Aspect ratio (AR)	10	9	12	0.5
Taper ratio (τ)	0.5	0.45	0.55	0.025

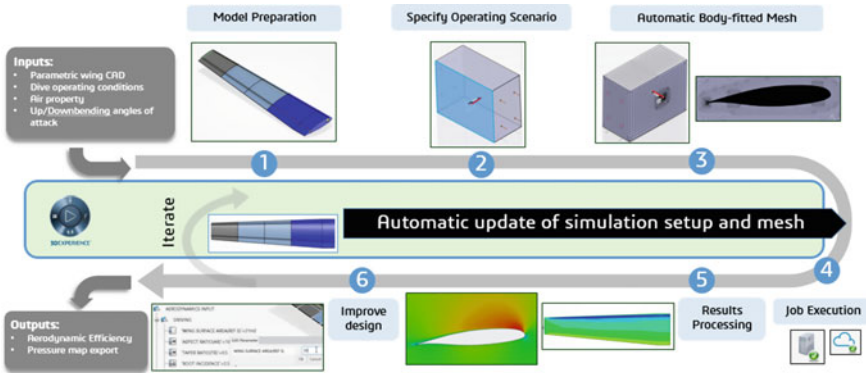


Fig. 5 CFD workflow

The fully automatic, body-fitted, hex-dominant mesh (HDM) consists of hex elements at the core, prism elements at the boundary layer, and tetrahedron & pyramid elements at the transition layer. The mesh parameters are as follows: global element size max = 2000 mm, min = 2 mm, local surface refinement (wing top and bottom surfaces) size = 8 mm. The boundary layer elements are meshed with prism-type elements having 15 number of layers with first cell height equal to 0.01 mm (targeting $y^+ = 1$) as represented in Fig. 6.

The flow solver in place uses implicit Reynolds-averaged Navier–Stokes (RANS) approach with a segregated pressure-based compressible solver offering 2nd-order spatial discretization. The turbulence model used is Spalart—Allmaras (typical in concept aircraft aerodynamics), and the boundary conditions include velocity inlet, pressure outlet, symmetry wall attached to the wing root, and free slip wall at top, bottom, and wing-tip side of the bounding domain box (represents virtual wind tunnel) as shown in Fig. 7.

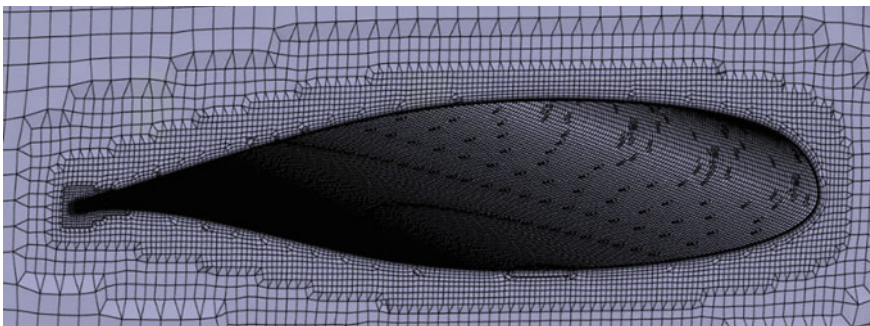


Fig. 6 Hex-dominant body-fitted CFD mesh

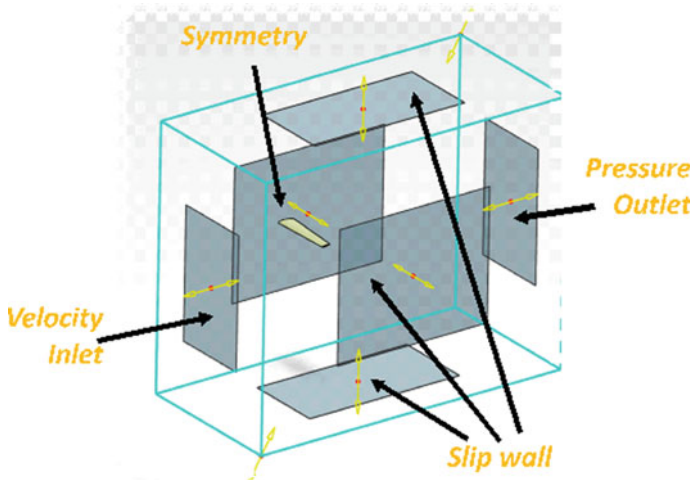


Fig. 7 CFD boundary conditions

Computation is run for 1000 iterations, and flow convergence is checked by monitoring the graphs of axial (Fx) and normal (Fz) forces, momentum, and energy residuals vs. number of iterations. Sample flow results and force convergence graph are presented in Fig. 8.

Sensors are introduced to measure the wing surface average pressure, axial, and normal forces. The 3D CFD surface average pressure data of the wing are stored in a tabular data format that is subsequently mapped to the FEA solver as a boundary condition (pressure load) in structural simulations. Two major advantages offered by this mapping capability include (i) Map is stored within the platform and hence no need to export and import files (ii) The map is tied to the geometry and CFD model; hence, it gets updated automatically when the CFD model is updated after a design change within the optimization loop.

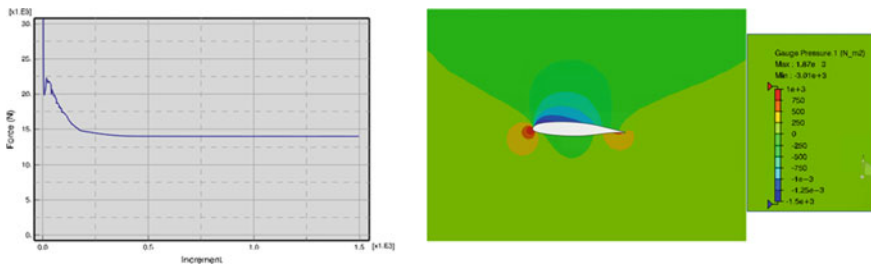


Fig. 8 CFD flow convergence and filed plots

2.3 Structural Model

The structural model is built using simulation model preparation app inside the 3DEXPERIENCE platform. The wing from root to tip is divided into four zones (Fig. 9), namely inboard (IB), zone A (ZA), zone B (ZB), and zone C (ZC).

The entire wing planform is discretized with a structured first-order shell element in maintaining connectivity across all sections of the wing. The process of meshing is automated such that every time design evolves in the design exploration phase, the mesh is generated automatically without any human intervention maintaining acceptable good element quality. Since the wing is assumed to be made up of aluminum, corresponding material properties such as Young's modulus, Poisson's ratio and density are considered under the material property definition. Considering the variable stiffness distribution along the length of the wing, skin surface over the wing (from leading edge to trailing edge) and the spars are also divided into zones of variable thickness as shown in Fig. 10a, b. All the major structural features like number of ribs across the cross-section, the thickness of the ribs and the thickness of the surface skin, and spars are considered as design variables for the optimization study.

Due to the seamless associativity between the CAD geometry and the simulation model (Fig. 11), all the changes made on the geometry are updated on the mesh model automatically including addition and removal of ribs and change in spar location. The structural simulation on the wing is performed for 2 pressure load cases that are coming from the CFD simulation.

The mapping of pressure data on structural model from CFD simulation is highly accurate (Fig. 12) and is done automatically by invoking the tabular data file generated by the CFD simulation during the structural model setup.

The boundary conditions applied on the structural model are as below:

1. Structural constraints applied in 'Y' direction at the central face
2. Constraints applied in 'Z' direction at the support brackets that connect to fuselage
3. Structural constraints applied in 'X' direction for drag bracket

The analyses carried out are as follows:

1. Stress analysis to check the strength of the structure against pressure load from CFD simulation.
2. Buckling analysis to check the Eigen value buckling factor against pressure load from CFD simulation.

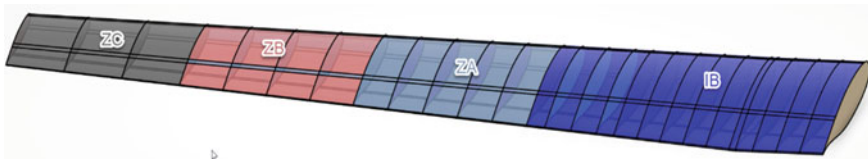
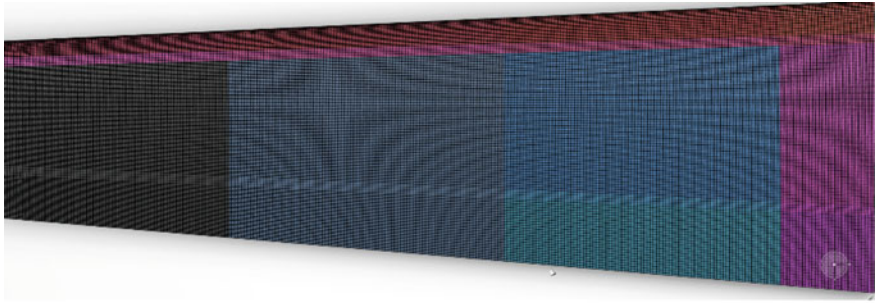
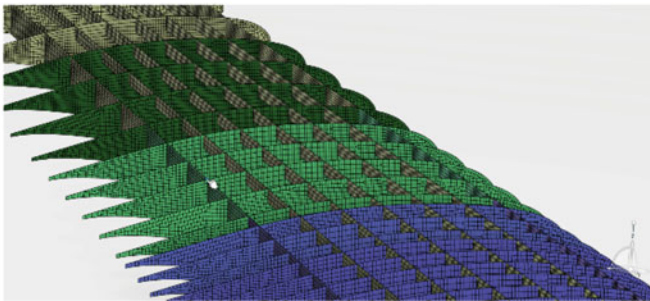


Fig. 9 Wing divided into four zones



(a). Surface Skin divided for Thickness Definition



(b). Ribs and Spars for Thickness Definition

Fig. 10 a Surface skin divided for thickness definition b ribs and spars for thickness definition

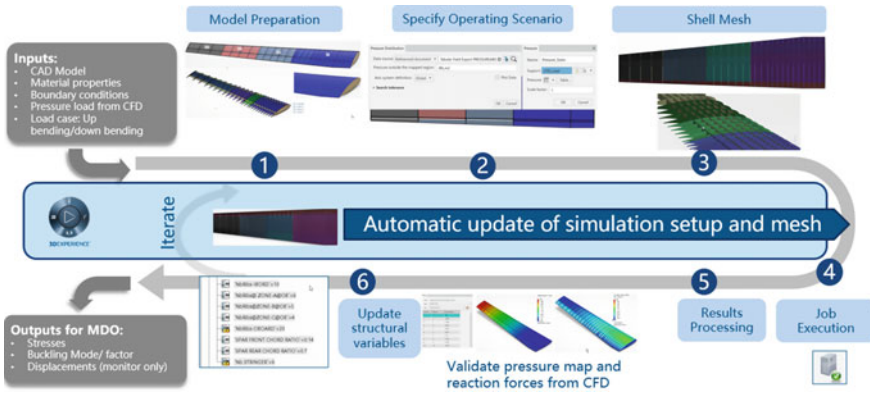


Fig. 11 Structural simulation workflow

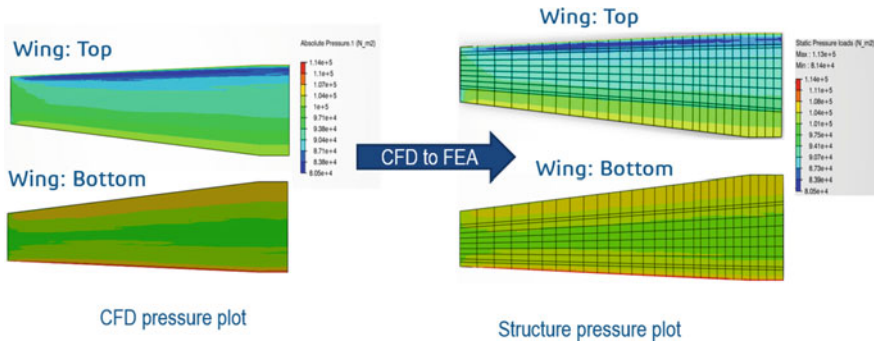


Fig. 12 Pressure mapping

3 Multidisciplinary Optimization Workflow

The multidisciplinary optimization workflow is structured in a way to consider all the design requirements of the wing. The workflow involves multiple activities (as shown in Fig. 13) like DOE, fuel volume calculation, angle of attack (AoA) estimator, CFD simulations for both upbending, downbending load cases, and also the cruise condition, encapsulated structural optimization for each CFD design. The workflow was initially proposed by CSIR-NAL and refined jointly. It has conditional checks for fuel volume and CFD model convergence. The whole workflow is driven by the DOE adapter on top which gives the planform variables as inputs.

Details of each activity labeled in Fig. 13 are mentioned below:

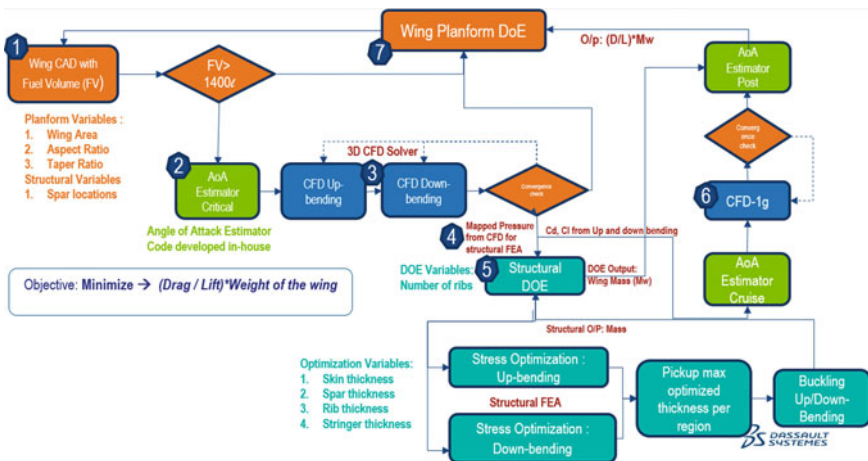


Fig. 13 Multidisciplinary wing optimization workflow process

3.1 Fuel Volume Calculation

The fuel volume calculation activity updates the geometry of the wing according to the inputs given by the DOE adapter and measures the fuel volume of updated geometry using CAD utilities available. There is conditional check next to fuel volume adapter where the decision is made; if the fuel volume is within the limits, the process will continue further; else, it will go back to the DOE adapter and start with the next design point.

3.2 Angle of Attack (AoA) Estimator

The angle of attack estimator is a FORTRAN code built to generate AoA values for the given input planform variables. The legacy data of aerodynamic efficiency for different angles of attack are considered as base by the AoA estimator to compute the AoA for limit load cases like upbending, downbending, and cruise conditions. This greatly reduces the size of DOE thereby improving the turnaround time. The angle of attack estimator activity takes the input values and runs a FORTRAN code for 3 main computations.

1. Use legacy data to compute AoA for upbending and downbending limit load cases.

Compute ratio of lift curve slope to 2π

Substitute values into the equation with initial guess for kapa. Iterate on kapa to solve.

where

$$C_{L\alpha} = \frac{2\pi \cdot AR}{2 + \sqrt{\left(\frac{AR \cdot \beta}{k}\right)^2 \left(1 + \frac{\tan^2 \Lambda_{c/2}}{\beta^2}\right) + 4}}$$

$\beta = (1 - M^2)^{0.5}$, Prandtl-Glauert Mach number parameter.

k = ratio of two-dimensional lift curve slope to 2π .

$\Lambda_{c/2}$ = Sweepback of mid-chord.

Ref: "General Aviation Aircraft Design," Snorri Gudmundsson, p.346.

Spanwise lift efficiency: $\sigma_{\text{eff}} = \frac{1}{C_{L\alpha} \pi \cdot AR}$.

2. Use CFD results from the limit load cases to estimate AoA for the cruise case.

Least-squares fit currently uses the tow limit load cases for linear regression.

Solve for AoA where:

$$C_L = C_{L\alpha}(\text{AoA} - \text{AoA}_{(CL=0)})$$

$$C_D = C_{D0} + C_l^2 / (\pi \cdot AR \sigma_{\text{eff}})$$

$$C_{L\alpha} = \frac{2\pi \cdot AR}{2 + \sqrt{\left(\frac{AR \cdot \beta}{k}\right)^2 \left(1 + \frac{\tan^2 \Lambda_{c/2}}{\beta^2}\right) + 4}}$$

$$W_{\text{cruise}} = CLqS$$

3. Fit CFD results from limit load cases and cruise case to refine estimate of L/D for the cruise point and compute objective function.
 - Least-squares fit currently uses the three CFD cases for linear regression.
 - Adjusts coefficients to cruise condition
 - Resolve for AoA
 - Computes objective function: $O_j = (D/L) W_{\text{wing}}$ at the adjusted cruise point where W_{wing} is the wing weight.

3.3 CFD Solver

The CFD solver activity solves the CFD simulation models for the upbending and downbending load cases considering the input planform variables for wing geometry and angle of attack from the AoA estimator. There is a conditional check after the CFD solver activity to proceed to the structural optimization only if the models have converged. If the model is not converged, it will go back to the DOE activity directly to generate next set of design points.

3.4 Mapped Pressure from CFD to Structural FEA

The output pressure data from the CFD model are automatically saved in the 3DEXPERIENCE database. This file is already called into the structural model at the time of model building. As the entire workflow runs in a single environment, the pressure data file will automatically get mapped on to the structural model before the structural simulation activity.

3.5 Structural Optimization

The structural optimization activity is encapsulated within the workflow to find an optimal structural model for each set of planform variables. The objective is to minimize the mass of the wing model for the given planform variables considering the

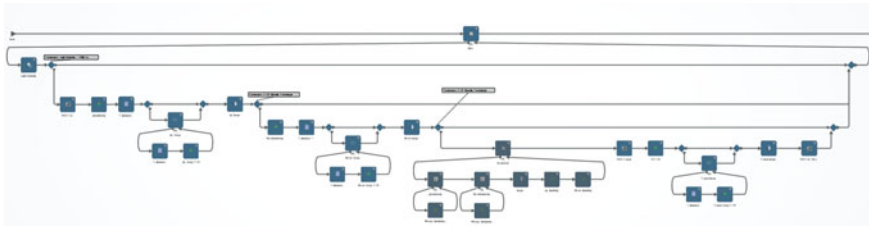


Fig. 14 Complete MDO workflow in 3DEXPERIENCE platform

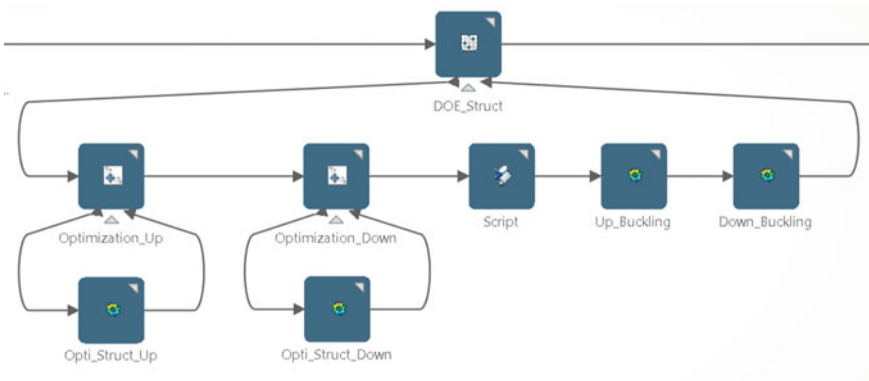


Fig. 15 Structural optimization workflow

thickness parameters and number of ribs as design variables and keeping the stress and buckling factor values within limits. The structural optimization as shown in Figs. 14 and 15 is driven by DOE component on top which gives the number of ribs at zone inboard, zone A, zone B, and zone C as inputs. The optimization activity has all the thickness parameters of the structural model, total 55 parameters as design variables and stress limits as constraints. The optimization activity for upbending and downbending load-cases is executed separately. The script after the optimization compares the optimal thickness values for each variable between upbending and downbending models, picks the higher value between the two and gets updated accordingly on to the buckling model. Fully stress design (SFD) structural optimization technique which is specific to thickness parameter changes is used for optimization.

3.6 CFD-1 g

The CFD 1 g activity is for the CFD cruise condition. It gets the inputs from the input planform variables and AoA estimator for cruise.

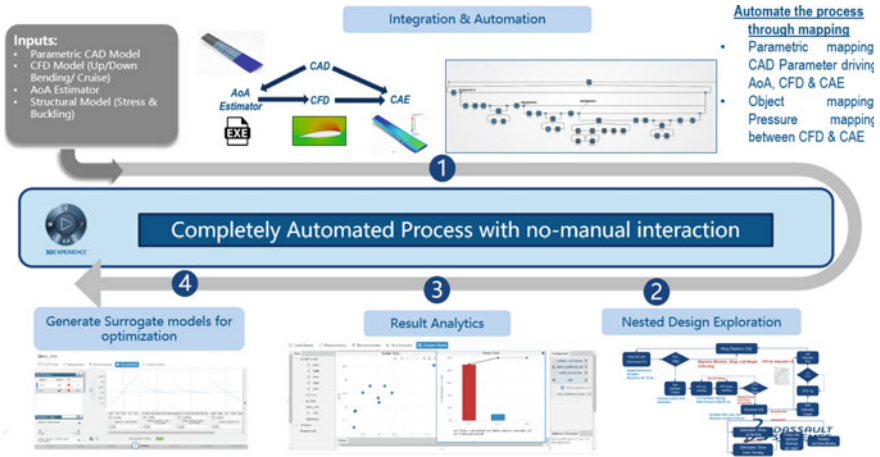


Fig. 16 MDO workflow

3.7 Doe

The DOE adapter is the driver which gives the planform variable wing area, aspect ratio, taper ratio, and also the front and rear spar location parameters as inputs and take the responses L/D ratio and mass which are defined as the objectives. The DOE technique used is Optimal Latin Hypercube, and the total number of design points considered is 40 (Fig. 16).

4 Results and Discussion

The MDO workflow is executed, and the results are analyzed in the results analytics app in the 3DEXPERIENCE platform. The final results are listed in a tabulated form as shown in Fig. 17 with all the inputs and outputs for the corresponding 40 design points. All the designs are given a specific rank based on the output values, and the

Rank	Aspect Ratio (AR)	Span	ASPECT	CD_Post	CL_Post	F.L.C.C	L.LOO	Mass (kg)	Objective	SP/SL F	SP/SL R	L/D	
1	0	1	0	0.05	0.0	0.0	1.14285	0.0	0.0	0.0	0.130414	0.62879	0.4
2	0	2	0	0.151	0.0	0.0	1.09184	0.0	0.0	0.0	0.1003	0.595	0.5
3	7	3	62.20	0.227	0.02235	0.47403	1.47731	21.226	390.224	20.25784	0.142206	0.70444	0.4
4	4	4	70.82	0.252	0.02144	0.46812	1.46854	21.834	413.857	19.89992	0.146524	0.70262	0.4
5	1	5	100	0.277	0.02015	0.46641	1.46122	22.549	350.963	18.51701	0.121628	0.605	0.4
6	0	8	0	0.2036	0.0	0.0	1.27912	0.0	0.0	0.0	0.128166	0.57146	0.5
7	0	7	0	0.4204	0.0	0.0	1.02016	0.0	0.0	0.0	0.137034	0.60732	0.5
8	2	8	97.45	0.504	0.021920	0.46365	1.42705	22.621	383.705	18.63434	0.123242	0.74851	0.4
9	0	9	0	0.36	0.0	0.0	1.30767	0.0	0.0	0.0	0.158172	0.68852	0.5
10	0	10	0	0.668	0.0	0.0	1.18872	0.0	0.0	0.0	0.130296	0.60207	0.5
11	4	11	74.85	0.731	0.02069	0.47111	1.43585	22.775	445.068	19.67639	0.131312	0.69734	0.4
12	0	12	0	0.807	0.0	0.0	1.22283	0.0	0.0	0.0	0.12817	0.66913	0.4
13	0	13	0	0.905	0.0	0.0	1.28714	0.0	0.0	0.0	0.155336	0.65895	0.4
14	8	14	47.20	0.983	0.02115	0.47211	1.41342	22.322	467.445	20.8468	0.122842	0.6797	0.5
15	6	15	63.12	10.008	0.02218	0.49146	1.43131	22.158	447.923	20.21572	0.128884	0.76815	0.4
16	0	16	0	10.094	0.0	0.0	1.26481	0.0	0.0	0.0	0.148852	0.75383	0.4
17	3	17	62.10	10.185	0.02126	0.46927	1.40756	22.787	430.204	19.34132	0.146524	0.75915	0.4
18	0	18	0	10.226	0.0	0.0	1.18254	0.0	0.0	0.0	0.128884	0.66261	0.5

Fig. 17 Final results table

best design is given rank no.1 (highlighted in light green color). Since the fuel volume calculation has a conditional check, 10 designs have passed fuel volume above 1.4 kL criteria. All the designs that failed the criteria are shown in orange label.

The best configuration is found to have the following properties:

- Aspect ratio: 9.277.
- Taper ratio: 0.46.
- Wing surface area: 30.2 sq.m
- L/D ratio: 22.55.
- Half-wing weight: **350.6 kg.**

Only, about 11 configurations from the 40 candidate configurations are found to meet the constraints. This is examined carefully, and it is found that the fuel volume constraint (minimum 1427L) dominated the results.

Another wing configuration with aspect ratio of approximately 12 is also found to be feasible with the following parameters:

- Aspect ratio: 11.72.
- Taper ratio: 0.54.
- Wing surface area: 31.97 m²
- L/D ratio: 23.
- Half-wing weight: 393.8 kg.

As seen from the above, the higher aspect ratio wing results in a higher wing area as well as overall weight and marginally better lift-to-drag ratio at cruise. This can be explained from the first-order analysis for the fuel volume dependence on the wing area and aspect ratio that goes as:

$$V \approx S^{1.5} / AR^{0.5}$$

It is clear from the above that if the solution is already at the limit value of the fuel volume, an increase in aspect ratio will result in requiring us to increase the wing area slightly to meet the fuel volume constraint.

The plots in Fig. 18 show the relation between planform variables vs L/D. It can be inferred from the graphs that the wing aspect ratio is directly proportional to L/D

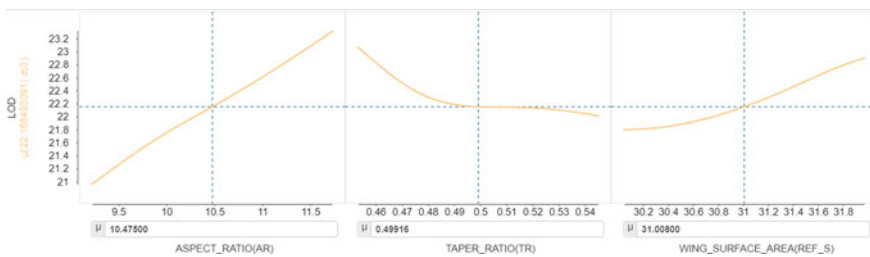
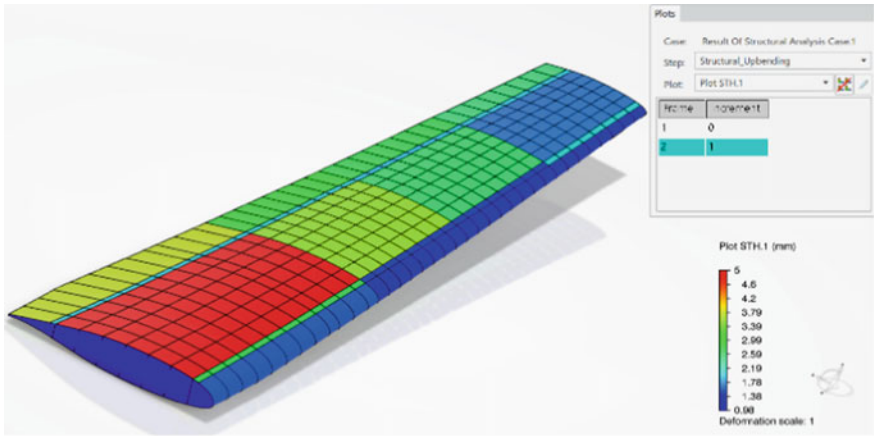


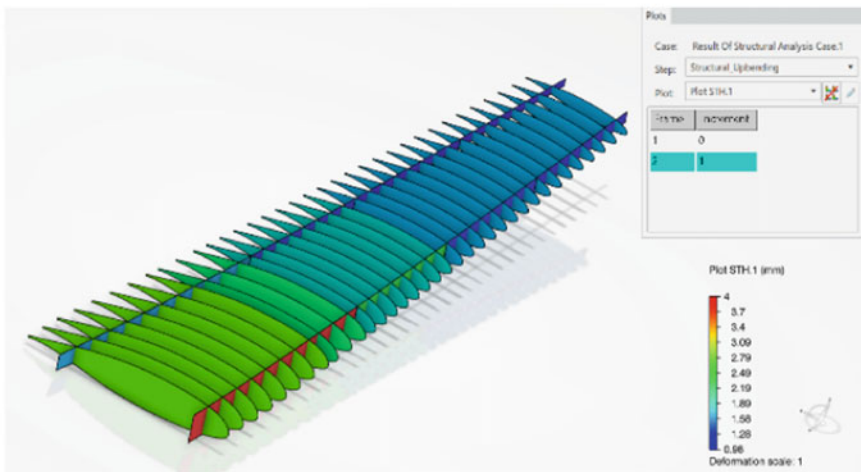
Fig. 18 Planform variables versus L/D

ratio. Increase in taper ratio affects L/D ratio for the given wing configuration. The twist applied to the wing CAD may also contribute to the L/D ratio along with taper ratio parameter. Increase in wing surface area and a higher aspect ratio increases the lifting surface area, thereby increasing the overall lift to drag ratio.

The corresponding structural model parameters for the best design from Fig. 17 are shown Fig. 19a, b.



(a). Final Thickness Values of the Outer Skin



(b). Final Thickness Values of Ribs & Spars

Fig. 19 a Final thickness values of the outer skin b final thickness values of ribs and spars

5 Conclusion

The MDO workflow shows the power of the **3DEXPERIENCE** platform from Dassault Systemés to enable seamless associativity between modeling and simulation by synchronizing fully parametrized CAD with automated multi-physics simulation workflows to perform multidisciplinary optimization studies. Benefits of the overall process help in transforming industry challenges to business values by accelerating product development time significantly. The proposed multidisciplinary optimization framework comprising of industry-standard methodology has great potential to influence the early conceptual design phase from coupon level to full scale. Based on this project experience, the turnaround time for the conceptual design process could be cut down by approximately 60% leveraging the described methodology.

Acknowledgements The First Author acknowledges Mr. Mark Beyer (A&D Industry Expert), Mr. Ganesh Prasad (Modeling Expert), Mr. Pradeep Ramadoss (Process Automation), Dr. Ravishankar Mariayyah (Process Automation), Mr. Gregory Laskowski (Global Fluids Application team), Mr. Benjamin Duda (Global Fluids Application Team), Mr. Michael Sacks (Global Fluids Application Team), Mr. Lin Sun (CFD R&D), Mr. Asif Khan (FEA R&D), Mr. David Lau (FEA R&D), Mr. Kaushik Das (Mapping R&D) from Dassault Systemés for their guidance and continuous support.

References

1. Fundamentals of Aerodynamics by John D. Anderson, 5th edn, McGraw Hill Education
2. Brown A, Harris WL (2020) Vehicle design and optimization model for urban air mobility. Aerospace Research Central.
3. Title 14 CFR Part 23—Airworthiness Standards for Normal Category Aircraft
4. Sobieszczanski-Sobieski J, Morris A, van Tooren M (2017) Multidisciplinary design optimization supported by knowledge based engineering, Wiley Publishers
5. Cavagna L, Ricci S, Travaglini L (2011) An integrated tool for structural sizing, aeroelastic analysis and MDO at conceptual design level. Prog Aerosp Sci 47(8):621–635
6. Mastroddi F, Tozzi M, Capannolo V On the use of geometry design variables in the MDO analysis of wing structures with aeroelastic constraints on stability and response. Aerospace Sci Technol 15(3):196–206

On–Off Control Scheme Using Reaction Control Thrusters for Pitch Stability During Atmospheric Abort of Crew Module



Swetha Sakunthala, Nikunj Gupta, Aprameyo Roy, and Kapil Kumar Sharma

1 Introduction

Crew modules are capsule modules housing astronauts and are critical to any human space mission. However, in the event of an abort condition in the atmospheric phase, the CM detaches itself from the launch vehicle and splashes down at an acceptable impact velocity, using parachute deployment. Body rates of the CM need to be actively controlled in order to ensure safe deployment of parachute before touchdown. Phase-1 atmospheric abort is the condition, wherein the CM is to be separated from the launch vehicle at a height of about 13–14 km. Once the CM separates from the launch vehicle, attitude is unfavourable for initiating the parachute deployment process as the module is at a high angle of attack and experiencing high tumbling rates.

The CM has two stable trim points, making it statically stable. Hence, self re-orientation is achieved mainly through the flight path angle changes and partly through aerodynamic moments [1]. However, this is a slow process, and some forms of active control are required to bring the system to stability in lesser time to meet the mission objectives. Motion in the pitch plane is controlled using 2 RCS thrusters, located at Pitch+ ($P+$) and Pitch– ($P-$) directions, respectively. RCS thrusters used provide a thrust capability of 100N each with only two operating states, either on

S. Sakunthala (✉) · N. Gupta · A. Roy · K. K. Sharma
Vikram Sarabhai Space Centre, Trivandrum, India
e-mail: swetha@vssc.gov.in

N. Gupta
e-mail: nikunj_gupta@vssc.gov.in

A. Roy
e-mail: aprimeyo_roy@vssc.gov.in

K. K. Sharma
e-mail: kk_sharma@vssc.gov.in

or off, implying they produce either a constant force or a null force. To design a controller of such nonlinear actuators, either nonlinear control algorithms must be developed, or the control command is to be modulated to pulses.

The mission objective requires the safe deployment of parachute within 50 s from the CM separation for the abort condition discussed. From control point of view, this translates to bringing the pitch rate to within $1^\circ/\text{s}$ and angle of attack to a stable trim point within the duration of 50 sec or less.

2 System Dynamics

Whilst designing any controller, an accurate model is required which captures the basic dynamics of the system. Following sections highlight the coordinate system and relevant parameters used to develop the system equations of motion. The assumptions used whilst deriving these equations are discussed, and initial conditions used for the simulation are presented. Finally, a model of the system is simulated, and the results are discussed.

2.1 Equations of Motion

The CM axes are defined as shown in Fig. 1a which is a right-handed triad system with the CM's centre of gravity (CG) as origin. Whilst looking from the base of the module, clockwise roll is positive (rotation about Z_b). Y_b is defined as the pitch axis, with pitch down (from Z_b axis towards X_b axis) being positive rotation. Similarly, rotation about X_b axis signifies yaw motion. The coordinate system and other parameter definition used for deriving the equations of motion of the crew module is given in Fig. 1b. α is the body angle of attack; θ is the yaw angle, and γ is the flight path angle. The crew module is at an altitude of h from the Earth's centre.

The following assumptions are taken into account whilst deriving the equations of motion:

- (i) Motion is restricted to a plane (movement along pitch axis).
- (ii) Earth is spherical and non-rotating.
- (iii) Crew module is rigid, and its mass is constant throughout the flight.
- (iv) Effective length to diameter ratio of the crew module is small.
- (v) Value of acceleration due to gravity (g) is constant throughout the trajectory.
- (vi) Aerodynamic derivatives are a function of Mach number and angle of attack.
- (vii) The effects of atmospheric winds are neglected.

The equations of motion are as follows [2]:

$$\dot{h} = V \sin(\gamma) \quad (1)$$

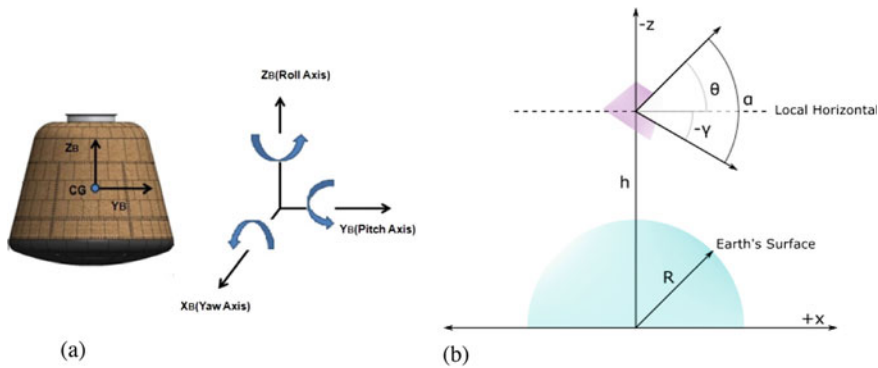


Fig. 1 a Crew module axes definition **b** coordinate system for equations of motion

$$\dot{V} = \frac{-\rho V^2 C_D A}{2m} - g \sin(\gamma) \quad (2)$$

$$\dot{\gamma} = \frac{\rho V A C_L}{2m} - \left(\frac{g}{V} - \frac{V}{R} \right) \cos(\gamma) \quad (3)$$

$$\theta = \alpha + \gamma \quad (4)$$

$$\ddot{\theta} = \frac{\rho V^2 A D}{2I} (\alpha C_{m\alpha} + \frac{\dot{\theta} D}{2V} C_{mq} + \frac{\dot{\alpha} D}{2V} C_{m\dot{\alpha}}) \quad (5)$$

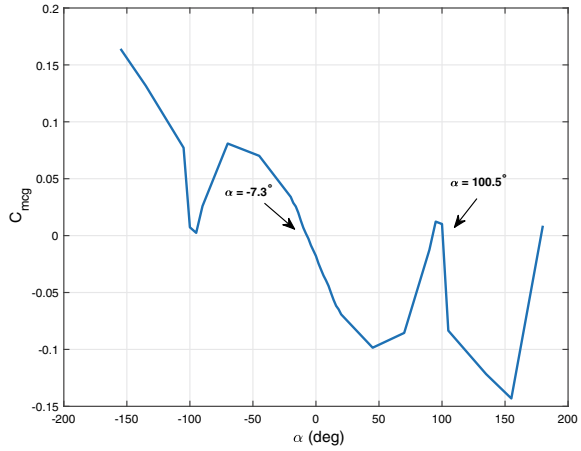
Here, mass (m), reference diameter (D), reference area (A) and inertia (I) are parameters of the CM. C_d , C_L and C_m are the drag, lift and pitching moment coefficients, respectively, and are obtained using wind tunnel testing of the CM.

Equation 1 shows the change in altitude of the CM taking into account vertical component of the velocity vector (V). Equation 2 describes the sum of the forces acting on the CM in the direction of motion. Equation 3 describes the change in flight path angle (γ) due to forces normal to the direction of motion, gravity and centrifugal forces. Equation 4 comes from the definition of the angles as described in the coordinate system above. Finally, Eq. 5 sums the inertial, static and dynamic moments acting on the CM.

It can be shown that $\dot{\theta}$ and $\dot{\alpha}$ are almost equal as $\dot{\gamma}$ tends to zero over the course of time. As a result, Eq. 5 can be modified such that:

$$\ddot{\theta} = \frac{\rho V^2 A D}{2I} \left(\alpha C_{m\alpha} + \frac{\dot{\theta} D}{2V} (C_{mq} + C_{m\dot{\alpha}}) \right) \quad (6)$$

Fig. 2 $C_{m_{cg}}$ versus angle of attack



2.2 Initial Conditions

The following initial conditions are used for simulating the vehicle dynamics. These values come from the description of the Phase-1 atmospheric abort discussed earlier.

- Initial Flight path angle = 1° Initial velocity = 68 m/s
- Initial altitude = 13240 m Initial pitch rate = $-2^\circ/s$
- Initial angle of attack = 150°

2.3 Trajectory Plots

A Simulink® model is created using Eq. 1– 6 with the initial conditions mentioned previously. The aerodynamic coefficients of the system are obtained from the wind tunnel tests conducted on the CM. These are stored as a look-up table in the model with angle of attack as the input. The dynamic damping derivatives, C_{mq} and $C_{m\dot{\alpha}}$, are obtained as a sum during the wind tunnel tests. For the default conservative case, the sum of these derivatives is taken to be positive. Further, the density variation in the atmosphere with altitude has been captured using the standard atmospheric model as reference. The nonlinear differential equation solver (ode4) with a fixed step time of 0.1 s is used for solving the system dynamic equations.

CM is longitudinally statically stable with two stable trim points (at -7.3° and 100.5°) as shown in the plot of $C_{m_{cg}}$ versus α in Fig. 2. This shows that the CM aligns itself to the desired trim angle irrespective of the initial attitude given sufficient time. This can be further verified from Fig. 3a, where initial $\alpha = 50^\circ$, and Fig. 3b, where initial $\alpha = 100^\circ$.

Figure 4a shows that the flight path angle (FPA) builds up to almost a vertical fall ($\gamma = -90^\circ$), which favours the parachute deployment landing scheme. There are

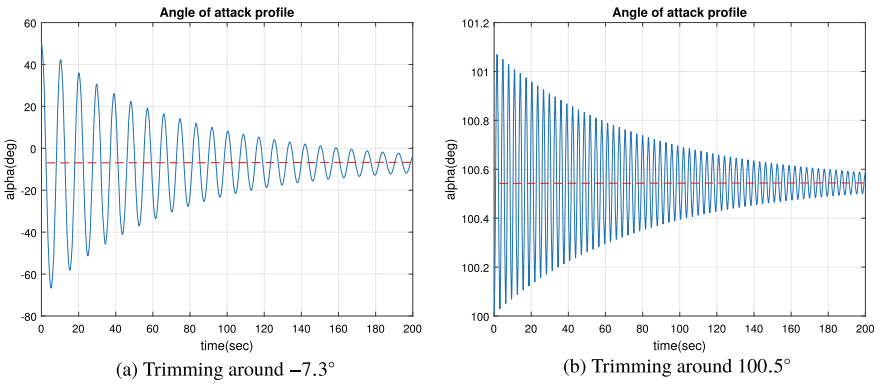


Fig. 3 Angle of attack profile over time

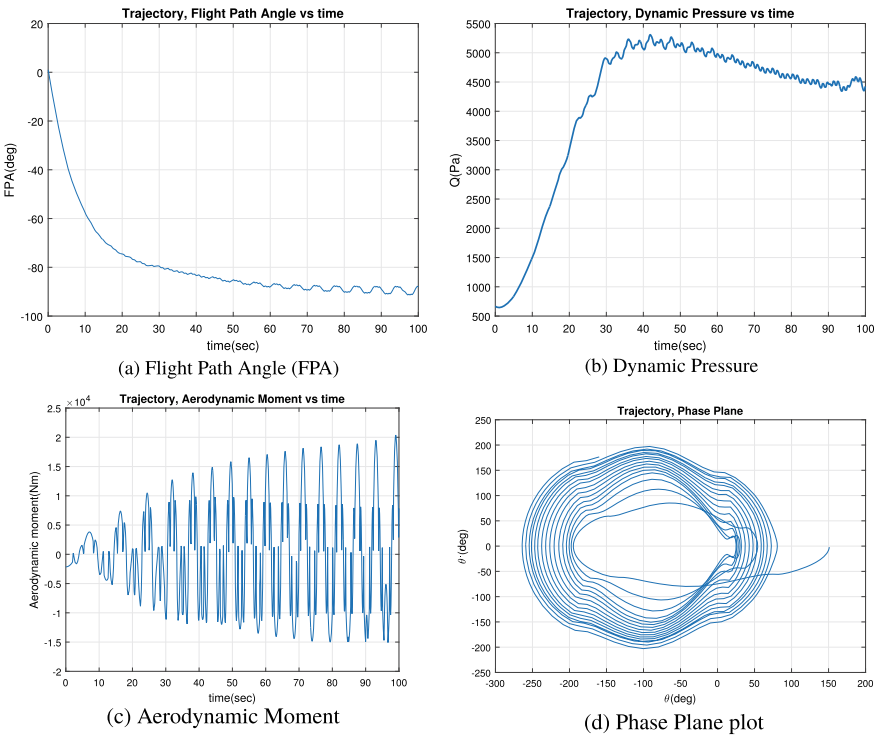


Fig. 4 Trajectory plots

small oscillations in FPA profile as well beyond the 20s mark corresponding to the dynamic instability of the system. The maximum dynamic pressure experienced by the CM is around 5300 Pa, as seen in Fig. 4b.

Aerodynamic moment acting on the CM is plotted in Fig. 4c showing a maximum moment of 2×10^4 Nm. This moment is also sinusoidally varying. Figure 4d shows the phase plane plot between pitch angle (θ) and pitch rate ($\dot{\theta}$) of the CM. It can be seen that the curve spirals away over time showing high limit cycle amplitude and, hence, dynamic instability of the system.

3 Controller Design

The control scheme proposed is a PD controller with a combination of hysteresis and dead zone, as shown in Fig. 5. Hysteresis block is required to modulate the control output to pulses, which is essential for driving the RCS thrusters. Increasing the hysteresis value decreases the number of times the output will cycle. Decreasing the hysteresis band improves the controllability of the system but may result in output chattering. Dead-band regions are used to prevent oscillations. Dead band and hysteresis width are chosen depending upon the requirements on rate and attitude as well as to minimise chattering and fuel consumption of the system [3].

Hysteresis and dead zone region in the control logic as shown in Fig. 6a gives rise to nonlinearity in the system, whose behaviour cannot be observed with the help of superposition. Hence, phase plane analysis is used. This graphical analysis designed for second-order systems is an effective tool to check the stability of the system without solving the nonlinear equations.

The hysteresis controller logic has a few disadvantages. A lot of chattering ensues in the control moments in the presence of disturbance resulting in the wearing of RCS thrusters. As the logic is entirely based on composite error, the system keeps overshooting desired set-points resulting in the thrusters consuming excess fuel from continuous and non-optimal firing commands. In order to overcome these disadvan-

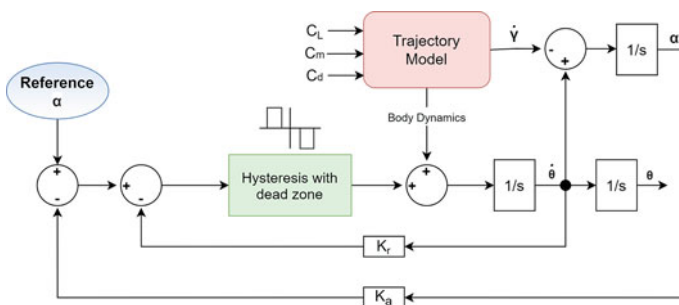


Fig. 5 Controller schematic for on-off control with hysteresis and dead zone

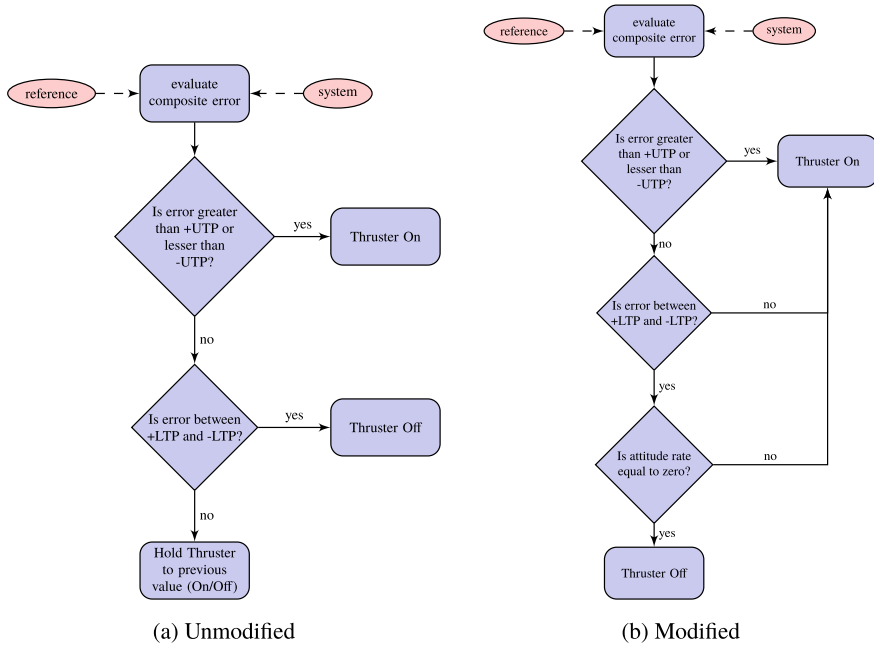


Fig. 6 Thruster on off logic flowchart

tages, a modified controller logic, as shown in Fig. 6b, is proposed that takes into account the current body rate whilst switching off the thrusters. The switch-on logic remains the same. Thruster is switched off only when the composite error is within limit as well as attitude rate is zero. As a result, number of switching cycles of the RCS thrusters is reduced without any change in controller performance.

4 Results and Discussion

Figure 7a, b shows that the controlled vehicle reaches a stable trim point and pitch rate comes down below 1°/s within 75 s, suggesting that more powerful thrusters are required to meet the requirement of stabilising the CM within 50 s. Phase plane plot of Fig. 7d shows that the limit cycle amplitude of the system has reduced significantly using the on-off controller.

In Fig. 7c, aerodynamic moment experienced by the vehicle is shown with respect to the control moment provided by the RCS thrusters. It can be seen that if the aerodynamic moment increases further due to environmental disturbances, the controller will take more time to bring the system to stability. Hence, RCS with a higher thrust capability is required. Also, some chattering of the thrusters around the 70 s mark is observed.

To overcome the chattering of RCS thrusters, system is simulated with the proposed modified control logic. From Fig. 8b, we can see that there is almost no difference in the performance for the modified control logic. Desired angle of attack value

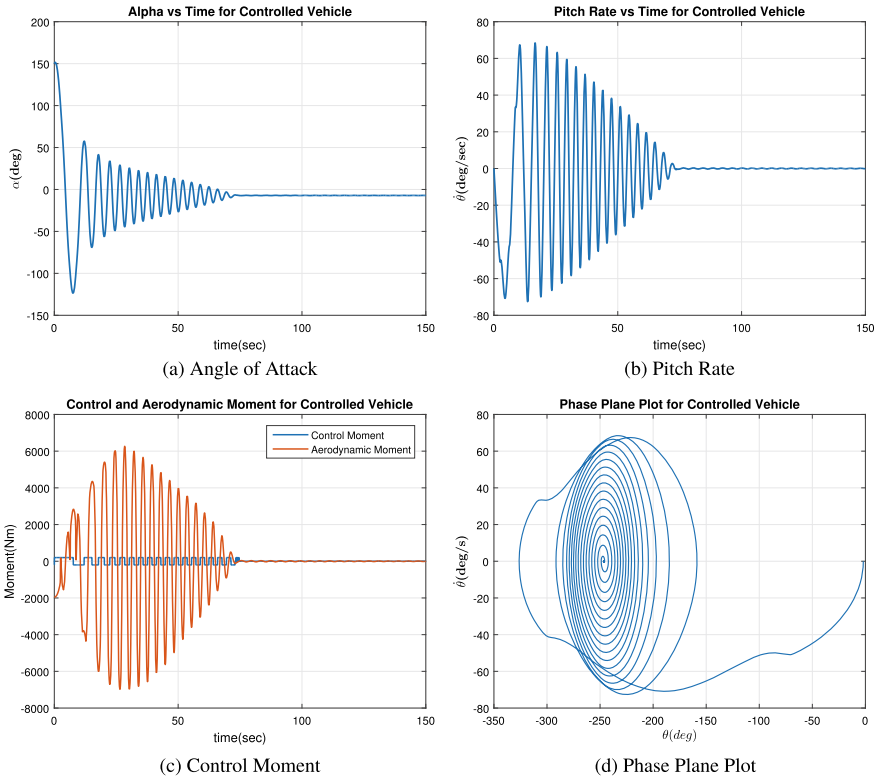


Fig. 7 Plots for controlled vehicle

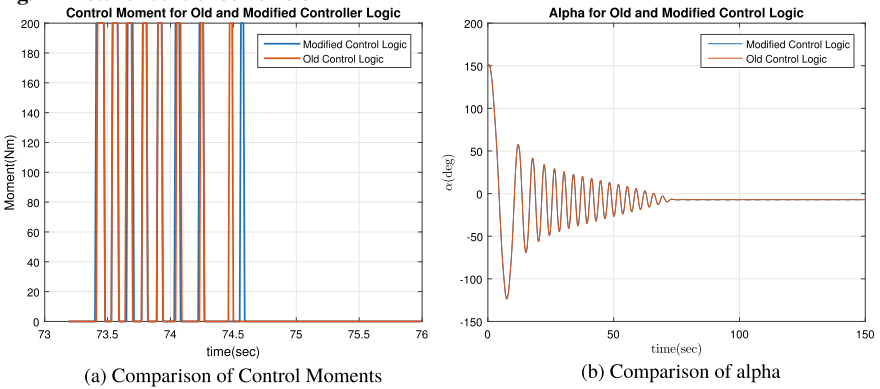


Fig. 8 Plots for modified control logic

is achieved in almost the same time as the previous controller. However, the amount of chattering is reduced, as seen in Fig. 8a.

5 Conclusion

Stability aspects of the crew module are discussed, and an on-off controller using PD algorithm for the RCS thrusters is designed to assist in safe deployment of parachute during the abort phase. It is seen that 100N RCS thrusters are insufficient to bring the module to a stable orientation in the given time. This signifies a need for using thrusters with a higher thrust value. However, this can cause significantly higher limit cycle amplitudes. Further, it is seen that the limit cycle amplitude and frequency can be kept within a specified range by appropriately modifying the dead zone and hysteresis bands whilst designing the controller.

Due to inherent problem of chattering in the on-off control algorithm, there is unnecessary firing of RCS thrusters which is fuel inefficient and reduces the life of these thrusters. To prevent this, a modification to the existing control algorithm is made, and results are presented.

Reaction control system and other nonlinear systems are actively used for launch vehicle control, especially during roll control. Given the inherent issue of chattering in these systems, the modified controller logic can be used to increase reliability and life of these systems. Further, the relation between hysteresis and dead band with the limit cycle characteristics of the system can be exploited whilst designing such a control algorithm.

Acknowledgements We express our sincere gratitude to Dr. Gopal Jee (DH, CLD, CGSE, VSSC) for his continuous guidance throughout the course of this work. We would also like to thank SWTD, AERO for granting us permission to use their resources for running the simulations and Library, VSSC for extending its resources which proved invaluable for the completion of the project.

References

1. Kazemba CD, Braun RD, Clark IG, Schoenenberger MA (2017, January–February) Survey of Blunt body supersonic dynamic stability. *J Spacecraft Rockets* 54(1):109–127
2. Soumya N, Nair AP, Brinda V, Sheela DS, Lalithambika VR, Dhekane MV (2018) Attitude control schemes for crew module atmospheric re-entry experiment mission. *IFAC-PapersOnLine*, vol 51, issue 1, 2018, pp 627–632. ISSN 2405-8963
3. Koshy T, Ushakumari S, Gopal J (2014) Stability assessment and control law design of crew capsule module in re-entry phase. Master thesis report, Department of Electrical Engineering, College of Engineering, Thiruvananthapuram

Sensitivity Analysis and Optimization for a Trainer Aircraft Configuration



M. B. Subrahmanya, V. K. Suman, K. N. Kaushik, S. Raghavendra Rao, and Gopinath L.

1 Introduction

Flow sensitivities are the derivatives of the variable which we would like to minimize/maximize (lift, drag, etc.) with respect to a set of parameters that describe the flow for example the shape of the body. These are interesting as they reveal the amount of change of these parameters to the flow variable. Three-dimensional, compressible equations using open source SU2 [1] has been used to derive the drag sensitivities for optimization studies. The full wing shape optimization has been performed using the discrete adjoints. This resulted in a 28 counts reduction in drag on the wing alone [2].

2 Methodology and Results

A 25.5 million mesh has been used for the computation. The governing equations have been discretized using the Jameson Schmidt and Turkel (JST) scheme with

M. B. Subrahmanya · V. K. Suman · K. N. Kaushik (✉) · S. Raghavendra Rao · G. L.
CSIR -NAL, Bangalore, India
e-mail: kaushik@nal.res.in

M. B. Subrahmanya
e-mail: subrahmanya@nal.res.in

V. K. Suman
e-mail: suman@nal.res.in

S. Raghavendra Rao
e-mail: srrao@nal.res.in

G. L.
e-mail: lgopinath@nal.res.in

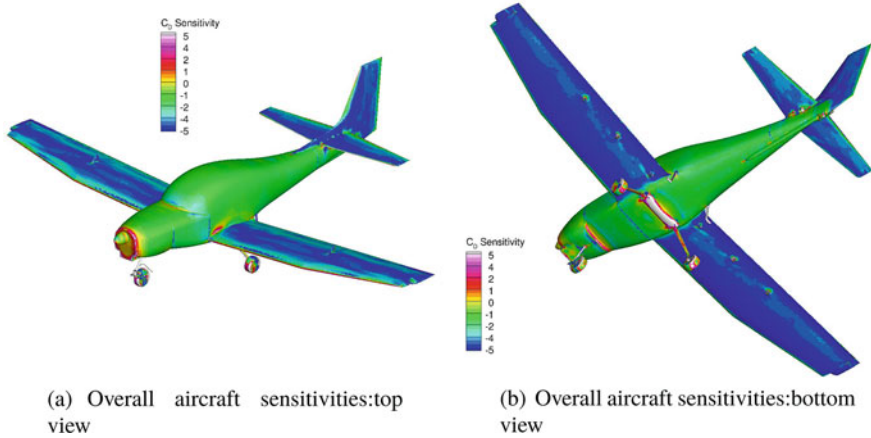


Fig. 1 Overall sensitivities on the full aircraft

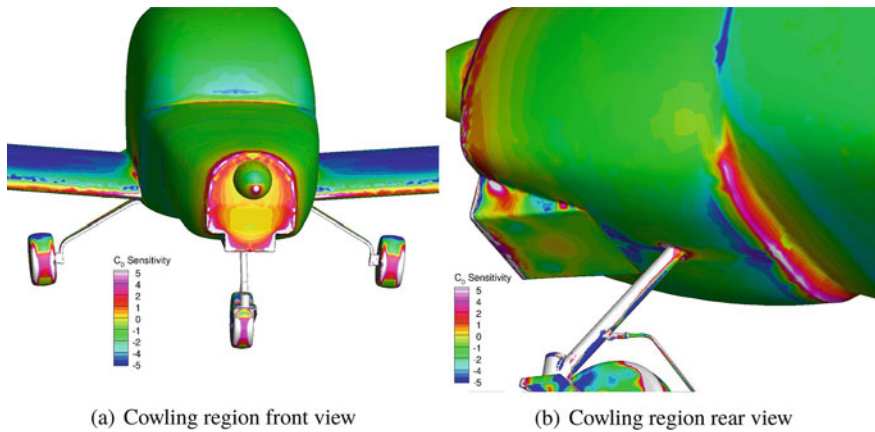


Fig. 2 Sensitivities on the cowling region

Spalart Alamaras (SA) turbulence model, both for the direct as well as the adjoint solver. Implicit Euler is used for time discretization. Mach number of 0.15, Reynolds number of 4 million and an angle of attack of 5° have been chosen in this study. A drag-based cost functional has been used for the adjoint solver. The adjoint solver has been validated against standard configurations as in [2].

The direct solver has been validated with the experimental data. Figure 1 shows results for overall drag sensitivities of the full aircraft. As observed the major contribution of the drag is due to the wing, landing gears and cowling which need a geometric modification.

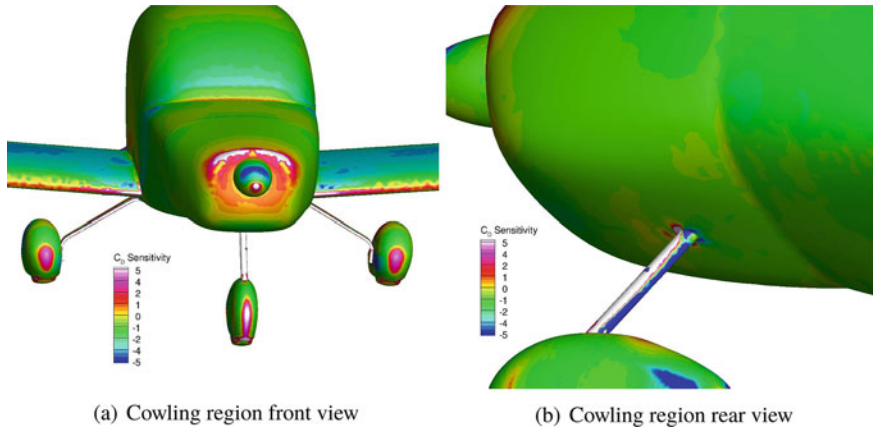


Fig. 3 Sensitivities on the cowling region after modification

As shown in Fig. 2 the vertical step at the interface of the cowling with the fuselage shows a high value of sensitivity. Also high values of sensitivities is observed on the cowling edges and the landing gear assembly.

In a joint work with the CAD designers the following modifications were further proposed for further drag reduction. As a first step, the bottom vertical step at the inter-junction of the front fuselage and cowling is eliminated and the front portion is made smoother as compared to the flat vertical face of the existing cowling. The main concern was to make the cowling surface more convergent and reduce the exposed wet area for the air flow. The sensitivities after modification shown in Fig. 3 shows a significant reduction.

The modification helps in streamlining the flow better as seen in the reduction of the values at the cowling-fuselage junction. However there is still a significant high values around the top edge of the cowling, suggesting areas where further shape modifications possible. Since it is well known that bluff bodies generate more pressure drag, we have identified the original landing gear assembly to represent the bluff body configuration. The RANS computations also clearly demonstrate this by showing a high pressure drag contribution from the landing gear assembly. Hence, we opted for wheel fairings similar to [3] which are aerodynamically shaped covers enclosing the wheel, wheel hub and the strut partially. This gives a streamlined configuration around these regions.

The belly fairing (MLG and fuselage fairing) in the initial configuration was a bluff body. To reduce the drag from this geometry, the fairing is widened and maintaining continuity with fuselage in all directions.

The sensitivities for the belly fairing and MLG strut is shown in Fig. 6. There is a reduction in the sensitivities after modification, both on the MLG strut and the bottom fairing due to the streamlining of the flow in these regions. The modified configuration resulted in a drag reduction of approximately 72 counts (Figs. 4, 5 and 6).

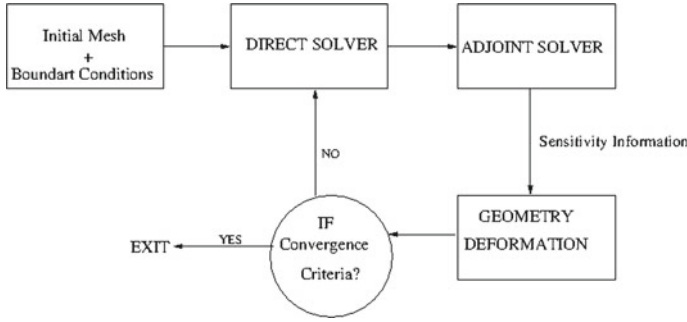


Fig. 4 Overall optimization procedure

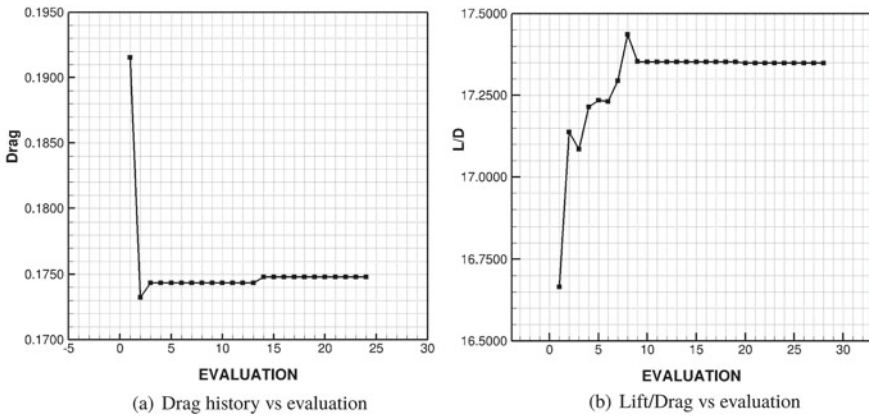


Fig. 5 Drag and lift history

For the optimization procedure minimization of a drag-based cost functional has been proposed. To perform the deformation an FFD box of size $11 \times 9 \times 2$ has been used in this study as shown in Fig. 7. The discrete adjoint solver is used backwards in time to compute the functional gradients which is then fed into a built in elastic solver of SU2 to deform the geometry and the mesh. The process is repeated until a predefined convergence criteria on the gradient to obtain the improved shape. The overall optimization procedure is shown in Fig. 4.

The whole procedure has been run on a cluster of 480 processors. The overall computational time of the complete optimization process is around 7 days. Figure 5 shows the drag evaluation versus the number of evaluation and the corresponding lift drag ratios. The optimization has resulted in a reduction of around 28 counts of drag on the wing. The minimum thickness changes by around 5 mm during the optimization process.

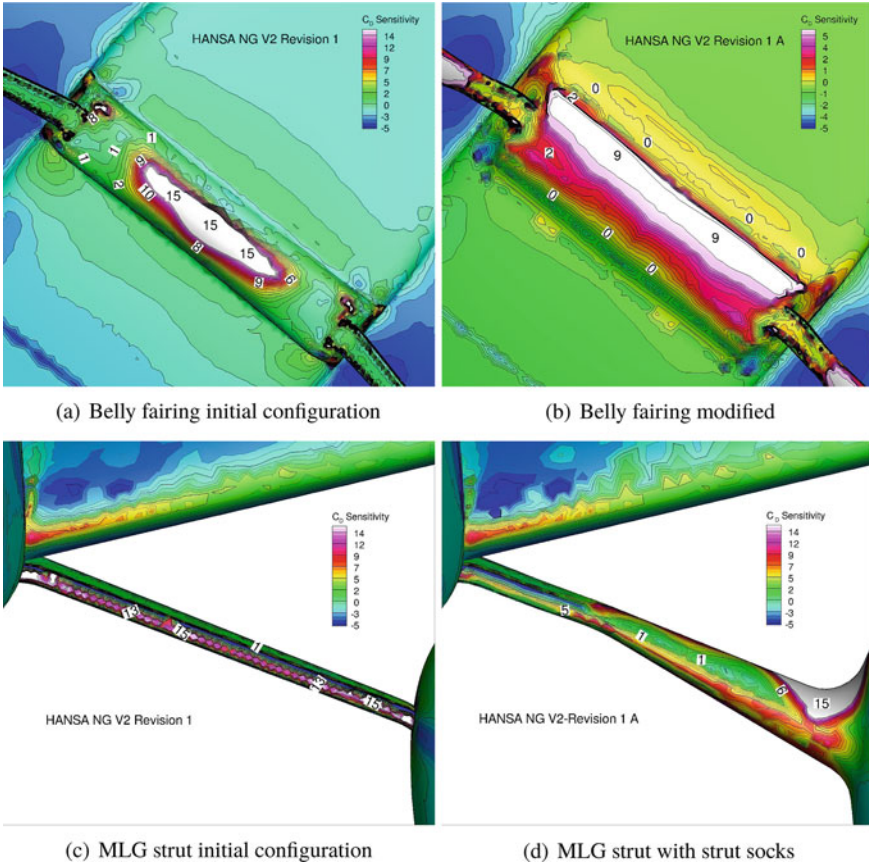
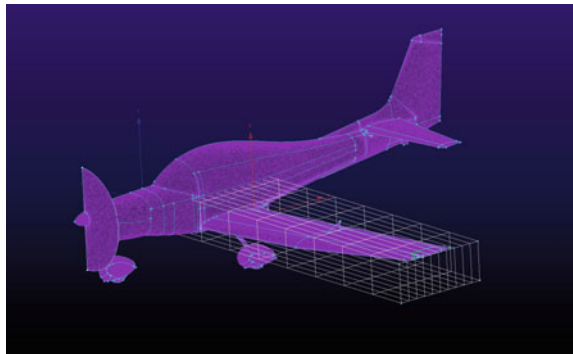


Fig. 6 Sensitivity analysis comparison of belly fairing and MLG strut

Fig. 7 Mesh with FFD box



3 Conclusions

1. Drag sensitivity study based on discrete adjoints of a trainer aircraft configuration has been carried out.
2. Regions which are sensitive to geometry modifications have been identified. Modification based on the sensitivity analysis resulted in a drag reduction of 72 counts.
3. An adjoint-based shape optimization based on minimizing a drag-based cost functional has been performed. This has further resulted in a 28 drag count reduction on the wing.

References

1. Palacios F, Economon TD, Wendorff AD, Alonso JJ (2015) Large-scale aircraft design using SU2. In: AIAA Paper 2015-1946, AIAA SciTech: 53rd AIAA Aerospace Sciences Meeting, Kissimmee, Florida, 5–9 Jan 2015
2. Kaushik KN, Subrahmanya MB, Suman VK (2018) Sensitivity analysis of aerospace configurations using open-source tool SU2. In: 20th AESI CFD conference
3. Herrnstein WH, Biermann D (1934) The drag of wheel, wheel fairings and landing gears -I. Report number 485, National Advisory Committee on Aeronautics

Mathematical Modelling and Numerical Simulations of Underslung Dynamics



K. L. N. Sai Nitish, S. Kumanan, N. Remesh, and B. Karthik

1 Introduction

Applications of helicopters carrying externally suspended loads (underslung) are of significant interest in the aerospace research community. The underslung, usually, is a streamlined winged body such as jet trainer or a bluff body like container used in rescue missions in disaster-stricken areas. Early works by Nagabhushan [1] in this field considered the underslung as a point mass with aerodynamic drag acting on it. Point mass approximation can predict the pendulum dynamics of the underslung accurately although this model fails to predict the yaw plane instabilities arising due to aerodynamic excitation of the underslung. Therefore, it is imperative to study the six DoF helicopter-underslung system and its stability in the presence of unsteady aerodynamics through different regimes of flight, especially the limit cycle oscillations in yaw and roll plane engendering due to insufficient aerodynamic restoring moments. Works carried out by Ronen et al. [2], Stuckey [3] do bring out various modes of oscillations by modelling the coupled dynamics of the helicopter and the underslung, but focus of the current work is to study the dynamics of underslung with unsteady helicopter accelerations as input. Pal [4] modelled the helicopter-underslung dynamics using Kane's method which is an intermediate form between the Lagrange's equations and Euler equations where the system constraint forces can

K. L. N. Sai Nitish (✉) · S. Kumanan · N. Remesh · B. Karthik
Vikram Sarabhai Space Centre, I.S.R.O, Trivandrum, India
e-mail: nitish_k@vssc.gov.in

S. Kumanan
e-mail: kumanan@vssc.gov.in

N. Remesh
e-mail: n_ramesh@vssc.gov.in

B. Karthik
e-mail: b_karthik@vssc.gov.in

be eliminated. In the current formulation, the equations of motion are obtained from the Newton–Euler equations represented in generalised coordinates and velocities as used in [3].

2 Mathematical Modelling

The present work focusses on modelling the translational and rotational dynamics of a generalised two-body underslung system. The model consists of a parent body and an underslung attached together through two slings, constituting a double pendulum. For a pre-defined trajectory of the parent body, underslung body rates, attitudes and accelerations are arrived at. Two coordinate reference frames are used throughout this paper, namely the Earth-fixed inertial frame and the body frame. The body frame (of the helicopter or the underslung) is centred at respective body's centre of gravity (C.G.) and is represented by the subscript i . The body axis is defined in coherence with the standard aircraft body axis convention. The inertial frame coincides with the body frame of the helicopter at the time of liftoff and is denoted by subscript N . The Newton-Euler equations of motion for a system of two rigid bodies can be expressed in six DoF as

$$(m_k g)_N + (FA_k)_N + (FC_k)_N - m_k \dot{V}_{kN}^* = 0 \quad (1)$$

$$(MA_k)_i + (MC_k)_i - J_k \dot{\omega}_k - S(\omega_k) J_k \omega_k = 0 \quad (2)$$

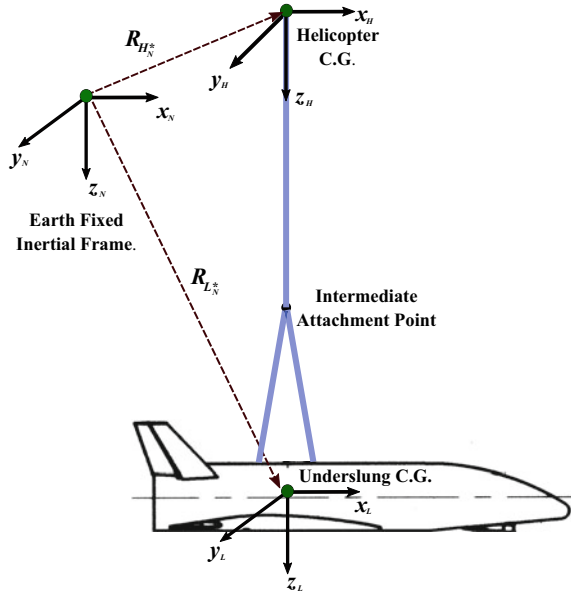
Equation (1) represents the balance of translational forces, whilst Eq. (2) depicts the sum of moments about individual body's C.G. The inner subscript k denotes the body for which the equations are written (subscript H refers to the helicopter and subscript L refers to the underslung), whilst the outer subscript denotes the reference frame in which the forces and moments are represented. The equations comprise of terms due to gravity, aerodynamics and inertia, succinctly derived and explained in [3].

These equations, for the two bodies, can be represented in a single expression using matrices. The position vector r and velocity vector v for the two-body system is represented as,

$$r = \begin{bmatrix} R_{H_N}^* \\ R_{L_N}^* \\ \alpha_H \\ \alpha_L \end{bmatrix}; \quad v = \begin{bmatrix} V_{H_N}^* \\ V_{L_N}^* \\ \omega_{H_H} \\ \omega_{L_L} \end{bmatrix} \quad (3)$$

where Rk_N^* and Vk_N^* are the rigid body C.G. positions and velocities in the inertial frame as shown in Fig. 1 and $\alpha_k = [\phi_k \quad \theta_k \quad \psi_k]^T$ denotes the Euler angle triplet used in the transformation between the inertial and body frame, whilst ω_k denotes the angular velocity in respective body frame.

Fig. 1 Illustration of the helicopter-underslung system with coordinate frames



Using f_g , f_a , f_c , and f^* , for the combined force-moment vectors due to gravity, aerodynamics, cable suspension and inertia plus coriolis effects, the equations of motion can be written in matrix form as

$$f_g + f_a + f_c + f^* = 0 \tag{4}$$

where

$$f_g = \begin{bmatrix} m_H g_N \\ m_L g_N \\ 0 \\ 0 \end{bmatrix} \quad f_a = \begin{bmatrix} (FA_H)_N \\ (FA_L)_N \\ (MA_H)_N \\ (MA_L)_N \end{bmatrix} \quad f_c = \begin{bmatrix} (FC_H)_N \\ (FC_L)_N \\ (MC_H)_N \\ (MC_L)_N \end{bmatrix} \tag{5}$$

and

$$f^* = -D\dot{v} - X \tag{6}$$

where D is a block-diagonal matrix with body masses and inertia occupying the diagonal, \dot{v} is the configuration velocity vector containing the linear and angular accelerations, whilst the matrix X contains the Coriolis terms due to the use of rotational coordinates in body-axes, as used in [3].

Equation (4) must be numerically solved for the respective body accelerations using the system states and net forces acting on each body. This is done by transforming the equations of motion to a set of generalised coordinates. The transformation

to the generalised coordinates follows relationship as shown in Eq. (7), where v and u represent the configuration and generalised velocities, respectively.

$$v = Au \quad (7)$$

Upon differentiating Eq. (7) and using \dot{v} into expression for f^* yields

$$f^* = -D\dot{A}u - DA\dot{u} - X \quad (8)$$

The equations of motion can then be simplified by using the expression for f^* in Eq. (4)

$$fo + fc - DA\dot{u} = 0 \quad (9)$$

where vector fo can be expressed as a net sum of inertia, aerodynamic and Coriolis forces

$$fo = fg + fa - D\dot{A}u - X \quad (10)$$

From Eq. 9, the generalised acceleration equation is given by

$$\dot{u} = A^{-1}D^{-1} [fo + fc] \quad (11)$$

The matrix A , is a 12×12 nonsingular matrix, and therefore, its inverse exists. Now, the constraint force fc , which is the tension in the cable, needs to be computed before arriving at the generalised accelerations. The constraint force is expressed as function of fo as shown below

$$fc = Kfo \quad (12)$$

Detailed derivation and expression of K is taken from [3]. This then leads to the final expression required to obtain the system states given by

$$\dot{u} = A^{-1}D^{-1} [fo + Kfo] \quad (13)$$

At this juncture, Eq. (13) is rearranged to use the helicopter accelerations as the input to solve for the generalised accelerations of the underslung. The resultant set of algebraic equations is solved numerically using Runge–Kutta (RK4) method to obtain the system states as function of time.

All the joints used in the simulation are spherical and assumed to be frictionless. The sling (or cable) aerodynamics and helicopter dynamics as a response to slung body disturbances are not included. Using Kane's method for problem involving multiple bodies and constraints drastically reduces the number of algebraic equations over classical Newton–Euler equations. Although results obtained from the current formulation compare exceptionally well with Kane's method formulation.

3 Results and Discussions

A planar helicopter trajectory with steady climb and straight flight, as shown in Fig. 2, is envisaged to understand the behaviour of a winged body underslung from a helicopter through six DoF simulations. For the underslung simulations, point mass trajectory of the parent body (helicopter) in the inertial reference frame, aerodynamic forces and moments of the underslung, as a function of angle of attack (α) and angle of sideslip (β), and mass properties are used as inputs.

Maximum cruise velocity of the helicopter is limited to 35 m/s with an ascent rate of 3 m/s. The trajectory is designed by limiting the peak acceleration and their derivatives. From the numerical simulations, it is observed that the underslung tracks the velocity of the helicopter, and oscillations in the total velocity correspond to the first pendulum mode. As shown in Fig. 3a, the underslung experiences a negative pitch angle and α , due to the aerodynamic drag acting on it and accelerating motion of the helicopter. Difference between the pitch angle and α corresponds to the ascent rate of the helicopter during the climb phase which is absent in the peak altitude. This dynamics is precisely predicted by the model. The underslung exhibits stable limit cycle behaviour about a non-zero β corresponding to the natural trim of the winged body in the lateral plane at that operating α due to the coupling of aerodynamics and pendulum motion of the winged body. The lateral pendulum motion results in the rolling motion of the winged body. The initial build up in the roll angle is due to the end of accelerated phase of the helicopter as shown in Fig. 3b.

3.1 Validation

For the planar helicopter trajectory, the results of the numerical simulations are validated against the commercially available multibody dynamic simulation software MSC ADAMS[®]. Figure 4a brings out the comparison between α from the current

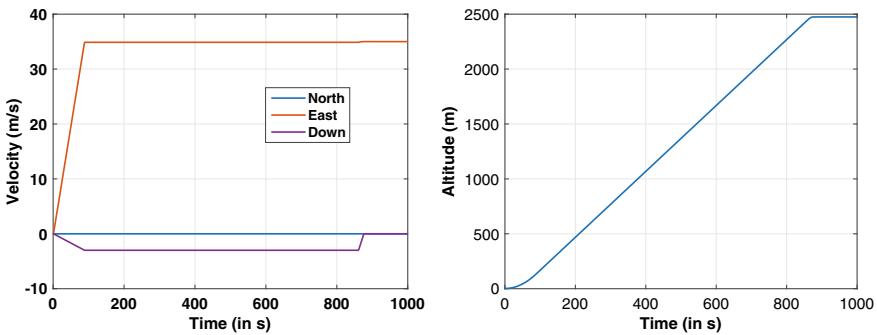


Fig. 2 Input helicopter velocity and altitude profile for the planar trajectory

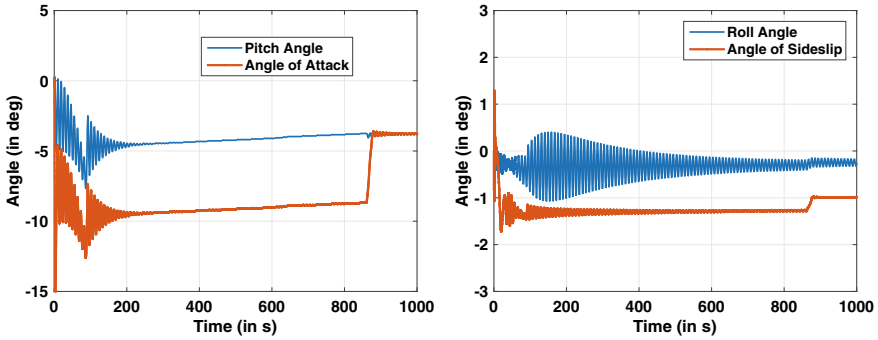


Fig. 3 Variation of the underslung body attitudes and aerodynamic angles for the planar helicopter trajectory

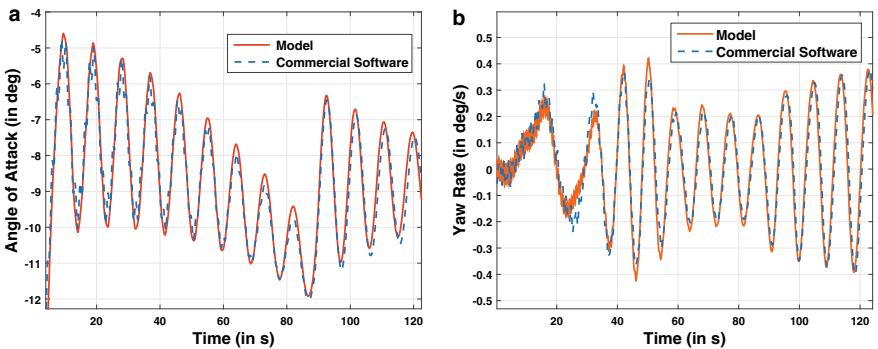


Fig. 4 Comparison of simulation results for $t = 0$ to 120 s showing **a** angle of attack, **b** Yaw rates

model and the commercial software. Change in mean α at $t = 90$ s corresponds to transition from accelerated to uniform velocity flight. The level of match between the numerical simulations further corroborates the accuracy of the mathematical model. Figure 4b shows the comparison of the underslung yaw rates for the first 120 s. The second pendulum mode can be identified in the beginning of the simulation when the dynamic pressure is low, resulting in lower aerodynamic excitation. Inertial forces govern the dynamics of the wing body in this period. As the velocity increases, the aerodynamic forces become significant, dampening the second pendulum mode. Similar observation is seen in the pitch rates of the underslung during this phase of flight. In addition, the frequency of oscillations in the longitudinal and lateral plane is inline with the theoretical pendulum frequency corresponding to the underslung length.

3.2 Sensitivity Studies

Sensitivity studies with respect to helicopter parameters and aerodynamic dispersions are carried out to understand the stability of the underslung through various regimes of flight. One such study is the effect of yaw damping derivative on the lateral plane dynamics. Parameter perturbation studies of the yaw damping derivative show that perturbing the derivative to its upper bound significantly reduces the yaw plane oscillations and precludes any possibility of divergence due to yaw-roll coupling. This is substantiated by Fig. 5 which shows the variation of β and yawrate of the underslung during the level flight. The case with reduced aerodynamic damping has the highest peak to peak lateral plane oscillations, in turn resulting in higher body rates. Since the aerodynamic data used for the simulations are that of a stable winged body, the body rates, attitudes and aerodynamic parameters do not diverge with time which is evident from Fig. 5. In contrast, for a directionally unstable winged body, the body rates build up due to yaw-roll coupling, leading to an undesirable situation for the helicopter which is also captured by the model as shown from the body attitudes and rates in Fig. 6. This model can be used to design stabilisers to help arrive at directional stability characteristics of the underslung, required to facilitate safer helicopter operations.

Another study is carried out to understand the effect of pendulum length parameters where the overall length of the pendulum and the length ratios of the two pendulums are varied. The first pendulum mode is a function of the overall length of the cable connecting the helicopter and the underslung. When the overall length of the pendulum increases, stability of the underslung in the lateral plane reduces leading to increasing oscillations which is unfavourable for the helicopter-underslung system. On the other hand, increasing the length ratio, i.e. augmenting the length of the second pendulum results in increase in the amplitude of the second pendulum

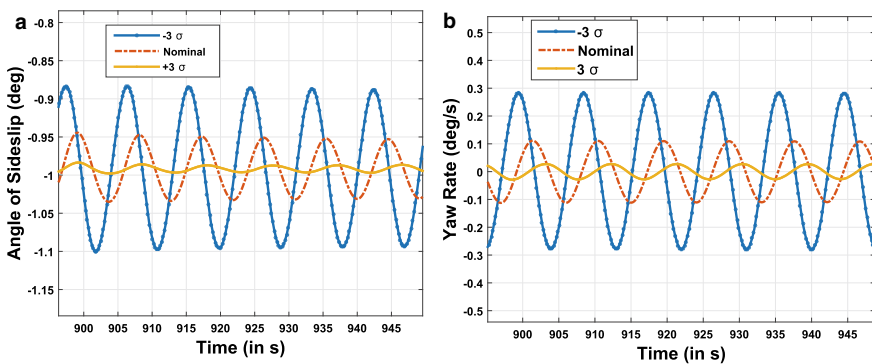


Fig. 5 Comparison of simulation results for the parameter perturbation case of yaw damping derivative showing **a** angle of sideslip, **b** Yaw rates during the level flight regime

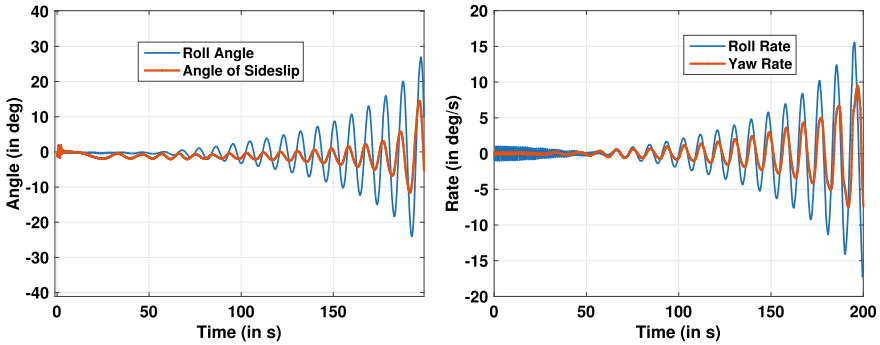


Fig. 6 Variation of body attitudes and rates of the winged body in the lateral plane for a directionally unstable configuration

mode, without affecting the first pendulum mode. The simulation model, therefore, can be used arrive at the length of the underslung and optimise the length ratios to ensure stability of the helicopter-underslung system.

4 Conclusion

A mathematical model is developed to simulate the underslung dynamics of a winged body from a helicopter, using point mass trajectory of the latter as the forcing function. This model is validated with a commercially available software, accurately capturing the dynamic behaviour of the double pendulum configuration. Parameter-sensitivity studies are carried out to understand the effect of aerodynamics on the directional stability of the underslung winged body. This model can be used to determine the stability requirements of certain unstable underslung bodies and operational limits of helicopter parameters such as climb rate, lateral accelerations and rates of accelerations. The current study can be extended to elastic cables whilst also solving for the helicopter dynamics, thus improving the fidelity of the simulations.

Acknowledgements The authors express their sincere gratitude to Shri.Jaison Joseph, Shri. Ravikumar C., Shri. Abhay Kumar, Dr. M. Jayakumar, Shri. V. T. Basker, Shri. Shyam Mohan N., Dr. V. Ashok and Director, VSSC for their technical guidance and motivation throughout the course of the work. Additionally, the authors would like to thank Shri. Vijith Mukundan for generating the required input helicopter trajectories for the parameter-sensitivity studies.

References

1. Nagabhushan BL (1977) Systematic investigation of models of helicopter with a slung load. Ph.D. thesis, Department of Aerospace Engineering, Virginia Polytechnic Institute and State University
2. Ronen T, Bryson AJ, Hindson W, Dynamics of helicopter with sling load. In: AIAA atmospheric flight mechanics conference, AIAA-86-2288, American Institute of Aeronautics and Astronautics
3. Stuckey RA, Mathematical modelling of helicopter slung-load systems. DSTO-TR-1257, Department of Defence, USA
4. Pal RS (2020) Modelling of helicopter underslung dynamics using Kane's method. IFAC PapersOnLine 53(1):536–542 (ScienceDirect)

A Genetic Algorithm-Based Optimization of a Generic Winglet



V. K. Suman, Abhijith J. Patil, M. B. Subrahmanya, K. N. Kaushik, Sintu Singha, Raghavendra, Abhay Pashilkar, and V. R. Ramesh

1 Introduction

Winglets have been used in typical aircraft's to improve the aerodynamic performance, thereby increasing the fuel efficiency. However, winglet design poses a challenge as the aerodynamics performance is sensitive to a large number of operating conditions and therefore an optimal winglet needs to be obtained. Therefore, it becomes necessary to choose the right parameters such that an optimization procedure can evolve an improved design. Critical parameters which influence winglet design are noted as cant angle, root radius and length as discussed in [1]. Along with these parameters, other parameters such as leading edge sweep, transition length and

V. K. Suman · A. J. Patil · M. B. Subrahmanya · K. N. Kaushik (✉) · S. Singha · Raghavendra · A. Pashilkar · V. R. Ramesh
CSIR-NAL, Bangalore, India
e-mail: kaushik@nal.res.in

V. K. Suman
e-mail: suman@nal.res.in

A. J. Patil
e-mail: abhijitpatil12@outlook.com

M. B. Subrahmanya
e-mail: subrahmanya@nal.res.in

S. Singha
e-mail: ssingha@nal.res.in

Raghavendra
e-mail: knrag@nal.res.in

A. Pashilkar
e-mail: apash@nal.res.in

V. R. Ramesh
e-mail: vramesh@nal.res.in

© The Author(s), under exclusive license to Springer Nature Singapore Pte Ltd. 2023
P. Pradeep Pratapa et al. (eds.), *Advances in Multidisciplinary Analysis and Optimization*,
Lecture Notes in Mechanical Engineering,
https://doi.org/10.1007/978-981-19-3938-9_14

transition width have also been included making it a total of 7 parameters for optimization. The main contribution of this work is to set up an optimization workflow using HEEDS for winglet design optimization. In this work, we have adopted the open source CFD software SU2 to evaluate the aerodynamic forces and thereby the objective function. We have chosen to optimize the SARAS winglet geometry. The knowledge and experience gained in this optimization study will be used for ongoing and future aircraft projects in NAL.

2 Methodology

A numerical optimization approach has been set up by coupling a parametric CAD model, mesh generator [2], open source CFD solver SU2 [3] in a genetic algorithm-based framework as shown in Fig. 1 using the optimization software HEEDS [4]. A cost functional based on maximizing $\frac{C_L}{C_D}$ is chosen. The design parameters identified previously such as cant angle, root radius, winglet length, are varied during each design cycle as in 2. A total of 125 samples are considered for the optimization algorithm (Fig. 2).

All CFD simulations are performed at a Mach number of 0.35 and Reynolds number of 6.5 million which are the typical parameters for cruise condition.

Fig. 1 Optimization methodology

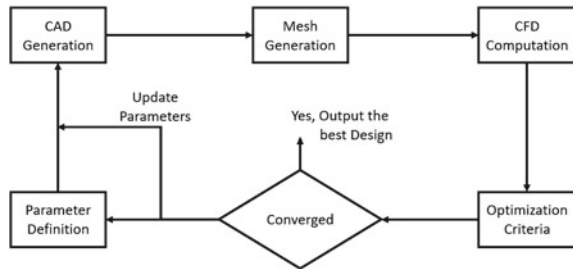


Fig. 2 Optimization methodology

Optimization Statement	
Objective	Maximize L/D
Parameters	30 ≤ Cant angle ≤ 80
	20 ≤ LE sweep ≤ 35
	640 ≤ Winglet root chord ≤ 650
	4 ≤ Winglet Setting ≤ 8
	810 ≤ Winglet Span ≤ 850
	-4 ≤ Tip airfoil twist ≤ -1

3 Results

The typical design parameter space is shown in Fig. 3 for the different aerodynamic performance indicators including the objective function. We observe a clustering around the optimal solution indicating that the process has achieved convergence. One observes that among all feasible designs about 10 designs meet the desired performance in maximizing $\frac{C_L}{C_D}$ compared to the baseline design as shown in Fig. 4, we

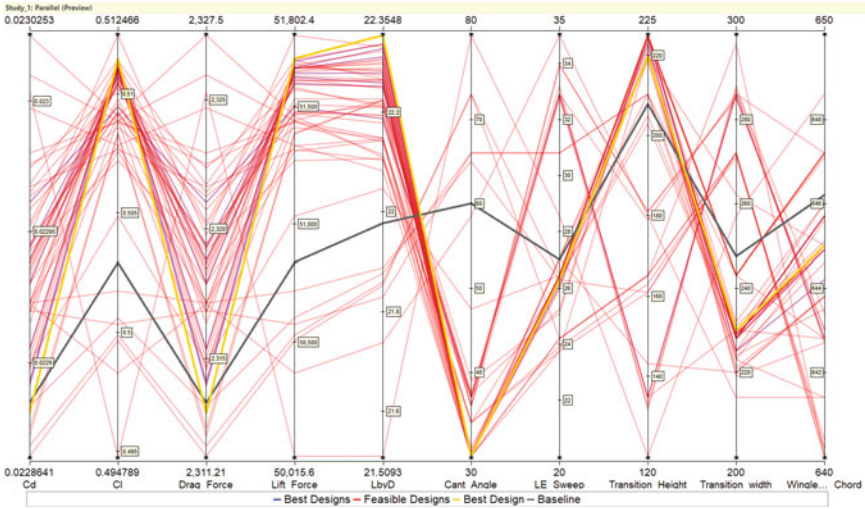


Fig. 3 Chart map of all feasible designs

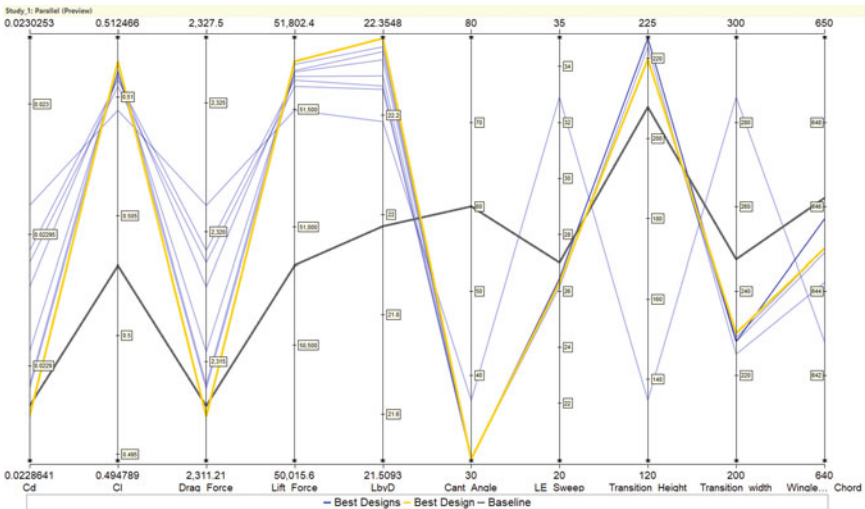


Fig. 4 Chart map of all feasible designs

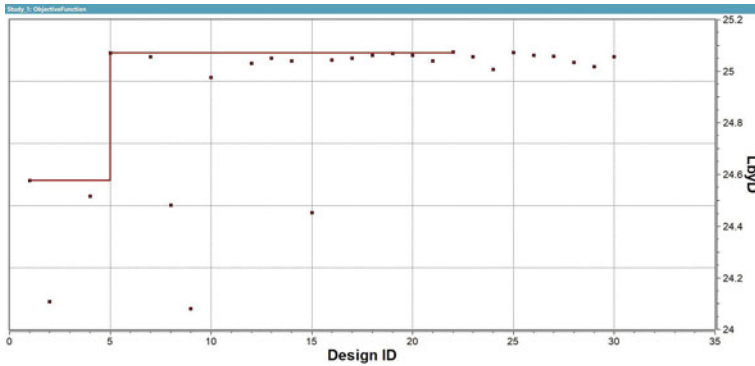


Fig. 5 Chart map of all feasible designs

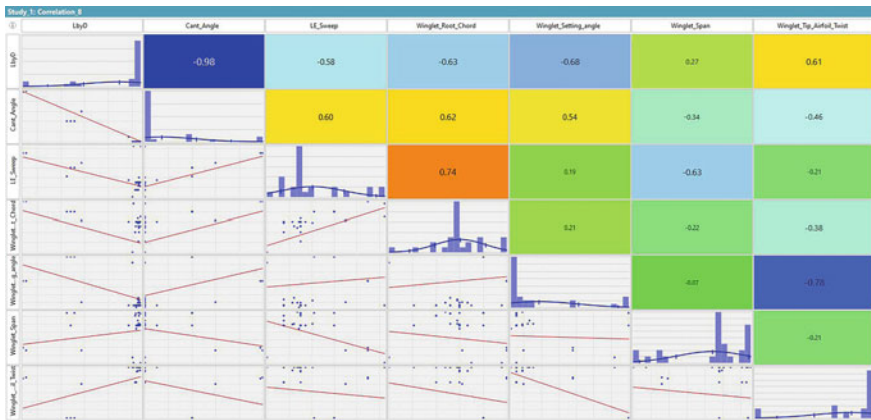
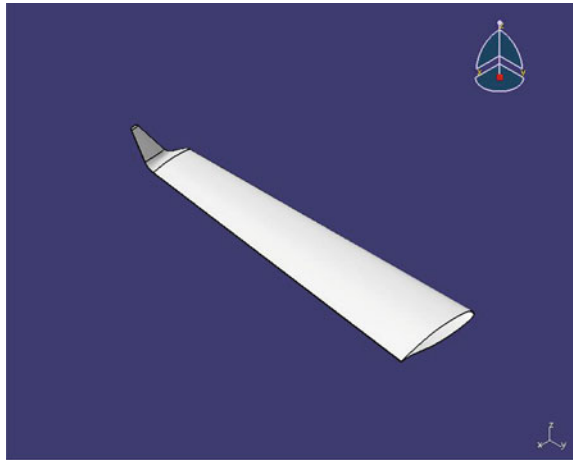


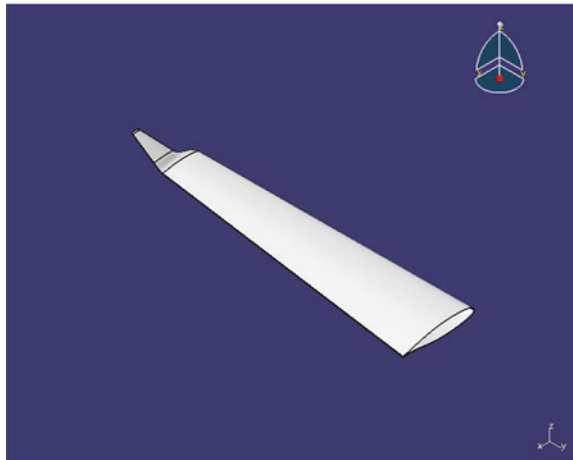
Fig. 6 Chart map of all feasible designs

call these set of designs as best designs. The evolution of objective function with iteration is shown in Fig. 5. The optimization procedure converges at around 25 iterations. The best design gave a performance improvement of 2.5% over the baseline design. The reason for the improvement is the decreased strength of the wingtip vortex, which results in a lower drag. The correlation plot of the various parameters influencing the maximization of $\frac{C_L}{C_D}$ ratio is shown in Fig. 6. One observes that the winglet cant angle, root chord and setting angle has a high negative correlation to the performance, whereas winglet length and airfoil twist have a positive correlation. Comparison of the baseline geometry with the best design is shown in Fig. 7. The total time for the optimization cycle is around 96h on a workstation with 96 cores.

Fig. 7 Comparison of baseline design with optimized design



(a) Baseline design



(b) Optimized design

4 Conclusions

1. Aerodynamic shape optimization of SARAS wing-winglet configuration using a genetic algorithm approach is demonstrated.
2. The optimization resulted in a best design which offers a 2.5% improvement in $\frac{C_L}{C_D}$ over the baseline SARAS wing with winglet.
3. Sensitivity analysis shows that maximization of $\frac{C_L}{C_D}$ is typically sensitive to the winglet cant angle and root radius

Acknowledgements We would like to thank the HEEDS support team for providing the initial training and demo licenses during the course of this work.

References

1. Takenaka K et al (2008) Multidisciplinary design exploration for a winglet. *J Aircraft* 45(5)
2. <https://www.pointwise.com/>
3. Palacios F, Economon TD, Wendorff AD, Alonso JJ (2015) Large-scale aircraft design using SU2. AIAA paper 2015-1946, AIAA SciTech: 53rd AIAA Aerospace Sciences Meeting, Kissimmee, Florida, 5–9 Jan 2015
4. <https://www.plm.automation.siemens.com>

Optimization of Oil Cooler Duct Shape of a Generic Transport Aircraft Using Numeca



A. Shikhar Jaiswal, C. K. Niranjanan, and T. N. Venkatesh

1 Introduction

An initial design of oil cooler duct for a generic transport aircraft was developed at CSIR-NAL [1]. Current study has been carried out in order to optimize the performance of this oil cooler duct. CFD simulations are carried out using Numeca software to study the performance of oil cooler duct. Several modifications to oil cooler duct geometry are studied. Modifications like changing inlet scoop position, inlet lip shape, and outlet profile are considered. This paper discusses the performance of these designs.

2 Methodology

In this study, RANS with SA turbulence model from Numeca has been used to carry out the simulations. Propeller effects are modeled in Numeca using the multiple reference frame (MRF) method with mixing plane approach [2]. In this method, the propeller domain is solved in rotating reference frame, and the aircraft domain is solved in a fixed reference frame, and solution is transferred between the two domains for every iteration at the interface. Heat exchanger in oil cooler duct is modeled by using a constant heat flux in the heat exchanger domain. The flow through heat

A. Shikhar Jaiswal (✉) · C. K. Niranjanan · T. N. Venkatesh
CSIR-NAL, Bangalore, India
e-mail: shikhar@nal.res.in

C. K. Niranjanan
e-mail: ckniranjanan@nal.res.in

T. N. Venkatesh
e-mail: tnv@nal.res.in

exchanger in oil cooler duct is obstructed during the heat exchange process. This causes pressure drop across the heat exchanger. This can be modeled by considering heat exchanger to be a porous media. In this study, Ergun law which is available in Numeca has been used to model porous media [3].

3 Mesh and Modified Oil Cooler Design Details

Generic transport aircraft geometry and oil cooler geometry (with transparent nacelle) used in this study are shown in Fig. 1a and b, respectively. Mesh generation is carried out using Numeca. Separate blocks were made for oil cooler internal duct, propeller, and external aircraft. 15 anisotropic layers with a first grid height of $3E-5$ are used. Surface mesh and sectional volume mesh (Y-normal section at center of nacelle) for initial design are shown in Fig. 2a and b. The total mesh size is of the order of 50 million.

The initial design of oil cooler duct was developed subject to many constraints of volume requirements, structural requirements, etc. In order to optimize the oil

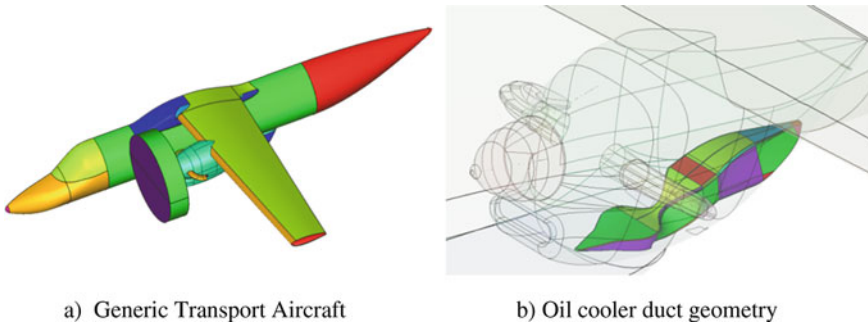


Fig. 1 Geometric details of the configuration

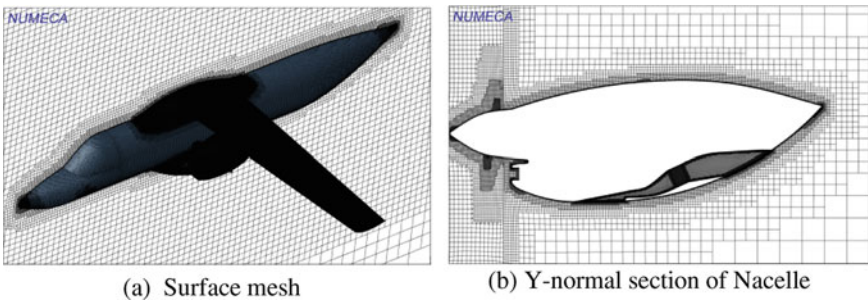


Fig. 2 Mesh details

cooler duct design for this transport aircraft, the traditional way of optimization is not suited because there are many constraints and parameters. For example, some sub-systems placed in nacelle around the oil cooler duct do not allow shape or profile change of oil cooler duct in those regions. Also, parameterizing the whole geometry would have resulted in large number of parameters due to which overall time taken for optimization process would have increased enormously. So, due to these constraints, modified designs are made by changing inlet scoop position, inlet lip shape, outlet profile, etc. The performance of the new designs is studied at static sea-level conditions.

4 Results and Discussion

Simulations are carried out for the new designs of oil cooler duct. Figure 3 shows total pressure contour of Y-normal section (at center of nacelle) for some new designs and initial design of oil cooler duct. The percentage change of mass flow rate through oil cooler duct for some of the new designs is shown in Table 1. From the study, it was found that one new inlet lip-shape design increased the mass flow rate in oil

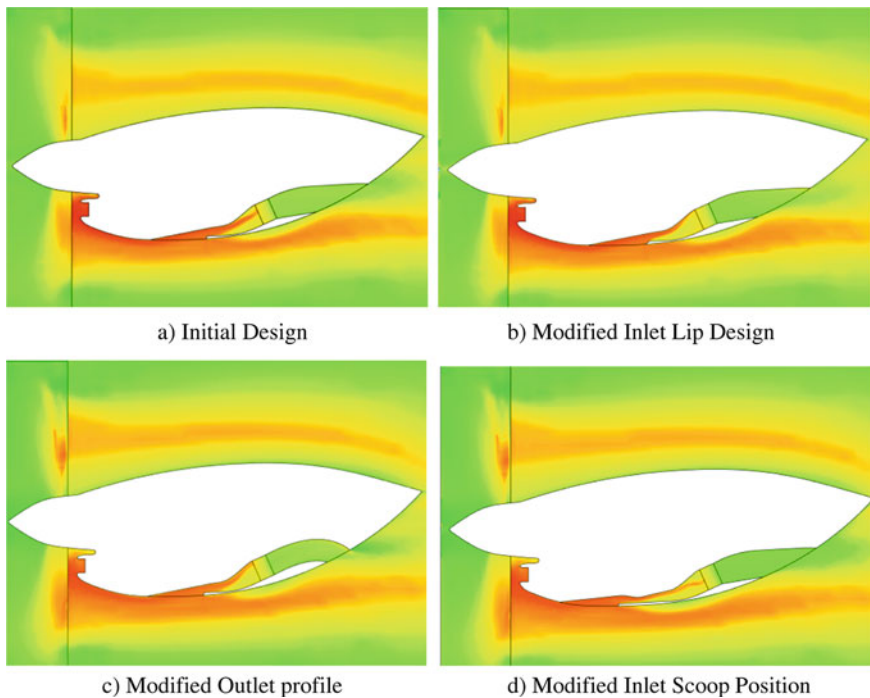
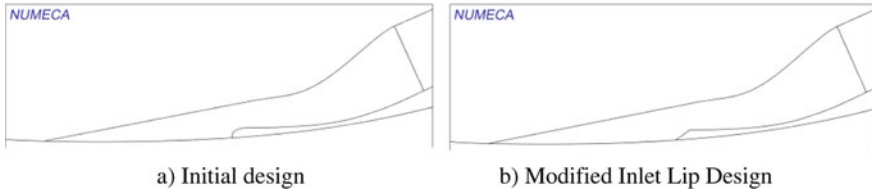


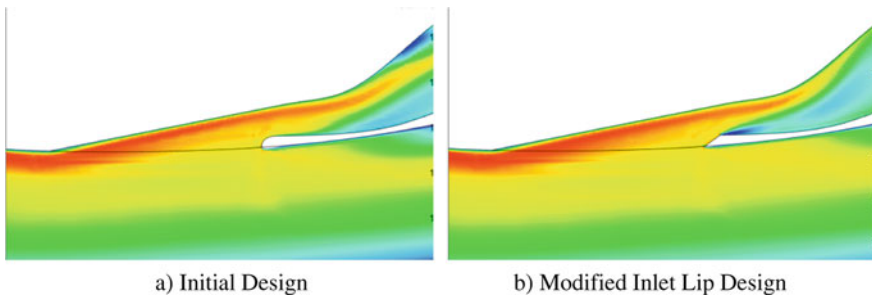
Fig. 3 Total pressure contour

Table 1 Mass flow through oil cooler duct

Case No.	Geometry	Δm (%)
1	Modified inlet lip	+ 4.3
2	Inlet scoop position-1	- 1.5
3	Outlet profile-1	+ 1.4

**Fig. 4** Sectional inlet lip profile

cooler duct by 4.3%. The sectional profile of initial oil cooler duct inlet lip shape and modified inlet lip shape which gives improved performance is shown in Fig. 4. The results for initial oil cooler duct design and the new inlet lip-shape designs are compared in detail. Figure 5 shows zoomed view of total pressure contour near the inlet lip for the initial oil cooler design and modified new inlet lip-shape design. Figure 6 shows velocity vectors (Y-normal section at center of nacelle) for the above two designs. Static pressure contour is shown in Fig. 7. Figure 8 shows magnitude of velocity contour of oil cooler inlet face on nacelle. Magnitude of velocity contour for an X-normal section at start of inlet lip is shown in Fig. 9.

**Fig. 5** Total pressure contour zoomed near inlet lip

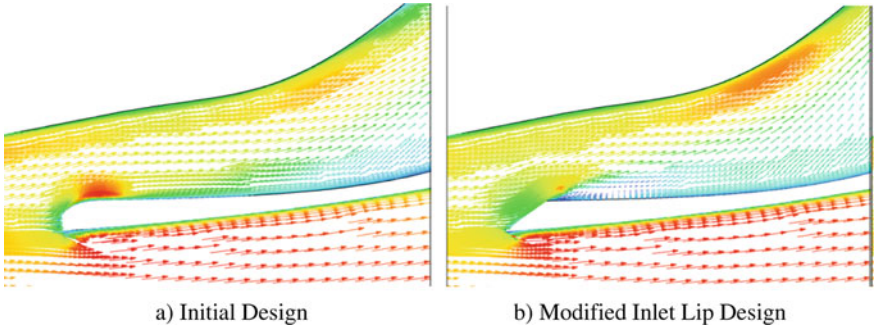


Fig. 6 Velocity vectors

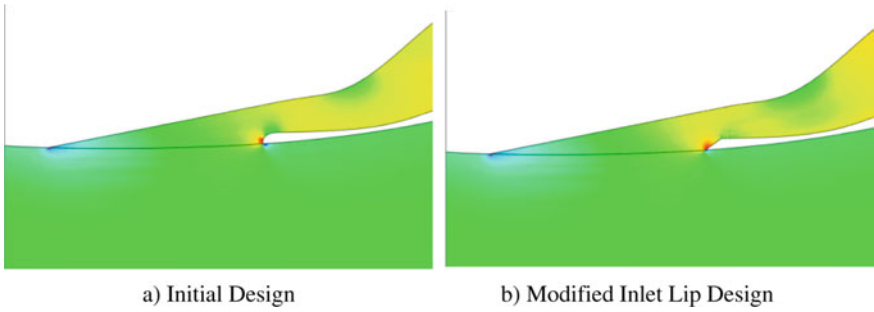


Fig. 7 Static pressure

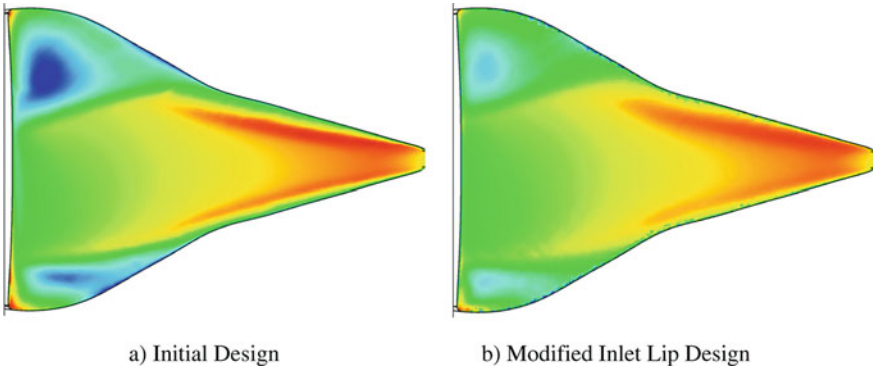


Fig. 8 Magnitude of velocity contour of oil cooler inlet face

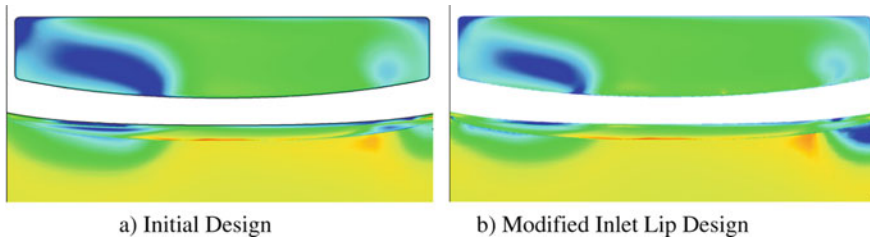


Fig. 9 Magnitude of velocity contour, x-normal section at start of inlet lip

5 Conclusion

Studies have been carried out to optimize the performance of oil cooler duct. Optimized oil cooler duct with new inlet lip-shape design improves the oil cooler duct performance. The new lip shape increased the mass flow rate through the oil cooler duct by 4.3%.

Acknowledgements The authors gratefully acknowledge Director, CSIR-NAL for his constant encouragement. We thank Mr. Vinay C. and C-CADD team for their support during the work. We also thank, Dr. V. Ramesh, Head CTFD Division, CSIR-NAL, for his support and helpful technical suggestions during the course of the work. We also thank Numeca Bangalore team for their support. Finally, we would like to thank CSIR-4PI, Anantha supercomputing facility and its support team.

References

1. Kalia S, Vinay CA, Hegde SM (2016) CFD analysis of turboprop engine oil cooler duct for best rate of climb condition. IOP Conf Ser: Mater Sci Eng
2. Franzke R, Sebben S, Bark T, Willeson E, Broniewicz A (2019) Evaluation of the multiple reference frame approach for the modelling of an axial cooling fan. *Energies* 12:2934. <https://doi.org/10.3390/en12152934>
3. www.numeca.com

External Aerodynamic Optimization of a 19-Seater Turboprop Aircraft During Preliminary Design Stage



C. K. Niranjanan, A. Shikhar Jaiswal, Raghavendra, and T. N. Venkatesh

1 Introduction

Components like nacelle, blister, and wing fairing generally produce huge drag with almost zero contribution toward lift. The profile drag (interference and pressure drag) and skin friction drag are the major type of drag on these components. Skin friction drag may reduce if wetted area reduces, but reducing wetted area sometimes increases the profile drag. In order to keep the total drag within limits, during preliminary design stage, empirical estimates are used for profile and skin friction drag. Using CFD to estimate total drag and performing a basic optimization, studies around baseline at this stage can result in a better design and significantly reduce the design changes required at later stages, and the current work was carried out to achieve the same.

2 Problem Definition and Formulation

Nacelle, blister, and wing fairing of the aircraft, which is in preliminary design stage, have to be optimized to reduce drag and increase L/D after considering the space constraint due to aircraft systems/components and structural members (e.g., engine systems inside nacelle and landing gear systems inside blister).

C. K. Niranjanan (✉) · A. Shikhar Jaiswal · Raghavendra · T. N. Venkatesh
CSIR-National Aerospace Laboratories, Bangalore, India
e-mail: ckniranjanan@nal.res.in

A. Shikhar Jaiswal
e-mail: shikhar@nal.res.in

T. N. Venkatesh
e-mail: tnv@nal.res.in

3 Methodology

Five to six samples were generated for each of nacelle, blister, and wing fairing. Navier–Stokes simulation with SA turbulence model was carried out on each of these models. All the simulations were carried out at Reynolds number 2 million and Mach 0.2, with tail portion of the aircraft excluded from simulation to reduce mesh size. Samples for nacelle and wing fairing were generated by using the morphing vector approach available in OMNIS [2]. In this approach, all the points on surface of a non-parametric triangulated geometry moves in the direction of the defined morphing vector with magnitude of displacement decided based on an inverse distance function. Multiple morphing vectors can be defined at suitable locations based on the problem. Different samples can be generated by controlling these morphing vectors. Samples for blister were generated using a commercial CAD modeling tool CATIA [1]. Morphing (only for nacelle and fairing) and mesh generation were automated using OMNIS Python interface. Due to space constraints from engine systems, nacelle samples were generated by morphing the profile of the nacelle beyond 80% of its length. The morphing vectors for nacelle were defined such that symmetry of the nacelle is not lost due to morphing. Figure 1 shows the samples studied for nacelle drag reduction. For fairing, only, the front profile was morphed. Figure 2 shows the fairing samples. Apart from morphing, studies were also carried out for optimum location of nacelle and fairing. Figure 4 shows positional variation studied for nacelle and fairing. For blister, front profile, back profile, width, and length were all changed during the studies. Figure 3 shows some of the blister samples used in drag reduction studies.

4 Results and Discussion

Changing the nacelle profile beyond 80% gave a significant reduction in drag with slight increase in L/D. The best performing nacelle sample gave around 17 counts reduction in drag compared to baseline. Figure 5 shows pressure distribution on baseline and least drag nacelle sample. Also, moving the nacelle forward by 27 cm reduced drag by another 3 counts.

Optimization of fairing by changing its front profile yielded only 1 count reduction in drag, but reducing the fairing height by 9 cm reduced the drag by 8 counts. Figure 6 shows pressure distribution on baseline fairing and fairing with reduced height.

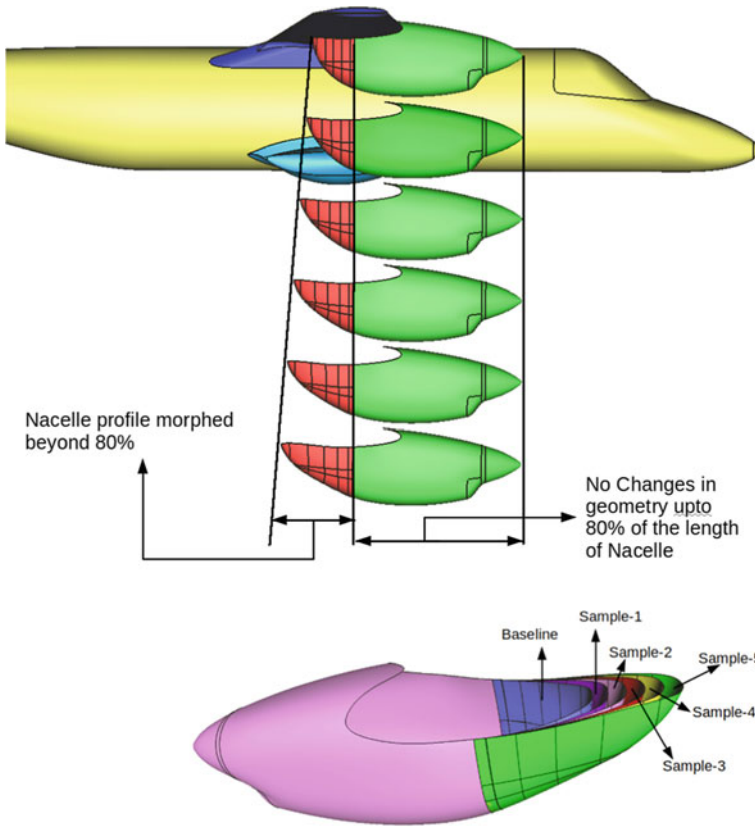


Fig. 1 Morphed samples of nacelle

For blister, drag reduction achieved by optimization was offset by increase in size of blister midway during studies due to change in space constraint from landing gear systems. The final optimized design by implementing changes to all three components resulted in a drag reduction of around 28 counts, with slight increase in L/D and more volume inside blister for landing gear systems.

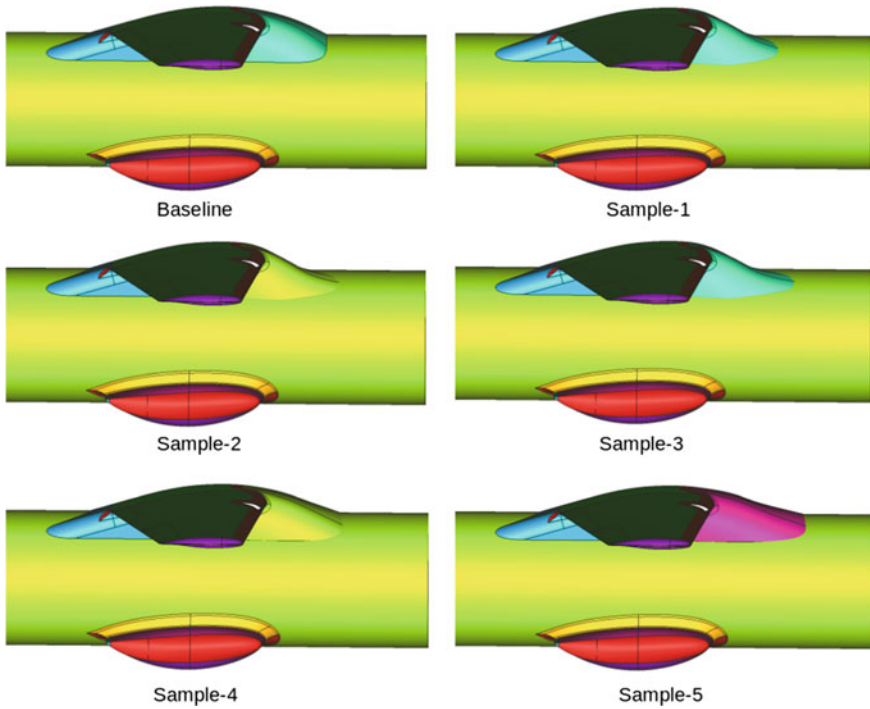


Fig. 2 Morphed samples of fairing

5 Conclusion

Initial aerodynamic drag reduction studies were carried out on a 19-seater turboprop aircraft during preliminary design stage. CFD simulations were run by varying shape and position of nacelle, fairing, and blister. Configurations with least drag were suggested to be carried forward to the next stage of design. Further, optimization of each of these parameters will be taken up in the future.

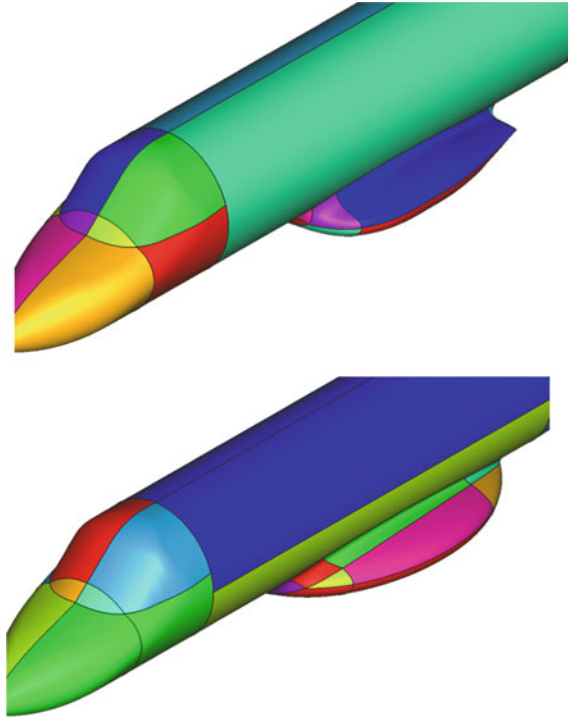


Fig. 3 Few morphed samples of blister

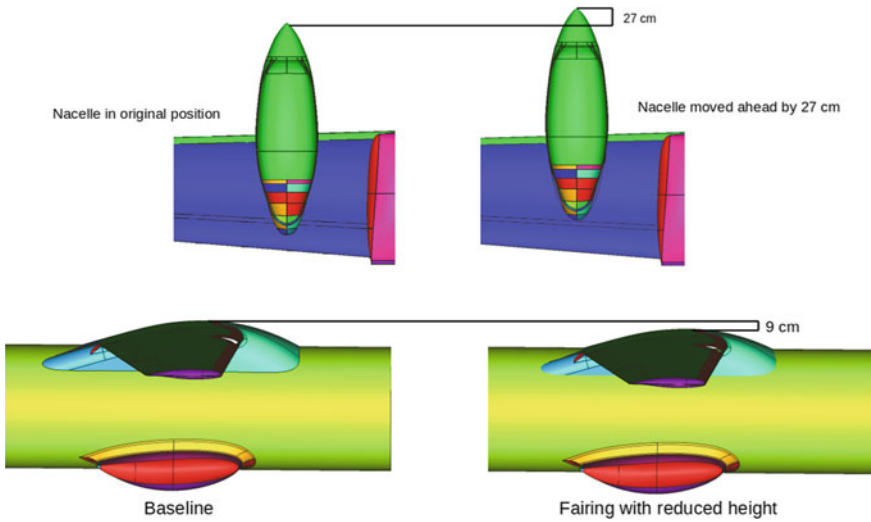


Fig. 4 Nacelle and fairing positional studies samples

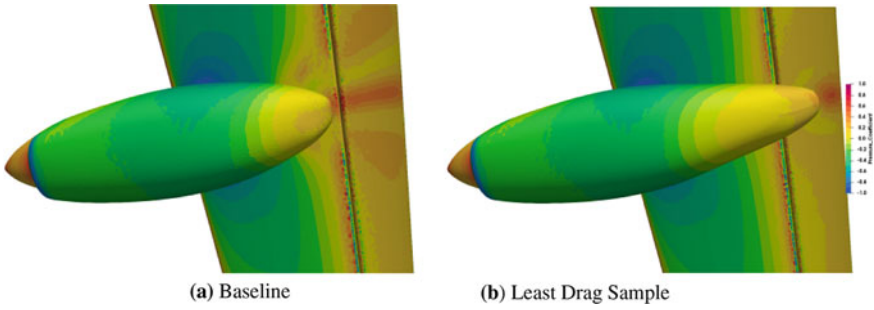


Fig. 5 Comparison of pressure coefficient on nacelle

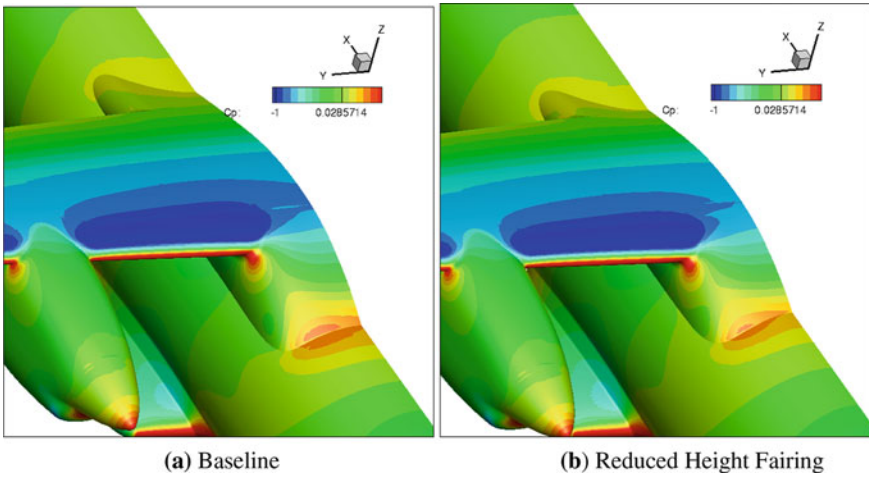


Fig. 6 Comparison of pressure coefficient on fairing

Acknowledgements Authors would like to acknowledge the efforts by Mr. Arshad Shameem C., Mr. Jyothi Kumar Puttam, and Mr. Madhubabu K, CTFD Division, CSIR-NAL for independently verifying the results of optimized nacelle geometry using SU2. Authors would also like to thank Dr. Ramesh V. Head, CTFD Division, CSIR-NAL and Mr. Bhaskar Chakravarthy CCADD, CSIR-NAL for their support during the course of work.

References

1. CATIA. A multi-platform software suite for computer-aided design. <https://www.3ds.com/products-services/catia>
2. Numeca multi-physics CFD solver. <http://www.numeca.com>

Winglet Aerodynamic Optimization of a 19-Seater Turboprop Aircraft



C. K. Niranjana, C. Arshad Shameem, A. Shikhar Jaiswal,
and T. N. Venkatesh

1 Introduction

For problems like aerodynamic optimization of winglets, the numbers of design variables to be considered is very large. This increases the dimension of the design space. For a problem with 'k' dimensional design space, to construct a reliable response surface for an objective function, around '10K' samples are suggested in literature [1, 2]. In our case, increase in design variables leads to increase in number of samples on which high-fidelity CFD flow solver has to be run to evaluate the objective function. Due to this reason, automation of the entire process from sample geometry generation to aerodynamic evaluation of samples (using CFD) is inevitable. But, automation of geometry modification and quality mesh generation still remain difficult. OpenVSP with its C-style API [3] (to generate new geometries) and HexpressHybrid/Hexpress with its volume to surface meshing approach [4] were utilized for this purpose.

In present work, Gaussian process regression response surface along with genetic algorithm was used to arrive at optimum winglet design. Response surface methodology allowed for faster evaluation of multiple objective functions using same set of sampled CFD solutions. Latin hypercube method was used to select the initial sampling locations in the design space, due to its space-filling property. Gaussian process regression was considered to construct the response surface due to its capability to model complicated responses. They also allow for computation of a metric

C. K. Niranjana (✉) · C. Arshad Shameem · A. Shikhar Jaiswal · T. N. Venkatesh
CSIR-National Aerospace Laboratories, Bangalore, India
e-mail: ckniranjana@nal.res.in

C. Arshad Shameem
e-mail: arshad@nal.res.in

A. Shikhar Jaiswal
e-mail: shikhar@nal.res.in

called expected improvement (EI), which can be used to choose additional sampling points required to re-calibrate the response surface to make it more accurate [1, 5–7]. Genetic algorithm was preferred as an optimizer due to the ease of implementation (a simple genetic algorithm-based optimizer [8] was developed in-house). Monte-Carlo method was also implemented as an optimizer to check the solutions from in-house developed genetic algorithm code. The number of function evaluations from response surface required by Monte-Carlo was found to be significantly higher and is expected to drastically increase with increase in design variables.

2 Problem Definition and Formulation

The current development version of the aircraft under consideration consists of a baseline winglet was carried over from preliminary design stage. Parameters (design variables) like cant angle, sweep angle, twist angle, span, chord, and toe angle (see Fig. 1) of the winglet had to be optimized for better aerodynamic performance. Based on quick survey into historical trends and literature [2, 9], it was found that drag is most sensitive to cant angle, twist, span, and sweep; hence, these four parameters were considered as the design variable for the optimization problem. The lower and upper bounds considered for each of these design variables are as follows:

$$0.74 < \frac{\text{Span}}{\text{Span}_{\text{Baseline}}} < 2.23, \quad 0.47 < \frac{\text{Cant Angle}}{\text{Cant Angle}_{\text{Baseline}}} < 1.32,$$

$$-5^\circ < \text{Twist} - \text{Twist}_{\text{Baseline}} < 9^\circ \quad \text{and} \quad 0.37 < \frac{\text{Sweep}}{\text{Sweep}_{\text{Baseline}}} < 1.67$$

Maximization of L/D of the aircraft was the primary objective, but due to the possibility of solution converging at upper and lower bound of span and cant angle, respectively, there exist a probability for drag to increase at maximum L/D location. At this point, the winglet becomes more like an extended wing and can give higher L/D despite increase in drag due to proportionally larger increase in lift. This scenario can be avoided by maximizing a drag-weighted L/D function (DF(x)) given in Eq. (1). Maximization of DF(x) ensures drag reduction while maximizing L/D.

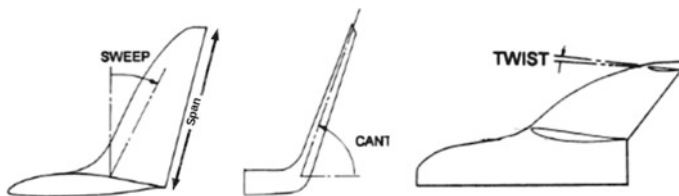


Fig. 1 Design variables. Taken from Lappas and Ikenaga [9]

$$\begin{aligned} & \text{Drag Weighted L/D Cost Function}(DF(x)) \\ &= \frac{L(x)}{D(x)} \cdot \frac{D_{\text{SampleMax}} - D(x)}{D_{\text{SampleMax}} - D_{\text{SampleMin}}} \end{aligned} \quad (1)$$

where $L(x)$ and $D(x)$ are the lift and drag, respectively, at x in the design space, $D_{\text{SampleMax}}$ and $D_{\text{SampleMin}}$ are the maximum and minimum drag from the sampled CFD solutions.

3 Methodology

3.1 Latin Hypercube Sampling

Based on the list of design variables and their limits, the sample space was populated using Latin hypercube sampling approach. Initially, 50 samples were generated; the suggested number of initial samples is around 40 for 4 variables [1, 2]. Latin hypercube was chosen due to its space-filling property, which ensures that there exists a sample in all the intervals of design variables partitioned by number of samples.

3.2 Geometry Modeling

Geometry modeling of samples from Latin hypercube was carried out using OpenVSP. Only, wing with winglet was modeled in OpenVSP; for various samples, remaining components of the aircraft were taken from the master CAD geometry. The wing was modeled by specifying three sections in OpenVSP, one each for main wing, winglet, and wing–winglet transition region. Span, root chord, tip chord, sweep, dihedral, and airfoil sections were specified for each of these sections. The span, twist, sweep, and dihedral (for cant angle) of the winglet section were varied to generate various sample geometries. Figure 2 shows some of the sample winglet geometries generated using OpenVSP. A Python code was used to generate OpenVSP scripts for each of the samples based on output from Latin hypercube module. These scripts were used to automate geometry generation process.

3.3 Mesh Generation and CFD Simulation

HexpressHybrid/Hexpress and FineOpen (Navier–Stokes CFD solver) were used for mesh generation and CFD flow simulation, respectively, through their Python interface. To make the automation of mesh generation easy and to maintain quality

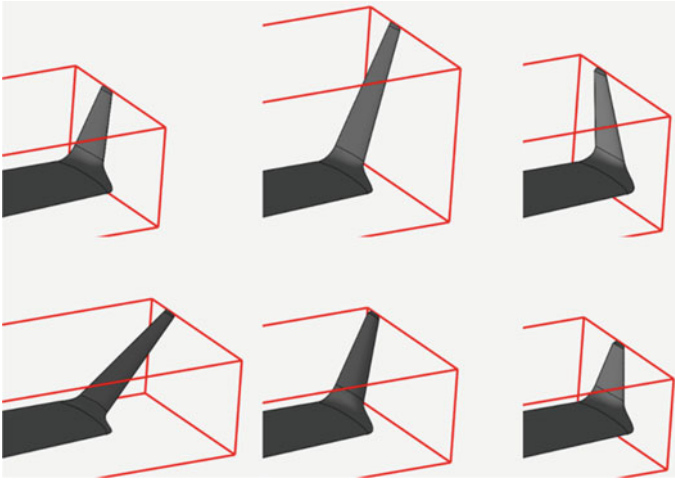
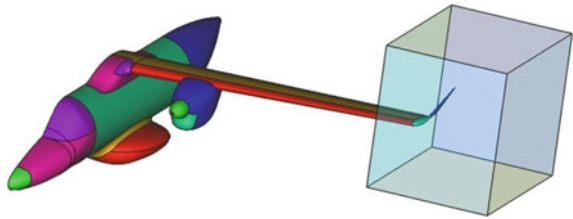


Fig. 2 Few sample winglets generated using OpenVSP

Fig. 3 Winglet domain for re-meshing



of mesh, the flow domain was split into two, a larger domain which includes the entire aircraft along with far field except winglet and a small domain surrounding the winglet (see Fig. 3). For each sample, the mesh was re-generated only in winglet domain. Full Navier–Stokes simulation was carried out with SA-turbulence model and JST flux scheme on all the samples. Latin hypercube sample generator, OpenVSP, HexpressHybrid/Hexpress, and FineOpen were integrated into single module using Python. Given a list of design variables and limits for each of these variables, the module will populate the design space, generate geometries, generate mesh, run flow solver, and post-process the results to give the value of integrated aerodynamic quantities (Lift, drag, pitching moment, etc.) for every sample.

3.4 Gaussian Process Regression

A response surface was fit to both L/D and drag-weighted L/D cost functions ($DF(x)$) using Gaussian process regression. GPpy, an open-source Python frame work, was used for Gaussian process regression. Squared radial basis function was used as the

kernel to obtain the co-variance matrix in Gaussian process regression. GPy optimizes the length scales and variance of the kernel using the sampled values by evaluating maximum likelihood estimates to construct an accurate response surface [1, 7, 10].

3.5 Optimizer

A simple genetic algorithm-based [8] code was developed and utilized to find the optimum solution on the response surface. Genetic algorithm generates a random initial population (initial parent), which is evaluated to find the fittest individuals. Offsprings are generated by combining fittest individuals. Offsprings which are fit enough will replace weak parents to form a new parent population for next generation. Some offsprings in every generation are mutated to improve the exploratory nature of the algorithm (i.e., to avoid early convergence into a local optimum). This process continues iteratively till an optimum is found. For maximization of L/D and $DF(x)$, a parent population of 100 individuals was used to start with; 100 offsprings with 20% of them mutated were generated in every generation, and the fittest 100 from combined population of parent and offspring of current generation were carried forward as parent population for next generation. A simple Monte-Carlo optimization was also performed to re-confirm the results from genetic algorithm. The optimum predicted by genetic algorithm and Monte-Carlo was the same, but Monte-Carlo required objective function evaluation, using response surface, at around 1 million locations in the design space, whereas genetic algorithm made query at less than 2000 locations to converge to optimum (took less than 20 generations with 100 offspring each to converge, ref Fig. 4). Figure 5 shows the entire methodology of winglet optimization in graphical representation.

Fig. 4 Semi-log plot of genetic algorithm convergence

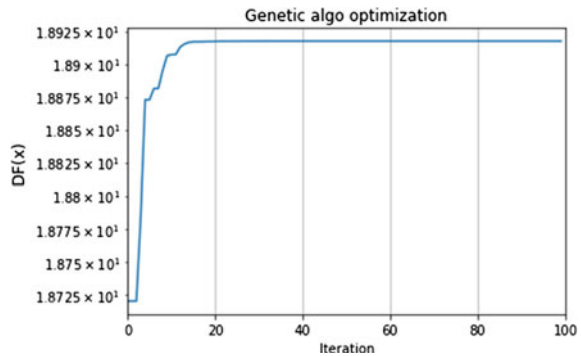
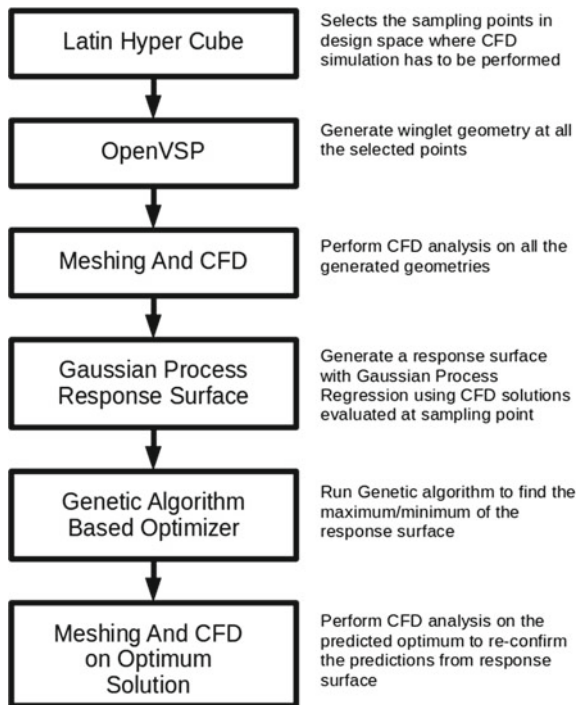


Fig. 5 Winglet optimization methodology



4 Results and Discussion

The maximization of L/D , as anticipated, converged to a solution where span and cant angles were at their maximum and minimum bound, respectively, for the reasons mentioned earlier (sec-Problem Definition and Formulation); at this point, the twist and sweep angles were 4.5° more and 9° less, respectively, than baseline. The improvement in L/D was 8%, with a slight increase in drag (0.2%). Maximization of drag-weighted L/D function ($DF(x)$) converged to a solution where drag reduced 1.6% and L/D improved 4.5%. The span at this optimum was 1.93 times baseline; cant angle and sweep were 18° and 6° lesser, respectively, than baseline and twist remained same. CFD simulations were carried out at optimum points obtained from response surface to validate the predicted optimum. The drag and L/D from CFD matched the values predicted by response surface. CFD and response surface matched at two other randomly chosen location as well; hence, expected improvement (EI) metric was not explored to add more samples.

Both the predicted optimum solutions have large span. From weight, aesthetic, flutter, and other structural standpoint, such a high span may not be realistic. Due to these reasons and assuming that weight and other structural characteristics do not vary much with considered variables other than span; maximization of $DF(x)$ was carried out by fixing span to baseline value. The span-constrained optimum yielded

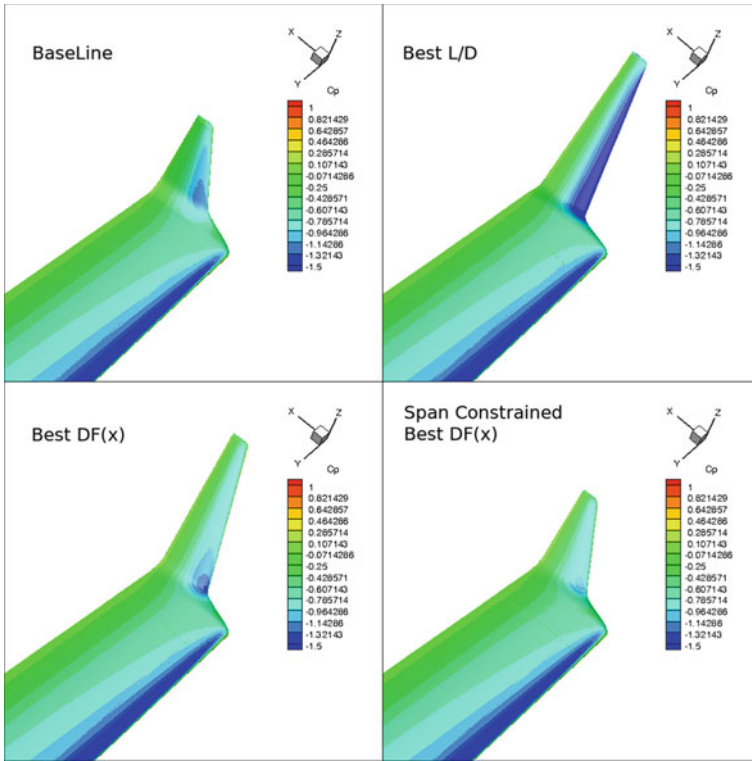


Fig. 6 Pressure coefficient on various optimum

1.3% improvement in L/D with 0.4% drag reduction. The cant angle and twist reduced by 20° and 3°, respectively, from base line for span-constrained optimum, whereas sweep increased by 4°. Figure 6 shows the pressure contour on winglet for various optimum solutions. For the current aircraft under consideration, the span-constrained optimum was found to be the most practical solution, unless a multi-disciplinary optimization is performed.

5 Conclusion

Maximization of L/D and drag-weighted L/D ($DF(x)$) of a 19-seater turboprop aircraft was carried out by exploring various winglet designs. Around 50 sample winglets were generated, and CFD simulations were carried out on them. Response surfaces for L/D and $DF(x)$ were fit on these samples using Gaussian process regression (Kriging method). Genetic algorithm-based optimizer was used to find the global maximum on these response surfaces. CFD simulations were carried out at the maximum obtained

from response surface to re-confirm the predictions. This study aided in choosing a suitable winglet for the aircraft under consideration.

Acknowledgements Authors would like to thank Dr. Ramesh V., Head, CTFD Division, CSIR-NAL for his support during the course of work. Authors would also like to thank the entire team at High Performance Computing (HPC) facility, CSIR-4PI for ensuring that HPC was available for the entire course of work.

References

1. Jones DR, Schonlau M, Welch WJ (1998) Efficient global optimization of expensive black-box functions. *J Glob Optim*
2. Takenaka K, Hatanaka K, Nakahashi K (2008) Multi-disciplinary design exploration for winglet. In: 26th International congress of the aeronautical sciences
3. NASA open source parametric geometry modeller. <http://openvsp.org>
4. Numeca multi-physics CFD solver. <http://www.numeca.com>
5. Skinner SN, Zare-Behtash H (2018) State-of-the-art in aerodynamic shape optimisation methods. *Appl Soft Comput* 62:933–962
6. Jeong S, Murayama M, Yamamoto K (2005) Efficient optimization design method using Kriging model. *J Aircr* 42(2)
7. Rasmussen CE, Williams CKI (2005) Gaussian processes for machine learning. The MIT Press. ISBN 026218253X
8. Heris MK (2015) Binary and real-coded genetic algorithms in MATLAB. Yarpiz. <https://yarpiz.com/23/ypea101-genetic-algorithms>
9. Lappas I, Ikenaga A (2019) Conceptual design and performance optimization of a tip device for a regional turboprop aircraft. *MDPI Aerosp J*
10. GPY (2012) A Gaussian process framework in python. <http://github.com/SheffieldML/GPY>

Design and Position Sensitivity Analysis of Close-Coupled Canard for Naval Fighter Aircraft



Sathish Sunnam, C. Muthuraj, and S. Ragul

1 Introduction

Canard-wing combination plays an essential role in achieving the performance like carrier approach, launch, trans-supersonic acceleration and combat ceiling for the naval fighter aircraft design. In addition, the canard provides better manoeuvrability and controllability of an aircraft. The selection of canard for delta wing aircraft has been explored by using the knowledge of various literatures [1–3] and available information from the in-house project and also from the contemporary fighter planes in the world. The demand of reduced approach speed emerged as the most important requirement for the naval fighters which necessitates higher lift. The addition of lift from close-coupled canard is mainly due to the favourable mutual interaction of wing-canard vortex systems which can stabilize the vortices up to higher AOA. The CFD code is validating against a test case from open literature [1] to build the confidence of an important flow features of canard-wing interactions on delta wing aircraft which is also captured in this paper. Subsequently, the selection of canard design parameters has been carried out by using the simplified fuselage to get the desired results in minimum turn-around time. Various canard positions, canard area, leading edge (LE) and trailing edge (TE) sweep angles of canard are explored to get the best possible canard for 50° delta wing configuration.

S. Sunnam (✉) · C. Muthuraj · S. Ragul
Aeronautical Development Agency, Bangalore, India
e-mail: sathishsunnam@gmail.com

© The Author(s), under exclusive license to Springer Nature Singapore Pte Ltd. 2023
P. Pradeep Pratapa et al. (eds.), *Advances in Multidisciplinary Analysis and Optimization*,
Lecture Notes in Mechanical Engineering,
https://doi.org/10.1007/978-981-19-3938-9_18

2 Objectives and Constraints

The naval aircraft naturally demands for higher lift towards achieving the lowest possible approach speed and better launch capability during its operations from aircraft carriers. To attain the higher lift at lower speeds, all movable canard surfaces have been introduced on delta wing aircraft. From the [1], it was understood that the close-coupled canard provides additional lift and also can act as an additional control device for an aircraft; however, the benefit is purely dependent on canard parameters. Therefore, it is essential to understand the geometrical parameter of canard to achieve the maximum benefits from the canard. The main constraints and objectives of low speed regime are discussed below:

1. The target approach speed is restricted from the arresting gear system of the carrier. To attain a lower speed of the aircraft requires higher lift for a given approach angle.
2. The size and location of canard surface are restricted by space available on the fuselage, internal layout considerations and intake design.
3. The slope of pitching curve should have linear trend that means without any pitch-up tendency. It is also preferred to have better high AOA pitch recovery control during launch and high 'g' manoeuvres.
4. Further, it should also improve lateral-directional characteristics to achieve the desired usable AOA max.

3 CFD Methodology

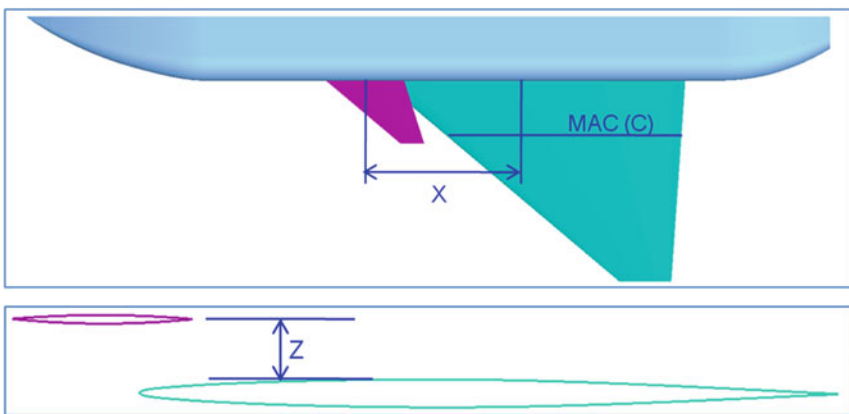
The analyses are carried out by using commercial CFD++ solver with high-fidelity RANS CFD methods using 2-eqn $k\omega$ SST turbulence modelling. Meshing is accomplished in ANSYS ICEM CFD, Version 15.0–1. The reason for this tool selection is because of simple and powerful, unstructured grid generation algorithm with good quality. For an accurate prediction of vortex and flow separations, adequate grid density at volume was adopted based on previous experience on low speed, high AOA flow simulations to capture nonlinear flow phenomenon. Surface mesh with triangular elements and unstructured volume mesh with tetrahedron grid elements is generated using Delaunay method. Quadratic elements were generated in the prism layer to capture the growth of boundary layer near the wall region by keeping the $y^+ = 1.0$ and total height of ~ 35 mm as shown in Table 1. Sensitivity analysis is conducted by varying its geometric parameters of canard and its relative positions using CFD methods. The design decisions are made based on low speed launch and approach speed requirements.

Table 1 Mesh details for delta-canard aircraft

Mesh details	
Mesh method	Unstructured
Total number of mesh elements ($\times 10^6$)	44
Total number of surface cells ($\times 10^6$)	1
Reynolds number ($\times 10^6$)	Flight conditions
1st layer height, mm	0.0018
Prism layers growth rate	1.25
Total height of prism layers, mm	35

4 CFD Evaluation of Canard Design

Various canard positions, shapes and area variations are studied as shown in Figs. 1, 2, 3. Three canard sweeps have been studied which in turn change the shape of canard and have same area but differ in LE sweep from 45° , 50° and 55° . In addition, one more shape, called as “edge matching”, which has same LE and TE sweep angle of main wing is also studied as shown in Fig. 3. Since area of canard has more impact on actuator size requirements, design space for area variation is limited with three areas of 4, 5.5 and 7% of wing area. It also may be noted that canard area percentage is calculated as a normalization by the exposed canard area of both sides to the theoretical wing area of both sides. Similarly, canard relative position such as X&Z separation with respect to wing has been normalized as shown in Fig. 1 which is the



X	Distance between 25% of MAC and 40% exposed root chord of canard.
Z	Distance between wing upper surface to exposed root chord of canard.
MAC (C)	Wing Mean Aerodynamic Chord

Fig. 1 Canard position definitions

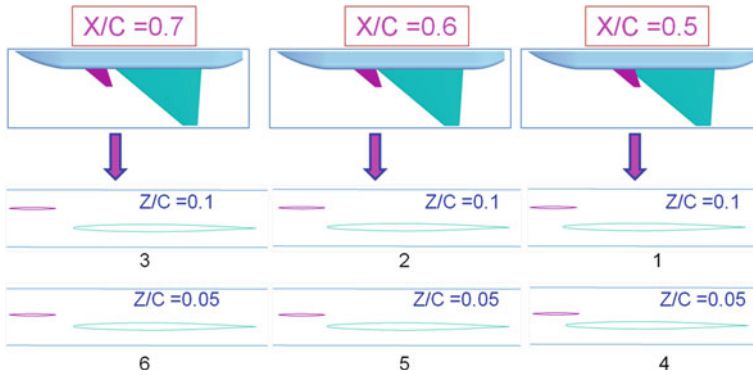
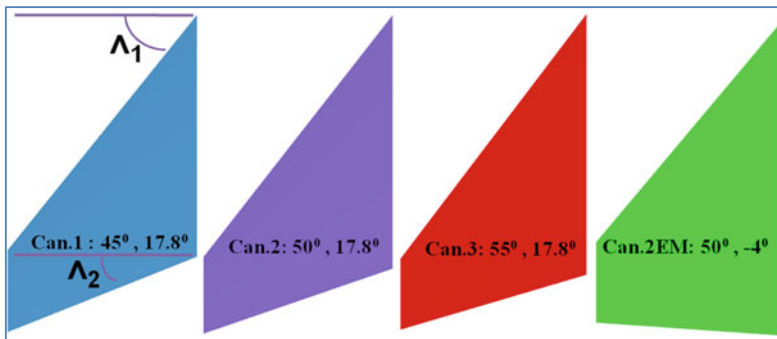


Fig. 2 Various canard positions in X/C and Z/C



S.No	Canard 01	Canard 02	Canard 03	Canard 02EM (Edge Matching)
S_c, m^2	5.5% of Wing area	5.5% of Wing area	5.5% of Wing area	5.5% of Wing area
LE, deg	45°	50°	55°	50°
TE, deg	17.8°	17.8°	17.8°	-4°

Fig. 3 Same swept wing family shapes with variation of LE and TE sweep angles

same expression as shown in [1] as well. Six relative positions of canard have been investigated for the 50° sweep canard as shown in Fig. 2, and the optimal position is obtained based on the approach speed value with canard upward deflected condition of -20° (approach phase) and usable AOA_{max} and CL_{max} characteristics with canard neutral position (launch phase).

5 Results and Discussions

5.1 CFD Validation

Towards building the confidence on CFD process, validation exercise has been carried out with the same research test model geometry and the test data provided in open literature from Lacey [1]. The given dimensions of wing-body and the canard taken from [1] and also shown in Table 2 are modelled by using CATIAV5, and CFD simulations were employed on that model with a same wind tunnel conditions mentioned in [1]. CFD grids are made similar standard as mentioned in Sect. 3, and the RANS solver of CFD++ with 2-eqn kwSST has been employed. CFD simulations were performed at two speeds ($M = 0.2$ and 0.6) and each Mach number has different location of canard as shown in Table 2. CFD results show fairly good agreement with an experimental predictions, and the error in uncertainty is minimum for both with and without canard configurations Figs. 4 and 5. CFD results show that the presence of canard generates more lift coefficient and pitching moment due to favourable mutual interaction of canard downstream vortices with wing vortices, thereby delaying the wing stall and flow separations up to higher AOA.

Table 2 Wing and canard details from [1]

Parameters	WT test model dimensions	Wing-canard relative positions
Wing S_{ref} , m^2	0.1961	All dimensions are same but the relative position with respect to wing is normalized accordingly as per [1] Pos.3 ($M = 0.6$) X/C = 1.0 & Z/C = 0.2 Pos.5 ($M = 0.2$) X/C = 1.25 & Z/C = 0.1
Wing Δ_{LE} , deg	50°	
Wing Δ_{TE} , deg	0°	
Canard exposed area (both sides), m^2	0.0257	
Canard Δ_{LE} , deg	45°	
Canard Δ_{TE} , deg	0°	

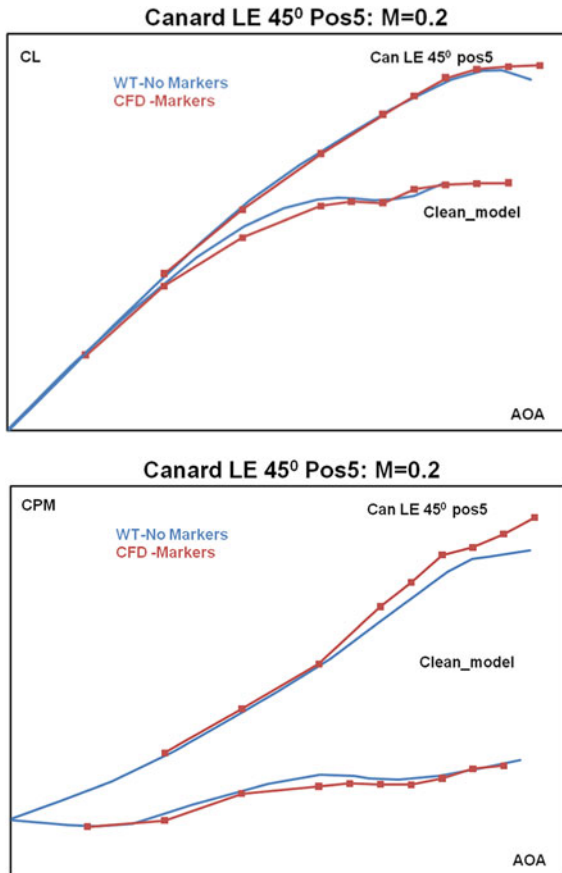


Fig. 4 CL, CPM validation with experiment data at $M = 0.2$

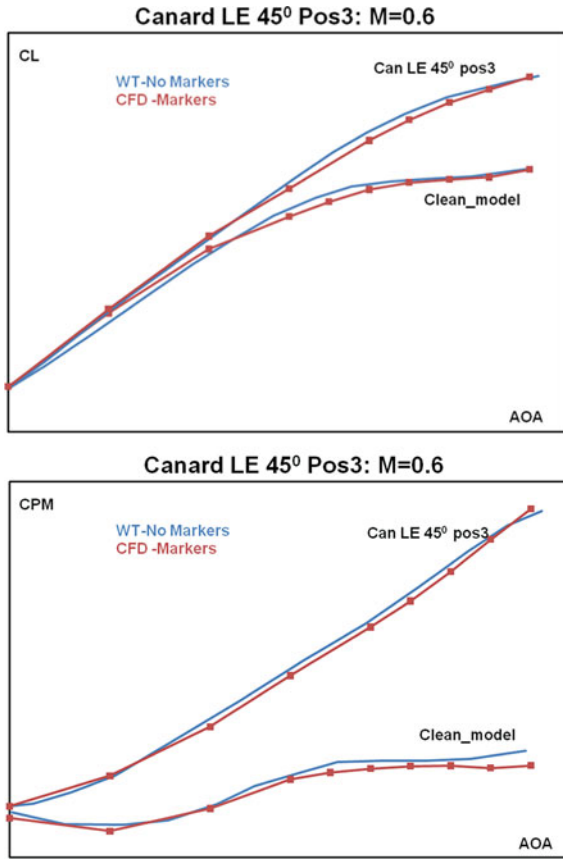


Fig. 5 CL, CPM validation with experiment data at $M = 0.6$

5.2 Canard Position Sensitivity

It is essential to identify the optimum position of canard with respect to wing to obtain the better lift characteristics up to higher AOA. Six positions are considered for analysis in which four positions are having non-overlap with wing and other two positions are overlap with wing as shown in Fig. 2. From the literature [1], it was understood that the canard Z-positions should be placed above or in-line with the wing surface to get favourable wing-canard vortex interactions instead of placing the canard to lower than wing plane. Thus, all the Z-position sensitivity analysis in this study was restricted to only above the wing plane to have better longitudinal characteristics. The CFD results on these six positions along with a clean wing configuration are plotted in Figs. 6, 7 and 8. Results indicate that the

Fig. 6 CL plots for various canard positions

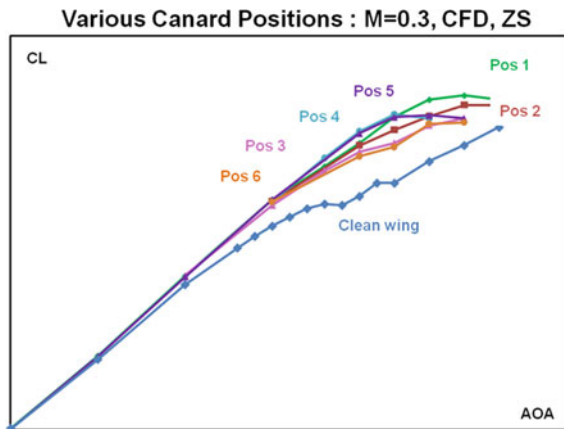


Fig. 7 CPM plots for various canard positions

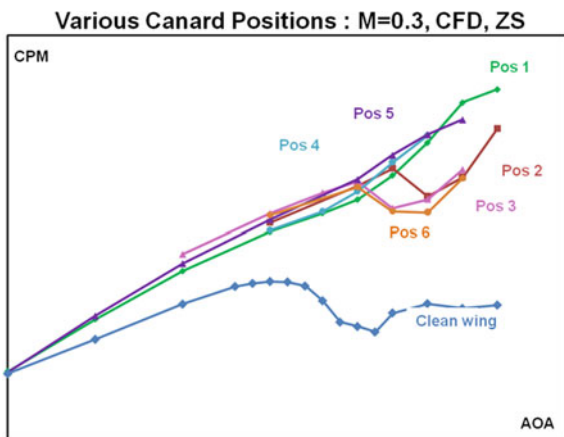
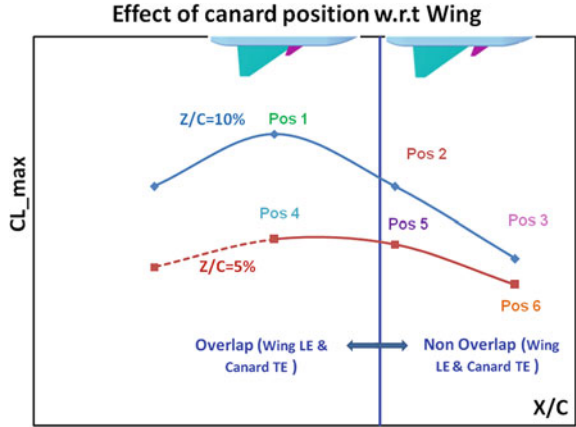


Fig. 8 CL_{max} plots for various canard positions



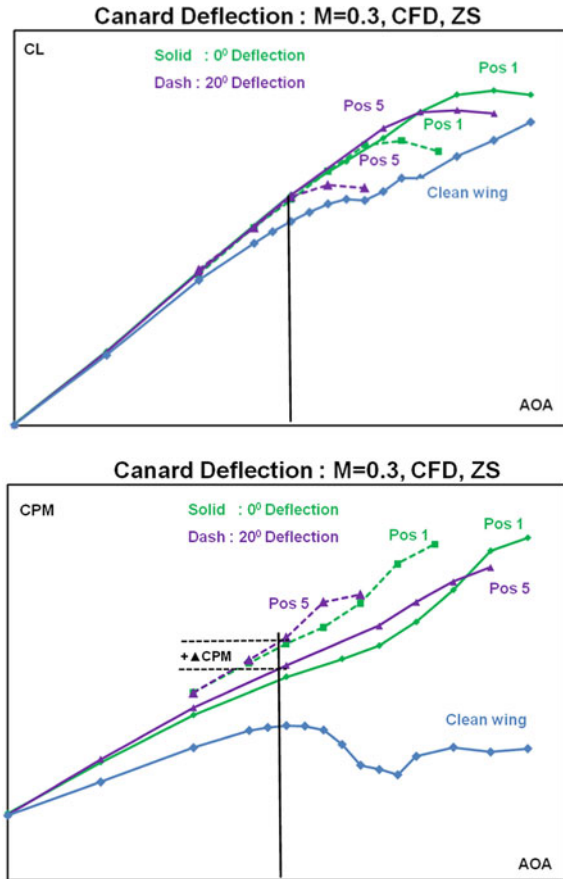
presence of canard increases the flow linearity up to higher AOA compared to clean wing configuration and attained higher CL_{max} .

Based on the low speed requirement of higher CL_{max} for launch and linearly increasing $CPM\alpha$ without having sudden pitch-up tendency improve the aircraft handling qualities, Pos.1 and Pos.5 have been selected from the analysis among six canard positions. From Fig. 8, it is seen that CL_{max} increases with increase of Z/C location. Pos.1 with Z/C of 10% shows better CL_{max} than other positions, and both Pos.1 and Pos.5 show linear CPM characteristics up to high AOA. More overlapping with wing or too much of forward placement of canard leads to the lower lift than slight overlap or just in front of overlap regions as shown in Fig. 8. Generally, it can be concluded that optimum position of canard is mostly realized close to the wing-canard overlap region.

5.3 Canard Deflection Analysis

For naval aircraft, the approach speed is of prime importance in engaging the aircraft in carrier operations; therefore, it is essential to have maximum possible CL and CPM linearity for the given approach angle to get desired approach speed. The selected positions (i.e. Pos.1 and Pos.5) have been investigated for longitudinal characteristics of CL and CPM with canard LE deflected upwards by 20° towards attaining higher CPM , thereby attaining higher trim lift and reducing approach speed. Both positions show similar CL for the design AOA, but Pos.1 is relatively better than Pos.5 in terms of CPM nonlinearity (pitch-up) as shown in Fig. 9. However, due to space constraints available on aircraft geometry, Pos.1 requires large Z -separation over wing plane which is not a feasible option for integrating with aircraft. Thus, Pos.5 has been explored in detail in follow-up studies along with Pos.1.

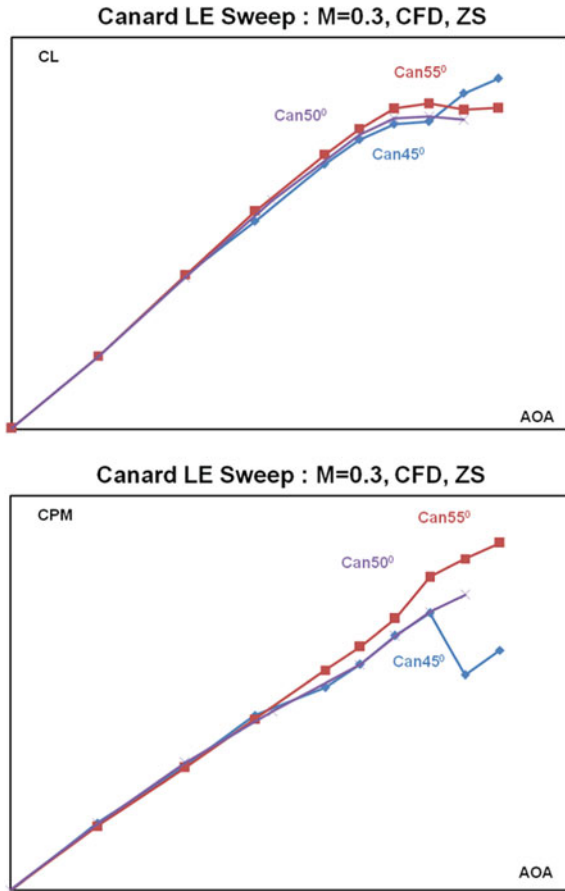
Fig. 9 CL and CPM plots for two different canard LE deflections (0, 20°)



6 Selection of Canard Sweep

Canard leading edge sweep: For selecting the canard plan form shape, three leading edge sweeps and two trailing edge sweep variations are studied with a fixed selected position of Pos.5 to obtain a canard shape which has better aerodynamic characteristics. From Fig. 10, it is found that higher LE sweep (50° and 55°) of canard has better CL and CPM characteristics than lower sweep of canard for a given wing of 50° sweep. In addition, the individual contribution of canard and wing surface for various leading edge sweeps has been plotted in Figs. 11 and 12, showing that canard alone and wing alone integration of CL and CPM characteristics is found to be better with the leading edge of 50° and 55° than lower sweep canard of 45°. Though, 55° LE sweep has shown relatively better CL and CPM characteristics than 50° sweep, the 50° sweep has been presently adopted in the baseline model due to having the same sweep angle of wing.

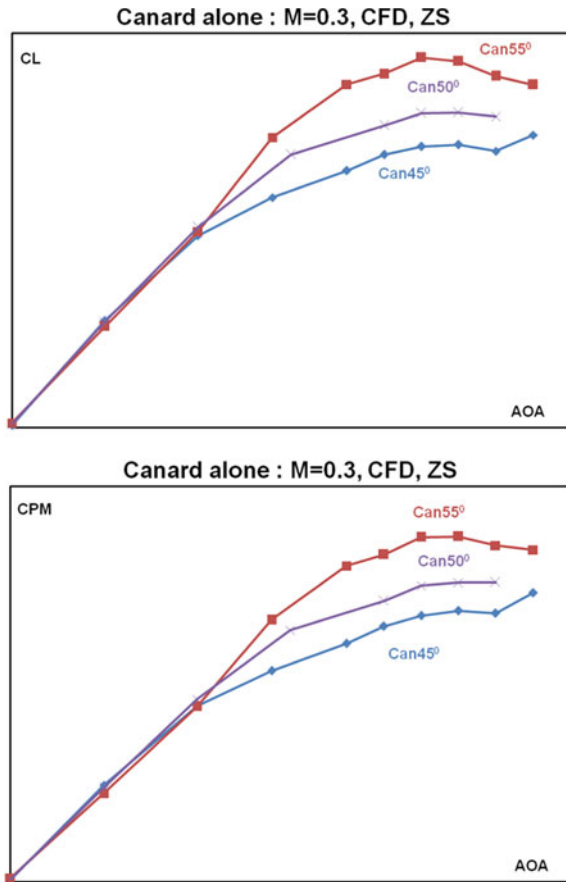
Fig. 10 CL and CPM plots for different canard LE sweep (45°, 50°, 55°)



Canard trailing edge sweep: Two trailing edge sweeps are studied, first one is the selected baseline canard of 50° LE sweep which has TE sweep of 17.8°, and the second variant of canard has TE sweep of 4° which is actually to acquire same LE and TE sweeps of wing to get edge matching towards improving the stealth features of aircraft. From Fig. 13, it is shown that the lower TE sweep edge has better CL and CPM characteristics than higher TE sweep at high AOAs. The individual contribution of canard and wing surface shown in Figs. 14 and 15 exposed that lower TE sweep has better CL from canard and wing than other one. It has also shown more linear CPM trend than higher TE sweep of baseline canard.

Selection of canard area (Sc): The canard to wing area ratio (S_c/S_w) has shown strong correlation with lift characteristics of aircraft as discussed in [1]. However, it should be noted that better positioning of canard can provide additional lift than the sum of the lift of individual contribution from canard and wing size. A study has been made to investigate three area ratios of 4.0, 5.5 and 7.0% for sensitivity analysis. From Fig. 16, it is found that the increase of canard to wing area does not contribute

Fig. 11 Canard alone characteristics for different LE sweep canard (45°, 50°, 55°)



to increase in CL, except in CLmax. However, the pitching moment increases with an increase in canard area which eventually amplifies the hinge moment requirements of actuator and its structural requirements. Thus, canard area ratio of 5.5% has been considered for the baseline aircraft as per the information available from contemporary aircraft canard sizes.

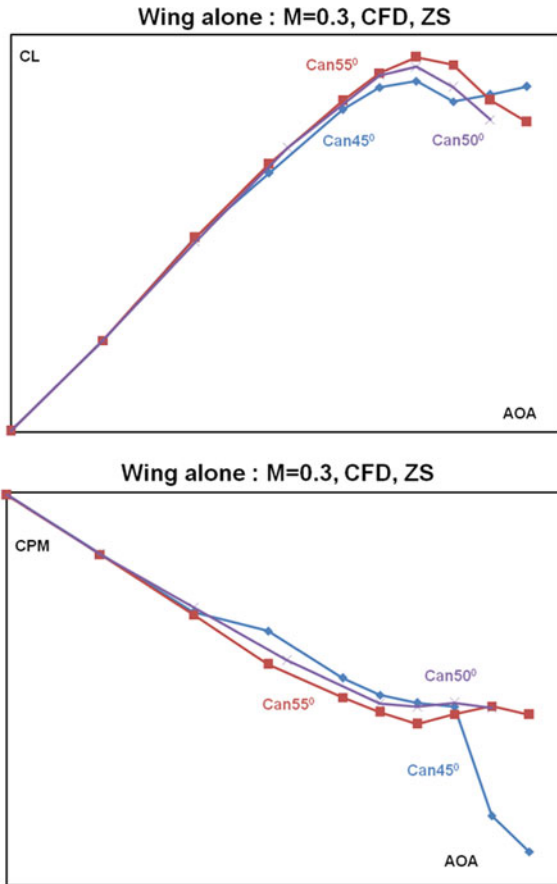


Fig. 12 Wing alone characteristics for different LE sweep canard (45°, 50°, 55°)

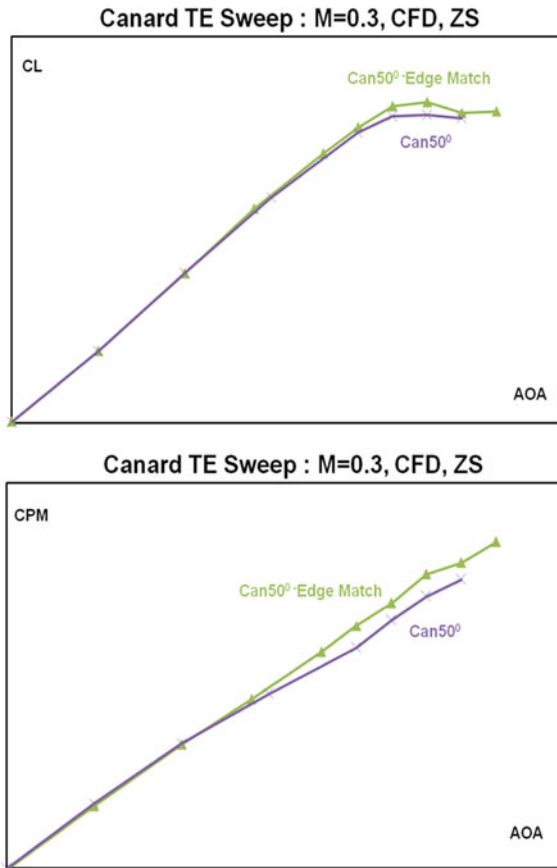


Fig. 13 CL and CPM plots for different TE sweep (4°, 17.8°)

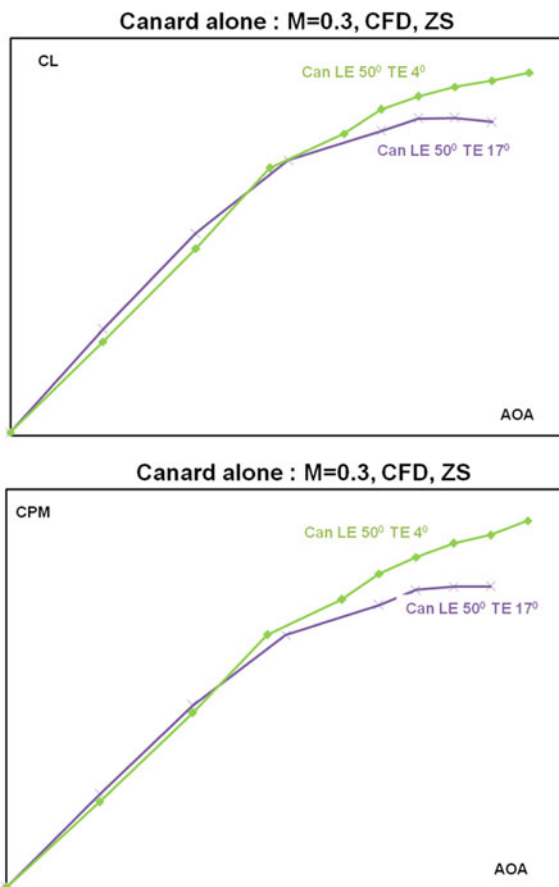


Fig. 14 Canard alone characteristics for different TE sweep (4°, 17.8°)

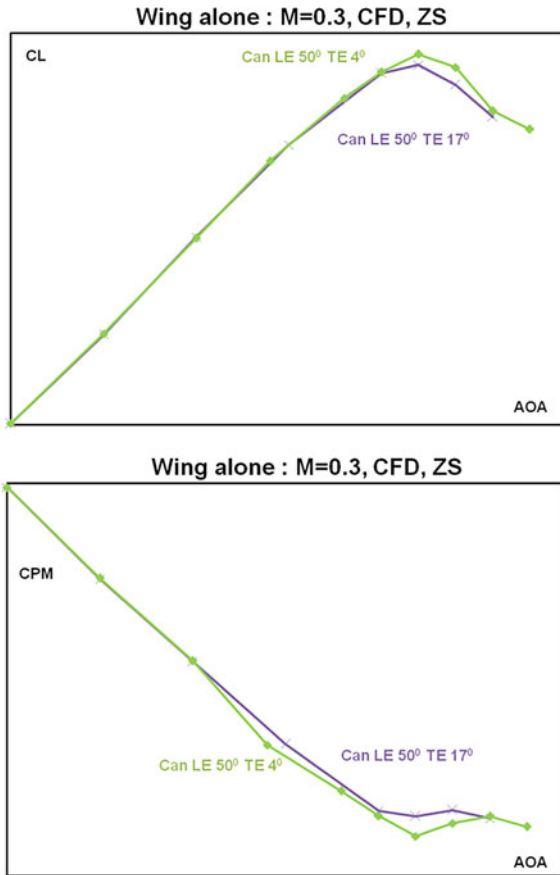


Fig. 15 Wing alone characteristics for different TE sweep (4°, 17.8°)

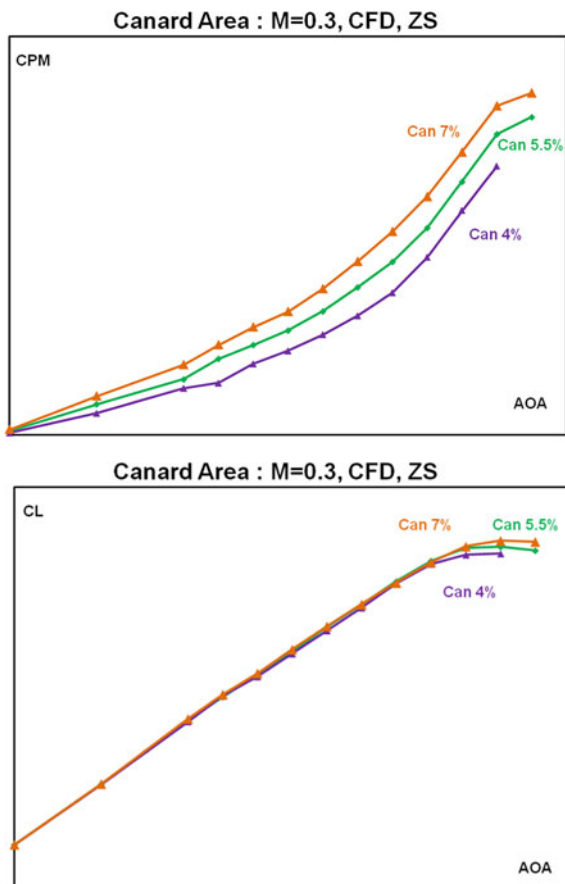


Fig. 16 CPM and CL plots for different canard sizes at Pos.5 (4.0, 5.5 and 7.0%)

7 Conclusion

Sensitivity analysis has been carried out on various canard positions, shapes and its area on simplified fuselage using CFD++ commercial CFD solver. Based on the results, the most preferred design is identified which could meet the essential requirement of carrier-based naval aircraft launch and recovery aspects. The following conclusions are drawn:-

1. The test case from literature [1] is validated with CFD results and shown fairly good agreement with an experimental predictions.
2. Introduction of canard on delta wing aircraft improves CL and pitching moment characteristics of aircraft which can be further enhanced by placing the canard at its optimum location with respect to the wing location.
3. **Canard position sensitivity:** Six positions of canard have been explored, and two positions of canard are found to be better in terms of CL_{max} and CPM linearity characteristics which are Pos.1 and Pos.5.
4. **Canard deflection sensitivity:** Canard upward deflection of 20° for two positions—Pos.1 and Pos.5—has been investigated for longitudinal characteristics of CL and CPM towards attaining higher CPM, thereby higher trim lift and reduced approach speed. Both positions have shown similar CL for the design AOA, but Pos.1 is relatively better than Pos.5 in terms of CPM nonlinearity (pitch-up).
5. Due to the space constraints available with aircraft geometry, Pos.5 which has lower Z-separation with wing plane has been selected for baseline configuration.
6. **Canard sweep angle sensitivity:** Higher leading edge sweep of 55° and lower trailing edge sweep of 4° have shown better longitudinal characteristics of CL and CPM than other shapes for a given 50° wing configuration.
7. **Canard area sensitivity:** Three area ratios are studied, and it is found that increase in canard area shows small increase in CL_{max} and large increase in pitching moment. Thus, to achieve the desired performance with reasonable actuator and structural demands, canard area ratio of 5.5% has been considered for the baseline aircraft configuration.

Acknowledgements The authors are thankful to the senior scientists of Ms. Valliammai Soma-sundaram and Shri Balmiki kumar and management of Aeronautical Development Agency for supporting this research and permitting the presentation to conference.

References

1. Lacey DW (1979, January) Aerodynamic characteristics of the close-coupled canard as applied to low-to-moderate swept wings 1–4. DTNSRDC-79/001, David W. Taylor Naval Ship Research and Development Center, Naval Air Systems Comand (NavAir)
2. McKay K (2000) “Eurofighter: aerodynamics within a multi-disciplinary design environment” as part of the report “Aerodynamic design and optimization of flight vehicles in a concurrent multidisciplinary environment”. Defence Technical Information Centre
3. Re RJ, Capone FJ (1978) Longitudinal aerodynamic characteristics of a fighter model with a close-coupled Canard at Mach numbers from 0.40 to 1.20. NASA-TP-1206

Optimization Applications: Automobile

Seating System in Indian Public Transport



Surya Chaurasiya and Tripti Singh

1 Introduction

(Transportation) [1] In India, the rapid growth of the urban population, development of cities, and migration has resulted in increasing transportation demand among the mass. Many people in cities such as Delhi and Mumbai spend a significant amount of time standing on their daily commute to and from work, and many a time, in some cases, it becomes very risky. The major cause of this situation in India is the rapid growth of the urban population. Although a large percentage of the population own private vehicles, the lack of availability and access to transport has proven to be a hindrance in the overall development of an area. This includes different modes of transport, such as railways, buses, auto-rickshaw, and many others. The consequences of this result in exceeded road capacity, increased traffic, high level of pollution, crowding, and accidents. Public transportation is important and needs in many areas like medical care, community resources, and employing across several countries [2]. The fast growth of cities, as well as the increase in their population, highlighted a transit challenge [3].

S. Chaurasiya (✉) · T. Singh
Design Discipline, Indian Institute of Information Technology Design and Manufacturing,
Jabalpur, India
e-mail: 1914029@iiitdmj.ac.in

T. Singh
e-mail: ts@iiitdmj.ac.in

© The Author(s), under exclusive license to Springer Nature Singapore Pte Ltd. 2023
P. Pradeep Pratapa et al. (eds.), *Advances in Multidisciplinary Analysis and Optimization*,
Lecture Notes in Mechanical Engineering,
https://doi.org/10.1007/978-981-19-3938-9_20

1.1 Background Study

Motor Vehicle

“Motor vehicle or vehicle means any mechanically propelled vehicle adopted for use upon roads whether the propulsion is transmitted there to from an external or internal source and includes a chassis to which body has not been attached and a trailer, but does not include a vehicle running upon fixed rails or a vehicle of special type adopted for use in factory or enclosed premises or a vehicle having less than four wheels fitted with engine capacity of not exceeding twenty five cubic centimeters.” [4, 5] (AIS-053 Automotive Vehicles—Types—Terminology) (Section 2(28) in The Motor Vehicles Act, 1988)

1.2 Types of Public Transport

In India, there is a variety of transportation options. Airways, waterways, railways, metro, bus service, and auto-rickshaw are some of the most common modes of transportation. Every system has flaws, some of which are listed below:

Airways: Flight delays and cancelations have become common due to poor aircraft maintenance. Increasing air traffic, slow policy implementation, congested airspace, a scarcity of runways, and a dearth of facilities for the physically impaired have all proven to be significant hurdles for India’s aviation business [6].

Waterways: As a capital-intensive business, providing and maintaining waterway ports necessitate even more investment. Vehicle costs, fuel expenses, staff costs, maintenance costs, and so on are all examples of operating costs. Increased water use for drinking, agriculture, construction, and other purposes affects overall water flow in downstream regions and complicates transportation operations.

Railways: Network capacity restrictions are one of the most significant concerns. Low infrastructure and service investment have led to slow speeds, delays, and safety concerns. Lack of overall hygiene and maintenance, hawker intervention at train stations, and a lack of facilities for the differently abled are just a few of the issues that appear to be difficult to solve.

Metro: The stages of metro construction—the development of a metro line road closures during construction cause traffic congestion and congestion. These clogs can also be a nuisance in residential areas. Even if ongoing expansion is necessary, it frequently comes at the expense of the environment. Deforestation and clearing of land for structural expansion are a major issue.

Bus: The majority of buses in operation today have numerous maintenance and hygiene difficulties, causing them to be overlooked as the ideal means of transportation for any Indian passenger. The majority of overcrowding occurs during rush hours due to a scarcity of buses on a route, a lack of clear-cut laws on passenger capacity on a bus, or people’s unwillingness to wait for another vehicle.

Auto-rickshaw/Taxi: Due to its high energy consumption and high exhaust emissions, it is one of the most significant contributors to the deterioration of air quality in urban areas. Due to its poor structure and lack of safety, it is the most vulnerable to damage and injuries following a collision.

1.3 Common Types of Bus in India

There are two types of buses, according to AIS 052(Rev. 1):

- A. High capacity buses such as articulated bus, double-decker bus, double-deck articulated bus.
- B. Special purpose buses such as sleeper coach, school bus, tourist bus, prison vehicles, vehicles specially designed for the carriage of the injured or sick person (ambulances), off-road vehicles, vehicle designed for use by police, securities, and armed forces [7].

“**Type I**” vehicles are medium and high-capacity vehicles with areas for standing passengers, designed and constructed for urban and suburban/city transportation with frequent stops, and low-capacity vehicles designed and constructed for urban and suburban/city transportation exclusively for carrying seated passengers [7]. Low-capacity vehicles of this type can transport standee passengers if they fulfill the requirements for low-capacity standee buses [4, 7].

“**Type II**” Vehicles are those intended and built for inter-urban/inter-city transportation that does not have a designated location for standing passengers but can transport standing passengers over a short distance in the gangway unless otherwise forbidden by the State Transport Department [7].

Vehicles classified as “**Type III**” are those designed and built for long-distance passenger transport, with the sole purpose of providing comfort to seated passengers, and are not intended to carry standing passengers [7].

“**Type IV**” vehicles are created for special purposes and built for such purposes as:

“School bus” refers to vehicles with a seating capacity of 13 or more individuals, excluding the driver, that is intended and built specifically for transporting students to and from schools (Page No. 5/14 clause 3.1.7.5). [4] “Sleeper coach” refers to vehicles with a seating capacity of 13 passengers or more, excluding the driver, that is designed and built with an additional berth for passengers to sleep while traveling (Page No 5/14 clause 3.1.7.6). [4]

1.4 Low-Capacity Vehicles Include

- (1) Micro buses, which have a maximum seating capacity of 12 passengers including the driver.
- (2) Mini bus: Seating capacity ranges from 13 to 22 passengers, including the driver.

1.5 Medium-Capacity Vehicles

- (1) Midi bus*, which has a seating capacity of 23–34 passengers including the driver.
- (2) Standard bus: Capacity ranges from 35 to 70 passengers plus the driver.

* “Provisions of this code are not applicable to Micro Buses.”

High-Capacity Vehicles are those that can seat more than 70 passengers plus the driver and include vehicles such as the single-deck articulated bus, single-deck double articulated bus, double-deck bus, double-deck articulated bus, and single-deck tandem axle bus, among others.

Articulated bus: A bus made up of two rigid parts joined by an articulated joint, with passenger accommodation compartments in each rigid segment communicating with one another. The articulated joint ensures that passengers can freely move from one stiff segment to the other (AIS-053) [4, 7].

“Low floor vehicle” refers to a vehicle in which at least 35% of the space available for standing passengers (or front portion in the case of articulated vehicles) constitutes a single space without steps, accessible by at least one service entrance via a single step from the ground (Page 10/122 clause 1.1.74) [7].

1.6 Methodology

The data collection framework included several methods such as desk research, direct observation, interviews, task analysis, and a survey questionnaire. The desk research was used to get an overview of existing services. Photography and videography were used as tools to collect relevant information for in-depth study whenever possible. To gain a better understanding of the problems, users (of various ages, genders, and professions) and service providers were interviewed.

More than 50 auto-rickshaw drivers of various ages were interviewed, to gain insight into the actual problem they are facing in the current situation and their daily struggle with passengers. The drivers who took part in the interviews were from the Jhansi District of Uttar Pradesh, India.

1.7 Current Scenario in India

The current situation in India varies from state to state, which means that each state has its own set of rules and laws regarding public transportation. When it comes to railways, trains are subject to certain regulations. Some states are on complete lockdown, while others are on partial lockdown. Furthermore, most Indians are not traveling because of the added concern of infection, as public transportation is one of the most afflicted systems.

During COVID-19, the situation of India has changed a lot due to this pandemic. There are a lot of restrictions for the people going out from their home, most of the work they have to do from their home only. Mass gatherings have been suspended for few months [8]. As a result, there is less congestion in the transportation mediums and reduced transportation service as a result of the lower number. People are often hesitant to use public transportation due to fear of infection [8].

Before COVID-19, a public transit system was overcrowded. Passengers have to face issues like mechanical noise while traveling in the buses. Passengers had to deal with pain in the seats because some of the older buses had vertical back support. There is a lot of litter inside the vehicle, which indicates that there are a lot of maintenance and hygiene issues.

1.8 Transport in Auto-Rickshaw and Buses

In India, the auto-rickshaw is the most popular mode of transportation. It can be found in almost every part of the country. For short trips, they are the preferred mode of transportation. Two of the key reasons for increased demand for auto-rickshaws are because they are very convenient and easily located and hired for first and last mile connections. This vehicle's compact size and thin shape make it ideal for navigating India's congested roads.

Due to the weak structure and lack of safety equipment, an auto-rickshaw is most vulnerable to damage and injuries during a collision. It is considerably more perilous due to a lack of substantial girdles and covers and an unsteady frame. Daily, many school children use auto-rickshaws as a mode of transportation. It is frequently picked at the expense of their genuine ability. Three-wheelers are dangerous because they easily topple during sharp turns at high speeds, despite their ease of manufacture.

Buses are one of India's most popular and convenient modes of transportation, with the majority of the population using them. For the past decade, bus transportation has been the primary mode of transportation in most Indian cities.

The majority of buses currently in use in India have numerous maintenance and hygiene issues, causing buses to be overlooked as the best mode of transportation for any Indian passenger [3]. The majority of overcrowding occurs during rush hour due to a shortage of buses on a specific route. By efficiently utilizing seating capacity, bus transportation must provide comfortable travel [3].

1.9 Seating System in Foreign Countries

Most countries use the common practice of pasting stickers with the words "Do not sit here" on alternative seats in buses and metros. A plastic sheet is used to separate the driver and passengers' areas in auto-rickshaws and taxicabs.

India is a developing country, and it, like any other country, faces a complex set of challenges that must be addressed. Due to a lack of willingness to follow the rules, this solution will not work in most parts of the country. The mindset of Indians, their reactions when confronted with a particular situation, and the potential for them to exploit the solution provided. The developing country's financial constraints make putting a solution in place even more difficult. It is difficult for any solution to remain in practice.

1.10 Crowding in Indian Public Transport

When buses and trains carry a small number of passengers, everyone can find a seat, passengers are transferred smoothly at stations, and passenger-related interruptions that cause unexpected delays are infrequent. As the number of passengers grows, there comes a point where not everyone can find a seat, and some passengers must stand inside the vehicle [9]. However, because of the well-known virus, only a few people are using public transportation, and it can also be noted that the number of vehicles is also decreasing due to the low number of passengers [3]. However, if the transport vehicle is occupied to more than half of its capacity, the vehicle is considered overcrowded. Because of rapid population growth, public and transit facilities are becoming overloaded, producing social discomfort [3].

1.11 Ergonomics and Anthropometric Analysis of Seating

Guidelines from the Government of India

The CMVR—Technical Standing Committee, chaired by Shri B. Bhanot at the time, addressed the issues, and the entire exercise was aimed at standardizing the essential aspects involved in the construction of the bus body while keeping in mind the minimum requirements of passenger safety and comfort [7]. The CMVR-Technical Standing Committee was asked by the former Ministry of Surface Transport, currently known as the Ministry of Shipping, Road Transport and Highways, to draught necessary recommendations on bus body standardization [7] (Table 1).

To determine the maximum seating capacity, a conventional 3×2 arrangement with a seat spacing of 686 mm and a seat width of 400 mm per passenger was used [7]. The calculation takes into account places that are not suitable for the passenger sitting, such as the driver's compartment, the engine compartment, the step-well gangway, and so on [7]. Clause 2.2.11 of the AIS-052 Code of Practice for Bus Body Design and Approval should be taken into account for additional seating specifications of all types of buses in India.

Table 1 Recommendations for urban bus specification, according to the Government of India Ministry of Urban Development Urban Transport Division [10]

Parameter	Details	Recommended specification	
		Standard bus (Type 1 bus as per AIS 052)	Mini/midi buses
Seats	Seat layout	1 × 1 or 2 × 0 in low floor area 2 × 2 in the high floor area	2 × 1 2 × 2 (for non-standee bus)
	Seating area/space per passenger (total width X depth)	400 × 350 mm (AIS 052)	400 × 350 (AIS 052)
	Seat spacing (AIS 023)	650 mm—Type 1	As per AIS 023
Seat belt requirement		Not required other than driver	Not required other than driver

1.12 Ergonomic Measurements in Sitting Posture

For several decades, it is well observed that human breadth and circumference measures have increased at a faster rate than heights [12]. Increases in body mass relative to height are evidence of this. The body mass index (BMI) is calculated by dividing a person’s weight in kilograms by the square of his or her height in meters [12] (Table 2).

In ISO 7250-2 technical report, on average, around 32% of men and 78% of women from the seven nationalities are accommodated at a seat and shoulder width by an overall width of 447.4 mm [13].

Only the information required to determine the measurements that are appropriate for Indian passengers is provided here.

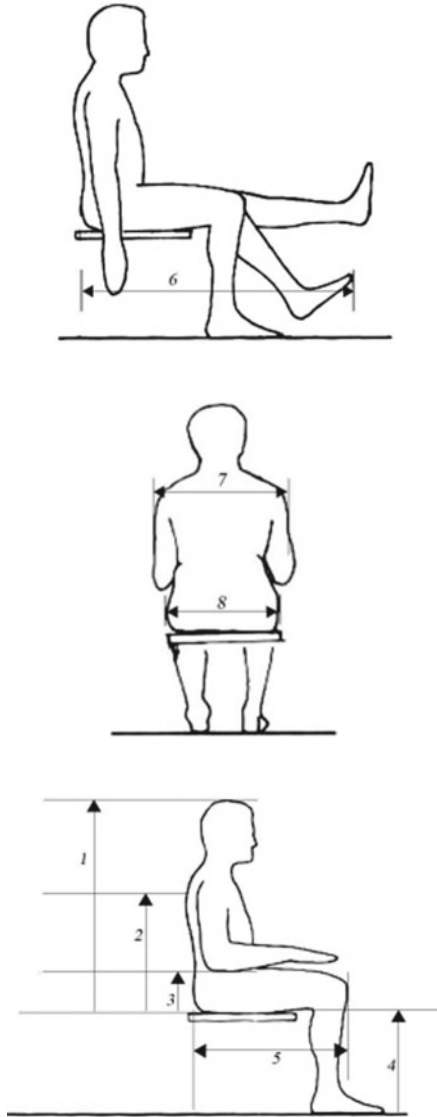
The normal setting is measuring the head in a normal relaxed position [11]. The 95th percentile data for both men and women must be combined in order to estimate the seat height. The appropriate height for the sitting can therefore be measured from 1000 to 1050 mm. The backrest must be at least 800 mm tall for Type I, 1000 mm tall for Type II, and 1100 mm tall for Type III, according to AIS-052.

The acromion is the most lateral point on the acromion process of the scapula’s superior surface [11]. People lay their backs on the seat at this point. To determine the suitable dimension for the acromion height, it is needed to extend the area of the acromion support from the 25th percentile to the 95th percentile. The suitable range can be 509–603 mm.

The lowermost part of the elbow is called elbow rest [11]. To determine the height of the elbow rest, the combined data of males and females of the 50th percentile is needed. The suitable height for the elbow rest can be taken as 210 mm. The minimum height for the armrest is 175 mm according to AIS-052.

Popliteal angle point at the underside of the thigh immediately behind the knee, where the tendon of biceps femoris muscle inserts into the lower leg [11]. It can help

Table 2 Required dimensions for Indian bus seats and can be determined



(continued)

Table 2 (continued)

No	Parameters	Min	Percentiles					Max	Mean	SD	Ratio
			5th	25th	50th	75th	95th				
1	Normal sitting	650	715	768	805	836	886	929	803	50	0.49
2	Acromion	426	475	509	541	566	603	657	540	40	0.33
3	Elbow rest	102	150	188	210	234	268	335	211	36	0.13
4	Popliteal	605	374	399	419	439	466	540	420	33	0.26
5	Buttock to knee length normal sitting	400	479	520	549	575	613	861	549	44	0.34
6	Buttock to extended (rested on floor) leg comfortable length	660	739	849	905	979	1069	1210	910	99	0.56
7	Bi-deltoid	276	349	393	417	443	479	672	418	41	0.26
8	Hip breadth	209	269	304	326	353	406	550	331	45	0.2

For men and women, all statistics are combined [11]

All the measurements are in mm

in determining the height of the seat from the floor of the bus. The combined data of males and females of 50th percentile is needed to determine the height of the seat. The suitable height of the seat can be taken as 420 mm. According to AIS-052, the height of the uncompressed seat cushion shall be between 450 + 50 mm.

To determine the depth of the seat, refer to AIS-052 as depth can be taken as 400 mm as it is given for Type II and Type III buses and 350 mm as the minimum depth.

Buttock to knee length is the horizontal distance from the most posterior point on the uncompressed buttocks to the most anterior point on the knee [11]. It can help in determining seat spacing. The combined data of males and females of the 95th percentile is needed. The suitable seat spacing can be taken as 650 mm. According to AIS-052, the minimum length for seat spacing is 650 mm for Type I and 680 mm for Type II buses [14].

Bi-deltoid is the maximum horizontal distance across the shoulders, breadth measured to the protrusions of the deltoid muscles. This parameter can help in calculating the minimum width of available space for each seating position. The combined data of males and females of 95th percentile (479 mm) is needed to find the suitable dimension. The suitable width of available space can be 500 mm. Measurement of 500 mm in the case of individual seats and 450 mm in the case of continuous seats for two or more passengers is provided according to AIS-052.

Hip breadth is the maximum horizontal distance across the hips [11]. This parameter can help in calculating the seat width. The combined data of males and females of the 95th percentile (406 mm) is needed to find a suitable dimension. The dimension of seat width can be taken as 410 mm. The minimum dimension for seat width is 400 mm according to AIS-052.

1.13 Results and Discussion

Some conclusions were drawn from conversations with the auto-rickshaw drivers and from the data that was collected. The ages of the participants range from 21 to 62 years old. The majority of the drivers own their vehicles, while others do so on a rental basis. They have 3–5 years of driving experience, while some of them have more than ten years. The majority of the drivers use low-cost smartphones, with only a few using keypad-based phones, and the majority of them are over 40 years old who use keypad-based cellphones. The auto-rickshaw drivers go around in circles on a predetermined route of 15–20 km. The drivers do not take more than 2–3 passengers at a time due to the pandemic. The majority of the passengers wear safety precautions such as masks, but the driver stated that those who do not wear masks will be refused service. When there is not a pandemic, the drivers usually take 5 to 6 passengers, and sometimes even more. The drivers request that their children's parents or guardians hold them in the appropriate position for their safety. Before starting the vehicle, they make sure that the elderly are properly seated. The drivers ask for extra money for more luggage and tie the goods and bags with ropes at the back and top of the vehicle for passengers who approach with extra luggage. The majority of drivers are satisfied with their vehicle's capacity; they only experience congestion when passengers arrive with more luggage than intended.

Public transportation, as a whole, has a variety of challenges and other features that must be properly considered. In India, buses and auto-rickshaws are widely used modes of transportation. Several difficulties concerning areas such as safety, vehicle operation, sanitation, psychological elements, government engagement, and system planning have been raised. Each of the areas raised several difficulties that needed to be investigated to effect systemic change. Several COVID-19 crisis rules and regulations for public transportation services in cities can be projected in the medium and long term, even though there is a lot of ambiguity and the debate is just getting started.

In India, public transportation is a mess and could be drastically improved, but there is also the need to recognize the Indian way of looking at it. It is needed to explore a schematic redesign of bus and auto-rickshaw seating that can improve transit conditions while also lowering infection fears. Another option is to go back to the source of it all: school. Educating students on the significance of transportation. There is also a need for a useful mobile application that can direct passengers based on real-time conditions, a solution that not only saves time but also addresses the major issue with bus transportation—overcrowding.

2 Conclusion

The COVID-19 crisis, as well as its medium and long-term implications, point to an emerging research agenda based on sustainable and healthy urban mobility, as

well as solid guidelines for future pandemics. It is important to understand how people's needs and desires, as well as their willingness to change, influence solution development and execution. Failure to implement a solution teaches us about what the public is willing to accept and how quickly such change should be implemented. It not only enhances their experience but also dispels common myths and misconceptions. It makes it easier for systems to integrate into their lives.

The conclusion of the research, interviews, and survey is that overcrowding is a system loop problem that can be reduced for a limited period of time but that, due to population growth, things will revert to their previous state. Also, when it comes to public transportation, Indian mentality is very different in terms of following rules and regulations.

Public transportation in India is a mess that could be drastically improved, but there is also a need to recognize the Indian perspective. It is necessary to look into a schematic redesign of bus and auto-rickshaw seating in order to improve transit conditions. It's critical to comprehend how people's needs and desires, as well as their willingness to change, influence the development and implementation of solutions. Failure to implement a solution teaches us about the public's willingness to accept change and the speed with which it should be implemented. It not only improves their experience, but it also debunks common myths and misunderstandings. It facilitates the integration of systems into their daily lives.

References

1. Hrelja R, Khan J, Pettersson F (2019, October 25) How to create efficient public transport systems? A systematic review of critical problems and approaches for addressing the problems. <https://doi.org/10.1016/j.tranpol.2019.10.012>
2. The Importance of Public Transportation. <https://www.fhwa.dot.gov/policy/2002cpr/pdf/ch14.pdf>
3. Simha BV, Lamani BN, Nithin HS, Shreyas LS, Shruthi BS (2018) Smart seating management in public bus transportation. http://ijariie.com/AdminUploadPdf/SMART_SEATING_MANAGEMENT_IN_PUBLIC_BUS_TRANSPORTATION_ijariie8474.pdf
4. AIS 053 Automotive Vehicles-Types-Terminology. https://hmr.araiindia.com/Control/AIS/1122018124347PMAIS-053_7amds_and_Corri_1.PDF
5. Central Government Act. <https://indiankanoon.org/doc/1873380/>
6. Duerstock BS Report on the challenges of air transportation experienced by people with disabilities. <https://docs.lib.purdue.edu/cgi/viewcontent.cgi?article=1001&context=ugcw>
7. AIS-052 Code of Practice for Bus Body Design and Approval, September 2001. https://www.araiindia.com/cpanel/Files/PUB_10~4~2011~10~12~04~AM~AIS-052_Rev_1_and_Amd_1.pdf
8. Gutiérrez A, Miravet D, Domènech A (2020, August 12) COVID-19 and urban public transport services: emerging challenges and research agenda. <https://doi.org/10.1080/23748834.2020.1804291>
9. Tirachini A, Hensher DA, Rose JM (2013) Crowding in public transport systems: effects on users, operation and implications for the estimation of demand. <https://doi.org/10.1016/j.jtra.2013.06.005>
10. Government of India, Ministry of Urban Development Urban Transport Division, November 2008. http://www.indiaenvironmentportal.org.in/files/urbanbus_spec.pdf

11. Chakrabarti D (1997) Indian anthropometric dimensions for ergonomic design practice. India: National Institute of Design, 161 pp. National Institute of Design Original, The University of Michigan Digitized. 7 October 2008
12. Molenbroek JFM, Albin TJ, Vink P (2017) Thirty years of anthropometric changes relevant to the width and depth of transportation seating spaces, present and future. <https://doi.org/10.1016/j.apergo.2017.06.003>
13. Mitchell C (2007) Research on the ergonomic capabilities of public transport passengers. <https://www.researchgate.net/publication/295688992>
14. AIS 023 Automotive Vehicles-Seats, their Anchorages and Head Restraints for Passenger Vehicles of Categories M2, M3 and Goods Vehicles of Category N-Specifications. https://hmr.araiindia.com/Control/AIS/1010201710501PMAIS_023.pdf

Strategic Optimization of Lubricant Base Oil Formulations and Supply Portfolio



Senthil K. Vadivelu, G. R. Gauri Shanker, Sudarshan Kasthurirangan, and Ben Bosmans

1 Problem Definition and Modeling Framework

Let x_{ij} be the composition of the i th group j th grade base oil in any formulation. A superscript could be used to track the current and future year formulations as x_{ij}^{curr} , x_{ij}^{1yr} , x_{ij}^{2yr} , etc. The aim is to start with a current formulation and arrive at optimized year-by-year formulations for the next ten years, satisfying the following classes of constraints:

- The viscosity constraint $\text{visc}(x_{ij}) = \text{visc}(x_{ij}^{\text{curr}})$ is imposed to maintain it during a blend reformulation. This strict equality can be relaxed as a weaker inequality as $0.95 \text{visc}(x_{ij}^{\text{curr}}) \leq \text{visc}(x_{ij}) \leq 1.05 \text{visc}(x_{ij}^{\text{curr}})$. We optimize future formulations by maintaining the kinematic viscosity constraints at two different temperatures to ensure good performance over the entire operating range. Constraints for other performance indicators like solvent power, seal compatibility index, and volatility can be added if blend models or datasets are available [2, 3].
- Additional inequalities arise from max and min values for select components as $x_{ij}^{\text{min}} \leq x_{ij} \leq x_{ij}^{\text{max}}$; these are called as the balance groups. In every scenario to be optimized, there should be at least one balance group for tuning. Additional equalities arising from a component that should be absent or to be maintained constant as in $x_{ij} = 0$ or constant; these can be cast as weaker inequalities as

S. K. Vadivelu (✉) · G. R. Gauri Shanker · S. Kasthurirangan
Shell India Markets Pvt. Ltd., Bengaluru, India
e-mail: senthil.v.kumar@gmail.com

G. R. Gauri Shanker
e-mail: gauri-shanker.gr@shell.com

B. Bosmans
Shell Lubricants Supply Company BV, Hague, The Netherlands

described above. Thus, setting x_{ij}^{\min} and x_{ij}^{\max} for all the components (balance, as-is or zero groups) would be a complete specification of a formulation.

- Composition positivity and normalization constraints would be $x_{ij} \geq 0$ and $\sum_{i,j} x_{ij} = 100$ (excluding the additives).
- Other business and technical constraints like the balance among different BO grades so that the entire product slate is optimally used, the current or future capacity and supply chain constraints, etc., can often be put in the form $\sum \phi_{ij} x_{ij} = \text{constant}$.

The objective function is the summed term-by-term product of a prioritization matrix p_{ij} and the composition matrix x_{ij} , $J = \sum p_{ij} x_{ij}$. The prioritization matrix is an abstraction of preference and cost so that the erstwhile heuristics can be coded as levels of preference (1, 2, 4, ... or 1, 10, 100, ... etc.) and later be replaced with actual costs. Note that minimizing the objective function would then ensure that a preferred BO grade gets prioritized. Such bridging abstractions are needed to transition from the purely heuristic and spreadsheet-based tools to an automatable optimization-based solution.

2 Methodology

Since the objective function and all constraints except viscosity are linear, we chose the derivative-free nonlinear optimization algorithm constrained optimization by linear approximation (COBYLA), developed by Powell [4]. Though it is known to be slower than gradient-based algorithms, it is stable even with non-smooth objective function or constraints and has lesser number of tuning parameters. Excluding the nonlinear viscosity constraints, an approximate solution is generated using the standard linear programming (LP) routine. Adding a little noise to this LP solution, we generated a better initial guess for nonlinear problem. This numerical trick enhanced its speed and allowed us to efficiently process thousands of scenarios covering Shell's global lube portfolio.

3 Sample Results

Table 1 shows a sample set of model inputs; from these inputs, we calculate total cost = 81,324 and overall viscosity = 4.696. Table 2 shows the model results; from these, we calculate total cost = 71,007 and overall viscosity = 4.696.

Table 1 Sample set of model inputs

Base oil grade	Current composition	Min	Max	Viscosity1	Viscosity2	Cost
B1	30.53	0	100	19.5	4.26	1063
B2	40.05	0	100	19.86	4.043	731
B3	29.42	0	100	40.8	6.431	666
B4	0	0	10	101.9	12.03	760

Table 2 Sample model output

Base oil grade	Current composition	Min	Max	Viscosity1	Viscosity2	Cost	New composition
B1	30.53	0	100	19.5	4.26	1063	0
B2	40.05	0	100	19.86	4.043	731	67.34
B3	29.42	0	100	40.8	6.431	666	32.34
B4	0	0	10	101.9	12.03	760	0.32

4 Discussion and Conclusions

The first epoch of the model predicts the optimal first-year reformulations using the current formulations as the input. Further, epochs cover the succeeding years, generating multi-year strategic predictions. This framework as stated optimizes at an individual LOBP level. However, it can be easily extended to optimize at a regional hub or global-level factoring interactions among the LOBPs, global supply chain constraints, etc., by simply extending the composition notation as x_{ij}^k , standing for the composition of i th group and j th grade BO at the k th LOBP.

References

1. Chevron (2012) Modern base oils & blending for optimal performance. Lube-Tech 107(80):2–7
2. Roegiers M, Zhmud B (2011) Property blending relationships for binary mixtures of mineral oil and elektrionised vegetable oil: viscosity, solvent power, and seal compatibility index. Lubr Sci 23:263–278
3. Zhmud B (2014) Viscosity blending equations. Lube-Tech 121(93):1–4
4. Powell MJD (1994) A direct search optimization method that models the objective and constraint functions by linear interpolation. In: Gomez S, Hennart J-P (eds) Advances in optimization and numerical analysis. Kluwer Academic, Dordrecht

Optimization of Lot Size in Lubricant Blending Plants



**G. R. Gauri Shanker, Ramya C. Sreeram, Michael Mortlock,
and Danielle Zennemers**

1 Introduction

Shell is a global supplier of lubricant products across its network of many blending plants worldwide that demands careful and meticulous upfront planning. It is often very challenging to make an optimal choice between producing bigger batches of lubricants, i.e., lesser unit operating expense (OPEX) vs smaller batches, i.e., reduce working capital. A common dilemma is where plants would like to have a larger filling lot size to improve OEE and reduce set up changes (line flushing and changeover). However, this leads to higher working capital and impacts logistics costs. Evaluating the impact of such decisions on the end-to-end (E2E) supply chain performance is often complex and subjected to individual's assessment.

As illustrated in Fig. 1, the complexity of the problem is mainly due to the competing cost parameters and finding a balanced state between waste/flush optimization, OEE and days inventory outstanding (DIO). Hence the need of a model that maps the full complexity of operations, setup and inventory parameters.

Adding to the complexity of the competing key performance indicators like inventory vs operations, the model must find the optimal lot size for thousands of products

G. R. Gauri Shanker (✉) · R. C. Sreeram
Shell India Markets Pvt. Ltd, Bangalore, India
e-mail: gauri-shanker.gr@shell.com

R. C. Sreeram
e-mail: ramya.c-sreeram-i@shell.com

M. Mortlock
Shell Eastern Trading Pvt. Ltd., Singapore, Singapore
e-mail: michael.mortlock@shell.com

D. Zennemers
Société des Pétroles Shell, Paris, France
e-mail: danielle.zennemers@shell.com

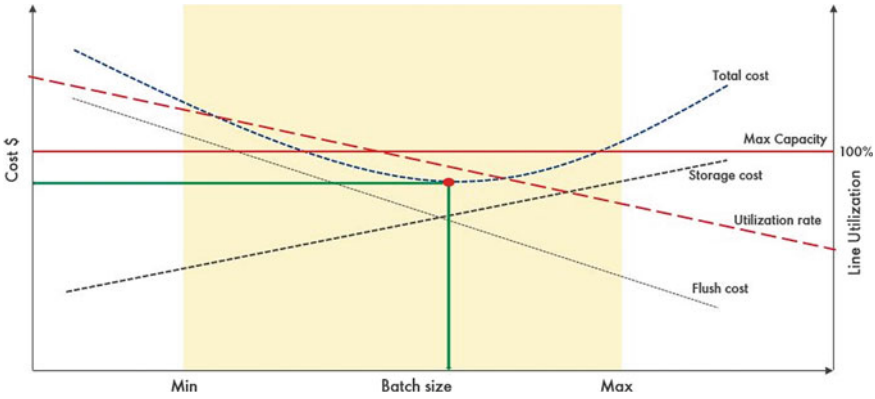


Fig. 1 2-D representation of the problem (lot size vs cost and utilization) for one product

within the portfolio. The products are allocated to specific production lines that have minimum and maximum volume limits for the operation. They are also limited by the number of operating hours for a given period, which is based on runtime, setup and maintenance time and shift hours. Hence, the objective of this optimization problem is to find optimal lot size for producing lubricant products at the lowest total E2E cost subject to plant constraints such as operating capacity of the machineries and storage capacity of the warehouses.

2 Mathematical Formulation of the Problem

$$\text{Minimize } Z = \sum_{i=1}^N \left(s_i * \frac{x_i}{2} \right) + \left(f_i * \frac{d_i}{x_i} \right) \tag{1}$$

$$\text{subject to } \sum_{i=1}^{N_l} \left[\left(t_l * \frac{d_i}{x_i} \right) + (d_i * R_l) \right] \leq C_l \quad \forall l \in \{1, 2, 3, \dots, L\} \tag{2}$$

$$\sum_{i=1}^N \left(\frac{x_i}{2} \right) \leq W \tag{3}$$

$$x_i \geq 0 \quad \forall i \in \{1, 2, 3 \dots N\} \tag{4}$$

$$x_l^{\min} \leq x_i \leq x_l^{\max} \quad \forall i \in \{1, 2, 3 \dots N\} \& \forall l \in \{1, 2, 3, \dots, L\} \tag{5}$$

In the above formulation, the objective function minimizes total E2E cost of production by finding the optimal values of x for each product i , where s and f are the storage and set up costs (per unit), respectively, d is the demand projection

of the product, N is the total number of products. Constraint in Eq. (2) stipulates that total operating time of the specific production line should be within the monthly capacity, where L is the total number of production lines, N_l is the total number of products produced in the specific line, R is the runtime of each production line, t is the setup time before each batch and C_l is the capacity of line l . Constraint in Eq. (3) specifies the average inventory volume should not exceed the warehouse capacity W . The model is run for different scenarios of W (-20% to $+15\%$ of capacity) that acts as a sensitivity metric. The users can decide to choose a scenario based on the flexibility of warehouse capacities. Constraints in Eqs. (4) and (5) establish that lot size should be non-negative and within the upper (x_l^{\max}) and lower (x_l^{\min}) bounds of the specific production line.

3 Modeling Framework and Methodology

As seen in Fig. 2, the objective function is convex [1] for realistic (non-negative) values of lot size and the underlying constraints form convex sets, thus the model is a nonlinear convex optimization problem, and we deduce that a nonlinear solver would yield a global optimum.

The algorithm was implemented in the pyomo modeling environment, and we used an open-source programming solver ipopt short for “Interior point optimizer” suitable for solving large-scale [2] nonlinear optimization problems. Ipopt uses a primal–dual interior point algorithm and uses line searches based on filter methods. Filter methods guarantee global convergence in algorithms for nonlinear programming.

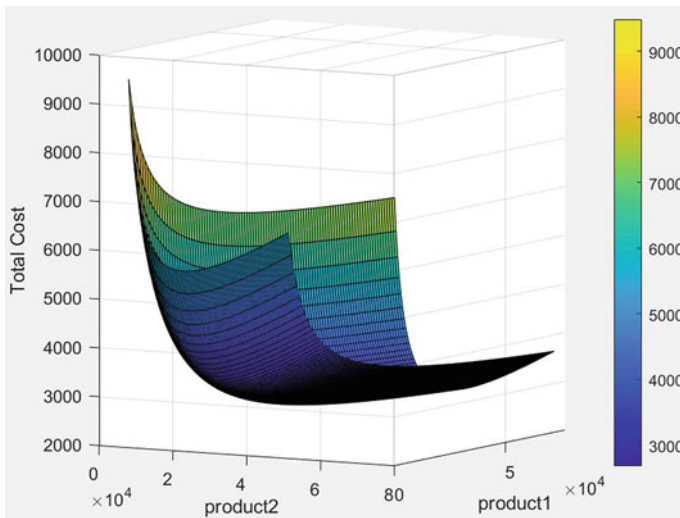


Fig. 2 A 3-D representation of cost function with two products

Interior point methods maintain feasibility but use barrier functions to avoid leaving the feasible set. The barrier problem is interpreted as a bi-objective optimization problem with the two goals of minimizing the objective function and the constraint violation (with a certain emphasis on the latter quantity). Then a trial point is considered during the backtracking line search and accepted if it leads to sufficient progress toward either improving the objective function or constraint violation compared to the current iterate.

Ipopt provides the feasibility of automatic differentiation, and any initial value assigned for the lot size leads to the lowest possible E2E cost. Before stepping into the model, the algorithm performs a feasibility check by considering the x_l^{\min} and x_l^{\max} values and calculates the upper and lower limits of the operating time for each line. This is a crucial step to ensure that the model has a feasible solution space to search for the optimal solution. If any line is found to be having both upper and lower limits of capacity above 100%, it is highlighted to the user for correction in the allocation of products in that specific line to find a feasible solution.

4 Inputs and Results

Key inputs to the model include product demand, lower and upper bounds of lot size (depends on production line), cost components of each product (storage, set up costs), capacity of production lines (maximum minutes each line can operate per month), warehouse capacity for the entire portfolio of the products.

Table 1 provides a sample input data for 10 products allocated to 2 production lines. Table 2 provides the capacity input data for each production line and warehouse. Table 3 lists the optimal lot size obtained from the model for each product and the

Table 1 Inputs to the model

Product	Line	Min	Max	Demand	Unit runtime	Unit set up cost	Unit storage cost
Prod1	L1	25,080	100,320	165,528	0.0048	62.66	0.13
Prod2	L1	25,080	100,320	36,784	0.0048	46.50	0.13
Prod3	L2	7524	87,780	9196	0.0057	72.37	0.15
Prod4	L2	7524	87,780	32,186	0.0057	99.94	0.16
Prod5	L2	7524	87,780	68,970	0.0057	122.36	0.16
Prod6	L2	7524	87,780	96,558	0.0057	146.85	0.17
Prod7	L2	7524	87,780	41,382	0.0057	179.35	0.18
Prod8	L1	25,080	100,320	18,392	0.0048	28.07	0.12
Prod9	L1	25,080	100,320	133,342	0.0048	48.25	0.12
Prod10	L1	25,080	100,320	514,976	0.0048	63.13	0.13

Table 2 Capacity of lines (in minutes), warehouse (in liters)

Asset	Capacity
L1 (line)	8910
L2 (line)	4500
W1 (warehouse)	191,334

Table 3 Results from the model

Product	Line	Optimal lot size	Total cost	Total runtime
Prod1	L1	43,542	5717	849
Prod2	L1	25,080	2394	198
Prod3	L2	10,397	1536	66
Prod4	L2	22,293	3463	205
Prod5	L2	35,385	5724	422
Prod6	L2	44,866	7585	582
Prod7	L2	31,588	5639	255
Prod8	L1	25,080	1703	99
Prod9	L1	35,198	4387	695
Prod10	L1	77,091	10,121	2564

utilization details based on the model output are provided in the last column of Table 4.

From the above computations, minimum total E2E cost for all the products = 48,269.

We introduced a sensitivity metric m on the inventory constraint that relaxes or restricts the solution space based on the input provided. The Eq. (6) is a modified version of Eq. (3) for J number of warehouses

$$\sum_{i=1}^N \left(\frac{x_i}{2}\right) \leq W * m_j \quad \forall j \in \{1, 2, 3, \dots, J\} \tag{6}$$

We run the model for each instance of m which is the percentage change in the capacity of warehouse j . The storage and set up costs from each instance of model run are plotted in Fig. 3. This plot enables the users to understand how all

Table 4 Capacity (input) and utilization (model output) of lines (in minutes), warehouse (in liters)

Asset	Capacity	Utilization
L1 (Line)	8910	4405
L2 (Line)	4500	1530
W1 (Warehouse)	191,334	172,844

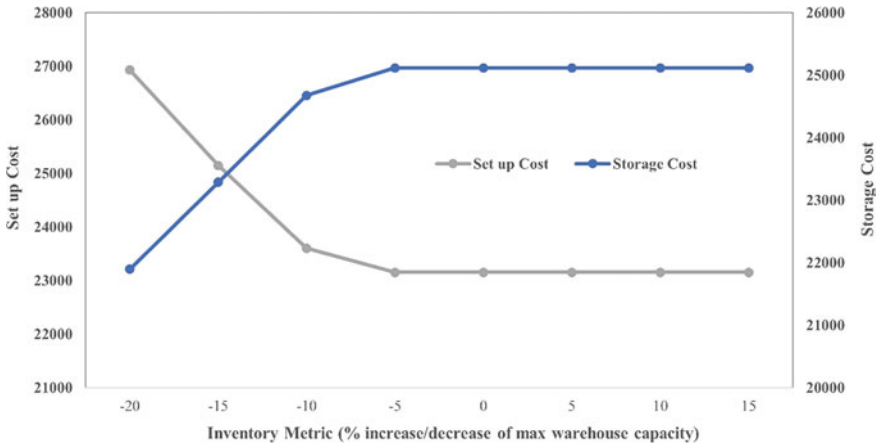


Fig. 3 Sensitivity chart for storage cost vs set up cost for m in the range of -20% to $+15\%$

the cost and utilization elements move with respect to the inventory. It also provides multiple alternate solutions for some plants that are restricted by warehouse capacity limitations and few others that have an option to increase their capacity. The users can decide the inventory metric based on these flexibilities and run the model to get the best solution for that scenario.

5 Conclusions

The model has been tested in two plants and the resulting total cost using the recommended lot sizes is found to be the lowest possible value. Using the sensitivity metric, the model has the flexibility to simulate variations in the warehouse capacity to understand the impact of inventory on other parameters. This model is easily scalable and replicable to any size of a lubricant plant. It can work on the entire portfolio (thousands of products) with limited computing power and in a short span of time.

Future directions of this work could include the below developments.

- Model to dynamically choose the allocation of products to production lines, thereby deciding the optimal way of running the lines depending on the capacity and availability. Currently, the products are allocated to the production lines manually by the planners.
- Overlay this model on a scheduling optimization framework to choose the order of production of the products based on demand, inventory and changeover process. This can also help in maintaining an optimal inventory level.
- Factoring the demand uncertainties to the model: With uncertainty in demand being a significant concern, users can have the flexibility of using the demand

based on the market and their policies. This can be very useful during the uncertainties in demand caused by the factors like COVID-19.

- CO₂ reduction as an additional constraint: We are planning to introduce an additional constraint that limits the CO₂ emission in the production process. This feature can also be an additional sensitivity metric to enable users understand the impact of increasing/decreasing lot size on CO₂ emissions.

Acknowledgements We thank Senthil Kumar Vadivelu (Chemical process analytics manager in Shell) for his review and comments that greatly improved this paper. We thank our colleagues from lubricants supply chain business in Shell who provided insight and expertise that helped in development of this work.

References

1. Boyd S, Vandenberghe L (2004) Convex optimization. Cambridge University Press
2. Wächter, Biegler LT (2006) On the implementation of a primal-dual interior point filter line search algorithm for large-scale nonlinear programming. *Math Program* 106:25–57

Optimization of Aluminum Extrusion Battery Side Rail for Crashworthiness



Rajapandian Ramamoorthy, Sriram Seshadri, Gaurav R. Kanvinde,
and Tejas Bhavsar

1 Problem Definition

Baseline design in our problem has extruded Aluminum which was overdesigned for side crash. Our main objective is to optimize crushability of battery side rail resulting in reduced mass of battery system (Fig. 1).

To achieve this objective, one can use topology optimization of complete battery side rail. To solve for topology from full scale model, side rail should be finely meshed due to minimum web thickness of extrusion. Another shortcoming of linear topology optimization is it cannot accommodate non-linearity. It takes approximately 1 h solver run time in HPC to get non-linear subsystem crush model with MMP cores. If one wants to use non-linear loading for topology using modern optimization tools, it will add exponential computational cost.

Performing topology optimization of entire side rail of battery is not computationally efficient considering the worst case impact location and non-linear crush load case which needs to be solved in order to arrive at more accurate intrusion within battery and understand the load distribution between rocker and battery side rail. Because these studies are performed at early stage of vehicle development, architecture level decisions are driving based on the performance of critical load

R. Ramamoorthy (✉) · S. Seshadri · G. R. Kanvinde
Tata Consultancy Services, Bangalore, India
e-mail: rajapandian.ramamoorthy@gm.com

S. Seshadri
e-mail: sriram.seshadri@gm.com

G. R. Kanvinde
e-mail: gaurav.kanvinde@gm.com

T. Bhavsar
General Motors LLC, Detroit, USA
e-mail: tejas.bhavsar@gm.com

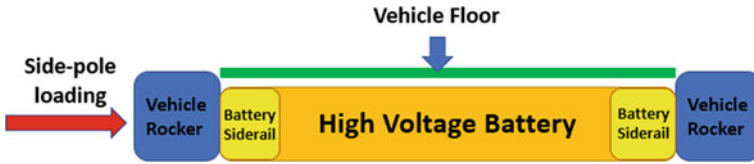


Fig. 1 Battery structures for the high voltage battery protection in side impact

transfer elements rather than finer interaction within various sub-components of vehicle during side crash.

To benefit from the positives of above two methods, in this paper we present two step approach.

2 Methodology Adopted for Solution

In this paper, we propose a method (as shown in Fig. 2) to breakdown the activity of “finding critical load transfer of web structure (extrusion ribs)” by using linear topology described in Sect. 2.1 and perform the “Gauge optimization” using non-linear crash analysis of buck model to optimize further in Sect. 2.2.

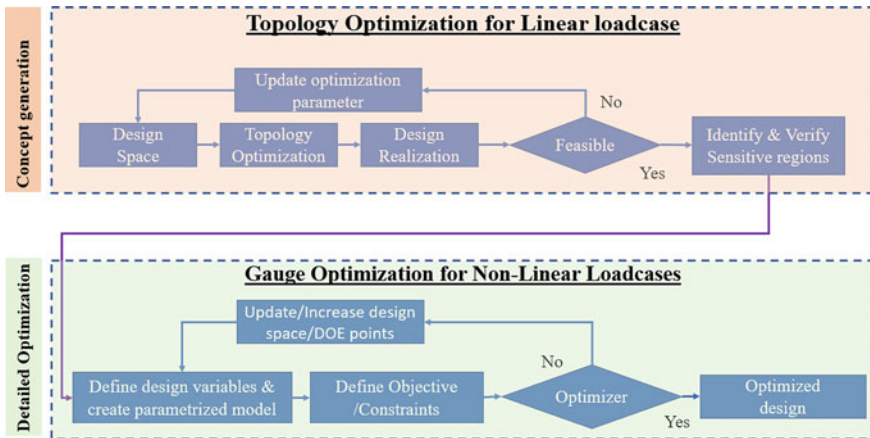


Fig. 2 Two-step optimization methodology adopted in this paper

2.1 Concept Generation Using Linear Topology

In first step, we simplify and perform the linear topology optimization by converting 3-D crush analysis into a reduced thickness cross section problem. To do that we need to transform boundary conditions and loads into cross section equivalent conditions. As we are performing linear optimization, we need take average of the force over pole intrusion and downscale it to reduced thickness cross section problem as shown in Fig. 3. This is performed using Altair Optistruct® [3] solver. Some of the optimization setups include defining the design space (which is usually the area which needs to be optimized, in our study entire envelope needs to be maintained as in original design and all of the internal structure can be derived based on loading and boundary conditions).

For linear topology only cross section considered for optimization and hence all the loads need to be normalized for specific thickness and applied on to the model. We have also considered web thickness restrictions considering manufacturing limitations. Further steps in process helps to obtain required thickness for each web structure, here interest to get critical load members for the side crash. Finite element modeling size also plays role in determining the rib thickness and hence finer mesh is considered in this paper. Draw constraint is defined to maintain uniform cross section along the length of cross section.

Results of linear topology is shown in Fig. 4. Totally 30 optimization iterations are

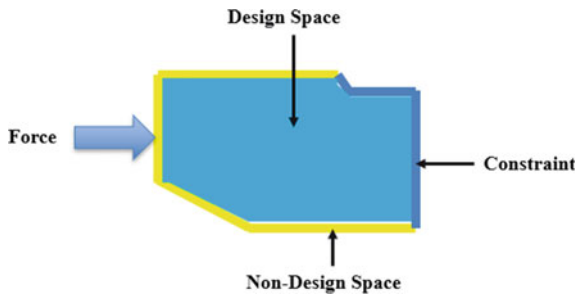


Fig. 3 Battery side rail topology optimization setup—linear loadcase

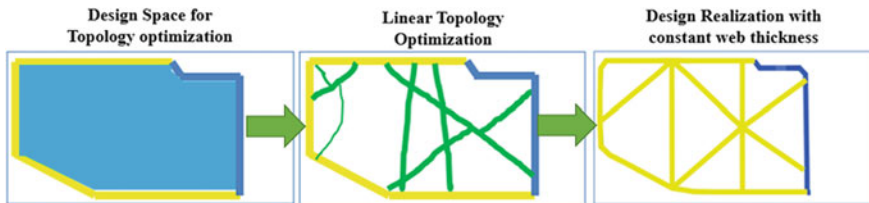


Fig. 4 Concept generation using linear topology results

performed to arrive at the feasible solution. As first step in process, we have considered webs which are having minimum thickness to be carried over for further studies to isolate the load path. Design realization is performed along with manufacturing feasibility to align and re-orient the webs coming out of topology.

This design is then validated in actual side crash analysis results shown in Fig. 6. Linear topology helps to find out the critical load members and helps to improve crushability of pack without compromising the intrusion requirement.

2.2 Detailed Optimization Using Non-linear Analysis

Gauge Optimization uses Response Surface Method (RSM) to solve design problems by incorporating relevant non-linear loadcase. Mathematical representation of optimization problem definition as shown below. Now that we have defined the objective function, design variables and constraints.

$$\begin{array}{ll} \text{Minimize} & f(x) - \text{Mass of battery side rail structure} \\ \text{by varying} & x \in R^n - \text{Rail thickness} \\ \text{Subject to Constraints} & c_j(x) < 0; \quad j = 1, 2, \dots, m \end{array}$$

- f objective function, output (Minimizing the mass of side rail structure).
- x vector of design variables, inputs (e.g., side rail thickness); bounds can be as summed based on manufacturing.
- c_j Intrusion constraint at inner wall of Battery Side rail.

where f is the objective function, x is the vector of n design variables, c_j is the constraint.

Detailed optimization process flowchart is shown in Fig. 5.

Number of thickness (sensitive regions) were 15 variables considered. Thickness changes were implemented in a parameterized model to minimize the mass while determine the optimum side rail structure design with satisfying the crush load case.

The Design of Experiment (DOE), Kriging meta-model surface creation and optimization is done by GM internal tool. Totally 150 DOE points were considered. Optimal design results are shown in Fig. 6. Ansys LS-DYNA® [4] solver used for performing the simulations.

3 Results

Outcome from 2 step optimization method is presented in Fig. 7. Linear topology identifies web structure with identical thickness that increases crushability and at the same time meets the overall intrusion requirement when compared with baseline

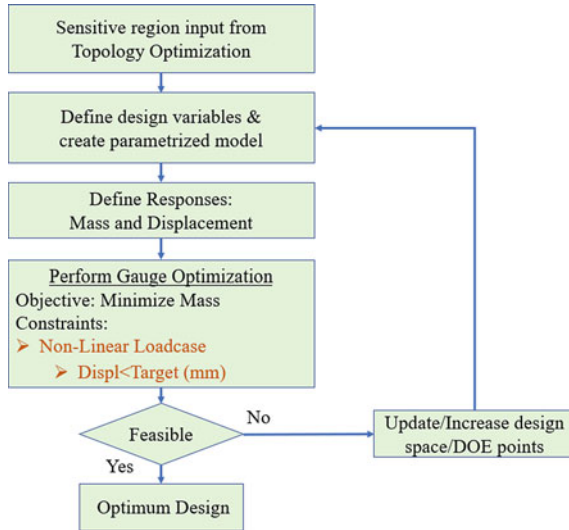


Fig. 5 Detailed optimization process flow chart

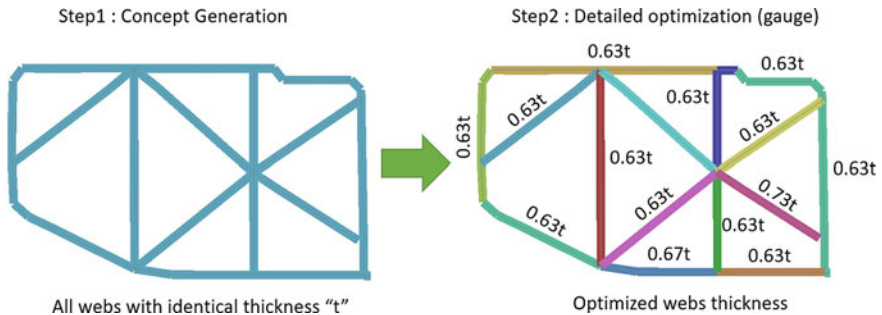


Fig. 6 Optimal design based on gauge optimization using non-linear crush analysis

results. Detailed gauge optimization using subsystem crash model ensures to maintain the same performance by reducing the mass further. Flat response line from detailed gauge optimization improves crushability of outer surface for side rail and optimally prevents the inner wall of battery side rail to intrude into critical areas of battery.

4 Conclusion

In this paper, optimization of battery side rail extrusion is performed accounting for vehicle level side pole loads. As first step, Linear Topology optimization of

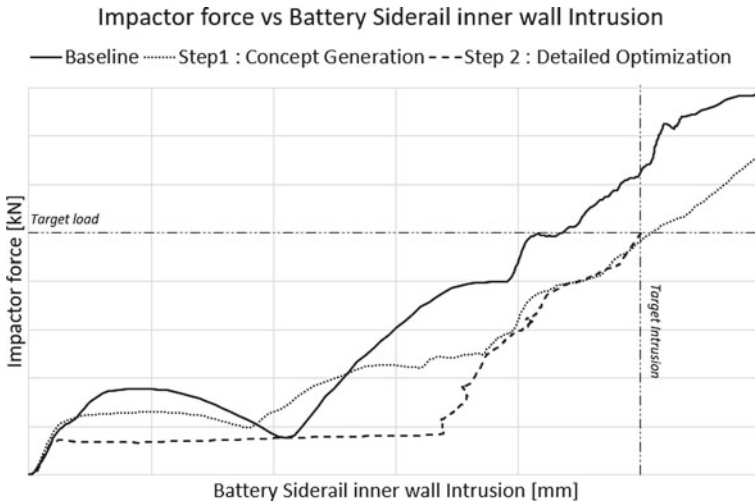


Fig. 7 Battery side rail inner wall intrusion versus Impactor force comparison at subsystem level crush study

battery side rail is carried out to identify the web structure. Using linear optimization, approximately 25% mass reduction achieved with constant internal web thickness, further mass reduction up to 35% achieved from the topology optimized design using size optimization with variable rib thickness. By combining the linear topology and non-linear size optimization overall turnaround time is found to be improved compared to conventional topology optimization in subsystem model.

References

1. Arora S, Shen W, Kapoor A (2016) Review of mechanical design and strategic placement technique of a robust battery pack for electric vehicles. *Renew Sustain Energy Rev* 60:1319–1331. ISSN 1364-0321. <https://doi.org/10.1016/j.rser.2016.03.013>
2. Christensen J, Bastien C, Blundell MV, Gittens A, Tomlin O (2011) Lightweight hybrid electrical vehicle structural topology optimization investigation focusing on crashworthiness. *Int J Veh Struct Syst* 3(2). <https://doi.org/10.4273/ijvss.3.2.06>
3. Altair OptiStruct® Optimization-enabled structural analysis. <https://www.altair.com/optistruct/>
4. LS-DYNA® Keyword user's manual. <https://www.dynasupport.com/manuals/ls-dyna-manuals/>

A Methodology for Multi-objective Design Optimization (MDO) of Automotive Transmission Systems



Saurabh Sameer Kamat, Srinivas Gunti, Bonda Veerababu, and Shankar Venugopal

1 Introduction

In order to have a sustainable growth in the automotive market, Original Equipment Manufacturers (OEM) should innovate ways to optimize the product costs meeting the changing customer expectations without sacrificing the functional and stringent regulatory requirements. In the past, there are many optimization studies done using advanced algorithms to solve various domain-specific problems.

Deb [1] explained and demonstrated the benefits of evolutionary optimization algorithms in solving real-world optimization problems. The architecture of NSGA-II is discussed in detail and relevant algorithms are applied to solve a multi-objective optimization problem. Deb and Jain [2] in their work discussed a gearbox design optimization methodology using evolutionary algorithms. Fazeley et al. [3] in their work demonstrated a multidisciplinary—multi-objective design optimization approach to select the optimal system parameters of a space propulsion system under conflicting requirements with an objective of minimizing the wet mass and maximizing the total impulse. Mohan et al. [4] have demonstrated the efficacy of using machine learning-based optimization methods in solving complex CFD-based optimization problems. A machine learning-based super learner model is created that will assist in quickly arriving at the optimal bowl shape. Zheng et al. [5] in their work performed multi-objective optimization in order to reduce the B-pillar accelerations, intrusions, and vehicle mass—simultaneously.

S. S. Kamat
Vellore Institute of Technology, Vellore, Tamil Nadu 632014, India

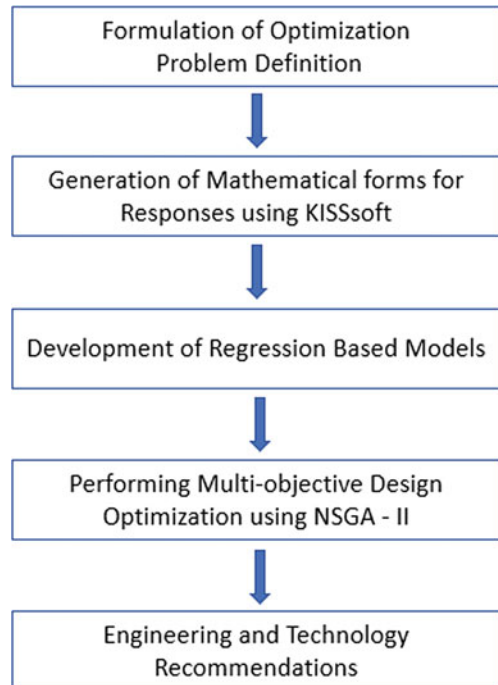
S. Gunti (✉) · B. Veerababu · S. Venugopal
Mahindra & Mahindra Ltd., Mahindra Research Valley, Mahindra World City, Chengalpattu,
Tamil Nadu 603004, India
e-mail: srinivas.gunti@mahindra.com

To the best of our knowledge, there are no studies available in the public domain related to optimization of “Transmission Bandwidth” by considering the aspects of commonality and configurability of gear pairs and considering constraints pertaining to durability and Noise Vibration Harshness (NVH). Authors [6–9] came up with various definitions of “commonality” and highlighted the importance of commonality and configurability in realizing cost benefits. Authors [10, 11] explained various practical and response surface method-based optimization methods applied to vehicle body design. The present work focuses on multi-objective design optimization of a transmission gear pair using NSGA-II [12].

2 Optimization Methodology

Automotive transmission systems consist of several interdependent variables. The optimization of a particular variable with respect to an objective function subsequently changes the values of other dependent variables. Often times, it yields non-optimal or impractical values for design variables. Multi-objective optimization allows to solve for multiple objective functions and find a Pareto of Solution sets. Figure 1 describes the optimization methodology adopted in this paper.

Fig. 1 Flowchart describing optimization methodology



2.1 Formulation of Optimization Problem Definition

The first step in solving an optimization problem is defining a set of mathematical models that accurately describe the system. The scope of this work involves optimization of the gearbox design with an objective of minimizing the cost and maximizing the transmission bandwidth considering the constraints from durability and gear manufacturing quality. The transmission bandwidth is represented as percentage variation from two existing gearbox designs of different torque ratings using cosine similarity.

Equation (1) represents the optimization problem definition subject to constraints shown in Eq. (2). The matrix of variables X is shown in Eq. (3) with X_{\min} and X_{\max} being the lower and upper bounds, respectively. The objectives are three independent functions f_1 , f_2 , and f_3 subjected to six constraints from g_1 to g_6 . All equations are derived by performing linear regression on a dataset produced using physics-based KISSsoft models of gear pairs with two different torque ratings.

$$z = \text{minimize}(f_1, f_2, f_3) \tag{1}$$

$$\text{Subject to constraints: } g_1, g_2, g_3, \dots, g_6 \tag{2}$$

$$\text{Where: } X_{\min} \leq X \leq X_{\max} \tag{3}$$

Each objective function is described by the following equations.

$$f_1 = \text{cost of gear pair} \tag{4}$$

$$f_2 = \text{variation from Gearbox1 } (T_1 \text{ Nm}) \tag{5}$$

$$f_3 = \text{variation from Gearbox2 } (T_2 \text{ Nm}) \tag{6}$$

The variation described in Eqs. (5) and (6) is calculated using cosine similarity formula shown in Eq. (7), where A_i is a collection of base design values, and B_i is the collection of calculated values. The similarity is obtained in the form of percentages.

$$\text{similarity}(A, B) = \frac{\sum_{i=1}^n A_i \times B_i}{\sqrt{\sum_{i=1}^n A_i^2} + \sqrt{\sum_{i=1}^n B_i^2}} \tag{7}$$

Equations (8) to (13) describe the constraints for the optimization problem.

$$g_1 = \text{tooth root stress of Gear 1} \tag{8}$$

$$g_2 = \text{tooth root stress of Gear 2} \quad (9)$$

$$g_3 = \text{contact root stress} \quad (10)$$

$$g_4 = \text{axial force} \quad (11)$$

$$g_5 = \text{root safety} \quad (12)$$

$$g_6 = \text{flank safety} \quad (13)$$

2.2 Generation of Mathematical Forms for Responses Using KISSsoft

As shown in Fig. 2, the gear train is modeled as each individual gear pair in KISSsoft. A DoE is formulated using a fractional factorial approach for the variable ranges in Table 1. Design of Experiment (DoE) based approach is used to generate the regression-based mathematical models for the responses (factor of safety, tooth root stress, contact stress, and axial force) that are function of the design variables shown in Table 1.

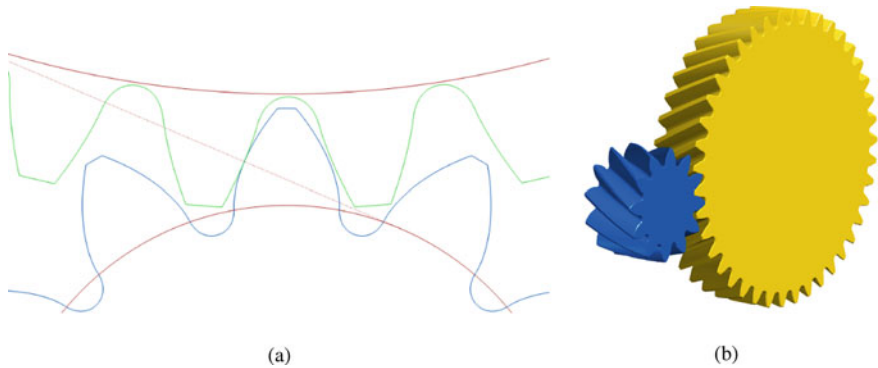


Fig. 2 a 2D geometry and meshing of cylindrical gear pair, b 3D geometry and meshing of cylindrical gear pair

Table 1 Gear parameters for optimization

S. No.	Design parameter of gear	Limits
1	Module (m)	$m_1 \leq m \leq m_2$
2	Face width (b)	$b_1 \leq b \leq b_2$
3	Quality (Q)	DIN6, DIN9
4	Helix angle (β)	$\beta_1 \leq \beta \leq \beta_2$
5	Pressure angle (α)	$\alpha_1 \leq \alpha \leq \alpha_2$
6	Profile shift coefficient (x^*)	$x_1^* \leq x^* \leq x_2^*$
7	Ratio (i)	$i_1 \leq i \leq i_2$
8	Material (M)	M_1, M_2

2.3 Identification of Design Variables and Constraints

Correlation studies were done using the heat map shown in Fig. 3 generated using

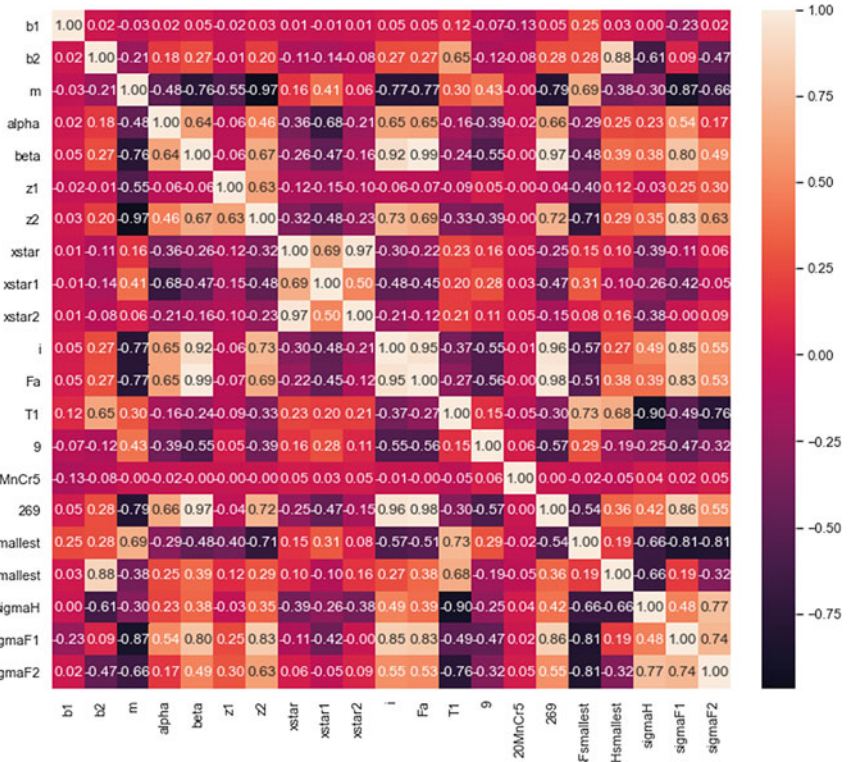


Fig. 3 Correlation heatmap of independent and dependent variables

the response dataset. The design variables for optimization are selected based on the insights obtained from the heatmap.

2.4 Development of Regression-Based Equations

Multivariate linear regression is an effective machine learning technique to model the behavior of dependent variables in relation to the variation in independent variables. The constraint equations are modeled by applying this to the dataset containing factors and responses described in Eqs. (14) to (19).

$$\sigma_{F_1} = f(b_{G_1}, m, \alpha, \beta, x_1^*, i, \text{DIN}) \quad (14)$$

$$\sigma_{F_2} = f(b_{G_2}, m, \alpha, \beta, x_1^*, i, \text{DIN}) \quad (15)$$

$$\sigma_H = f(b_{G_1}, b_{G_2}, m, \alpha, \beta, x^*, i, \text{DIN}, M) \quad (16)$$

$$F_a = f(b_{G_2}, m, \alpha, \beta, x_1^*, x_2^*, i, \text{DIN}, M) \quad (17)$$

$$S_F = f(b_{G_2}, m, \alpha, \beta, x^*, i, \text{DIN}) \quad (18)$$

$$S_H = f(b_{G_2}, m, \alpha, \beta, x^*, i, \text{DIN}) \quad (19)$$

Here, σ_{F_1} is tooth root stress in Gear 1, σ_{F_2} is tooth root stress in Gear 2, σ_H is contact root stress, F_a is axial force, S_F is the minimum factor of safety for tooth root, S_H is the minimum factor of safety for tooth flank, b_{G_1} is the face width of Gear 1, b_{G_2} is the face width of Gear 2, m is the module, α is the pressure angle, β is the helix angle, i is the gear ratio, and x^* is the sum of profile shift coefficients, where $x^* = x_1^* + x_2^*$ and x_1^* , x_2^* are the profile shift coefficients of Gear 1 and Gear 2, respectively, DIN is the gear quality, and M is the material.

The regression models are created using the Scikit-learn library for Python. Figure 4 shows the scatter plot of each response. This is used to analyze the data to tune the parameters of the linear regression algorithm. During pre-processing the dataset, the values for DIN and M are encoded as 0 and 1. A 30% split of data is made to generate distinct sets for training and testing. The training set is used for curve fitting, and the testing set is used purely for the purpose of finding the accuracy of each model. A list of model accuracies is shown in Table 2.

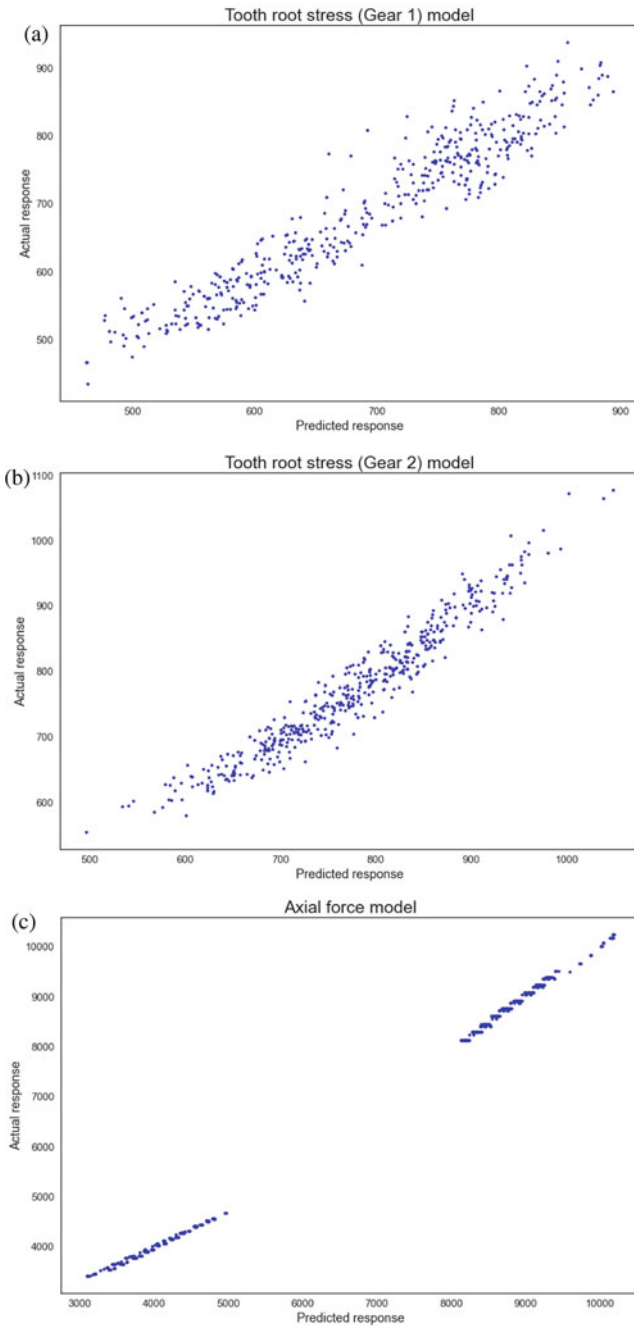


Fig. 4 **a** Scatter plot of tooth root stress model of Gear 1, **b** scatter plot of tooth root stress model of Gear 2, **c** scatter plot of axial force model, **d** scatter plot of contact root stress model, **e** scatter plot of root safety model, and **f** scatter plot of flank safety model

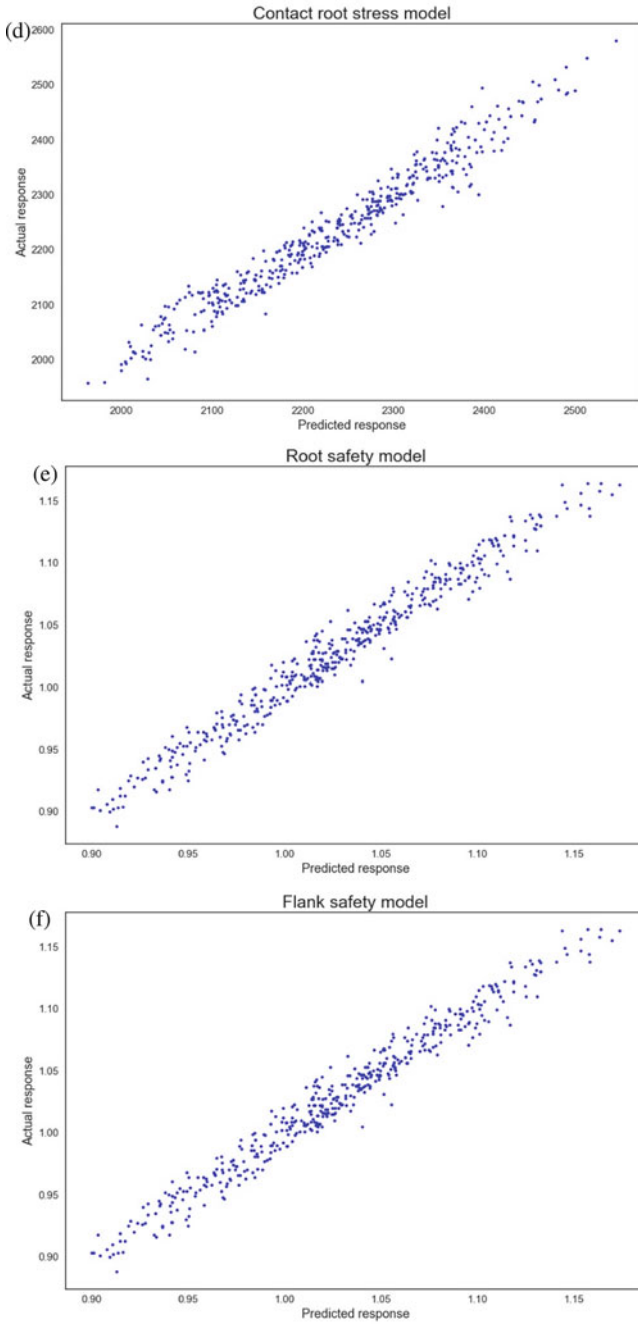


Fig. 4 (continued)

Table 2 Accuracies of regression models for constraint equations

S. No.	Model	Accuracy (%)
1	Tooth root stress of Gear 1	91.68
2	Tooth root stress of Gear 2	93.83
3	Contact root stress	95.53
4	Root safety	96.62
5	Flank safety	96.62
6	Axial force	99.81

Table 3 Constraint limits for MDO

S. No.	Constraint variable	Limit
1	Tooth root stress of Gear 1 (σ_{F_1})	$\sigma_{F_1} \leq \sigma_{F_1}^{\max}$
2	Tooth root stress of Gear 2 (σ_{F_2})	$\sigma_{F_2} \leq \sigma_{F_2}^{\max}$
3	Contact root stress (σ_H)	$\sigma_H \leq \sigma_H^{\max}$
4	Axial force (F_a)	$F_a \leq F_a^{\max}$
5	Root safety (S_F)	$S_F \leq S_F^{\max}$
6	Flank safety (S_H)	$S_H \leq S_H^{\max}$

2.5 Performing Multi-objective Design Optimization Using NSGA-II

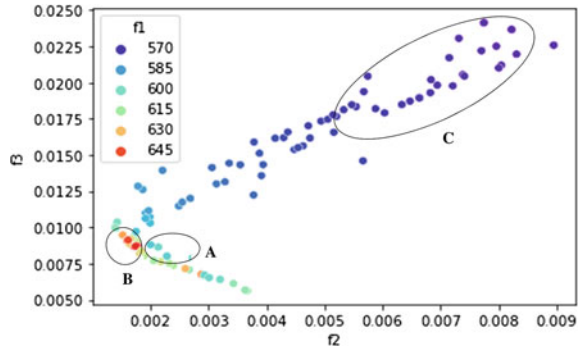
The presence of multiple conflicting objective functions subject to multiple constraints requires the adoption of a fast non-dominated sorting function with quick convergence. NSGA-II by Deb et al. [12] is one such algorithm that has an elitist strategy to ensure the passing of favorable traits to the next generation and reduce genetic drift. The intention is to obtain a set of multiple optimal solutions in form of a Pareto front. Prior to performing, the constraints limits are fixed and listed in Table 3.

3 Technology and Engineering Recommendations

The MDO is carried out by applying the Pymoo framework and Python programming. The parameters are tuned for optimization of three objectives subject to six constraints using NSGA-II. Running the algorithm for a finite number of generations yields the following scatter plot in Fig. 5. The x-axis and y-axis represent the configurability with respect to Gearbox 1 and Gearbox 2, respectively. The color represents the total cost of each solution. A Pareto front is formed near the origin with multiple feasible solutions.

The scatter plot has the X and Y axes as percentage variation with respect to Gearbox 1 and Gearbox 2, respectively. The cost is displayed using color depth with

Fig. 5 Multi-objective optimization results as a color-coded scatter plot



hotter colors showing higher cost and vice versa. Solutions pertaining to regions A and B showed lesser variation from the two gearboxes. However, solutions falling in region A showed lesser cost than their region B counterparts making them most economical. The solutions residing in region C showed minimal cost but maximum variation from the baseline. *Upon further analysis of each region in the scatter plot, it can be said that the points falling inside **region A** are optimal solution sets that show relatively lower cost with the lowest variation from each gearbox.* These solutions can be selected in cases where the objective is part standardization for minimal cost. The points inside region B are non-optimal by the aspect of cost as they exhibit similar variation to solutions in region A for a higher cost. All solutions inside region C are optimal solutions with respect to cost but sub-optimal with respect to percentage variation from defined baselines. Such solutions can be selected in cases where cost has greater importance than part standardization.

4 Conclusions

The present work demonstrated a methodology that can solve a practical multi-objective gearbox optimization problem formulated as minimization of cost and maximization of transmission bandwidth. Authors demonstrated the application of cosine similarity to estimate the commonality and configurability aspects (transmission bandwidth). Tradespace explorations were done, and the solution set corresponding to region A in Fig. 5 is recommended as the optimal solution set. This work can be further extended by including—entire gear box as the design space, and methodology being the same.

References

1. Deb K (2011) Multi-objective optimisation using evolutionary algorithms: an introduction.

In: Multi-objective evolutionary optimisation for product design and manufacturing. Springer, London

2. Deb K, Jain S (2003) Multi-speed gearbox design using multi-objective evolutionary algorithms. *ASME J Mech Des* 125(3):609–619
3. Fazeley HR, Taii H, Naseh H, Mirshams M (2016) A multi-objective, multidisciplinary design optimization methodology for the conceptual design of a spacecraft bi-propellant propulsion system. *Struct Multidiscip Optim* 53(1):145–160
4. Mohan B, Tang M, Badra J, Pei Y et al (2021) Machine learning and response surface-based numerical optimization of the combustion system for a heavy-duty gasoline compression ignition engine. *SAE Technical Paper* 2021-01-0190
5. Zheng L, Gao Y, Zhan Z, Li Y (2017) Multi objective optimization of vehicle crashworthiness based on combined surrogate models. *SAE Technical Paper* 2017-01-1473
6. Eynan A (1996) The impact of demands correlation on the effectiveness of component commonality. *Int J Prod Res* 34(6):22
7. Ashayeri J, Selen W (2005) An application of a unified capacity planning system. *Int J Oper Prod Manag* 25(9):917–937
8. Mirchandani P, Mishra AK (2002) Component commonality: models with product-specific service constraints. *Prod Oper Manag* 11(2):199–215
9. Meyer MH, Lehnerd AP (1997) The power of product platforms. In: *The power of product platforms*. The Free Press, New York
10. Chen M, Wang D, Lee H, Jiang C et al (2014) Application of CAE in design optimization of a wet dual clutch transmission and driveline. *SAE Int J Passenger Cars Mech Syst* 7(3):1128–1137
11. Deb A, Srinivas G, Chou C (2016) Development of a practical multi-disciplinary design optimization (MDO) algorithm for vehicle body design. *SAE Technical Paper* 2016-01-1537
12. Deb K, Pratap A, Agarwal S, Meyarivan T (2002) A fast and elitist multiobjective genetic algorithm: NSGA-II. *IEEE Trans Evol Comput* 6(2):182–197

Numerical Investigation and Multi-objective Optimization of the Aerodynamics of a Hyperloop Pod



Nivedan Vishwanath, Tushar Maloo, Prithvi Ramesh, and Dheeraj Agarwal

1 Introduction

Rising environmental concerns have led people to shift from cars to public transportation systems. In order to account for the large influx of new users, existing mass transportation systems are required to be very efficient in ferrying a large number of people in less time. Currently, the high-speed rail systems are capable to reach a top speed of approximately 500 km/h; however, they operate at much lower speeds of ~300 km/h. This could be attributed to many reasons: at high speeds, the contact friction between the rail and the wheels produce excessive heat, thus limiting their performance. Moreover, since trains currently operate at ambient conditions, the form drag increases rapidly at high speeds. Maglev trains, which operate on the principle of magnetic levitation [1, 2], are able to address the issue associated with friction heating, as they do not make contact with rails; however, the limitations of pressure drag at high speeds still exists. These operational limitations of current vehicles motivated the scientific community to develop Hyperloop systems [3].

A Hyperloop consists of pods that can be accelerated in partially evacuated tubes to over 1000 km/h. They are magnetically levitated on a central rail and are propelled

N. Vishwanath (✉)

Department of Mechanical Engineering, BITS Pilani, Hyderabad Campus, Hyderabad, India
e-mail: f20181005@hyderabad.bits-pilani.ac.in

T. Maloo · P. Ramesh

Department of Mechanical Engineering, BITS Pilani, K K Birla Goa Campus, Goa, India
e-mail: f20180848@goa.bits-pilani.ac.in

P. Ramesh

e-mail: f20180502@goa.bits-pilani.ac.in

D. Agarwal

School of Engineering, University of Liverpool, Liverpool, UK
e-mail: Dheeraj.Agarwal@liverpool.ac.uk

using linear induction motors (LIM). Inside the tube, the low-pressure environment ensures low air density, leading to lower form drag than vehicles travelling at similar speeds in ambient conditions. This combined with the absence of contact friction would enable operational speeds well beyond the capability of the existing railway systems. The Hyperloop is planned to provide point-to-point connections at speeds resembling air travel. Maintaining efficiency at high operating speeds of $M_{\text{Operational}} \sim 0.9$ would require an efficient aerodynamic design. While the pressure inside the tube is nearly 0.1% of the atmospheric pressure [3], it is necessary to carefully model the remaining air. Since transonic flow in confined tubes produce complex flow structures, it is difficult to simulate the phenomenon with high fidelity.

Due to low operating pressure inside the tube, the Reynolds number (Re) of the current flow is $\mathcal{O}(10^5)$. This makes it susceptible to laminar to turbulent transition [4]. Since the flow can become locally supersonic over certain regions of the pod, they can also trigger boundary layer separations [5]. All of these factors would contribute to increase in drag, apart from the drag caused due to the choked flow [6].

The flow becomes choked when the area between the pod and the surrounding tube reaches a minimum and when it occurs, any increase in the pressure difference across the pod does not produce a further rise in the mass flow rate downstream of the pod. There are two ways to ensure that the pod does not violate the Kantrowitz limit [7]. The first option tackles this issue by reducing the blockage ratio, which is defined as a ratio of cross-sectional areas of the pod and the tube $B_r = A_{\text{Pod}}/A_{\text{Tube}}$. The other option is to introduce a compressor in front of the pod that can redirect excess mass flow rate to the back of the pod even when the B_r is high. Although compressors were originally proposed in the Hyperloop white paper as a means to prevent choking, it is difficult to simulate the aerodynamics of the pod in the presence of a compressor.

The objective of this study is to develop an aerodynamic shape optimization framework for a Hyperloop pod, taking into consideration the drag coefficient and the Kantrowitz limit. This is realized by performing two-dimensional numerical simulations using ANSYS fluent, coupled with the ANSYS DesignXplorer optimization interface. The optimization routine controls the geometry using Bezier control points and produces a geometry that minimizes the drag force while staying within the Kantrowitz limit. The baseline pod geometry is designed in accordance with the minimum geometry requirements set by Hyperloop India, a student team at BITS Pilani, India. This paper is structured as follows: Sect. 2 outlines the numerical methods employed in this work, followed by the problem definition and computational methodology in Sect. 3. Section 4 provides detailed results for the developed optimization framework, followed by the conclusions in Sect. 5.

2 Numerical Methodology

We carry out a goal-driven optimization (GDO) study based on the multi-objective genetic algorithm (MOGA) formulation. It lays emphasis on producing a diverse set

of non-dominating solutions and introduces elitism in a controlled manner. Both the objective function and the constraint-handling technique use the same non dominance principle. They allow the algorithm to rank the feasible solutions higher than the infeasible ones. MOGA performs cross-over operation in which two parent chromosomes are combined to produce a new chromosome that performs better than its parents by inheriting their best characteristics. The chromosomes then undergo mutation, where one or more gene values of the chromosome is altered to produce better results. These two processes together generate new population sets. The algorithm repeats the process to arrive at progressively better solutions in every iteration. The objective functions for the MOGA algorithm are the minimization of the coefficient of drag (C_D) and the coefficient of lift (C_L). In addition to drag minimization, we also minimize the lift to prevent the pod from taking off the ground unevenly. The input parameters are the y-coordinates of the 12 control points that make up the pod spline.

$$y_1, y_2, \dots, y_{12} \in \text{Control Points}$$

The constraint functions are specified as bounds to the control points—each control point is bounded between a highest possible value (H_n) and a lowest possible value (L_n), such that the pod’s overall shape is not altered. Therefore, the constraints are of the form:

$$L_n \leq x_n \leq H_n, n \in (1, 2, \dots, 12)$$

The spatial constraints in our problem are governed by the Kantrowitz limit, which is calculated using the following relation [7],

$$\frac{A_{\text{flow}}}{A_{\text{tube}}} = M_0 \left(\frac{\gamma + 1}{2} \right)^{\frac{\gamma+1}{2(\gamma-1)}} \times \left(1 + \frac{\gamma - 1}{2} M_0^2 \right)^{-\frac{\gamma+1}{2(\gamma-1)}}$$

The values of L and H are constants defined for each control point. To retain the pod’s shape, the control points maintain their relative position as follows:

- For the nose section of the pod (y_1, y_2, \dots, y_6), the ranges represented by the bounds are mutually exclusive for those control points, that is, $L_n > H_{n-1}$.
- For the control points of the pod (y_7, y_8, \dots, y_{12}), the shape has slight upward incline that reaches a maximum height and then has a considerable downward incline. For this region, the ranges represented by the bounds are not mutually exclusive as the upward and downward inclines are not very steep. Here, the parameter relations are as shown in Table 1.
- The point y_8 is the topmost point of the pod, whose upper bound H_n is calculated from the Kantrowitz limit relation.
- The point y_{12} is the bottom most point of the main body of the pod, whose lower bound L_n is set according to the geometric constraints imposed by the minimum volume requirement of the pod.

Table 1 Constraint relations on the pod geometry

Left expression	Operator	Right expression
y_6	\leq	y_7
y_7	\leq	y_8
y_8	\geq	y_9
y_9	\geq	y_{10}
y_{10}	\geq	y_{11}
y_{11}	\geq	y_{12}

3 Computational Method

We study the transonic flow aerodynamics of a Hyperloop pod for multiple design configurations. The objective is to converge to a design that experiences the least drag and lift force during its motion through the tube. A baseline pod of length (L) of 3.5 m and a height (H) of 0.355 m is considered. The values of L and H are in accordance to the designs made by Hyperloop India, a student team at BITS Pilani. The flow domain is modelled according to a scaled-down version (1:100) of the test tube at the SpaceX site and has a height of 1.4 m. The upstream and downstream lengths are taken as $5L$ and $10L$, respectively. The blockage ratio $B_{r,i}$ is defined as the ratio of the projected area of the pod to the height of the computational domain. $B_{r,i}$ for this baseline geometry is computed to be 0.253. Figure 1 represents the schematic of the computational domain. The permissible pod velocity, as calculated as Mach 0.5, for which the flow around the pod is exactly sonic. For our study, we have considered the pod velocity to be equal to 163.2 m/s, corresponding to $M = 0.476$.

The flow is assumed to be steady, inviscid and adiabatic. Since the current case dealt with accelerating flows, entropy was considered to be a constant. [8] The flow resides in the continuum regime, since the Knudsen number (K_n) is of the order 10^{-6} . The $k-\omega$ SST RANS model is used for the turbulence modelling. A constant mass flow rate enters the domain at the inlet, with a pressure far-field condition imposed at the outlet. All the walls in the domain are non-slipping, to simulate the pod motion through the tube. An operating pressure of 1000 Pa is considered. A grid independence study is performed to determine the most optimum grid for the subsequent simulations. Four cases with increasing mesh refinement were simulated, and the force coefficients were compared as shown in Table 2.

For the subsequent optimization study, Mesh 2 was chosen because the per cent change in the drag and lift coefficient values were less than 0.02% between Mesh 2 and Mesh 3.



Fig. 1 Schematic of 2D computational domain with boundary conditions

Table 2 Results from the mesh convergence study carried out to ensure grid independence of the solution for the case of flow past the Hyperloop pod at $Re = 3.89 \times 10^5$

Mesh no.	Mesh 1	Mesh 2	Mesh 3	Mesh 4
Mesh count	225,340	345,238	547,008	1,136,185
C_d	1.4206	1.4116	1.4116	1.4114
C_l	6.8800	6.8387	6.8374	6.8423

4 Results

The optimization algorithm is run for 85 design points, generated from the constraints entered for the 12 spatial coordinates that make up the pod geometry. The *MOGA* routine is such that it outputs the global extrema for the set of constraints provided for the design variables. Figure 2 compares the initial and final design parameters obtained from the simulation. The nose radius of the optimized geometry is marginally lesser than that of the baseline geometry. There is also a slight reduction in the overall height of the pod, which would allow more mass rate to pass around the pod at any given point in time.

The optimized geometry is simulated to obtain the values of aerodynamic coefficients. Table 3 compares the force coefficients of the baseline geometry with the optimized one. We can observe that the drag coefficient reduced by around 22% along with a 15% decrease in the lift coefficient. This decrease in the aerodynamic coefficient values clearly indicates an improvement in the aerodynamic flow characteristics as a result of the optimization step.

Figures 3 and 4 present the pressure and velocity contours for the baseline and optimized configurations, respectively. The contours for both the configuration are plotted on a common range to visualize the changes effectively. Upon observation, it

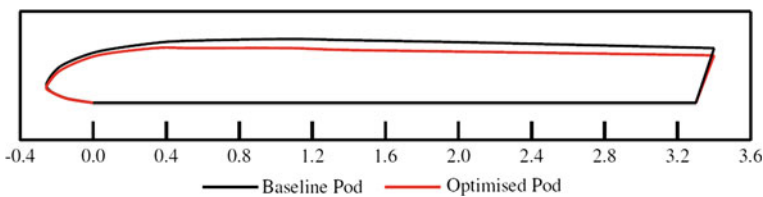


Fig. 2 Comparison of baseline and optimized pod geometry

Table 3 Summary of force coefficients obtained from 2D simulations of the baseline and the optimized pod geometry

Case	Baseline geometry	Optimized geometry	% change
C_d	1.4113	1.0946	-22.44
C_l	6.8362	5.8196	-14.87

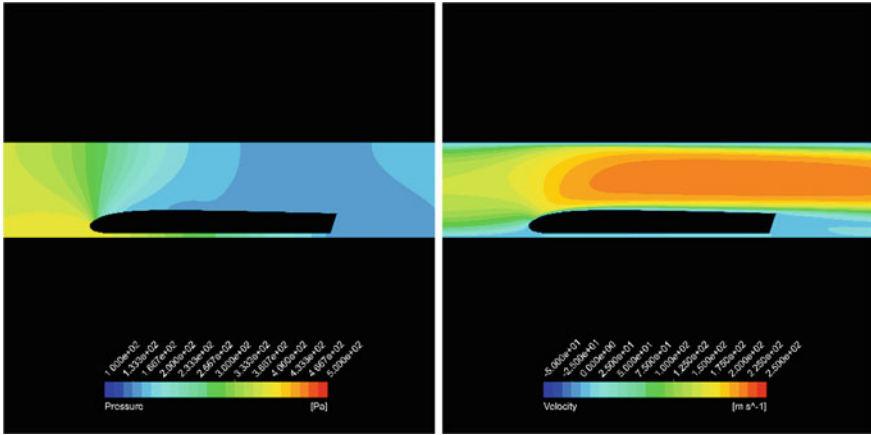


Fig. 3 Pressure and velocity contours for the baseline pod

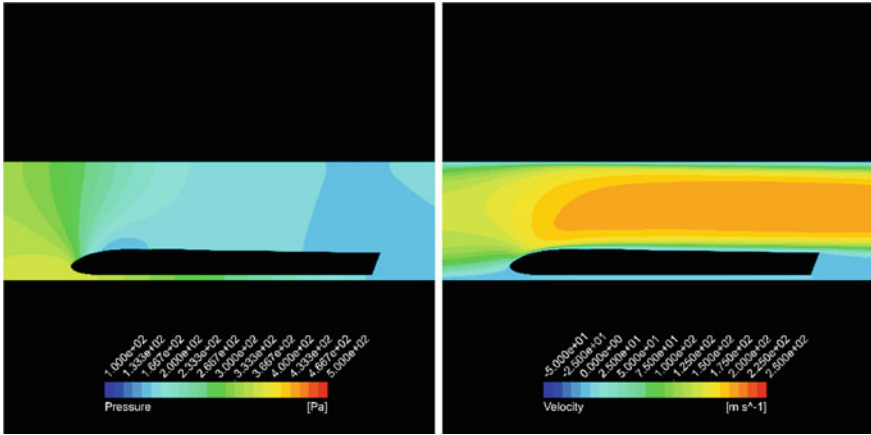


Fig. 4 Pressure and velocity contours for the optimized pod

was found that the flow velocity over the pod for the optimized case is lower than that of the baseline case. This indicates that the pressure difference between the forward and rear portions of the pod is lesser in case of the optimized case. A lower pressure difference means that lesser drag is experienced by the pod as it moves through the tube.

5 Conclusion

The current study focused on the aerodynamic optimization of a Hyperloop pod using multi-objective global optimization algorithm. The optimization environment was created on ANSYS, and simulations were run for 85 different configurations. The results from the simulations demonstrate the fact that the optimized configuration of the pod would be aerodynamically efficient as compared to the baseline, while adhering to the minimum volume limit to safely pack all internal components inside the pod. Future studies can focus on geometries in which the flow is predominantly choked. That would test the robustness of the routine to find the best possible geometries.

Acknowledgements The authors would like to thank the Department of Mechanical Engineering, BITS Pilani, K.K. Birla, Goa Campus, for providing the required computational facilities.

References

1. Lee HW, Kim KC, Lee J (2006) Review of maglev train technologies. *IEEE Trans Magn* 42(7):1917–1925
2. Yan L (2008) Development and application of the maglev transportation system. *IEEE Trans Appl Supercond* 18(2):92–99
3. Musk E (2021) Hyperloop alpha. https://www.tesla.com/sites/default/files/blog_images/hyperloop-alpha.pdf. Accessed 14 June 2021
4. Opgenoord M, Caplan P (2016) On the aerodynamic design of the hyperloop concept. *AIAA J*
5. Schlichting H, Gersten K (2017) *Boundary layer theory*, 9th edn. Springer
6. Braun J, Sousa J, Pekardan C (2017) Aerodynamic design and analysis of the hyperloop. *AIAA J* 55(12):4053–4060
7. Van Wie DM, Kwok FT, Walsh RF (1996) Starting characteristics of supersonic inlets. In: 32nd joint propulsion conference and exhibition, p 2914
8. Fox R, McDonald A, Pritchard P (2011) *Introduction to fluid mechanics*, 8th edn, 10, vol 4. Wiley

Molecular Dynamics of Carbon Capture from the Emissions of an IC Engine Using ZSM-5



L. Deepak, A. Ganesh, R. S. Dit, S. H. Sreehari, V. Vinod,
and G. P. Krishnamohan

1 Introduction

Rising CO₂ levels in the atmosphere is a growing concern of current times. Recently, the field of carbon capture and storage has received much interest worldwide. Despite a major part of CO₂ emissions in the atmosphere being from automobiles, the matter of carbon capture from IC engines has not been taken into consideration in present automotive exhaust systems. The problem of carbon dioxide emissions from an IC engine can possibly be reduced by incorporating an auxiliary carbon capture unit. The capturing process involves two stages; physical adsorption and chemisorption. In this work, we focus on the physical adsorption of CO₂ by several layers of porous zeolite where adsorption takes place.

This work proposes the use of a zeolite (ZSM-5) to capture CO₂ emissions from IC engines. ZSM-5 has been known to have an affinity towards CO₂ [1]. It is required to determine how efficient ZSM-5 will be in CO₂ adsorption and for that purpose, the analysis in this paper will include molecular dynamics simulations of a ZSM-5 and CO₂ mixture in an attempt to replicate automotive exhaust conditions. Molecular dynamics (MD) simulation is a computational tool used to describe how positions, velocities, and orientations of molecules change over time. The simulation is based on a set of models that describe molecular-scale interactions. These models

L. Deepak (✉) · A. Ganesh · R. S. Dit · S. H. Sreehari · V. Vinod
Department of Mechanical Engineering, MBCET, Thiruvananthapuram, Kerala, India
e-mail: 28deepak12000@gmail.com

V. Vinod
e-mail: vinodv@mbcet.ac.in

G. P. Krishnamohan
Department of Science and Humanities, MBCET, Thiruvananthapuram, Kerala, India
e-mail: krishna.mohan@mbcet.ac.in

relate energy/force to configuration which are then used to calculate acceleration via Newton's law. OpenMD is an open-source molecular dynamics simulation tool that is based on force field type intermolecular interactions [2] which has been used for the simulations in this paper.

2 Numerical Simulations

In order to perform MD simulations, a force field is required. For this purpose, CLAYFF set is used, which is a general force field suitable for the simulation of hydrated and multicomponent mineral systems including zeolites, and their interfaces. The initial velocities of the CO₂-zeolite system are given by thermalizer programme. Here in Fig. 1, the initial velocities for the system at different temperatures are calculated by using the Maxwell-Boltzmann distribution function. The configuration of CO₂ and ZSM-5 mixture was similar to high pressure conditions in an automotive exhaust, i.e. thirty six CO₂ molecules in a $22 \times 22 \times 30$ Å unit cell where CO₂ pressure is around 10267 kPa. Here, NVT ensemble is used for thermalizing the system and for diffusion data, MD calculations were performed using NVE ensemble up to 10 ps. In all calculations, 1 fs is used as the time step in the Velocity-Verlet integration technique [3].

The mean square displacement (MSD) of CO₂ molecule depends on position vector of the CO₂ molecule and number of steps. Number of steps refers to number of iterations or instances in the trajectory obtained from the OpenMD simulation. The mean square deviation of a single CO₂ molecule from the trajectory file of the simulation is obtained. The self-diffusion coefficient was determined from the time plot. This is used to calculate the self-diffusion coefficient of CO₂ alone and CO₂ in presence of ZSM-5. The results reveal the restriction of CO₂ movement in zeolites.

The Knudsen number is an important indicator of flow nature which depends on the mean free path (λ) and characteristic length (L) of the zeolite super cage. Using

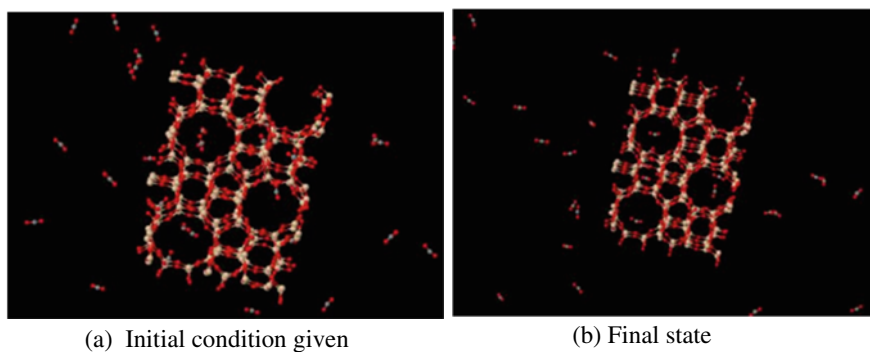
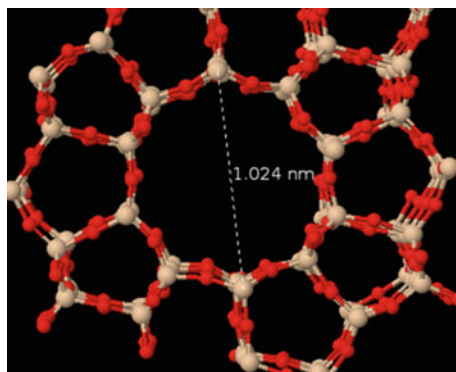


Fig. 1 a Initial condition given. b Final state

Fig. 2 Diameter of the ZSM-5 supercage visualized in JMol



the trajectory file, it was possible to determine the mean free path (distance between two intermolecular collisions that result in a change of energy or direction of the molecule) of CO_2 molecules. The molecules in a simulation do not move in straight lines due to various intermolecular forces which makes calculating the mean free path complicated. A programme was written in Python3 which would calculate the direction cosines of a CO_2 molecule at all instances of motion from the trajectory and then measure the angular deviations from the origin. If the angular deviation between two instances is above an assumed tolerance of 0.05 radians, then the point is assumed to be a collision point. Distances between the collision points are averaged to obtain the mean free path of CO_2 at a fixed temperature.

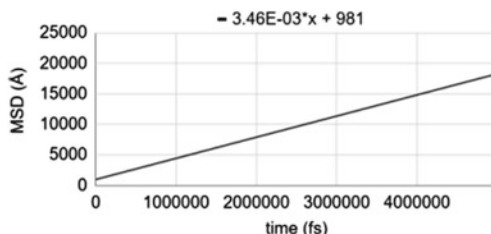
The Knudsen number of CO_2 flow through ZSM-5 can be calculated by dividing the mean free path with the characteristic length of ZSM-5, i.e. internal diameter of a ZSM-5 supercage as shown in Fig. 2.

3 Results and Discussion

Molecular dynamics simulations are done in OpenMD and trajectory file obtained which could be visualized in JMol. From the molecular dynamics simulations, it is observed that the CO_2 molecules that are within the super cages at start of simulation remain there, which is verified in Fig. 1a, b. This shows the retention capacity of ZSM-5. From slope of MSD-time plot in Fig. 3, it is possible to determine the self-diffusion coefficient (D_c) of CO_2 alone and CO_2 in presence of ZSM-5. D_c of CO_2 alone = $1.43 \times 10^{-7} \text{ m}^2/\text{s}$, D_c of CO_2 with zeolite = $6 \times 10^{-9} \text{ m}^2/\text{s}$.

On comparing diffusion coefficients, we find that the D_c of CO_2 alone is greater than the combined CO_2 -zeolite system. This shows that the molecules have their mobility limited by the ZSM-5 structure. CO_2 in zeolite shows two important processes adsorption (can be quantified by DFT adsorption energy calculations) and diffusion. Knudsen number quantitatively indicates the nature of diffusion and its temperature dependence [4]. At 300 K, the mean free path of CO_2 from the

Fig. 3 MSD versus time of CO₂ in presence of ZSM-5



programme was determined to be 9.894 Å, and the characteristic length was measured at 11.024 Å, shown in Fig. 2. This results in a Knudsen number of 0.949. The mean free path varies with molecular density and temperature. Since the obtained Knudsen number is between 0.1 and 10, it shows that the flow is transitional.

4 Conclusions

Molecular dynamics simulations were done to study the carbon capture capabilities of ZSM-5 using OpenMD-based molecular dynamics. Self-diffusion coefficients were obtained from NVE-based MD for CO₂ molecules with and without ZSM-5. The results show that the motion of CO₂ molecules is effectively controlled by the presence of ZSM-5 structure and gas molecules entraps in its various channels. The work done revealed that ZSM-5 is a viable material for the carbon retention from the emissions of an IC engine.

References

1. Hefti M, Marx D, Joss L, Mazzotti M (2015) Adsorption equilibrium of binary mixtures of carbon dioxide and nitrogen on zeolites ZSM-5 and 13X. *Microporous Mesoporous Mater* 215:215–228
2. Loudon P et al (2017) OpenMD-2.5 molecular dynamics in the open. *OpenMD*
3. Della Valle E, Marracino P, Setti S, Cadossi R, Liberti M, Apollonio F (2017) Magnetic molecular dynamics simulations with velocity Verlet algorithm In: 2017 XXXIInd general assembly and scientific symposium of the international union of radio science (URSI GASS). IEEE
4. Clark MM (2009) *Transport modeling for environmental engineers and scientists*, 2nd edn. Wiley

Surrogate Modelling of the Retaining Ring Shrink Fit in a Turbogenerator



Abhishek Sharma, Aditi Khandelwal, and Rishi Relan

1 Introduction

Thermal power plants produce the majority of power in the world today and are likely to continue to do so in the near future until renewable energy sources take over. Although new thermal power plants are not as likely to be installed, the old power plants need to be more robust and reliable than before as they age [1]. Turbogenerators are synchronous electric machines that are coupled with a turbine (either a gas turbine or a steam turbine) to operate on a specific frequency of 50 or 60 Hz, depending on the grid frequency to which it is connected [2]. Retaining rings are one of the most critical components of a turbogenerator rotor, installed at the rotor ends by shrink fitting at a high temperature. Retaining rings are used to protect end windings on both ends of the generator rotor from damaging and, therefore, suffer from large centrifugal forces, which increase with the size of the turbogenerator. Therefore, these components are carefully designed. Unfortunately, most interference fit assemblies fail due to the presence of stress concentration, which can be induced due to shrink fit on the rotor shaft [3]. Static structural analysis of the retaining ring is necessary to ensure the safety of end windings and blockings and to ensure that the retaining ring assembly has enough life cycles as per the customer specification.

There are four prominent shrink-fit locations between the rotor and retaining ring, which play a crucial role in the calculation of stresses and low-cycle fatigue [4]. Shrink-fit values between the shaft and retaining ring should be enough to hold it on

A. Sharma (✉) · R. Relan
Generator R&D, Siemens Limited, Gurgaon, India
e-mail: abhishek.sharma02@siemens.com

R. Relan
e-mail: rishi.relan@siemens.com

A. Khandelwal
Department of Electrical Engineering, IIT Delhi, New Delhi, India

the rotor shaft, and no contact should be loose. Moreover, stresses on the retaining ring should not be high enough to cause crack propagation. Numerical analyses are generally performed to assess the structural integrity of mechanical components. Therefore, in standard industrial practice, techniques like finite element method [5] and computer-aided design [6] are very helpful to perform such analyses to optimize the process and reduce the production time. In the structural analysis of the retaining ring assembly, it is generally observed that optimizing the stresses in one component may lead to an increase in other components of the assembly. The stresses and low-cycle fatigue at shrink-fit locations in a retaining ring assembly are susceptible to shrink-fit design parameters between the rotor and retaining ring used for assembly. The shrink-fit design parameters are generally optimized by performing multiple iterations through computationally expensive FEM simulations. The accuracy of FEM simulations depends on the quality of meshing, and refining mesh will lead to increase in simulation time from hours to a few days [7]. Therefore, it becomes impractical to perform numerous high-fidelity simulations for retaining ring shrink-fit optimization especially when the focus of the industry is to reduce the service turnaround time and maintenance interventions. Hence, for faster design optimization turnaround time and quick service interventions, a better alternative lies in the use of approximations of the original models, which are often called metamodels (or surrogate models).

Metamodels aim to construct the mathematical representation (either black-box or grey-box) to define the relationship between the system's inputs–outputs. Furthermore, metamodels are also used to facilitate the integration of discipline-specific computer analyses and can provide better insight to stem performance (output) responses [8]. In the general scope of metamodeling, the system's response may be evaluated via a physical experiment or a computer simulation at several points in the domain. However, our case study primarily focuses on high-fidelity computer simulations. Therefore, it considers metamodeling to be the general process of creating a computationally inexpensive abstraction through either an approximation or an interpolation of data gathered over a particular domain (with a well-defined set of inputs and outputs). In structural and multidisciplinary optimization, the metamodeling approach is much older, and approximation methods have their remote origins in structural synthesis [9]. Both global (metamodels which are valid throughout the entire design space or a large portion of it) and local (valid in the vicinity of a specific design point) metamodeling approaches have been applied to a wide variety of structural design problems [10]. In the literature, reference for midrange approximations can also be found for creating local metamodels having certain degree of global qualities [11].

Many industrial research questions involve the collection and analysis of multivariate input–output data. Generally, in these scenarios, the first common step is the identification of predictor variables that are associated or correlated with the multivariate output. Multivariate multiple regression (MMR) [12] and multivariate analysis of variance (MANOVA) [13] are typical methods that are used to accomplish such research. However, the MMR method assumes that the output variables jointly follow

a multivariate normal distribution. Still, many industrial problems require the collection and analysis of outputs that violate this assumption and cannot be transformed to satisfy this assumption. To overcome this limitation, another method to identify the predictor variables associated with a multivariate output, namely the multivariate distance matrix regression (MDMR), is suggested in the literature [14, 15]. In this paper, we first utilize the MDMR method to identify the dominant shrink-fit design parameters associated with stresses at each shrink-fit sensitive location. Thereafter, we use both univariate, i.e. multiple linear regression, and multivariate regression, e.g. partial least squares surrogate modelling techniques for approximating the relationship between the shrink-fit design points and the observed stresses at pre-specified locations on the retaining ring assembly structure.

The paper is organized as follows: Sect. 2 briefly describes all the steps involved in the collection of data, high-fidelity simulations details and a short description of the MDMR method. Section 3 explains the univariate and multivariate surrogate modelling techniques used in the case study. And finally, the discussion of the results and conclusions are made in Sect. 4.

2 Data Collection and Modelling Workflow

Figure 1 shows the workflow followed in this paper to develop a surrogate model of the relationship between the stresses at specific locations on a retaining ring assembly and the design points. First, for the collection of input output data, a high-fidelity nonlinear elastic FE analysis was carried out by applying the appropriate thermal and structural boundary conditions. The finite element package, “Ansys Workbench”, is used to simulate the retaining ring assembly. Finally, the data collected from these simulations on the chosen design points based on the design of experiments (DoE)

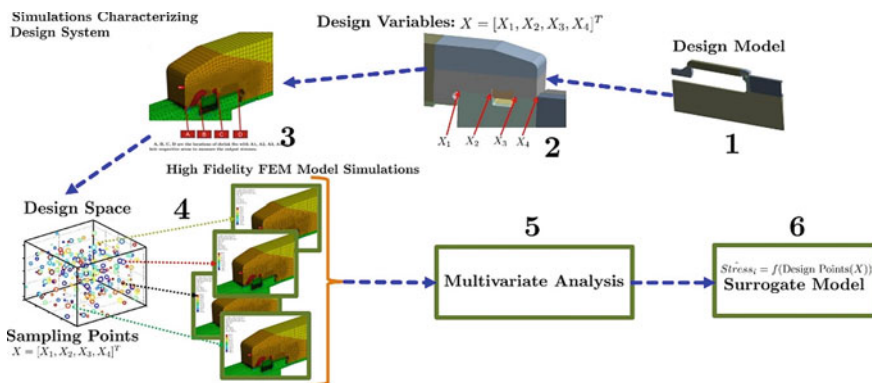


Fig. 1 Surrogate modelling workflow

are then used to create the surrogate model. The following sections explain all the steps briefly.

2.1 *Computer-Aided Design Model*

In this step, a computer-aided design model was prepared for the retaining ring assembly. We made certain assumptions while importing the retaining ring assembly in Ansys Workbench for performing a thermal/structural analysis. In Fig. 1, the 1st stage shows the design model which is used in the present case study. It is a half-tooth solid geometry representation of the retaining ring assembly consisting of a rotor shaft, retaining ring, wedge, filler, liner, endplate and a key. The complete assembly of the retaining ring is approximately symmetric about a 4-degree section, i.e. this half-tooth geometry includes a radial section of the rotor that encompasses $\frac{1}{2}$ of the thickness of a rotor tooth and $\frac{1}{2}$ thickness of rotor slot space. Based on the previous design and manufacturing experience, it is usually considered a good approximation for finding the pattern of stresses around the shrink-fit area of the rotor tooth. Although some details, e.g. ovalization of retaining ring, are not captured in half-tooth model, present study does not focus on it.

2.2 *Selection of Design Variables*

Tapered shrink fit is present in the retaining ring at inboard and outboard locations. At least four radial locations of shrink fit are selected to perform the DoE and capture the appropriate shrink-fit behaviour. Other parameters like shrink-fit length, diameter, tooth radius, etc., in the retaining ring geometry may also affect the principal stresses at the shrink-fit location. Still, in this paper, we focus only on the sensitivity of radial shrink fits between the rotor and the retaining ring. These radial locations are designated as X_1 , X_2 , X_3 and X_4 . Some nodes are chosen at all four locations as shown in the 3rd stage of Fig. 1, where the principal stresses are recorded. Maximum principal stresses are measured at a load step corresponding to speed hot conditions. In contrast, minimum principal stress is measured at a standstill cold. These conditions cover the worst-case scenario for life cycle evaluation for a retaining ring.

2.3 *Design of Experiment*

Formally speaking, a necessary condition to the successful surrogate modelling is the exploration of the design space $X \subset \mathbb{R}^d$ of the input variables $x \in X$ (here the shrink-fit design points). Let us consider, $Y = G(X) \in \mathbb{R}^q$, here Y is the output variable and represents the principal stresses in this case study, and G refers to some

mathematical representation of the engineering problem, e.g. a high-fidelity FEM or a physical asset. Generally, the system G is simulated or perturbed at pre-selected input points selected from the domain of input variables such that the nonlinear behaviour of Y can be captured by the surrogate model \hat{G} efficiently. A careful selection of such inputs and input sample points is often called the design of experiments (DoE). It is one of the most crucial steps for successful statistical modelling, as evident in the plethora of literature about experimental designs for computer experiments [16, 17]. Among many strategies available for designing computer experiments, e.g. orthogonal arrays [18] and Hammersley designs [19], we have used Latin hypercube designs [20] because of their space-filling property and flexibility. For example, the computer experiments can be performed on a small set of dimensions chosen from an existing Latin hypercube design by dropping a few dimensions. Although suboptimal, the resulting design is still a Latin hypercube design due to the orthogonality of the sampling points. Furthermore, this paper uses a constrained version of the Latin hypercube design by including the prior knowledge of the relationship among the shrink-fit input design points at the DoE stage itself. For that purpose, we omit the design points outside the defined linear constraints defined for each input dimension.

2.4 Finite Element Modelling

The present study performs a nonlinear elastic finite element analysis by applying the appropriate thermal and structural boundary conditions. For example, we do not consider material nonlinearity, but contact nonlinearity is considered in the form of shrink fits and frictional contacts. We use Ansys Workbench 19.2 to evaluate the results of thermal and structural analysis. As the first step, we perform steady-state thermal analysis. We consider bonded contacts between the components such that the temperatures are transferred through conduction. Different values of temperatures are then assigned to each component based on field experience. While performing thermal analysis, we consider isotropic thermal conductivity as the material property. Based on thermal conductivity and calculated thermal contact conductance, temperature contours of assembly are obtained.

Next, nodal temperatures are then transferred as thermal boundary conditions in the static structural model. Linear elastic material properties (Young's modulus, Poisson ratio, density, coefficient of thermal expansion, thermal conductivity) are assigned to each component, and contacts are modelled wherever required between the components. Contact pairs for the structural analysis are chosen in a way that agrees with the design intent during normal rotor operation.

For a shrink fitted assembly, failures generally occur on the contact surface due to low-cycle fatigue, so necessary precautions are taken during the finite element analysis. The type of contacts considered during the FEA is based on proven design experience. Although thermal analysis is not very sensitive to contact modelling, it severely affects the structural results. Therefore, special attention is given to contact settings and mesh convergence. Different values for the coefficient of friction are

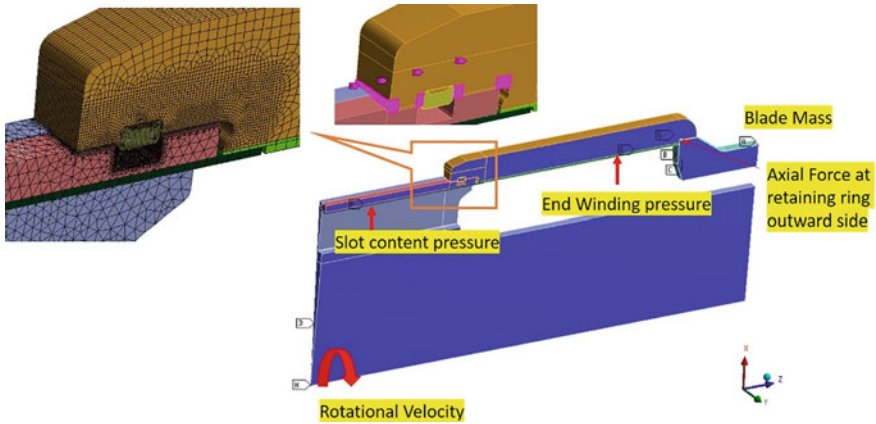


Fig. 2 FEA model boundary conditions and close-up view of mesh at shrink-fit region

assigned to various contacts of mating parts, and these values are chosen based on the interaction of materials. The augmented Lagrangian method is used as a contact algorithm which is generally preferred over the penalty and the normal Lagrangian method [21].

The shrink fit of the ring on the wedges/shaft is modelled by geometric interference between contact surfaces. The loading conditions considered in the structural analysis are shown in Fig. 2. The following steps explain the details of these boundary conditions.

- Due to rotation of the complete assembly, centrifugal force will be acting on each component. Therefore, rotational velocity is applied at the centreline of the rotor and based on density inputs; these forces act upon the respective components in the FE model.
- End winding/slot winding components that are not modelled during the analysis but contribute to calculating the total centrifugal force acting on assembly are applied as normal pressure value at the bottom of the desired components. End arc pressure due to end windings and pressure on wedges due to slot contents are applied as shown in Fig. 2
- Axial loading due to thermal expansion of coils is also taken into account, and it is applied to the retaining ring on the outboard surface next to the endplate.
- Blower blades are not modelled explicitly; therefore, it is considered as a point mass attached on the end plate. Behaviour of these point masses are kept deformable.

We use a preconditioned conjugate solver for the analysis, and the Newton–Krylov method is used as a nonlinear resolution option. This solver is used as a black-box solver in Ansys Solution Phase [22]. For the analysis, we perform seven load steps, three load steps for overspeed cases and the rest four load steps for the normal duty

cycle. Maximum and minimum principal stresses are extracted on design points at speed hot and speed cold conditions, respectively.

2.5 Multivariate Analysis

As briefly described in the introduction, we use MDMR to identify the dominant predictor variables associated with the multivariate output. From here on, the shrink-fit design points are referred as the set of independent input variables $\mathbf{X}_{n \times p}$ and the outcome stress locations as the dependent variable $\mathbf{Y}_{n \times p}$. MDMR proposed by Anderson [23] focuses on the differences between the rows of \mathbf{Y} rather than concentrating on the covariances among its columns. It quantifies the structure in data based on similarities between subjects rather than those between variables. Such a method is used to assess if \mathbf{X} can be used to explain individual differences among the subjects' response profiles on \mathbf{Y} which are quantified in a distance matrix \mathbf{D} .

MDMR is essentially a two-step procedure that first computes the (dis)similarity between each pair of subjects' multivariate response profiles, that is, the distance between each pair subjects' scores along all variables comprising \mathbf{Y} . The Eq. (1) computes the distance between two vectors of scores on a multivariate outcome which quantifies the dissimilarity present in the response profiles of subjects i and j . That is, this function quantifies the distance between $q \times 1$ vectors of scores on the variables comprising the target stress locations \mathbf{Y} . Different distance metrics can be used to quantify the distance between $d(Y'_i, Y'_j)$. In this paper, we use Manhattan distance as it is more robust to the outliers due to the absolute difference between the two. So, our d can be written as:

$$d_M(Y'_i, Y'_j) = \sum_{k=1}^q |Y_{ik} - Y_{jk}| \tag{1}$$

Using this d , we create our distance matrix \mathbf{D} which is a symmetric matrix of size $n \times n$ computed based on dis(similarities) in \mathbf{Y} . Each entry in this matrix denotes the distance between response profiles of subjects i and j . It is simple to understand that the diagonal of \mathbf{D} is zero as there is no dissimilarity between response profile and itself.

$$SSD = \sum_{i < j} D_{ij}^2 = \sum_{j < i} D_{ij}^2 \tag{2}$$

In the next step, the sum of squared distances (SSD) (2) is decomposed into a portion that is attributable to regression onto \mathbf{X} and a portion that attributes to the residual. We use δ -statistics to measure the effect size of each stress location, comprising \mathbf{Y} by dissociating one stress location at a time from the predictors and then

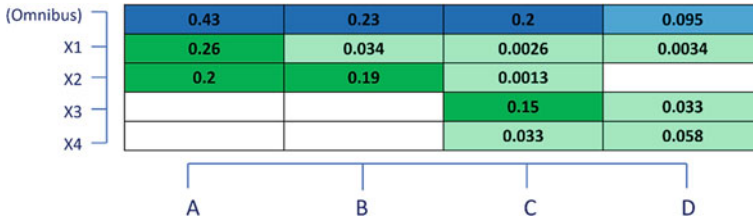


Fig. 3 Influence matrix for predictor selection

constructing again the distance matrix using Manhattan distance with the remaining stress locations as well as the dissociated stress location. We then again regress the new distance matrix onto **X**. The extent to which the pseudo-R2 from this regression decreases relative to the estimate of pseudo-R2 from regressing **D** onto **X** measures the effect on the dissociated outcome variable [24]. The following Fig. 3 describes a heatmap which shows the δ -statistics where the rows correspond to the omnibus effects and the columns correspond to conditional effects of the multivariate outcome where $X_1 \dots X_4$ are the shrink-fit design point locations and A, B, C and D are the shrink-fit locations at which the stresses are observed.

It can be clearly seen in the figure above that the shrink-fit design point X_1 influences the stresses observed at location A and B to some extent. The shrink-fit design point X_2 has a stronger influence on the stresses observed at location A as compared to location B, C or D, whereas the major contributor to the stress observed at location C is shrink-fit design point X_3 . The omnibus effects tend to be larger than the conditional effects. Design points X_3 and X_4 have little effect on maximum stress at location A. Similar inference can be made regarding the relationship between the design points and stresses at other locations by looking at the heatmap.

3 Surrogate Modelling

In this step, we use the information about the dominant predictors obtained from the influence matrix calculated using the MDMR method explained in the section above; we performed a feature engineering step. Firstly, independent exploratory features are constructed using domain knowledge to estimate the surrogate model. Then, to improve the performance of the estimated model, new features, e.g. higher-order, cross-terms, etc., of the dominant features were introduced iteratively based on statistical analysis. The final set of features were selected based on the *P* values [25] and residual analysis. Based on the final set of features, we developed univariate surrogate models for each location separately first and, in the next step, estimated a multivariate model to account for multiple inputs and outputs in a single model.

3.1 *Multilinear and Multivariate Models*

In this section, we discuss the multilinear and multivariate models that are created using the chosen dominant predictors that explain the underlying target function to accurately predict the stresses in the retaining ring.

1. **Multilinear regression model:** We create a univariate regression model for each stress location using the engineered features to estimate the relationship between design points and the stresses. We initially use 100 data points which are generated using the high-fidelity FEM simulations. Out of these 100 data points, we use 70 randomly chosen samples for training and the rest 30 for validating the results. We use coefficient of determination, i.e. R^2 score as an accuracy metric for assessing the goodness of fit. We perform the 5-fold cross-validation to select the best multilinear model for each location.
2. **Multivariate regression model:** Multilinear regression models are used to model the relationship between multiple independent variables and single dependent variables. But such models do not take into account the interaction between multiple independent and dependent variables. Therefore, instead of creating a number of individual multilinear models for all the stress locations separately, a single multivariate model is created in the step using the partial least squares regression [26]. PLS is a method that takes into account the covariance structure of the \mathbf{Y} . The experiments were performed on 395 data points which were split in 70:30 ratio as training and validation set, respectively. An accuracy of 94.5% is obtained using the PLS regression technique on the training set, whereas on the validation set, the observed accuracy was 93.39%.

4 Discussion and Conclusion

Figure 4 shows the surrogate model's performance on training and testing dataset for stress locations A and B. Similar results were observed for other locations. Table 1 shows the results for all four stress locations on the training and validation set, where the accuracy metric is chosen to be coefficient of determination R^2 score. Figure 5 shows the performance of the multivariate model on training and testing dataset for stress locations A and B. Similar prediction performance was observed both on the training and validation datasets for other stress locations. Finally, in this paper, we have proposed an MDMP-based predictor selection technique that is further used for feature engineering before the surrogate model identification step. The developed surrogate models, i.e. both univariate and multivariate models, can predict the pattern of the stresses developed at the pre-specified locations. The future goal of this work is to extend the dimensionality of the input space by introducing more relevant factors and physical design parameters of the retaining ring assembly that affect the stresses at the chosen locations in the feature set and, finally, use the extended surrogate model for sensitivity analysis, reliability assessment, design optimization and several other studies that require many function evaluations.

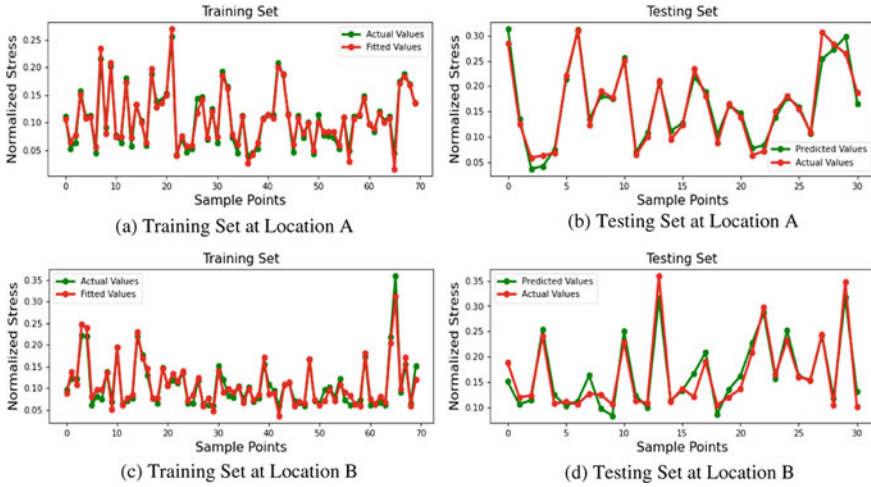


Fig. 4 Multilinear model performance at location A and B

Table 1 Performance of the multilinear model for stress locations A, B, C and D

Stress location	Accuracy on training set	Accuracy on validation set
A	0.968	0.962
B	0.931	0.952
C	0.857	0.924
D	0.995	0.988

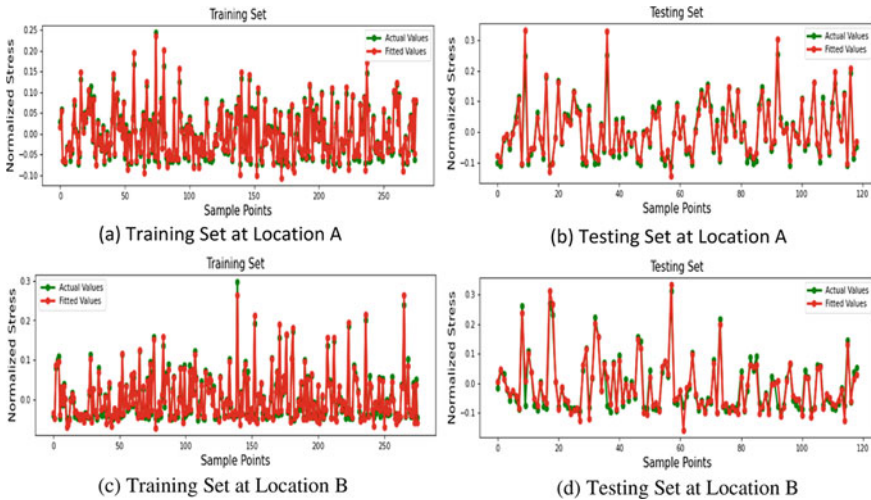


Fig. 5 Model performance at locations A and B with multivariate partial least squares model

Acknowledgements We thank our colleague Vishvendra Pratap Singh from the Generator R&D department of Siemens India, Limited for the discussions on development and analysis of high-fidelity FEM simulation model of retaining ring assembly.

References

1. Harmukh SK, Haran KS, Salon S, Stein J (2016) Root cause analysis of arcing in retaining rings of turbogenerators. *IEEE Trans Ind Appl* 53(3):3129–3136
2. Klempner G, Kerszenbaum I (2011) Handbook of large turbo-generator operation and maintenance, vol 38. Wiley
3. Pedersen NL (2016) On optimization of interference fit assembly. *Struct Multidiscip Optim* 54(2):349–359
4. Clarke GA (1979) Fracture mechanics evaluation of generator rotors. In: Application of fracture mechanics to design. Springer, pp 233–249
5. Stasa FL (1985) Applied finite element analysis for engineers. Harcourt College Pub
6. Lee K (1995) Principles of cad/cam/cae systems
7. Biron G, Vadean A, Tudose L (2013) Optimal design of interference fit assemblies subjected to fatigue loads. *Struct Multidiscip Optim* 47(3):441–451
8. Forrester A, Sobester A, Keane A (2008) Engineering design via surrogate modelling: a practical guide. Wiley. ISBN 9780470770795. <https://books.google.co.in/books?id=ulMHmeMnRCcC>
9. Schmit LA Jr, Farshi B (1974) Some approximation concepts for structural synthesis. *AIAA J* 12(5):692–699
10. Barthelemy J-FM, Haftka RT (1993) Approximation concepts for optimum structural design—a review. *Struct Optim* 5(3):129–144
11. Toropov VV (2001) Modelling and approximation strategies in optimization—global and mid-range approximations, response surface methods, genetic programming, low/high fidelity models. In: Emerging methods for multidisciplinary optimization. Springer, pp 205–256
12. Su Y, Gao X, Li X, Tao D (2012) Multivariate multilinear regression. *IEEE Trans Syst Man Cybern Part B (Cybern)* 42(6):1560–1573
13. Bray JH, Maxwell SE (1985) Multivariate analysis of variance. Number 54. Sage
14. Anderson MJ (2001) A new method for non-parametric multivariate analysis of variance. *Austral Ecol* 26(1):32–46
15. McArdle BH, Anderson MJ (2001) Fitting multivariate models to community data: a comment on distance-based redundancy analysis. *Ecology* 82(1):290–297
16. Lin DKJ, Simpson TW, Chen W (2001) Sampling strategies for computer experiments: design and analysis. *Int J Reliab Appl* 2(3):209–240
17. Pronzato L, Muller WG (2012) Design of computer experiments: space filling and beyond. *Stat Comput* 22(3):681–701
18. Owen AB (1992) Orthogonal arrays for computer experiments, integration and visualization. *Statistica Sinica*, 439–452
19. Hammersley JM (1960) Monte Carlo methods for solving multivariable problems. *Ann New York Acad Sci* 86(3):844–874
20. McKay MD, Beckman RJ, Conover WJ (2000) A comparison of three methods for selecting values of input variables in the analysis of output from a computer code. *Technometrics* 42(1):55–61
21. Lanoue F, Vadean A, Sanschagrin B (2009) Finite element analysis and contact modelling considerations of interference fits for fretting fatigue strength calculations. *Simul Model Pract Theory* 17(10):1587–1602

22. Poole EL, Heroux MA, Vaidya P, Joshi A (1995) Performance of iterative methods in ansys on cray parallel/vector supercomputers. *Comput Syst Eng* 6(3):251–259
23. McArdle BH, Anderson MJ (2001) Fitting multivariate models to community data: a comment on distance-based redundancy analysis. *Ecology* 82(1):290–297. [https://doi.org/10.1890/00129658\(2001\)082\[0290:FMMTCD\]2.0.CO;2](https://doi.org/10.1890/00129658(2001)082[0290:FMMTCD]2.0.CO;2)
24. McArtor DB, Extending a distance-based approach to multivariate multiple regression. PhD thesis. <https://curate.nd.edu/show/qb98mc90825>
25. James G, Witten D, Hastie T, Tibshirani R (2014) *An introduction to statistical learning: with applications in R*. Springer Publishing Company, Incorporated. ISBN 1461471370
26. Geladi P, Kowalski BR (1986) Partial least-squares regression: a tutorial. *Analytica Chimica Acta* 185:1–17

A Methodology for Multi-objective Design Optimization (MDO) of Automotive Suspension System



Lingadalu Ganesh, Srinivas Gunti, N. Balaramakrishna, and Shankar Venugopal

1 Introduction

Deb [1] demonstrated how evolutionary optimization algorithms can be used to solve real-world optimization problems. This paper discusses NSGA II architecture in-depth and proposes an algorithm for solving a multi-objective optimization problem. Deborah and Sachin [2] presented a gearbox design optimization method utilizing evolutionary algorithms. Fazeley [3] demonstrated a multi-objective design optimization approach to determine the optimal system parameters for a space propulsion system that focuses on minimizing wet mass and maximizing total impulse. Moiz [4]: machine learning-based optimization methods are demonstrated as being efficacious for solving complex CFD-based optimization problems. Machine learning-based algorithms are used to generate an optimal bowl shape using a super learner model. Zheng et al. [5] performed multi-objective optimization to reduce accelerations of B-Pillars, foot-well intrusions, as well as vehicle mass. To the best of our knowledge, there are no studies done till date on optimizing vehicle suspension design, for both ride and handling requirements, simultaneously.

2 Optimization Methodology

Figure 1 shows the optimization methodology. A calibrated vehicle dynamics model is developed and used for generating the desired responses. A Design Of Experiments (DOE) is populated, and machine learning-based predictive models were generated

L. Ganesh · S. Gunti (✉) · N. Balaramakrishna · S. Venugopal
Mahindra & Mahindra Ltd., Mahindra Research Valley, Mahindra World City, Chengalpattu,
Tamil Nadu 603004, India
e-mail: srinivas.gunti@mahindra.com

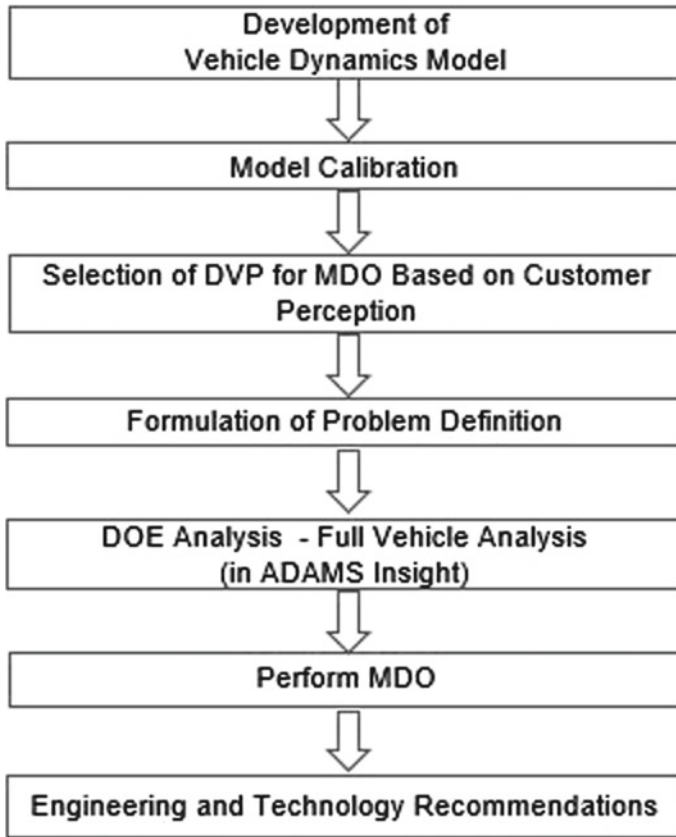


Fig. 1 Flowchart describing optimization methodology

to obtain the mathematical forms of the objective functions and constraint variables. Multi-objective optimization is performed, and trade-studies are done to arrive at practically optimal design decisions.

The subsequent sections show the details of the optimization methodology.

2.1 Development of Vehicle Dynamics Model

Figure 2 shows sub-system level and full vehicle physics-based models that are developed using commercially available solver ADAMS. Steering system, front suspension, rear suspension, Anti Roll Bar (ARB) and tires were modeled in detail. Body in white (BIW) and powertrain are considered as lumped masses. Front subframe, lower control arm, knuckle, ARB and rear twist beam (RTB) were modeled as flexible bodies.

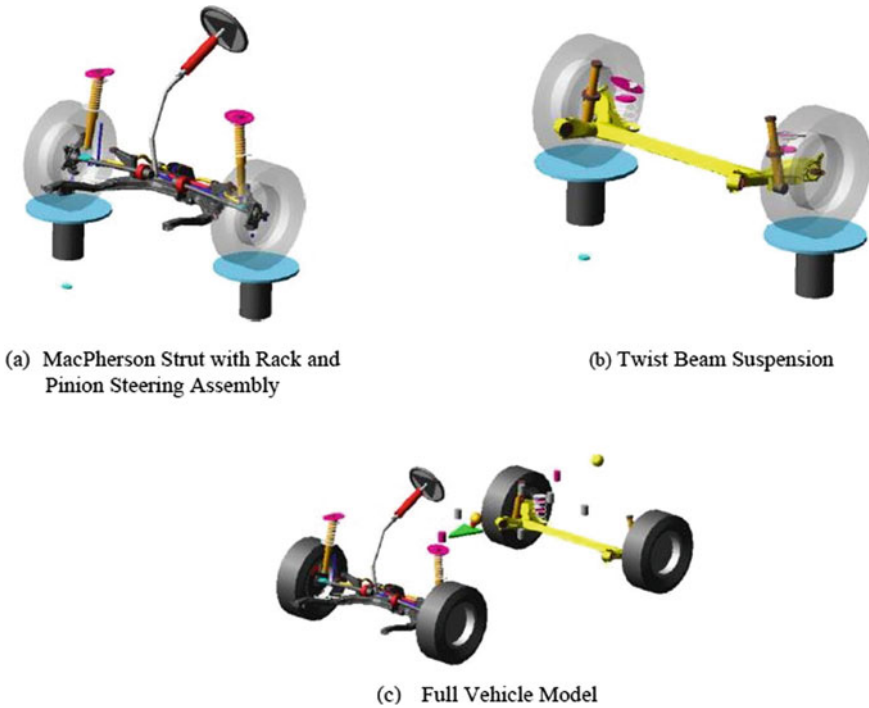


Fig. 2 Vehicle dynamics model (front and rear suspension, steering and full vehicle model)

Table 1 gives the details of the suspension, steering and vehicle system configuration.

Table 1 Vehicle suspension and steering system details

<i>Steering</i>	
Rack and pinion type. Electric power steering	
<i>Suspension</i>	
Front-MacPherson strut rear twist beam-type suspension	
Antiroll bar	Front only
Tire size	215/55R17
Wheelbase (mm)	2500–2600
Overall width (mm)	1750–1850
Overall length (mm)	3500–4500
Front track (mm)	1500–1600
Rear track (mm)	1500–1600

2.2 Model Calibration

The sub-system level models (front suspension and rear suspension) are validated through kinematics and compliance, and full vehicle model is validated for handling performance. Figure 3 shows the experimental versus numerical results, and it is noted that a correlation of more than 90% is achieved.

Figure 4 shows the comparison of test versus simulation results of the steering wheel angle (SWA) gradient and yaw rate. It is noted that there is a good correlation between the experimental and numerical results, and therefore, the full vehicle calibrated model is for optimization studies.

Fig. 3 **a** Front suspension toe angle versus wheel travel correlation. **b** Rear suspension wheel normal force [Fz] versus wheel travel correlation

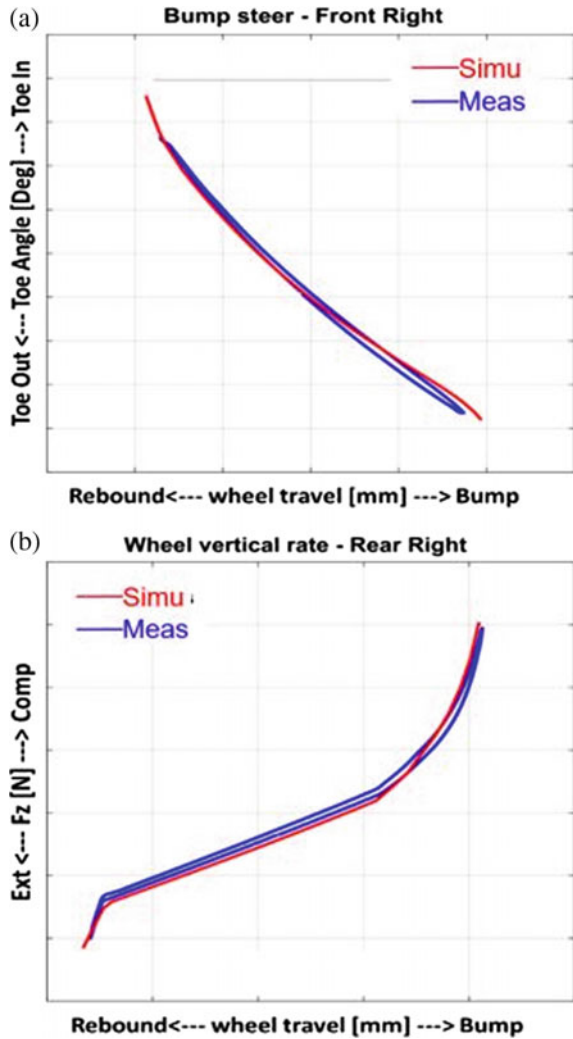
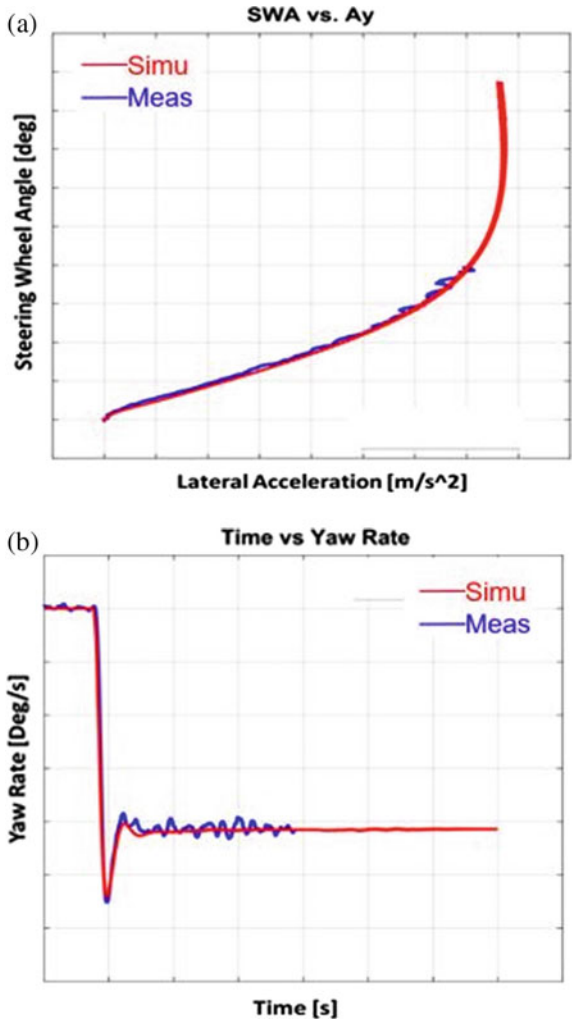


Fig. 4 **a** Steady-state velocity test: SWA gradient.
b Transient test: Yaw rate



3 Selection of Design Verification Plan (DVP) for MDO Based on Customer Perception

Figure 5 shows the linkage between customer perception, subjective feel and the corresponding objective metrics.

Table 2 gives the details of the DVPs selected based on the objective metrics.

Evaluation Items		Customer Perception	Subjective feel	Objective metrics
Handling		Sporty/fun	Sporty/fun (Response, Agility)	Steering Wheel Angle Gradient Lateral acceleration Response time 90% Yaw Rate Response time 90%
Stability		confidence/Safety	Confidence/Safety (Body control/Yaw stability)	Roll gradient & Side slip gradient
Comfort		Ride	Ride comfort (Deterministic impacts)	Seat Longitudinal and Vertical Acceleration

Fig. 5 Mapping of subjective feel with objective metrics

Table 2 Subjective feel mapping with objective data

ISO	DVP	Metrics
ISO 4138	Steady-state cornering Constant speed (continuous)	Steering wheel angle gradient Roll gradient and side slip gradient
ISO 7401	Step Steer	Lateral acceleration 90% time Yaw rate 90% time Yaw rate overshoot
As per OEM	Straightline driving on deterministic inputs-40 kmph	Seat longitudinal and Vertical acceleration

4 DOE Analysis Using Full Vehicle Model (in ADAMS Insight)

Figure 6 show the workflow of DoE-based analysis. Machine learning-based predictive models were generated, and Table 3 shows the details of the accuracy pertaining to various attributes (Fig. 7).

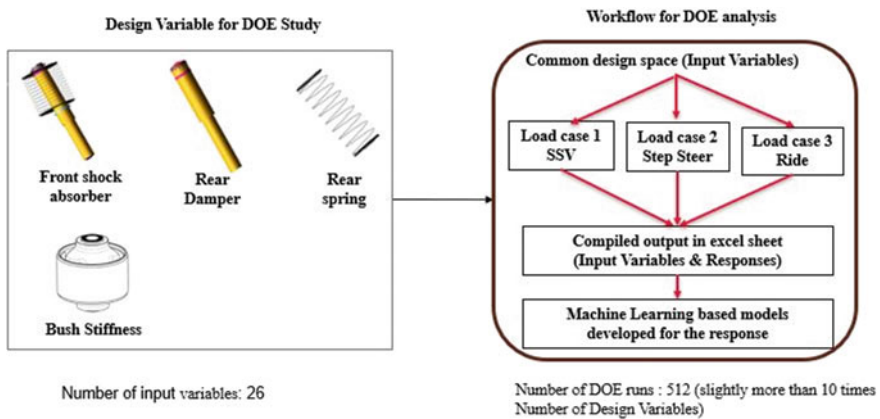


Fig. 6 Workflow for DOE analysis

Table 3 Accuracies of regression models of R&H responses

S. no.	Responses	Accuracy (%)
1	SWA gradient	99.05
2	Roll gradient	98.84
3	Side slip gradient	98.72
4	Lateral acceleration 90% response time [Ay]	99.2
5	Yaw rate acceleration 90% response time [γ]	99.3
6	Yaw rate overshoot	98.6
7	Peak-to-peak driver seat longitudinal acceleration	95.4
8	Peak-to-peak driver seat vertical acceleration	95.6

4.1 Identification of Important Design Variables by Using Heat Map

Correlation studies were performed to arrive at important design variables that influence the ride and handling responses. Figure 8 shows the heatmap generated for SWA_GRADIENT, and similar heatmaps were generated for the remaining ride and handling attributes that were considered in the present study.

From the initial set of 26 design variables, top 10 variables that influence the ride and handling parameters were shortlisted and shown in Table 4.

5 Formulation of Problem Definition

Improving ride performance without the deterioration of handling is a challenging task. In this MDO, the main objective is to improve ride and handling performance considering the relevant DVPs.

The **objective function** is defined as shown in the Eq. 1.

$$\text{Objective function} = \text{minimize}(w1 * f_{\text{ride}} + w2 * f_{\text{handling}}) \tag{1}$$

f_{ride} = peak-to-peak seat longitudinal accelerations and peak-to-peak seat vertical acceleration, f_{handling} = roll gradient and side slip gradient, $w1$ = ride weighting factor, $w2$ = handling weighting factor.

Top 10 critical variables that are shown in Table 4 were considered as the **design variables**. The **constraints** and their limits are shown in Table 5.

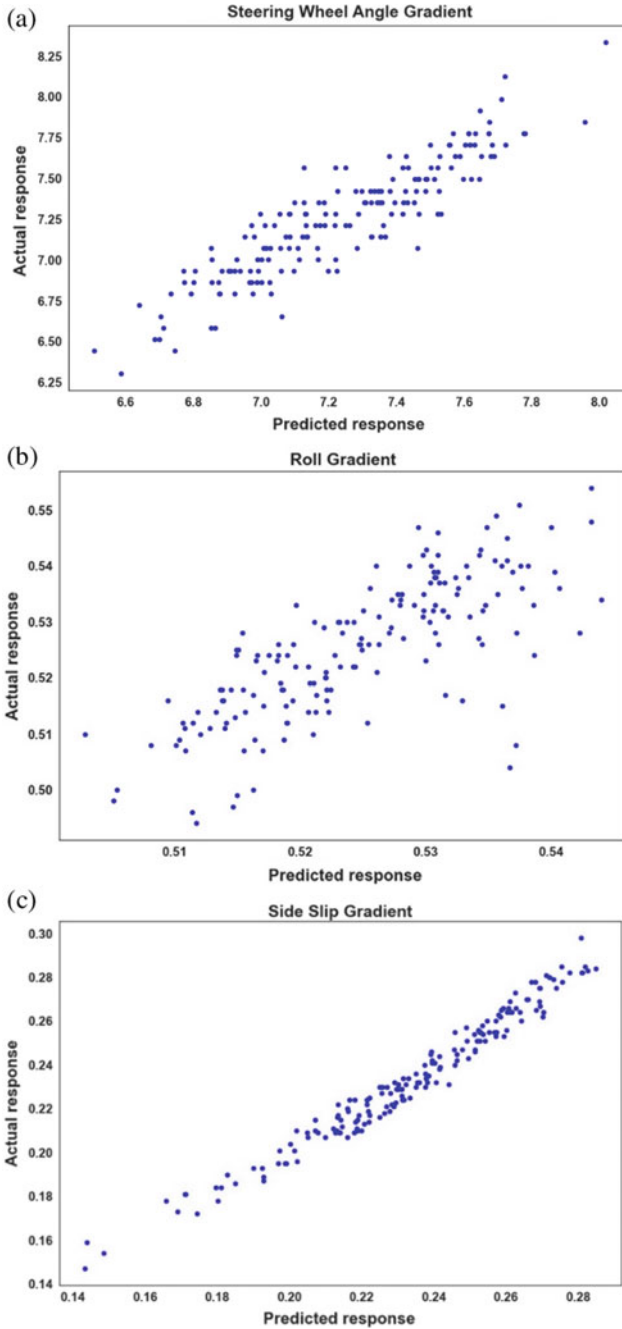


Fig. 7 **a** Scatter plot of SWA gradient. **b** Scatter plot of roll gradient. **c** Scatter plot of side slip gradient. **d** Scatter plot of lateral acceleration 90% response time. **e** Scatter plot of yaw rate 90% response time. **f** Scatter plot of raw rate overshoot. **g** Scatter plot of peak-to-peak driver seat longitudinal acceleration (A_x). **h** Scatter plot of peak-to-peak driver seat vertical acceleration (A_z)

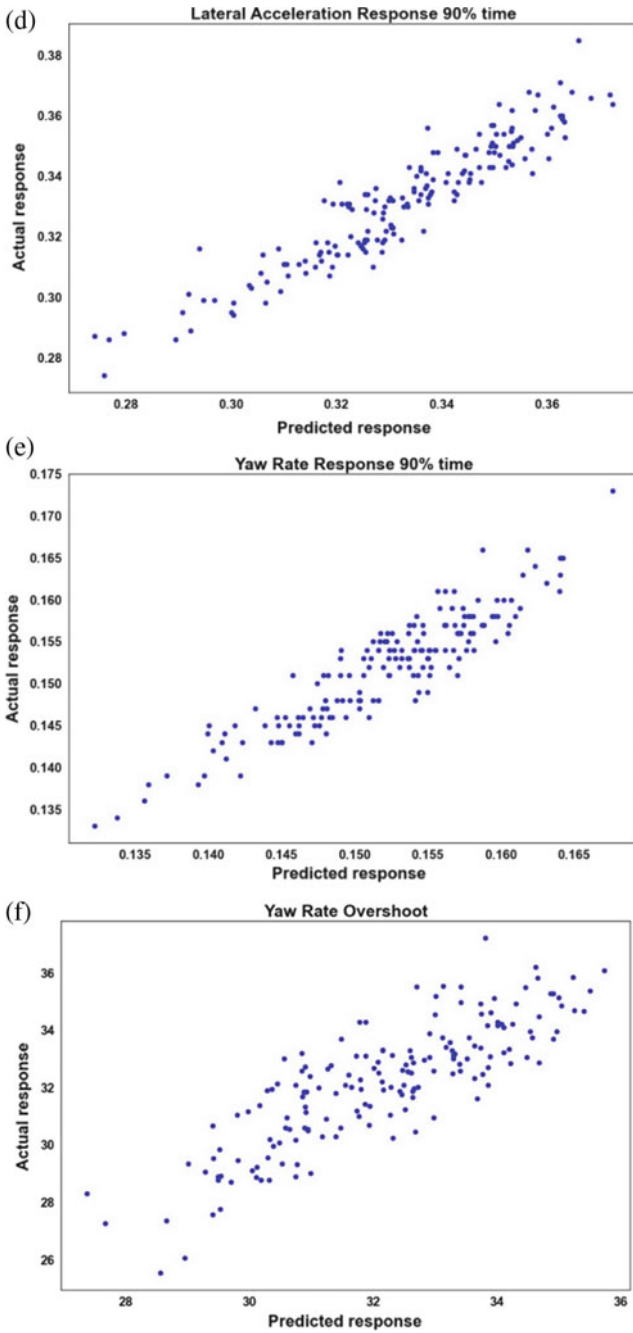


Fig. 7 (continued)

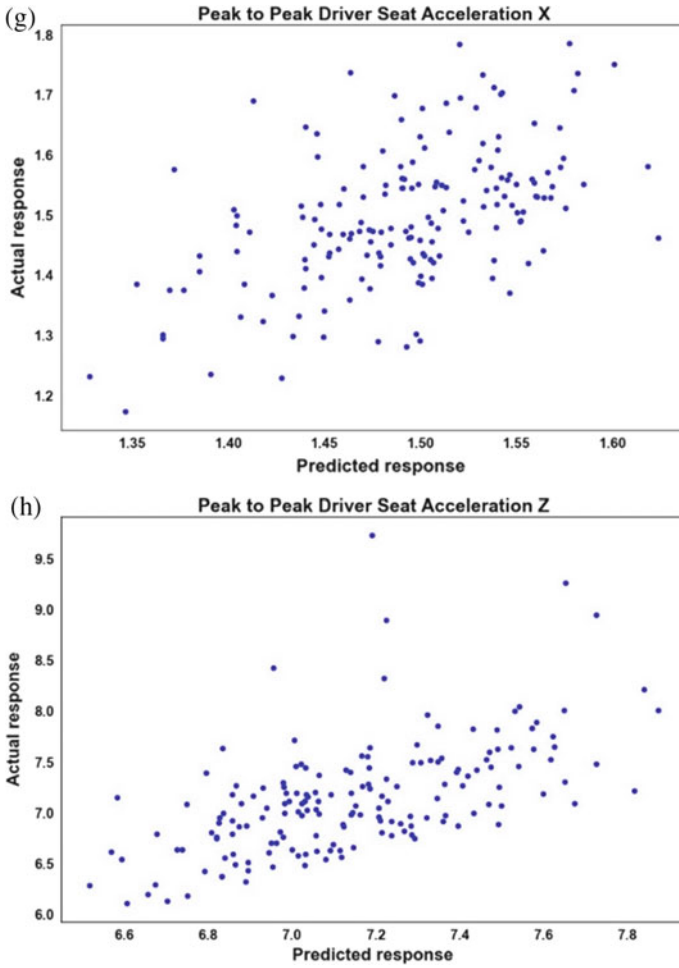


Fig. 7 (continued)

6 Performing Multi-objective Design Optimization Using NSGA-II

When there are multiple conflicting objective functions subject to multiple constraints, a fast and non-dominated sorting function is required. The NSGA-II algorithm by Deb et al. [6] is one example of such an algorithm that uses an elitist strategy to minimize the objective function. The main objective of this MDO is to minimize objective function without deteriorating the base vehicle ride and handling performance. Using NSGA-II algorithm, an overall improvement of 13% was achieved with minimal changes to the design variables. Comparison of results (SWA gradient,

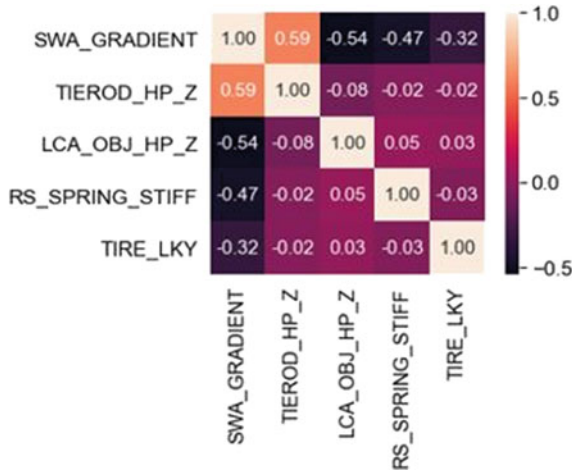


Fig. 8 Heatmap—SWA gradient response

Table 4 Top 10 critical design variables that effect ride and handling attributes

S. No.	Design variable	Variable description
1	Tie rod HP Z	Tie rod hard point Z direction
2	LCA OBJ HP Z	LCA outer ball joint hard point Z direction
3	RS spring stiff	Rear suspension coil spring stiffness
4	Tire LKY	Tire cornering stiffness
5	FS spring stiff	Front suspension coil spring stiffness
6	FS arb stiff	Front Suspension anti-roll Bar Stiffness
7	RS bump stop clr	Rear suspension bump stopper clearance
8	TB to BIW Kx	Twist beam to BIW bush X-direction stiffness
9	FS damper stiff compression	Front suspension damper stiffness-compression
10	FS damper stiff rebound	Front suspension damper stiffness-rebound

Table 5 Constraint limits for MDO

S. No.	Constraint variable	Limit
1	SWA gradient	$SWA_g \leq SWA_g^{target}$
2	Lateral acceleration 90% response time [Ay]	$A_y \leq A_y^{target}$
3	Yaw rate acceleration 90% response time [γ]	$\gamma \leq \gamma^{target}$

roll gradient, side slip gradient, etc.) baseline versus optimal solution is shown in Fig. 9 on a relative scale.

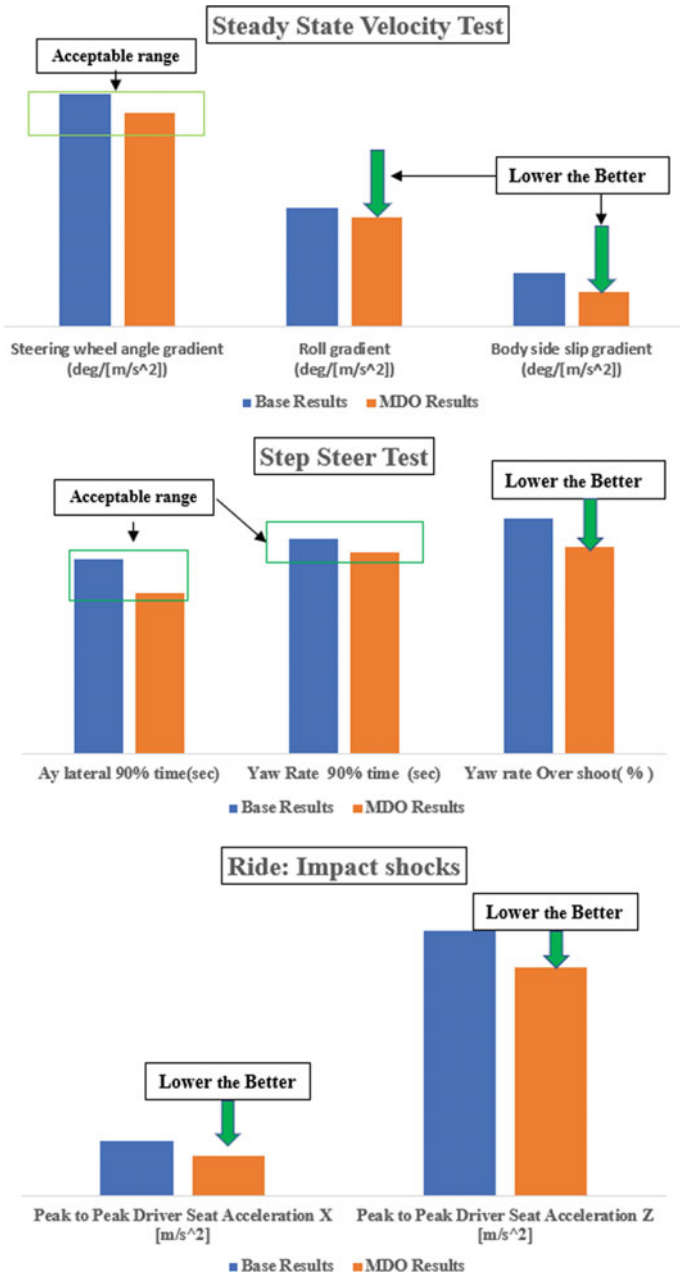


Fig. 9 Comparison of baseline with multi-objective design optimization (MDO) results

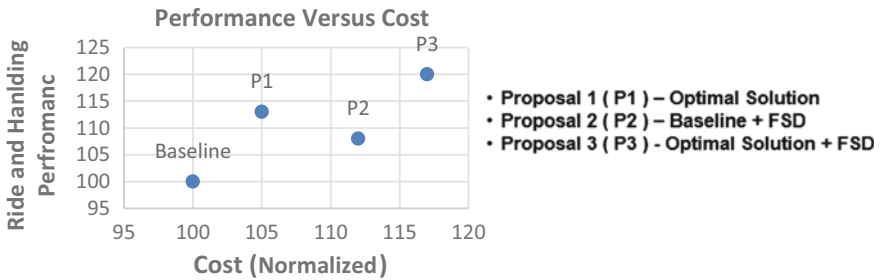


Fig. 10 Trade space studies

7 Technology and Engineering Recommendations

As shown in Fig. 10, the optimal results (P1) show a significant improvement in ride and handling performance with respect to the baseline design. Proposal 2 is the design configuration that is obtained by adding Frequency Selective Damping (FSD) to baseline design. It is noted that proposal 2 is costly and yet underrated in performance with respect to proposal 1, and therefore, proposal 2 can be discarded. Proposal 3 is obtained by adding FSD to the optimal solution (P1), and it gives the best performance but is a costly solution. Authors recommend proposal 3 for high-end variant and proposal 1 for entry-level variant (Fig. 10).

References

1. Deb K (2011) Multi-objective optimisation using evolutionary algorithms: an introduction. In: Multi-objective evolutionary optimisation for product design and manufacturing. Springer, London
2. Deb K, Jain S (2003) Multi-speed gearbox design using multi-objective evolutionary algorithms. *ASME J Mech Des* 125(3):609–619
3. Fazeley HR, Taei H, Naseh H, Mirshams M (2016) A multi-objective, multidisciplinary design optimization methodology for the conceptual design of a spacecraft bi-propellant propulsion system. *Struct Multidiscip Optim* 53(1):145–160
4. Moiz A, Pal P, Probst D, Pei Y et al (2018) A Machine learning-genetic algorithm (ML-GA) approach for rapid optimization using high-performance computing. *SAE Int J Commer Veh* 11(5):291–306. <https://doi.org/10.4271/2018-01-0190>
5. Zheng L, Gao Y, Zhan Z, Li Y (2017) Multi objective optimization of vehicle crashworthiness based on combined surrogate models. *SAE Technical Paper* 2017-01-1473
6. Deb K, Pratap A, Agarwal S, Meyarivan T (2002) A fast and elitist multiobjective genetic algorithm: NSGA-II. *IEEE Trans Evol Comput* 6(2):182–197

Optimization Applications: Materials and Structures

Optimization and Prediction of Transverse Shear Property of the Bioinspired Cell Core Using PSO and ANN



Muthukumaran Gunasegeran and P. Edwin Sudhagar

1 Introduction

The ultra-light, low-density core structures with stiff facings were impressive for research in significant weight-saving applications. The aviation and marine industries reduce the mass of structures to reduce production and operating costs. Sandwich core design analysis with finite element analysis has been developed into a promising concept with maximum strength, rigidity, and weight reduction in sandwich structures. A profound examination of geometric and mechanical properties in the transverse plane is necessary to obtain the multifunctional behaviour of sandwich panels since they are highly susceptible to any kind of charge. The design of lightweight structures is one of the critical aspects of structural optimization, which does not simply involve ensuring a complex construction but also identifying the constraints and solving problems by producing optimal values of the main parameters. Optimization provides the most satisfactory fitting solution to a problem underneath assumed conditions. Optimization states equal minimization and maximization tasks. Subsequently, the maximization of any function is scientifically equal to the minimization of its additive inverse. The terms minimization and optimization are used interchangeably.

In their research, Ming et al. [1] examined the relationship between the compositions of alloys and mechanical properties. The results show that the proposed PSO-BP model can define the quantitative association concerning the composition of the Mg–Li–Al alloy. Chen et al. [2] suggested a technique that combines PSO and finite element analysis (FEA). And, examples of the optimization of the durability design (RDO) of a laminate and a composite cylindrical shell are carried out to illustrate

M. Gunasegeran · P. Edwin Sudhagar (✉)

School of Mechanical Engineering, Vellore Institute of Technology (VIT), Vellore, Tamil Nadu 632014, India

e-mail: edwinsudhagar.p@vit.ac.in

the method's effectiveness. Mohan et al. [3], using the PSO technique, tested the use of the frequency response function (FRF). After comparing the results between the two approaches, the robustness and efficiency of the above approach have been developed. Chen et al. [4] projected that the surrogate simulation technique and PSO combined with the SBPSO algorithm. It is applied to composite pressure vessels reliability-based robust nature (RBRD) and is demonstrated by numerical examples. Zhang et al. [5] suggested a method for the Barcelona basic model (BBM) to define parameter values, utilizing inverse analysis of the pressure–cavity strain curve of the experimental cavity from pressuremeter tests in unsaturated soils. Lee et al. [6] aimed to determine the superlative number and locations of locking compression plates (LCPs) screws to attain adequate fixation stability and to minimize energy dissipation from thermoelastic dissipation (TED). Lake et al. [7] improved the MEMS slotted resonator's geometry. They moved through the complex design space resulting from multiple physical complications. Vosoughi and Gerist [8] suggested a mixed optimization method incorporating FEA, continuous GA, and PSO to detect damage for a laminated composite beam. Ribeiro et al. [9] examined the geometric effects of the auxetic structures through recycled rubber composites via numerical and experimental data. Kitak et al. [10] developed a procedure for calculating the heat transfer coefficients for the FEM housing a medium voltage switchgear cell model. The proposed technique focused on the PSO algorithm, an equivalent numerical FE model, and an accurate partition wall test model was developed. Kalatehjari et al. [11] used to test the vital slip surface of the soil slopes using PSO. Previous publications have also been limited to the study of 2D slope stability. ANSYS performs the optimization task to obtain the new design of the sandwich cores with optimum design and improved transverse shear modulus. The design variables used to carry out the optimization method are the model and dimensions.

Artificial neural networks are ideal for applying real-world issues in research and science, business, and industry. ANNs are a logical method of programming that replicates the human brain's characteristics, such as learning, recalling, deciding, and inference. The artificial neural network architecture comprises mainly parallel adaptive processing elements with interconnected hierarchical ordered networks. Ramada et al. [12] addressed damage characteristics of a composite beam by employing an ANN environment. Reddy et al. [13] studied and were predicted by ANN the natural frequency of laminated composite plates under clamped boundary conditions. Chandrasekaran and Devarasiddappa [14], using ANN methodology, indicated surface roughness for the cylindrical grinding of MMC. The research showed that as feed increases, surface roughness raises while it reduces with a rise in wheel velocity. Kurt and Oduncuoglu [15] studied the impact on the wear properties of ultra-high molecular weight polyethylene of load applied, speed of sliding, form, and reinforcements weight percentages. Mohit et al. [16] used a single-input and single-output approach to evaluate active vibration control of plates with ANN. Dey et al. [17] presented the stochastic natural frequency for laminated composite plates which was compared to conventional Monte Carlo simulation, and then compared via ANN model the sample size and computational cost were minimized by using the current method. Guo and Wang [18] examined the characteristics of an adhesively bonded

double-strap joint with an adhesive viscoelastic layer under free vibration. Three-dimensional finite element analysis verified the suggested procedure. The impact on the joint of the adhesive material properties and joint geometric parameters was analysed with detailed dynamic characteristics. Bui et al. [19] proposed using the optimized ANN of pure cohesive slopes for the design. FE limit balance analysis was performed to run training and research datasets to prepare ANN-based predictive models. The optimum design for the ANN structure has been identified. Expected outcomes for ANN model datasets were evaluated based on R^2 , RMSE, and VAF. Suresh et al. [20] investigated the prediction of tool wear by response surface method and ANN.

The literature evaluates the transverse shear elastic property for various cores such as honeycomb, cork, foam, and lattice which have been studied using ASTM C393. The present study investigates the numerical evaluation of the transverse shear property of a bioinspired core by the alternative dynamic method. PSO is used to optimize the geometric parameters of bioinspired cell core and predict the transverse shear property using an ANN.

2 Numerical Evaluation of the Transverse Shear Elastic Property of Bioinspired Core

Refs. [21, 22] have formulated a technique to evaluate the transverse shear modulus of honeycomb core in both experimental and numerical methods. An alternative dynamic method of core property evaluation is employed to reduce the cost and time spent in experimentation.

The proposed method can be considered for the bioinspired core to evaluate the transverse shear modulus.

$$G_{yz} = \left[\frac{(-E_z \times m \times a_c^4 \times h_c \times \omega_{yz}^2) + (12I_{mx} \times m \times h_c^2 \times \omega_{yz}^4)}{(-E_z \times a_c^6) + (3hc \times m \times a_c^2 \times h_m^2 \times \omega_{yz}^2) + (12I_{mx} \times h_c \times a_c^2 \times \omega_{yz}^2)} \right] \tag{1}$$

$$G_{xz} = \left[\frac{(-E_z \times m \times a_c^4 \times h_c \times \omega_{xz}^2) + (12I_{mx} \times m \times h_c^2 \times \omega_{xz}^4)}{(-E_z \times a_c^6) + (3hc \times m \times a_c^2 \times h_m^2 \times \omega_{xz}^2) + (12I_{mx} \times h_c \times a_c^2 \times \omega_{xz}^2)} \right] \tag{2}$$

$$E_z = E_2 \times \left(\frac{A_{\text{foot}}}{A_{\text{cell}}} \right) \tag{3}$$

where $G_{xz,yz}$ —shear modulus; E_z —Young’s modulus (Z-direction); m —the mass of the steel block; a_c —core width/length; h_c —core height; h_m —steel block height; $\omega_{xz,yz}$ —radial velocity; I_{mx} —the mass moment of inertia of the steel block; A_{cell} —cell area; A_{foot} —footprint area.

Figure 1 shows the detailed interface between ANSYS and the MATLAB tool, combined as a fitness function for the optimization problem. Geometric parameters and material properties of the composite material were determined and provided as an input to the ANSYS modelling programme. The Solid185 element is chosen for the steel block and bioinspired core. An APDL (Ansys parametric design language) script is developed for four different bioinspired cores, and the created geometry was glued, and the core’s bottom face was constrained. Modal analysis was carried out for the developed model using block Lanczos method. The first two modal frequencies were extracted and used to calculate the transverse shear modulus (G_{xz} and G_{yz}) (Table 1).

The present FE analysis has a good argument with the alternative dynamic approach in the existing literature.

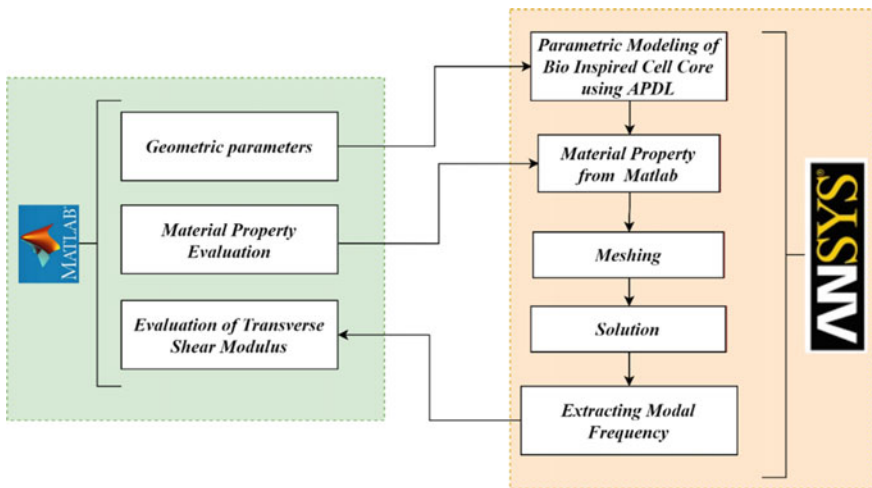


Fig. 1 MATLAB and ANSYS–APDL interface

Table 1 Reviewed and measured honeycomb material properties

Reviewed approaches	E_z (Gpa)	G_{xz} (MPa)	G_{yz} (MPa)
Alternative dynamic method [21]	1.89	369	217
FE analysis [21]	1.89	369	217
Present method	1.89	391	234

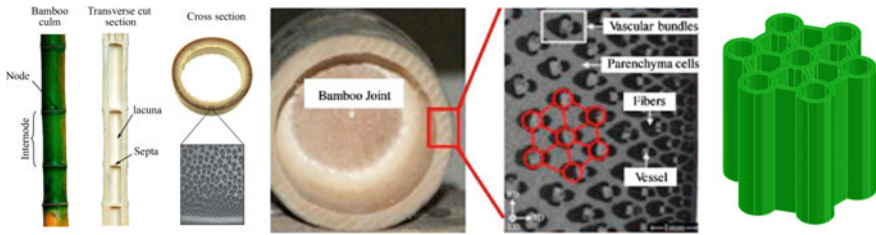


Fig. 2 Bioinspired model from bamboo [26]

3 Selection of Bamboo-Based Bioinspired Model

Bamboo has a higher stiffness–mass ratio than some metallic materials such as steel and aluminium, probably a lightweight composite. It also has good mechanical properties of biological materials displaying non-self-similar classified structures such as penetration resistance, fracture toughness, and fracture toughness. The mechanical efficiency of model materials with non-self-similar hierarchical structures was examined [23]. The bioinspired composite plate with equal spatial was subjected to an underwater impulsive loading setup mass by Tran et al. [24]. Zhang et al. demonstrated new biomedical honeycomb system uses and also explored the engineering bioinspired materials and devices based on honeycomb structures has been used for various practical applications to better understand the design principles underlying honeycomb structure creation and the accompanying scientific discovery and technology growth [25] (Fig. 2).

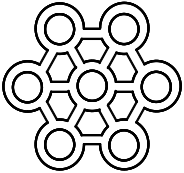
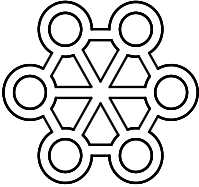
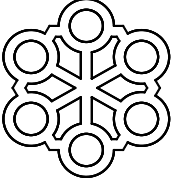
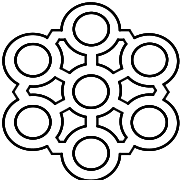
3.1 Design Modification in the Bamboo Bioinspired Model

Modified bamboo-based bioinspired model is formulated by performing certain modifications such as eliminating the centre circular portion of the base model and shifting the circular edge portion to the middle portion. The design modification was carried out and considered for optimization and prediction. The modified bamboo-inspired models are given in Table 2.

4 Particle Swarm Optimization (PSO)

Swarm intelligence theories were influenced by the societal behaviour of gathering animals like birds, ants, and swarms from the fish school. PSO algorithm is population-based, using an individual population to examine the capable areas of the search space. Each individual’s output is calculated using a fitness function like evolutionary algorithms (Fig. 3).

Table 2 Four different bamboo bioinspired models design modification details

Core name	Core sketch	Description
BIM		Bamboo-inspired model [26] <ul style="list-style-type: none"> The base model was taken as a reference for optimization and prediction
MBIM01		Modified bamboo-inspired model_01 <ul style="list-style-type: none"> First modified model, the central circular portion is eliminated, about the base model
MBIM02		Modified bamboo-inspired model_02 <ul style="list-style-type: none"> The circular portion in the edge is transferred to the middle. It eliminates the central circular part of the base model
MBIM03		Modified bamboo-inspired model_03 <ul style="list-style-type: none"> The circular portion in the edge is transferred to the middle, about the base model

Considering n -dimensional design space in an optimization problem. Assuming M swarm, particles and i th swarm particle are denoted as vectors [27].

$$X_i, X_i, \in R^n$$

$$X_i = (X_{i1}, X_{i2}, \dots, X_{in})T, i = 1, 2, \dots, M$$

in n -dimensional search space, the velocity of the particle moving is given as

$$V_i = (V_{i1}, V_{i2}, \dots, V_{in})T, i = 1, 2, \dots, M$$

and the best position met by the particle is

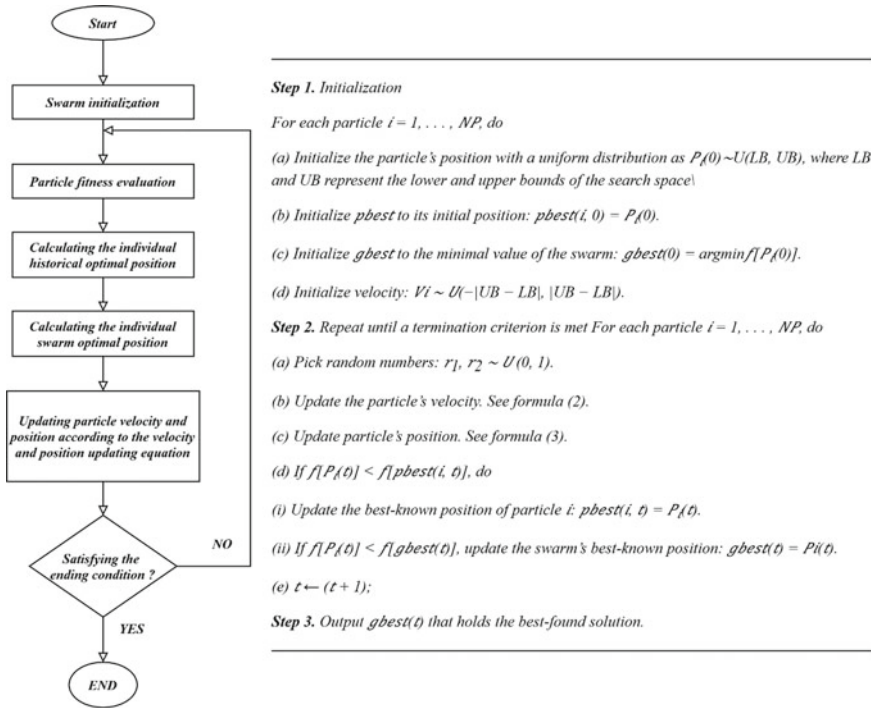


Fig. 3 Flowchart and standard pseudocode for particle swarm optimization [27]

$$B_i = (B_{i1}, B_{i2}, \dots, B_{in})T, i = 1, 2, \dots, M$$

Assuming that the particle j reaches the best position in the present iteration (1), then the particles' position and velocity are modified using the succeeding equations.

$$V_i(l + 1) = wV_i(l) + c_1r_1(B_i(l) - X_i(l)) + c_2r_2(B_i(l) - X_i(l))$$

$$X_i(l + 1) = X_i(1) + v_i(l + 1)$$

where w is the inertia weight, c_1, c_2 denote positive acceleration constants, and r_1, r_2 are uniformly distributed random numbers $r_1, r_2 \in [0, 1]$. The initial term in the above equation narrates to the present swarm velocity, and the subsequent term denotes the local search, while the 3rd term denotes the global search directing to the optimum solution.

The weight of inertia (w) is used to monitor the outcome of the earlier antiquity of velocities on each particle's present velocity. The w parameter thus controls the trade-off among the swarm's global and local search capacity.

The optimization technique for determining the optimal design of the transverse shear elastic modulus can be defined in Fig. 4. Three segments are involved in the

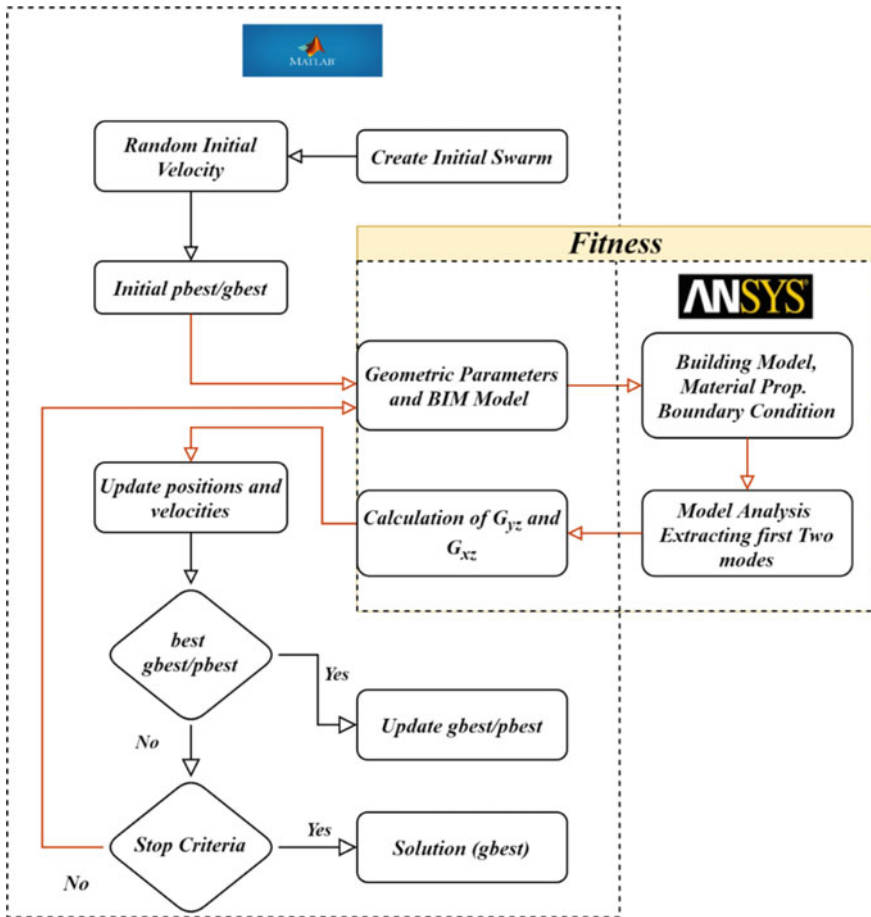


Fig. 4 PSO optimization using MATLAB-APDL interface

method: (1) evaluating the natural frequency via model analysis by ANSYS-APDL; (2) calculation of out of plane elastic modulus; and (3) optimization. The method is written in the programming software MATLAB and ANSYS-APDL. Initially, the particles are adjusted with random position values and random velocities. Next, to evaluate the natural frequency of the bioinspired cell core, ANSYS-APDL is in the background, and the results are extracted in an external file. After that, the extracted file is read by MATLAB, and the transverse shear elastic modulus is calculated. The optimization algorithm assesses each swarm's fitness. It then records for the best previous experience at the current iteration and the best experience of all other swarms. Over the best solutions stated above, each swarm updates itself. The upgraded swarms are transferred to ANSYS-APDL for additional iteration. This procedure is repeated until iterations reach the programmed determined iteration

Table 3 Three-variable problem—maximum shear modulus

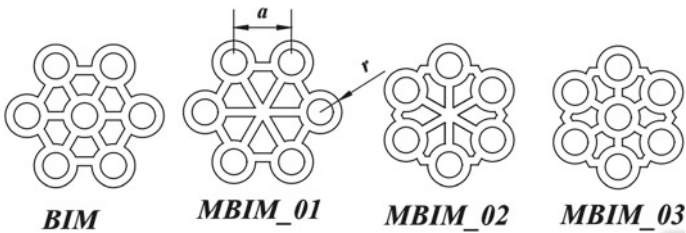
BIM_Model	Optimized side length (a) in mm	Optimized edge radius (r) in mm	Shear Modulus (G_{xz}) in MPa	Shear Modulus (G_{yz}) in MPa
MBIM_02	4	2	319.71	316.28

number. The data as of ANSYS–APDL and MATLAB are shared, from side to side, in the whole optimization process.

4.1 Result and Discussion on Optimization of Modified Bioinspired Cell Core

Considering three variables for the optimization problem, four different bioinspired models with varying side length and edge radius.

- Find: (G_{yz}, G_{xz}) .
- Maximize: $f = f(\text{BIM_model}, a, r)$.
- Subject to: BIM_model :



- Side length (a): $4 \leq a \leq 8$.
- Edge radius (r): $1.5 \leq r \leq 4$.

In the seventh iteration, the convergence of the objective value, search position, objective value variance, and shear position variance has occurred. Table 3 shows the optimized parameters for the selected variable problem for maximization problem using the PSO optimization. The maximum transverse shear modulus is observed in the MBIM_02 model with a side length of 4 mm and edge radius of 2 mm.

5 Artificial Neural Network (ANN) on Bioinspired Cell Core

The numerically simulated data shown in Table 4 were randomly separated into three

Table 4 ANN parameters for bioinspired cell core

Input layers in (nos.)	Hidden layers in (nos.)	Training algorithm	Output layers in (nos.)
03	10–50	Levenberg–Marquardt backpropagation	02

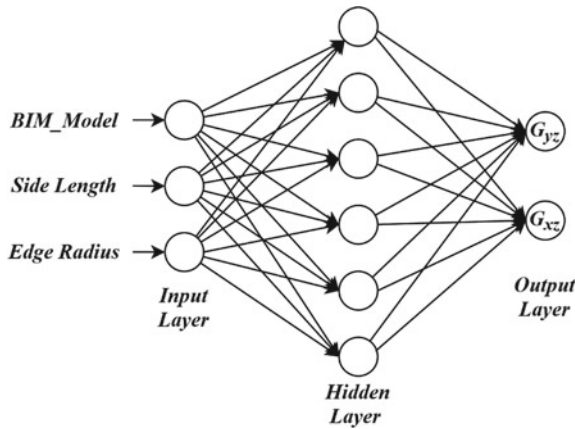


Fig. 5 Artificial neural network architecture

categories. The data for training the network were 70%, 15% to validate to prevent overfitting of the generalized network and then the last to test the network 15% of the data. The architecture of the artificial neural network is shown in Fig. 5. A momentum backpropagation was used in the learning stage to prevent trapping into the local minimum. The constant momentum was set as 0.98. The tansig transfer function was applied in the hidden, and output layers normalized range 0 to 1 were used for inputs and output. Mean squared error was 0.001, the learning rate was after the training when the neural networks mean square error met the minimum; the network model was saved.

6 Result and Discussion on ANN of Modified Bioinspired Cell Core

Hidden layers for the ANN were varied from 10 to 50, and the most acceptable optimum outcome was obtained in the 24th hidden layers, the results were recorded, and the plot concerning the number of hidden layers versus RSME, Val performance, number of epochs, and best epoch is shown in Fig. 6. The R^2 value should be closer to one which replicates the accuracy of the prediction of the ANN. The R^2 of 0.99979 is the best possible value in this study, considering different hidden layers.

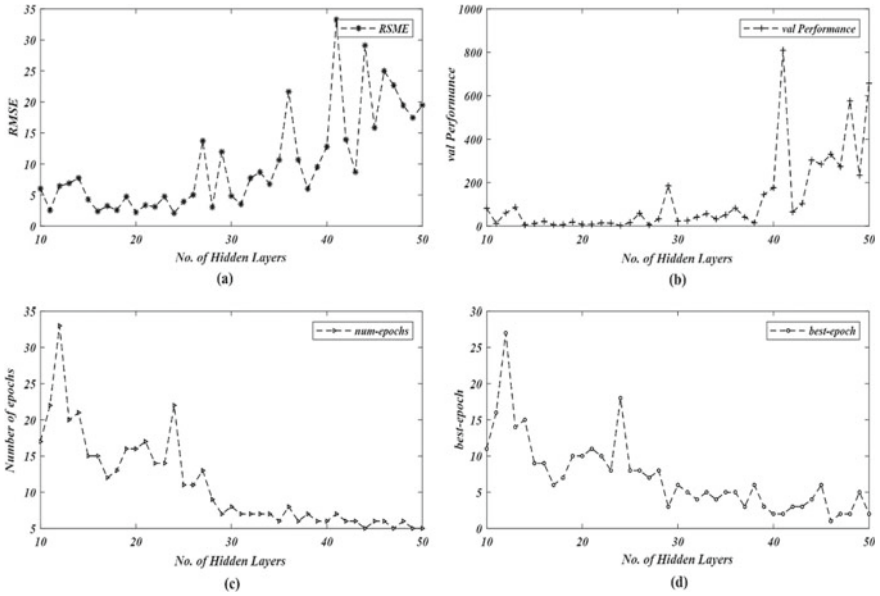


Fig. 6 **a** Plot between RSME and number of hidden layer. **b** Plot between Val performance and number of hidden layer. **c** Plot between number of epochs and number of hidden layer. **d** Plot between best epoch and number of hidden layer

Compare the numerical data and ANN predicted with the BIM_model, side length, and edge radius. The bioinspired core’s transverse shear modulus holds a good argument providing consistent results with the error percentage between the numerically simulated and predicted ranging from -1.92 to 6.85% , as shown in Fig. 7.

An evaluation of the predicted and numerically simulated data of the transverse shear elastic modulus is presented in Fig. 8. A close correlation among the predicted and numerically simulated data records was observed. Yet, there are errors in approximately specific values. The errors might be in the training of the network. So far, the models projected can define and predict the transverse shear elastic modulus G_{xz} and G_{yz} . These results provide us assurance in predicting transverse shear elastic modulus from the models. The limitation of the models is that a mathematical expression cannot be attained immediately. The advancement of computer technology and artificial intelligence indicates that the ANN is the best tool for predicting various unknown factors with better accuracy, as shown in Table 5 (Table 6).

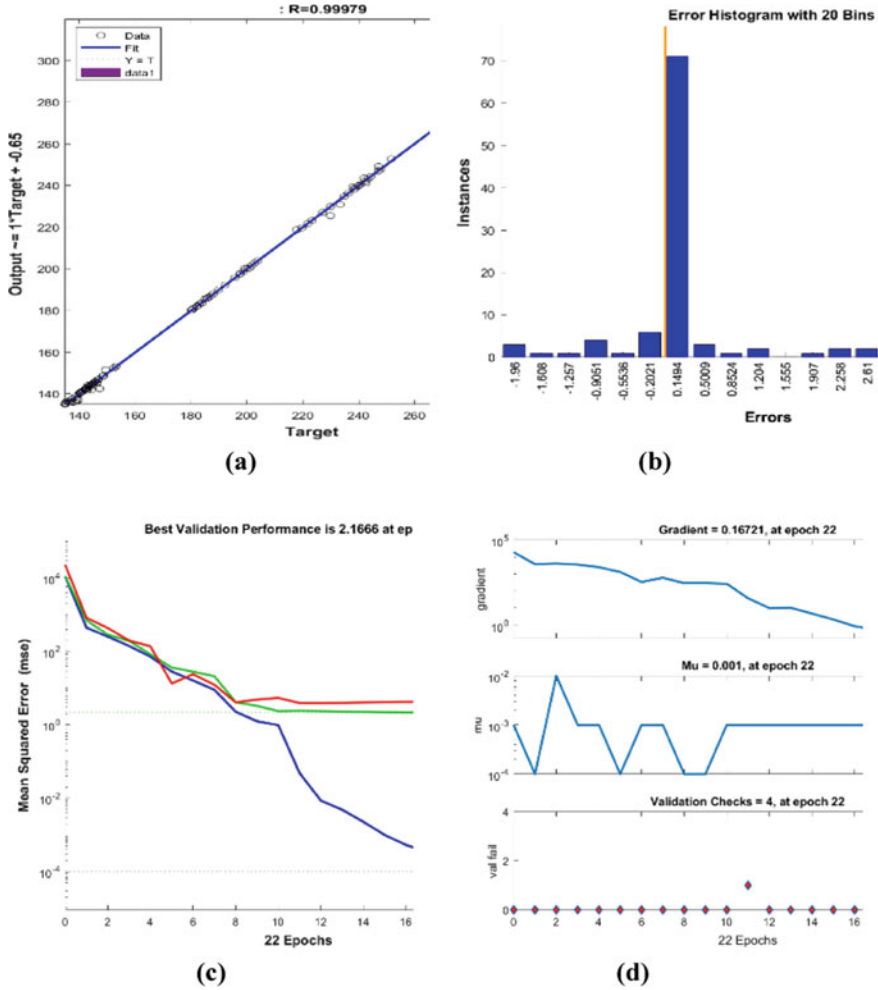


Fig. 7 a Regression plot. b Error histogram plot. c Performance plot. d Train state plot

7 Conclusion

In this study, the optimal novel bamboo-based bioinspired core with a maximum transverse shear modulus was predicted. Also, it signified the influences of the bioinspired model and geometric parameters. The optimum model and geometric parameters such as side length and edge radius were obtained by PSO. It was observed that the maximum transverse shear modulus of the bioinspired cell core in the modified bioinspired model MBIM_02. Apart from the modified bioinspired model, the geometric parameters such as side length and the edge radius play a significant part in maximizing the out of plane elastic modulus. Using ANN, the transverse shear

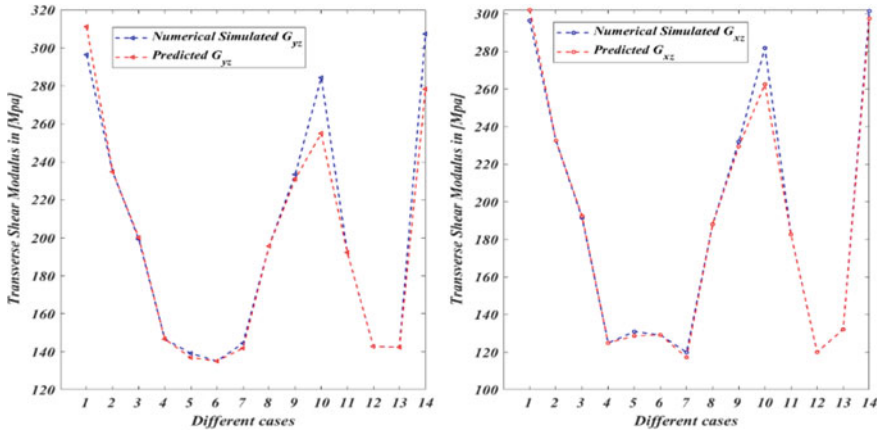


Fig. 8 Comparison of transverse shear modulus with numerically simulated and ANN predicted

modulus of the bioinspired cell core was predicted by considering ranges of parameters such as bioinspired model, side length, and edge radius. Better results were obtained. And also, when experimental approaches are unavailable, FE characterization can be a viable alternative. This research is beneficial for designers to customize structures with better strength and lighter weight.

Table 5 Numerically simulated and predicted transverse shear modulus G_{yz} and G_{xz} , error percentage

Case	BIM_Model	Side length (a) in mm	Edge radius (r) in mm	Simulated transverse shear modulus in MPa		Predicted transverse shear modulus in MPa		Error %	
				G_{xz}	G_{yz}	G_{xz}	G_{yz}	G_{xz}	G_{yz}
1	1	4	1.5	296.41	296.41	311.20	302.1	-1.92	-1.92
2	2	5	2	234.8	232.58	234.80	232.58	0.00	0.00
3	3	6	2.5	199.3	191.51	200.18	192.39	-0.44	-0.46
4	4	7	3	146.73	124.92	146.72	124.91	0.01	0.01
5	1	8	3.5	139.21	130.95	136.94	128.68	1.63	1.73
6	2	8	4	135.11	129.18	135.11	129.18	0.00	0.00
7	3	7	1.5	144.51	119.88	141.91	117.28	1.80	2.17
8	4	6	2	195.66	188.03	195.66	188.03	0.00	0.00
9	1	5	2.5	233.36	231.97	230.96	229.57	1.03	1.03
10	2	4	3	284.31	281.83	255.01	262.53	6.79	6.85
11	1	6	1.5	192.35	182.63	192.34	182.62	0.01	0.01
12	2	7	2	142.83	120.06	142.83	120.06	0.00	0.00
13	3	8	2.5	142.47	132.15	142.43	132.11	0.03	0.03
14	4	4	3	307.37	301.51	278.31	297.54	1.29	1.32

Table 6 Predicted transverse shear modulus G_{yz} and G_{xz} for geometric parameters

Case	BIM_Model	Side length (a) in mm	Edge radius (r) in mm	Predicted transverse shear modulus in MPa	
				G_{xz}	G_{yz}
1	1	3.5	2.5	318.95	310.58
2	2	3.5	2.5	320.57	318.32
3	3	3.5	2.5	317.44	316.76
4	4	3.5	2.5	319.98	311.96

Acknowledgements The authors would like to thank the Vellore Institute of Technology, Vellore, Tamil Nadu, India-632014, for providing the research facilities.

Authors' Contributions

Muthukumar Gunasegeran—Conceptualization, methodology and investigation.

Edwin Sudhagar P—original draft preparation—content writing and visualization, supervision.

References

- Ming L, Hai H, Aimin Z, Yingde S, Zhao L, Xingguo Z (2012) Modeling of mechanical properties of as-cast Mg-Li-Al alloys based on PSO-BP algorithm. *China Foundry* 9(2):119–124
- Chen J, Tang Y, Ge R, An Q, Guo X (2013) Reliability design optimization of composite structures based on PSO together with FEA. *Chin J Aeronaut* 26(2):343–349. <https://doi.org/10.1016/j.cja.2013.02.011>
- Mohan SC, Maiti DK, Maity D (2013) Structural damage assessment using FRF employing particle swarm optimization. *Appl Math Comput* 219(20):10387–10400. <https://doi.org/10.1016/j.amc.2013.04.016>
- Chen J, Tang Y, Huang X (2013) Application of surrogate based particle swarm optimization to the reliability-based robust design of composite pressure vessels. *Acta Mech Solida Sin* 26(5):480–490. [https://doi.org/10.1016/S0894-9166\(13\)60043-9](https://doi.org/10.1016/S0894-9166(13)60043-9)
- Zhang Y, Gallipoli D, Augarde C (2013) Parameter identification for elasto-plastic modelling of unsaturated soils from pressuremeter tests by parallel modified particle swarm optimization. *Comput Geotech* 48:293–303. <https://doi.org/10.1016/j.compgeo.2012.08.004>
- Lee CH, Shih KS, Hsu CC, Cho T (2014) Simulation-based particle swarm optimization and mechanical validation of screw position and number for the fixation stability of a femoral locking compression plate. *Med Eng Phys* 36(1):57–64. <https://doi.org/10.1016/j.medengphy.2013.09.005>
- Lake JJ, Duwel AE, Candler RN (2014) Particle swarm optimization for design of slotted MEMS resonators with low thermoelastic dissipation. *J. Microelectromechanical Syst* 23(2):364–371. <https://doi.org/10.1109/JMEMS.2013.2275999>
- Vosoughi AR, Gerist S (2014) New hybrid FE-PSO-CGAs sensitivity base technique for damage detection of laminated composite beams. *Compos Struct* 118(1):68–73. <https://doi.org/10.1016/j.compstruct.2014.07.012>
- Filho SLMR, Silva TAA, Vieira LMG, Panzera TH, Boba K, Scarpa F (2014) Geometric effects of sustainable auxetic structures integrating the particle swarm optimization and finite element method. *Mater Res* 17(3):747–757. <https://doi.org/10.1590/S1516-14392014005000024>

10. Kitak P, Glotic A, Ticar I (2014) Heat transfer coefficients determination of numerical model by using particle swarm optimization. *IEEE Trans Magn* 50(2):933–936. <https://doi.org/10.1109/TMAG.2013.2282409>
11. Kalatehjari R, Rashid ASA, Ali N, Hajihassani M (2014) The contribution of particle swarm optimization to three-dimensional slope stability analysis. *Sci World J* 1:2014. <https://doi.org/10.1155/2014/973093>
12. Ramdas C, Balasubramaniam K, Joshi M, Krishnamurthy CV (2008) Detection of transverse cracks in a composite beam using combined features of lamb wave and vibration techniques in Ann environment. *Int J Smart Sens Intell Syst* 1(4):970–984 (2008). <https://doi.org/10.21307/ijssis-2017-331>
13. Reddy MRS, Reddy BS, Reddy VN, Sreenivasulu S (2012) Prediction of natural frequency of laminated composite plates using artificial neural networks. *Engineering* 04(06):329–337. <https://doi.org/10.4236/eng.2012.46043>
14. Chandrasekaran M, Devarasiddappa D (2014) Artificial neural network modeling for surface roughness prediction in cylindrical grinding of Al-SiCp metal matrix composites and ANOVA analysis. *Adv Prod Eng Manag* 9(2):59–70. <https://doi.org/10.14743/apem2014.2.176>
15. Kurt HI, Oduncuoglu M (2015) Application of a neural network model for prediction of wear properties of ultrahigh molecular weight polyethylene composites. *Int J Polym Sci* 2015. <https://doi.org/10.1155/2015/315710>
16. Mohit DC, Kumar S (2015) Active vibration control of the smart plate using artificial neural network controller. *Adv Aerosp Eng* 2015:1–20. <https://doi.org/10.1155/2015/137068>
17. Dey S, Mukhopadhyay T, Spickenheuer A, Gohs U, Adhikari S (2016) Uncertainty quantification in natural frequency of composite plates—an artificial neural network based approach. *Adv Compos Lett* 25(2):43–48. <https://doi.org/10.1177/096369351602500203>
18. Guo Q, Wang S (2020) Free vibration analysis and optimal design of adhesively bonded double-strap joints by using artificial neural networks. *Lat Am J Solids Struct* 17(4):1–19. <https://doi.org/10.1590/1679-78255878>
19. Bui X-N, Muazu MA, Nguyen H (2020) Optimizing Levenberg–Marquardt backpropagation technique in predicting factor of safety of slopes after two-dimensional OptumG2 analysis. *Eng Comput* 36(3):941–952. <https://doi.org/10.1007/s00366-019-00741-0>
20. Suresh R, Joshi AG, Manjiaiah M (2021) Experimental investigation on tool wear in AISI H13 die steel turning using RSM and ANN methods. *Arab J Sci Eng* 46(3):2311–2325. <https://doi.org/10.1007/s13369-020-05038-9>
21. Schwingshackl CW, Aglietti GS, Cunningham PR (2006) Determination of honeycomb material properties: existing theories and an alternative dynamic approach. *J Aerosp Eng* 19(3):177–183. [https://doi.org/10.1061/\(ASCE\)0893-1321\(2006\)19:3\(177\)](https://doi.org/10.1061/(ASCE)0893-1321(2006)19:3(177))
22. Mujika F, Pujana J, Olave M (2011) On the determination of out-of-plane elastic properties of honeycomb sandwich panels. *Polym Test* 30(2):222–228. <https://doi.org/10.1016/j.polymertesting.2010.12.005>
23. An B, Zhao X, Zhang D (2014) On the mechanical behavior of bio-inspired materials with non-self-similar hierarchy. *J Mech Behav Biomed Mater* 34:8–17. <https://doi.org/10.1016/j.jmbbm.2013.12.028>
24. Tran P, Ngo TD, Mendis P (2014) Bio-inspired composite structures subjected to underwater impulsive loading. *Comput Mater Sci* 82:134–139. <https://doi.org/10.1016/j.commat.2013.09.033>
25. Zhang Q et al (2015) Bioinspired engineering of honeycomb structure—using nature to inspire human innovation. *Prog Mater Sci* 74:332–400. <https://doi.org/10.1016/j.pmatsci.2015.05.001>
26. Hu D, Wang Y, Song B, Dang L, Zhang Z (2019) Energy-absorption characteristics of a bionic honeycomb tubular nested structure inspired by bamboo under axial crushing. *Compos Part B Eng* 162(September 2018):21–32. <https://doi.org/10.1016/j.compositesb.2018.10.095>
27. Poli R, Kennedy J, Blackwell T (2007) Particle swarm optimization. *Swarm Intell* 1(1):33–57. <https://doi.org/10.1007/s11721-007-0002-0>

Adaptable and Robust Origami Metamaterials with Controllable Poisson's Ratio Over Large Deformations



Siva P. Vasudevan and P. Pradeep Pratapa

1 Introduction

Poisson's ratio, determined as the negative ratio of lateral and longitudinal strains in a material stretched along a single direction, is an important metric in characterizing the elastic response. For instance, properties such as shear resistance, toughness, fracture resistance, compressibility, and behavior in bending are dependent on the Poisson's ratio of a material [1]. The significance of this elastic parameter served as a motivation for earlier studies to architect materials that are tunable to a wide range of Poisson's ratio [2–4]. A majority of these developments are origami inspired. Origami metamaterials are 3D structured lattice systems obtained by folding 2D sheets about a crease pattern that acts as line hinges. Because the kinematics of origami systems are primarily governed by geometry, they can be conveniently architected for a target Poisson's ratio. Nevertheless, conventional origami systems' behavior is geometrically nonlinear, so the designed value are retained only within a narrow strain range; when deformed finitely, the Poisson's ratio and the associated mechanical properties of these systems change significantly. To overcome this limitation, some of the recent studies designed soft-material-based structures capable of displaying an almost constant value of Poisson's ratio over finite strains [5–7]. But, such systems were designed for a single target value of Poisson's ratio and therefore may require re-fabrication when the design requirement is even slightly modified. Deriving properties predominantly from geometry, existing metamaterials can also be sensitive toward geometric imperfections, if not explicitly designed for it [8, 9]. In recent work, we designed a class of hybrid origami metamaterials for constant

S. P. Vasudevan · P. Pradeep Pratapa (✉)
Indian Institute of Technology Madras, Chennai 600036, India
e-mail: ppratapa@civil.iitm.ac.in

S. P. Vasudevan
e-mail: ce19d750@smail.iitm.ac.in

Poisson's ratio, specifically in the range of -0.5 to 1.0 over a large strain of up to 200% with a minimum of 10% [10]. In the current study, we show through optimization that these systems can adapt for slight variations in the target Poisson's ratio and are further robust against minor geometric imperfections. We achieve these features by leveraging the following two properties characteristic of origami structures: (i) tunability: the ability to change the mechanics depending on the folded configuration of the system, and (ii) modularity: the ability to add (remove) compatible cells to (from) an existing pattern.

The rest of the paper is organized as follows. At first, we explain the geometry and Poisson effects in a Morph origami cell. Subsequently, we describe a hybrid Morph strip obtained by combining more than one Morph cell. Here, we also briefly discuss the optimization of hybrid Morph structure for behavior with constant Poisson's ratio over finite strains. Following this, we highlight the adaptable and robust nature of the proposed hybrid Morph systems by solving a set of optimization problems where the tunability and modularity parameters are taken as design variables. Finally, we summarize the findings and draw salient conclusions from this study.

2 Morph Origami Cell

A single Morph cell is built with four parallelogram panels meeting at a common vertex [4, 11]. Quite analogous to kite shape, the panels can be grouped into two pairs of identical sets adjacent to each other. The angle at the vertex of one pair of parallelograms is $\alpha_1 (< \pi/2)$, and that of the other pair is $\alpha_2 (< \alpha_1)$. Due to its geometry, a Morph cell can exist in two modes—the eggbox mode and the Miura mode (Fig. 1a, b). When the panels are assumed rigid, the Morph structure deforms as a single degree of freedom system, and therefore, its folded state can be described in terms of a single folding angle $\psi \geq 0$ when the mode of the Morph cell is known. The dimensional changes in the cell as it folds–unfolds give rise to an apparent Poisson effect which varies with the folded state ψ . Interestingly, and unlike other origami patterns, a Morph cell can display both positive and negative Poisson's ratio by switching between eggbox and Miura modes, respectively [4]. At any reference state $\psi = \psi_0$, a Morph cell in the eggbox mode has a positive Poisson's ratio, which increases with increase in ψ . In contrast to this, the Miura mode has a negative Poisson's ratio at the reference configuration ψ_0 , and the value becomes more negative for $\psi > \psi_0$. The Poisson's ratio ν_s of a single Morph cell is expressed as [10]

$$\nu_s(\psi) = -\left(\frac{\sin(\psi_0/2)}{\sin(\psi/2) - \sin(\psi_0/2)}\right) \left[\left(\frac{\cos(\psi_0/2)}{\cos(\psi/2)}\right) \left(\frac{\zeta(\psi) \pm \xi(\psi)}{\zeta(\psi_0) \pm \xi(\psi_0)}\right) - 1 \right], (1)$$

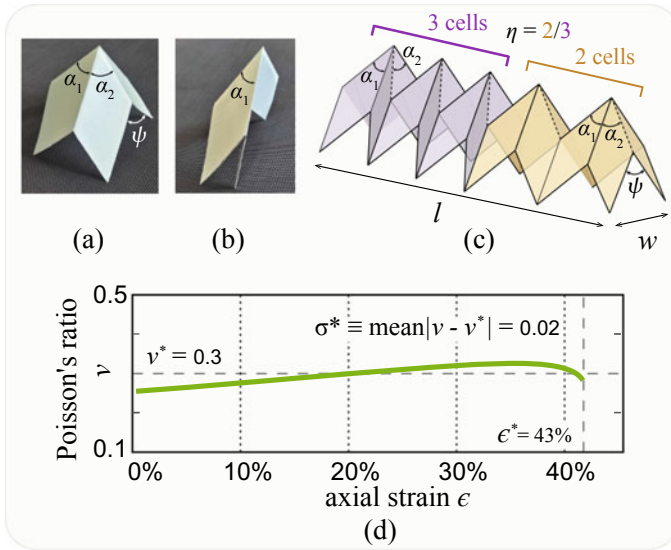


Fig. 1 A hybrid origami system built as a compatible combination of two sets of cells exhibiting contrasting Poisson effects displays strain-independent Poisson’s ratio over large deformations [10]. **a** Eggbox mode of Morph cell. **b** Miura mode of Morph cell. **c** Hybrid Morph obtained by combining the two modes of the Morph cell. **d** Variation of Poisson’s ratio with strain in hybrid Morph optimized for constant Poisson’s ratio of 0.3 over strain of 43%

where ‘+’ is for the eggbox mode and ‘-’ is for the Miura mode, and the intermediate variables ζ and ξ are expressed as

$$\zeta(\psi) = \cos \alpha_2 \sqrt{\cos^2(\psi/2) - \cos^2 \alpha_1} \tag{2}$$

$$\xi(\psi) = \cos \alpha_1 \sqrt{\cos^2(\psi/2) - \cos^2 \alpha_2} \tag{3}$$

3 Hybrid Morph

The kinematics of Morph origami allow for a compatible deformation letting any proportion say η , of the cells in eggbox mode to combine with that in the Miura mode to form a hybrid structure as shown in Fig. 1c [11]. Since the Poisson effects due to cells in eggbox mode and Miura mode are contrasting to each other, the global Poisson’s ratio ν_h of the hybrid strip vary less with deformation angle ψ when compared to the variation of Poisson’s ratios in the individual cells. When the mode of each cell is fixed, the hybrid Morph can be described using a single current state parameter ψ , which equals ψ_0 in the reference state. The Poisson’s ratio for the strip is expressed as [10]

Table 1 Optimized geometric parameters of hybrid Morph for constant Poisson’s ratio of 0.3 over strain of 43% [10]

α_1^*	α_2^*	ψ_0^*	η^*
39.15°	30.36°	41.96°	2/3

$$v_h(\psi) = -\left(\frac{\sin(\psi_0/2)}{\sin(\psi/2) - \sin(\psi_0/2)}\right)\left(\frac{(\eta + 1)l_1(\psi) + (\eta - 1)l_2(\psi)}{(\eta + 1)l_1(\psi_0) + (\eta - 1)l_2(\psi_0)} - 1\right), \tag{4}$$

where

$$l_1(\psi) = a_1\sqrt{1 - \cos^2\alpha_1\sec^2(\psi/2)}, \tag{5}$$

$$l_2(\psi) = a_2\sqrt{1 - \cos^2\alpha_2\sec^2(\psi/2)}. \tag{6}$$

By taking the objective function as

$$\sigma(\eta, \alpha_1, \alpha_2, \psi_0) = \int_{\psi_0}^{\psi^*} (v_h(\psi) - v^*)^2 \frac{\cos(\psi/2)}{2\sin(\psi_0/2)} d\psi, \tag{7}$$

we had shown recently that the ratio of cells in each mode η , the panel angles α_1 and α_2 , and the initial deformed state ψ_0 can be optimized for the hybrid structure to display a constant Poisson’s ratio at the target value v^* , which is within the range of -0.5 to 1.0 , over large strains of up to 200% with a minimum of 10% [10]. The constraints on the optimization problem are

$$\psi^* \leq 2\alpha_2, \tag{8}$$

$$\cos\alpha_1/\cos\alpha_2 \leq 0.9, \tag{9}$$

where ψ^* is the folding angle of the strip corresponding to the target strain ϵ^* . The first constraint ensures that the desired strain ϵ^* is attainable by the hybrid Morph structure. The second constraint prevents α_2 from getting too close to α_1 , which can otherwise limit the level of extreme folded state of the structure in the Miura mode. In the subsequent sections, we illustrate the adaptability and the robustness of these designs through a case study. Consider a hybrid Morph structure designed to exhibit Poisson’s ratio of $v^* = 0.3$ over a target strain $\epsilon^* = 43\%$. The mean deviation of the Poisson’s ratio v_h from the target value v^* is estimated as $\sigma^* = 0.02$ (Fig. 1d) [10]. The geometric parameters of this optimized structure are summarized in Table 1.

4 Optimization for Adaptability

We observe from Fig. 1d that the designed structure performs well with minimal deviation, $\sigma = 0.02$, for the considered target Poisson's ratio of $\nu^* = 0.3$. But, when there is a minor change in the design requirement, say the target Poisson's ratio is modified as $\nu_{\text{mod}}^* = 0.25$; the deviation of ν_h from the target value ν_{mod}^* increases significantly to about 0.045 in the original design (Fig. 2a). Therefore, such changes in the design requirements typically demand for a re-fabrication of the entire structure. Origami metamaterials can offer better flexibility in this aspect as they allow for a change in the initial configuration described by ψ_0 (due to tunability), and further permit addition/removal of cells (due to modularity), allowing for a change in the η value. Leveraging on these aspects, we study the adaptability of the existing design by formulating an optimization problem with an objective to minimize the error σ between ν_h and the modified target value ν_{mod}^* . Here, in addition to the input parameters ν_{mod}^* and ϵ^* , panel angles α_1^* and α_2^* are also kept constant; the design variables are ψ_0 and η . The objective to be minimized is

$$\sigma(\psi_0, \eta) = \int_{\psi_0}^{\psi^*} (\nu_h(\psi) - \nu_{\text{mod}}^*)^2 \frac{\cos(\psi/2)}{2 \sin(\psi_0/2)} d\psi. \quad (10)$$

We solve the optimization problem using the interior-point algorithm of the *fmincon* sub-routine in-built in MATLAB. The results are summarized in the form of graphs in Fig. 2a. We observe (from the solid line in the plot) that when ψ_0 and η are allowed to vary (possible due to the tunability and modularity features of origami systems), the error measure σ is significantly reduced for values of ν_{mod}^* close to $\nu^* = 0.3$, in comparison to the error in the original design (represented by the dashed line of the plot). For instance, for $\nu_{\text{mod}}^* = 0.25$, σ drops to about 0.015 from a value of 0.04 observed in the originally designed system. The findings highlight the unique adaptability of the proposed origami structures, unlike designs from most of the studies in the literature, which require a re-fabrication of the lattice.

5 Optimization for Robustness

Deriving properties based on geometry, mechanical metamaterials are prone to be sensitive toward geometric imperfections, for example, as observed in topology optimized architectures [8, 9]. We observe a similar behavior in our proposed designs—when α_1 and α_2 are perturbed slightly with all other parameters put constant, the error σ can increase drastically (Fig. 2b). This sensitive behavior can be a source of a challenge when the system is manufactured for applications. To overcome this issue in the proposed origami structures, we again take advantage of the tunability and modularity aspects of the origami systems. Thereby, we set up an optimization

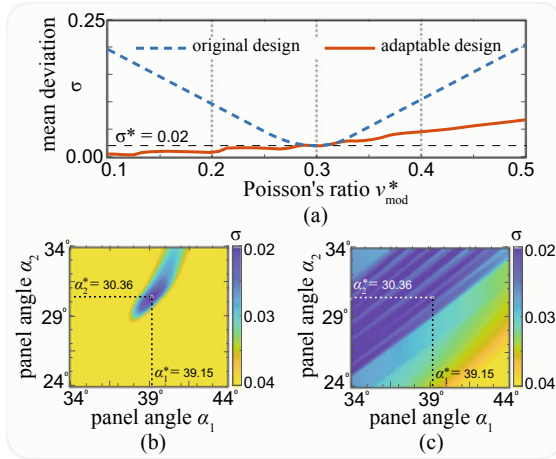


Fig. 2 Illustration of robustness and adaptability in proposed origami metamaterials with controllable Poisson’s ratio over large deformations. **a** Variation of error σ with modified target Poisson’s ratio values ν_{mod}^* in original design and that modified for adaptability. **b** Error σ contours for varying panel angles (α_1, α_2) in the original design. **c** Reduced error σ values for varying panel angles (α_1, α_2) in the design modified for robustness

problem to minimize the error σ between ν_h and the target value ν^* for perturbed values of α_1 and α_2 ; here again, the parameters ψ_0 and η are taken as design variables. The objective function here is the same as that given by Eq. 7, except for the difference in the number of design variables. The problem is solved similar to that described in previous sections, and the results are graphically illustrated in Fig. 2c. By comparing Fig. 2b, c, we observe that σ reduces drastically for any minor imperfections (of about 5°) in the panel angles α_1 and α_2 . The results imply that the designed system can be altered to have a different η and a new reference state (described by ψ_0) once the perturbed panel angles are known after fabrication. We thereby illustrate the robustness of the designed system to allow for small manufacturing errors in the modified structure.

6 Summary and Conclusions

In summary, we demonstrated the adaptability and robustness of a class of origami metamaterials with near-constant Poisson’s ratio over large strains. Due to tunability and modularity aspects, the origami systems from the present study were shown to be easily re-configurable for any slightly modified design requirements. This feature is unique to the proposed origami metamaterials, as other systems typically require a re-fabrication when the target Poisson’s ratio is changed. Moreover, origami designs from this study were found to be capable of being altered to display

reduced sensitivity toward geometric imperfections. These aspects of the proposed metamaterials provide increased control on the desired response toward Poisson's ratio. We expect the current study to open new avenues in the design of 2D lattice metamaterials with multi-functional characteristics.

Acknowledgements Siva P. Vasudevan acknowledges the support from the fellowship offered by the Prime Minister's Research Fellows (PMRF) Scheme, Ministry of Human Resource Development, Government of India. Phanisri P. Pratapa acknowledges the support from the Indian Institute of Technology Madras through the seed grant and the Science & Engineering Research Board (SERB) of the Department of Science & Technology, Government of India, through award SRG/2019/000999. The information provided in this paper is the sole opinion of the authors and does not necessarily reflect the views of the sponsors or sponsoring agencies.

References

1. Greaves GN, Greer AL, Lakes RS et al (2011) Poisson's ratio and modern materials. *Nat Mater* 10(11):823–837
2. Schenk M, Guest SD (2013) Geometry of Miura-folded metamaterials. *Proc Natl Acad Sci* 110(9):3276–3281
3. Wei ZY, Guo ZV, Dudte L et al (2013) Geometric mechanics of periodic pleated origami. *Phys Rev Lett* 110(21):215501
4. Pratapa PP, Liu K, Paulino GH (2019) Geometric mechanics of origami patterns exhibiting Poisson's ratio switch by breaking mountain and valley assignment. *Phys Rev Lett* 122(15):155501
5. Clausen A, Wang F, Jensen JS et al (2015) Topology optimized architectures with programmable Poisson's ratio over large deformations. *Adv Mater* 27(37):5523–5527
6. Liu J, Zhang Y (2018) Soft network materials with isotropic negative Poisson's ratios over large strains. *Soft Matter* 14(5):693–703
7. Wang F (2018) Systematic design of 3D auxetic lattice materials with programmable Poisson's ratio for finite strains. *J Mech Phys Solids* 114:303–318
8. Sigmund O (2009) Manufacturing tolerant topology optimization. *Acta Mech Sin* 25(2):227–239
9. Wang F, Sigmund O, Jensen JS (2014) Design of materials with prescribed nonlinear properties. *J Mech Phys Solids* 69:156–174
10. Vasudevan SP, Pratapa PP (2021) Origami metamaterials with near-constant Poisson functions over finite strains. *J Eng Mech* 147(11):04021093
11. Pratapa PP, Liu K, Vasudevan SP et al (2021) Reprogrammable kinematic branches in tessellated origami structures. *J Mech Robot* 13(3):031004

Design and Optimization of Bio-inspired Fluidic Diode for Wave Energy Harvesting System



Doddamani Hithaish and Abdus Samad

1 Introduction

An oscillating water column (OWC) is a well-studied wave energy converter (WEC), which contains a power take-off device (typically a turbine-generator assembly) and an air chamber [1] (Fig. 1). The air chamber has an opening submerged in seawater while the other end connects to a duct. The approaching ocean waves enter through the opening and compress the air inside the chamber. A couple of air turbines can be arranged in the duct called a twin turbine or turbine duo (Fig. 2) [2, 3]. These turbines extract energy from the air, so they are called air turbines. The compressed air tries to escape through the duct, which energizes one turbine while another restricts the airflow. Similarly, the receding wave sucks air through the duct, and the above operation of the turbines reverses. The performance of this unit is affected by the incomplete flow blockage [4]. Researchers have proposed using a fluidic diode (FD) that offers variable resistance to flow with the turbine duo. It forces more airflow through one turbine, restricting the airflow of the other turbine [5, 6]. The performance parameter of an FD is diodicity (Eq. (1)) which should be higher for better performance.

It is defined as:

$$\text{Diodicity}(\Psi) = \frac{\text{Pressure drop } (\Delta p) \text{ for reverse flow direction } [2 - 1]}{\text{Pressure drop } (\Delta p) \text{ for forward flow direction } [1 - 2]} \quad (1)$$

There are ample designs proposed for different applications. Figure 3 shows a few FD models proposed for the WEC. From the literature on FD, it was inferred that the problem and design requirements guide the design of the FD [7]. Hence, new designs are being proposed by the designer based on the application. In this article, an FD is proposed for the WEC application inspired by the shark fish shape and is

D. Hithaish · A. Samad (✉)

Department of Ocean Engineering, IIT Madras, Chennai, India
e-mail: samad@iitm.ac.in

Fig. 1 Oscillating water column

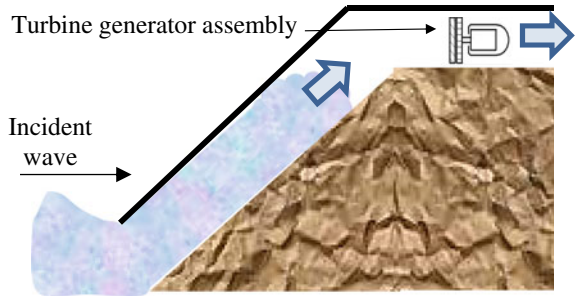


Fig. 2 Schematic of turbine arrangements

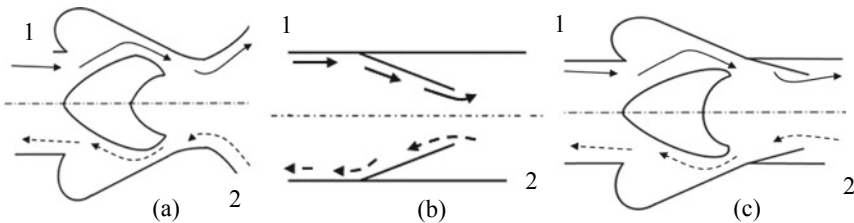
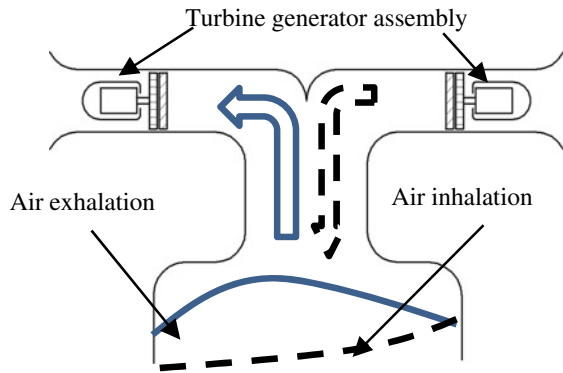


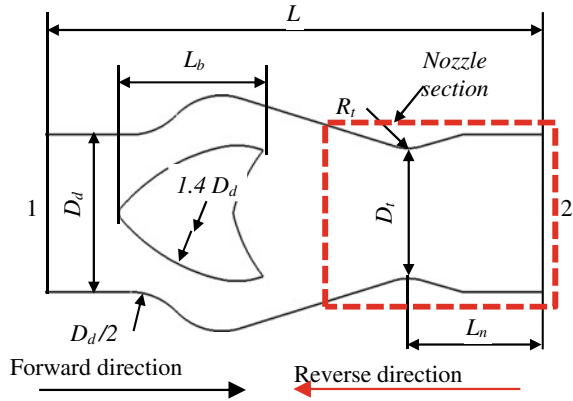
Fig. 3 Schematic of the FD **a** bluff body type [6], **b** nozzle type [5], **c** cascade bluff body type [8]

called a fish fluidic diode (FFD). The model is studied numerically by solving three-dimensional Reynolds Navier–Stokes (RANS) equations, and its shape is optimized for higher performance using a surrogate model. The article also presents a detailed flow analysis of the model and the optimization procedure followed for the study.

2 Geometrical Details

Figure 4 shows the geometrical details of the FFD. Its outer shape is similar to the

Fig. 4 Schematic of the FH-FD



streamlined body of a shark fish which is a fusiform shape, and a bluff body is placed at the center (length of the bluff body (L_b) = 200 mm and diameter of the duct (D_d) = 240 mm). The change in the internal shape of the FFD affects the flow behavior, which offers a variable resistance to the flow, thereby altering its performance. The increment in the diodicity of an FD can restrict flow reversal better. The internal shape is needed to be optimized for achieving higher diodicity.

3 Methodology

The optimization framework followed for the present study is as follows.

Formulation of objective function: The objective function of the study is to maximize the diodicity (Eq. 1) of the FFD.

1. *Selection of design variables:* The fluid flow characteristics of the FFD are affected by its shape. The geometrical parameters such as length of the bluff body (L_b), throat diameter (D_t), and the length of the nozzle (L_n/L), which constitute its shape, are chosen as design variables.
2. *Design of Experiments (DOE):* It provides the effect of the geometrical variables on the performance of the model. For the study, the full factor method was employed to obtain the sample points. Later, the performance of the model is evaluated at these points.
3. *Construction of surrogate model:* An approximate model (surrogate model) replicates the behavior of the objective function similar to the numerical simulation or experiments. The artificial neural network (ANN) is one of the surrogate models that a biological computer algorithm trained using the set of inputs and can predict the output. A radial basis neural network, which is one of the variants of the ANN, is used for the study.

Table 1 Estimation of uncertainty due to discretization

Parameter	Values	
Number of cells (10^6)	$N_1/N_2/N_3$	6.063, 2.599, 1.151
Grid refinement factor	r_{21}, r_{32}	1.31, 1.33
Performance parameters	$\varphi_1, \varphi_2, \varphi_3$	183.15, 184.24, 190.51
Apparent order	P	6.18
Extrapolated values	$\theta_{\text{ext}}^{21}, \theta_{\text{ext}}^{32}$	182.89, 182.91
Approximate relative error	e_a^{21}, e_a^{32}	0.005951, 0.03403
Extrapolated relative error	$e_{\text{ext}}^{21}, e_{\text{ext}}^{32}$	0.00137, 0.00725
GCI	$\text{GCI}_{\text{fine}}^{21}, \text{GCI}_{\text{coarse}}^{32}$	0.170, 0.90%

4. *Searching optimal point and verification:* The optimum point is found using the sequential quadratic programming (SQP) algorithm. The study uses an in-house optimization code that was earlier used to optimize the other engineering problems [9–13].

4 Results and Discussions

4.1 Numerical Validation

The grid convergence index (GCI) [14] was used to arrive at the optimum number of mesh elements required for the numerical investigation. Based on the GCI calculations (Table 1), the change in the GCI values for the successive grid is less than 3% ensuring that grid convergence was achieved. The medium grid was retained for further analysis. The commercial computational fluid dynamic software ANSYS FLUENT 16.2 was used for the study. The flow parameters were obtained numerically, solving the three-dimensional Reynolds Navier–Stokes equations with the realizable $k - \varepsilon$ turbulence closure model. Figure 5 shows the validation of the numerical model with the experimental results of the cascade body type FD.

4.2 Optimization Results

Figure 6 shows the comparison of the diodicity of both models for the $0.35 \text{ m}^3/\text{s}$ flow rate. The diodicity of the optimized model improved by 185% than the initial (base) model. Figure 7 shows the superimposing of the initial model over the optimized

Fig. 5 Numerical validation

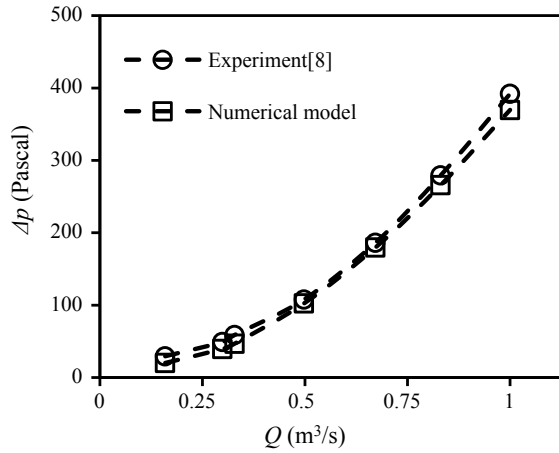


Fig. 6 Diodicity of the base and optimized FD

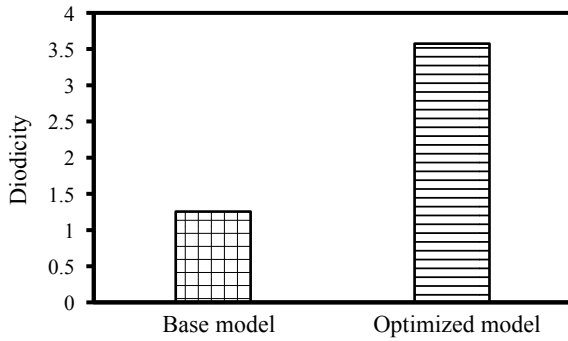
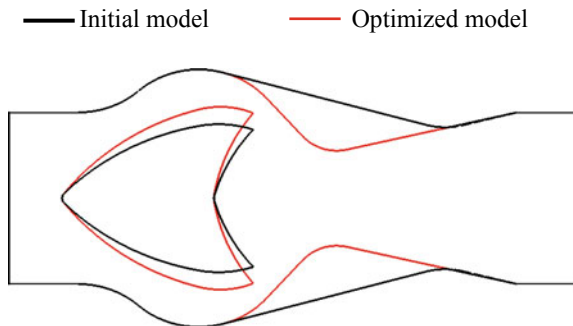


Fig. 7 Superimpose of the initial and optimized model



model. The nozzle throat diameter of the optimized case is smaller than the initial model and is placed near the bluff body.

4.3 Fluid Flow Analysis

To understand the fluid flow characteristic inside the FD, the streamline and pressure contours are drawn at the mid-section along the length of the model for $0.35 \text{ m}^3/\text{s}$. Consider the streamline contour (Fig. 8) fluid flowing in a forward direction smoothly passes over the bluff body. Later, it separates at the end of the bluff body due to the adverse pressure gradient, generating a wake region (highlighted in red circle). Finally, the fluid leaves the nozzle section smoothly. The above flow pattern is similar for both models. Like the forward direction, consider the reverse direction (Fig. 8). Flow enters through the nozzle section where it gets diffused, offering additional resistance to the incoming fluid. This pattern is similar for both models. The fluid leaving the nozzle experience the presence of the bluff body. The fluid tries to follow the shape of the bluff body. The sharp change in the shape of the bluff body of the optimized model causes an adverse pressure gradient on the surface, which causes the fluid to separate and detach on the surface, forming the vortex pattern (highlighted in red circle).

Figure 9 shows the static pressure distribution inside the FD. It can be seen that fluid experiences a higher pressure drop around the bluff body for both models in the forward direction compared to other sections. For reverse flow direction, both the models experience a higher pressure drop at the nozzle section. The optimized model experiences a higher pressure drop in reverse than the base model. Hence, the diodicity of the optimized model is higher than the base model.

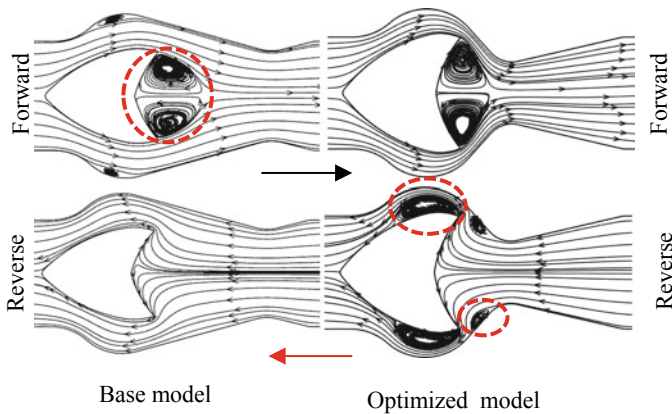


Fig. 8 Streamline contours

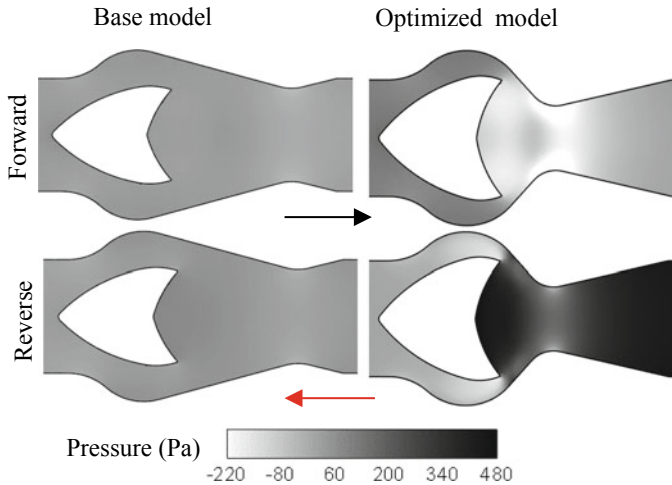


Fig. 9 Pressure contours

5 Conclusions

A fluidic diode (FD) model is proposed for the wave energy system. The FD was studied numerically using commercial fluid dynamics software. The shape of the model was optimized for higher performance using a surrogate model. The optimized model has a diodicity of 3.54. The nozzle throat diameter of the optimized case has reduced from the 37.5% to the initial design, which offers higher resistance to the fluid in the reverse low. Among all the design parameters, the throat diameter of the nozzle has more effect on the performance of the FD.

References

1. Das TK, Halder P, Samad A (2017) Optimal design of air turbines for oscillating water column wave energy systems: a review. *Int J Ocean Clim Syst* 8(1):37–49
2. Jayashankar V, Anand S, Geetha T, Santhakumar S, Jagadeesh Kumar V, Ravindran M, Setoguchi T, Takao M, Toyota K, Nagata S (2009) A twin unidirectional impulse turbine topology for OWC based wave energy plants, *Renew Energy* 34(3):692–698
3. Takao M, Takami A, Okuhara S, Setoguchi T (2011) A twin unidirectional impulse turbine for wave energy conversion. *J Therm Sci* 20(5):394–397
4. Pereiras B, Valdez P, Castro F (2014) Numerical analysis of a unidirectional axial turbine for twin turbine configuration. *Appl Ocean Res* 47:1–8
5. Okuhara S, Sato H, Takao M, Setoguchi T (2014) Wave energy conversion: effect of fluidic diode geometry on the performance. *Open J Fluid Dyn* 4:433–439
6. Dudhgaonkar PV, Jayashankar V, Jaliha P, Kedarnath S, Setoguchi T, Takao M, Nagata S, Toyota K (2011) Fluidic components for oscillating water column based wave energy plants. In: ASME-JSME-KSME 2011 joint fluids engineering conference, AJK 2011, Hamamatsu, Shizuoka, JAPAN, 24–29 July 2011

7. Thomas SK, Muruganandam TM (2018) A review of acoustic compressors and pumps from fluidics perspective. *Sens Actuators A* 283:42–53
8. Okuhara S, Ashraful Alam MM, Takao M, Kinoue Y (2019) Performance of fluidic diode for a twin unidirectional impulse turbine. In: IOP conference series: earth and environmental science 2019
9. Badhurshah R, Samad A (2015) Multiple surrogate based optimization of a bidirectional impulse turbine for wave energy conversion. *Renew Energy* 74:749–760
10. Badhurshah R, Dudhgaonkar P, Jaliha P, Samad A (2018) High efficiency design of an impulse turbine used in oscillating water column to harvest wave energy. *Renew Energy* 121:344–354
11. Das TK, Samad A (2020) Influence of stall fences on the performance of Wells turbine. *Energy* 194:116864
12. Kumar PM, Seo J, Seok W, Rhee SH, Samad A (2019) Multi-fidelity optimization of blade thickness parameters for a horizontal axis tidal stream turbine. *Renew Energy* 135:277–287
13. Bellary SAI, Adhav R, Siddique MH, Chon BH, Kenyery F, Samad A (2016) Application of computational fluid dynamics and surrogate-coupled evolutionary computing to enhance centrifugal-pump performance. *Eng Appl Comput Fluid Mech* 10(1):172–182
14. Celik IB, Ghia U, Roache PJ, Freitas CJ, Coleman H, Raad PE (2008) Procedure for estimation and reporting of uncertainty due to discretization in CFD applications. *J Fluids Eng Trans ASME* 130(7):0780011–0780014

Prediction of the Propagation of Fatigue Cracks for a Beam Specimen in Four-Point Bending Using CASCA and FRANC2D



H. M. Vishwanatha, Pawan Kumar, Anshuman Das, Ashish Agrawal, Ch. Satheesh Kumar, and B. B. Verma

1 Introduction

Aluminum 5754 alloy is an alloy in the wrought Al–Mg alloy family that possesses significant weldability and is widely used in automotive, rivets making, tread plates engineering, and shipbuilding industries [1]. In regular engineering operations, various kinds of loads are acting on shipbuilding structures, rivets, and other engineering structures made of aluminum 5754 alloy. These loadings can be tension,

H. M. Vishwanatha

Department of Mechanical and Manufacturing Engineering, Manipal Institute of Technology Manipal, Manipal Academy of Higher Education, Manipal, Karnataka 576104, India

P. Kumar (✉)

Department of Engineering Metallurgy, Faculty of Engineering and the Built Environment, University of Johannesburg, Johannesburg 2028, South Africa

e-mail: pkumar@uj.ac.za

A. Das

Department of Mechanical Engineering, DIT University, Dehradun 248009, India

e-mail: anshuman.das@dituniversity.edu.in

A. Agrawal

Department of Mechanical Engineering, Madhav Institute of Technology and Science, Gwalior, Madhya Pradesh 474005, India

e-mail: ashish.agr@mitsgwalior.in

Ch. Satheesh Kumar

Department of Mechanical Engineering, Madanapalle Institute of Technology & Science, Madanapalle, Andhra Pradesh 517325, India

e-mail: drsateeshkumarch@mits.ac.in

B. B. Verma

Department of Metallurgical and Materials Engineering, National Institute of Technology Rourkela, Rourkela 769008, India

e-mail: bbverma@nitrkl.ac.in

compression, internal pressure, bending, or any combination of all. These dissimilar types of loading conditions may initiate a new crack and/or propagate an existing crack. Therefore, the prediction of fatigue life of such an important class of alloy is important. Qiao Yaxia et al. investigated fatigue crack growth in aluminum 5754 alloy using standard compact tension specimens [2]. The same studies were also done by Lukacs et al. using the staircase method and FCG limit curves [3]. Meilinger et al. studied crack propagation in a different direction of FSW joints made of such alloy [4]. The various researchers also investigated fatigue crack growth using an experimental route [5–7]. The experimental approach for predicting the crack is time consumables and/or required destructive testing methods. However, analytical methods can be used to predict fatigue crack propagation based on the finite element method and applying the boundaries conditions. The three-dimensional (3D) partial circumferential cracks require multifaceted computation; however, 3D problems can be simulated using 2D hypothesis using deflection and stress intensity factors the same while keeping the sample thickness to be same. Kumar et al. used an extended finite element method to simulate quasi-static crack growth of aluminum 5754 alloy [8]. In context to these investigations, Kumar et al. predicted the fatigue crack growth in circumferential cracked pipes of steel using CASCA and FRANC2D [9]. However, this hypothesis was not used for beam specimens of aluminum. In the present investigation, an attempt has been made to predict the propagation of the fatigue cracks for a beam specimen in four-point bending using CASCA and FRANC2D.

2 Materials and Methods

The alloy under investigation was aluminum 5754. The chemical composition and mechanical properties are shown in Tables 1 and 2, respectively. The beam samples having a cross-section of $25 \times 25 \text{ mm}^2$, span length of 300 mm, and notch length of 2.70 mm (at the center) were subjected to four-point bending using an ultimate tensile strength (UTM) testing machine INSTRON 8800. The samples were tested up to a large-scale deformation with periodic loading and unloading. It leads to the beach sign created on the edge. The load had a sine wave shape. The load range was

Table 1 Chemical composition of the material

Element	Mn	Fe	Mg	Si	Al
Weight %	0.50	0.40	2.60–3.20	0.4	Balance

Table 2 Mechanical properties of the material

Mechanical property	Yield strength (MPa)	Shear strength (MPa)	Ultimate tensile strength (MPa)	Poison's ratio
Value	276	160	580	0.34

on the order of 7.8 kN (below the elastic limit of the beam material) at a load ratio of 0.3 for the slit dimensions. It was confirmed that the crack growth was in a thick elastic state. A load of 7.8 kN was applied to calculate the number of cycles to failure with the corresponding stress intensity factor (SIF).

3 Results and Discussion

The four-point bending test was done using INSTRON 8800 apparatus; the experimental crack length corresponding to the number of cycles is shown in Fig. 1. The central section of the sample was confined pre-notched which was imperiled to pure bending. The experimental log da/dN data conforming to log K is shown in Fig. 2. The stress intensity factor was calculated using below empirical formula below [10].

Stress intensity factor

$$K = \frac{6M}{BW^2}(\pi a)^{0.5} * f(a/w)\pi r^2 \tag{1}$$

$$f(a/w) = 0.8 - 1.7(a/w) + 2.4(a/w)^2 + \frac{0.66}{(1 - \frac{a}{w})^2} \tag{2}$$

where

- M maximum bending moment
- B depth of specimen
- W width of specimen

Fig. 1 Crack length versus number of cycles (experimental)

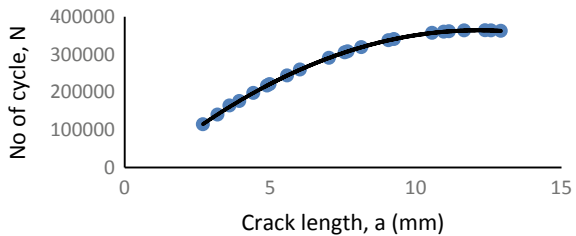
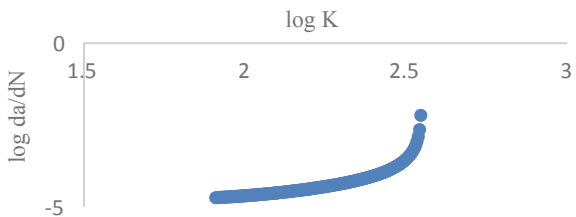


Fig. 2 Log da/dN versus log K (experimental)



a crack length.

The contemporary premise was to predict the “propagation of an existing crack” in beam specimen using finite element methods. The stiffness of a three-dimensional beam was equated with a proposed two-dimensional model using the stiffness and stress intensity quantification approach. FEM simulation was performed using a beam geometry design of the desired dimension. It was created with a preprocessor, and a grid pattern was created for it. The generated network is saved in the preprocessor and can be reopened in FRANK2D for the simulation. The boundary condition was determined and appropriate material properties/parameters were generated for the beam sample following the text. Next, it was required to reformulate the stiffness matrices of the elements. This was done using the ELEM STIFF option. The next step was to define the boundary conditions. Once boundary conditions were provided, loads were given by selecting point loading. The corresponding loading values were then entered and the loading point was determined for both simulations. Then, a stress analysis was performed. This provided an answer that summarized the size of the model and the time required for analysis. After analysis, the boundary conditions were again validated. The post-treatment option was then selected, followed by the outline option which provided colored stress charts to indicate main tensile stress, effective stress, and shear stress. The variance of the stress intensity factor concerning the slit length was plotted by FRANC2D for the beam dimensions, using both methods and compared to experimental data. The S–N curve for simulated data was plotted, and compared with experimental data under four-point bending loading conditions. Also, a graph of stress intensity range versus crack growth rate in logarithmic scale was compared. It was observed experimental and predicted results were in agreement. The generated mesh using CASCA, the deformed mesh using boundaries conditions, crack initiation and crack propagation is shown in Figs. 3, 4, 5, and 6, respectively.

The experimental crack length corresponding to the number of cycles was compared using FRANC2D modeling and the trend showed that the predicted results showed a similar trend as experimental as shown in Fig. 7.

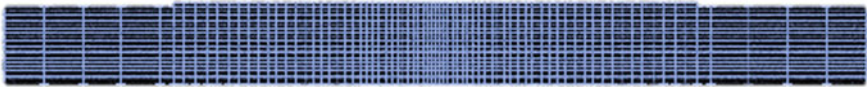


Fig. 3 Mesh generated in CASCA

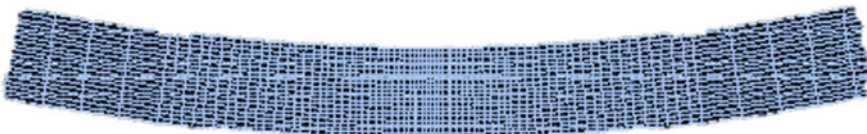


Fig. 4 Deformed mesh after applying boundaries conditions

Fig. 5 Crack initiation in the beam

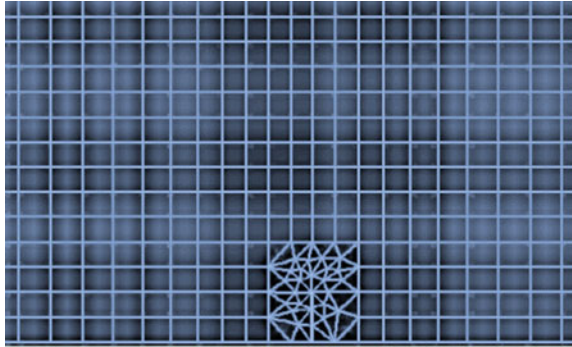


Fig. 6 Crack propagation in the beam

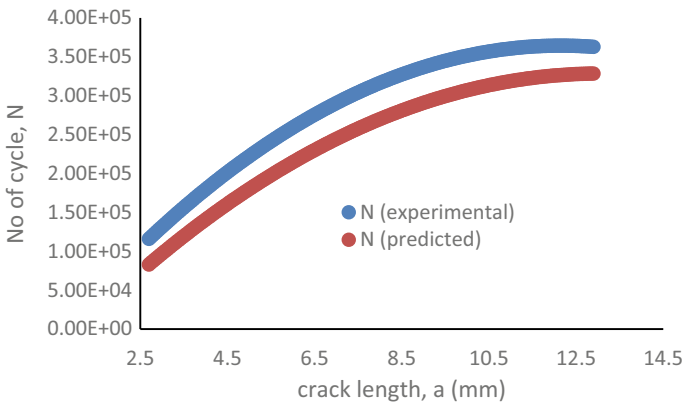
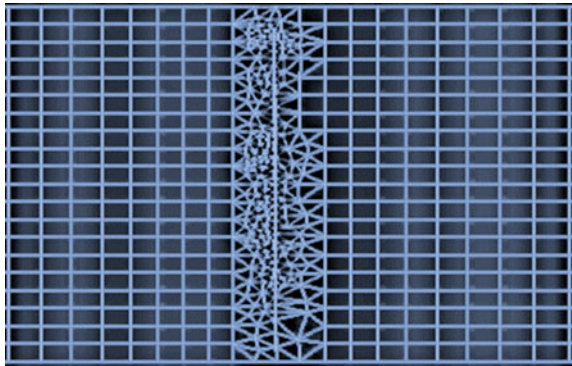


Fig. 7 Experiment and predicted crack length-number of cycles data

4 Conclusion

The predicted results using FRANC2D showed agreement with the experimental data obtained under bending for beam specimen replicates the typical nature of fatigue crack propagation. The constants were found to be in the range of ASTM standards. It was also observed a nearly constant or marginally increasing slope of crack growth rate versus stress intensity range which indicated that crack propagation falls in the region-II. The simulated results using FRANC2D simulation methods were comparable to the experimental data generated. However, the prediction can be improvised using more appropriate boundary conditions near the crack tip.

References

1. Rudawska A, Wahab MA (2019) The effect of cataphoretic and powder coatings on the strength and failure modes of EN AW-5754 aluminium alloy adhesive joints. *Int J Adhes Adhes* 89:40–50
2. Qiao Y et al (2020) Fatigue crack growth properties of AA 5754 aluminum alloy gas tungsten arc welding and friction stir welding joints. *J Mater Eng Perform* 29(4):2113–2124
3. Lukács J, Meilinger A, Pósalaky D (2017) Fatigue curves for aluminium alloys and their welded joints used in automotive industry. *Mater Sci Forum* 885
4. Meilinger Á, Lukács J (2014) Characteristics of fatigue cracks propagating in different directions of FSW joints made of 5754-H22 and 6082-T6 alloys. *Mater Sci Forum* 794
5. Tran V-X, Pan J, Pan T (2008) Fatigue behavior of aluminum 5754-O and 6111-T4 spot friction welds in lap-shear specimens. *Int J Fatigue* 30(12):2175–2190
6. Tran V-X, Pan J, Pan T (2010) Fatigue behavior of spot friction welds in lap-shear and cross-tension specimens of dissimilar aluminum sheets. *Int J Fatigue* 32(7):1022–1041
7. Kumar P, Singh A (2010) Experimental and numerical investigation of strain rate effect on low cycle fatigue behaviour of AA 5754 alloy. *IOP Conf Ser: Mater Sci Eng* 346(1)
8. Kumar P, Pathak H, Singh A (2021) Fatigue crack growth behavior of thermo-mechanically processed AA 5754: experiment and extended finite element method simulation. *Mech Adv Mater Struct* 28(1):88–101
9. Kumar P et al (2020) Prediction of the propagation of fatigue cracks in part-through cracked pipes with CASCA and FRANC2D. *Trans Indian Inst Metals*, 1–4
10. Tarafder S, Tarafder M, Ranganath VR (1994) Compliance crack length relations for the four-point bend specimen. *Eng Fract Mech* 47(6):901–907

Topology Optimization

Topology Optimization of Vehicle Components for Nonlinear Load Cases



Rajapandian Ramamoorthy

1 Introduction

In the early 1980s, the topology optimization-based conceptual design is explored with an iterative process for the best positioning of elements on a limited volume of the structural domain. In order to obtain the optimized design through minimum or maximum of specified objective, this optimization process symmetrically finds the material distribution based on load path.

The traditional gradient-based method incurs more variables for the performance of the optimization process. This brings attention to computational techniques to arrive at the optimal material distribution which was first introduced by Bendsoe and Kikuchi [1]. Considering the assumption of elastic material properties, linear deformations, and static loading conditions, topology optimization is used for simple problems at inception stages which can be found in the literature by Bendsoe and Sigmund [2], Rozvany [3], and Eschenauer and Olhoff [4].

2 Problem Definition

The main objective of topology optimization is to find the maximum use of the material. In most linear static problems, regulatory compliances and strain energy density are generally used as an objective. In the case of safety crashworthiness simulations, the dynamic behavior of the structure should absorb maximum energy which ensures the structural integrity and limits the peak load transmission to the occupants. The

R. Ramamoorthy (✉)
Tata Consultancy Services, Bangalore, India
e-mail: rajapandian.ramamoorthy@gm.com

© The Author(s), under exclusive license to Springer Nature Singapore Pte Ltd. 2023
P. Pradeep Pratapa et al. (eds.), *Advances in Multidisciplinary Analysis and Optimization*,
Lecture Notes in Mechanical Engineering,
https://doi.org/10.1007/978-981-19-3938-9_33

309

purpose of obtaining uniform energy density in the structure is proposed and formulated by Patel [5] as an objective for optimization and mass is constrained. Also, the conceptual design of the fully stressed and uniform strain energy method (Haftka and Gurdal [6]; Patnaik and Hopkins [7]) is well established in the literature for linear static problems. The optimization problem is defined as below,

$$\min_x \sum_{i=1}^N \sum_{j=1}^L (w_j U_j(x_i) - U_i^*) \quad (1)$$

subject to:

$$\sum_{i=1}^N \rho(x_i) V_i \leq M^* \quad (2)$$

$$x_{\min} \leq x_i \leq 1.0$$

where represents the internal energy density of the i th element, is the volume of the i th element, U^* represents an internal energy density set point, and there are L load cases. In general, density-based approach is one of the methods to define the design variable x for each cell with its own material model. The material properties are interpolated from the solid isotropic material with penalization (SIMP [6]) model as shown below,

$$\rho(x) = x \rho_0 \cdot E(x) = X^p E_0 \cdot \sigma(x) = X^q \sigma_0 \cdot E_h(X) = X^q E_{h0} \quad (3)$$

The subscript of ‘0’: base material properties. The design variable x as relative density which varies from ‘0’ to ‘1’, where ‘0’ represents void and ‘1’ represents the whole material availability. Refer Bendsoe and Sigmund [2] and Patel [5] for further details of material model parameterization. The user-defined minimum value of the design variable decides the element retention criteria as well as improve numerical stability.

3 Methodology

3.1 Hybrid Cellular Automata Method

To address the highly nonlinear and dynamic behavior of crash simulation with the inclusion of plasticity, the gradients of elements cannot be calculated analytically. And also needs huge computational effort and cost for the simulation. Given this, non-gradient-based methods are more suitable. LSTaSC with hybrid cellular automata (HCA) method is a non-gradient topology optimization method that was initially

developed as a linear static problem. In the recent approach of the hybrid cellular automata method [8], the internal energy density of structure is considered as homogeneously distributed by heuristics which is derived from biological growth rules. The discretization of the computation domain with voxel is represented as cellular auto. From iteration to iteration, the density of voxel is controlled by transition and neighborhood rules which correlate the state of a cellular auto lattice with the state of neighbors from time to time. An example of this rule is that the internal energy density (U_i) of the i th cellular auto lattice is the average of its von Neumann with n neighbors

$$U_i = \frac{\sum_{j=1}^n U_j}{\sum_{j=1}^n 1} \tag{4}$$

Considering HCA heuristic rules, the field variables are enforced to neighborhood update rule first, and then, the design variables are revised as the iteration progress until the equilibrium of all state variables arrives. Hence, adaption of relative density of each element with respect to current density is to arrive at the structure with uniform internal energy density (IED) as an objective of HCA, where the mass of the whole structure is kept constrained. Figure 1 explains the workflow of the procedure. Design variables are the relative density in each finite element. Material properties such as E-Modulus, yield stress and hardening parameter within every parameterized function of the relative density using SIMP [9].

By importing the baseline FE model, cellular automata lattice is assigned to this FE model. And neighbors of FE model cell are estimated which is used for updating element density. Initially, uniform density is assumed for all elements so that mass is constrained.

In the iterative process of optimization workflow for each FE analysis (LS-DYNA), the relative density of the element is calculated with an internal energy density of a respective element and its neighbors and the target mass. When the

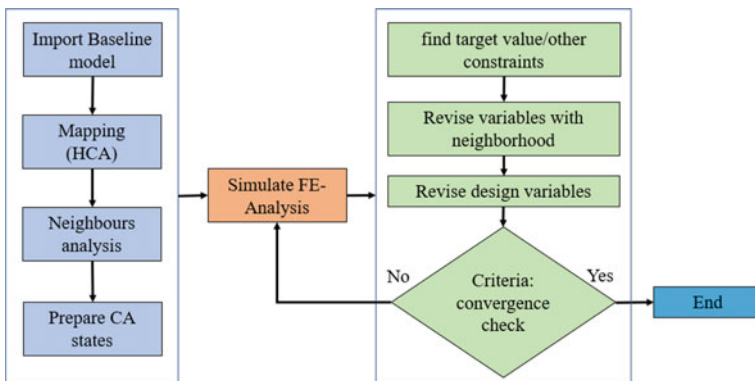


Fig. 1 Workflow of hybrid cellular automata-based topology optimization procedure

internal energy of a cell is less than an internally calculated target value, density is reduced. Likewise, the internal energy density of a cell is greater than an internally calculated target value, density is increased. Based on the density, material properties and stiffness of each element are altered. In the case of the element, density is lower than the lower threshold value, the element vanishes from this iteration. This iteration is continued till the convergence criteria are met which refers to small changes in density.

3.2 Content of This Contribution

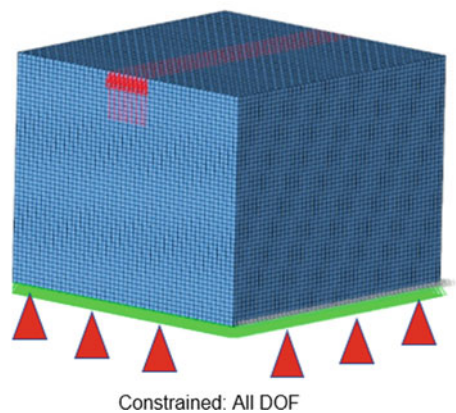
In this paper, HCA-based LS-TaSCTM [10] optimization software is evaluated and presented here.

3.3 Application 1—‘Linear Static Load Case’

A square box meshes with solid elements and loading conditions are shown in Fig. 2. The square box of base area is constrained, and a uniform distributed load is applied on the top surface of the box. The total number of mesh elements of the square box is 125 K with an element size of 1 mm and a mass fraction of 0.3. The mass constraint is defined as the amount of material removed which is specified by the user through the mass fraction parameter. The mass redistribution is the convergence criteria at which the fraction of the total mass of the structure has been redistributed per iteration. A maximum of 30 iterations are specified to arrive at the best optimal topology based on the load path.

Objective: Homogenization of internal energy density (IED)

Fig. 2 Geometry and load condition



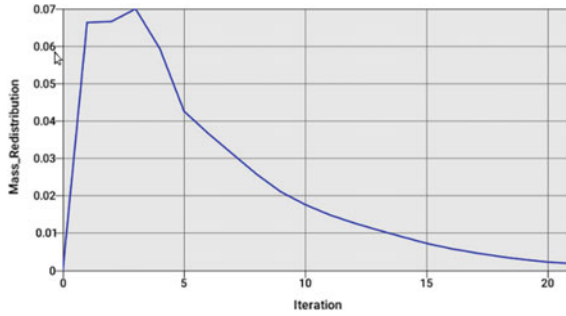


Fig. 3 Mass redistribution; convergence history

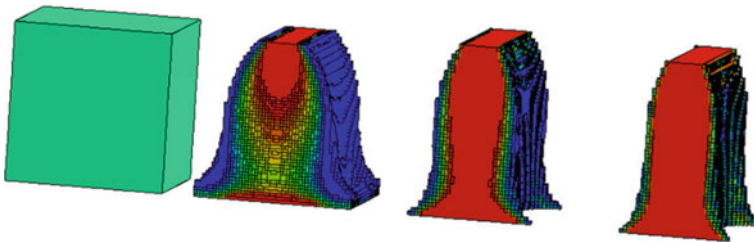


Fig. 4 Topology evolution changes

Design variables: Relative density in every finite element
 Constraints: Mass constraint; here a relative mass $M_{rel} = 0.3$.

From Fig. 3, the convergence history of topology optimization is shown. There is a monotonic reduction of topology changes noticed and convergence arrives at the 21st iteration.

The topology evolution change is shown in Fig. 4.

The final form of the evolved structure shows the material redistribution and low-density elements removal which are not actively contributing load path and obtain homogenous material distribution at the end of convergence of 21st iteration. The base of the square box is unaffected due to support constraints.

3.4 Application 2—‘Static Displacement Load Case’

A beam is modeled with solid mesh elements, and loading conditions are shown in Fig. 5. Both beam ends are constrained, and a rigid ram hits the beam with applied static displacement. The total number of mesh elements of the beam is 65 K with an element size of 5 and a mass constraint of 0.3. To design the topology of the beam, the maximum reaction force with mass constraint is considered.

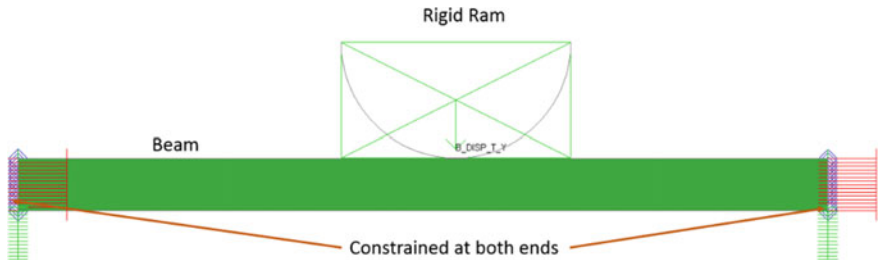


Fig. 5 Geometry and load condition

Objective: Homogeneous of internal energy density (IED)
Design variables: Relative density in every finite element
Constraints:

- (i) Mass constraint; here a relative mass $M_{rel} = 0.3$
- (ii) Reaction force constraint; $RCFORCE1 > 600$.

From Fig. 6, the convergence history of topology optimization is shown. There is a monotonic reduction of topology changes noticed and convergence arrives after the 30th iteration. The final form of the evolved structure shows a high internal energy density at both fixed ends and rigid ram impact region, where the elements have a huge deposition. There are intermediate density elements as thin walls are observed. And also the reaction force constraint is met, and the final structure has adequate support at both ends and impact region as shown in Fig. 7. The topologies at different

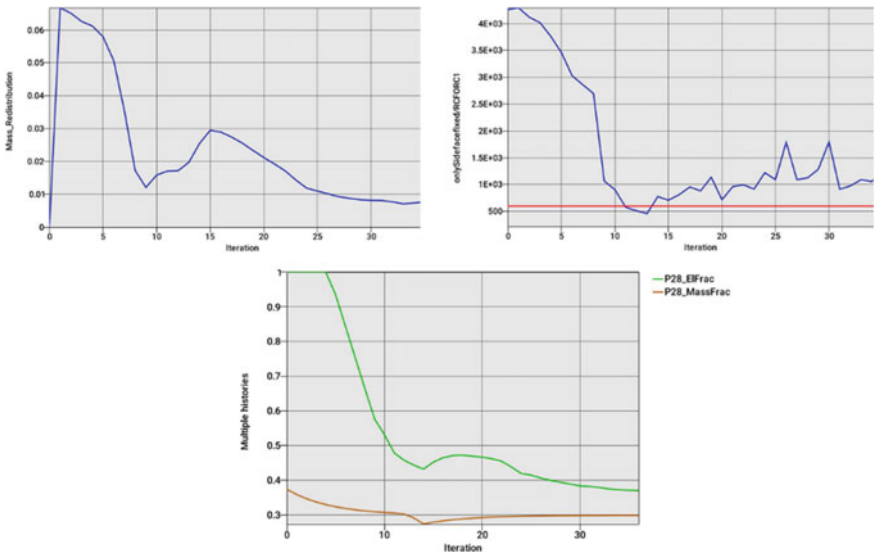


Fig. 6 Convergence history

Fig. 7 Solid density plot—initial and final design

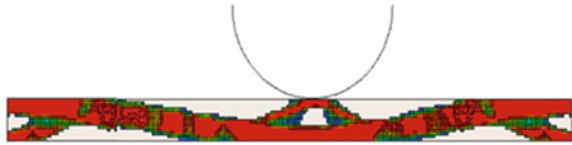


Fig. 8 Evolution of the geometry



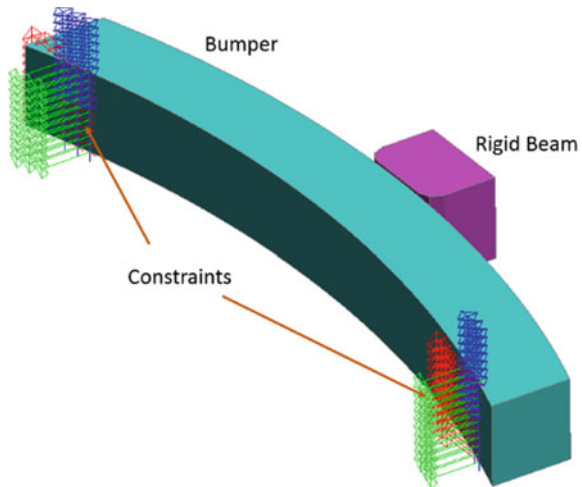
iterations during the evolution process are shown in Fig. 8.

3.5 Application 3—‘Dynamic Load Case’

A curved bumper beam is modeled with solid elements which are constrained at both ends of its either side faces. A rigid block is impacting at the center of a curved beam with initial velocity in the y-direction as shown in Fig. 9. The rigid material model is used for the impactor and the beam material model is represented with elastic piecewise linearly plastic material (MAT024 from DYNA). The total number of elements for the curved beam is 3120 and the mass fraction is 0.3. To minimize the intrusion of the rigid block, the topology of the curved bumper beam is designed with mass constraint.

Objective: Homogeneous of internal energy density (IED)

Fig. 9 Geometry and load condition



Design variables: Relative density in every finite element

Constraints:

- (i) Mass constraint; here a relative mass $M_{rel} = 0.3$
- (ii) Displacement constraint; $NODOUT1 < 30$.

From Fig. 10, the topology change arrives from the normalized mass distribution and intrusion based on optimization convergence at the 18th iteration. There were significant changes in the topology till the 17th iteration, later small changes were taken place in the topology for convergence stability.

The final topology is visualized in Fig. 11. The topologies at different iterations during the evolution process are shown in Fig. 12. By reducing the non-uniformity distribution of the internal energy density, the final topology arrived with carved elements profile in line with intrusion constraints.

Adequate homogenous material distribution is noticed on the final structure as desired. The evolution of topology at different stages shows the main feature of the changes in structure till the 17th iteration. Thereafter, material removal based on the load path and associate zones brought the necessary elements by redistributing the same for the final structure.

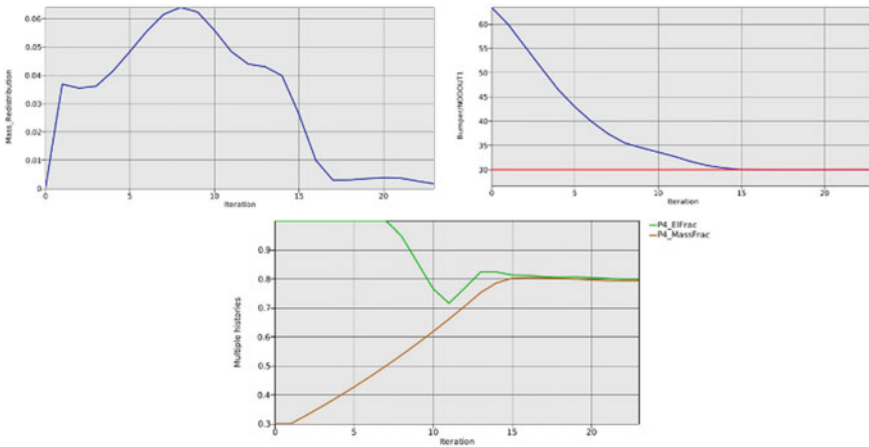


Fig. 10 Convergence history

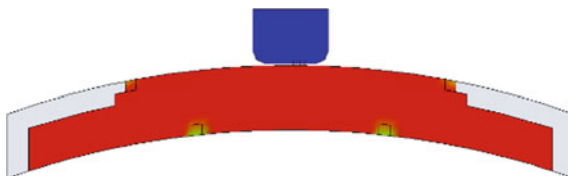


Fig. 11 Solid density plot—initial and final design

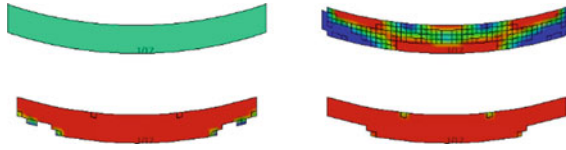


Fig. 12 Evolution of the geometry

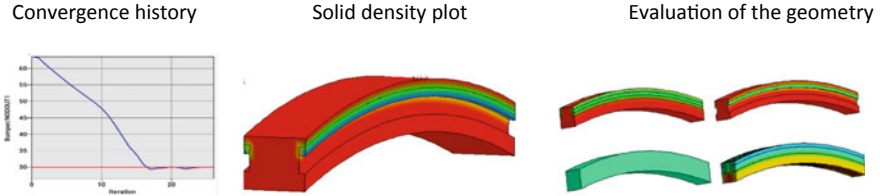


Fig. 13 Convergence history; solid density plot; evaluation of the geometry

Similarly, extrusion and casting of the bumper beam are analyzed. Figure 13 shows the different phases of topology evolution. The optimized final structure arrives at the 20th iteration. At the initial stage, a notable amount of material was removed, and the final geometry is completely different than earlier cases without manufacturing constraints. The resultant structure evolved as an I-section.

4 Summary/Conclusions

From this paper, the application of topology optimization for nonlinear load cases is studied in detail.

And the convergence of this study is found to be excellent in different optimization formulations involving different load cases and constraints. The tool has an excellent interface with LS-DYNA solver and is hence easy to use. It can deal with both shell and solid elements and also manufacturing constraints. The topologies obtained for complex dynamic load cases are often intuitive, which adds to the value the method delivers. The method can deal with displacement and force constraints, however, the inclusion of complex constraints such as head impact criteria (HIC) poses a challenge. The other capability of the tool is the multipoint method, where an additional objective can be defined (by converting a constraint) in addition to minimizing mass fraction, however, the quality of results depends on the specific load case used.

Acknowledgements The author would like to thank Dr. Biswajit Tripathy for the exploratory study on LSTaSC nonlinear load cases outcome and value addition for future scope of work

References

1. Bendsoe MP, Kikuchi N (1988) Generating optimal topologies in optimal design using a homogenization method. *Comput Methods Appl Mech Eng* 71:197–224
2. Bendsoe MP, Sigmund O (1989) *Topology optimization: theory methods and applications*. Springer, Berlin
3. Rozvany GIN (1997) *Topology optimization in structural mechanics*. Springer
4. Eschenauer HA, Olhoff N (2001) Topology optimization of continuum structures: a review. *Appl Mech Rev* 54:331–390
5. Patel NM (2004) *Crashworthiness design using topology optimization*. Ph.D. thesis, University of Notre Dame
6. Haftka RT, Gurdal Z, Kamat MP (1990) *Elements of structural optimization*, 2nd edn. Kluwer Academic Publishers, Dordrecht, The Netherlands
7. Patnaik SN, Hopkins DA (1998) Optimality of fully-stressed design. *Comput Methods Appl Mech Eng* 165:215–221
8. Patel NM, Kang BS, Renaud JE, Tovar A (2009) Crashworthiness design using topology optimization. *J Mech Des* 131(6):061013-12
9. Bendsoe MP (1989) Optimal shape design as a material distribution problem. *Struct Optim* 1:193–202
10. Livermore Software Technology Corporation (2019) *The LS-TaSC™ tool, Theory manual, r10.1.0*

Topology Optimization of a Coupled Aerothermoelastic System



Pankil N. Mishra and Abhijit Gogulapati

1 Introduction

Topology optimization (TO) of structures in multi-disciplinary environments has been explored in a number of studies [1–3]. The present work is motivated by interest in aerothermoelastic applications in which the coupled fluid-thermal-structural interactions (FTSI) play a prominent role. Several previous studies [4–9] have highlighted the importance of the feedback between the aerothermal loads and the structural response.

In particular, this coupling introduces a path dependency into the response problem that creates a wide variety of challenges for both the modeler and the designer. As separate topics of research, topology optimization strategies and aerothermoelastic modeling and analyses have produced a number of publications. However, topology optimization of a coupled aerothermoelastic system has received limited attention.

Reference [10] describes an optimization framework based on a transient adjoint sensitivity analysis approach to obtain optimal configurations of a fully coupled aerothermoelastic system. Finite element-based structural, compressible flow, and transient thermal solvers, are coupled using a monolithic approach. The author however notes that additional work is required before meaningful results can be obtained. Optimization of metallic panels for the flutter and buckling metric was considered in [11]. The structural response was coupled to piston theory-based aerodynamic pressure. However, the temperature of the panel was assumed to be constant throughout the analysis. It was observed that flutter and thermal buckling

P. N. Mishra (✉) · A. Gogulapati

Department of Aerospace Engineering, Indian Institute of Technology Bombay, Powai, Mumbai, Maharashtra 400076, India
e-mail: pankilmishra@iitb.ac.in

A. Gogulapati

e-mail: abhijit@aero.iitb.ac.in

metrics were competing objectives when the panel was subjected to prescribed temperature conditions.

A boundary variation method based on a level-set approach was used to optimize the topology of a static aeroelastic system in [12]. Mass minimization study was carried out with a flutter constraint. The authors note that the optimal designs may be dependent on the initial design itself. An evolutionary-based topology optimization study with stress minimization as the objective is described in [13]. The aerodynamic pressure is described using piston theory. The effect of material degradation on structural response was included. The authors concluded that the optimal configurations were dependent on the effect of material degradation and the application of non-uniform temperature loading resulted in optimal designs governed by thermal stresses. An aerothermoelastic framework was developed by coupling a flexible supersonic wedge to a fluid solver in [14]. The structural optimization of a panel on the wedge for steady state aerothermoelastic response was implemented using gradient-based approach.

It is evident from the review of literature presented above that such a study has not been considered prior to this work. The principal objective of the proposed study is to explore topology optimization of a coupled aerothermoelastic systems. The specific objectives are:

1. To maximize the non-linear normalized thermal buckling metric of the panel using density-based topology optimization approach.
2. To explore the impact of periodic cellular structure using variable linking method on optimal topology with potential applications to manufacturing constraint.

2 Configuration and Modeling

A panel of length L and thickness h shown in Fig. 1 is selected as the structural system. The third dimension of the panel is assumed to be infinitely long and the L/h ratio is fixed as 25. The panel is fixed on both the ends while its top surface is subjected to a hypersonic flow conditions mentioned in Table 1. The panel material is Ti-6Al-2Sn-4Zr-2Mo and thickness is 5 mm.

A basic implicit scheme is used to couple the aerothermoelastic framework developed obtained by coupling finite element-based structural and thermal solvers. The pressure and heat loads are computed using piston theory and Eckert's reference

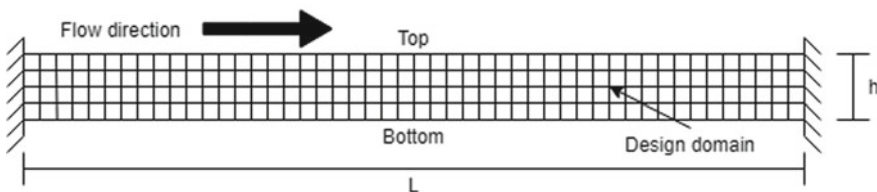


Fig. 1 Schematic of the panel configuration

Table 1 Flow conditions

Property	Value
Free-stream Mach No. (M_∞)	7.0
Altitude	30.0 km
Free-stream pressure (P_∞)	1090 Pa
Free-stream temperature (T_∞)	227 K
Upstream transition to turbulence	1.0 m

enthalpy approaches, respectively [2]. The description of various models is provided in the following subsections.

2.1 Aerodynamic Pressure Model

The aerodynamic pressure p_a at a point along the top surface of the panel is calculated using the third order piston theory given by:

$$p_a = 2 \cdot \frac{q_\infty}{M_\infty} \cdot \left[\left(\frac{1}{U_\infty} \cdot \frac{\partial w}{\partial t} + \frac{\partial w}{\partial x} \right) + M_\infty \cdot \frac{\gamma + 1}{4} \cdot \left(\frac{1}{U_\infty} \cdot \frac{\partial w}{\partial t} + \frac{\partial w}{\partial x} \right)^2 + M_\infty^2 \cdot \frac{\gamma + 1}{12} \cdot \left(\frac{1}{U_\infty} \cdot \frac{\partial w}{\partial t} + \frac{\partial w}{\partial x} \right)^3 \right] \quad (1)$$

where q_∞ is the dynamic pressure, w is the panel displacement in transverse direction, x is the free-stream direction along the flow as shown in Fig. 1 and t is time. Note that the undeformed configuration of the panel is parallel to the free-stream flow.

2.2 Aerodynamic Heating Model

The thermal loads generated due to the flow over the panel's top surface are estimated using the Eckert's reference enthalpy method [15]. The aerodynamic thermal load is determined from the Eq. 2, where U_e , St^* , ρ^* , H_w and H_{aw} are the velocity of the flow at the edge-of-boundary-layer, the Stanton number, density of the flow at the reference condition, the enthalpy at the wall and at the adiabatic wall condition, respectively.

$$Q_{\text{aero}} = St^* \cdot \rho^* \cdot U_e \cdot (H_{aw} - H_w) \quad (2)$$

Note that the coupling between panel deformation and thermal load is incorporated by updating the edge-of-boundary-layer pressure using piston theory, mentioned in Sect. 2.1.

2.3 Finite Element Models

In-house finite element code is used in the present case study. Bi-linear Q4 finite elements are used for both the structural (2 displacement degrees of freedom per node) and thermal (1 temperature degree of freedom per node) solvers discussed below. Identical finite element mesh with consistent matrices are used for both the solvers. More information about the finite element procedure and analysis is available in [16].

2.3.1 Thermal Solver

The finite element formulation of the heat transfer governing equation is used to perform transient thermal analysis of the panel using a *Backward difference* scheme. The thermal load vector \mathbf{R}_{T_n} is computed based on thermal boundary conditions specified for the panel based on a staggered scheme.

$$\left(\frac{\mathbf{C}_T}{\delta t_{AT}} + \mathbf{K}_T \right) \cdot \mathbf{T}_{n+1} = \frac{\mathbf{C}_T}{\delta t_{AT}} \cdot \mathbf{T}_n + \mathbf{R}_{T_n} \quad (3)$$

where δt_{AT} is the thermal time-step. The thermal boundary condition along the top surface includes aerodynamic and radiation heat load. Adiabatic boundary conditions are assumed for remaining surfaces of the panel, unless stated otherwise.

2.3.2 Structural Solver

The element temperature T_e is assumed to be spatially uniform within each finite element e , calculated using the average of nodal temperatures extracted from the vector \mathbf{T} at a given time-step. The elastic stress due to thermal expansion within each element is given by:

$$\sigma_{0_e} = \frac{-\alpha \cdot (T_e - T_{ref}) \cdot E_e}{1 - \nu} \cdot \begin{bmatrix} 1 \\ 1 \\ 0 \end{bmatrix} \quad (4)$$

where α , ν and E_e are the coefficient of thermal expansion, the Poisson's ratio and the elastic modulus of the element, respectively. They are assumed to be independent of the temperature. Note that the stresses produced due to the thermally induced displacements in the panel are not considered in the current study. Thus, the geometric stress stiffness matrix \mathbf{K}_σ of the structure is then obtained using:

$$\mathbf{K}_\sigma = \sum_{e=i}^N \mathbf{G}_e^T \cdot \mathbf{S}_e(\sigma) \cdot \mathbf{G}_e \cdot \mathbf{V}_e \quad (5)$$

Table 2 SIMP model

Relation	Property
$E_e = x_e^3 \cdot E_0$	Elastic modulus
$\mathbf{M} = \sum_e (x_e \cdot \mathbf{M}_e)$	Mass matrix
$\mathbf{C}_T = \sum_e (x_e \cdot \mathbf{C}_{Te})$	Heat capacity matrix
$\mathbf{K}_T = \sum_e (x_e^3 \cdot \mathbf{K}_{Te})$	Thermal conductivity matrix
$\mathbf{K} = \sum_e \left(\frac{x_{\min} + (1-x_{\min}) \cdot x_e^3}{1-\nu^2} \cdot \mathbf{K}_e \right)$	Stiffness matrix
$\mathbf{K}_\sigma = \sum_{e=i}^N \mathbf{G}_e^T \cdot \mathbf{S}_e(\sigma) \cdot \mathbf{G}_e \cdot \mathbf{V}_e$	Geometric stress stiffness matrix

where \mathbf{G}_e , \mathbf{V}_e and \mathbf{S}_e are the shape differentiation matrix, volume of the element and matrix reordering of the element stress σ_{0_e} , respectively.

2.3.3 Thermal Buckling Metric

The stability of the panel in terms of thermal buckling is obtained from the Eigenproblem defined below:

$$\{(\mathbf{K} + \mathbf{K}_\sigma) - \lambda_b \cdot \mathbf{I}\} \cdot \phi_b = \mathbf{0} \quad (6)$$

where \mathbf{K} is the linear stiffness matrix and terms in parentheses comprise a net stiffness matrix \mathbf{K}_{net} . The Eigenvector ϕ_b is associated with the b th eigenvalue λ_b of the net stiffness matrix. Thermal buckling means loss of stability of an equilibrium configuration due to thermal loads. In mathematical terms, \mathbf{K}_{net} becomes singular, i.e., the lowest eigenvalue λ^* obtained from Eq. 7 becomes zero.

$$\lambda^* = \min(\lambda_b) \quad (7)$$

2.4 Solid Isotropic Material with Penalization (SIMP) Model

In density-based SIMP method, each finite element is assigned a relative density x_e , a continuous design variable that varies between x_{\min} (void) to 1 (solid). The material property relations used in the current study based on the SIMP model are given in Table 2.

3 Sensitivity Analysis

The design derivatives required for the topology optimization problem are calculated analytically. The adjoint-based sensitivity analysis provides the design derivatives of the thermal buckling metric shown below:

$$\frac{d\lambda^*}{d\mathbf{x}} = \frac{(\boldsymbol{\phi}_b)^T \cdot \left(\frac{\partial \mathbf{K}}{\partial \mathbf{x}} + \frac{\partial \mathbf{K}_\sigma}{\partial \mathbf{x}} \right) \cdot (\boldsymbol{\phi}_b)}{(\boldsymbol{\phi}_b)^T \cdot \mathbf{I} \cdot (\boldsymbol{\phi}_b)} + (\boldsymbol{\beta}_T)^T \cdot \left(\frac{\partial \mathbf{C}_T}{\partial \mathbf{x}} \cdot \left(\frac{\mathbf{T}_x - \mathbf{T}_c}{\delta t_{AT}} \right) + \frac{\partial \mathbf{K}_T}{\partial \mathbf{x}} \cdot \mathbf{T}_x \right) \quad (8)$$

where the adjoint vector $\boldsymbol{\beta}_T$ is obtained from:

$$\left(\frac{\mathbf{C}_T}{\delta t_{AT}} + \mathbf{K}_T \right) \cdot \boldsymbol{\beta}_T = - \frac{(\boldsymbol{\phi}_b)^T \cdot \frac{\partial \mathbf{K}_\sigma}{\partial \mathbf{T}_x} \cdot (\boldsymbol{\phi}_b)}{(\boldsymbol{\phi}_b)^T \cdot \mathbf{I} \cdot (\boldsymbol{\phi}_b)} \quad (9)$$

4 Topology Optimization Methodology

The current study is inspired based on the work carried out in [11, 21]. The design variables $\tilde{\mathbf{x}}$ are assigned to finite elements of a unit cell. A variable linking sparse mapping matrix \mathbf{G} defined in Eq. 10, links the design variables of the unit cell to finite elements of other cells in the structural system [17].

$$\mathbf{G} = \begin{bmatrix} 1 & 0 & \dots & 0 & \dots \\ 0 & 1 & \dots & 0 & \dots \\ \vdots & \vdots & \ddots & \vdots & \vdots \\ 1 & 0 & \dots & 0 & \dots \\ 0 & 1 & \dots & 0 & \dots \\ \vdots & \vdots & \ddots & \vdots & \vdots \\ 0 & 0 & \dots & 1 & 0 \\ 0 & 0 & \dots & 0 & 1 \end{bmatrix}_{N_e \times n_e} \quad (10)$$

where N_e is the total number of finite elements in the whole design domain and n_e is the number of finite elements in the single design cell, i.e., the number of design variables $\tilde{\mathbf{x}}$. If the density of element j is linked to the i -th design variable then $\mathbf{G}(j, i) = 1$

A density filter [18, 19] is used to obtain the element densities \mathbf{x} from the design variables $\tilde{\mathbf{x}}$ using the density filter \mathbf{H} . Note that the density filter is applied on to the whole design domain. The topology optimization is performed using the below mentioned steps:

1. Initialization of design variables and set $i = 0$
2. Map the design variables to the whole domain using matrix \mathbf{G}
3. Apply the density filter to obtain the element densities from the design variables

4. Perform the aerothermoelastic analysis for the stipulated simulation time, N_s seconds or till the thermal buckling event happens
5. Perform the sensitivity analysis and map it to the design variables using transpose of the matrix \mathbf{G}
6. Perform optimization of Eq. 11 using MMA algorithm [20]
7. Update the design variables and set $i = i + 1$
8. Perform the steps 2-7 till the convergence criteria is fulfilled.

The objective function is to maximize the normalized thermal buckling metric, where the baseline thermal buckling metric $\lambda_{\text{baseline}}^*$ is calculated once initially for the baseline design domain shown in Fig. 2. The mathematical formulation of the topology optimization problem considered here is shown below:

$$\begin{aligned}
 &\text{Maximize } \frac{\lambda^*}{\lambda_{\text{baseline}}^*} \\
 &\text{w.r.t. } \tilde{\mathbf{x}} \\
 &\text{subject to } \mathbf{v}^T \cdot \mathbf{x} \leq \mathbf{V}^* \\
 &\quad \tilde{x}_e \in [\mathbf{x}_{\text{min}}, \mathbf{1}] \quad \mathbf{e} = \mathbf{1}, \dots, \mathbf{N}_e
 \end{aligned} \tag{11}$$

where V^* is the volume constraint on the element densities \mathbf{x} . The density filter radius reduces each time the iterations converge within the specified tolerance, according to the following sequence [3.1, 2.9, 2.3, 2.1, 1.5, 1.1, 1.0, 0.1]. The optimization algorithm terminates either when the number of iterations are equal to N_I or when the filter radius value is less than 1.0

5 Results and Discussion

The value of various parameters related to the topology optimization problem are given in Table 3. Note that the flow is over the undeformed (flat) panel which means that effect of pressure load is not considered since the focus is on thermal-structural coupling.

Table 3 Common parameters

Parameter	Value
Number of elements	1600
Max. number of iterations, N_I	700
Min. change	0.0001
Volume fraction, V^*	0.350
Thermal time-step, δt_{AT}	0.1 s
Reference temperature, T_{ref}	300 K



Fig. 2 Topology of baseline design and initial design for case study A



Fig. 3 Optimal topology for case study-A, $N_s = 3 s$

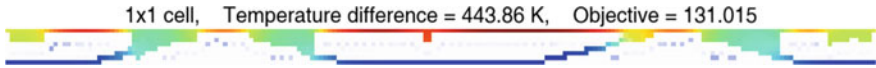


Fig. 4 Optimal topology for case study-A, $N_s = 6 s$

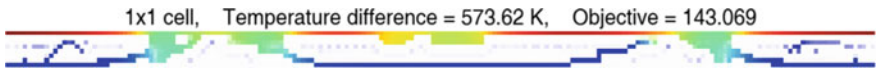
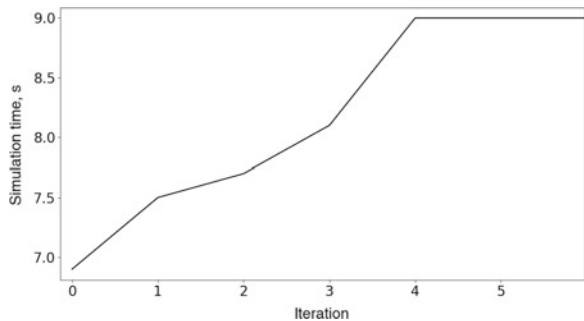


Fig. 5 Optimal topology for case study-A, $N_s = 9 s$

Fig. 6 Simulation time of initial iterates for case study A, $N_s = 9 s$



The topology optimization problem Eq. 11 is solved here for the case study A with an implicit periodic cell constraint as shown in Fig. 2. The optimal topology obtained for the simulation time of 3 s, 6 s and 9 s are shown in Figs. 3, 4 and 5, respectively. The temperature distribution is shown using the *jet* color scheme, where the *red* color indicates the maximum temperature and the *blue* color indicates the minimum temperature across the panel.

The thermal buckling of baseline design takes place at 3.4 s. Due to which the change in objective function value from simulation time of 3–6 s is quite large as compared to that of 6–9 s. As mentioned earlier, the analysis module terminates either when the stipulated simulation time, N_s seconds is achieved or when the thermal buckling of the panel occurs. For simulation time of 9 s, the iterate $i = 0$ terminates at 6.8 s due to the thermal buckling of the panel as shown in Fig. 6. One can observe that the thermal buckling of the panel is delayed and from iterate $i = 4$

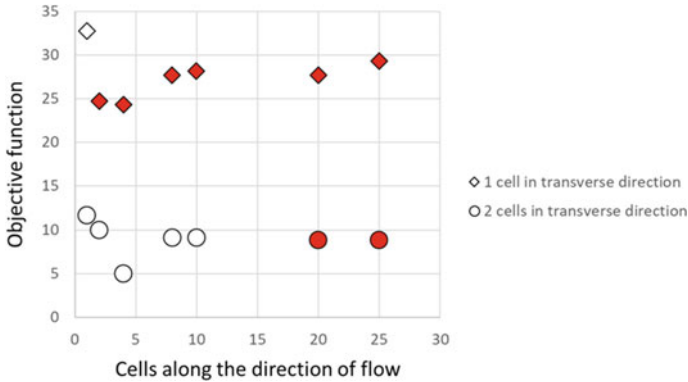


Fig. 7 Objective function for different periodicity

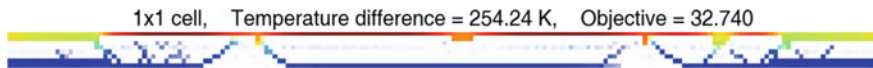


Fig. 8 Optimal topology for 1 × 1 periodic cell

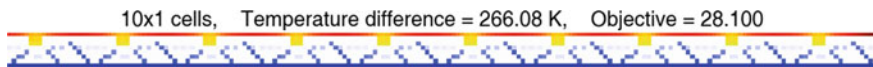


Fig. 9 Optimal topology for 10 × 1 periodic cells

on-wards the analysis module terminates only when the stipulated simulation time of 9 s is achieved.

The design space of case study A ($N_s = 3s$) for different periodic cell structure is shown in Fig. 7. The solid red markers as compared to solid white markers produced configurations where the top and bottom part of the panel were disconnected from each other. The heat transfer from top to bottom takes place through conduction in the internal part of the panel. The absence of internal radiation model leads to the removal of material just below the solid top surface of the panel. They are mathematically feasible solutions to the topology optimization problem Eq. 11 as the thermal buckling metric is calculated for the whole panel (Fig. 8). The panel configuration obtained for 10 × 1 periodicity shown in Fig. 9 is an example of the topology denoted by solid red markers in Fig. 7.

The value of objective function in Fig. 7 is highest for a 1 × 1 periodicity while it decreases as the number of cells in the transverse direction increase from 1 to 2. This is mainly due to the presence of material in middle part which reduces the thermal buckling characteristic of the panel. For example the objective metric of topology 1 × 2 periodicity as shown in Fig. 10 is almost one-third of that for 1 × 1 periodicity as shown in Fig. 8. The optimal topology obtained for 8 × 2 and 10 × 2 periodicity resembles to traditionally manufactured stiffened panels found in aerospace applications shown in Figs. 11 and 12, respectively.

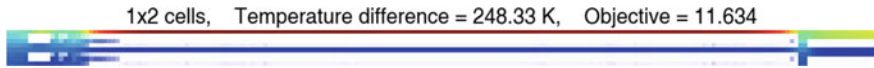


Fig. 10 Optimal topology for 1×2 periodic cells



Fig. 11 Optimal topology for 8×2 periodic cells



Fig. 12 Optimal topology for 10×2 periodic cells

6 Conclusions

Topology optimization for a normalized thermal buckling metric of a 2-D panel heated by the flow is described. The effect of periodic cell constraint on the panel topology is considered implicitly using variable linking method. The investigations revealed the following insights:

- Normalizing of the objective function metric improves the rate of order of convergence 2 to 3 times as compared to non-normalized metric
- Overall the thermal buckling metric of the panel decreases with increase in the periodicity
- Panel configurations with top and bottom part being disconnected are produced due to the absence of internal radiation model
- Periodicity as a manufacturing constraint generates configuration similar to traditionally manufactured stiffened aerospace panels at the cost of optimal panel topology.

Acknowledgements The authors acknowledge the Department of Aerospace Engineering, IIT Bombay for the computational resources and wall time.

References

1. McNamara JJ, Friedmann PP (2011) Aeroelastic and aerothermoelastic analysis in hypersonic flow: past, present, and future. *AIAA J* 49(6):1089–1122
2. Culler AJ, McNamara JJ (2010) Studies on fluid-thermal-structural coupling for aerothermoelasticity in hypersonic flow. *AIAA J* 48(8):1721–1738
3. Gogulapati A, Brouwer KR, Wang X, Murthy R, McNamara JJ, Mignolet MP (2017) Full and reduced order aerothermoelastic modeling of built-up aerospace panels in high-speed flows. In: 58th AIAA/ASCE/AHS/ASC structures, structural dynamics, and materials conference, p 0180
4. Bendsoe MP, Sigmund O (2013) *Topology optimization: theory, methods, and applications*. Springer Science & Business Media

5. Sigmund O, Maute K (2013) Topology optimization approaches. *Struct Multidiscip Optim* 48(6):1031–1055
6. Feppon F, Allaire G, Dapogny C, Jolivet P (2020) Topology optimization of thermal-fluid-structure systems using body-fitted meshes and parallel computing. *J Comput Phys* 417:109574
7. Deaton JD, Grandhi RV (2014) A survey of structural and multidisciplinary continuum topology optimization: post 2000. *Struct Multidiscip Optim* 49(1):1–38
8. Wang X, Xu S, Zhou S, Xu W, Leary M, Choong P, Qian M, Brandt M, Xie YM (2016) Topological design and additive manufacturing of porous metals for bone scaffolds and orthopaedic implants: a review. *Biomaterials* 83:127–141
9. Liu J, Gaynor AT, Chen S, Kang Z, Suresh K, Takezawa A, Li L, Kato J, Tang J, Wang CC et al (2018) Current and future trends in topology optimization for additive manufacturing. *Struct Multidiscip Optim* 57(6):2457–2483
10. Howard MA (2010) Finite element modeling and optimization of high-speed aerothermoelastic systems. Ph. D. Thesis, Colorado University
11. Stanford B, Beran P (2013) Aerothermoelastic topology optimization with flutter and buckling metrics. *Struct Multidiscip Optim* 48(1):149–171
12. Dunning PD, Stanford B, Kim HA (2015) Level-set topology optimization with aeroelastic constraints. In: 56th AIAA/ASCE/AHS/ASC structures, structural dynamics, and materials conference, p 1128
13. Munk DJ, Verstraete D, Vio GA (2017) Effect of fluid-thermal-structural interactions on the topology optimization of a hypersonic transport aircraft wing. *J Fluids Struct* 75:45–76
14. Smith LJ, Halim LJ, Kennedy G, Smith MJ (2021) A high-fidelity coupling framework for aerothermoelastic analysis and adjoint-based gradient evaluation. In: AIAA Scitech 2021 Forum, p 0407
15. Eckert E (1956) Engineering relations for heat transfer and friction in high-velocity laminar and turbulent boundary-layer flow over surfaces with constant pressure and temperature. *Trans ASME* 78(6):1273–1283
16. Cook RD et al (2007) Concepts and applications of finite element analysis. Wiley
17. Kai W, Sigmund O, Jianbin D (2021) Design of metamaterial mechanisms using robust topology optimization and variable linking scheme. *Struct Multidiscip Optim* 63:1975–1988
18. Bruns TE, Tortorelli DA (2001) Topology optimization of non-linear elastic structures and compliant mechanisms. *Comput Methods Appl Mech Eng* 190(26–27):3443–3459
19. Bruns T (2005) A reevaluation of the SIMP method with filtering and an alternative formulation for solid-void topology optimization. *Struct Multidiscip Optim* 30(6):428–436
20. Svanberg K (1987) The method of moving asymptotes | a new method for structural optimization. *Int J Numer Methods Eng* 24(2):359–373
21. Mishra PN, Gogulapati A (2021) Topology optimization of fully coupled aerothermoelastic system. In: Proceedings of the international conference on multidisciplinary design optimization of aerospace systems (AEROBEST 2021), p 192

Topology Optimization for Designing a Wheel Rim



Pilla Sai Priyatham, Dheeraj Agarwal, and Amit Kumar Gupta

1 Introduction

Automobiles play an important role in our day-to-day life. Automobile parts are made from various manufacturing components and we strive for making highly efficient component always. Traditionally these components are processed by casting and forging. Even after the development in manufacturing technology these processes are still used due to its strong efficacy. The advancement can be done in the area of design for the betterment of the manufacturing components by using optimization tools. One of such tools is the topology optimization which is an emerging field and is often used in early phase of conceptualizing designs, which in turn is used to determine the optimal approach of material distribution within the given design domain. Topology is derived from a Greek word “*Topos*” which means location, space, or domain. Optimization intends to obtain best alternative design that satisfies all the required criterion for a specified objective. Topology optimization aims to provide the best alternative of material configuration by reducing the weight without compromising the functioning of the component. The four-wheel automobiles are extensively used in day-to-day life due to its ability to carry loads, among which cars are at high demand due to the versatile comfort that it offers to a passenger as per their needs. A reason for these advantages lies on to the wheels that transmits the

P. S. Priyatham (✉) · A. K. Gupta

Department of Mechanical Engineering, BITS Pilani Hyderabad Campus, Secunderabad, Telangana, India

e-mail: h20201060271@hyderabad.bits-pilani.ac.in

A. K. Gupta

e-mail: akgupta@hyderabad.bits-pilani.ac.in

D. Agarwal

School of Engineering, University of Liverpool, Liverpool, England

e-mail: Dheeraj.Agarwal@liverpool.ac.uk

load uniformly. The different types of loads that it experiences are: static load (due to chassis), dynamic load (due to movement of vehicle), impact load (due to collision of vehicle), inertial load (due to breaks), and momentary duration load (due to vehicle turn). Hence, it is very important to perform topology optimization of wheels and static load is considered as the first step in this direction.

2 Related Literature

Alonso et al. [1] provided an advanced and integrated approach for collaborative multidisciplinary design that included consistent interdisciplinary analysis as well as multi-objective optimization of wing semi-span, outer wing, and sweep angle. They greatly enhanced the design, validating the industry's belief that multidisciplinary design optimization is critical for improving plans to meet market demands. The distinct hybrid optimization methods for optimal multi-objective low thrust spaceship trajectories and earth mass trajectories were discussed by Carroll et al. [2]. Wang et al. [3] used two separate strategies topology optimization and sizing optimization, to increase the stiffness of an automobile. Harzheim and Graf [4] did a review of optimization for casted parts and topology optimization was done for the same. Using a compromise programming technique, Xiao et al. [5] optimize the topology of steel wheel under static load conditions for eight distinct types of models to obtain maximum stiffness or minimal compliance. When compared to its original design, the optimized wheel disc does have a mass decrease 4.57%. Zhang et al. [6] described the Static analysis of finite element analysis of foundation construction, which is used to determine how the structures respond to specified limitations under different load. Christensen et al. [7] developed a model in Catia and imported it to Ansys, where they implemented various forms of boundary conditions. After performing crash simulation studies, the body in white (BIW) was optimized in two primary areas: overall topology and mass reduction. The impact of proposed revisions to the FMVSS 216 standard on the roof topology of a body in white for hybrid electric vehicle was investigated in this study. Li et al. [8] created an optimized 3-D suspension model. The model's strength, stiffness, and safety factor were then simulated and verified under three different conditions: turning, braking, and sharp turning. The suspension front upright's basic geometry model was optimized for weight reduction, resulting in a lightweight front upright with a mass reduction of 60.43%. The wheel's CAD model was made using the parameters, and the model was then simulated in Hypermesh, using standard load conditions (radial loads and bending loads). In one of the other works, Razak and Ikhwan [9] achieved weight reduction by using aluminum and magnesium alloy instead of steel and cast iron.

3 Problem Definition and Formulation

The wheel is a cylindrical component that rotates around an axle bearing and is one of the simple machines. The wheels and axles allow heavy things to be moved more readily, allowing for easier mobility or transit while sustaining defined loadings. The excessive weight of the wheel would demand more power from the engine, which may reduce the vehicle performance. The aim of this work is to obtain an optimal design of a wheel rim using topology optimization techniques by applying two different loading conditions for two different materials viz, aluminum and steel. These material configurations are chosen as these are commonly used for manufacturing components. The wheels are essential to the vehicle's safety, and they require careful attention to preserve their life. The development of the automobile industry is largely impacted by the wheel design, material selection, and manufacturing methods. They are loaded in a complex manner, and better understanding of these loadings would enable further refinements to produce an efficient wheel design. Two requirements must be met to achieve the best possible wheel design: precise knowledge of the material's loading, mechanical properties, and permitted stresses, which are influenced by vehicle attributes, service circumstances, and manufacturing methods. It would matter less, if you have highly efficient engine, but the wheel is very heavy and using all the available power to move its own weight. Therefore, it is a requirement to optimize the wheel design, so that better efficiency can be achieved in the given design domain.

4 Methodology

Topology optimization can be performed on various simulation platforms such as Fusion 360, Alter inspire, Creo 6.0, Siemens NX, Opti struct, Ansys, etc. The present optimization is done on Fusion 360, which is a multi-component part system that includes tools for parametric, direct, and mesh modeling. It is also completely cloud-based, making it ideal for distant teams. The different functionalities are separated into distinct workspaces, so the entire screen changes depending on the activity at hand (CAM, rendering, etc.), eliminating unnecessary space by removing unnecessary tools and features. Fusion 360 offers easy simulation packages that may be more beneficial in the early stages of the design to better understand how parts would react under different situations.

4.1 Materials Used

The wheel is manufactured by using casting technique. Casting is the process of pouring hot molten metal into the mold to get the desired shape. In the twenty-first

Table 1 Material properties of steel and aluminum

Material	Steel	Aluminum
Density (kg/mm ³)	7.85E-06	2.7E-06
Initial weight of specimen (kg)	61.848	20.874
Youngs modulus (GPa)	210	68.9
Poisons ratio	0.3	0.33
Yield strength (MPa)	207	275
Ultimate tensile strength (MPa)	345	310

century with the advancements in technology, new materials have been invented with different combination of alloys, ceramics, and natural composites. However, in this work we have used only the basis materials viz., aluminum and steel, as they are more readily available in workshops, making it ideal for this study. The properties of these materials are shown in Table 1. Steel is an iron alloy with a percent of carbon added to improve the material's strength and fracture resistance. It also includes a variety of additional ingredients. Corrosion and oxidation-resistant stainless steels normally require an additional % chromium to be added. Steel is widely applied in buildings, tools, ships, railroads, infrastructure, cars, machineries, and weapons due to its high strength and low cost. Aluminum is a chemical compound having a lower density than other common metals. When exposed to air, aluminum has a strong affinity for oxygen and produces a protective layer of oxides on the surface. Aluminum has a silver-like appearance, both in appearance and in its ability to reflect light. It is ductile, soft, and non-magnetic. The advantages of an aluminum profile system start with the material's basic properties. Despite being much lighter than steel, aluminum is a very robust material. Corrosion does not pose a serious threat to it, so no time-consuming preventative actions are necessary. As a result, two traditional steel-related cost issues, such as routine maintenance and corrosion prevention, becomes obsolete. The properties of aluminum and steel are shown in Table 1.

The initial sketching and design of the circular component which is intended to be a wheel is done in the sketcher of fusion 360. Simulations are performed by using an optimum mesh density (3% of the average mesh size). Primarily two conditions are considered for the simulation and only static analysis is performed. The weight of the car for simulation is estimated to be approximately 900 kg (without any passenger) and considering 5 adults with luggage to be approximately 1350 kg (including the passenger's weight). When these masses are converted into weights and equally distributed on to four wheels for static analysis, it results as 2.25 kN and 3.375 kN, respectively. The initial thickness and diameter of the wheels are considered as 53 mm and 432 mm, respectively [9].

4.2 Meshing

Meshing is the act of breaking down an object's continuous geometric space into thousands or more shapes in order to adequately define the object's physical shape. The more intricate a mesh, the more accurate would be the results from the high-fidelity simulations. One of the most important aspects of getting correct results from a FEA model is meshing. To accurately discretize stress gradients, the elements in the mesh must take into consideration a variety of factors. Because the designs are better sampled over the physical domains, the smaller the mesh size, the more accurate the solution.

Finer meshes can provide a more accurate solution, but as a mesh becomes finer, computing time increases, therefore a good balance between accuracy and available computational resources must be struck. The entire process is shown in Fig. 1. Mesh refining is a useful tool for fine-tuning finite element meshes and improving solution accuracy. Refinement is done through an iterative process that involves finding a solution, calculating error estimates, and refining elements in high-error areas and it is much more needed to make sure the mesh size is less than 3% for a finer mesh.

The loading condition for the finite element simulations for the starting models is shown in Fig. 2, while the preliminary result with the optimized design of steel wheel with a load of 2.250 kN is shown in Fig. 3. The results after performing the topology optimization for two different materials and loadings are shown in Table 2.

5 Conclusions and Future Work

Using the approach of topology optimization, entirely different configuration of the wheel designs was obtained when the material and loading conditions were changed. For the steel material, weight reduction of 69–73% was obtained when the load condition was changed from 2.250 to 3.375 kN. However, using aluminum, the mass reduction obtained was between 61 and 71% when the load condition is considered from 2.250 to 3.375 kN.

In the current study, the loads were only applied in static analysis and further work would be done by applying different loads like inertial load, dynamic load and impact load, etc. The materials considered would be altered according to the current industry standards and simulations would be extended to obtain better design than the existing one.

Fig. 1 Flow chart showing the entire procedure for simulation

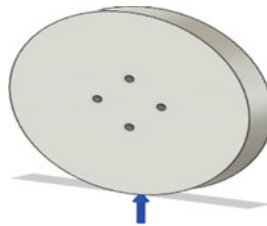
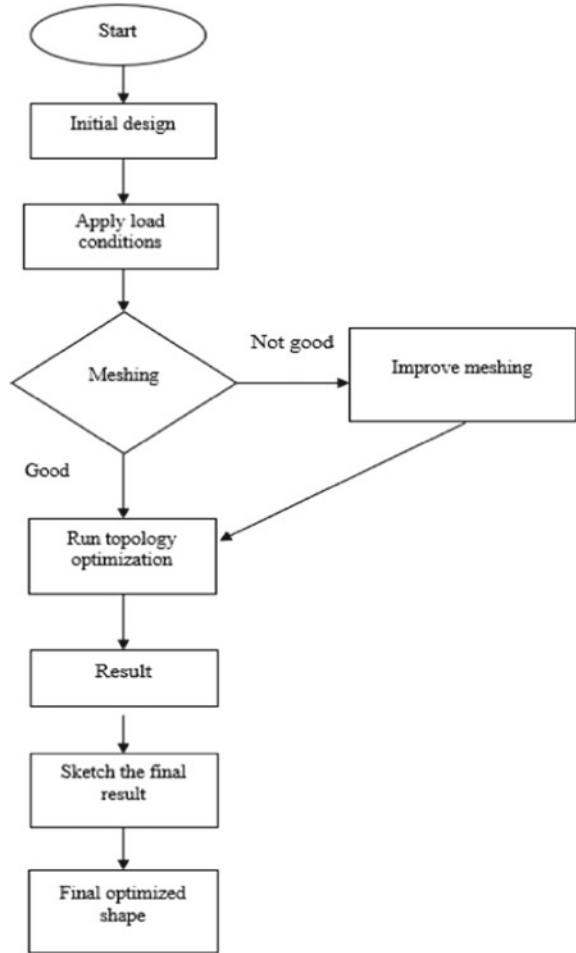


Fig. 2 Load of 2.25 kN applied on steel wheel

Fig. 3 Final optimized design of steel wheel

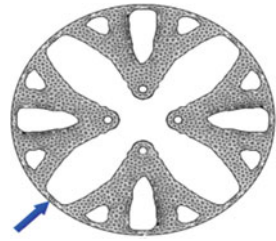


Table 2 Optimization designs of wheel with respect to load conditions

S. No.	Material used	Load condition (in kN)	Initial weight (in Kg)	Final weight (in Kg)	Mass reduction (percentages)	Optimum designs obtained
1	Steel	2.250	61.848	16.524	73.28	
		3.375	61.848	18.608	69.13	
2	Aluminum	2.250	20.874	6.330	69.67	
		3.375	20.874	8.090	61.24	

References

1. Alonso J, LeGresley P, Pereyra V (2009) Aircraft design optimization. *Math Comput Simul* 79(6):1948–1958. <https://doi.org/10.1016/j.matcom.2007.07.001>
2. Coverstone-Carroll V, Hartmann J, Mason W (2000) Optimal multi-objective lowthrust spacecraft trajectories. *Comput Methods Appl Mech Eng* 186(2–4):387–402. [https://doi.org/10.1016/S0045-7825\(99\)00393-x](https://doi.org/10.1016/S0045-7825(99)00393-x)
3. Wang L, Basu PK, Leiva JP (2004) Automobile body reinforcement by finite element optimization. *Finite Elem Anal Des* 40(8):879–893. [https://doi.org/10.1016/S0168-874x\(03\)00118-5](https://doi.org/10.1016/S0168-874x(03)00118-5)
4. Harzheim L, Graf G (2005) A review of optimization of cast parts using topology optimization. *Struct Multidiscip Optim* 31(5):388–399. <https://doi.org/10.1007/s00158-005-0554-9>
5. Xiao D, Zhang H, Liu X, He T, Shan Y (2014) Novel steel wheel design based on multi-objective topology optimization. *J Mech Sci Technol* 28(3):1007–1016. <https://doi.org/10.1007/s12206-013-1174-8>
6. Zhang GH (2012) The research on modal analysis and topology optimization in car clutch parts. *Appl Mech Mater* 189:486–490. <https://doi.org/10.4028/www.scientific.net/amm.189.486>
7. Christensen J, Bastien C, Blundell MV (2012) Effects of roof crush loading scenario upon body in white using topology optimisation. *Int J Crashworthiness* 17(1):29–38. <https://doi.org/10.1080/13588265.2011.625640>
8. Li C, Kim IY, Jeswiet J (2014) Conceptual and detailed design of an automotive engine cradle by using topology, shape, and size optimization. *Struct Multidiscip Optim* 51(2):547–564. <https://doi.org/10.1007/s00158-014-1151-6>
9. Razak MI (2015) Design and development of alloy wheel. <https://doi.org/10.13140/RG.2.1.1049.7367>

Topology Optimization with Orthotropic Material Model for Design-Dependent Loads



Rahul Ramachandran, Sourav Rakshit, and G. Saravana Kumar

1 Introduction

Topology optimization is an optimization technique used to find the optimal material layout for a structural design problem. Most of the structural problems in topology optimization try to find the stiffest structure with material volume as a constraint and fixed loading conditions [1–3]. Nevertheless, there are many scenarios where the loading conditions change as the design changes (i.e., these are design-dependent loads). The classification of topology optimization according to the loading conditions is shown in Fig. 1. To find the optimal layout for these kinds of problems, the loading boundary, load magnitude, and direction must be changed from one iteration to another.

Many researchers have explored the area of topology optimization with design-dependent loads [4–10]. The main difficulty of these problems is the identification of the structures' load surfaces at each and every step of optimization. Due to this, a simple boundary identification method is proposed in this work for finding the load curve in each iteration. In all the research works in this area, the material model is assumed to be isotropic. However, there are many applications in which the design-dependent loads act on an anisotropic medium. In this work, topology optimization with design-dependent loads is carried out for an orthotropic material.

R. Ramachandran · G. Saravana Kumar

Department of Engineering Design, Indian Institute of Technology Madras, Chennai, India
e-mail: ed19s001@smail.iitm.ac.in

G. Saravana Kumar

e-mail: gsaravana@iitm.ac.in

S. Rakshit (✉)

Department of Mechanical Engineering, Indian Institute of Technology Madras, Chennai, India
e-mail: srakshit@iitm.ac.in

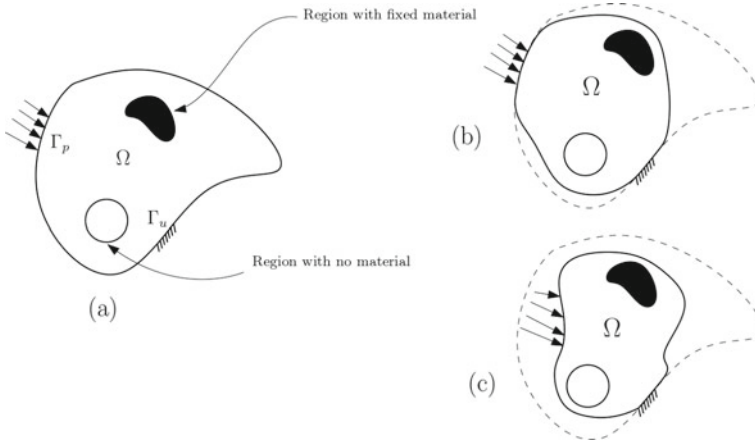


Fig. 1 A component with **a** its initial material layout along with its loading/boundary conditions, **b** new material layout due to fixed load, and **c** new material layout due to design-dependent load (dashed boundary line in (b) and (c) represent the initial material layout (a))

2 Problem Formulation

A two-dimensional design domain $\Omega \in R^2$ is considered for the problem formulation. The optimal structural layout for a given volume and pressure loads is found by minimizing the compliance of the structure. The boundary of the domain Γ is composed of two regions Γ_u and Γ_p . The former is where the displacements are prescribed, and in the latter, the traction boundary conditions (design-dependent loads) are applied. The structural compliance is given by

$$C(u) = \int_{\Omega} bu \, d\Omega + \int_{\Gamma_p} pu \, d\Gamma \tag{1}$$

where b , p , and u are body forces, traction loads, and displacements, respectively. The topology optimization problem can be mathematically written as

$$\min_{\rho(x)} C(u^*) \tag{2}$$

$$V = \int_{\Omega} \rho(x) d\Omega = V_0 f \tag{3}$$

$$0 \leq \rho(x) \leq 1 \tag{4}$$

In the above equation, x is any point in the two-dimensional domain Ω , $\rho(x)$ is the pseudo-density at that given point x , and u^* is the displacement vector that satisfies

equilibrium equations. V_0 is the total volume of the design domain, and f is the desired volume fraction. The solid anisotropic material with penalization (SAMP) model relates the element stiffness to the element material density. Young's elastic moduli E_1 , E_2 and shear modulus G are used as material properties for FE analysis. These properties can be written as a function of pseudo-density $\rho(x)$ as

$$E_1(\rho) = \rho^n E_1^0 \tag{5}$$

$$E_2(\rho) = \rho^n E_2^0 \tag{6}$$

$$G(\rho) = \rho^n G^0 \tag{7}$$

The plane stress constitutive matrix for orthotropic material can be written as

$$\mathbf{C}(\rho) = \rho^n \begin{bmatrix} \frac{E_1^0}{(1-\nu_{12}\nu_{21})} & \frac{E_2^0 \nu_{12}}{(1-\nu_{12}\nu_{21})} & 0 \\ \frac{E_2^0 \nu_{12}}{(1-\nu_{12}\nu_{21})} & \frac{E_2^0}{(1-\nu_{12}\nu_{21})} & 0 \\ 0 & 0 & G^0 \end{bmatrix} \tag{8}$$

Here, E_1^0 , E_2^0 , and G^0 are the corresponding modulus of solid material. Penalization factor (n) is used to minimize the formation of intermediate densities. The optimization problem can be written as

$$\min_{\rho} : \mathbf{U}^T \mathbf{K} \mathbf{U} = \sum_{e=1}^N \mathbf{u}_e^T \mathbf{K}_e \mathbf{u}_e \tag{9}$$

$$\text{s.t.: } \mathbf{K} \mathbf{U} = \mathbf{F}$$

$$:g(V(\rho)) = V/V^* - 1 = \sum_{e=1}^N v_e \rho_e / V^* - 1 \leq 1 \tag{10}$$

$$:0 < \rho_{\min} \leq \rho_e \leq 1$$

where N is the total number of elements in the mesh. \mathbf{K} , \mathbf{U} , \mathbf{F} , \mathbf{K}_e , v_e , and \mathbf{u}_e are the global stiffness matrix, global displacement vector, load vector, element stiffness matrix, volume of the finite element cell, and element displacement vector, respectively. ρ_{\min} is used to circumvent any singularities.

3 Sensitivity Analysis and Filtering

For gradient-based topology optimization, sensitivity analysis is a crucial step. In order to perform sensitivity analysis, i.e., to find the gradient of the objective function, we have used adjoint method. A Lagrangian function of the density design variable ρ is defined with the help of a Lagrange multiplier:

$$C^* = \mathbf{U}^T \mathbf{K} \mathbf{U} - \lambda^T (\mathbf{K} \mathbf{U} - \mathbf{F}) \quad (11)$$

Sensitivity analysis is concerned with finding the derivative of the objective function with respect to design variable ρ .

$$\begin{aligned} \frac{\partial C^*}{\partial \rho} &= \frac{\partial \mathbf{U}^T}{\partial \rho} \mathbf{K} \mathbf{U} + \mathbf{U}^T \mathbf{K} \frac{\partial \mathbf{U}}{\partial \rho} \\ &+ \mathbf{U}^T \frac{\partial \mathbf{K}}{\partial \rho} \mathbf{U} - \lambda^T \left(\frac{\partial \mathbf{K}}{\partial \rho} \mathbf{U} + \mathbf{K} \frac{\partial \mathbf{U}}{\partial \rho} - \frac{\partial \mathbf{F}}{\partial \rho} \right) \end{aligned} \quad (12)$$

After re-arranging, we get

$$\frac{\partial C^*}{\partial \rho} = 2\mathbf{U}^T \mathbf{K} \frac{\partial \mathbf{U}}{\partial \rho} + \mathbf{U}^T \frac{\partial \mathbf{K}}{\partial \rho} \mathbf{U} - \lambda^T \left(\frac{\partial \mathbf{K}}{\partial \rho} \mathbf{U} + \mathbf{K} \frac{\partial \mathbf{U}}{\partial \rho} - \frac{\partial \mathbf{F}}{\partial \rho} \right) \quad (13)$$

Assigning the arbitrary λ as $2\mathbf{U}$, the above equation becomes

$$\frac{\partial C^*}{\partial \rho} = -\mathbf{U}^T \frac{\partial \mathbf{K}}{\partial \rho} \mathbf{U} + 2\mathbf{U}^T \frac{\partial \mathbf{F}}{\partial \rho} \quad (14)$$

The first term on the RHS of the above equation can be easily calculated; the term $\frac{\partial \mathbf{F}}{\partial \rho}$ is the sensitivities of the external load vector with respect to the variation of the element density. The load vector acting on a finite element is decided by whether the element is a boundary element or not. This, in turn, is dependent on the threshold density, which decides the boundary elements. Therefore, the load vector acts as a Heaviside function. Also, the derivatives of the force vectors require the derivatives of a Heaviside function, a Dirac delta function. This function is zero everywhere except at the threshold density value. Therefore, the term $\frac{\partial \mathbf{F}}{\partial \rho}$ can be neglected [11, 12]. Hence, the sensitivity of the objective function w.r.t the design variable for each element becomes

$$\frac{\partial C^*}{\partial \rho_i} = -\mathbf{u}_e^T \frac{\partial \mathbf{K}_e}{\partial \rho_i} \mathbf{u}_e = -n\rho_i^{n-1} \mathbf{u}_e^T \mathbf{K}_e \mathbf{u}_e \quad (15)$$

A mesh-independency filter developed by [13] is used to prevent numerical instabilities.

4 Stiffness Matrix for Solid ($\rho = 1$) Four Noded Bi-linear Element

The stiffness matrix is the same for all solid elements. This can be calculated by the same procedure employed in a four noded rectangular isoparametric element. The interpolation functions of the rectangular elements can be calculated from corresponding one-dimensional interpolation functions by taking the tensor product two orthogonal one-dimensional interpolation functions. Let x and y coordinates be taken along element sides, with the origin of the coordinate system at the center of the rectangle. Then for an element with dimensions $2a$ and $2b$ along the x and y directions, respectively, the interpolation functions are given as follows:

$$\begin{aligned} N_1 &= \frac{1}{4ab} (x - x_2) (y - y_4) \\ N_2 &= -\frac{1}{4ab} (x - x_1) (y - y_3) \\ N_3 &= \frac{1}{4ab} (x - x_4) (y - y_2) \\ N_4 &= -\frac{1}{4ab} (x - x_3) (y - y_1) \end{aligned} \quad (16)$$

Let $u(x, y)$ and $v(x, y)$ be approximated over the domain by the finite element interpolations:

$$\begin{aligned} u(x, y) &\approx \sum_{i=1}^4 N_i(x, y) u_i \\ v(x, y) &\approx \sum_{i=1}^4 N_i(x, y) v_i \end{aligned} \quad (17)$$

The strain displacement matrix for the element, \mathbf{B}^e , is given by

$$\mathbf{B}^e \equiv \nabla_S \mathbf{N}^e = \begin{bmatrix} \frac{\partial N_1^e}{\partial x} & 0 & \frac{\partial N_2^e}{\partial x} & 0 & \dots & \frac{\partial N_{nen}^e}{\partial x} & 0 \\ 0 & \frac{\partial N_1^e}{\partial y} & 0 & \frac{\partial N_2^e}{\partial y} & \dots & 0 & \frac{\partial N_{nen}^e}{\partial y} \\ \frac{\partial N_1^e}{\partial y} & \frac{\partial N_1^e}{\partial x} & \frac{\partial N_2^e}{\partial y} & \frac{\partial N_2^e}{\partial x} & \dots & \frac{\partial N_{nen}^e}{\partial y} & \frac{\partial N_{nen}^e}{\partial x} \end{bmatrix} \quad (18)$$

$$\mathbf{B}^e = \frac{1}{4ab} \begin{bmatrix} y - y_4 & 0 & y_3 - y & 0 & y - y_2 & 0 & y_1 - y & 0 \\ 0 & x - x_2 & 0 & x_1 - x & 0 & x - x_4 & 0 & x_3 - x \\ x - x_2 & y - y_4 & x_1 - x & y_3 - y & x - x_4 & y - y_2 & x_3 - x & y_1 - y \end{bmatrix} \quad (19)$$

The plane stress constitutive relation for an orthotropic medium is given by

$$\begin{Bmatrix} \sigma_{xx} \\ \sigma_{yy} \\ \sigma_{xy} \end{Bmatrix} = \begin{bmatrix} \hat{c}_{11} & \hat{c}_{12} & 0 \\ \hat{c}_{12} & \hat{c}_{22} & 0 \\ 0 & 0 & \hat{c}_{66} \end{bmatrix} \begin{Bmatrix} \varepsilon_{xx} \\ \varepsilon_{yy} \\ 2\varepsilon_{xy} \end{Bmatrix} \quad (20)$$

$$\begin{aligned} \hat{c}_{11} &= \frac{E_1}{(1 - \nu_{12}\nu_{21})}, & \hat{c}_{22} &= \frac{E_2}{(1 - \nu_{12}\nu_{21})} \\ \hat{c}_{12} &= \nu_{12}\hat{c}_{22} = \nu_{21}\hat{c}_{11}, & \hat{c}_{66} &= G_{12} \end{aligned} \quad (21)$$

The stiffness matrix can be evaluated using the below given equation.

$$k_0^e = \int_{\Omega_e} \mathbf{B}^{eT} \mathbf{C} \mathbf{B}^e dx \tag{22}$$

The stiffness matrix for an arbitrary density value is given by

$$k^e(\rho) = \rho^n k_0^e \tag{23}$$

5 Load Curve Identification

Identification of boundary elements (load curve) is an important step in problems having design-dependent loads. The four-node bi-linear elements discretize the design domain. A threshold density ρ_T is used to define the boundary of the domain in each iteration. The threshold density is gradually increased as the optimization progresses. Initially, ρ_T is assigned a low value (typically 0.15–0.2), and then for every iteration, a constant value ‘ k ’ is added. The value of ‘ k ’ generally varies from 0.01 to 0.03 and this is fine tuned manually by looking at the rate of convergence of the problem. The loads are applied directly to the nodes of elements that are on the boundary. A start point and an end point as shown in Fig. 3 are defined such that, when we traverse along the element boundaries, (from start point to end point) the load curve is defined. The representation of the element nodes is given in Fig. 2.

The load curve is found out by tracing the path taken from start point to end point. The path is created by joining a series of vector lines from one node to another with four different directions: left, right, up, and down. The rules for determining the direction are given below.

For the interior nodes, when traversing up alongside the boundary of element I , the possible directions to move to the next node are left, up, and right, as shown in Fig. 4a. The dashed arrow shows the possible directions to move from one node to another. The direction for the next move is decided by the density values of neighboring elements (J and K). If the density of element K is greater than threshold density ρ_T , then left is taken. If not, we check the same condition for element J . If the density of element J is greater than ρ_T , we continue upward; else, we take a right. Similar steps, as shown in Fig. 4b–d, are taken when moving rightward, leftward, and downward.

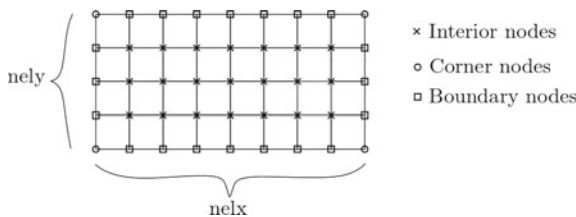


Fig. 2 Classification of the nodes in design domain (nelx and nely are the number of elements along x and y axis)

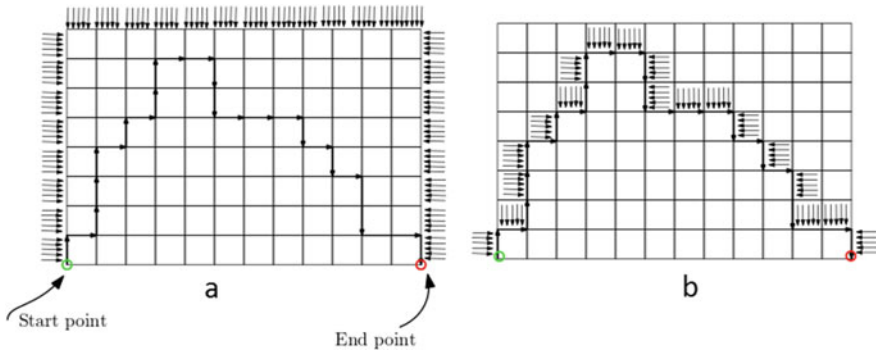


Fig. 3 Schematic showing **a** identification of load curve, **b** loads applied on the load curve

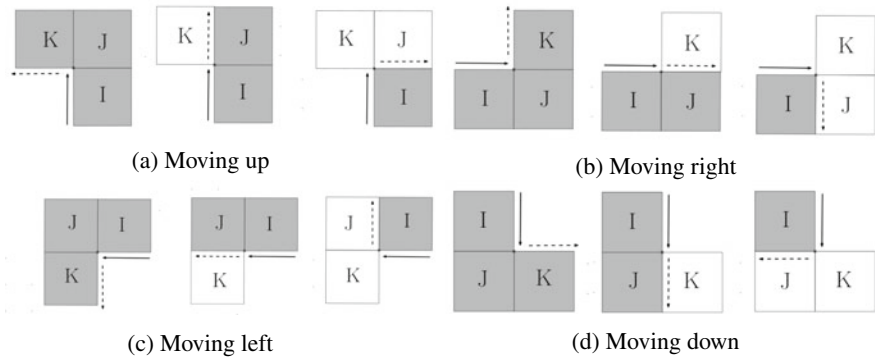


Fig. 4 The rules for determining the advancing direction for interior nodes

For the boundary nodes, the process remains the same except that the location of the boundary node decides the rules for advancing direction, instead of the direction of the previous step as in the interior node. This process is illustrated in Fig. 5. For the upper boundary node, if element K 's density is greater than ρ_T , then right is taken. If not, we check the density of element J . If the density of element J is greater than ρ_T , we move downwards; else, we take a left. Similar steps are taken for right, left, and lower boundary nodes. For corner nodes, only one element decides the direction of the next step. This is shown in Fig. 6. For a upper left node, if the density of element K is greater than ρ_T , then right is taken or else we move downward. Similar steps are taken for upper right, lower left, and lower right corner nodes. Once we reach the end point, the identification of the load curve is complete. The load vector is then directly applied to the new boundary.

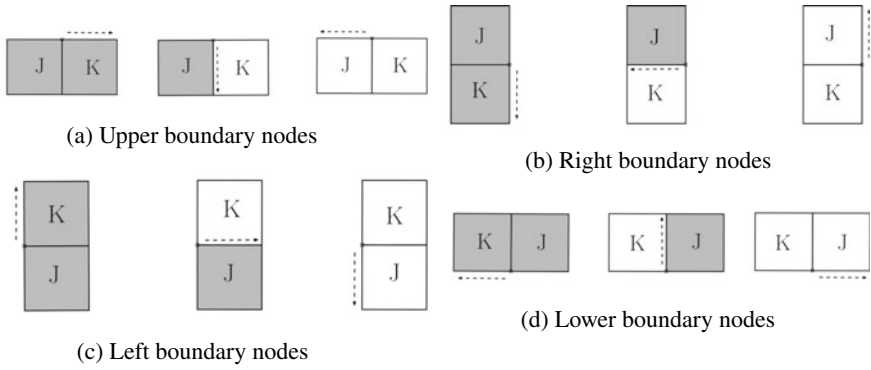


Fig. 5 The rules for determining the advancing direction for boundary nodes

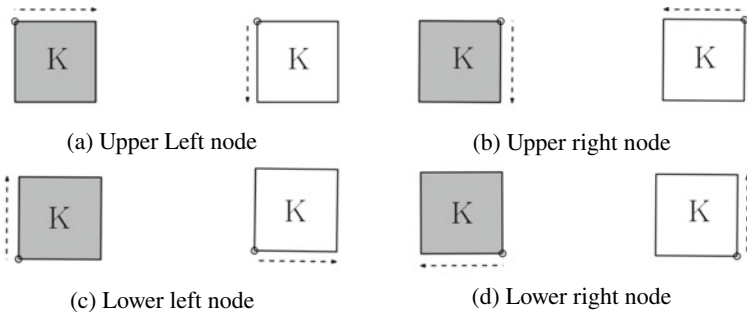


Fig. 6 The rules for determining the advancing direction for corner nodes

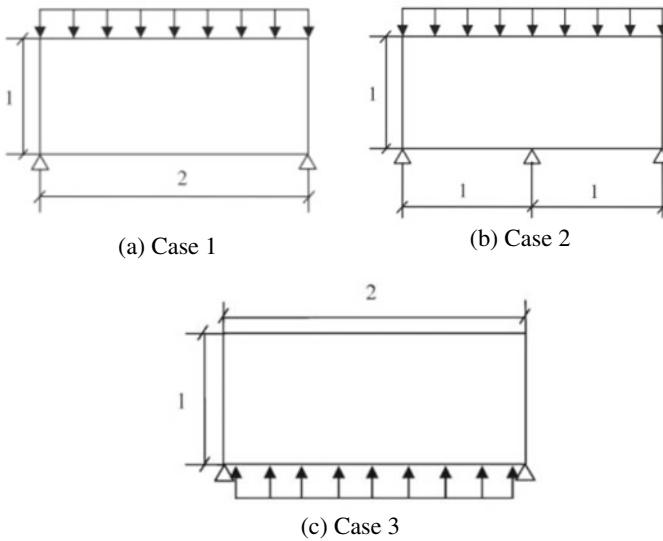


Fig. 7 Loading and boundary conditions for different cases

6 Numerical Illustration

Three example case studies are considered to illustrate the method and results of optimization.

Case (1) Short beam subjected to pressure: Optimization of a beam which is simply supported and carrying a pressure load on the top surface is considered. The finite element mesh consists of 800 elements (40 along x -axis and 20 along y -axis). The boundary conditions are shown in Fig. 7a. The pressure value is 1 Pa. The material properties are $E_1 = 100$ Pa, $E_2 = 150$ Pa, and $\nu_{12} = 0.3$ and $G = 40$ Pa. The volume fraction is kept as 0.5. Figure 8 shows loading conditions and material layout (in left and right panel, respectively) at different iterations.

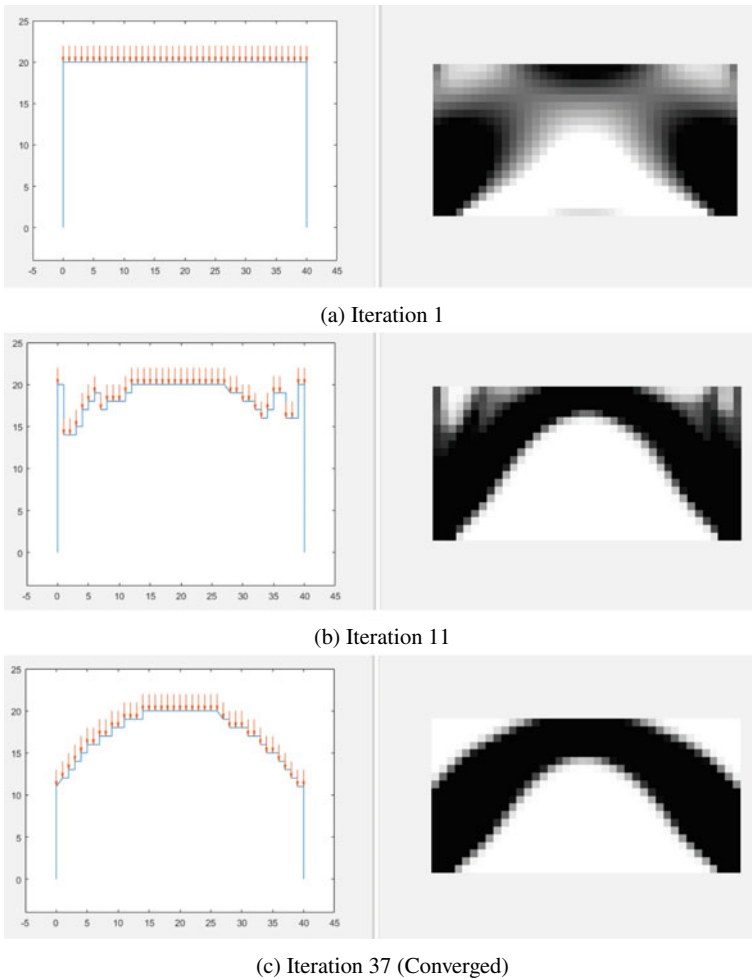


Fig. 8 Boundary and loading conditions (left) and structure (right) at different iterations for Case 1

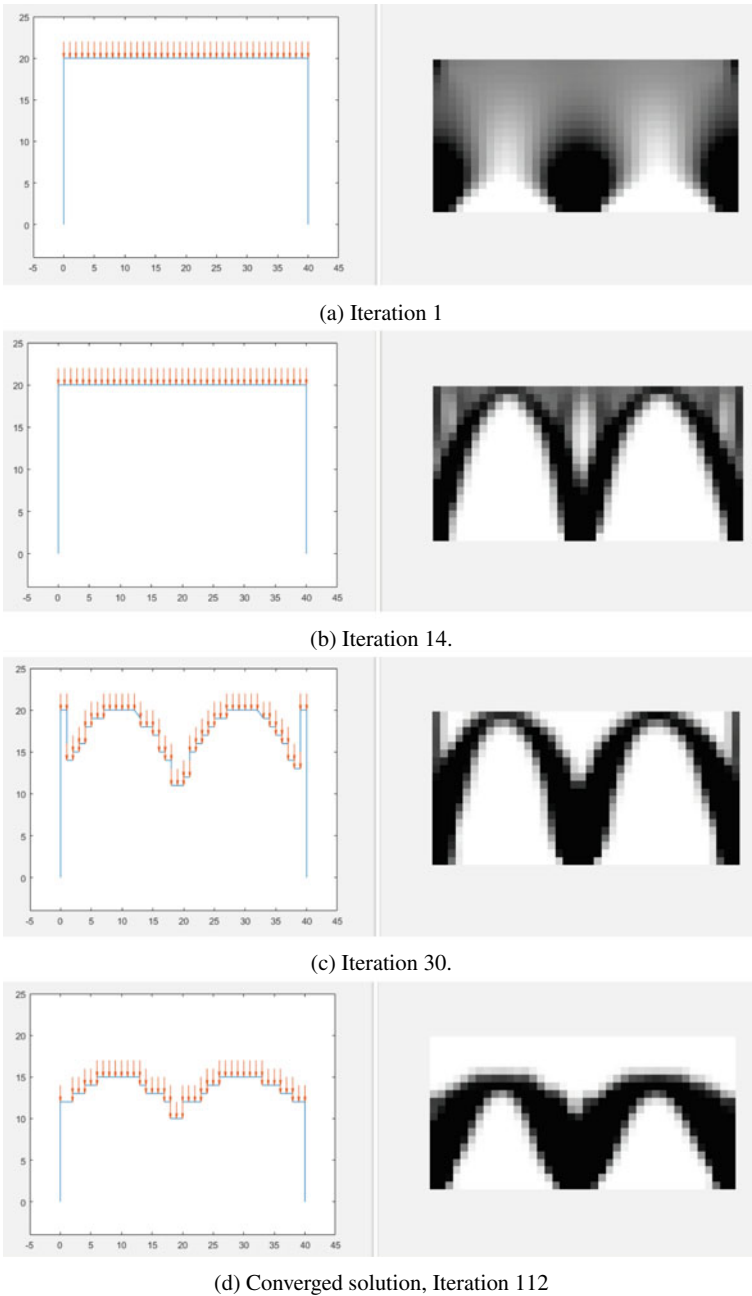
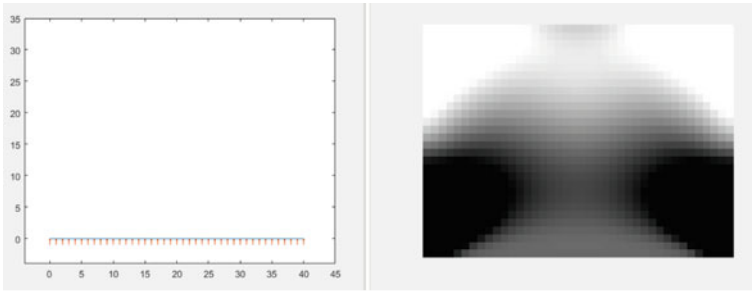
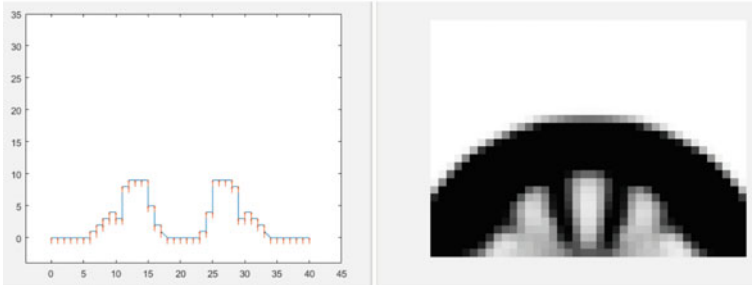


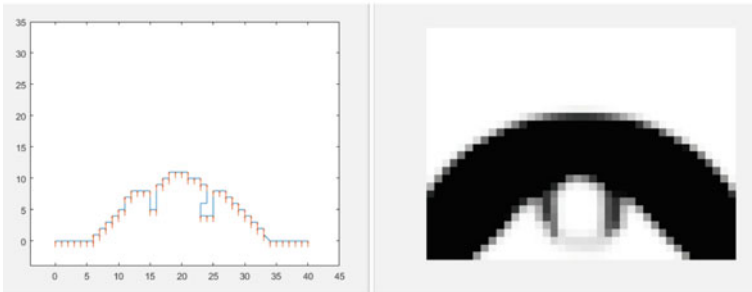
Fig. 9 Boundary and loading conditions (left) and structure (right) at different iterations for Case 2



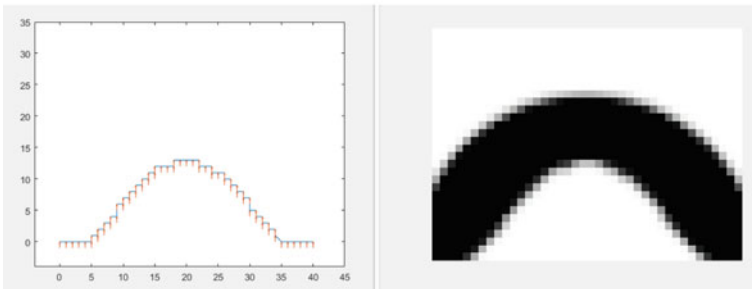
(a) Iteration 1.



(b) Iteration 26.



(c) Iteration 35.



(d) Iteration 78 (Converged).

Fig. 10 Boundary and loading conditions (left) and structure (right) at different iterations for Case 3

Case (2) Pressurized short beam with three supports: A short beam with three supports with a surface load is optimized. The material properties are $E_1 = 100$ Pa, $E_2 = 150$ Pa, and $\nu_{12} = 0.3$ and $G = 40$ Pa. The design domain, initial load, and boundary conditions are shown in Fig. 7b. The evolution of structure and loading conditions is shown in Fig. 9.

Case (3) Internally pressurized cover-like structure: Optimization of a structure, which is pressurized internally, is performed. The FE mesh consists of 800 elements (40 along x -axis and 20 along y -axis). The boundary conditions along with the initial load conditions are shown in Fig. 7c. The load value is 1 Pa. The material properties are $E_1 = 100$ Pa, $E_2 = 150$ Pa, and $\nu_{12} = 0.3$ and $G = 40$ Pa. The volume fraction is set to 0.4. The evolution of structure and loading conditions is shown in Fig. 10.

7 Conclusion

Most structural topology optimization methods reported in literature try to find the stiffest structure with material volume as a constraint and fixed loading conditions. Some recent works explore topology optimization and design-dependent loads but are restricted to the isotropic material model. The work reported here has developed techniques and demonstrated topology optimization with design-dependent loads for an orthotropic material model. Also, a simple boundary identification method is proposed for topology optimization with design-dependent loads. Once the boundary is identified, the loads are directly given to the nodes of the finite element. The SAMP model is used to describe the elemental stiffness as a function of element density. The validity of this method is shown using various numerical examples. Only vertical loads are considered in this work. When pressure loads were applied (where the loading directions are normal to the evolving boundary), the optimization did not converge and kept fluctuating between two values. The authors intend to work further to resolve the convergence issue and extend the work to include pressure loads.

References

1. Bendsøe MP, Kikuchi N (1988) Generating optimal topologies in structural design using a homogenization method. *Comput Methods Appl Mech Eng* 71(2):197–224
2. Bendsoe MP (1989) Structural optimization optimal shape design as a material distribution problem. Technical report
3. James KA, Hansen JS, Martins JRRRA (2009) Structural topology optimization for multiple load cases using a dynamic aggregation technique *Structural topology optimization for multiple load cases using a dynamic aggregation technique*. *Eng Optim* 41(12):1103–1118
4. Hammer VB, Olhoff N (2000) Topology optimization of continuum structures subjected to pressure loading. *Struct Multidiscip Optim* 19(2):85–92
5. Fuchs MB, Shemesh NNY (2004) Density-based topological design of structures subjected to water pressure using a parametric loading surface. *Struct Multidiscip Optim* 28(1):11–19

6. Du J, Olhoff N (2004) Topological optimization of continuum structures with design-dependent surface loading - Part I: new computational approach for 2D problems. *Struct Multidiscip Optim* 27(3):151–165
7. Bendsøe MP, Lund E, Olhoff N, Sigmund O (2005) Topology optimization—broadening the areas of application. *Control Cybern* 34(1):7–36
8. Lee E, James KA, Martins JRRR (2012) Stress-constrained topology optimization with design-dependent loading. *Struct Multidiscip Optim* 46(5):647–661
9. Bruggi M, Cinquini C (2009) An alternative truly-mixed formulation to solve pressure load problems in topology optimization. *Comput Methods Appl Mech Eng* 198(17–20):1500–1512
10. Zhang H, Zhang X, Liu S (2008) A new boundary search scheme for topology optimization of continuum structures with design-dependent loads. *Struct Multidiscip Optim* 37(2):121–129
11. Ibhadoe O, Zhang Z, Rahnama P, Bonakdar A, Toyserkani Ehsan (2020) Topology optimization of structures under design-dependent pressure loads by a boundary identification-load evolution (BILE) model. *Struct Multidiscip Optim* 62(4):1865–1883
12. Zheng B, Gea HC (2005) Structural topology optimization under design-dependent loads. In: *Proceedings of IDETC/CIE*, vol 41, pp 530–541
13. Sigmund O (2001) A 99 line topology optimization code written in matlab. *Struct Multidiscip Optim* 21(2):120–127

Lattice Topology Optimization of Hip Bone Microstructure



S. Rajaraman and Sourav Rakshit

1 Introduction

The human hip bone performs the vital task of transferring the upper body's weight to the lower limbs. Walking forms an integral part of routine activities, and hence walking loads have a significant effect on hip bone adaptation. The hip bone typically consists of a sandwich structure with a thin cortical outer shell and a highly porous cancellous (or trabecular) bone inside [1]. This unique sandwich architecture gives the hip bone the load-bearing capacity, which ranges up to six times the body weight. Hence, researchers are interested in finding the optimal global geometry and microstructure relevant for bone replacement and implant applications. Numerous studies have been carried out to find the optimal microstructure of femur bone, whilst very little research has been carried out on the hip bone design. This gap could be partly because of the need for 3-D finite element models for the hip bone, which are computationally intensive as against 2-D femur bone approximations, which needs relatively lesser computational power. Jang and Kim [2] have used topology optimization to study the trabecular architecture of femur bone with an extensive study on Wolff's law. Park et al. [3] have optimized the bone internal microstructure of femur bone with Solid isotropic material with penalization (SIMP)-based topology optimization and felt the need for additional constraints in the form of perimeter constraints to mimic the femur bone microstructure. Zaharie and Phillips [4] have predicted the pelvic construct based on a structural modelling approach with strain driven bone adaptation algorithm. The method of topology optimization has been used by Iqbal et al. [5] to optimize the hip bone global geometry at various resections for the hip prosthesis application. SIMP-based topology optimization has been used to study the optimal global geometry of pelvic bone by Kumar and Rakshit [6],

S. Rajaraman · S. Rakshit (✉)

Department of Mechanical Engineering, Machine Design Section, Indian Institute of Technology Madras, Chennai, Tamil Nadu 600036, India

e-mail: srakshit@iitm.ac.in

© The Author(s), under exclusive license to Springer Nature Singapore Pte Ltd. 2023
P. Pradeep Pratapa et al. (eds.), *Advances in Multidisciplinary Analysis and Optimization*,
Lecture Notes in Mechanical Engineering,
https://doi.org/10.1007/978-981-19-3938-9_37

353

but have ended up with a hip bone mass that is significantly higher than that of the natural hip bone due to ad-hoc strategies implemented to preserve volume for binary densities of 0 or 1 (void or solid). There has been limited research in the optimal design of hip bone geometry and microstructure as against the finite element analysis of hip bone which is well established [1, 7, 8].

Although density-based topology optimization with the SIMP method, in particular, has been a valuable tool for mimicking the internal bone microstructure, manufacturing optimized designs with a multitude of intermediate densities has been highly complicated. Algorithms adopt ad-hoc ways to steer the optimized body into either void or solid to ease the manufacturing, which finally becomes a sub-optimal solution with the loss of heterogeneity. To alleviate the shortcomings as mentioned above and with the advancements in additive manufacturing, a method of integrating lattice cells and topology optimization is used here similar to the seminal works of Bendsoe and Kikuchi [9]. The lattice-based topology optimization using homogenization is a relatively older technique but had minimal applications owing to its complex manufacturing needs back when it was introduced. With the significant advances in additive manufacturing, the method of lattice topology optimization is gaining impetus and is now an active area of research with advantages of tailor-made material properties and increased stiffness to weight ratio. The optimal porous yet stiff hip bone microstructure find applications in reducing pelvic implant's stress shielding effect and promoting osseointegration for stable implant fixations.

In this current work, we use pre-defined lattice cell units and integrate these lattice cells with topology optimization utilizing homogenization with the weighted multi-loads of walking gait cycle to design porous yet stiff optimal microstructures and understand how much lattice topology optimization can help replicate actual hip bone microstructure. Further, the resulting optimal solutions are compared to the natural hip bone with the information available in the literature. Finally, the effect of the choice of lattice cell on the weighted compliance is studied.

2 Hip Bone Model

2.1 *Material and Geometric Model*

Figure 1a, b shows the hip bone model purchased from Turbosquid domain [10]. The model is built from laser topography (LT) using a 3-D laser scanner with 0.1 mm accuracy. The cloud data of coordinates are converted to a meshed file and hence to a CAD file and further corrected for self-intersections. The CAD file is then scaled and mirrored to match the anthropometric characteristics as given in Dostal and Andrews [11]. The baseline material properties of cortical bone with a density of 1800 kg/m^3 , isotropic elastic modulus of 17 GPa and Poisson's ratio of 0.3 are adopted from Dalstra et al. [1]. The total hip bone mass comprises the cortical shell and cancellous core mass. The mean value of elastic modulus of cancellous or

Table 1 Hip bone mass parameters

Parameter	Value	Units
Total volume of hip bone (V)	290,563.503	mm ³
Cortical shell (2 mm) volume (V_c)	105,877.005	mm ³
Trabecular bone volume ($V_t = V - V_c$)	184,686.498	mm ³
Density of cortical bone (ρ_c)	1800	kg/m ³
Density of trabecular bone (ρ_t)	483	kg/m ³
Cortical bone mass ($m_c = \rho_c \times V_c$)	0.190	kg
Trabecular bone mass ($m_t = \rho_t \times V_t$)	0.090	kg
Actual total mass of hip bone (m_0)	0.280	kg
Initial mass for optimization of hip bone		
Full cortical (m_1)	0.523	kg
Mass Fraction (m_0/m_1)	0.535	—

trabecular bone of pelvis as suggested by Anderson et al. [7] is 338 MPa, and this value is used to compute the average mass of the trabecular bone as shown below in Eq. 1. The apparent density of bone is the ratio of the solid mass of bone to the total volume occupied by the bone (including the void spaces). An empirical relation that relates apparent density (ρ_a) in g/cm³ of pelvic trabecular bone to its elastic modulus in (MPa) is given by Dalstra et al. [12] and is shown below.

$$E = 2017.3(\rho_a)^{2.46} \quad (1)$$

Using Eq. 1 and with the trabecular elastic modulus of 338 MPa, we estimate the ρ_a to be 0.483 g/cm³ or 483 kg/m³. Different works [7, 8] suggest different average cortical thickness, though, in reality, cortical thickness varies from 0.44 to 4 mm as given by Anderson et al. [7]. Dalstra et al. [1] suggested that a homogeneous cortical thickness and elastic modulus for trabecular bone was appropriate for comparative studies. An average cortical thickness of 2 mm was suggested by Phillips et al. [8] and is incorporated in this analysis. The mass parameters are shown in Table 1.

2.2 Boundary Conditions

The muscle force directions of the 21 muscles are obtained by subtracting the coordinates of the proximal and distal insertion points from the works of Dostal and

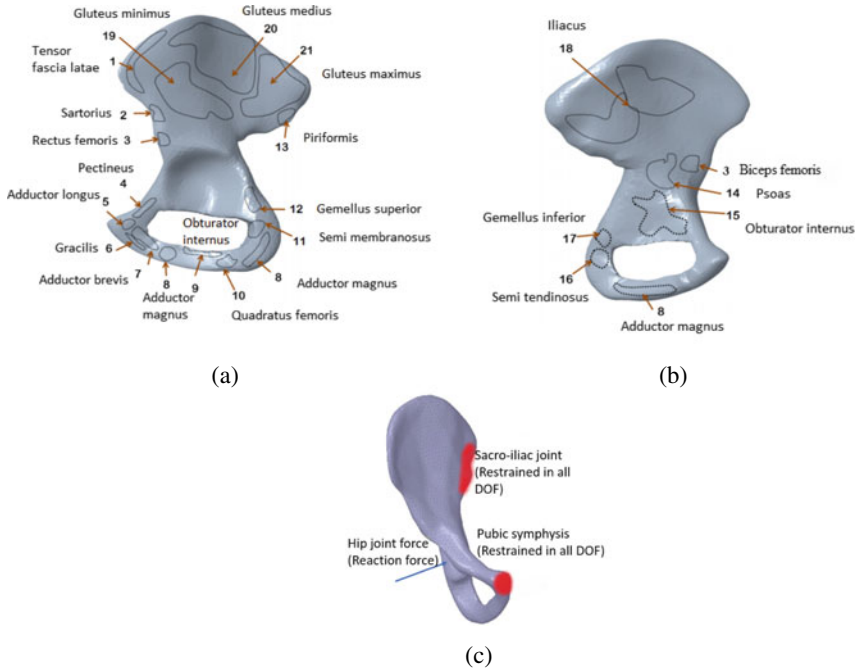


Fig. 1 Hip bone model with boundary conditions and muscle attachment areas. **a** and **b** are the representative muscle attachment areas on the hip bone adapted from [6]. **c** Hip bone boundary conditions (the red zones represent the fixed constraints at sacro-iliac joint and pubic symphysis) and the hip joint force is applied as a reaction force at the acetabulum region

Andrews [11]. The 21 muscle attachment areas and the corresponding load values are adopted from Dalstra and Huiskes [13] for the eight phases of walking gait. The sacro-iliac joint and pubic symphysis are constrained at all degrees of freedom as shown in Fig. 1c, whilst the acetabulum region is applied with a reaction force. The directions for the hip joint force are adopted from [14]. Finite element analyses are carried out with a mesh of ten noded tetrahedral elements (quadratic) with 33,135 elements with an average mesh size of 4 mm obtained after a mesh convergence study.

3 Methods

3.1 Homogenization

The lattice topology optimization method helps distribute optimal material in lattice cells that conform to the actual input global geometry. The computation cost would be extremely high if we explicitly model lattice cells and optimize them individually on a

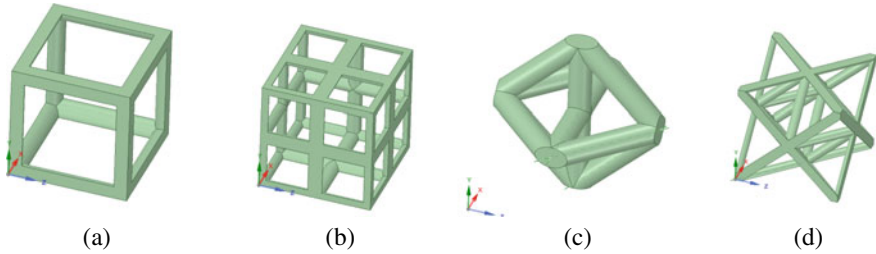


Fig. 2 Lattice units for topology optimization: **a** Cubic. **b** Mid-point. **c** Octahedral. **d** Octet

single scale. Homogenization is a technique used to evaluate the material properties of microstructure, which are further used for design and analysis. The method of homogenization implemented through the Ansys® Academic Research Material Designer, Release 2020 R1 module helps to ascertain the microscopic material properties of the lattice cells. The lattice unit cell is considered a representative volume element (RVE) for homogenization. The design variable relative density (ρ) is given by the ratio of the total volume occupied by the lattice cell to the volume of a solid unit cell. Ten noded tetrahedral elements of mesh size 0.5 mm was used to obtain the constitutive material properties of the lattice cells by applying periodic boundary conditions.

Lattice cells of cubic, mid-point, octet and octahedral (double pyramid with a cross) lattice cells are used for the optimization study as depicted in Fig. 2. The cubic, mid-point and octet have cubic symmetry, resulting in homogeneous and isotropic material properties in all three perpendicular axes. In contrast, the octahedral lattice has transverse symmetry and hence orthotropic material properties. A lattice unit with transverse symmetry is considered to examine the effect of symmetry on the overall weighted compliance and density contours. Similarly, the effect of a stretch dominated lattice cell (octet) is as well compared against bend dominated lattice cells (cubic, mid-point and octahedral). Ansys® Academic Research Material Designer, Release 2020 R1 uses a computational homogenization model to estimate the material properties. For further understanding of RVE and homogenization interested readers can refer the works of [15, 16]. Typically for 3-D unit lattice cells, nine independent terms of the stiffness matrix are to be evaluated. Only six independent load case analyses are needed due to the reflection symmetry of lattices about the three principal coordinate axes. Hence three mutually perpendicular uni-axial tension (or compression) and shear load cases are applied individually. The loads are generally applied as strains rather than forces to reduce the computational time in evaluating the effective homogenized material properties. The boundary conditions for the loading are such that the faces parallel to the loading face in the direction of loads are fixed. For the other set of faces, periodic boundary conditions are applied. Interested readers can refer to Li [17] for detailed discussions on periodic boundary conditions. Further, if there are more than one rotational symmetries, only two load cases are needed to estimate the material stiffness matrix, which is the case for cubic, mid-point and octet lattice cells.

Table 2 Weights of gait phases for compliance minimization

Phase	Name	Weight
1	Double support beginning stance phase	0.04
2	Beginning single support phase	0.11
3	Halfway single support phase	0.22
4	End single support phase	0.13
5	Double support end stance phase	0.04
6	Beginning swing phase	0.11
7	Halfway swing phase	0.22
8	End swing phase	0.13

3.2 Lattice Topology Optimization

Although the constituent materials of the cortical and trabecular bone are the same, the difference in material and elastic properties comes from the anisotropic microarchitecture of the trabecular bone. Similar to this principle, the initial input for the optimization comprises cortical bone material properties and is optimized to decrease compliance (or increase the stiffness). Mass constraints are imposed to ensure that the mass of the optimized hip bone is similar to that of the natural hip bone as evaluated in Table 1. The homogenization technique is used to evaluate the elastic properties \mathbf{E} of the individual lattice cells with different relative densities, and the material elastic properties are fitted over a polynomial called the scaling laws that are a function of relative density ρ . The muscle attachment areas are part of the non-design domain to facilitate mechanical load transfer across the muscle fibres. Hence we impose this additional non-design domain along with the boundary conditions for optimization study.

The lattice topology optimization is carried out in the Ansys® Academic Research Mechanical, Release 2020 R1 topology optimization module. Compliance is represented as c , which is a function of relative density ρ and m_e being the mass of individual finite elements. ρ of value 1 specifies a solid lattice, whilst $\rho = 0.5$ represents a half-filled lattice and $\rho = 0$ represents a void. For the lattices considered, the diameter of the struts varies whilst the lattice cell size is constant and fixed at 4mm. The lattice cell size is chosen to capture the trabecular strut sizes effectively in the mesoscale, whose diameter value ranges from 0.2 to 4 mm [4, 18]. \mathbf{K} here represents the global stiffness matrix, and n is the total number of ten noded tetrahedral mesh elements. Hence the problem formulation is posed as shown below in Eq. 2.

$$\begin{aligned}
\min_{\rho_1, \rho_2, \dots, \rho_n} \quad & c(\rho) = \sum_{i=1}^N w_i \mathbf{f}_i^T \mathbf{u}_i \\
\text{s.t.} \quad & \mathbf{K} \mathbf{u}_i = \mathbf{f}_i \\
& \sum_{e=1}^n \rho_e m_e \leq m_0 \\
& \mathbf{E} = \mathbf{E}(\rho_e) \\
& \rho_{\min} \leq \rho \leq 1
\end{aligned} \tag{2}$$

\mathbf{u}_i , \mathbf{f}_i corresponds to the global displacement and load vector corresponding to i th gait cycle load. m_0 refers to the actual mass of hip bone obtained from Table 1 and N refers to the total number of gait phases. A lower limit of 10^{-3} is capped on the relative density (ρ) to overcome numerical singularities. ρ_e is the relative density of element e . The Ansys® Academic Research Mechanical, Release 2020 R1 topology optimization module uses a sequential convex programming (SCP) technique in addition to the method of moving asymptotes (MMA) to ensure rapid convergence as given by [19]. Convergence is achieved when the weighted compliance of the subsequent three iterations differ not more than 0.5%. The loading effects of the gait cycle phases are considered weighted based on the proportion of cycles each phase contributes to the walking gait cycle. Table 2 specifies the gait phase and its corresponding weight for compliance minimization. The weight values are estimated from the works of Dalstra and Huiskes [13].

3.3 Sensitivity Analysis

The derivative of the objective function gives vital information on search directions for the optimal solutions and ensures quicker convergence. Substituting \mathbf{f}_i as $\mathbf{K} \mathbf{u}_i$ from Eq. 2 we get

$$c(\rho) = \sum_{i=1}^8 w_i \mathbf{f}_i^T \mathbf{u}_i = \sum_{i=1}^8 w_i \mathbf{u}_i^T \mathbf{K} \mathbf{u}_i \tag{3}$$

The derivative of the compliance c is obtained by taking the first derivative of Eq. 3 with respect to ρ

$$\frac{\partial c(\rho)}{\partial \rho} = \sum_{i=1}^8 w_i (2 \mathbf{u}_i^T \mathbf{K} \frac{\partial \mathbf{u}_i}{\partial \rho} + \mathbf{u}_i^T \frac{\partial \mathbf{K}}{\partial \rho} \mathbf{u}_i) \tag{4}$$

Differentiating $\mathbf{K} \mathbf{u}_i = \mathbf{f}_i$ with respect to ρ is given as

$$\frac{\partial \mathbf{K}}{\partial \rho} \mathbf{u}_i + \mathbf{K} \frac{\partial \mathbf{u}_i}{\partial \rho} = 0 \tag{5}$$

$$\mathbf{K} \frac{\partial \mathbf{u}_i}{\partial \rho} = - \frac{\partial \mathbf{K}}{\partial \rho} \mathbf{u}_i \quad (6)$$

Substituting the value of $\mathbf{K} \frac{\partial \mathbf{u}_i}{\partial \rho}$ in Eq. 4 we get

$$\frac{\partial c(\rho)}{\partial \rho} = - \sum_{i=1}^8 w_i (\mathbf{u}_i^T \frac{\partial \mathbf{K}}{\partial \rho} \mathbf{u}_i) \quad (7)$$

4 Results and Discussion

Figure 3 shows the functionally graded cubic lattices across a cross section. The graded lattices typically represent the trabecular core. It is found that there are no significant differences in density contours from one lattice type to the other. Only very small local changes in density contours are found between the four lattice types. Typically the red zones in the density contours of Fig. 4 represent the cortical shell, and blue contours represent the porous trabecular zones. The cortical shell has predominantly red zones with a few blue patches as well seen on the cortical surface. It was also seen that from homogenization analysis of inner blue regions of low relative density, the elastic modulus of the homogenized cells was within the range of elastic modulus of actual trabecular bone 2.5–3829 MPa as estimated by Anderson et al. [7]. Through a cut section view, we see an approximate sandwich architecture with the thin cortical shell filled with a porous trabecular layer as shown in Fig. 6b. Similar to the estimates of [7], we see the high cortical thickness in the gluteal area and along the rim of the acetabulum. Low cortical thickness was seen in ischial tuberosity, iliac fossa, pubic tubercle and acetabular cup in conformance with [7]. Figure 6a shows a cut section view of a pelvis-femur CT-image. The scan shows

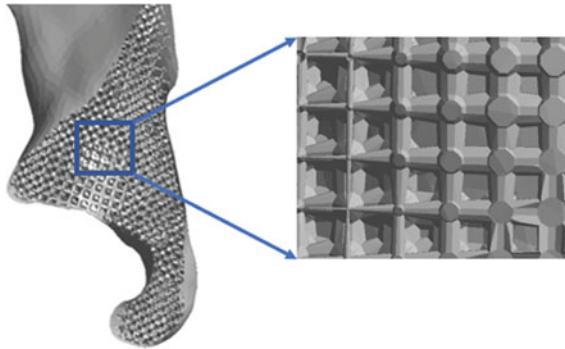


Fig. 3 Functionally graded cubic lattice cells representing the trabecular microstructure after lattice topology optimization

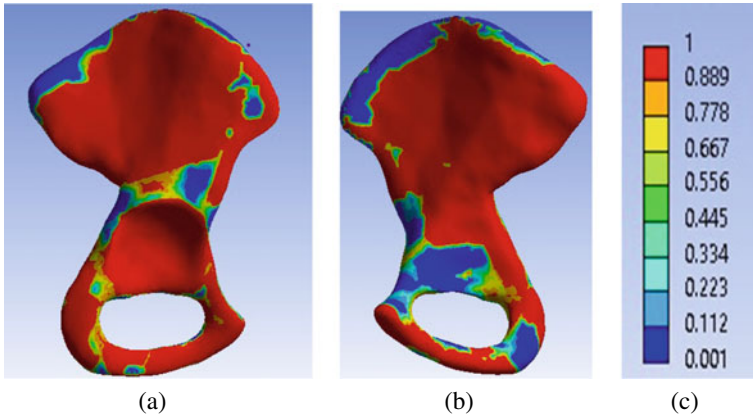


Fig. 4 Density contours for lattice topology Optimization with cubic lattice: **a** Exterior view. **b** Interior view. **c** Legends for the density contours from 0 to 1

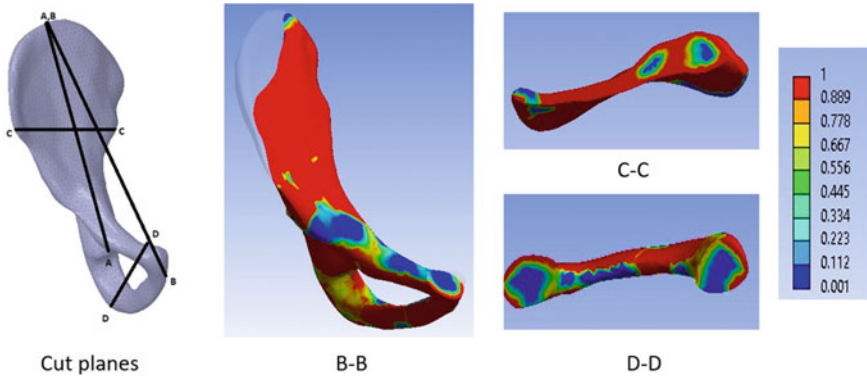


Fig. 5 Density contours of the section views along 4 different planes A-A, B-B, C-C, D-D with corresponding density legends

a sandwich architecture with the thin white zone representing cortical bone and thin grey struts of the trabecular bone. The optimized model with density contours of a similar cross-section is shown in Fig. 6b for comparison. We see a higher cortical thickness around the gluteal area as depicted by Fig. 5. Typically iliac crest is a bone marrow rich region with lesser muscle activity, and this could be one of the reasons for low-density contours (blue region) seen on the iliac crest surface Fig. 4b. Cross-sections along D-D (Fig. 5) shows low cortical thickness around the pubic tubercle area and cross-sections along B-B (Fig. 5) we see lower cortical thickness zones in ischial tuberosity. Lower cortical thickness was seen further in regions of the acetabular cup as in Fig. 6b, and iliac fossa as shown in Fig. 4b. Hence the estimated areas of high and low cortical thickness are in good agreement with that of Anderson et al. [7] and Zaharie and Phillips [4].

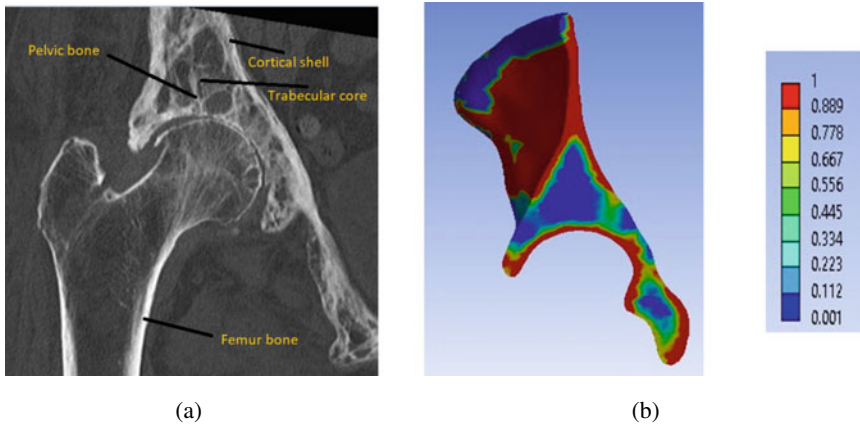


Fig. 6 Comparison of CT-image of hip bone with the density contours of cubic lattice-based optimal hip bone microstructure: **a** CT-cut section image of hip bone and femur, the white shell represents cortical bone and the inner struts represent trabecular region. **b** The density contours of hip bone along section A-A of Fig. 5

Although the optimization technique captures the microarchitecture reasonably well, there are certain regions where the low-density regions are seen on the cortical surface. The critical factor of this variation could be that walking has not much influenced these blue zones towards bone adaptation. The results of Zaharie and Phillips [4] augment this fact where the regions on blue zones (beneath obturator foramen) of interior view in Fig. 4b are influenced by stair descent, sit-to-stand and stand-to-sit activities. The other factors might be the approximation of a uniform cortical shell with a thickness of 2 mm and the non-inclusion of ligamentous boundary conditions. Nevertheless, the optimization technique serves as a valuable tool in capturing the microstructural details of the natural hip bone. Further, the compliance values across the eight walking phases with various lattice cells are depicted in Table 3. We see that octet lattice provides the maximum stiffness followed by the cubic, mid-point and lowest stiffness is generated by octahedral lattice cells. Octet lattice has efficiently packed stretch dominated struts that offer the highest stiffness compared to other lattice cells though the difference was insignificant. The weighted compliance between the octet and octahedral differed not more than 2 %. The results show that the hip bone model, independent of the choice of lattice symmetry, whether cubic or transverse, results in insignificant differences in the optimum weighted compliance value. We also see that stretch dominated or bend dominated lattices have no considerable effect on compliance due to the weighted multi-loads of muscles. Further studies can include stochastic lattice cells and the effect on optimal weighted compliance from a range of routine activities can be studied.

Table 3 Compliance values of the optimum hip bone for the eight phases of walking gait cycle in N-mm

Walking gait phase	Cubic	Octet	Mid-point	Octahedral
Double support beginning stance phase (1)	491.43	487.71	492.58	494.44
Beginning single support phase (2)	503.06	498.52	504.17	513.09
Halfway single support phase (3)	902.40	893.48	903.97	911.31
End single support phase (4)	983.49	974.84	985.20	991.15
Double support end stance phase (5)	1136.62	1132.07	1138.13	1144.89
Beginning swing phase (6)	1541.32	1533.41	1542.85	1546.85
Halfway swing phase (7)	89.02	87.92	89.19	88.63
End swing phase (8)	243.84	242.06	244.38	243.88
Weighted combination of gait phases	667.668	662.409	668.742	672.705

5 Conclusions and Future Work

Lattice topology optimization serves as a valuable computational method to optimize and study the microstructure of the hip bone. Many morphological similarities were found between the optimized hip bone model and that of information available in literature corresponding to the hip bone. This in-silico optimization strategy can help us build pelvic constructs after tumour resections and injuries with pre-defined custom lattice shapes, matching the weight and architecture of natural hip bone. Prosthesis with comparable bone material properties and architecture are said to offset stress shielding effects, so with additional bone in-growth/pore sizes constraint and additive manufacturing constraints, it is possible to develop a patient-specific custom prosthesis that would resemble near the natural hip bone. Compared to other topology optimization techniques, the optimized designs can be translated into additive manufacturing with minimal post-processing and retention of heterogeneity. Further studies can include the weighted effect of daily activities such as sit-to-stand, stair climbing with additional objectives of metabolic cost reduction and adopting stochastic tailor-made lattice units.

Acknowledgements The authors would like to thank Prof. C. Sujatha from the Department of Mechanical Engineering, IIT Madras for sharing the CAD model of the human hip bone.

References

1. Dalstra M, Huijskes R, van Erning LJTO (1995) Development and validation of a three-dimensional finite element model of the pelvic bone
2. Jang IG, Kim IY (2008) Computational study of Wolff's law with trabecular architecture in the human proximal femur using topology optimization. *J Biomech* 41(11):2353–2361
3. Park J, Sutradhar A, Shah JJ, Paulino GH (2018) Design of complex bone internal structure using topology optimization with perimeter control. *Comput Biol Med* 94:74–84 (2018)
4. Zaharie DT, Phillips A (2018) Pelvic construct prediction of trabecular and cortical bone structural architecture. *J Biomech Eng* 140(9)
5. Iqbal T, Wang L, Li D, Dong E, Fan H, Jun Fu, Cai Hu (2019) A general multi-objective topology optimization methodology developed for customized design of pelvic prostheses. *Medical Eng Phys* 69:8–16
6. Kumar KES, Rakshit S (2020) Topology optimization of the hip bone for gait cycle. *Struct Multidiscip Optim* 62:2035–2049
7. Anderson AE, Peters CL, Tuttle BD, Weiss JA (2005) Subject-specific finite element model of the pelvis: development, validation and sensitivity studies. *J Biomech Eng* 127(3):364–373
8. Phillips ATM, Pankaj P, Howie CR, Usmani AS, Simpson AHRW (2007) Finite element modelling of the pelvis: inclusion of muscular and ligamentous boundary conditions. *Med Eng Phys* 29(7):739–748
9. Bendsøe MP, Kikuchi N (1988) Generating optimal topologies in structural design using a homogenization method. *Comput Methods Appl Mech Eng* 71(2):197–224
10. Turbosquid (2000) <https://www.turbosquid.com>
11. Dostal WF, Andrews JG (1981) A three-dimensional biomechanical model of hip musculature. *J Biomech* 14(11):803–812
12. Dalstra M, Huijskes R, Odgaard AV, Van Erning L (1993) Mechanical and textural properties of pelvic trabecular bone. *J Biomech* 26(4–5):523–535
13. Dalstra M, Huijskes R (1995) Load transfer across the pelvic bone. *J Biomech* 28(6):715–724
14. Bergmann G, Deuretzbacher G, Heller M, Graichen F, Rohlmann A, Strauss J, Duda GN (2001) Hip contact forces and gait patterns from routine activities. *J Biomech* 34(7):859–871
15. Hollister SJ, Kikuchi N (1991) A comparison of homogenization and standard analysis for periodic porous composites. *Comp Mech* 83:143–198
16. Kouznetsova V (2002) Computational homogenization for the multi-scale analysis of multi-phase materials. PhD thesis, Mechanical Engineering
17. Li S (2008) Boundary conditions for unit cells from periodic microstructures and their implications. *Compos Sci Technol* 68(9):1962–1974
18. Nägele E, Kuhn V, Vogt H, Link TM, Müller R, Lochmüller E-M, Eckstein F (2004) Technical considerations for microstructural analysis of human trabecular bone from specimens excised from various skeletal sites. *Calcified Tissue Int* 75(1):15–22
19. Zillober C (2001) Global convergence of a nonlinear programming method using convex approximations. *Numer Algorithms* 27(3):265–289

Optimization Applications: Manufacturing

Optimization of Fused Filament Fabrication for Maximum Stiffness Considering Anisotropy



Rahul Ramachandran and G. Saravana Kumar

1 Introduction

Fused filament fabrication (FFF) is one of the many additive manufacturing (AM) process in which a three-dimensional object is printed layer-by-layer directly from a CAD model. Due to the layer-by-layer approach of the printing process, FFF objects usually exhibit anisotropic mechanical properties. Hence, the build orientation (BO) significantly affects the structural and non-structural properties of the printed part. Even though many researchers have shown that BO has significant implications on the non-structural properties (like surface roughness [1, 2], build time [3, 4], support structures [5], and cost [6]) of the parts manufactured through FFF, the influence of BO on the structural properties is studied only experimentally and that too, in a limited fashion. In this work, we present a numerical approach to analyze the effect of BO on part anisotropy and stiffness and present an optimization framework for maximizing the stiffness. This problem is formulated for minimizing the mean compliance (C) of the structure for a given loading condition.

2 Problem Definition and Formulation

2.1 Build Orientation Optimization

The orientation of a part with respect to x , y , and z -axis of the build platform in AM is known as build orientation (BO). It can be represented mathematically by three

R. Ramachandran (✉) · G. Saravana Kumar

Department of Engineering Design, Indian Institute of Technology Madras, Chennai, India
e-mail: ed19s001@smail.iitm.ac.in

G. Saravana Kumar

e-mail: gsaravana@iitm.ac.in

© The Author(s), under exclusive license to Springer Nature Singapore Pte Ltd. 2023
P. Pradeep Pratapa et al. (eds.), *Advances in Multidisciplinary Analysis and Optimization*,
Lecture Notes in Mechanical Engineering,
https://doi.org/10.1007/978-981-19-3938-9_38

367

Table 1 Parameters used for GA

Parameter	Value
Population size	30
Crossover fraction	0.8
Function tolerance	1e-6
Constraint tolerance	1e-3
Elite count	2

Euler angles (α , β and γ) of rotation of the part (from its base orientation) about the x , y , and z -axis, respectively. The Euler angle of rotation about the z -axis (γ) does not affect the printed part, as it is the layer stacking direction, i.e., BO does not change. Thus, BO optimization considers instantaneous rotation of part about x and y -axis to minimize strain energy (a measure of mean compliance) and can be mathematically described as

$$\min E (\text{Strain energy}) = f_1(\alpha, \beta) = U^T K U \quad (1)$$

subject to

$$0 \leq \alpha \leq 2\pi \quad (2)$$

$$0 \leq \beta \leq 2\pi \quad (3)$$

where U and K are the global stiffness matrix and global displacement vector, respectively, from a FE model of the part under consideration. MATLAB's in-built GA with parameters shown in Table 1 was used for optimization. MATLAB's parallel processing in global optimization toolbox was used to speedup the process.

2.2 Material Characterization

The directional dependencies caused by the layer-by-layer approach are manifested in the form of anisotropic material properties in printed parts. This makes the structural response of the FFF part heavily dependent on BO. In this work, we have chosen an orthotropic model with nine independent material constants (Young's modulus, shear modulus, and Poisson's ratios) to represent the material behavior. These are determined through experiments as described in the next section.

2.2.1 Experimental Setup

In the experimental phase, we have used ASTM D638-14 standard to print the tensile coupons. The printed coupons were 5 mm thick and were printed using Flashforge-Creator 3TM 3D printer with polylactic acid (PLA) material. The tensile coupons were modeled using Autodesk Fusion360® and then exported in STL file format.

FlashPrint® software was used to generate the G-code. A total of 24 tensile coupons were printed (6 orientations and 4 coupons in each orientation) to obtain the elastic properties. The orientations of the tensile coupons are shown in Fig. 1. The tensile tests were carried out using Dak series 9000™ UTM machine performed at 2 mm/min. The engineering constants were determined from the stress-strain curves obtained from the tensile test, and for shear moduli, we use the Eq. 4, as given in [7]. To obtain the Poisson’s ratio, bidirectional strain gauges were used.

$$G_{ij} = \frac{1}{\frac{4}{E_x^{45}} - \frac{1}{E_i} - \frac{1}{E_j} + \frac{2\nu_{ij}}{E_i}} \tag{4}$$

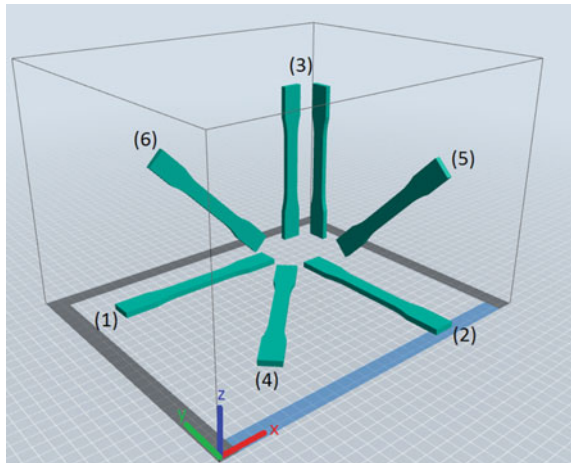
where E_x^{45} is the Young’s modulus of 45° angle tensile coupon.

2.2.2 Constitutive Model

For an orthotropic model, the compliance matrix is given by,

$$S_m = \begin{bmatrix} \frac{1}{E_1} & -\frac{\nu_{21}}{E_2} & -\frac{\nu_{31}}{E_3} & 0 & 0 & 0 \\ -\frac{\nu_{12}}{E_1} & \frac{1}{E_2} & -\frac{\nu_{32}}{E_3} & 0 & 0 & 0 \\ -\frac{\nu_{13}}{E_1} & -\frac{\nu_{23}}{E_2} & \frac{1}{E_3} & 0 & 0 & 0 \\ 0 & 0 & 0 & \frac{1}{G_{23}} & 0 & 0 \\ 0 & 0 & 0 & 0 & \frac{1}{G_{31}} & 0 \\ 0 & 0 & 0 & 0 & 0 & \frac{1}{G_{12}} \end{bmatrix} \tag{5}$$

Fig. 1 Orientations for tensile samples used for experiments



The inverse of the compliance matrix is known as stiffness matrix, given by

$$D_m = S_m^{-1} \quad (6)$$

D_m is the stiffness matrix in the local frame of reference and to obtain the stiffness matrix D in the global coordinate systems for an arbitrary BO; the same is obtained by performing the Euler rotations, and the combined transformation matrix is given by

$$L = \begin{bmatrix} \cos^2 \beta & \sin^2 \alpha \sin^2 \beta & \cos^2 \alpha \sin^2 \beta & \sin \alpha \sin 2\beta & \sin 2\alpha \sin^2 \beta & \cos \alpha \sin 2\beta \\ 0 & \cos^2 \alpha & \sin^2 \alpha & 0 & -\sin 2\alpha & 0 \\ \sin^2 \beta & \sin^2 \alpha \cos^2 \beta & \cos^2 \alpha \cos^2 \beta & -0.5 \sin \alpha \sin 2\beta & \sin 2\alpha \cos^2 \beta & -\cos \alpha \sin 2\beta \\ 0 & 0.5 \sin 2\alpha \sin \beta & -0.5 \sin 2\alpha \sin \beta & \cos \alpha \cos \beta & \cos 2\alpha \sin \beta & -\sin \alpha \cos \beta \\ 0 & 0.5 \sin 2\alpha \cos \beta & -0.5 \sin 2\alpha \cos \beta & -\cos \alpha \sin \beta & \cos 2\alpha \cos \beta & \sin \alpha \sin \beta \\ -0.5 \sin 2\beta & 0.5 \sin^2 \alpha \sin 2\beta & 0.5 \cos^2 \alpha \sin 2\beta & \sin \alpha \cos 2\beta & 0.5 \sin 2\alpha \sin 2\beta & \cos \alpha \cos 2\beta \end{bmatrix} \quad (7)$$

where α and β are the angles of rotation along x and y axis, respectively. The global stiffness matrix can be written as,

$$D = LD_mL^T \quad (8)$$

2.3 FE Formulation

In order to obtain the strain energy for a given boundary conditions and build orientation, we perform a FE analysis. The equations which govern the system defined in the domain Ω with boundary Γ for a 3D linear elastic static problem is given by

$$\nabla_s \cdot \boldsymbol{\sigma} = \mathbf{0} \quad (9)$$

in Ω . The boundary is split into Γ_u and Γ_t such that $\Gamma = \Gamma_u \cup \Gamma_t$, $\Gamma_u \cap \Gamma_t = \emptyset$. The boundary conditions are

$$\begin{aligned} \mathbf{u} &= \widehat{\mathbf{u}} & \text{in } \Gamma_u \\ \boldsymbol{\sigma} \cdot \mathbf{n} &= \widehat{\mathbf{t}} & \text{on } \Gamma_t \end{aligned} \quad (10)$$

where $\boldsymbol{\sigma}$ is the Cauchy stress tensor. The Galerkin weak for this problem can be formulated as:

$$\int_{\Omega} (\nabla \delta \mathbf{u})^T \mathbf{D} (\nabla \mathbf{u}) d\Omega - \int_{\Omega} (\delta \mathbf{u})^T \mathbf{b} d\Omega - \int_{\Gamma_t} (\delta \mathbf{u})^T \mathbf{t} d\Gamma = \mathbf{0} \quad (11)$$

In Eq. 11, \mathbf{u} and $\delta \mathbf{u}$ are called the trial and test functions, respectively, and \mathbf{D} is the global constitutive matrix. The finite element approximations for these functions are given below:

$$\mathbf{u}^h(\mathbf{x}) = \sum_{I=1}^{N_p} \mathbf{N}_I(\mathbf{x}) \mathbf{u}_I, \quad (12)$$

$$\delta \mathbf{u}^h(\mathbf{x}) = \sum_{I=1}^{N_p} \mathbf{N}_I(\mathbf{x}) \delta \mathbf{u}_I \quad (13)$$

where N_p , \mathbf{N} and \mathbf{u}_I are the total number of nodes, the matrix associated with shape function, and the displacement vector of node I . Upon substituting Eqs. 12 and 13 into Eq. 11, we get a system of linear equations, which can be represented in matrix form:

$$\mathbf{K} \mathbf{u} = \mathbf{f} \quad (14)$$

with

$$\mathbf{K} = \int_{\Omega^h} \mathbf{B}^T \mathbf{D} \mathbf{B} d\Omega \quad \mathbf{f} = \int_{\Omega^h} \mathbf{N}^T \mathbf{b} d\Omega + \int_{\Gamma_f} \mathbf{N}^T \widehat{\mathbf{t}} d\Gamma \quad (15)$$

where \mathbf{K} and \mathbf{B} are the global stiffness matrix and strain-displacement matrix, respectively. The strain-displacement matrix is defined as:

$$\mathbf{B}_I(\mathbf{x}) = \nabla_s N_I(\mathbf{x}) = \begin{bmatrix} N_{I,x} & 0 & 0 \\ 0 & N_{I,y} & 0 \\ 0 & 0 & N_{I,z} \\ N_{I,y} & N_{I,x} & 0 \\ 0 & N_{I,z} & N_{I,y} \\ N_{I,z} & 0 & N_{I,x} \end{bmatrix} \quad (16)$$

The stiffness matrix is first calculated locally for each element and then assembled to get the global stiffness matrix. The domain was discretized with 1394 four-noded tetrahedral element. An in-house MATLAB code was developed to perform the FE analysis. Open-source software, Gmsh [8], was used to create the three-dimensional finite element mesh. The post-processing of the results was carried out in MATLAB.

3 Results

3.1 Tensile Properties of Printed Samples

The load displacement curves for six different build orientations are shown in Fig. 2. The data obtained from the experiments were processed in MATLAB. Average elastic modulus and ultimate stress for different build orientations are given in Table 2. The lowest Young's modulus was found in z -direction, which is similar to the results found in other works [7, 9]. The material constants and Poisson's ratio are deduced

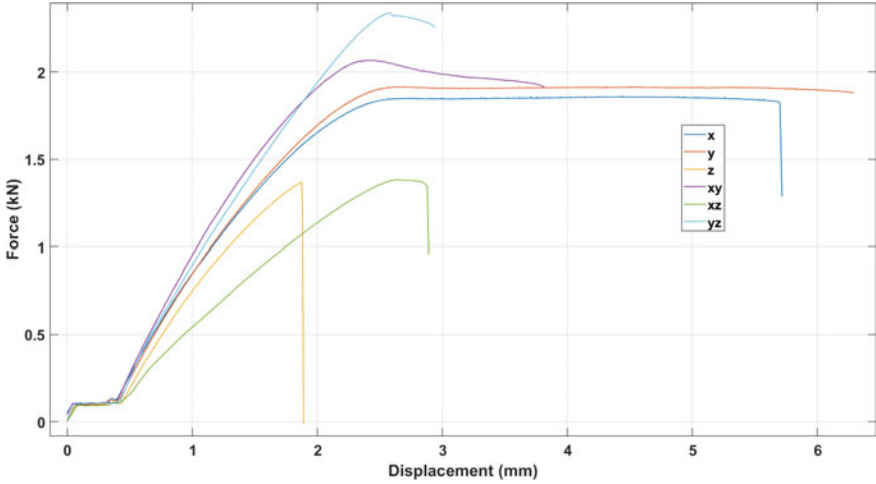


Fig. 2 Load-displacement curve for 6 different build orientations

Table 2 Experimental results

Sample	Build direction	Young’s modulus (GPa)	Ultimate strength (GPa)
1	x	9.6088	28.634
2	y	9.3304	29.501
3	z	9.2061	21.0618
4	xy	11.080	31.831
5	yz	7.1739	35.991
6	xz	9.7977	21.3

Table 3 Material constants

E_x (GPa)	E_y (GPa)	E_z (GPa)	ν_{xy}	ν_{xz}	ν_{yz}	G_{xy} (GPa)	G_{yz} (GPa)	G_{zx} (GPa)
9.608	9.33	9.206	0.285	0.333	0.375	4.782	3.665	2.414

from these curves and are given in Table 3. The difference of maximum and minimum values of Young’s modulus, Poisson’s ratio, and bulk modulus are 4.36%, 31.57%, and 49.33%, respectively, which clearly shows the anisotropy of the fabricated parts.

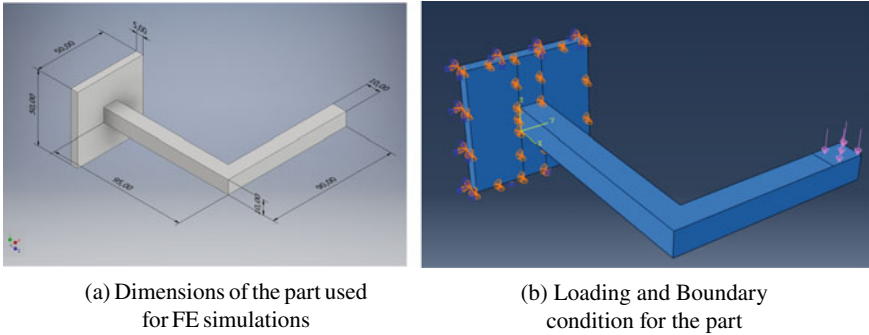


Fig. 3 Part specifications

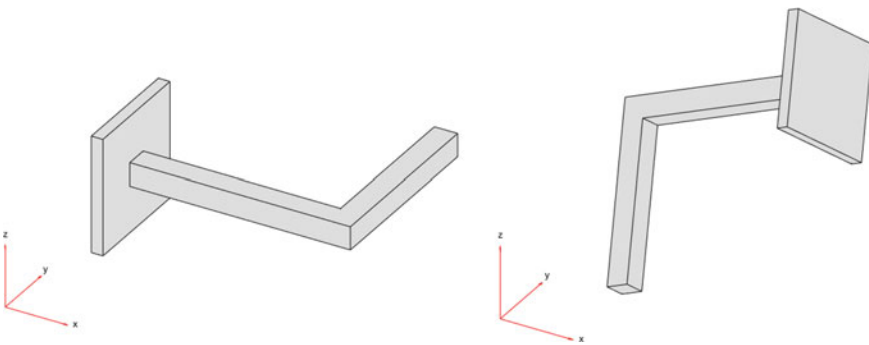


Fig. 4 Initial BO $[0^\circ, 0^\circ]$ (left) and optimal BO $[132.7^\circ, 157^\circ]$ (right)

3.2 Numerical Illustration

A simple load carrying part adapted from [9] is used as a numerical example. The dimensions of the part and the loading and boundary conditions are shown in Fig. 3a, b, respectively. The part sample, loading, and boundary conditions were selected in such a way that it produces stresses in several directions. The initial and the optimum BO are shown in Fig. 4. The computational cost of objective function evaluation was 9.74 s. The optimization converges after 25 generations, as shown in Fig. 5, with each generation taking 292 s. In this case, the use of gradient-based optimization can reduce the computational cost since the gradients can be calculated analytically and passed onto the solver. But, the drawback of such a method is that it will not guarantee global optima.

For analyzing the strain energy function, we have plotted it as a function of BO, α and β , as shown in Fig. 6. A total of 1296 data points were used to create the surface plot. The optimum BO $(132.7^\circ, 157^\circ)$ is marked as a green point on the plot. As this is an arbitrary orientation, it may not be build friendly. Standard orientations (SOs) that have surfaces parallel to the build plane (x - y) will have better properties like

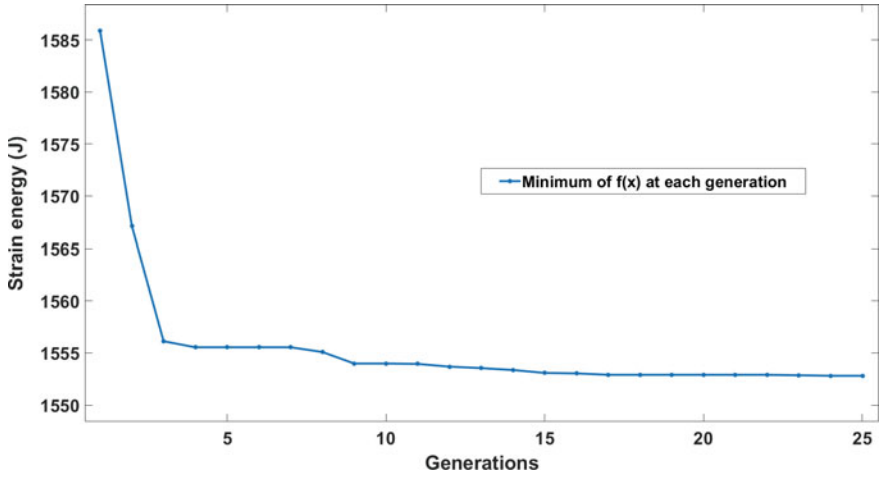


Fig. 5 Convergence plot for strain energy

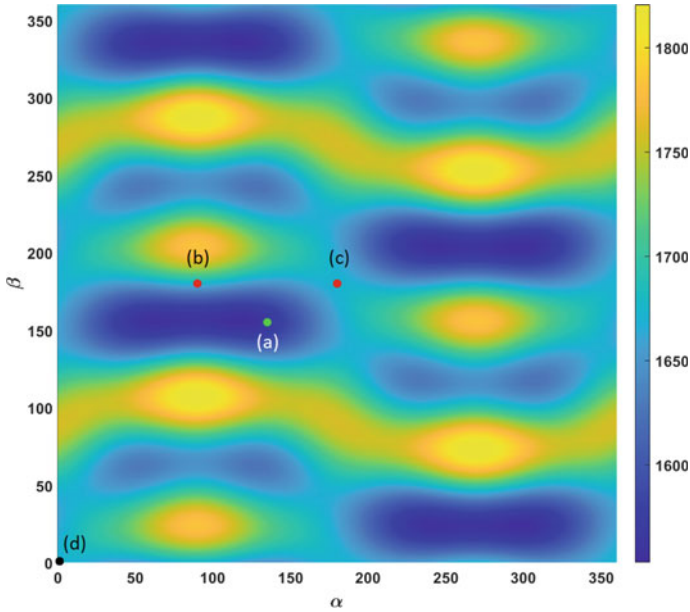


Fig. 6 Strain energy plot for all BO. **a** shows the optimum orientation. **b**, **c** are other standard orientations near the optima, **d** initial orientation of the STL file

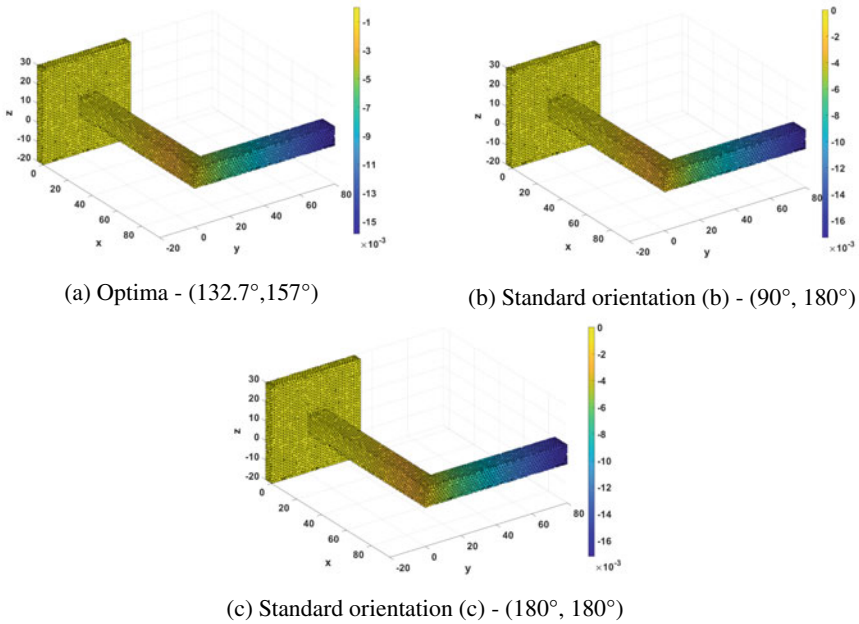


Fig. 7 FE analysis showing displacement field (m) in z -direction for different BO

Table 4 Comparison of different BO

Build orientation	Strain energy (J)	Max z deflection (mm)
Optimum—(132.7°, 157°)	1551.1	15.877
SO (a)—(90°, 180°)	1671.9	17.305
SO (b)—(180°, 180°)	1670.6	17.193
Initial BO—(0°, 0°)	1670.6	17.193

surface finish and support volume. These standard BO which are near the optima are found manually and are marked in red and the initial orientation (0°, 0°) of the STL file, in black. In the future works, this formulation can be extended to include multiple objectives so that BO can be selected from the pareto front instead of a single point. This is particularly helpful from a manufacturing point of view, as the manufacturer can decide the trade off among the objective functions according to his needs. The surface plot shows there are multiple local minima for strain energy function, which justifies the use of a global optimizer like GA. Figure 7 shows the z -direction displacement field for optimum and standard orientations obtained through FE analysis. Table 4 gives a comparison among the optimum, standard, and initial orientations with their corresponding strain energy and maximum z -direction deflection. The standard orientation (b) and initial BO have similar values because of the symmetry possessed by the geometry. The maximum deflection in z -direction has reduced from 17.193 to 15.877 mm (8.3% decrease).

4 Conclusion

In this work, anisotropy in FFF parts is characterized using an orthotropic model. The material constants were extracted from tensile test experiments. An AM-driven build orientation optimization was performed considering the Euler angles (α , β) as design variables and compliance of the structure as objective function. The results show that there is significant decrease in structural compliance, which shows that BO optimization is effective in finding the stiffest structure.

References

1. Xu F, Wong YS (1999) Considerations and selection of optimal orientation for different rapid prototyping systems. *Rapid Prototyping J* 5(2):54–60
2. Thrimurthulu K, Pandey PM, Reddy NV (2004) Optimum part deposition orientation in fused deposition modeling. *Int J Mach Tools Manuf* 44(6):585–594
3. Ahn D, Kim H, Lee S (2007) Fabrication direction optimization to minimize post-machining in layered manufacturing. *Int J Mach Tools Manuf* 47(3–4):593–606
4. Canellidis V, Giannatsis J, Dedoussis V (2009) Genetic-algorithm-based multi-objective optimization of the build orientation in stereolithography. *Int J Adv Manuf Technol* 45(7–8):714–730
5. Vanek J, Galicia JAG, Benes B (2014) Clever support: efficient support structure generation for digital fabrication. *Eurographics Symp Geometry Process* 33(5):117–125
6. Alexander P, Allen S, Dutta D (1998) Part orientation and build cost determination in layered manufacturing. *Comput-Aided Des* (97):343–356
7. Dai S, Deng ZC, Yu YJ, Zhang K, Wang SH, Ye J (2020) Orthotropic elastic behaviors and yield strength of fused deposition modeling materials: theory and experiments. *Polym Test* 87(November 2019):106520
8. Geuzaine C, Remacle JF (2009) Gmsh: a 3-D finite element mesh generator with built-in pre- and post-processing facilities. *Int J Numer Methods Eng* 79(11):1309–1331
9. Domingo-Espin M, Puigoriol-Forcada JM, Garcia-Granada AA, Llumà J, Borros S, Reyes G (2015) Mechanical property characterization and simulation of fused deposition modeling polycarbonate parts. *Mater Des* 83:670–677

Investigations on the Machining of Inconel X-750: Effect of Cutting Speed, Feed, Forces, Energy Consumption and MRR



Vishal Yashwant Bhise and Bhagwan F. Jogi

1 Introduction

Inconel X-750 is an austenitic nickel–chromium precipitation-hardenable alloy widely used in the aerospace engine applications. The material possesses high temperature strength up to 1300 °F and is highly resistant to corrosion and chemical oxidation. Inconel X-750 work hardens quickly and is difficult to machine due to its high stress rupture strength, abrasiveness and work hardening properties [1]. Consequently, high specific cutting forces are generated while machining. Therefore, the machine tool should have minimum backlash and adequate power so that the minimum vibrations are generated during cutting, and hence, the cutting forces are reduced. Besides, the tools must be rigid and have smooth finishes with sharp cutting edge to ensure smooth cutting action and eliminate work hardening effect. Harisha et al. analysed the tool geometry to reduce the cutting forces generated during turning of hardened steel. It was found that incorrect geometry leads to loss of energy which further results in loss of productivity [2].

Ahmadreza Hosseini et al. used coated carbide tools while turning Inconel X-750. The cutting forces are influenced by DOC and feed while cutting with coated carbide tool. Increasing DOC and feed severely increases cutting forces. However, the feed produced significant effect on cutting forces as compared to DOC [1]. Ezilarasan carried out machining on Nimonic C-263 with low DOC and feed along with higher cutting speed. It was observed that with this combination the lowest cutting forces were generated [3]. Vijayaraghavan et al. focussed on the development of a 3D FEM model in Abaqus software in oblique turning process. The effect of parameters

V. Y. Bhise (✉) · B. F. Jogi
Dr. Babasaheb Ambedkar Technological University, Lonere, India
e-mail: vishalbhise79@gmail.com

B. F. Jogi
e-mail: bfjogi@dbatu.ac.in

like angle of cutting edge, DOC, feed and cutting speed on power consumption and cutting forces is studied [4]. H. L'opez-G'alvez proposed a numerical model for finish turning of Inconel 718. The numerical predictions for thrust force, radial force and cutting force showed a good agreement with experimental results while machining at various speed ranges. [5]. P. C. Jindal et al. studied various PVD-coated tool inserts and found that TiAlN-coated tool inserts impart best machining performance [6]. It was concluded that the tools with PVD coating helped to reduce the cutting temperature 13.4% and cutting forces by 6.3% [7]. D. A Stephenson et al. carried out the turning with the aim to extend the tool life while machining Inconel X-750 by using supercritical CO₂-based MQL environment. The PVD-coated tool performed better than other tool inserts with same speed of 75 m/min [8]. The TiAlN coatings are highly resistant to crater and abrasive wear at higher speed. The TiAlN coatings resulted in better performance while machining with speed of 60 to 80 m/min [9].

Jinfu Zhao et al. worked on cutting forces and temperature while turning Inconel 718 under dry environment by using PVD TiAlN tool with 1 and 2 μm of coating thickness. The cutting temperature and forces were measured within speed range between 30 and 120 m/min. It was observed that cutting forces were decreased to 27.46% and 23.51% with 1 μm and 2 μm thickness, respectively. Hence, PVD TiAlN-coated tool was found to be suitable for high speed machining under dry environment [10]. Thakur et al. studied TiN/TiAlN-coated tool while machining Incoloy 825 under dry machining and observed that effect of tool coating on cutting force has great significance since the cutting forces directly effect on energy consumption and therefore environmental impacts [11]. Gupta et al. carried out the turning operation on C45 by using tools coated with TiAlN, AlCrN and TiN. Due to the higher hardness and self-lubricating ability, the TiAlN-coated tool was found to be most efficient while machining under various feed rates and cutting speed. It helped in improving tool life by avoiding adhesion of workpiece material on tool edge [12]. Ramanujam et al. studied different PVD-coated tools, viz. AlCrN (bottom layer)/TiAlN (top layer), AlCrN, TiAlN and uncoated carbide tools while turning Inconel 825. Further, GRA technique with multiple response optimization method was adopted to analyse the optimal machining parameters. It was observed that bilayer coating (TiAlN/AlCrN) performed better than TiAlN and AlCrN coatings [13]. In a comparative study, a lower flank wear was measured while machining Waspaloy as compared to Inconel 718 [14]. K. Vetri Velmurugan studied the tool wear for Waspaloy and Inconel X-750 by using PVD-coated carbide insert.

While machining Inconel X-750 with low feed, it was seen that the stages of tool wear range from built-up edge (BUI) to chipping and further mechanical breakage to diffusion wear. However, while machining Waspaloy the tool wear ranges only from BUI to diffusion without chipping [15]. Tool coatings also help to achieve sustainability while machining materials like nickel-based superalloys with higher cutting speeds. But the major drawback lies with the generation of high temperature and cutting forces. To overcome this problem, the lubrication is employed, and sometimes, flood cooling system is also adopted. However, such practice is unsustainable and affecting to the environment. Several studies have proved that the dry machining is a sustainable technique which completely eliminates the use of coolants [16].

Table 1 Chemical analysis of workpiece material Inconel X-750

Composition	C	Si	Mn	S	Cr	Ni	Al	Co	Cu	Nb	Ti	Fe
Weight (%)	0.02	0.15	0.70	0.008	14.63	74.05	0.55	0.22	0.25	0.85	2.64	5.55

From all above studies, it is found that a limited work on Inconel X-750 with high speed dry turning has been reported. Therefore, this study aims to investigate the effects of feed and high speed turning on cutting forces, energy consumption and material removal rate by using PVD-coated carbide inserts under dry environment.

2 Experimentation Procedure

In order to evaluate the effect of machining parameters in dry turning on output responses, viz. cutting forces, energy consumption and material removal rate, the experimentations were carried out on Inconel X-750 superalloy.

2.1 Workpiece Material

The austenitic nickel–chromium precipitation-hardenable superalloy Inconel X-750 in round bar form of size $\varnothing 50 \times 150$ mm length was chosen so that the L/D ratio remains below 10 to comply with the ISO 3685 standard. The Inconel X-750 is nickel–chromium superalloy which contains 70% nickel and 15% chromium; along with this, it contains Fe, Al, Si, Co, Mn, Nb and Ti in small proportion. Table 1 gives detailed chemical composition.

2.2 Cutting Tool Material

The PVD TiAlN-coated carbide insert (ISO Code: CNMG 120404-MF-1105, Make: Sandvik) having negative geometry with nose radius of 0.4 mm was chosen for turning of Inconel X-750 under dry environment as shown in Fig. 1. The details of tool insert are given in Table 2.



Fig. 1 **a** CNC turning centre used for experimentation. **b** Arrangement of tool, workpiece and dynamometer force sensor plate

Table 2 Details of cutting tool insert

Coating	PVD TiAlN-coated carbide insert
ISO code	CNMG 120404-MF-1105
Tool nose angle	80° (Rhombic)
Nose radius	0.4 mm
Clearance angle	0° (Negative insert)
Tool holder	PCLNL 2525 M12
Make	Sandvik

2.3 Machining Tests

For carrying out the turning experiments, a high-end CNC lathe machine (Make: Ace Micromatic, Model: JOBBER XL) has employed for machining Inconel X-750 round bar workpiece as shown in Fig. 1.

The length of cut for each experiment was fixed to 30 mm. The PVD TiAlN-coated negative geometry tool having nose radius 0.4 mm was chosen for turning Inconel X-750 under dry environment with feed range of 0.05–0.15 mm/rev and cutting speed 110–140 m/min with constant DOC of 0.5 mm. The piezoelectric sensor of lathe tool dynamometer (Make: Kistler, Model: 9257BA) was installed on tool post of CNC lathe connected with a desktop computer having ‘Dynoware’ software which was employed to measure the cutting forces in X , Y and Z direction. A three-phase energy meter was installed at input electrical connection of machine tool only to measure the energy consumption of CNC lathe during each experiment. Table 3 shows a detailed cutting conditions.

Table 3 Machining conditions for experimentation

CNC lathe	Ace micromatic, Model: JOBBER XL
Workpiece material	Inconel X-750 round bar \varnothing 50 X length 150 mm
Cutting tool insert	PVD TiAlN-coated carbide insert ISO code: CNMG 120404-MF-1105 Nose radius: 0.4 mm, tool nose angle: 80 Clearance angle: 0° (negative insert) (Make: Sandvik)
Tool holder	PCLNL 2525 M12
Machining parameters	Cutting speed (VC): 60, 80 and 100 m/min Feed (f): 0.05, 0.1 and 0.15 mm/rev Depth of cut (DOC): 0.5 mm (Constant)
Machining environment	Dry

3 Measurement of Output Responses

The turning experiments on Inconel X-750 superalloy were carried out under dry environment, and the output machining responses, viz. cutting force, electrical energy consumption and material removal rate, were measured as below.

3.1 Cutting Force Measurement

The multi-component dynamometer (Make: Kistler, Model: 9257BA) has employed to get the forces in X , Y and Z direction. The piezoelectric type dynamometer assembled with four numbers of 3-component preloaded force sensors installed between top and bottom base plate. The force sensor plate was installed on tool post of CNC lathe as shown in Fig. 2.

A desktop computer preloaded with 'Dynoware' software was connected to the force sensor via control unit (Kistler 5233a) to measure feed force (F_f), radial force (F_r) and main cutting force (F_c).

While turning the workpiece, forces are generated in X , Y and Z direction and displayed in graphical form as represented in Fig. 3. Further mean of cutting forces in each direction is recorded.

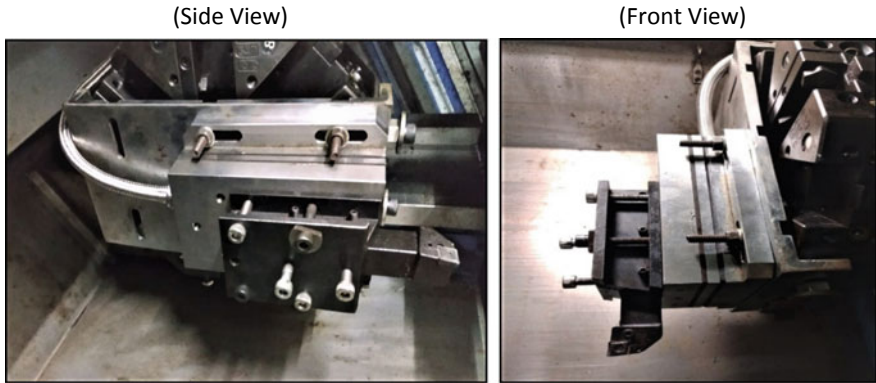


Fig. 2 Installation of force sensor plate on tool post of CNC lathe

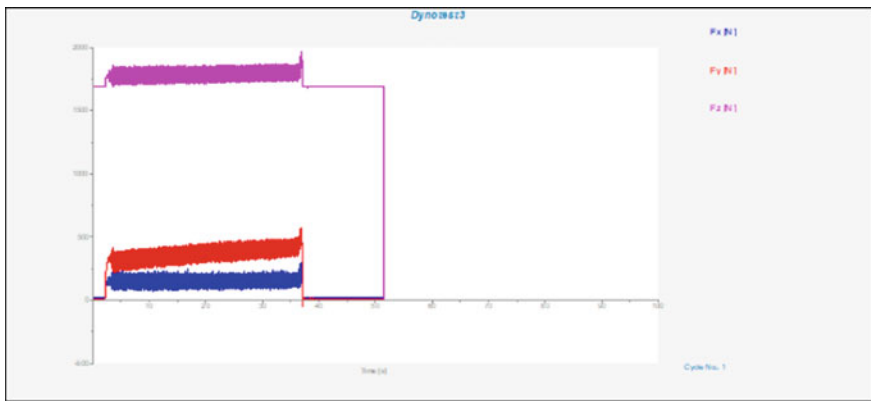


Fig. 3 A typical view of cutting forces generated by dynamometer

3.2 Measurement of Electrical Energy Consumption

A 3-phase, 4-wire energy meter (Make: L&T, Model: WR301BC6D20) has installed only to check the energy consumption of CNC lathe. The pulse rate of the meter is 450 lmp/kWh. It means that the 450 blinks of LED lamp on the top left hand side tend to consume 1 kWh electrical energy. Therefore, 1 blink of LED lamp is equal 2.22 W. The output reading of energy consumption is displayed in one decimal place format on the meter screen. The electrical energy consumption for each turning experiment on CNC lathe was recorded.

3.3 *Material Removal Rate (MRR)*

The MRR is defined as the volume of material removed during machining per unit time. The difference in weight before and after machining also helps to calculate the MRR. It is a measurement of how quick or slow the machining rate is, as well as an important machining performance measure. In finishing operations, however, it is a factor that should be ignored, allowing roughness and precision to give priority. In addition to increased machining productivity, a desired level of accuracy and surface quality must be achieved. The MRR is influenced by feed, cutting speed and DOC. The MRR is calculated as per the empirical relation below,

$$\text{MRR} = V_C \times f \times d$$

where

V_C = Cutting speed (m/min)

f = Feed (mm/rev)

d = Depth of cut (mm)

3.4 *Machining Time*

The machining time is the time taken to cut the specified length of material with the application of defined feed and speed for machining. The actual machining time was calculated with the help of stopwatch, and theoretical time for turning was calculated by using the empirical relation as below

$$\text{Machining Time} = (\text{length of cut}) / (\text{RPM} \times \text{Feed/rev})$$

4 **Results and Discussion**

The experiments were carried out, and all the results were recorded. The effect of feed and speed is discussed below.

4.1 *Effect of Feed and Cutting Speed on Cutting Forces*

As a general rule of turning, the cutting force increases with feed rate and decreases with increase in cutting speed.

Fig. 4 Effect of feed rate on cutting force

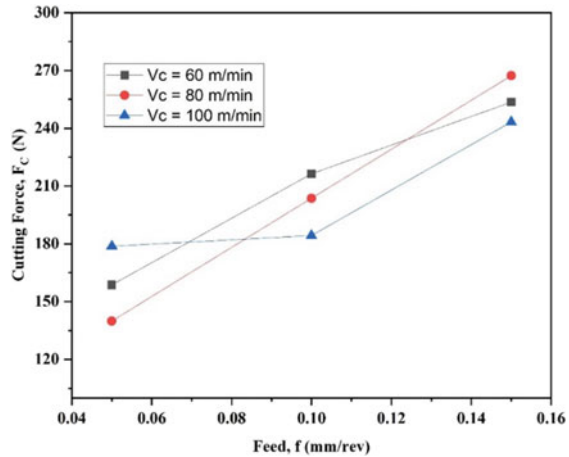
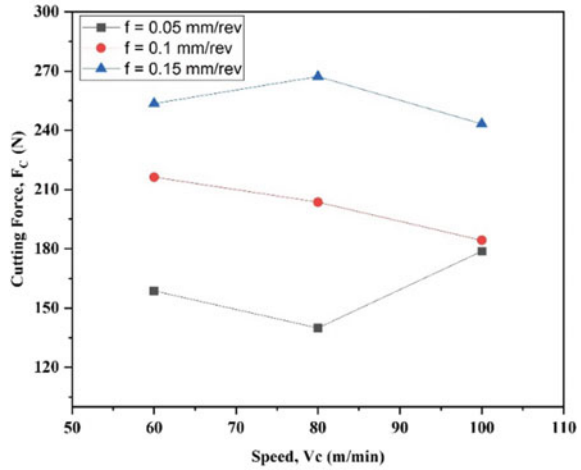


Figure 4 represents feed effect on cutting force. According to the general machining tendency, cutting forces tend to increase with feed rate. At feed 0.05 mm/rev and speed 60 m/min, the cutting force of magnitude 158.7 N is generated. Further, at feed 0.1 mm/rev, the cutting force is increased to 216.3 N and at feed 0.15 mm/rev again gradually increased to 253.6 N. At speed 80 m/min with feed 0.05 mm/rev, cutting force of magnitude 139.9 N is generated. Further, cutting force is increased to 203.6 N at feed 0.1 mm/rev and again gradually increased to 267.3 N at feed 0.15 mm/rev. Highest speed of 100 m/min with feed 0.05 mm/rev generates 178.8 N of force. Further, the force increased to 184.3 N at feed 0.1 mm/rev and again gradually increased to 243.3 N at feed 0.15 mm/rev. Therefore, it is found that cutting force is directly proportional to feed rate.

Figure 5 represents effect of cutting speed on cutting force. It is seen that with feed 0.05 mm/rev, the magnitude of force at 60 m/min is 158.7 N and slightly decreased to 139.9 at speed 80 m/min. Further, the cutting speed increased to 178.8 N at speed of 100 m/min, respectively. It is seen that force continued to decrease as speed increased from 60 to 80 m/min, and further, cutting force increased at highest speed of 100 m/min. With feed rate 0.1 mm/rev and speed 60 m/min, the magnitude of cutting force is 216.3 N which slightly decreased to 203.6 N at speed 80 m/min. Further, it is continued to decrease at speed 100 m/min with magnitude of 184.3 N. At 0.15 mm/rev of feed, the force of 253.6 N is generated at 60 m/min. Then, it is slightly increased to magnitude of 267.3 N at 80 m/min. Further, at highest speed 100 m/min the cutting forces are again slightly reduced to 243.3 N.

Fig. 5 Effect of cutting speed on cutting force



4.2 Effect of Feed and Cutting Speed on Electrical Energy Consumption

The evaluation of electrical energy consumed has a great significance in the machining as it is directly associated with the machining cost and environmental burden. The consumption of electrical energy increases with increase in load on machine tool. Therefore, increase in feed and speed increases the load on CNC lathe, which further increases the consumption of electrical energy. From Fig. 6, it can be noticed that as the feed increases, the total electrical energy consumption is reduced. The machining with speed 60 m/min along with initial feed 0.05 mm/rev, the energy

Fig. 6 Effect of feed rate on electrical energy consumption

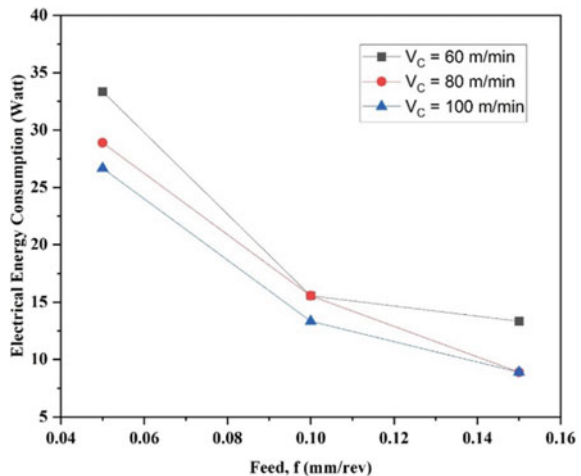
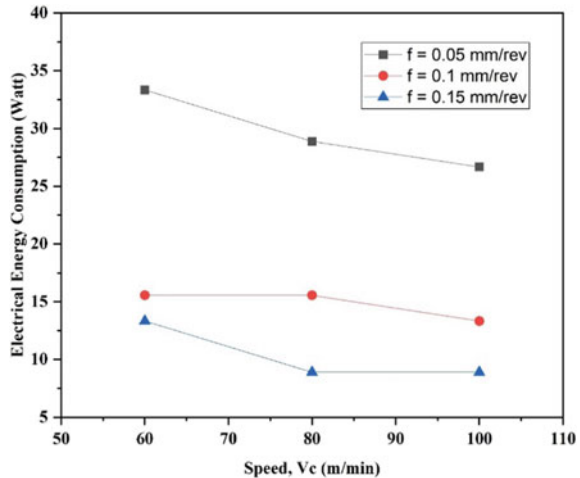


Fig. 7 Effect of cutting speed on electrical energy consumption



consumption is 33.33 W which is highest among the cutting range. Further, at medium feed of 0.1 mm/rev the consumption is drastically reduced to 15.56 watts, and at high range of feed 0.15 mm/rev, the consumption again goes down in a steady manner and reached to 13.33 W.

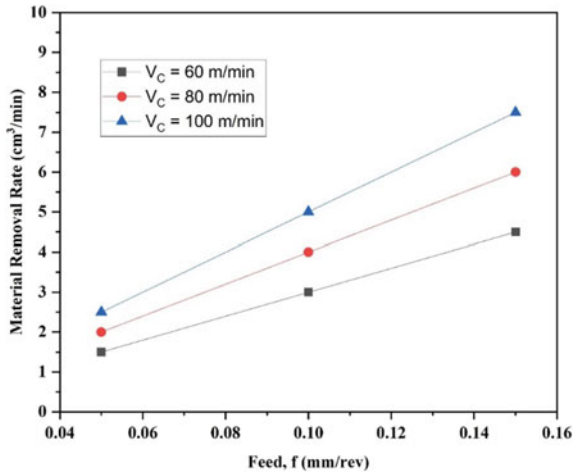
Further, at feed 0.05 mm/rev and speed 80 m/min, the consumption goes up to 28.89 W and it suddenly goes down to 15.56 W with feed rate 0.1 mm/rev. In the last range of feed rate 0.15 mm/rev along with same speed, the consumption steadily goes down to 8.89 watts. With cutting speed of 100 m/min and feed 0.05 mm/rev, the consumption goes up to 26.67 watts, and further with feed rate 0.1 and 0.15 mm/rev, the energy consumption goes down to 13.33 W and 8.89 W, respectively.

From Fig. 7, it is observed that with feed 0.05 mm/rev, the energy consumption steadily reduced from 33.33 W at cutting 60 m/min to 28.89 W at speed 80 m/min and then continued to decrease with consumption of 26.67 W at 100 m/min. Further, with feed of 0.1 mm/rev with speed 60 m/min the energy consumption is 15.56 W which continued to decrease to 15.56 and 13.33 W at 80 and 100 m/min, respectively. With highest rate of feed 0.15 mm/rev, the energy consumption steadily reduced with speed range 60–80 m/min with value 3.33–8.89 W, respectively. Further, at speed 80 to 100 m/min, the energy consumption is constant with consumption of 8.89 W.

4.3 Effect of Cutting Speed and Feed on Material Removal Rate

It is observed that the MRR is directly proportional to feed rate and hence constantly increases with feed rate as shown in Fig. 8. With a combination of lowest rate of feed and speed of 0.05 mm/rev and 60 m/min, respectively, the MRR is 1.5 cm³/min which is lowest among the cutting range. The MRR goes on increasing with increase

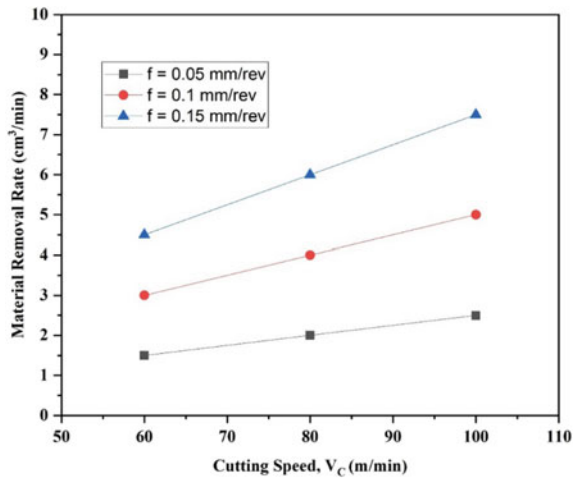
Fig. 8 Effect of feed on MRR



in feed and goes up to 7.5 cm³/min at highest cutting range of feed 0.15 mm/rev and speed 100 m/min.

It is observed that MRR steadily increases with speed and gives lowest range of MRR with feed 0.05 mm/rev as shown in Fig. 9. Further, with feed 0.1 and 0.15 mm/rev, the curve follows the same pattern and MRR steadily increased with middle and higher range, respectively.

Fig. 9 Effect of cutting speed on material removal rate



5 Conclusion

- The cutting forces steadily increased with increase in feed rate from 0.05 to 0.15 mm/rev.
- With increasing cutting speed, the cutting forces continued to decrease. However, at highest cutting speed 100 m/min along with lowest feed 0.05 mm/rev, the cutting force was found to be increased.
- The total energy consumption was found to be lowest at the highest range of feed and speed of 0.15 mm/rev and 100 m/min, respectively. This is because at high feed and cutting speed, machining time is less. Therefore, total energy consumption is also less. However, the rate of energy consumption is high due to increased load on machine tool.
- The total energy consumption greatly increases with increases in feed rate. On the other hand, energy consumption steadily increases with cutting speed. Hence, it is concluded that both feed rate and cutting speed have impact on energy consumption. However, it is found that the feed rate has a greater impact on energy consumption.
- The MRR is directly proportional to feed rate and therefore increases with increase in feed rate. Besides, with increase in cutting speed the MRR steadily increases with a comparatively low value. Therefore, the feed rate has a great influence on MRR than cutting speed.

Acknowledgements The authors are thankful to University Grants Commission, Government of India for award of fellowship (F1-17.1/2017-18/RGNF-2017-18-SC-MAH-34406/(SA-III/Website)) to carry out this work.

References

1. Tazehkandi AH, Shabgard M, Pilehvarian F, Farshfroush N (2017) Proc Inst Mech Eng Part B: J Eng Manuf 231(9):1516–1527
2. Harisha SK, Rajkumar GR, Pawar V, Keshav M (2018) Mater Today Proc 5:11277–11282
3. Ezilarasan C, Velayudham A (2013) Measurement 46(1):185–199
4. Vijayaraghavan V, Garg A, Gao L, Vijayaraghavan R, Lu G (2016) J Clean Prod 137:1619–1627
5. H. L'opez-G'alvez, Soldani X (2019) Determination of optimum numerical parameters in a 3D model of finish turning operation applied to Inconel 718. Simul Model Practice Theory
6. Jindal PC, Santhanam AT, Schleinkofer U, Shuster AF (1999) Int J Refract Metals Hard Mater 17(1):163–170
7. Hsieha JH, Lianga C, Yub CH, Wu W (1998) Surf Coat Technol 108–109:132–137
8. Stephenson DA, Skerlos SJ, King AS, Supekar SD (2014) J Mater Proces Technol 214:673–680
9. Settineri L (2005) CIRP Ann Manuf Techn 54(1):515–518
10. Zhaoa J, Liu Z (2020) J Manuf Process 56:1155–1165
11. Thakur A, Gangopadhyay S (2016) Dry machining of nickel-based super alloy as a sustainable alternative using TiN/TiAlN coated tool. J Clean Prod 129:256–268
12. Gupta KM, Ramdev K, Dharmateja S, Sivarajan S (2018) Cutting characteristics of PVD coated cutting tools. Mater Today Proc 5:11260–11267

13. Ramanujam R, Vignesh M, Tamiloli N, Sharma N, Srivastava S (2018) Patel Sens Actuators A Phys 279:331–342
14. Olovsjö S, Nyborg L (2012) Wear 282–283:12–21
15. Vetri Velmurugan K, Venkatesan K, Devendiran S, Mathew AT (2019) Investigation of parameters for machining a difficult-to-machine superalloy: inconel X-750 and waspaloy. In: Chandrasekhar U, Yang LJ, Gowthaman S (eds) Innovative design, analysis and development practices in aerospace and automotive engineering (I-DAD 2018). Lecture notes in mechanical engineering. Springer Nature, Singapore
16. Vitor FCS, Francisco JGS (2020) Recent advances in turning processes using coated tools—A comprehensive review. Metals 10:170

DMLS Support Structure Optimization Using Homogenized Model Distortion Prediction



A. Varun and G. Saravana Kumar

1 Introduction

Powder bed AM like DMLS is capable of printing complex part geometry by selectively sintering metal powders layer upon layer. This causes repeated heating and cooling of parts during the process and part will develop residual stresses in it, causing distortion and print failure. Using support structures minimizes part distortion and anchor's the part to the baseplate. These supports needs to be later separated from parts and scraped. So, there is a need to optimize support material use before printing to bring down the cost, energy and time associated with the over usage of support material [1]. FE-based simulation can help prevent costly trial and error processes by predicting part distortion and help choose only the essential supports.

In this paper, a support structure optimization technique based on support homogenization is introduced by integrating an optimization engine to a commercially available distortion prediction FEA software. Metal AM process simulation is a complex multiphysics problem that demands high computation load. So, using a detailed FE model will not be practical in the optimization approach as multiple iterations would be necessary to arrive at an optimal solution. Most of the commercially available FEA packages for AM use simulation in multiple levels for faster simulation, specific to the Ansys Additive™ the process flow is shown in Fig. 1. At Micro-level, the simulation is detailed, and it uses coupled analysis considering material microstructure.

A. Varun (✉)

Department of Aerospace Design, Honeywell, Bangalore, India
e-mail: varun.anand@honeywell.com

G. Saravana Kumar

Department of Engineering Design, IIT Madras, Chennai, India
e-mail: gsaravana@iit.ac.in

Additive Manufacturing Group, Centre of Excellence in Materials and Manufacturing for Futuristic Mobility, IIT Madras, Chennai, India

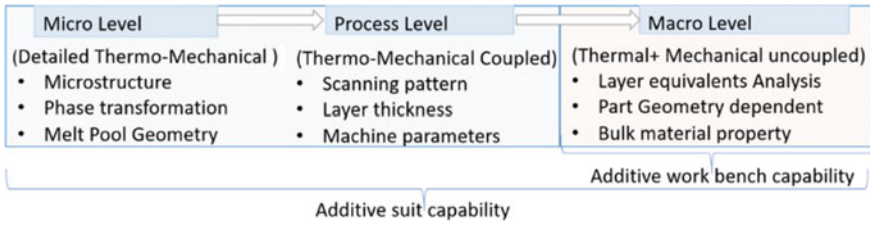


Fig. 1 Part geometry dependent macro-level FEA details in Ansys Additive™

Macro-level uses uncoupled simulation and mainly depends on part geometry [2]. In this work, Ansys Additive™ FE simulation package is specifically chosen because it provides a AM simulation workbench and optimization engine as well as APDL deployment for customization and integration. Ansys Additive™ workbench uses activation of an entire layer as molted metal using the element birth and death technique. However, DLMS process uses lattice supports with internal voids to reduce material consumption, this complex geometry will increase computation load. Hence, the support structure homogenization technique is used to reduce computation effort [3].

2 Methodology

The complete methodology followed in the present work is schematically described in Fig. 2. A cantilever overhang test sample with perforated block support, as shown

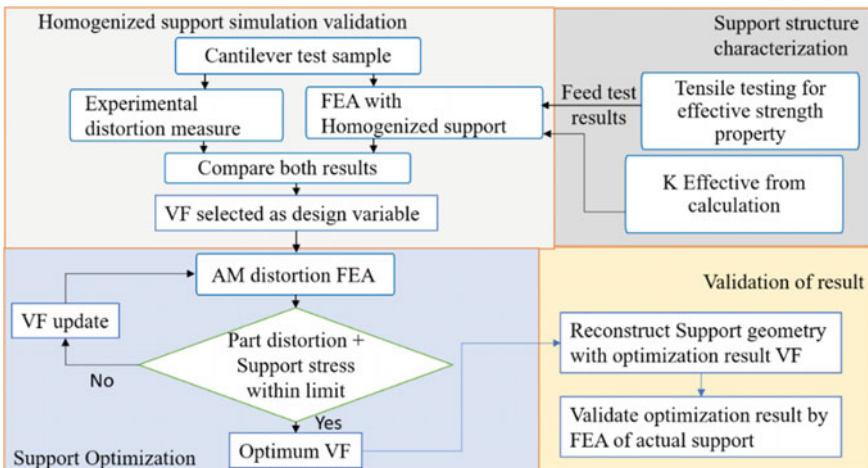


Fig. 2 Schematic of the methodology

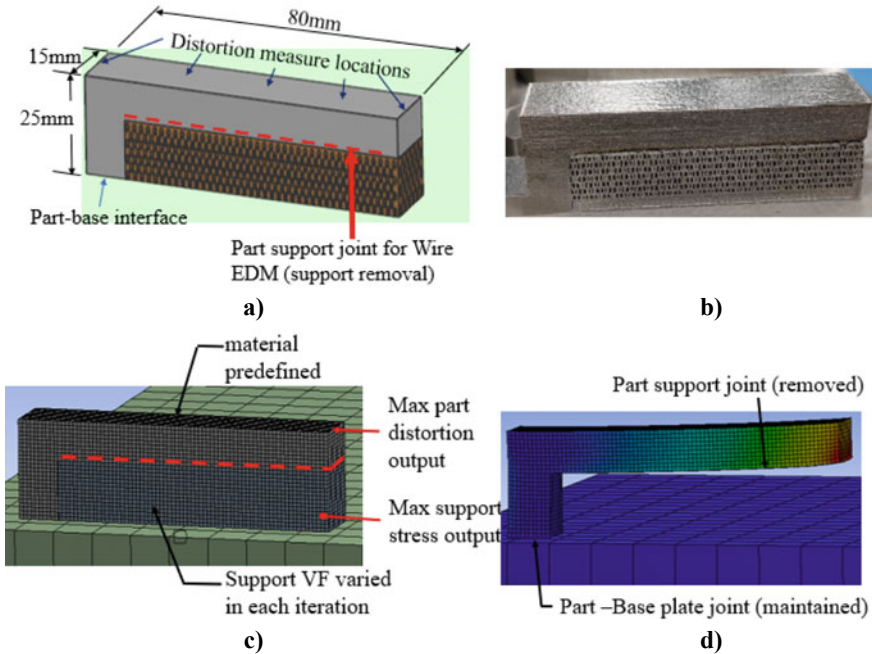


Fig. 3 a Details of cantilever test sample, b printed sample, c FE model and d FEA result

in Fig. 3a, is used to demonstrate the methodology. The test sample is made from Inconel 718 material, printed in an EOS M280™ machine using EOS™ standard process parameters [4] and support volume fraction (VF) of 0.3. The printed part is subjected to distortion measurement along cantilever length to compare and validate the distortion predicted using FEA. FE simulation is carried out by replacing complex support geometry with a homogenization technique to reduce the computational cost. With the aim of reducing the error, homogenized supports are loaded with effective strength characterized from tensile testing (refer to Fig. 2). The effective thermal conductivity is computed from an analytical calculation using Eq. (1), as per methodology described in a study from Zeng et al. [5]. The thermal conductivity of the support structure is a combined effect from the VF of the solid support and unsintered powder.

$$K_{\text{effective}} = K_{\text{solid}} * VF + K_{\text{powder}} * (1 - VF) \tag{1}$$

The FE simulation is modeled with AM simulation’s necessary mechanical and thermal boundary conditions. Cartesian mesh is used to get uniform mesh size in the build Z direction. The mesh size selected is 0.8 mm, 20 times the actual metal powder layer thickness of 40-microns, based on mesh sensitivity analysis. AM distortion FE model is linked to the optimization engine to run multiple iterations in loops and arrive at an optimal solution, as shown in Fig. 4a. The VF of the support is

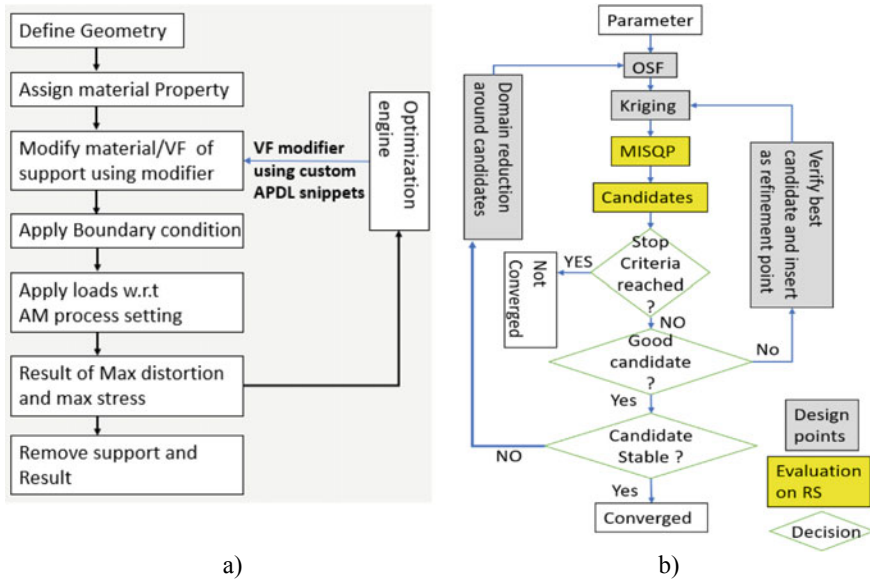


Fig. 4 a) FE simulation process schematic, b) Workflow of optimization method inside the optimization engine

considered a design parameter for optimization because it controls homogenized support’s effective strength and thermal conductivity. Minimization of the same VF is modeled as an objective for optimization. VF of support needs to be altered in each iteration; this is achieved by scaling of material property assigned to support geometry. Since the software package does not provide an option to vary the VF of support in each iteration, a custom APDL command snippet is created in the workflow to achieve VF scaling. The VF modifier is linked to the optimization engine and controlled as a variable. The effective strength of support structure is assumed to be directly proportional to VF of support, so the measured effective yield from the experiment is linearly scaled and added as an upper limit constraint for the maximum allowable stress. Maximum distortion of the cantilever sample allowed during the print is added as the second constraint. This limit is equal to twice the layer thickness the EOS M280™ printer can print without re-coater jam failure, i.e., 80 microns.

A single variable optimization with two constraints is formulated and an adaptive single-objective optimization is selected from the direct optimization module available in the Ansys™ workflow. It is a gradient-based algorithm based on response surface (RS) to obtain global optimization results. It uses the modified Latin Hypercube Sampling (LHS) called optimal space-filling (OSF) method for design of experiment. The sampling generated is used for Kriging meta-model construction. Then RS is used by mixed integer sequential quadratic programming (MISQP) optimization algorithm to find potential solutions as shown in Fig. 4b [2]. The output result is optimum VF of homogenized support. This VF is converted into actual support

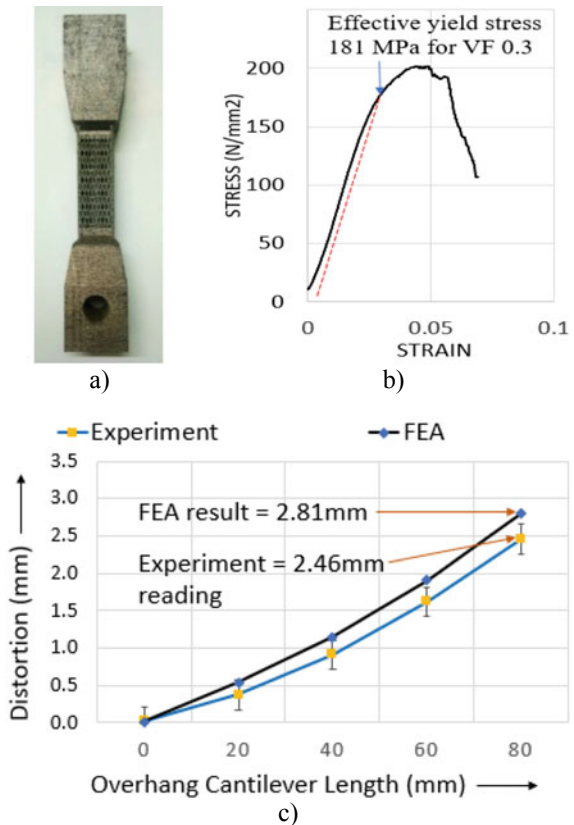
geometry of perforated block support and the generated optimal support geometry is simulated for validating the results.

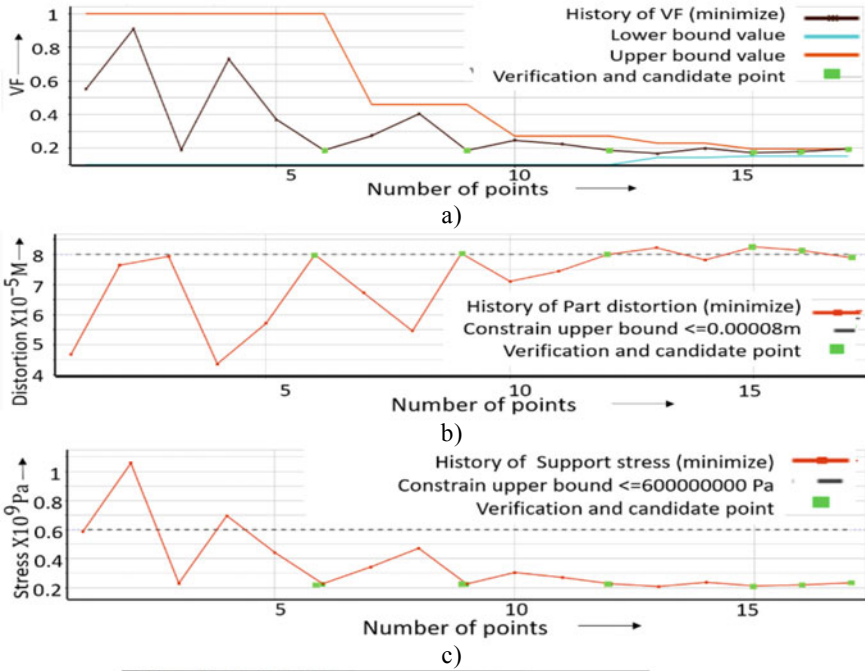
3 Results and Discussion

The tensile coupon used to find effective strength for perforated block, VF of 0.3, and its test result is presented in Fig. 5a and b. The stress–strain curve shows that effective yield strength is 181 MPa, and the equated yield strength for VF of 1 is 603 MPa. The result of effective property when loaded to homogenized support of cantilever sample for FE simulation, FEA result, and experimental measurement comparison are shown in Fig. 5c. Results show good agreement and validate the capability to apply the homogenization technique in an optimization framework.

The history of design points for optimization parameter and output are shown in Fig. 6a, b and c. OSF method scanned the entire range in the first 5 points to develop a response surface and the optimum solution has arrived at the 21st design

Fig. 5 a Printed tensile test coupon, b Stress–strain curve, c Cantilever sample distortion result experiment versus FEA result





d) Design points of optimization

Schematic C2: Optimization			
Name	P1 - VF	P2 - Deformation Maximum (m)	P3 - Stress Maximum (Pa)
1	0.55	0.000046764	5.8667E+08
2	0.91	0.000076399	1.0577E+09
3	0.19	0.000079311	2.3086E+08
4	0.73	0.00004367	6.9635E+08
5	0.37	0.000057131	4.4272E+08
6	0.18654	0.000079881	2.2762E+08
7	DP 1	✘	✘
8	0.2728	0.000067198	3.4309E+08
9	0.40424	0.000054587	4.718E+08
10	0.18557	0.000080295	2.2599E+08
11	DP 2	✘	✘
12	DP 3	✘	✘
13	0.24583	0.000071018	3.0494E+08
14	0.22322	0.000074386	2.7092E+08
16	0.16741	0.000082164	2.0926E+08
17	0.19866	0.000078135	2.3712E+08
18	0.17178	0.00008248	2.1295E+08
19	DP 4	✘	✘
20	0.17861	0.000081247	2.1977E+08
21	0.19415	0.000078864	2.3357E+08

Fig. 6 a history of design parameter VF in optimization, b history of cantilever part distortion, c history of support structure stress, d design points of optimization

point as shown in Fig. 6d. Optimization workflow encountered four bad candidates where AM simulation failed. These design points are eliminated, and design points were refined in further iterations. The optimization result for the cantilever sample considered in the study is VF 0.186. This value is used to generate actual support geometry and load it for FEA validation.

4 Conclusion

This paper presented a successful integration of distortion prediction AM simulation with optimization engine. A methodology for homogenization of support structure has been presented, which will help to reduce computation cost because to create RS, multiple simulation needs to be carried out. An example case study of cantilever beam test sample is taken up and the whole process is demonstrated for VF optimization.

References

1. Patterson AE, Messimer SL, Farrington PA (2017) Overhanging features and the SLM/DMLS residual stresses problem: review and future research need. *Technologies* 5(2):15
2. ANSYS (2019) ANSYS workbench design exploration and additive manufacturing guide, release 2019 R1, ANSYS Inc., Canonsburg, PA
3. Chen Q, Lianga X (2019) An inherent strain based multiscale modeling framework for simulating part-scale residual deformation for direct metal laser sintering. *Addit Manuf* 28:406–418
4. EOS Gmbh Electro Optical Systems. EOS Nickelalloy in718 Datasheet; EOS Gmbh Electro Optical Systems Munich, Germany (2014). Accessed 12 Aug 2021
5. Zeng K, Pal D, Tenga C, Stucker BE (2015) Evaluations of effective thermal conductivity of support structures in selective laser melting. *Addit Manuf* 6:67–73

Design Optimization of Nd:YAG Laser Welded Inconel 718 Alloy Joints by Taguchi Method



P. Thejasree and P. C. Krishnamachary

1 Introduction

Superalloy Inconel 718 is widely used for high temperature applications like aerospace engine parts, turbine blades and marine applications owing to its outstanding characteristics even at elevated temperatures. For fabricating superalloy joints, the narrow beam welding processes such as laser welding is preferred due to improved weld bead geometry when compared to conventional arc welding processes [1, 2]. The weld parameters play a major role in the achievement of sound quality welds [3]. By optimizing critical parameters during welding, one can fabricate a quality joint with minimal cost. Moreover, there is a need to optimize the process variables to fabricate very thin weldments of 1 mm thickness to achieve joints that last long during functioning [4]. To achieve this Taguchi technique is an effective tool. In this article, the influence of each parameter on the weld bead geometry was measured and optimized using Taguchi analysis.

2 Problem Definition and Formulation

The Nd:YAG laser welded thin joint of Inconel 718 alloy with dimensions 100 mm × 100 mm × 1 mm of joints was optimized with Taguchi technique by considering laser power, weld speed and the pulse duration as the process variables. Moreover, nine combination of the chosen weld parameters were analyzed through Taguchi method.

P. Thejasree (✉)
Sree Vidyankethan Engineering College, Tirupati, India
e-mail: thejasree.p@gmail.com

P. C. Krishnamachary
JB Institute of Engineering and Technology, Hyderabad, India

The effect of these parameters on Inconel 718 butt joints was measured in terms of the weld bead geometry comprising of the top width, bottom width and penetration. Taguchi method is an effective tool that reveals the key factor responsible for good quality weld joints.

3 Materials and Methodology

In the present investigation, laser fabrication technique is employed to join Inconel 718 sheets of 1 mm thick. The chemical composition of the base metal Inconel 718 is depicted in Table 1. The specimens were extracted with wire electrical discharge machining (WEDM) with dimensions of 50 mm × 100 mm size to get joints of 100 mm × 100 mm. Before proceeding for welding, the specimens were cleaned with acetone to prevent weld pool contamination. During welding, the specimens were firmly located with clamps to allow proper positioning and to prevent weld distortion.

Laser welding setup was shown in Fig. 1. The laser beam was perpendicular to the plate during welding. A pulsed Nd:YAG laser welding device with a power capacity of 4 kW was used to fabricate the welded joints.

To optimize the process parameters taken into consideration are laser power (LP), weld speed (WS) and pulse duration (PD). The three parameters were analyzed at three levels using Taguchi technique. The process parameters chosen for optimization and their levels are listed in Table 2. Taguchi technique is an effective tool to design

Table 1 Chemical composition of base metal Inconel 718

Element	Ni	Cr	Nb	Mo	Ti	Al	C	Si	B	S	P	Fe
wt. %	53.0	17.54	5.09	3.12	0.97	0.52	0.02	0.03	0.003	0.002	0.005	Bal

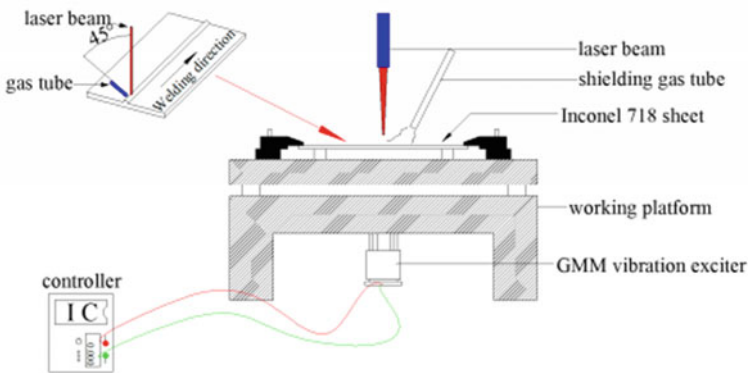


Fig. 1 Laser welding setup

Table 2 Process parameters during laser welding and levels

Symbols	Weld parameters	Levels		
		1	2	3
LP	Laser power (kW)	2.5	2.02	6.6
WS	Weld speed (mm/min)	2.9	2.2	7.5
PD	Pulse duration (ms)	3.3	2.38	8.4

a system with superior quality. It provides an easiest and economical means to optimize the designs for good performance characteristics and high quality. Moreover, Taguchi design technique optimizes the system performance by arriving at the best set of parameters subjected to variable source characteristics [5, 6]. Unlike the other optimization methods, Taguchi technique estimates not only the optimal solution but also the prevailing process variables that contributed during welding. In this investigation, three process variables were considered as three factors and three levels. The minimum and maximum levels for the parameters were set by running bead on trials to observe the level of penetration and weld appearance. Totally nine sets of parameters were resulted nine different joints to analyze the weld bead geometry in terms of its bead dimensions viz. top width, bottom width and penetration as these factors decide the quality and appearance of the weld joint [7–9].

4 Results and Discussion

The weld joints fabricated with nine sets of parameters designed by Taguchi as shown in Table 3, were mounted, polished and etched to observe the weld geometry. The bead dimensions viz., top width, bottom width and the depth of penetration were

Table 3 Weld process parameters

Laser power (kw)	Welding speed (mm/min)	Pulse duration (ms)	Top width (mm)	Bottom width (mm)	Penetration (mm)
2.5	2.02	6.6	1.5927	0.0875	0.5738
2.5	2.2	7.5	1.6199	0.1054	0.4242
2.5	2.38	8.4	1.6125	0.056	0.3054
2.9	2.02	7.5	1.7394	0.3566	0.7698
2.9	2.2	8.4	1.8645	0.5862	0.74
2.9	2.38	6.6	1.7012	0.315	0.3899
3.3	2.02	8.4	2.2036	1.0579	0.8352
3.3	2.2	6.6	1.8757	0.3305	0.7939
3.3	2.38	7.5	1.9685	0.4353	0.6748

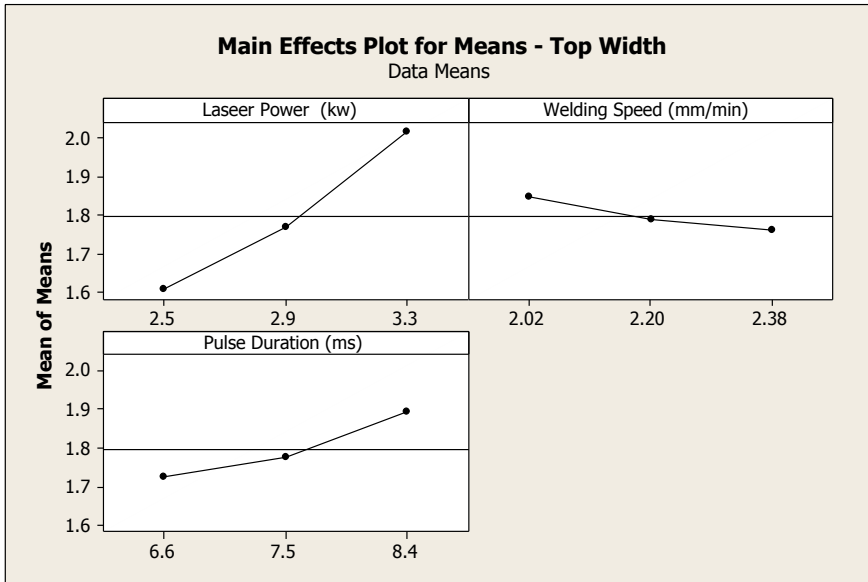


Fig. 2 Response graph for top width

measured through optical microscope. The effect of welding limit on these responses was analyzed to arrive at the best performance criterion through the main effect plot generated in Taguchi analysis as in Figs. 2, 3 and 4.

Figure 2 illustrates that the top width shows an upward trend due to the increase in laser power and pulse duration. Also, it is decreased with increasing values of welding speed. These trends are on account of the corresponding heat inputs. Figure 3 represents that the bottom width is increasing with respect to an increase in laser power and pulse duration, but decreased with rise in welding speed. This is because the bottom width will show similar trend with all the weld parameters like the top width. The width at the bottom is lesser than the width at the top as the heat input reduces from top to bottom. Figure 4 represents a trend depicting an increase in penetration during welding with an increasing value of laser power and pulse duration. Also, it is decreased with increasing values of welding speed due to proportional variations in heat input.

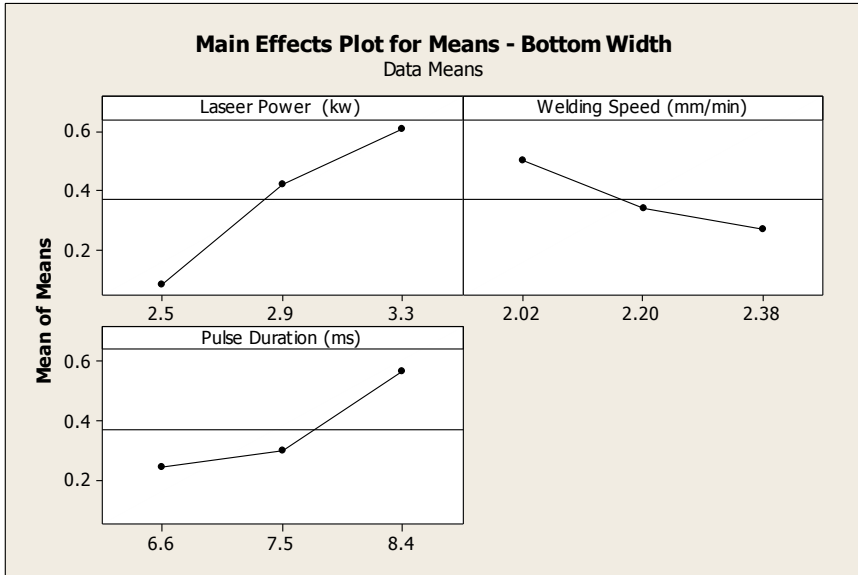


Fig. 3 Response graph for bottom width

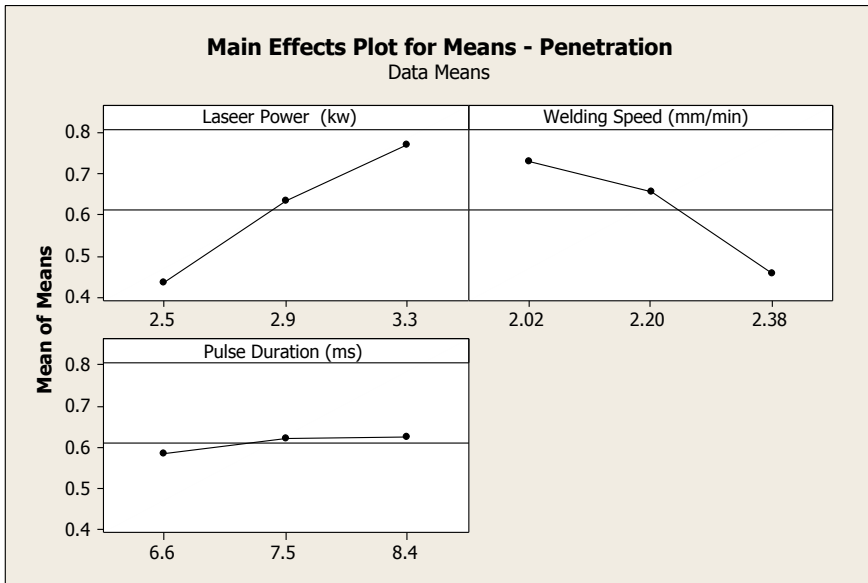


Fig. 4 Response graph for penetration

5 Conclusions

Using Taguchi design methodology, the experimental trials were designed and the performance of individual process variable was optimized. The influence of each process parameter on the response indicators was clearly depicted by using Taguchi technique. The results achieved through this investigation can be taken as a reference during the real-time fabrication processes through laser welding, especially in case of thin weld fabrications and repair welds. The procedure adopted to optimize the process by Taguchi design technique can be successfully employed to improve the performance of any suitable fabrication technique.

References

1. Madhankumar S, Ashwin S, Robert JA, Francis JC, Kalyan RB, Raj AK, Anton WJ (2021) Experimental investigation on ultimate tensile strength of laser butt welded inconel 718 alloy and 2205 duplex stainless steel. *Mater Today Proc*
2. Huang Y, Gao X, Ma B, Liu G, Zhang N, Zhang Y, You D (2021) Optimization of weld strength for laser welding of steel to PMMA using Taguchi design method. *Opt Laser Technol* 136:106726
3. Zhu J, Li W, Li Z, Jiao X, Feng C, Wang K (2020) Optimization of laser deep penetration TIG hybrid welding technology for stainless steel. In: *Transactions on intelligent welding manufacturing*. Springer, Singapore, pp 123–130
4. Thejasree P, Krishnamachary PC (2021) Effect of weld speed on joint quality of Nd: YAG laser welded Inconel 718 alloy weldments. *SAE Technical Paper*, No. 2021–28–0263
5. Palanivel R, Dinaharan I, Laubscher RF, Alarifi IM (2021) Effect of Nd: YAG laser welding on microstructure and mechanical properties of Incoloy alloy 800. *Opt Laser Technol* 140:107039
6. Canel T, Zeren M, Sinmazçelik T (2019) Laser parameters optimization of surface treating of Al 6082–T6 with Taguchi method. *Opt Laser Technol* 120:105714
7. Manikandan N, Binoj JS, Thejasree P, Sasikala P, Anusha P (2021) Application of Taguchi method on wire electrical discharge machining of inconel 625. *Mater Today Proc* 39:121–125
8. Maheswaran CB, Bharathi RJ, Srirangan AK (2018) Optimisation of laser welding parameters for incoloy 800HT joints using Grey-fuzzy Taguchi approach. *Mater Today Proc* 5(6):14237–14243
9. Gencalp Irizalp S, Koroglu BK (2020) Optimization of weld bead geometry of laser welded ANSI 304 austenitic stainless steel using grey-based Taguchi method. *Materialwiss Werkstofftech* 51(8):1120–1136

General Applications of Optimization

A State Estimation, Kalman Filter Auto-tuning and Uncertainty Quantification Framework with Application to Industrial Storage Tank-farms



Shirish Nanda Potu, Rihab Abdul Razak, and Senthil K. Vadivelu

1 Introduction

In the energy industry, tank-farms form an intermediate storage facility between production and need-based customer delivery (see Fig. 1). Miscalibration and sensor drift can lead to errors associated with the tank-farm's inlet and outlet line flow meters and result in mass loss amounting to several million USD every year. Since measured state is the sum of true state and some error (random or bias), gray-box modeling such as the Kalman filter (KF) is a reliable approach to estimate said true state of a system, such as the tank-farm, by statistically combining measurement data with physics-based predictions of system behavior [1]. The approach is however affected by measurement and modeling errors. In a KF framework, such epistemic uncertainties are accounted for by the initial state, process, and measurement noise covariance matrices which in most cases are assigned through heuristic hand-tuning. In this work, we propose a framework for combining KF, Bayesian optimization [2], bootstrapping, clustering, and confidence interval techniques for state estimation and uncertainty quantification with faster rate of convergence over a conventional KF. We primarily target flow meter bias estimation in a multi-tank system as an application for this framework. Section 2 of this paper discusses the operational and instrumentation complexities associated with storage tank-farms and introduces the system that is used as a case study for demonstrating the usage of the proposed framework. In Sect. 3, we describe the methodology for bias estimation, where we

S. N. Potu (✉) · R. A. Razak · S. K. Vadivelu
Shell India Markets Pvt. Ltd., Bengaluru, India
e-mail: shirish.nanda@shell.com

R. A. Razak
e-mail: rihab.abdulrazak@shell.com

S. K. Vadivelu
e-mail: s.vadivelu@shell.com

cover the formulation for the Kalman filter and Bayesian optimization and end with a description of bootstrap and clustering that forms the last segment of this three-staged framework. In Sect. 4, we present the results of the case study and conclude the paper with Sect. 5, where we discuss our ongoing work in this area.

2 Problem Statement

Consider the tank-farm system in Fig. 1. At any time, any number of inlet lines could be delivering any number of tanks, and any tank could be delivering to any measured or unmeasured outlet line. The tanks could also be interacting with each other. To satisfy tank-farm mass balance, net tank accumulation should equal the difference between net inlet and net outlet at this time. The inlet and outlet line flow rates are measured and have unknown biases, which contribute to mass imbalance. However, constant bias associated with tank levels gets canceled during tank accumulation calculation in the mass balance equation, and therefore, does not contribute to mass imbalance. As a case study for demonstrating the proposed framework, we abstract the above complexities through the three-tank system in Fig. 2a. The tanks are connected sequentially in which the liquid enters through a pipe connected to Tank 1 and exits the system through a pipe connected to Tank 3. Inflow and outflow rates, q_{in} and q_{out} , are controlled externally and their measurements are biased. Levels L_1 , L_2 , and L_3 are measured. q_1 and q_2 are unmeasured gravity-driven flows and are thus related to tank level through proportionality constants k_1 , k_2 as shown in the figure. We are interested in obtaining reliable estimates of flow meter bias and internal states k_1 , k_2 by combining the mass balance model with sensor measurements using the three-stage framework described in Sect. 3

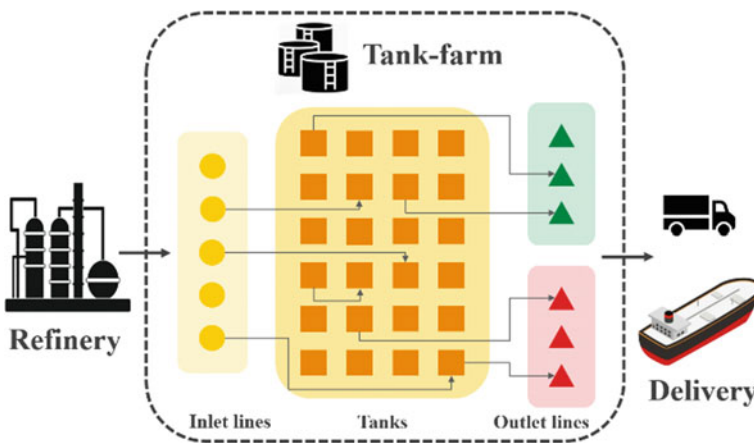
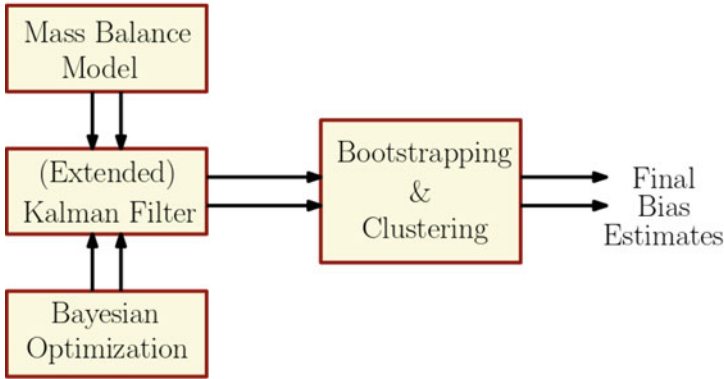
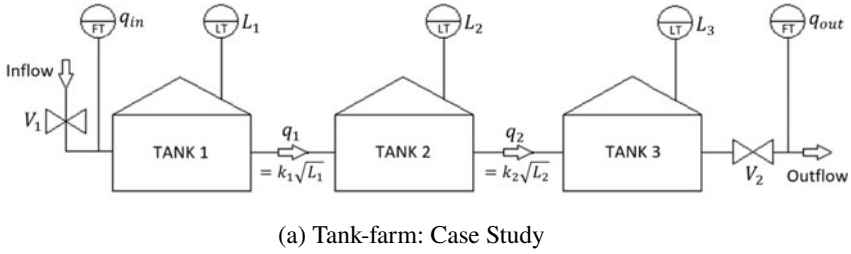


Fig. 1 Tank-farm schematic



(b) Bias estimation framework

Fig. 2 Set up

3 Methodology

The framework for bias estimation is shown in Fig. 2b. The idea is to use the dynamic mass balance equations in a state estimator (KF) to obtain flow bias. The KF hyper-parameters are auto-tuned using Bayesian optimization. The resulting bias sequence is further processed using a bootstrapping and clustering module to obtain a reliable value for the flow bias. The below subsections describe the formulation in greater detail.

3.1 Mass Balance Model

The tank-farm system is modeled using dynamic mass balance equations in discrete time. For the three-tank system used in the current study, the mass balance equations can be written as given below:

$$\begin{aligned}
L_1[n+1] &= L_1[n] + T \cdot \left(q_{\text{in}}[n] - k_1 \sqrt{L_1[n]} \right) + w_1[n] \\
L_2[n+1] &= L_2[n] + T \cdot \left(k_1 \sqrt{L_1[n]} - k_2 \sqrt{L_2[n]} \right) + w_2[n] \\
L_3[n+1] &= L_3[n] + T \cdot \left(k_2 \sqrt{L_2[n]} - q_{\text{out}}[k] \right) + w_3[n]
\end{aligned} \tag{1}$$

where L_1 , L_2 , and L_3 are the tank levels, T is the sampling interval at which measurements are available, k_1 and k_2 are constants such that $q_1 = k_1 \sqrt{L_1}$ and $q_2 = k_2 \sqrt{L_2}$ are the internal gravity-driven flows. w_1 , w_2 , and w_3 are the process noise terms which are assumed to be i.i.d Gaussian random variables. q_{in} and q_{out} are the true inlet and outlet flows, respectively. Assuming that the flow measurements have a constant bias, they are formulated as

$$\begin{aligned}
q_{\text{in}}^m &= q_{\text{in}} + b_{\text{in}} + v_1 \\
q_{\text{out}}^m &= q_{\text{out}} + b_{\text{out}} + v_2
\end{aligned} \tag{2}$$

where b_{in} and b_{out} are the bias, v_1 and v_2 are the measurement noise which are assumed to be i.i.d Gaussian random variables. Note that the model given by (1) is nonlinear due to the presence of gravity-driven flows. Implementing an extended Kalman filter will require computing the linearization of the system about the operating points.

3.2 Kalman Filter-Based Estimator

An extended Kalman filter is implemented to estimate the inflow/outflow bias as follows. An augmented model of the system (1) is constructed by augmenting the tank levels state vector with the unknown parameters k_1 and k_2 as well as one of the biases b_{in} or b_{out} . Only one of the biases is included so that the augmented system remains observable and the unknown parameters can be accurately estimated. To estimate b_{in} , we look at a period of operation where the outlet valve is closed and thus $q_{\text{out}} = b_{\text{out}} = 0$, and vice versa for b_{out} . The unknown parameters are modeled as random walks. In addition, we also construct a case-wise pseudo-measurement for k_1 or k_2 . For example, for estimating b_{out} , k_1 can be modeled as

$$k_1 = \frac{A \cdot (L_1[n] - L_1[n+1])}{T \cdot \sqrt{L_1[n]}} \tag{3}$$

The augmented process model then becomes the same as (1) along with the three additional equations

$$\begin{aligned}
k_1[n+1] &= k_1[n] + w_4 \\
k_2[n+1] &= k_2[n] + w_5 \\
b_{\text{out}}[n+1] &= b_{\text{out}}[n] + w_6
\end{aligned} \tag{4}$$

The augmented model (1), (2), and (4) can then be written together as

$$\begin{aligned} z[n+1] &= f(z[n]) + B \cdot u[n] + w[n] \\ y[n] &= H \cdot z[n] + v[n] \end{aligned} \tag{5}$$

where $z = [L_1, L_2, L_3, k_1, k_2, b_{out}]^T$ is the state vector, $u = [q_{in}^m, q_{out}^m]^T$ is the input vector, w is the process noise, y is the measurement vector, v is the measurement noise and H is the measurement matrix given by

$$H = \begin{bmatrix} 1 & 0 & 0 & 0 & 0 & 0 \\ 0 & 1 & 0 & 0 & 0 & 0 \\ 0 & 0 & 1 & 0 & 0 & 0 \\ 0 & 0 & 0 & 1 & 0 & 0 \end{bmatrix}. \tag{6}$$

The EKF is then implemented for estimating the augmented state z , as follows:

Predictor step:

$$\begin{aligned} \hat{z}_{n+1|n} &= f(\hat{z}_{n|n}) + Bu_n \\ P_{n+1|n} &= FP_{n|n}F^T + Q \end{aligned} \tag{7}$$

Corrector step:

$$\begin{aligned} \hat{z}_{n+1|n+1} &= \hat{z}_{n+1|n} + K_{n+1}[y_{n+1} - H\hat{z}_{n+1|n}] \\ K_{n+1} &= P_{n+1|n}H^T[HP_{n+1|n}H^T + R]^{-1} \\ P_{n+1|n+1} &= [I - K_{n+1}H]P_{n+1|n}[I - K_{n+1}H]^T + K_{n+1}RK_{n+1}^T \end{aligned} \tag{8}$$

where F is the linearized system matrix given by

$$F = \left. \frac{\partial f}{\partial z} \right|_{z=\hat{z}_{n-1|n-1}} = \begin{bmatrix} 1 & 0 & 0 & -\frac{\Delta t}{A}\sqrt{\hat{L}_1[n]} & 0 & 0 \\ 0 & 1 & 0 & \frac{\Delta t}{A}\sqrt{\hat{L}_1[n]} & -\frac{\Delta t}{A}\sqrt{\hat{L}_2[n]} & 0 \\ 0 & 0 & 1 & 0 & \frac{\Delta t}{A}\sqrt{\hat{L}_2[n]} & \frac{\Delta t}{A} \\ 0 & 0 & 0 & 1 & 0 & 0 \\ 0 & 0 & 0 & 0 & 1 & 0 \\ 0 & 0 & 0 & 0 & 0 & 1 \end{bmatrix}, \tag{9}$$

Q is the process noise covariance, R is the measurement noise covariance, P is the state covariance matrix, and K is the Kalman gain.

3.3 Bayesian Optimization (BO)

The Bayesian optimization is implemented for Kalman filter auto-tuning. Given the innovation e for the i th iteration of the Kalman Filter, the BO objective function's data point J_{NIS}^i is formulated as shown in (10) [2],

$$J_{NIS}^i = \left| \log\left(\frac{\overline{\epsilon^i}}{\epsilon_{\min}^i}\right) \right|, \quad (10)$$

where $\epsilon = e^\top S^{-1}e$, $e = Y_{n+1} - H\hat{z}_{n+1|n}$, and $S = HP_{n+1|n}H^\top + R$.

Its integration with the Kalman filter for auto-tuning the covariance matrices is shown in Algorithm 1.

Algorithm 1 Kalman Filter Auto-tuning with Bayesian Optimization

```

No. of Kalman Filter runs =  $N$ 
 $\epsilon_{list} = []$ 
for  $i$  in  $N$  do
     $P_0, Q, R \leftarrow \text{rand}$ 
     $\hat{z}^i, \epsilon^i = \text{Kalman Filter (system data, } P_0, Q, R)$ 
     $\triangleright$  Initial exploration of the KF hyper-parameter space
     $\epsilon_{list}.append(\epsilon^i)$ 
end for
while BO termination criteria not met do
    GPR based Surrogate Model =  $J_{NIS}$  function ( $\epsilon_{list}$ )
     $\triangleright$  Gaussian Process Regression on  $J_{NIS}$  (10)
    optimal  $P_0, Q, R = \text{Probability of Improvement (Surrogate Model)}$ 
     $\triangleright$  Acquisition function for global optima
     $\epsilon_{list} = []$ 
    for  $i$  in  $N$  do
     $\triangleright$  Hyper-parameter exploration over an updated neighborhood
     $\hat{z}^i, \epsilon^i = \text{Kalman Filter (system data, optimal } P_0, Q, R \pm \text{neighborhood)}$ 
     $\epsilon_{list}.append(\epsilon^i)$ 
    end for
end while
GPR based Surrogate Model =  $J_{NIS}$  function ( $\epsilon_{list}$ )
optimal  $P_0, Q, R = \text{Probability of Improvement (Surrogate Model)}$ 
 $\triangleright$  Auto-tuned  $P_0, Q, R$ 
 $\hat{z}^i, \epsilon^i = \text{Kalman Filter (system data, optimal } P_0, Q, R)$ 
 $\triangleright$  KF state estimate  $\hat{z}$  post auto-tuning

```

3.4 Bootstrapping and Clustering

To obtain point values and statistical uncertainty of the time-series state estimate from the Kalman filter, a representative distribution of \hat{z} is obtained through resampling with replacement as part of the bootstrapping method. We then perform a vector quantization on this distribution using k -means clustering, and the largest cluster of

which is chosen as representative dataset of the converged states. A 95% confidence interval on this dataset provides the desired mean and uncertainty of the converged state estimate.

4 Results

Figures 3 and 4 showcase the current outcome of the three-stage methodology described above when applied to the system in Fig. 2a. The baseline EKF was implemented using nominal values for the initial state, process and measurement noise covariance matrices P_0 , Q and R , respectively. The red curve for b_{out} in Fig. 3 shows that this setup can estimate the true state of the system. This estimate is used as input for the statistical uncertainty quantification step in Sect. 3.4.

The slow rate of convergence results in a bias estimate that shows significant difference from the truth. By auto-tuning the EKF with Bayesian optimization, we exhibit a marked performance improvement by way of faster convergence, resulting in a bias distribution that is not only significantly closer to the truth but also has a lower uncertainty (Fig. 5).

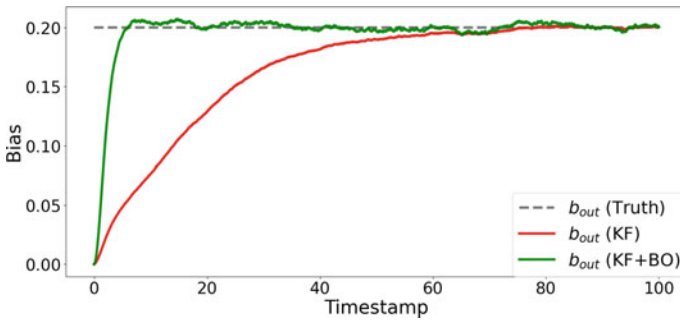


Fig. 3 Outlet flow bias

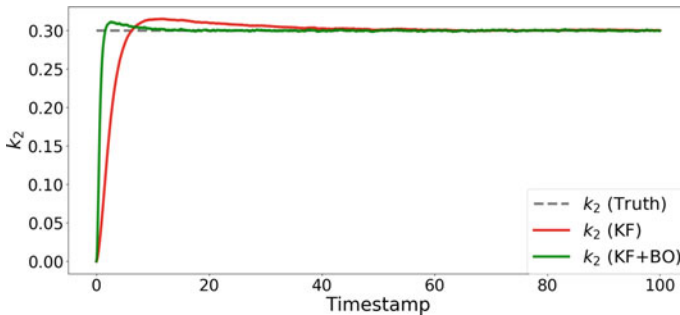
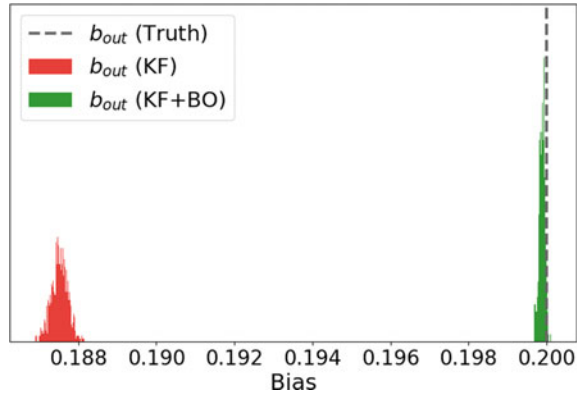


Fig. 4 Internal flow parameter k_2

Fig. 5 Bias estimate histograms



5 Conclusion

The proposed methodology meets the objective of providing reliable estimates of flowmeter bias, therefore, meeting the business goal of maintaining tank-farm mass balance to avoid potential capital loss. As part of the ongoing work, we aim to implement maximum likelihood estimation along with the Kitanidis-KF methodology [3], and also consider additional operational scenarios for validating the framework.

References

1. Sorensen HW (1985) Kalman filtering: theory and application. IEEE Press, New York
2. Chen Z, Ahmed N, Julier S, Heckman C (2019) Kalman filter tuning with Bayesian optimization. arXiv [arXiv:1912.08601](https://arxiv.org/abs/1912.08601)
3. Varshney D, Bhushan M, Patwardhan SC (2019) State and parameter estimation using extended Kitanidis Kalman filter. J Process Control 76:98–111

3-D Spatio-Temporal Prediction of Atmospheric Quantities for Cn² Modelling Using Machine Learning



Suraj Subramanian and Rishav Kanth

1 Introduction

Electromagnetic waves are used in various domains in the current times such as IR-Imaging, High Energy Laser Propagation, communication, object detection, object identification, long-distance optical imaging. These applications need the propagation of Electromagnetic waves through the atmosphere. During propagation, there are distortions induced in these waves due to turbulence in the media. These distortions are captured using optical turbulence profiling or rather, Cn² modelling. Cn² is a measure of these turbulent fluctuations and is mainly dependent on atmospheric parameters such as wind speeds, temperature, and relative humidity. This paper focuses on a 3-D spatio-temporal prediction model to get an altitude profile of these atmospheric parameters which can be used for Cn² modelling. The data used to build the model is of R4 type with variations in altitude, latitude, longitude, and time. In MDAO, regression on such type of multidimensional data is extremely essential, and to tackle this type of data, different machine learning, deep learning, and statistical learning tools are tried, to find a suitable model.

2 Problem Definition

This project aims to build a model which takes in scalar inputs of latitude, longitude, time at which the prediction is to be made and the atmospheric parameter to be predicted to get a predicted altitude profile of that atmospheric parameter.

S. Subramanian (✉) · R. Kanth
Zeus Numerix Pvt. Ltd., Pune, India
e-mail: suraj.subramanian@zeusnumerix.com

© The Author(s), under exclusive license to Springer Nature Singapore Pte Ltd. 2023
P. Pradeep Pratapa et al. (eds.), *Advances in Multidisciplinary Analysis and Optimization*,
Lecture Notes in Mechanical Engineering,
https://doi.org/10.1007/978-981-19-3938-9_43

415

3 Methodology

The dataset used to build this spatio-temporal model, taken from the NCMRWF websites RDS repository, focuses on a small part of the south Indian region for this initial stage, which has time variations, and for each time variation, there are variations in latitude, longitude, and altitude, meaning, for each time instance in the data, there is a corresponding 3-D bounding space. Hence, this problem has 4-dimensions to be tackled, one-dimension of time, and 3-dimensions of space. The model we propose consists of 2 sections viz, the 3-D spatial regression model, and the time series model. The spatial regression model performs regression on the bounding space for each time step individually, i.e., the spatial regression model will consist of a group of several models equal to the total number of time instances in the data. These spatial models will perform regression and give a predicted altitude profile for each time step. The python’s sklearn module was used for these algorithms. These output profiles are given as input to the time series part of the model, which is also a group of time series models equal to the number of altitude points considered for the altitude profile. Here, each time series model takes the atmospheric parameter value for one particular altitude level from all the altitude profiles to learn and perform univariate time series forecasting. The same is done for all the altitude levels via the different time series models. For the time series part, modules like tensorflow and pytorch were used. These forecasted parameters at multiple altitude levels are combined to get the final forecasted altitude profile. The visualization of this entire process flow has been shown in Figs. 1 and 2.

The algorithms compared for the spatial regression part of the model are Support Vector Regression (SVR) [1], Random Forest Regression (RFR) [2], Gradient boost regression (GBR) [3], and XG Boost regression (XGBR), and for the time series part of the model, Auto-Regressive Integrated Moving Average (ARIMA) [4], Long Short-Term Memory (LSTM) [5], and Gated Recurrent Units (GRUs) [5] are compared. The performance metrics used to compare the algorithms are the R2 score and Mean Absolute Percentage Error (MAPE).

Figure 3, shows how both the parts of the model will be combined to get the

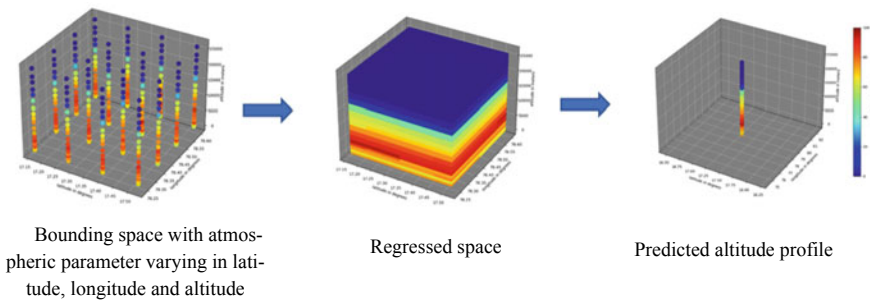


Fig. 1 Visualization of spatial regression for a single time step

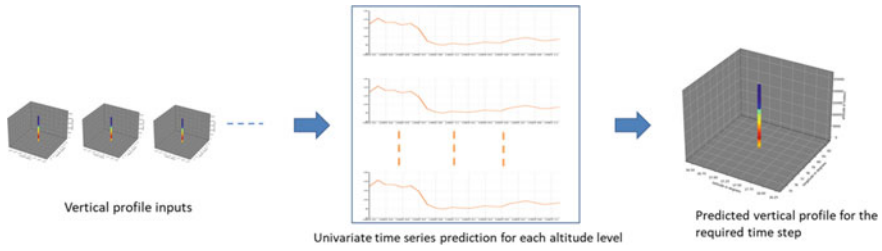


Fig. 2 Time series prediction model visualization

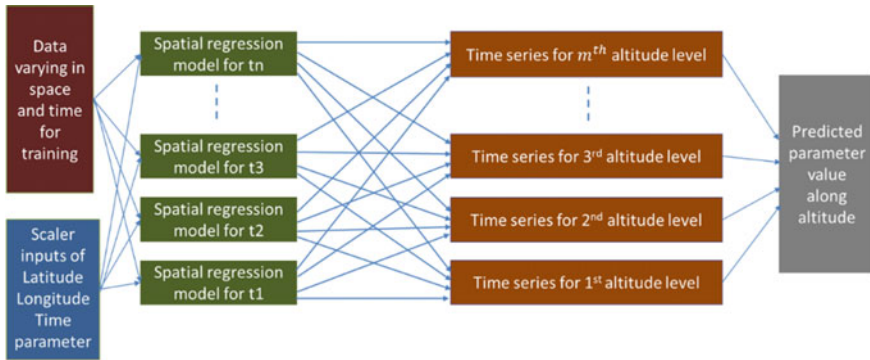


Fig. 3 Proposed spatial-temporal model

predicted output.

4 Dataset Overview

The dataset used in this project was taken from the NCMRWF website which is publicly accessible. In this dataset, after pre-processing, time is considered in seconds from the start of the year and the coordinates in degrees. The dataset has 24 different pressure levels, 4 latitude variations, 4 longitude variations, and 2726 time steps.

5 Results and Discussion

5.1 Spatial Regression

The MAPE and R2 scores for both, spatial and time series algorithms were compared. For the 3-D spatial regression part, the tree-based algorithms such as GBR, RFR,

Table 1 Hyperparameter tuning outputs for spatial regression

Hyperparameter	RFR	GBR	XGBR	SVR
Bootstrap	True	–	–	–
Max depth	5	5	10	–
Min sample leaf	2	1	–	–
Min samples split	5	4	–	–
n estimators	700	600	20	–
C	–	–	–	100
Epsilon	–	–	–	0.01
Gamma	–	–	–	0.1
Kernel	–	–	–	RBF

Table 2 Mean absolute percentage errors and R2 scores for spatial regression

Performance metric	RFR	GBR	XGBR	SVR
E_{in}	1.46%	0.014%	0.231%	8.47%
E_{out}	2.09%	0.314%	0.836%	8.61%
Train R2 score	0.972	0.999	0.999	0.551
Test R2 score	0.936	0.999	0.988	0.486

and XGBR performed better compared to SVR. Though there was a higher variance in the test dataset, the errors were comparatively very less for the GBR model. And the XGBR performed slightly less compared to GBR, but in terms of computational load and speed XGBR outperformed all the methods used, even so, since accuracy was of greater concern, GBR was selected for the 3-D spatial regression part of the model. Tables 1 and 2 shows the hyperparameter tuning outputs for these algorithms and the Mean absolute percentage errors for in-sample (E_{in}) and out of sample (E_{out}) points, and the R2 scores. These results are for one specific time instance (700th time step is considered for the table).

5.2 Time Series Prediction

Amongst the time series models, the deep learning models (LSTMs and GRUs) performed better compared to the statistical learning model (ARIMA). Overall, GRUs performed with the least errors, and hence GRUs were used for the time series part of the model. Tables 3 and 4 show the hyperparameters tuned and the performance metric for the time series models. These outputs are for a specific altitude level (10th altitude level in this case).

Some part of the dataset was kept aside to validate the results of the combined model. After the selection and training of the individual models, the combined model

Table 3 Hyperparameter tuning output for time series prediction

Hyperparameter	ARIMA	LSTM	GRU
Stacked layers	–	2	2
Hidden size	–	20	20
Sequence length	–	120	150
P	8	–	–
d	1	–	–
q	2	–	–

Table 4 Mean absolute percentage errors and R2 scores for time series prediction

Performance metric	ARIMA	LSTM	GRU
E_{in}	15.57%	3.96%	3.86%
E_{out}	25.07%	5.06%	4.90%
Train R2 score	0.805	0.847	0.854
Test R2 score	0.869	0.762	0.782

was used to predict the altitude profile at a particular time instance from the validation dataset. A particular value of latitude longitude was selected for a future time step and the atmospheric parameter was predicted using this model. Figure 4 shows the regressed altitude profile for the future time instance to be used as a reference to visualize the difference in the time series prediction output. Figure 5 shows the predicted altitude profile for the future time instance for a particular latitude and longitude value. The results were good with an accuracy of around 85%. This accuracy was based on the median percentage errors of the parameter values at the known altitude levels from the dataset and the predicted altitude profile.

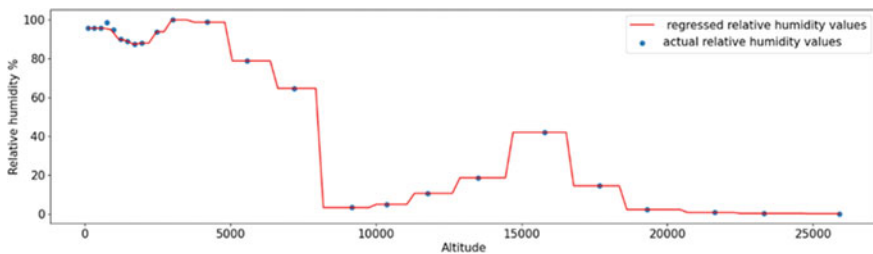


Fig. 4 Spatially regressed altitude profile (GBR)

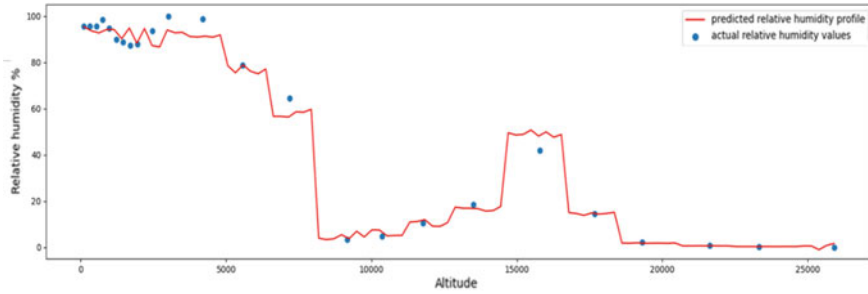


Fig. 5 Forecasted altitude profile (GRU)

6 Conclusion

From this comparison study and trying out different combinations, an accuracy of about 85% was achieved on a model for spatial-temporal prediction using a combination of machine learning and deep learning techniques. Even so, greater accuracies can be achieved by using a larger dataset.

References

1. Smola AJ, Schölkopf B (2004) A tutorial on support vector regression. *Stat Comput* 14(3):199–222. <https://doi.org/10.1023/b:stco.0000035301>
2. Liaw A, Wiener M (2002) Classification and regression by randomForest 2(3)
3. Zemel RS, Pitassi T (2000) Department of computer science university of Toronto. A gradient-based boosting algorithm for regression problems
4. Noureen S, Atique S, Roy V, Bayne S (2019) Analysis and application of seasonal ARIMA model in energy demand forecasting: a case study of small scale agricultural load
5. Hochreiter S, Fakultat fur Informatik (1997) Long short term memory

To Evaluate the Performance of Cooling Tower Using Different Filters



Rutuja Kapote, Kumar Vivek, and Ajit Dorwat

1 Overview

Cooling towers are most widely utilized in the HVAC industries to remove heat into the atmosphere by considering the surrounding environment. Among the various types of cooling tower, the counter-flow cooling tower is widely used and preferred over the other types and yields maximum tower performance in terms of gain in cooling domain. Heat transfer takes place within the tower between the hot water in droplets form and the ambient air through filters by exchanging the heat and mass. The cooling tower filters play a crucial role in increasing the contact area which is a vital parameter in temperature grid, between hot water droplets and air, hence promoting the better heat transfer. It is analytically unfeasible to calculate the performance of heat rejection inside the filters because of the difficulty in estimating the contact time and the surface area among air and the water, and hence, numerical methods are required to simulate and analyze the grid at microscopic level.

Different experiments were performed to evaluate and analyze evaporation losses from different types of filters. The calculations are performed for evaluating performance characteristics of cooling tower, efficiency, effectiveness, and different types of losses which include drift losses, windage losses, evaporation losses, and lastly blowdown losses. After performing the set of calculations and analyzing the experimental data which concludes that the composition of cooling tower is proportional to tower characteristics, and different types of losses generated in the cooling tower [2].

R. Kapote · K. Vivek (✉) · A. Dorwat
Sinhgad College of Engineering, S. No. 44/1, Off, Sinhgad Rd, Vadgaon Budruk, Pune,
Maharashtra 411041, India
e-mail: k.vivek3689@gmail.com

A. Dorwat
e-mail: aldorwat.scoe@sinhgad.edu

Cooling tower is designed on the concept of evaporative cooling where water is cooled down by the effect of high rate of flowing air. It provides a fruitful alternative at places where there is cooling water insufficiency and where hot water discharge causes an environmental apprehension.

The CFD analysis of wet cooling tower with various inlet conditions is done using ANSYS. Simulation of transport inside the tower is done using the code Fluent [3, 5]. The effect of process variable such as inlet water movement, inlet air velocity, and fill porosity is observed on temperature of water from the results [4, 12]. The effective cooling of water depends on various process parameters like dry-bulb temperature of air, wet-bulb temperature of air, material used for filters, size of filters, flow rate of inlet air, angle at which air is entering, water flow rate, and temperature gradient [5]. The packaging region is considered as porous zone, and accordingly, modeling of porous zone is done to get the pressure drop across this zone. In cooling tower model, two air flow rates in vertical direction and air inlet temperature, water inlet temperature is considered for analysis [6].

The cooling tower was analyzed with the help of artificial neural network (ANN). An ANN model used for a forced draft cooling tower with the experimental data as: the ratio of mass flow rate of water to that of mass flow rate of air, the inlet water temperature, and the outlet water temperature, and the inlet air wet-bulb temperature are chosen as input variables, while the output obtained is the coefficient of performance and come across that a trained model will give accurate results for the thermal performance of the cooling tower using limited number of data points also [1]. An ANN model was developed to foretell the thermal performance of natural draft wet cooling tower considering the cross-wind flow for the first time. However, water evaporation losses were not considered in these papers which motivated us to develop a model to optimize the water losses and the thermal performance of cooling tower using different types of packaging [2].

The present study focuses on application of computational fluid dynamics (CFD) and artificial neural network (ANN) for the prediction of the cooling tower performance. The obtained results are validated from experimental data. The optimization of cooling tower is done using data points received from the CFD obtained after simulation and is tested from the experimental data obtained from the [1], so in depth, the study evaluates the cooling tower in two different platforms, i.e., by creating the model and analyze the system in Ansys Fluent by implementing the boundary condition with respect mass and heat. And data considering from the experiments cited are used for building the model as ANN.

2 Methodology

The domain represents the cooling tower area through which the system evaluates in two sections, initially system is model, discretized with different meshing techniques and boundary conditions; by running the simulation, the different filters are incorporated, and same procedure is executed for finding out the best for getting

the maximum efficiency; also, the simulation results with different epochs with constrained environment are consider with sensitivity and accuracy matrix.

By gaining the flow in cooling tower attaining the simulation with the help of cited reference, the dataset is implemented in the building the ANN with the MATLAB tool.

3 Performance Analysis of Cooling Tower Using Computational Fluid Dynamics (CFD)

Analysis of cooling tower with different filter materials is performed using CFD. Starting first step with the creation of geometry then meshing (Discretization) and finally evaluation of results. For the simulation, ANSYS Fluent is used. The CFD process can be divided into three steps: preprocessing, solver, and post-processing. These processes are applied to cooling tower by taking fill of different materials (Fig. 1).

A 3D model of cooling tower is created in SOLIDWORKS. Height of cooling tower is taken to be 2.3 m, and the fill height is taken to be 0.4 m. The material of cooling tower is stainless steel, while the fill material is taken to be aluminum and wood [2]. ANSYS is used for further analysis of cooling tower. In Ansys workbench, (geometry) the fluid domain is define. The porous zone in Fig. 2 is formed in geometry using some Ansys geometry commands. The mesh is created over the domain to capture certain area of interest and achieve a robust solution. In fluent preprocessor, all the input data related to the required condition are given. Flow is

Fig. 1 3D model

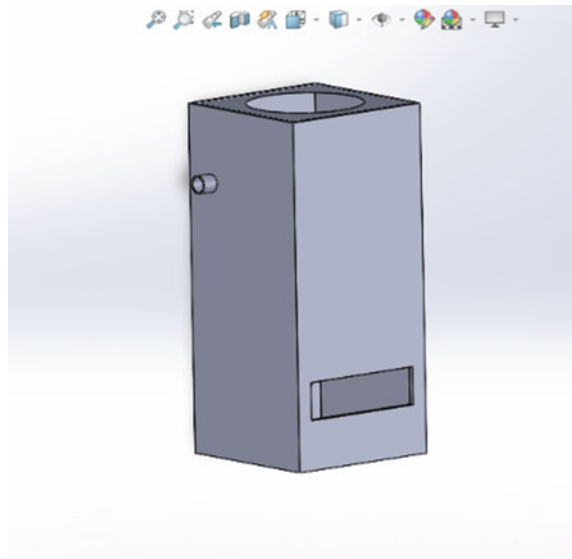
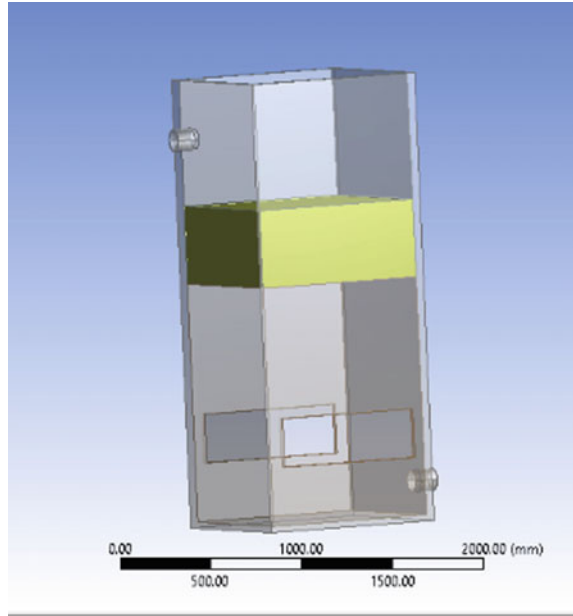


Fig. 2 Porous domain

transient, and turbulence model standard K-omega is used with energy equation on. As the cooling tower consists of two phases, i.e., water, air. Eulerian phases are given. Multiphase model is used, and materials are assigned for different cell zones. Porous zone conditions are given in fluent preprocessor (Figs. 2 and 4).

4 Simulation of Cooling Tower Using ANN Model on MATLAB

To obtain an optimized model of a cooling tower between its performance and evaporation losses, artificial neural network is created. A typical architecture of this ANN domain configuration has one input layer, one hidden layer, and one output layer. Each layer contains several neurons, and each neuron in the layer is connected to all the neurons in the adjacent layer with different weights. Signal flowing through the input layer flows through the hidden layer multiplied by weights and summed up with a bias contribution. While developing the ANN model, the available data were divided into three sets; one set is used for training the model (50% of the data), and the second set is used for the validation the model (30% of the data), and the remaining set is use for testing the mathematical model (i.e., 20% of the data) (Fig. 3).

Following steps were used while developing the ANN model:

1. Imported the data as a numeric matrix from csv file
2. Assigning the name to call inputs and the outputs

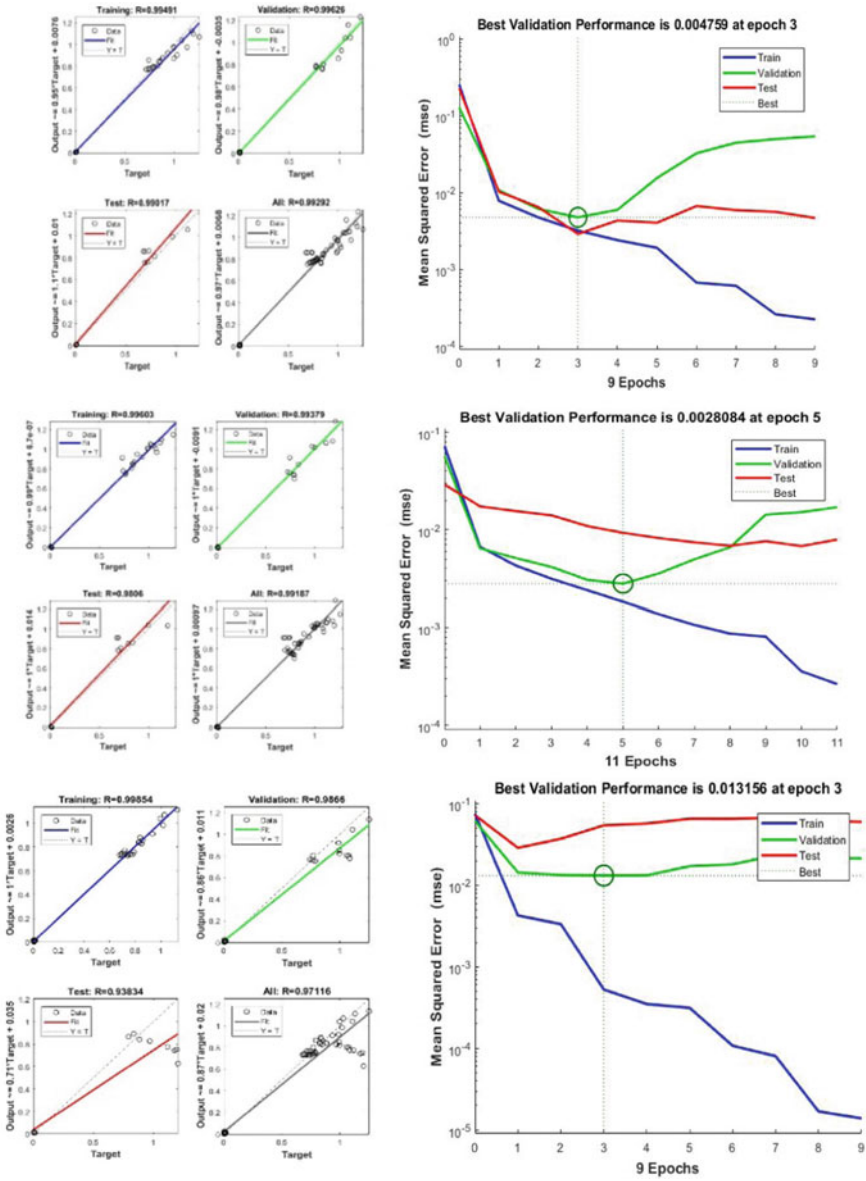


Fig. 3 ANN plot

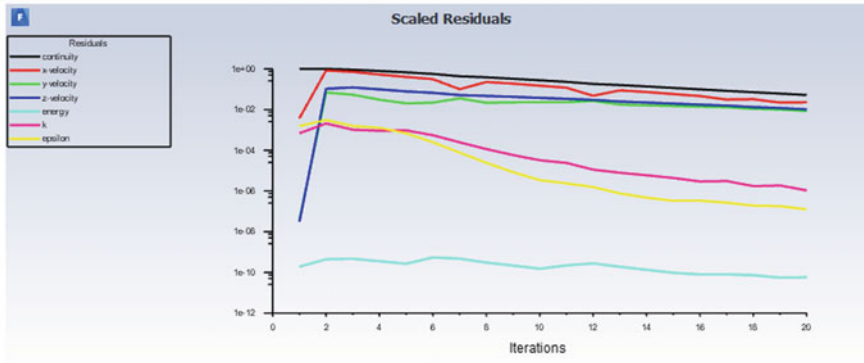


Fig. 4 Convergence plot

Fig. 5 Temperature contour for aluminum

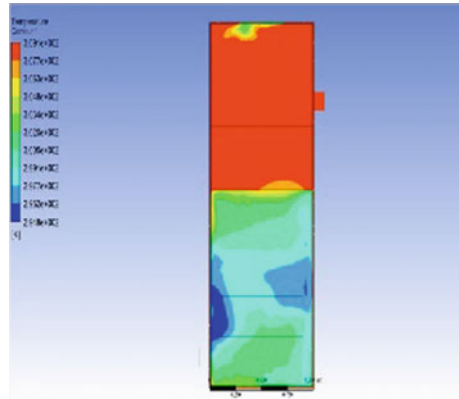
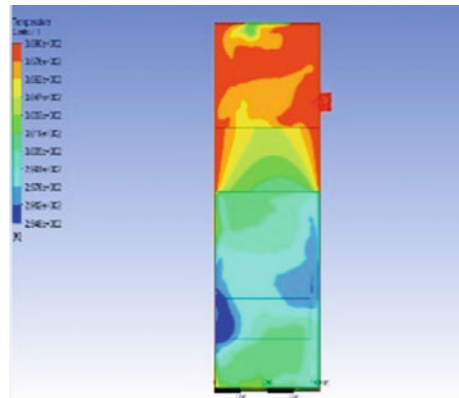


Fig. 6 Temperature contour for wood



3. Visualization of the data
4. Normalize the features and transform the output
5. Train the ANN
6. Read the different plots produced by the ANN model
7. If required, increase the number of neurons in the hidden layer to obtain more accurate results.

5 Results and Discussion

From the results obtained, we can see that the selection of filters depends upon its material, porosity, permeability, number of condensed droplets and surface area.

From the temperature gradient obtained in results, the heat transfer rate is more in wood material than in aluminum. As the porosity of wood is between 40 and 80% and that of aluminum is between 55 and 75%, the wood can take more water in, and by the transfer of ambient air through the fill material, reduction in the temperature of hot water is more. The post-processor shows the decrease in temperature of hot water in wood material is more as compared to aluminum material which leads to the selection of wood as a fill material.

The regression value for the validation is found to be 0.99626, and after testing, it is 0.99017. Overall regression value of the model is 0.99292. From the performance curve, the best validation performance is 0.004759 (Figs. 7 and 8).

Fig. 7 Pressure contour for aluminum

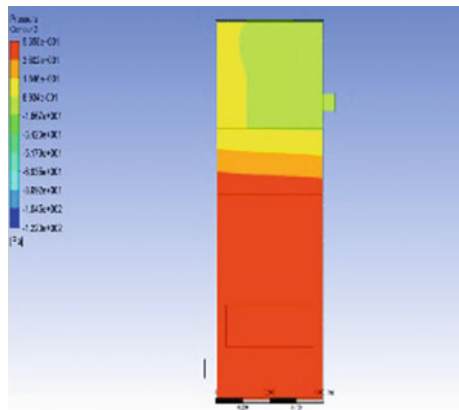
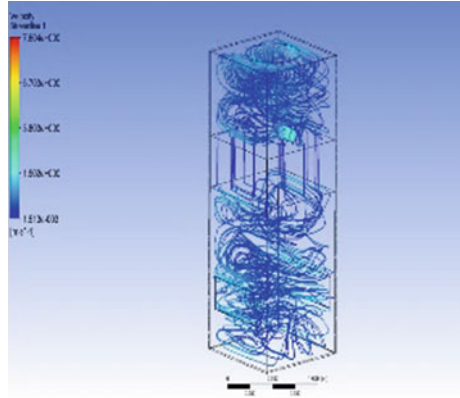


Fig. 8 Velocity streamlines

Acknowledgements We would like to express special Thanks of gratitude to our Assistant professor “Mr. Ajit Dorwat” sir for their guidance and support in completing our project.

References

1. Shublaq M, Sleiti AK (2020) Experimental analysis of water evaporation losses in cooling towers using filters Appl Therm Eng 175
2. Ronak S, Trupti R Thermal design of cooling tower. Int J Adv Eng Res Stud
3. Priyadarshini I, Akhil A, LakshmiShilpa V (2017) Flow analysis of cooling tower using CFD. Int J Creative Res Thoughts ISSN 2320–2882
4. Patel R, Asthana G (2014) CFD Analysis of FRP cooling tower. Int J Sci Res Dev 2(03) ISSN 2321–0613
5. Chitale PR, Gamare RK, Chavan SK, Chavan SR, Yekane AS (2018) Design and analysis of cooling tower. J Eng Res Appl 8(04):79–84
6. Grover DS, Hadgekar P (2019) Thermal and numerical analysis of wet cooling tower for shore based naval material boiler. Int J Eng Res Technol 8(04)
7. Islamoglu Y (2005) Modeling of thermal performance of a cooling tower using an artificial neural network. Heat Transf Eng 26(4):073–076
8. Gao M, Sun FZ, Zhou SJ, Shi YT, Zhao YB, Wang NH (2009) Performance prediction of wet cooling tower using artificial neural network under cross-wind conditions. Int J Therm Sci 48:583–589
9. Singh B, Mishra P (2019) Thermal & CFD analysis of induced draught cross flow cooling tower 56(156)
10. Arunraj VS, Parthasarthy P, Sundar Raj M, Akbar Ali A (2016) Performance and analysis of cooling tower 03(04)
11. Lu Y, Guan Z, Gurgenci H (2012) CFD simulations on small natural draft dry cooling towers
12. Chauhan B, Gajdhar D (2018) Optimization and CFD analysis of induced draft counter flow wet cooling tower 5(04)
13. Xia L, Gurgenci H, Liu D, Guan Z, Zhou L, Wang P (2018) CFD analysis of pre-cooling water spray system in natural draft dry cooling towers

Extension of Particle Swarm Optimization Algorithm for Solving Priority-Based Time Minimization Transportation Problem



Gurwinder Singh, Amarinder Singh, and Prabhjot Kaur

1 Introduction

Transportation problem (TP), a network-flow optimization problem, emerges as a process to strategically manage the marketing channels of an organization for the procurement, movement, and storage of parts and finished inventories (and the associated information flows). The TP plays an important role to meet such industrial and management needs by seeking a distribution plan that fulfills the availability and requirement restrictions and optimizes the total cost of transportation.

The complexity of the social and economic system, however, postulates establishing the parameter of optimization that may be other than the cost in the real-world problems. There are instances when the transportation time assumes significant prominence over the cost of the transportation. The transportation of artillery from depots to the border locations, the supply of biodegradable items for daily requirements and the provision of medical aids needed at urgent hours, etc., are some of the situations where the time-delay in the shipment will effect a substantial loss than gaining some advantage over other evaluation parameter. Thus, time optimization plays a key role in squeezing the transportation time limit and is formulated as the time minimization transportation problem (TMTP) that stipulates minimization of maximum time taken to ship the commodities from sources to destinations while satisfying the supply and demand constraints.

G. Singh (✉)
Chandigarh University, Gharuan, Mohali, Punjab, India
e-mail: singh1001maths@gmail.com

A. Singh
Chitkara University Institute of Engineering and Technology, Chitkara University, Rajpura,
Punjab, India
e-mail: amarinder77@gmail.com

P. Kaur
University Institute of Engineering and Technology, Panjab University, Chandigarh, India
e-mail: prabh.g3@gmail.com

© The Author(s), under exclusive license to Springer Nature Singapore Pte Ltd. 2023
P. Pradeep Pratapa et al. (eds.), *Advances in Multidisciplinary Analysis and Optimization*,
Lecture Notes in Mechanical Engineering,
https://doi.org/10.1007/978-981-19-3938-9_45

In real-world situations, there are destinations whose demand is to be met on time priority, so they are labeled with respect to deliverance of products. Such identification and labeling categorizes the destinations as primary and secondary destinations. The following instances are considered as priority-based TMTP as applications in real life:

- the outbreak of pandemic like COVID-19 across the world whereby the government bodies are imposing different restrictions and working hard to mobilize the movement of essential goods and services etc. Though the supplies are required everywhere, certain regions are in dire need of the critical supplies (oxygen, medicine, etc). Such regions are identified as prioritized destinations.
- during wartime soldiers at some locations need rapid supplies because of faster rate of stock depletion. Accordingly, such locations are classified as priority destinations.
- nowadays, different e-retailers are launching priority services, so that clients receive their items even within few hours, depending on product requirements, instead of the regular delivery period.

The solution techniques of TMTP have been developed by various authors. Hammer [1], Schwarz [2], and Garfinkel and Rao [3] used the labeling techniques, while Srinivasan [4] and Issermann [5] solved the problem using the cost operator theory. Bhatia et al. [6], Ramakrishnan [7], Sharma and Swarup [8], Prakash [9], and Nikolic [10] made noticeable enhancements to the common facets. Some alterations of TMTP, namely bi-level TMTP [11], capacitated two-stage TMTP [12] and a priority-based TMTP [13], have been studied by the researchers.

The heuristic or analytical methods proposed by these authors could not solve the large-sized problems as the computation time increases considerably. Thus, the interest in metaheuristics and evolutionary approaches has increased in the solution of such complex problems. The metaheuristic methods are widely known global search approach which have attracted considerable attention since they can be adapted to context of optimization problem. Techniques such as genetic algorithm (GA), spanning-tree-based GA, tabu search (TS) have been used to solve linear and nonlinear TPs by Vignaux and Michalewicz [14], Gen and Li [15], Gen et al. [16], Syarif and Gen [17], and Sun and Mckeown [18, 19]. Likewise Huang [20], Elsherbiny et al. [21], and Singh and Singh [22] solved TP using PSO.

The main objective of this work is to solve a PBTMTP through swarm intelligence and provide a method that explores the solution space without focusing on the count and positions of the non-zero allocations and also exploring the alternate solutions, if they exist, thereby providing a computationally efficiently solution procedure to the decision makers. The present study develops a hybridized PSO algorithm to solve a PBTMTP by integrating new algorithms. The computational competence of the proposed algorithm has been validated by implementing it on a wide variety of problems to obtain their optimal solutions.

2 Problem Definition and Formulation

Consider m sources S_1, S_2, \dots, S_m with respective supply levels a_1, a_2, \dots, a_m units and n destinations D_1, D_2, \dots, D_n with respective demand levels b_1, b_2, \dots, b_n units. The transportation time of any number of units of product from S_i to D_j is denoted by t_{ij} , while the actual number of units shipped from S_i to D_j is denoted by x_{ij} that is to be determined in a manner that minimizes the maximum transportation time. The mathematical representation of the problem is given below:

$$\text{Minimize } T(X) = \text{Max}(t_{ij} : x_{ij} > 0) \tag{1}$$

$$\text{subject to constraints } \sum_{j=1}^n x_{ij} = a_i \quad (i = 1, 2, \dots, m) \tag{2}$$

$$\sum_{i=1}^m x_{ij} = b_j \quad (j = 1, 2, \dots, n) \tag{3}$$

$$x_{ij} \geq 0 \quad (i = 1, 2, \dots, m; j = 1, 2, \dots, n) \tag{4}$$

where t_{ij} is the time to transport any number of units of the homogeneous commodity from S_i to D_j . The associated objective function $T(X)$ is a concave function that is minimized over a convex polytop; thus, TMTP belongs to a class of concave minimization problems [23].

However, in case of according priority to some destinations, they are labeled as primary (higher priority) destinations & secondary (lower priority) destinations and constitute the sets L_1 and L_2 respectively. The time of transportation to the destinations is recorded with respect to their priority, and the total time of transportation is evaluated using the function :

$$\min[\text{Max}_{L_1}(t_{ij} : x_{ij} > 0) + \text{Max}_{L_2}(t_{ij} : x_{ij} > 0)] \tag{5}$$

Thus, the priority-based time minimization transportation problem (PBTMTP) is mathematically defined to satisfy the objective function given by Eq. (5) while satisfying the constraints and feasibility conditions given by Eqs. (2)–(4).

3 Methodology

PSO is a metaheuristic algorithm which can explore very wide areas of possible solutions of an optimization problem without making few or no assumption of the problem. In addition, PSO does not optimize the problem by taking into account the gradient, i.e., derivative-based space exploration, as done by conventional optimization methods. It is a computational method which optimizes a problem by iteratively enhancing the candidate’s solution with respect to the objective function. The PSO

operates through a combination of solutions, called particles, and moving them in the solution space using velocity and position equations. The personal best position (Pbest) and the global best position (Gbest) interact to determine the next position of the particles and hence the path toward the optimal solution.

The position vector $X_i = (x_{i1}, x_{i2}, \dots, x_{in})$ represents the particle i of the swarm in an n -dimensional search space and is assigned velocity through the vector $V_i = (v_{i1}, v_{i2}, \dots, v_{in})$. $P_{i,best} = (p_{i1}, p_{i2}, \dots, p_{in})$, and $P_{g,best} = (p_{g1}, p_{g2}, \dots, p_{gn})$ denotes the personal best position attained by X_i and the global best position of the swarm. Subsequently, particles move through some velocity and reach new positions that are determined using the undermentioned equations:

$$V_i(t + 1) = \omega \cdot V_i(t) + c_1 r_1 (P_{i,best} - X_i) + c_2 r_2 (P_{g,best} - X_i) \tag{6}$$

$$X_i(t + 1) = X_i(t) + V_i(t + 1) \tag{7}$$

where ω is inertia weight, c_1 and c_2 are acceleration coefficients, r_1 and r_2 are random variables uniformly distributed between zero and one. Using these random weights, PSO improves the positions of all the particles and moves toward Pbest and Gbest locations.

The basic PSO is drawn up ahead:

Algorithm 1: Basic PSO

- 1 Assign values to inertia weight, acceleration coefficients, Popsizer, Maxiters, Maxrun.
 - 2 Randomly assign initial velocity and position to each particle.
 - 3 **do**
 - 4 **for each particle do**
 - 5 Determine the value of the objective function
 - 6 Upgrade best position visited by the particle
 - 7 Upgrade best position visited by the swarm
 - 8 Upgrade the inertia weight ω .
 - 9 **for every particle do**
 - 10 Upgrade velocity through the equation (6)
 - 11 Upgrade position through the equation (7)
 - 12 **while** the Maxiters are not completed
 - 13 **return** the global best solution
-

In this paper, a priority-based time minimization transportation problem has been solved to obtain a non-negative integral variable combination that not only meets the availability and requirement conditions but also optimizes transportation duration. Algorithm 2 generates random initial basic feasible solutions (IBFSs) by assigning non-negative integral values to the decision variables that meet all the constraints.

The solution procedure begins with the first module determining an IBFS using algorithm 2. The IBFS then moves with certain velocity through Eq. (6) and reaches the updated position given by Eq. (7). This updated position possesses some infeasible values, i.e., some of the basic variables assume fractional &/or negative values. PSO is then hybridized with two modules, viz., algorithm 3 and algorithm 4 to remove the infeasibility from the decision variables. The procedure is carried out in different phases owing to the value of the solution obtained & an attempt to further improve the same.

Algorithm 2: Initial Solution

Input: $TP, Supply, Demand$
Output: Initial Solution X

- 1 Set $[m, n] = size(TP)$
- 2 Set $a = Supply$ and $b = Demand$
- 3 Generate a random number matrix X of size $[m, n]$
- 4 Assign X as $X = zeros(m, n)$
- 5 **for** $iter = 1$ **to** mn **do**
- 6 Set $maxr = max(X)$
- 7 Determine the position of $maxr$ as (i, j) in X
- 8 Assign available amount to x_{ij} as $x_{ij} = min(a_i, b_j)$
- 9 Upgrade demand and supply as: $b_j = b_j - x_{ij}$ and $a_i = a_i - x_{ij}$
- 10 Set $maxr = 0$
- 11 **return** X

Algorithm 3: Repair Negatives

Input: Matrix X containing negative numbers
Output: Matrix X with non-negative numbers

- 1 **do**
- 2 **if** $x_{ij} < 0$ **then**
- 3 Select the largest element in column j and denote it as x_{hj}
- 4 Select elements x_{hj}, x_{ij} as
- 5 $x_0 = x_{ij}$
- 6 $x_{hj} = x_{hj} - |x_0|$
- 7 $x_{ij} = 0$
- 8 Upgrade elements in row i as
- 9
$$x_{ig} = \begin{cases} x_{ig} & x_{ig} = 0 \\ x_{ig} - \frac{|x_0|}{u} & x_{ig} > 0 \end{cases}$$
- (u is the number of positive elements in row i)
- Change elements in row h into
- $$x_{hg} = \begin{cases} x_{hg} & x_{ig} = 0 \\ x_{hg} + \frac{|x_0|}{u} & x_{ig} > 0 \end{cases}$$
- 10 **while** $(x_{ij} < 0; i \in \{1, 2, \dots, m\}, j \in \{1, 2, \dots, n\})$
- 11 **return** X

Algorithm 4: Repair Fractions

Input: A Matrix X containing fractional numbers
Output: Matrix X containing integers

- 1 Set IX as the matrix containing integral numbers of matrix X
- 2 Set FX as the matrix containing fractional numbers of matrix X
- 3 Set s_i =row sum of FX_{ij} and d_j =column sum of FX_{ij}
- 4 Upgrade FX_{ij} as follows:
 - 5 **for** $i = 1$ **to** m **do**
 - 6 **for** $j = 1$ **to** n **do**
 - 7 $FX_{ij} = \min(s_i, d_j)$
 - 8 $s_i = s_i - FX_{ij}$
 - 9 $d_j = d_j - FX_{ij}$
- 10 Update IX as : $IX=IX+FX$
- 11 **return** IX

4 Solution Procedure

The hybridized PSO is applied on a balanced transportation problem where the destinations are categorized as primary and secondary destinations. The constant parameters of PSO are assigned present values, and a population of particles (IBFSs) is raised through algorithm 2, and the respective total time of transportation is computed. The individual times are referred as PBest, and the global best time is referred as GBest. The objective is to minimize GBest as much as possible.

Algorithm 5: Solution Procedure

- 1 Generate initial particles in the swarm
- 2 Update the position of particles using equation (6) and (7)
- 3 **for each particle do**
 - 4 Remove the negative values using Repair Negatives algorithm
 - 5 Remove the fraction values using Repair Fractions algorithm
 - 6 Determine the fitness value of the updated solution
 - 7 Update personal best position of all the particles
 - 8 Update global best position of the swarm
- 9 **return** *the global best solution*

5 Results and Discussion

In this work, proposed PSO is assessed on five test problems of varying dimensions taken from literature. The proposed method is repeated, for each test problem, with 10 runs and 1000 iterations with population size 5 in MATLAB. When converging to an optimum solution, the sequence of the suggested algorithm is separated into single or multiple phases, as per need of particular problem. The phase-wise obtained results of each problem are outlined in Table 1.

Table 1 Obtained optimal solution for problem TP1 to TP5

Phases	TP1	TP2	TP3	TP4	TP5
Phase-I	23	25	14	63	80
Phase-II	21	21	10	58	75
Phase-III	–	–	–	40	–

6 Conclusion

The PBTMTP is solved through the PSO hybridized with repair negatives and repair fractions algorithms. The time of transportation is improved using phase-wise bounds created based on the previous known best bound. The present solution procedure has displayed many efficiencies over the classical techniques. The latter works on number and location of non-zero allocations and does not investigate solutions having more than $(m + n - 1)$ non-zero allocations, while the former works irrespective of these. The amend fractions algorithm works better than other techniques that simply round-off the fractional values. The effectiveness of the procedure is established through the RPD and t -test, thus, the procedure is a huge achievement for solving the PBTMTP.

References

1. Hammer PL (1969) Time-minimizing transportation problem. *Naval Res Logistics Q* 16(3):345–357
2. Wlodzimierz S (1971) Some remarks on the time transportation problem. *Naval Res Logistics Q* 18(4):473–485
3. Garfinkel RS, Rao M (1971) The bottleneck transportation problem. *Naval Res Logistics Q* 18(4):465–472
4. Srinivasan V, Thompson GL (1976) Algorithms for minimizing total cost, bottleneck time and bottleneck shipment in transportation problems. *Naval Res Logistics Q* 23(4):567–595
5. Isermann H (1984) Linear bottleneck transportation problem. *Asia Pac J Oper Res* 1:38–52
6. Bhatia HL, Swaroop K, Puri MC (1977) A procedure for time minimization transportation problem. *Indian J Pure Appl Math* 8(8):920–929
7. Ramakrishnan CS (1977) A note on time minimization transportation problem. *Opsearch* 14(3):207–209
8. Sharma J, Swarup K (1978) Time minimization in transportation problems. *NZ Oper Res* 6(1):75–88
9. Prakash S (1982) On minimizing the duration of transportation. *Proc Indian Acad Sci Math Sci* 91(1):53–57
10. Nikolić I (2007) Total time minimizing transportation problem. *Yugoslav J Oper Res* 17(1):125–133
11. Khandelwal A, Puri M et al (2008) Bilevel time minimizing transportation problem. *Discrete Optim* 5(4):714–723
12. Sharma V, Dahiya K, Verma V (2010) Capacitated two-stage time minimization transportation problem. *Asia Pac J Oper Res* 27(04):457–476
13. Kaushal B, Arora S (2018) Priority based time minimization transportation problem. *Yugoslav J Oper Res* 28(2):219–235

14. Vignaux GA, Michalewicz Z (1991) A genetic algorithm for the linear transportation problem. *IEEE Trans Syst Man Cybern* 21(2):445–452
15. Gen M, Li Y, Ida K (1999) Solving multi-objective transportation problem by spanning tree-based genetic algorithm. *IEICE Trans Fundam Electron Commun Comput Sci* 82(12):2802–2810
16. Gen M, Altiparmak F, Lin L (2006) A genetic algorithm for two-stage transportation problem using priority-based encoding. *OR Spectrum* 28(3):337–354
17. Syarif A, Gen M (2003) Solving exclusionary side constrained transportation problem by using a hybrid spanning tree-based genetic algorithm. *J Intell Manuf* 14(3–4):389–399
18. Sun J, Lai C-H, Wu X-J (2016) Particle swarm optimisation: classical and quantum perspectives. CRC Press
19. Sun M, Aronson JE, McKeown PG, Drinka D (1998) A Tabu search heuristic procedure for the fixed charge transportation problem. *Eur J Oper Res* 106(2–3):441–456
20. Huang H, Zhifang H (2009) Particle swarm optimization algorithm for transportation problems. In: Particle swarm optimization. Intech, Shanghai, pp 275–290
21. El-Sherbiny MM, Alhamali RM (2013) A hybrid particle swarm algorithm with artificial immune learning for solving the fixed charge transportation problem. *Comput Ind Eng* 64(2):610–620
22. Singh G, Singh A (2019) A hybrid algorithm using particle swarm optimization for solving transportation problem. *Neural Comput Appl* 1–18
23. Bansal S, Puri M (1980) A min max problem. *Zeitschrift Oper Res* 24(5):191–200

Parametric Modelling, Analysis and Design of Compact Diffuser for Heat Exchanger



Kumud Mittal, G. Saravana Kumar, K. Arul Prakash, Sreenivas Jayanti, and S. Vengadesan

1 Introduction

Computer-aided design (CAD) is extensively used in development of new products in today's market. To make the design process simpler, a set of parameters are often identified in the proposed geometry or model which makes it easier to modify the model during the iterative design process and fulfil the user requirement. These parameters are product elements that might contribute to the shape, material, tolerance or manufacturing process specification. The present work describes a parameter-based approach to the model building and involves design and analysis of an innovative compact diffuser which has applications in automotive, aerospace and other related fields. A diffuser is a thermodynamic device which is used for reducing the velocity of fluid passing through it. As the fluid slows down, the static pressure increases. This is also termed as pressure recovery. These are used in rocket exhaust systems to propel the vehicle forward; Bernoulli's principle is used for the calculations at low-velocity flows where friction is usually neglected. A typical subsonic diffuser profile is a duct that increases in area. This helps in decreasing the fluid velocity and rise the static pressure.

The data presented in Charles et al. [2] show the performance of typical subsonic diffuser and various design methodologies as well as an attempt by Yusha and Filkin

K. Mittal · G. Saravana Kumar (✉)
Department of Engineering Design, IIT Madras, Chennai, India
e-mail: gsaravana@iitm.ac.in

K. Mittal
e-mail: ed16b043@smail.iitm.ac.in

K. Arul Prakash · S. Vengadesan
Department of Applied Mechanics, IIT Madras, Chennai, India

S. Jayanti
Department of Chemical Engineering, IIT Madras, Chennai, India

to design short diffusers for heat exchangers [7]. The design methodology varies with the kind of diffuser being made and its use. For example, an attempt to improve the performance of S-shaped diffuser was made by Reichert and Wendt [5] using vortex generators. Another study done by Mayer [3] to design highly curved, light and short diffuser for fighter aircraft.

The paper presents design of a compact diffuser for heat exchanger which has much better heat exchange to weight ratio and could be easily manufactured via 3D printing. The model of diffuser was tested with CFD simulation which helps to understand the velocity patterns and pressure gradient. A sensitivity analysis was conducted based on the identified input parameters and performance parameters. Gradient-based optimisation was applied to find the optimal set of values for the parameters in order to get the best performance. A direct optimisation approach, namely Box complex method, was also used to search for the optima.

2 Design of Diffuser

The schematic of the optimum design framework employed in this work is described in Fig. 1. The proposed design concept consists of placing baffles as frustum with aerofoil cross-section inside a diffuser flow path. The diffuser model along with the geometric parameters of the four rows of baffles in the flow direction (left to right) is shown in Fig. 2. The aerofoil sections shown in the cross-section revolve about the axis of the diffuser to form the frustums of baffles. Three of the sections form frustums, whilst one forms a teardrop-shaped body. Aerofoil is the cross-sectional shape of a wing or a blade of a turbine or propeller rotor. This turning of the air in the vicinity of the aerofoil creates curved streamlines, resulting in higher pressure on one side and lower pressure on the other. Using Bernoulli’s principle, it is easy to see

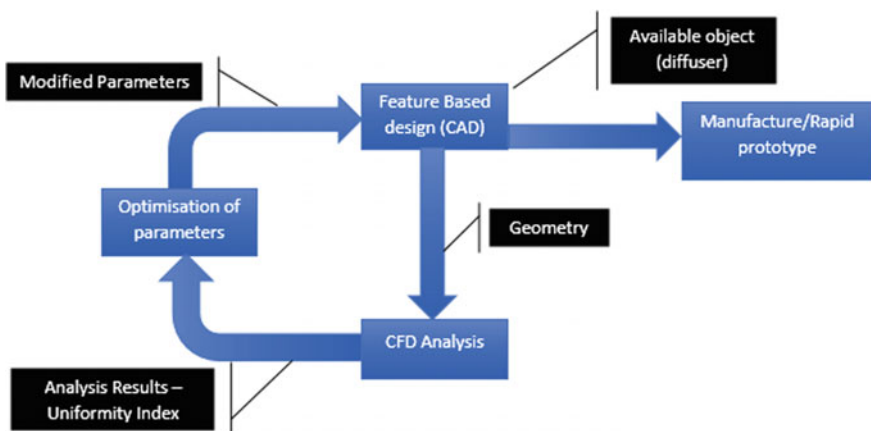


Fig. 1 Design and optimisation framework

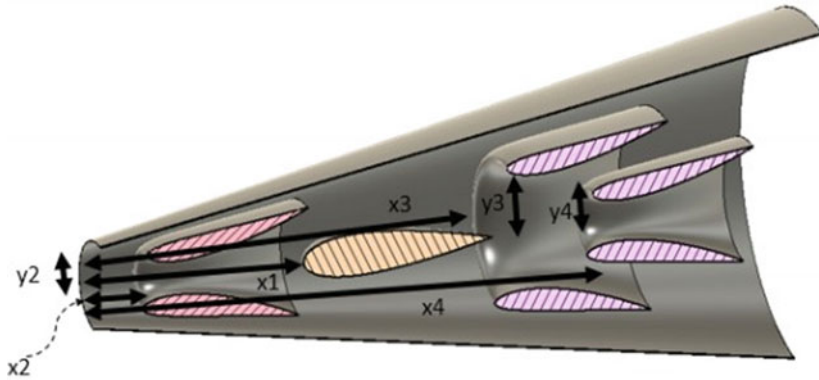


Fig. 2 Parametric geometric model of the diffuser (side section)

that this pressure difference is followed by a velocity difference, so the resulting flow field about the aerofoil has a higher average velocity on the upper surface than on the lower surface. Thus, using aerofoil-shaped baffles have the potential to improve flow uniformity with good pressure recovery when used in a diffuser.

In order to parameterize the design, seven parameters were used to define the diffuser geometry as shown in Fig. 2. These include the axial position of baffles and their respective radii. One of the geometry is in the form of a droplet for which no radius of revolution is required. The CFD analysis was done with ANSYS® software, and the design was optimised. Two important performance parameters that could be chosen for the optimisation are pressure rise and uniformity index. The uniformity index represents how a field variable varies over a surface. The uniformity index can be weighted by area or mass. The area-weighted uniformity index γ_a of a specified field variable is calculated using the following equation [1]:

$$\gamma_a = 1 - \frac{\sum_{i=1}^n [(|\phi_a - \bar{\phi}_a|) A_i]}{2|\bar{\phi}_a| \sum_{i=1}^n A_i}$$

where i is the facet index of a surface with n facets and $\bar{\phi}_a$ is the average value of the field variable over the surface:

$$\bar{\phi}_a = \frac{\sum_{i=1}^n \phi_i A_i}{\sum_{i=1}^n A_i}$$

For an inviscid flow, the standard deviation is 0, and uniformity index is 1. In this work, we aim at design of diffuser so that the performance is as close to this ideal situation as possible with maximum pressure increase across the diffuser.

3 CFD Analysis of Diffuser

The length of the diffuser has to be reduced for compact design. For the application considered, initially, plain diffusers with lengths 2400 mm and 4800 mm were designed for benchmark purpose. The CFD simulations were made with ANSYS Fluent®. $k-\omega$ sst turbulence model was used for all the simulations. The material of all the walls is chosen as aluminium and all the fluids to be air. All the walls exposed to the surroundings are assumed to be adiabatic. COUPLED scheme is used for the solution as the generated mesh has a high skewness. The CFD mesh for each case was optimised to give converged solutions. The elements consist of tetrahedral elements with around 630,000 nodes and 3,500,000 elements. The inlet and outlet has been extended to resolve the reverse flow. The convergence residual is kept at 10^{-5} for k , ω , continuity and 10^{-6} for energy. The results for benchmark simulation for lengths 2400 mm and 4800 mm are shown in Figs. 3 and 4. The performance

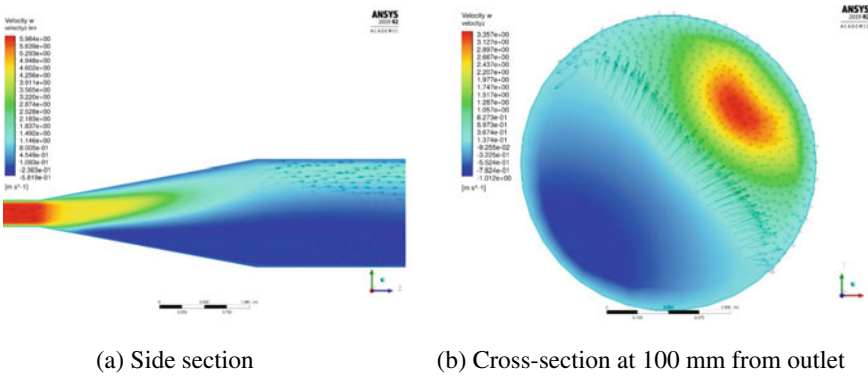


Fig. 3 Velocity profile for 2400-mm-length diffuser model

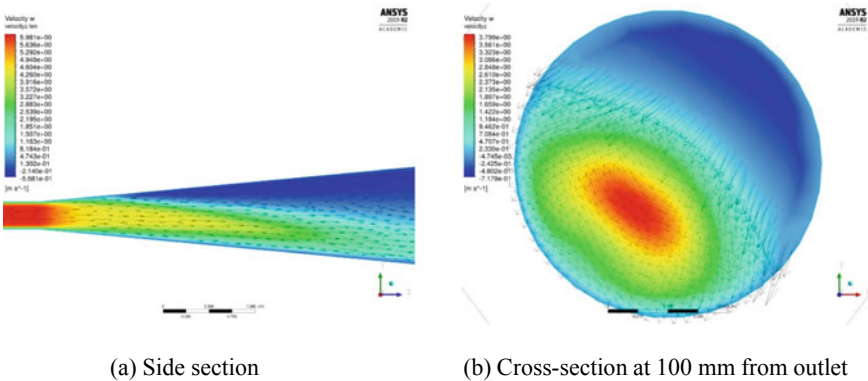


Fig. 4 Velocity profile for 4800-mm-length diffuser model

Table 1 Results for benchmark models and best optimised design

Length (mm)	Uniformity index	Pressure increase (Pa)	Ideal pressure recovery (Pa)
2400	-0.26	9.96	18.45
4800	0.18	12.79	18.45
2400	0.25	11.5	18.45

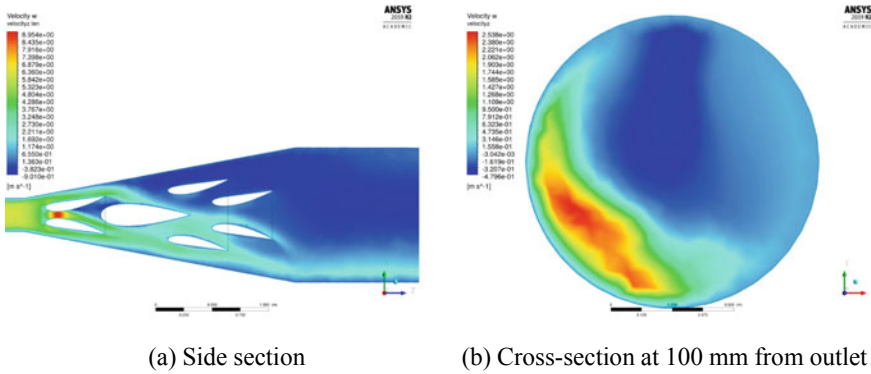


Fig. 5 Velocity profile for 2400-mm-length diffuser model with aerofoil baffles

indices, namely uniformity index and pressure rise for these designs, are given in Table 1. The 4800-mm-length diffuser gives very good results, but this dimension is not compact. Thus, to reduce the length and improve compactness, various baffle geometries were conceptualised in the flow path for a length of 2400 mm so as to improve the performance parameters and compare with the results of 4800-mm-length diffuser. Figure 5 lists all CFD simulation results for the diffuser with aerofoil baffle geometry.

4 Sensitivity Analysis and Optimisation

The baffle positions as described in Fig. 2 are the design variables, and design sensitivity and optimisation is performed by varying them with the constraints imposed by the diffuser section at each location, and this imposes variable limits as described in Table 2. In the present study, results obtained in the CFD analysis are used as input to numerically study the sensitivity, and optimisation of geometric parameters of diffuser was initially tried using traditional gradient-based technique [4]. The objective of optimisation was to maximise flow uniformity. The design sensitivity and Jacobian was evaluated by perturbing the design vector, X (7 variables corresponding to the geometric positions of the baffle) with respect the current design vector using $\pm X = 20$ mm one parameter at a time, thus creating 14 CFD models and computing

Table 2 Design variable limits (all units in mm)

Parameter	x1	x2	y2	x3	y3	x4	y4
Min	850	250	70	800	170	1350	150
Max	1900	1000	290	1550	390	2100	490
Mean taken	1000	400	120	1500	250	1900	150

the flow uniformity. The pressure recovery (increase) is also computed. Standard gradient descent algorithm was used with a step length of 0.008. The optimisation iterations converged in two iterations for the chosen objective. The design points after each iteration are listed in Table 3, and the flow uniformity and pressure increase for the solutions are shown in Fig. 6.

Since the convergence is quick, the solution could be a local optima, and a second approach was attempted to solve this optimisation problem. A direct optimisation strategy more commonly known as Box complex method [6] was used. The results obtained up to eleven iterations of this method are indicated in Fig. 7 and Fig. 8. Since each iteration of this algorithm takes in $2 * (n = \text{no. of variables})$, i.e. 14 points as an argument, Fig. 7 indicates how those 14 points converge for each iteration of this algorithm. A local optimum is indicated when all 14 points movement reduces so that

Table 3 Design points generated after two iterations of gradient-based descent method

S. No	x1	x2	y2	x3	y3	x4	y4
1	1	0.4	0.12	1.5	0.25	1.9	0.15
2	0.9768	0.4141	0.0902	1.5009	0.2426	1.8908	0.1407
3	0.9764	0.4140	0.0909	1.5009	0.2434	1.8912	0.1406

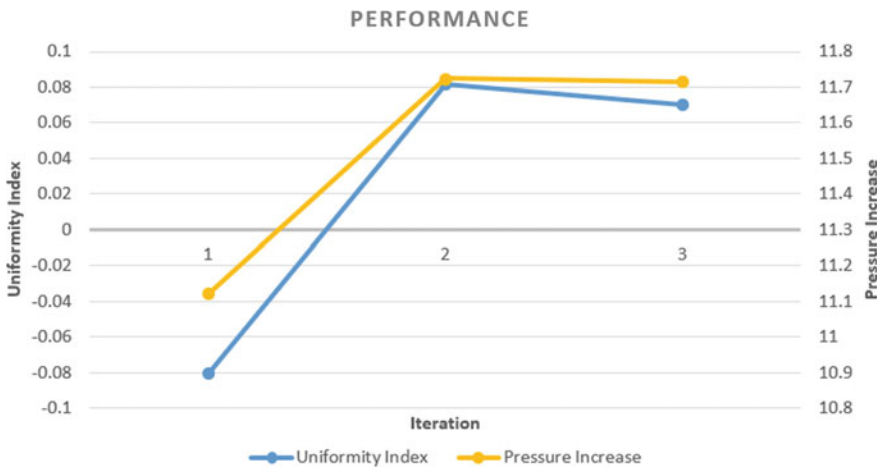


Fig. 6 Results of optimisation using gradient descent method

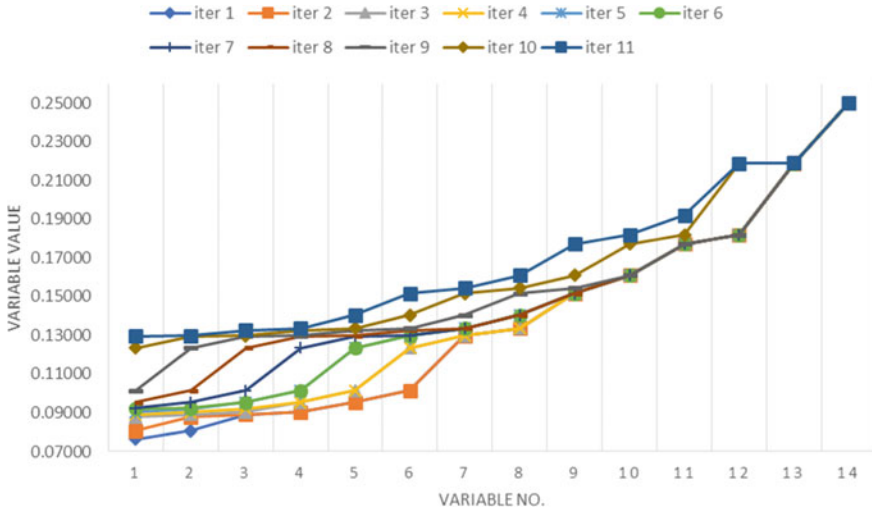


Fig. 7 Graph showing trend lines for different iterations of Box complex method



Fig. 8 Performance corresponding to centroid and worst point of the Box complex for different iterations

they are very close to each other indicating a local optimum value at that position. Figure 8 indicates the trend of the average performance and the worst performance over different iterations. Clearly, these figures indicate that the search is moving towards the optimum value. However, it is noted that the best value in each iteration remains the same. This indicates that the Box complex is not converged yet, and

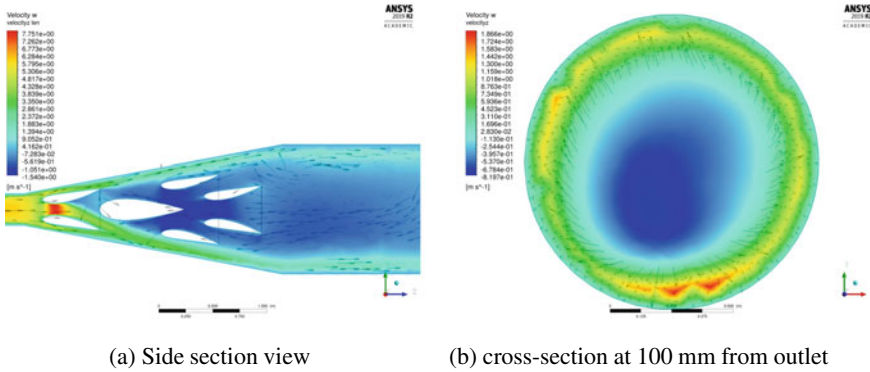


Fig. 9 Velocity profile for Box complex model optimisation

more iterations are required. The best point has a uniformity index = 0.25 (25%) and pressure rise = 11.5

Pa. comparing these results to that of the benchmark given in Table 1, these numbers are encouraging. The CFD results for this optima are shown in Fig. 9.

5 Conclusion

A concept of compact diffuser is presented with aerofoil baffle geometry. Initial results with CFD simulations showed that they result in better performance in terms of flow uniformity at outlet and pressure recovery as compared to plain diffuser twice the length. In order to further optimise the performance, a design optimisation framework was implemented using CFD simulation-driven numerical optimisation techniques. The Box complex method showed promising results.

References

1. ANSYS Fluent Theory Guide (2013)
2. Charles C, Wilbur SW, Henry JR, Wood (1956) Summary of subsonic-diffuser data. In NACA research memorandum, number 19930090284. National Advisory Committee For Aeronautics, Washington
3. Mayer D, Anderson B, Johnson T (1998 Jul) 3d subsonic diffuser design and analysis. In 34th AIAA/ASME/SAE/ASEE joint propulsion conference and exhibit. American Institute of Aeronautics and Astronautics
4. Meena R, Kumar GS, Shasrabudhe D (2006) Feature based modelling, analysis and design of axial fan impeller. In Proceedings of international conference on global manufacturing and innovation, Coimbatore, India, 07
5. Reichert BA, Wendt BJ (1996) Improving curved subsonic diffuser performance with vortex generators. AIAA J 34(1):65–72

6. Srinivasan K, Balamurugan V, Jayanti S (2016) Shape optimization of flow split ducting elements using an improved box complex method. *Eng Optim* 49(2):199–215
7. Yusha VL, Filkin NYu, Shipunova AA (2014) Theoretical analysis of short diffusers implementation efficiency in compact heat exchangers. In 2014 Dynamics of systems, mechanisms and machines (dynamics), pp 1–4

Thermal Frequency Stability Test for Multiple ICs



Merlyn Kuriakose and A. N. Aryadevi

1 Introduction

Frequency characteristics of sine wave references depend on the operating environment. Deviations in frequency can occur due to variations in circuit parameters, supply voltages, stray capacitances, output load, etc. Temperature and component aging also cause frequency drift. Frequency stability plays a very important role in applications like communication systems, radar, positioning, navigation, and timing systems. Frequency stability measurements provide very useful information for characterization of such systems.

Thermal characterization of ICs is carried out as part of qualification tests for high reliability applications such as satellites and launch vehicle applications [1]. This involves evaluating the ICs at different ambient temperatures. Temperature stability tests are one of the most time-consuming among other electrical tests. To reduce final product realization time, there is a need to improve throughput by some means without compromising on the quality of the tests.

This paper deals with the thermal frequency stability measurement and analysis for a fixed amplitude sine wave reference IC. The IC output frequency is programmable from 800 Hz to 10 KHz using two external high temperature stability capacitors C1 and C2. The IC output frequency is calculated as

$$f = \frac{10^{-5}}{\sqrt{C1 \times C2}} \quad (1)$$

M. Kuriakose · A. N. Aryadevi (✉)
VSSC, Thiruvananthapuram, India
e-mail: an_aryadevi@vssc.gov.in

M. Kuriakose
e-mail: k_merlynkuriakose@vssc.gov.in

$C1$ and $C2$ are selected to be 2 nF so that output frequency is 5 KHz nominal. The frequency stability is directly related to the stability of the capacitors; therefore, stable capacitors like NPO ceramic, polycarbonate, or polypropylene film should be used. CCR capacitor was used for the experimental setup. CCR ceramic capacitors have temperature compensating characteristics, and the temperature coefficient of the capacitor dielectric is within 30 ppm/°C over temperature range of -55 °C to +125 °C.

The IC is used for exciting a capacitive sensor whose output is used for a highly reliable liquid level sensing circuit. The IC has a frequency drift specification of 30 ppm/°C over temperature. The specifications are valid for the temperature range of -55 °C to +125 °C. Since we are using 30 ppm CCR ceramic type capacitor, we will get 20–30 ppm stability over specified temperature range.

2 Experimental Setup

The experimental test setup for thermal stability measurement of this IC is shown in Fig 1. It consists of a test PCB with socketed ICs fitted with connectors. The connectors provide means to connect individual outputs of each of the socketed IC to a relay switching card.

The test printed circuit board (PCB) also has provision for providing power to individual ICs and relay card using an external DC power supply. The relay card is controlled using a digital IO (input output) card inserted into a PC. Individual relays can be opened or closed on receiving command from PC. The relay switching card connects the individual IC outputs to a 6.5-digit digital multimeter (DMM) or frequency counter. The general purpose interface bus (GPIB) interface is used to control the DC power supply and DMM/frequency counter through the PC. Presently, the checkout uses an LXI-based equipment for implementing the switching relay part.

A program is written in LabVIEW [2] software to control the whole test sequence. Before start of program, the test PCB is placed in the oven and given time to stabilize for about 15 min after set temperature is reached.

Initially, oven temperature is set to the lowest operating temperature specified. DC power supply is switched on and relays are closed one by one. Individual output frequencies are noted for all ICs in sequential order. Next, the above procedure is repeated with oven set to highest operating temperature. The frequency stability is then calculated from the measurements as

$$\text{Frequency stability in ppm} = \frac{\text{Frequency}(-55\text{ }^{\circ}\text{C}) - \text{Frequency}(125\text{ }^{\circ}\text{C})}{\text{Frequency}(-55\text{ }^{\circ}\text{C}) \times 180} \times 10^6 \quad (2)$$

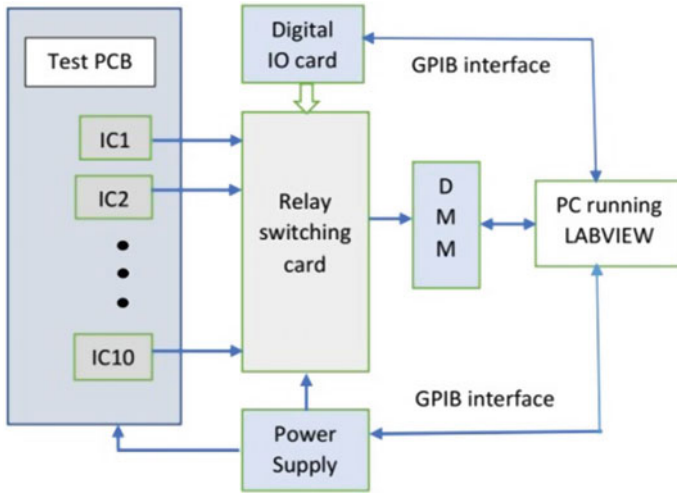


Fig. 1 Block diagram of test setup for measurement of thermal frequency stability

Table 1 Temperature stability test results for experimental setup

S. No.	Frequency at $-55\text{ }^{\circ}\text{C}$ (KHz)	Frequency at $-125\text{ }^{\circ}\text{C}$ (KHz)	Frequency stability (ppm/ $^{\circ}\text{C}$)
IC1	4.5328	4.5088	-29
IC2	4.5298	4.5067	-28
IC3	4.5099	4.4915	-22
IC4	4.5162	4.4939	-27
IC5	4.5107	4.4884	-27
IC6	4.5105	4.4877	-28
IC7	4.5217	4.4985	-28
IC8	4.5262	4.5034	-27
IC9	4.5070	4.4847	-27
IC10	4.5193	4.4992	-24

3 Results

The described system was used to measure frequency at temperatures of $-55\text{ }^{\circ}\text{C}$ and $+125\text{ }^{\circ}\text{C}$. Devices under test (DUT) are placed into the oven at $-55\text{ }^{\circ}\text{C}$ ambient, and LabVIEW program is used to measure the output frequency sequentially for 10 devices. Data is also logged in the PC. Oven temperature is then changed to $+125\text{ }^{\circ}\text{C}$, and the output frequency of each of the 10 ICs is measured at this temperature. Frequency stability was calculated as per equation (2), and the test results (Table 1) are found to be within 30 ppm/ $^{\circ}\text{C}$ over temperature.

4 Conclusion

In this paper, a PC-based automated test system is described which enables thermal frequency stability measurements for multiple ICs at the same time. A traditional checkout for the same IC would require about 8 h for measurements at different temperatures. The checkout as described in Figure 1 would require about 8 h for 10 ICs improving throughput by 10 times. Also, PC-based checkout ensures the test is done with least amount of human error once the initial setup is ready. The test results are also logged into the PC without any manual intervention.

References

1. MIL-PRF-55310D performance specifications. <https://nepp.nasa.gov/DocUploads/1F3275A6-9140-4C0C-864542DBF16EB1CC>
2. LABVIEW Core 1 Course manual, National Instruments

Synthesis and Fatigue Life Optimization of a Spring-Less Compliant Robot Leg Design



Rohan Vijay Khataavkar and Ajay Pandit Bhattu

1 Introduction

Legged mobile robots are advantageous over wheeled mobile robots in applications such as search and rescue during fires or earthquakes [1]. This is because the mobility of legged robots is more robust to varying tough terrains (encountered during search and rescue) than wheeled robots [2].

Many state-of-the-art legged robots have legs built with springs along with rigid links like in [3, 4] or rigid links with parallel hydraulic actuators like in [5–7]. Though such leg designs mimic the kinematics, elastics, and dynamics of animal locomotion, they generally make the leg assembly complex and expensive.

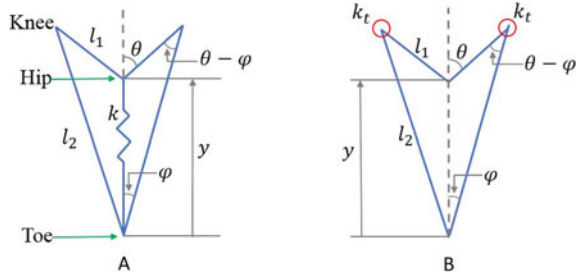
On the other hand, if compliant mechanisms are used to build legs, their inherent kinematic, elastic, and dynamic behavior may be exploited to mimic animal legs and simplify the leg assembly along with its control strategies. Moreover, compliant mechanism-based leg designs have previously been used in meso-scale-legged robots [8–10]. Further, [11], which uses such a design in a macro-scale-legged robot, provides only a single degree of freedom which limits the implementation of multiple gaits in the robot. Therefore, compliant mechanism based robot legs with multiple degrees of freedom need to be explored more.

In summary, the simplified leg assembly due to a compliant mechanism-based leg design in macro-scale-legged robots may, in turn, reduce the legs' weight, cost, and effort and time for replacement in critical situations. Thus, we report a two degree of freedom compliant mechanism-based robot leg design in the following sections.

R. V. Khataavkar (✉) · A. P. Bhattu
College of Engineering Pune, Pune, India
e-mail: khataavkarrv19.mech@coep.ac.in

A. P. Bhattu
e-mail: apb.mech@coep.ac.in

Fig. 1 **a** Leg design by Kenneally and Koditschek; **b** Torsional spring-loaded linkage equivalent to (a)



2 Methodology

2.1 Selection of the Linkage to be Converted into Compliant

As there are many spring-loaded rigid robot legs designs reported in robotics literature, it is reasonable to convert one of them into a compliant mechanism. This is because such a design could make the implementation of well-developed legged robot locomotion principles easier. Thus, the following designs reported earlier were considered.

In series elastic actuator-based leg designs like [3], all the actuating motors are placed at the hip, and the knee joint is actuated using chain drives to reduce the leg inertia. Strategies to eliminate the chain drive would have led to reduced actuated degrees of freedom making the control algorithm complicated, and thus, other similar designs were not considered. Parallel linkages on the other hand are actuated only at the hip by two motors. Hence, the coil spring-loaded symmetric five bar rigid robot leg design in [12] shown in Fig. 1a was found to be suitable for conversion into a compliant linkage. The linkage has a zero-length fixed link with two coaxial motors at the hip.

The referred rigid leg geometry, topology, and its stiffness have been optimized in [13] to maximize the transduction of battery energy to body energy during stance, minimize the collision losses upon toe touchdown, and maximize the storage and harvest of prior body energy in spring during stance. The optimization led to $k = 1565\text{N/m}$ on assuming $l_1 = 0.1\text{m}$, $l_2 = 0.2\text{m}$ and mass supported by the leg $M = 1.85\text{kg}$. Thus, the compliant linkage must not deviate from the original geometry or the overall leg stiffness, i.e., the compliant linkage must be kinematically and dynamically equivalent to the rigid linkage.

2.2 Synthesis of the Compliant Linkage

The pseudo-rigid body model of a compliant linkage consists of rigid links with revolute joints and a torsion spring at the rigid joints. Thus, the coil spring-loaded

rigid linkage was converted to a rigid linkage with torsion springs at the two knee joints as in Fig. 1b. To preserve the leg kinematics, the link lengths l_1 and l_2 were maintained the same. The torsional spring stiffness to preserve dynamic equivalence was determined as follows. Refer Fig. 1b.

$$l_2 \sin \varphi = l_1 \sin \theta \tag{1}$$

$$l_2 \cos \varphi - y = l_1 \cos \theta \tag{2}$$

The knee joint angle $\theta - \varphi$ in terms of the vertical coordinate y and link lengths

$$\begin{aligned} \theta - \varphi = \cot^{-1} & \left(\frac{-l_1^2 + l_2^2 - y^2}{\sqrt{-l_1^4 - (l_2^2 - y^2)^2 + 2l_1^2(l_2^2 + y^2)}} \right) \\ -\cot^{-1} & \left(\frac{-l_1^2 + l_2^2 + y^2}{\sqrt{-l_1^4 - (l_2^2 - y^2)^2 + 2l_1^2(l_2^2 + y^2)}} \right) \end{aligned} \tag{3}$$

Assuming horizontal position of the links of length l_1 corresponds to rest angle of the torsional springs at $y = y_0 = 0.17\text{m}$, the knee joint torque

$$T = k(y - y_0)l_1 \sin \theta \tag{4}$$

The knee joint torque in terms of y and link lengths

$$T = \frac{k}{2} \sqrt{-l_1^4 - (l_2^2 - y^2)^2 + 2l_1^2(l_2^2 + y^2)} \tag{5}$$

Knee joint torque (parameterized by y) v knee joint angular deflection from rest angle (parameterized by y) was plotted and observed to be fairly linear in Fig. 2. As y_0 corresponds to torsional spring rest angle, the plot was linearized at $y_0 = 0.1732\text{m}$ (red dot) to determine the required torsional stiffness $k_t = 7.826\text{Nm/rad}$.

The torsional spring-loaded rigid linkage was converted into four possible compliant linkages with the pseudo-rigid body method from [14]:

- compliant linkage with a small length flexure (SLF) along the link of length l_1 at the knee (variation A, Fig. 3a) or
- compliant linkage with a small length flexure (SLF) along the link of length l_2 at the knee (variation B, Fig. 3b) or
- compliant linkage with a slender beam (distributed compliance) along the link of length l_1 (variation C, Fig. 3c) or
- compliant linkage with a slender beam (distributed compliance) along the link of length l_2 (variation C, Fig. 3d) or

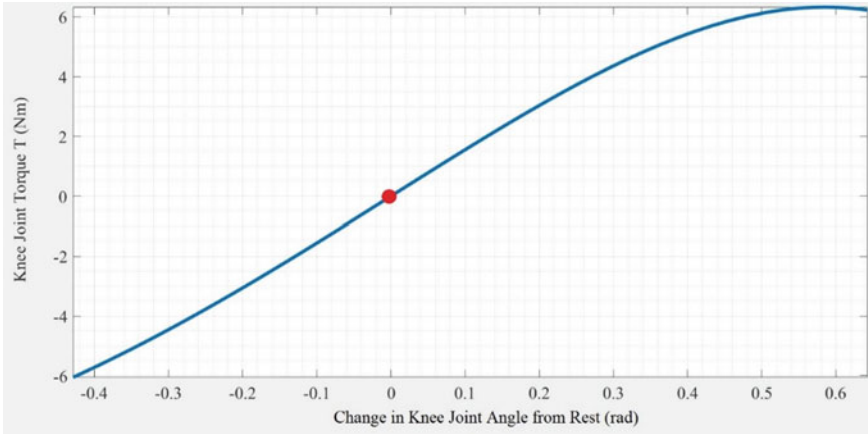


Fig. 2 Desired knee joint torque vs angular deflection

Fig. 3 a, b, c, and d Four compliant linkage variations synthesized based on the rigid linkage using pseudo-rigid body method

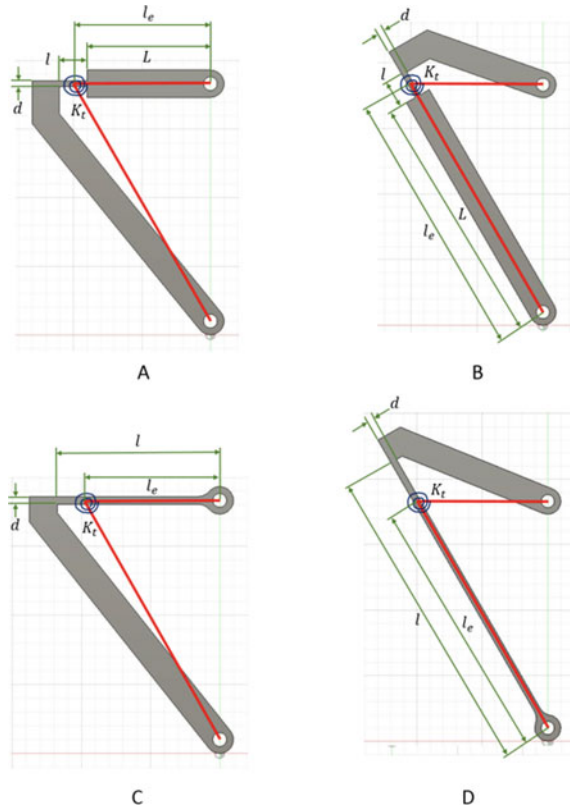


Table 1 Pseudo-rigid body method-based dimensions of the four variations

Variation	l	I	d
A	$l = 20\text{mm}, L = l_e - \frac{l}{2}$	$I = \frac{K_t l}{E}$	$d = \sqrt[3]{\frac{12I}{b}}$
B	$l = 20\text{mm}, L = l_e - \frac{l}{2}$	$I = \frac{K_t l}{E}$	$d = \sqrt[3]{\frac{12I}{b}}$
C	$l = \frac{l_e}{0.85}$	$I = \frac{K_t l}{2.25E}$	$d = \sqrt[3]{\frac{12I}{b}}$
D	$l = \frac{l_e}{0.85}$	$I = \frac{K_t l}{2.25E}$	$d = \sqrt[3]{\frac{12I}{b}}$

ABS ($E = 2.28\text{MPa}$) was assumed as the build material. l_1 and l_2 for all the four compliant linkage variations were the same as the spring-loaded rigid linkages. The depth (into the paper) b in Fig. 3 was assumed to be 10 mm for all the variations. The length of the small length flexures in variations A and B was assumed to be 20 mm. The lengths of the slender regions equivalent to the torsional spring-loaded rigid links were determined using pseudo-rigid body models in [14]. (Refer Table 1 and Fig. 3) The moment of inertia I of the slender regions of the variations was determined for obtaining the required stiffness k_t . Further, the thickness d of the slender regions in Fig. 3 for the variations was determined.

The four variations were numerically evaluated for their kinematic and dynamic equivalence with the rigid linkage using finite element method. The kinematic equivalence was verified by comparing the knee joint trajectory of the rigid linkage with that of the location corresponding to the pseudo-knee joint in the compliant linkage when the hip was vertically loaded, and toe was grounded. (Fig. 4 shows the compliant leg motion). The stiffness between the hip and the toe joint of the compliant linkage was compared with the stiffness of the coil spring for the dynamic equivalence.

3 Results

The numerical evaluation of the kinematic equivalence in Fig. 5a revealed that the four variations were lying within a maximum of -3% deviation from the rigid linkage. The dynamic equivalence evaluation in Fig. 5b revealed that the compliant variation D deviated the least (19.43% maximum) from the rigid linkage. Further, its fatigue life was optimized by maximizing the cross-sectional area a in Eq. (7) of the compliant link constrained by maintaining a constant area moment of inertia I in Eq. (8) and minimum thickness possible in FDM in Eq. (9). Fatigue life was determined using [15]:

$$\text{Stress Amplitude} = 164.28 \times (\text{Cycles to Failure})^{-0.199} \tag{6}$$

Maximize

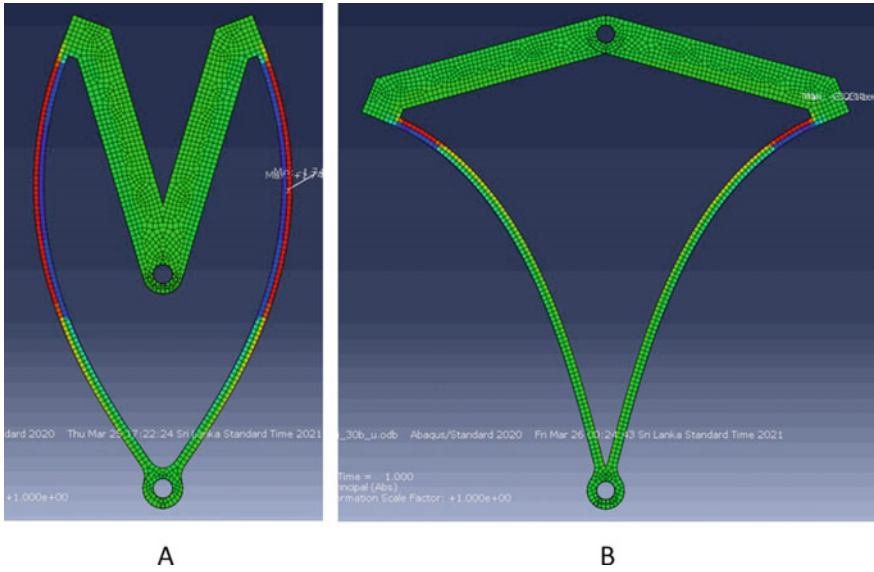


Fig. 4 Dynamic simulation of variation D

$$a = b \times d \tag{7}$$

Subjected to

$$I = \frac{bd^3}{12} = 304.8 \text{ mm}^4 \tag{8}$$

$$d \geq 5 \text{ mm} \tag{9}$$

This optimization resulted in 6x improvement (initial $b = 10\text{mm}$) in fatigue life at $b = 30\text{mm}$ as observed from Table 2. The optimization affected the kinematic equivalence negligibly as observed in Fig. 6a. The optimization of fatigue life also led to an improved dynamic equivalence with the maximum stiffness deviation reducing from 19.43% to 12.69% as observed in Fig. 6b

4 Conclusion

Two revolute joints and the coil spring in the rigid linkage were eliminated to simplify the assembly by using a 3-bar compliant structure. This structure’s dynamic and kinematic equivalence to the rigid linkage implies simpler implementation of the control strategies developed for the rigid-legged robot in the compliant-legged robot. The deviations in the kinematics and dynamics of the compliant linkage from the

Fig. 5 **a** Comparison of kinematic equivalence of the four compliant linkage variations with the rigid linkage; **b** Comparison of dynamic equivalence

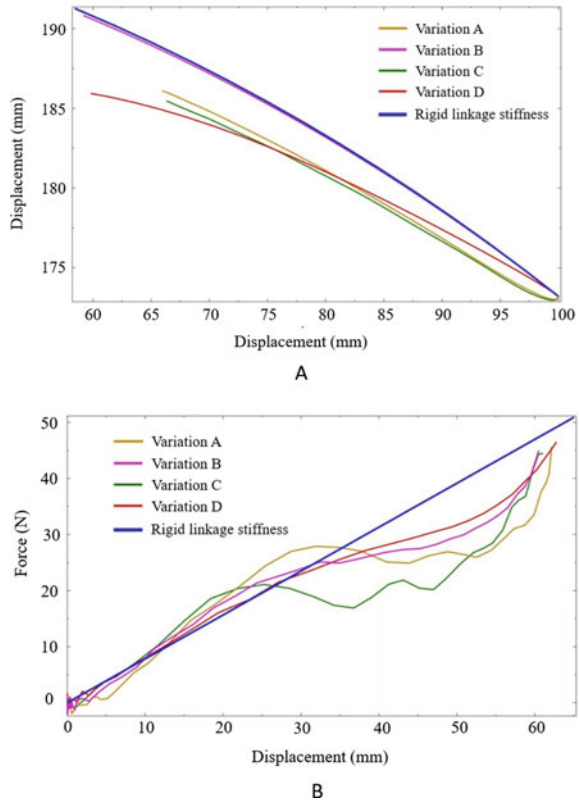
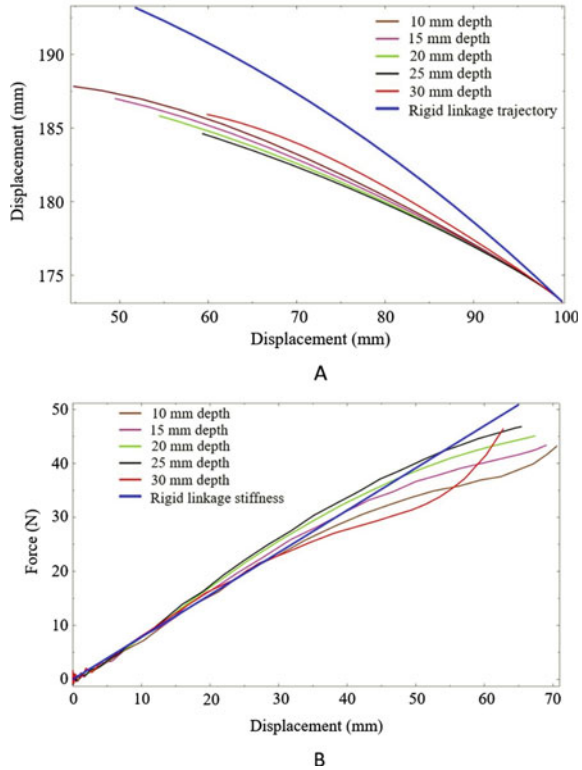


Table 2 Effect of increasing the depth of the compliant variation D

Depth (<i>b</i>) (mm)	Max stress (MPa)	Min stress (MPa)	Stress amplitude (MPa)	Life (cycles)
10	32.92	-34.49	33.705	2862
15	29.91	-21.91	25.91	10,733
20	31.64	-19.59	25.615	11,369
25	32.02	-17.41	24.715	13,607
30	31.11	-15.56	23.335	18,162

spring-loaded rigid linkage were lower when the longer link was made compliant (variations B and D) instead of the shorter link (variations A and C). This is because the longer link undergoes a smaller rotation during the full range of motion of the linkage, and the deviation of pseudo-rigid body models increases with increasing deflection. The stress amplitude was also minimum in this case. This is because it is subjected to a larger axial force than normal force. Further, fatigue life optimization led to a 6x increase in the fatigue life of the compliant linkage.

Fig. 6 a Effect of increasing depth of the compliant variation D on its kinematic equivalence with rigid linkage; **b** Effect on dynamic equivalence



References

1. Bellicoso CD et al (2018) Advances in real-world applications for legged robots. *J Field Robot* 35(8):1311–1326. <https://doi.org/10.1002/ROB.21839>
2. Rubio F, Valero F, Llopis-Albert C (2019) A review of mobile robots: concepts, methods, theoretical framework, and applications. *Int J Adv Robot Syst* 16(2). <https://doi.org/10.1177/1729881419839596>
3. Hutter M, Remy CD, Hoepflinger MA, Siegwart R ScarLETH: design and control of a planar running robot. *IEEE international conference on intelligent robots and systems*, pp 562–567. <https://doi.org/10.1109/IROS.2011.6048146>
4. Masia L et al (2018) Oncilla robot: a versatile open-source quadruped research robot with compliant pantograph legs. *Frontiers in Robotics and AI*, vol 1, p 67. www.frontiersin.org. <https://doi.org/10.3389/frobt.2018.00067>
5. Semini C, Tsagarakis NG, Vanderborght B, Yang Y, Caldwell DG (2008) HyQ—hydraulically actuated quadruped robot: Hopping leg prototype. In *Proceedings of the 2nd Biennial IEEE/RAS-EMBS international conference on biomedical robotics and biomechanics, BioRob 2008*, pp 593–599. <https://doi.org/10.1109/BIOROB.2008.4762913>
6. Semini C et al (2017) Design of the hydraulically actuated, torque-controlled quadruped robot HyQ2Max. *IEEE/ASME Trans Mechatron* 22(2):635–646. <https://doi.org/10.1109/TMECH.2016.2616284>
7. Products|Boston Dynamics. <https://www.bostondynamics.com/products>. Accessed 24 Jan 2022

8. Jung GP, Choi HC, Cho KJ (2017) The effect of leg compliance in multi-directional jumping of a flea-inspired mechanism. *Bioinspir Biomim* 12(2):026006. <https://doi.org/10.1088/1748-3190/AA575A>
9. Zhou X, Bi S (2012) A survey of bio-inspired compliant legged robot designs. *Bioinspir Biomim* 7(4):041001. <https://doi.org/10.1088/1748-3182/7/4/041001>
10. Hoffman KL, Wood RJ (2011) Passive undulatory gaits enhance walking in a myriapod millirobot. In 2011 IEEE/RSJ international conference on intelligent robots and systems, pp 1479–1486. <https://doi.org/10.1109/IROS.2011.6094700>
11. Saranli U, Buehler M, Koditschek DE (2001) RHex: a simple and highly mobile hexapod robot. *Int J Robot Res* 20(7):616–631. <https://doi.org/10.1177/02783640122067570>
12. Kenneally G, Koditschek DE Kinematic leg design in an electromechanical robot. kodlab.seas.upenn.edu
13. Kenneally G, Koditschek DE (2015) Leg design for energy management in an electromechanical robot. In: IEEE/RSJ international conference on intelligent robots and systems (IROS), vol 2015-December, pp 5712–5718. <https://doi.org/10.1109/IROS.2015.7354188>
14. Howell LL, Magleby SP, Olsen BM (2013) Handbook of compliant mechanisms. *Handb Compliant Mech*. <https://doi.org/10.1002/9781118516485>
15. Domingo-Espin M, Travieso-Rodriguez JA, Jerez-Mesa R, Lluma-Fuentes J (2018) Fatigue performance of ABS specimens obtained by fused filament fabrication. *Materials* 11(12):2521. <https://doi.org/10.3390/MA11122521>

Differential Evolutionary (DE) Method for Strut Performance Design and Optimization Using Machine Learning-Based Meta-Models Prediction



Balasubramanian Shanmugam, Arun Shanthkumar Bhaire, Sritharan Gopal, and Fan Li

1 Introduction

A typical automotive chassis suspension system, strut, plays a vital role to absorb and transfer the road loads of various vehicle event profiles. Suspension strut design and optimization is a key element for the ride and handling of vehicle performance based on the required stiffness and strength. As shown in Fig. 1, McPherson type of suspension strut use to be mounted on wheel knuckle with orientation based on the vehicle architecture packaging. During vehicle development, vehicles use to undergo multi-body dynamic road load profiles/events like full throttle, braking and bump road, etc.

Due to the orientation of strut as well as various road load events, strut is designed to withstand vertical and lateral load transfer path to the interface chassis structure. The overall performance design of the strut is to transfer the road load for the desired stiffness and strength without exceeding the allowable plastic strain and permanent deformation. In order to account for the orientation of strut and load path from various multi-body dynamic events, strut design highly depends on geometric/configurational parameters and the material grade used for the same. One of the mass-effective design solutions involves optimizing geometric parameters with the material grade for the range of road load in vertical as well as from lateral direction. Optimization of such a strut needs to satisfy the performance requirement of stiffness under linear load and nonlinear load case strength requirements. This paper proposes an ML-based meta-model for quick prediction of strut design performance parameters directly for the range of geometric/configuration parameters and road

B. Shanmugam (✉) · A. S. Bhaire · S. Gopal
Tata Consultancy Services, Bangalore, India
e-mail: balasubramanian.shunmugam@gm.com

F. Li
General Motors LLC, Detroit, USA

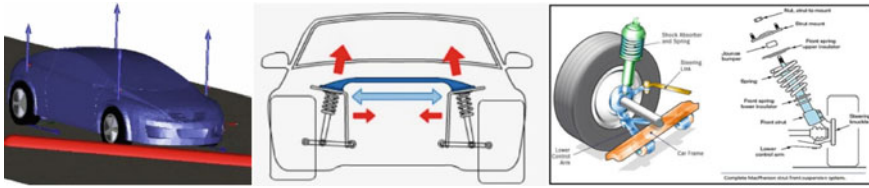


Fig. 1 A typical McPherson strut of automotive chassis suspension system

loads obtained from the DOE study. To arrive at an optimized design parameter with the desired material grade of the strut, a differential evolutionary method [1] is used to arrive at a minimum mass configuration abiding the same performance requirement targets of stiffness and strength.

2 Differential Evolutionary (DE) Algorithm

Evolutionary algorithms (EA) of nature-inspired metaheuristics approach are gaining a lot of interest in computational intelligence methods [2] and are very useful for global optimization problems which have been used in multiple applications [3]. Differential evolution algorithm is based on population-based evolutionary computation technique [4] that works with a population of vectors or solutions similar to genetic algorithm [5] and particle swarm optimization as shown in Fig. 2. Each vector is perturbed by adding the difference of two randomly chosen vectors from the population. DE algorithm works on three types of vectors like target, mutant, and trial vector.

Target vectors are being perturbed. A mutant vector is generated by adding the weighted difference between two randomly chosen vectors to a third vector from the population. The trial vector is generated by mixing the variables of the target vector and mutant vector.

For each target vector $x_i^{(t)}$, a mutant vector $v_i^{(t+1)}$ is generated as shown in Fig. 3,

$$v_i^{(t+1)} = x_{r_1}^t + F * (x_{r_2}^{(t)} - x_{r_3}^{(t)})$$

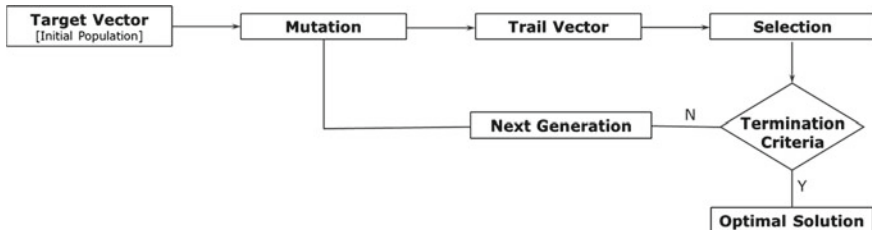


Fig. 2 Flowchart of differential evolutionary algorithm

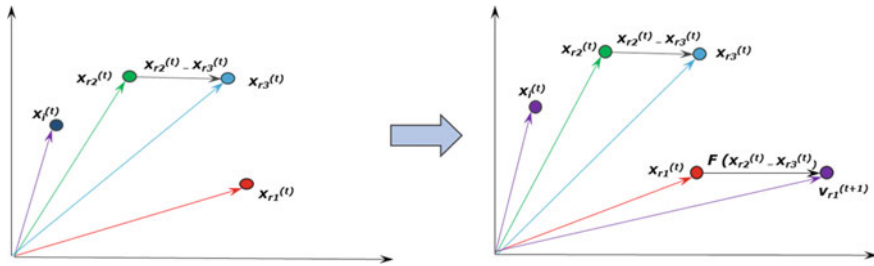


Fig. 3 Graphical illustration of mutation

where $r_1 \neq r_2 \neq r_3$ are randomly chosen vectors from the current population. F = User defined function.

2.1 Trial Vector Using Crossover

The purpose of creating a trial vector is for the diversity of solutions. This new vector has to be created using a crossover rate or probability of crossover.

A trail vector $u_i^{(t+1)}$ is generated as shown in Fig. 4,

$$u_{i,j}^{(t+1)} = \begin{cases} v_i^{(t+1)} & \text{if } (\text{rand_no} \leq p_c) \text{ or } j = \text{rnbr}(i) \\ x_{ij}^{(t)} & \text{if } (\text{rand no} > p_c) \text{ or } j \neq \text{rnbr}(i) \end{cases}$$

where $j \in 1, 2, \dots, n$, rand_no = random number $\in [0, 1]$, p_c : crossover rate/probability of crossover.

Using this differential evolutionary method [6], optimum strut design is arrived at using machine learning-based meta-models of stiffness and strength with a single

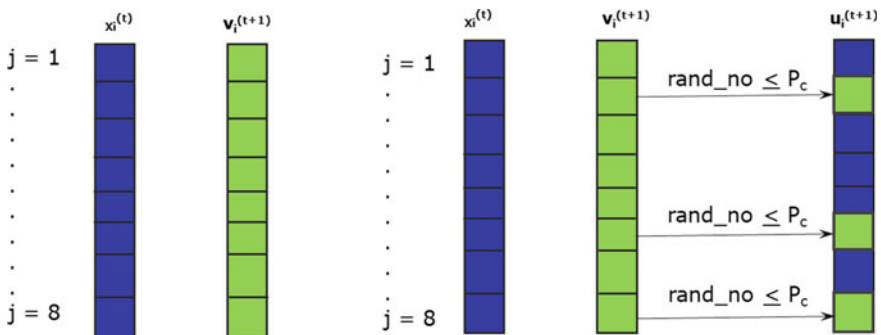


Fig. 4 Graphical illustration of trial vector

objective optimization problem formulation. Selection of optimal solution is arrived at based on termination criteria with respect to a number of population generations. Greedy selection criteria are applied over the number of generations to arrive the global optimum solution. This will ensure that the trailing vector can be replaced with the target vector based on the fitness value for the next population generation. The canonical differential evolution uses a greedy criterion for selecting one vector that to be included in the population.

$$x_i^{(t+1)} = \begin{cases} u_i^{(t+1)} & \text{if } F(u_i^{(t+1)}) < F(x_i^t) \text{ for minimization problem} \\ x_i^{(t)} & \text{Otherwise} \end{cases}$$

3 Problem Definition/Formulation and Methodology

The current design of the strut was able to meet the performances requirement of linear stiffness and nonlinear strength load cases through independent analysis but this iterative design of arriving at the performance target is not optimized and it involves a considerable time for the designer. The first step of this method is to generate strut DOE designs using strength to an orthogonal array with the range of geometrical parameters, material grade, and vertical and lateral loads. Using DOE design points of stiffness and strength responses analysis outcome, an ML-based meta-model is created using supervised regression algorithms (plastic strain and permanent deformation) which are used to arrive at correlations among the design variables. This direct way of predicting performance responses is obtained using meta-model-based prediction with respect to the design variables ranges of DOE design points. A prediction error (normalized mean absolute error) of 5–10% from the meta-model with 95% prediction interval which is in line with the actual values of stiffness and strength as shown in Fig. 5,

ML-based meta-model predictions are used to arrive at the desired performances targets through feature importance among the design variables from quick design synthesis.

3.1 Constraints Handling Technique—Penalty Function Method

When differential evolution techniques [7] are used to handle constraint optimum solution out of which few are feasible and infeasible regions on design space as shown in Fig. 6. If the solution violates any constraints, the solution is penalized by adding a penalty to the objective function. This will convert the constraint problem to an unconstraint problem by the penalty function.

Fig. 5 ML meta-model prediction error for stiffness and strength

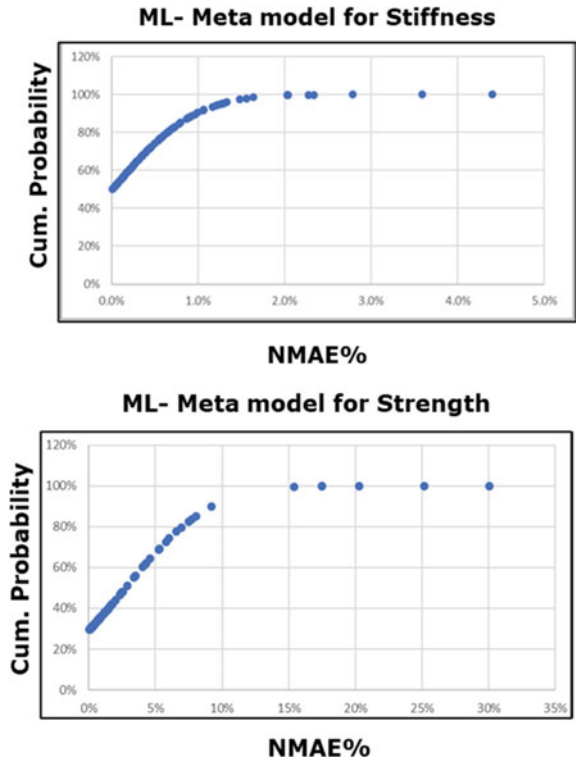
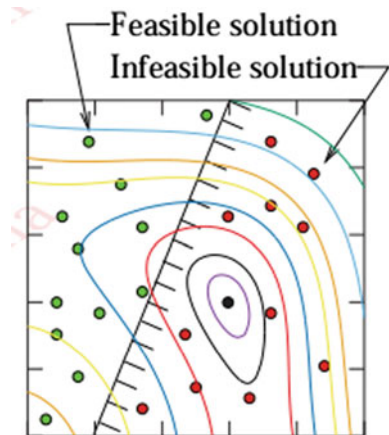


Fig. 6 Typical solutions of objective function on design space with constraints



3.2 Constraint Optimization Problem

In order to obtain the optimized strut design, a single objective of minimum mass with the constraints of desired performance targets is framed using an external penalty function to penalize infeasible points. A constraint optimization problem of single objective strut design is formulated as below,

Minimize $f(x) \rightarrow$ Mass of Sturt

Inequality Constraints :

Subject to:

$$g_j(x) \geq 0, \rightarrow \text{Stiffness} \geq \text{Target} - 1,$$

$$\text{Strength, PSET/PEEQ} \leq \text{Target} - 2$$

$$x_i^L < x_i \leq x_i^{(U)} \rightarrow \text{Design Space/Variables range}$$

The penalty function method is used to combine objective function and inequality constraints with static penalty parameters [6] as below,

$$P(x, R) = f(x) + \sum_{j=1}^J \left(R_j (g_j(x))^\beta \right)$$

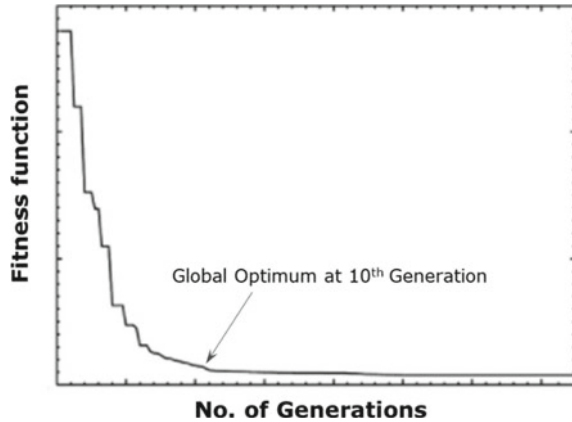
where R_j is the unique static penalty parameters for inequality constraints of stiffness and strength $g_j(x)$. $\beta = 1$.

A unique value of static penalty parameters has to be obtained to differentiate feasible and infeasible solutions and to avoid penalty function distortion as well as artificial local optimal solutions. In order to obtain an optimized design configuration of the strut with minimum mass, the differential evolutionary stochastic algorithm is used. This single objective optimization of the minimum mass of the strut design with the constraints of desired performance targets is framed using an external penalty function to obtain feasible optimum solutions. Optimum strut design configuration variables and grade of material for the given load are obtained from trail vector as a reverse prediction based on fitness values obtained using the greedy selection strategy with the best trail vectors from the intervals of population generations.

4 Results

It is shown in this paper that performance for the McPherson strut can be predicted with 90–95% accuracy using the machine learning-based meta-model. Differential evolution method of optimization is done on this meta-model for arriving at optimum strut design parameters to meet the desired performance. Best fitness of trial vector

Fig. 7 Convergence history of DE algorithm



over generations using greedy selection strategy [6] resulted in faster convergence of strut design configuration variables within 10 generations as shown in Fig. 7.

Using DOE design points within the range of strut configuration variables, material grades, and the stiffness and strength performance (due to road loads acting on the component) the problem is framed as a single objective optimization of minimum mass. Penalty function approach is used to take the constraints (stiffness and strength performance) into account. Typical strut optimization executed using the developed method is shown to result in 25% of reduction in mass. By combining machine learning-based meta-models for linear and nonlinear performance prediction, along with DE-based optimization on the surface, overall strut design synthesis is expediated significantly compared to the conventional and intuitive designs.

References

1. Sreedhar D, Rajan BM (2013) Differential evolution based multi objective optimization-a review. *Int J Comput Appl* (0975–8887) 63(15)
2. Karaboğa D, Ökdem S, (2004) A simple and global optimization algorithm for engineering problems: differential evolution algorithm, *Turk J Elec Eng* 12(1)
3. da Cunha CB (2000) Practical aspects of the application of vehicle routing models to real world problems. *Transportes* 8(2):1–23
4. Yang XS (2010) *Nature-inspired metaheuristic algorithms*, Luniver Press
5. Sharma D, IIT Guwahati. Evolutionary computation for single and multi-objective optimization
6. Zang H, Zhang S, Hapeshi K (2010) A review of nature-inspired algorithms. *J Bionic Eng* 7:S232–S237
7. Mezura-Montes E, Velázquez-Reyes J, Coello Coello CA (2006) A comparative study of differential evolution variants for global optimization. In: Genetic and evolutionary computation conference, GECCO 2006, proceedings, Seattle, Washington, USA